Review

Analytical methods for brain targeted delivery system in vivo: Perspectives on imaging modalities and microdialysis

Xingguo Zhang[a,b], Lin Liu[b], XiangYi Zhang[b], Kuifen Ma[b], Yuefeng Rao[b], Qingwei Zhao[b], Fanzhu Li[a,*]

[a] College of Pharmaceutical Science, Zhejiang Chinese Medical University, Hangzhou 310053, China
[b] The First Affiliated Hospital, College of Medicine, Zhejiang University, Hangzhou 310003, China

ARTICLE INFO

ABSTRACT

Since the introduction of microdialysis in 1974, the semi-invasive analytical method has grown exponentially. Microdialysis is one of the most potential analysis technologies of pharmacological drug delivery to the brain. In recent decades, analysis of chemicals targeting the brain has led to many improvements. It seems likely that fluorescence imaging was limited to ex vivo and in vitro applications with the exception of several intravital microscopy and photographic imaging approaches. X-ray computed tomography (CT), magnetic resonance imaging (MRI), and positron emission tomography (PET) have been commonly utilized for visualization of distribution and therapeutic effects of drugs. The efficient analytical methods for studies of brain-targeting delivery system is a major challenge in detecting the disposition as well as the variances of the factors that regulate the substances delivery into the brain. In this review, we highlight some of the ongoing trends in imaging modalities and the most recent developments in the field of microdialysis of live animals and present insights into exploiting brain disease for therapeutic and diagnostics purpose.

© 2011 Published by Elsevier B.V.

Contents

* Corresponding author. Tel.: +86 571 86633030; fax: +86 571 86633030.
  E-mail address: lifanzhu@zjtcm.net (F. Li).

1. Introduction

The advancement of pharmacological drug delivery to the brain has been constrained due to the existence of protective barriers which restricts the passage of foreign particles into the brain. The design of non-invasive brain delivery systems, such as nanoparticles [1], can facilitate controlled and targeted drug delivery to the specific regions of the brain become crucial to drug development and delivery for the neurological diseases. Once nanomaterials are enhanced with drug-carrying and transport capabilities, in vivo imaging markers, such as fluorescent dyes for optical imaging, and mini-invasive techniques, such as microdialysis for neurochemical and drugs measurements in brain, are the next landmarks to achieve.

In recent decades, analysis of chemicals targeting the brain has led to many improvements in our understanding. Making such analysis is fraught with difficulties related to complex and delicate tissues, requirements for stable measurements with high selectivity, temporal resolution, spatial resolution, and difficult interpretations of data. While progress has been made in such analysis, the techniques used to measure these chemicals are still limited in their ability to measure accurately the rapid and heterogeneous changes that occur in the special space of the brain [2]. Therefore, an efficient analytical method for studies of brain-targeting delivery systems is a major challenge in detecting the disposition as well as the variances of the factors that regulate the substances delivered into the brain.

Beyond improvements in overall image quality and spatial resolution, imaging modalities have been entrusted with the challenge of capturing dynamic processes involving various biological system components as well as their respective interactions. For example, the ability to resolve and monitor the transmigration ability of various types of bimolecular across the blood–brain barrier (BBB) in vivo is a daunting challenge. Initially, fluorescence imaging was limited to ex vivo and in vitro applications with the exception of several intravital microscopies and photographic imaging approaches [3–5]. Although helpful in some cases, these methods fall short to the potential of more recent trans-illumination and tomography techniques that allow non-invasive fluorescence images in vivo [6]. Over the last three decades, X-ray computed tomography (CT), magnetic resonance imaging (MRI), and positron emission tomography (PET) have been commonly utilized for visualization of distribution and therapeutic effects of drugs. These techniques are powerful when they are co-registered with precise in vivo anatomical views of the brain provided by MRI or X-ray CT. However, high costs, low sensitivity, and/or low spatial resolution associated with the existing well accepted clinical imaging modalities promoted the search for new approaches for in vivo visualization of brain-targeting nanocarriers, such as methods based on highly sensitive and specific optical contrast. Enormous potential lie ahead with the recent advances of high resolution optoacoustic molecular imaging approaches, such as multispectral optoacoustic tomography (MSOT) [7]. All of these are expected to facilitate the development of novel imaging-based diagnostic and therapeutic nanoprobes for early diagnosis and therapy of various disorders of the brain following systematic administration.

Another effective technology for studies of brain targeted delivery is microdialysis. Microdialysis emerged from the neurosciences where it was originally used for measuring concentrations of neurotransmitters in rat brain (1974). It became one of the most important and promising sampling techniques for the determination of tissue composition and pharmacokinetics. This is mostly due to its vital characteristics in for instance, continuous sampling in the same individual and area with minimal tissue perturbation, which has obvious advantages over homogenization. As there is no biological fluid loss, the technique can be applied in almost every tissue and individual, including small animals and neonates. Only the unbound fraction of the drug is collected, rendering extensive sample preparation unnecessary and eliminating the enzyme degradation processes. In pharmacokinetic studies this is especially important as the microdialysis only provides the pharmacologically active fraction of the drug [8]. Therefore, microdialysis (MD) has become an integral part of the modern biological and pharmaceutical discovery process, especially in pre-clinical small-animal-based research.

In this review, we highlight some of the ongoing trends in imaging modalities and the most recent developments in the field of microdialysis of live animals. We also present insights into exploiting brain diseases for therapeutic and diagnostics purposes.

2. Structures and function of the blood–brain barrier

The BBB is a separation of circulating blood and cerebrospinal fluid (CSF) in the central nervous system (CNS). Treatment of central diseases such as brain tumors, encephalic infectious disease, is a daunting challenge due to the unique environment of the CNS [9]. Protecting the brain from most substances, the BBB acts as a protective shield which supplies brain tissue with nutrients and filters harmful compounds back to the bloodstream [10]. Traditional drug delivery to the brain has been constrained due the existence of the protective BBB which restricts the passage of foreign substances into the brain. Therefore, the efficient design of non-invasive drug delivery systems that can facilitate controlled and targeted delivery to specific regions of the CNS is a major challenge in pharmaceutical science [11–13].

The BBB is constituted by cerebral microvascular endothelium and regulates the transport of solutes and other substances including drugs in and out of the brain. It maintains the homeostasis of the brain microenvironment, which is crucial for neuronal activity and proper functioning of the CNS [14]. The transport of solutes and other substances across the BBB is strictly constrained through both physical tight junctions (TJs) and adherents junctions (AJs), hence metabolic barriers exclude very small, electrically neutral and lipid soluble molecules. Thus, conventional pharmacological drugs or chemotherapeutic agents are unable to pass through the barrier [15].

TJs between endothelial cells of the BBB possess a complex of transmembrane proteins. They act as both a physiological and pharmacological barrier, thereby preventing influx of molecules from the bloodstream into the brain. The BBB is characterized by two membranes, namelyluminal and abluminal, facing blood capillary

and brain interstitial fluids (ISF), respectively [16]. With recent increasing pharmacological and toxicological studies and clinical trials, overcoming the brain drug delivery hurdle by special design are positioned to become a new generation of central pharmaceutical drugs for the treatment of human CNS disorders [17,18].

3. Different empirical methods for the assessment of brain targeted delivery in vivo

3.1. Homogenization

The benefit of homogenization is well known throughout the food and dairy sector. It provides a much more stable product, with a better shelf life, allows reduced use of additives, and helps manufacturers to fix the composition of products. Depending on the production conditions, it is possible to produce micro- as well as nanoparticulate systems without the use of organic solvents.

Liquid-based homogenization is the most widely used cell disruption technique for small volumes and sampling tissues. Several different types of homogenizers are in common use. A Dounce homogenizer consists of a round glass pestle that is manually driven into a glass tube. A Potter–Elvehjem homogenizer consists of a manually or mechanically driven polytetrafluoroethylene (PTFE) pestle shaped to fit a rounded or conical vessel. Both homogenizers can be obtained in a variety of sizes to accommodate a range of volumes. A French press consists of a piston that is used to apply high pressure to a sample volume of 40–250 mL, forcing it through a tiny hole in the press. Only two passes are required for efficient lyses due to the high pressures used with this process. Novel homogenization technologies have been proposed and developed, but most are designed for nanomaterial processing and industry producing [19,20]. However, the important defect of traditional detection methods was destructive, moved, and irreversible.

3.2. Imaging modalities

3.2.1. Traditional imaging modalities: microscope (fluorescence imaging); X-ray; CT

Several improvements in microscopy techniques have been invented in the 20th century and have resulted in increased resolution and contrast to some extent. The light radiation is non-ionizing, and therefore reasonable doses can be repeatedly employed without harm to the animal or patient. However, they did not overcome the diffraction limit. When a user wants to perform more than one assay on the same cells or tissue, multiple expensive fluorescent probes and filter sets are required. However, the overlapping fluorescence spectrum of many probes precludes the use of multiple dyes in routine use. Fluorescence imaging of biological samples using tunable filter systems helps the pathologist overcome the challenge of using multiple dyes for greater efficiency without sacrificing accuracy. CT or computed axial tomography (CAT) scanning uses a series of X-rays of the head taken from many different directions. Typically used for quickly viewing brain injuries, CT scanning uses a computer program that performs a numerical integral calculation (the inverse Radon transform) on the measured X-ray series to estimate how much of an X-ray beam is absorbed in a small volume of the brain. Typically the information is presented as cross sections of the brain. X-ray and CT technologies are also widely used in the life science.

3.2.2. Present imaging modalities: PET, MRI, diffuse optical tomography (DOT), fluorescence-mediated molecular tomography (FMT)

Microscope, X-ray and CT have been commonly utilized for visualization of distribution and therapeutic effects of drugs. However, with the limits of low sensitivity and low spatial resolution, exploring new approaches for in vivo visualization of brain targeted delivery is important to achieve.

Quantitative PET technology provides in vivo measurements of dynamic physiological and biochemical processes in the human body. It is non-invasive and has excellent sensitivity and specificity, which enables visualization of biodistribution of positron emitter-labeled compounds. A limitation of PET is an inability to provide precise anatomic localization due to relatively poor spatial resolution when compared to magnetic resonance imaging. Manual placement of region-of-interest is commonly used in clinical and research settings in analysis of PET datasets. However, this approach is operator dependent and time-consuming [21].

Magnetic resonance imaging (MRI or MR scanning) was developed by researchers including Peter Mansfield and Paul Lauterbur, who were awarded the Nobel Prize for Physiology or Medicine in 2003. In the early 1980s, MRI was introduced clinically, and during the 1980s a veritable explosion of technical refinements and diagnostic MRI applications took place. Scientists soon learned that the large blood flow changes measured by PET could also be imaged by the correct type of MRI. Functional magnetic resonance imaging (fMRI) was born. Since the 1990s, fMRI has come to dominate the brain mapping field due to its low invasiveness, lack of radiation exposure, and relatively wide availability.

Optical imaging techniques can be used in the field of molecular imaging to allow both visualization and quantification of molecular events associated with disease in a non-invasive and radiation-free manner using relatively simple equipment. Diffuse optical imaging (DOI) or diffuse optical tomography (DOT) is a medical imaging modality which uses near infrared light to generate images of the body. DOT is an emerging imaging modality for non-invasive brain functional mapping. The hemodynamic and metabolic images derived from optical properties are unique and complementary to those of MRI and PET. The technique measures the optical absorption of haemoglobin, and relies on the absorption spectrum of haemoglobin varying with its oxygenation status [22].

Fluorescence-mediated molecular tomography (FMT), a technique that can three-dimensionally image gene expression by resolving fluorescence activation in deep tissues, is a recent development in biomedical imaging. It is the non-invasive mapping of molecular events in intact tissues using fluorescence. Underpinning to this development is the discovery of bio-compatible, specific fluorescent probes and proteins and the development of highly sensitive imaging technologies for in vivo fluorescent detection. Of particular interest are fluorochromes that emit in the near infrared, a spectral window, whereas haemoglobin and water absorb minimally so as to allow photons to penetrate for several centimeters in tissue [23].

3.3. Microdialysis

3.3.1. Components and principle of MD

The MD system consists of a probe, a pump and vials in which the perfusate is collected. The system can be connected to an automated sampler/collector or to online (or even online bedside) analysis, and small, portable pumps for continuous use have been developed.

The probes act in a manner similar to a blood vessel, allowing substances to be removed or delivered to a specific site through diffusion with no net fluid loss. The probe containing a dialysis membrane with a specific molecular weight cutoff is implanted in the physiological region of interest. Small molecules in the extracellular fluid that are not present in the perfusate diffuse across the membrane based on their concentration gradient and are then transported to the analysis system. Likewise, compounds in the perfusate that are not present in the extracellular fluid can be delivered directly to the physiological site of interest. Cells and

macromolecules are excluded by the dialysis probe so centrifugation or protein precipitation steps are not required prior to analysis. Therefore, it is possible both to deliver and recover compounds from a single tissue site. This feature can be very useful for monitoring site-specific release of neurotransmitters, observing regional metabolism of neuropeptides [24,25], or comparing the metabolism of antineoplastic agents in tumor vs. healthy tissue [26].

The probes can be divided into four basic categories: the linear probe, the loop probe, the side-by-side probe and the concentric probe. In brain MD, a concentric cannula design is normally employed for neurochemical studies. The dialysis membrane is located at the end of the concentric cannula and is usually from 1 to 4 mm in length.

The probe is continuously perfused with a physiological fluid-the perfusate. This medium has to resemble the tissue in which the probe is placed. In brain MD the perfusate is most often an artificial cerebrospinal fluid or a Ringer solution. Depending on the lipophilicity of the drug, the perfusate medium may have to be modified to allow more lipophilic substances to enter the probe.

Calibration is necessary whenever the intention is quantitative MD. Since the MD probe is continuously perfused with fresh perfusate, a total equilibrium across the membrane cannot be established. Rather, a steady state rate of exchange across the MD membrane is rapidly reached. The ratio between the concentration in the dialysate and the concentration in the periprobe fluid is defined as the 'RR' and expressed in percentages:

$$RR = \frac{C_d}{C_e}$$

where C_d is the concentration of the dialysate and C_e is the concentration in the extracellular fluid [27]. The RR is influenced by many factors but is not affected by the periprobe concentration of the analyte, e.g. at steady state a fixed proportion of the extracellular analyte concentration (RR) is sampled by the probe. For a given compound, the transport (loss/recovery) across the membrane is theoretically symmetrical, although in practice this is not always the case due to the (predominantly lipophilic) substance of interest binding the probe material, or other artifactual situations [28].

3.3.2. Brain MD

In brain MD surgery, the animals (3 weeks to 12 weeks of age) are deeply anesthetized. The animal's head is shaved and positioned in a stereotaxic instrument with the head flat. The skull is exposed by a 2 cm coronal incision between the two ears along the interaural line using a pair of scissors and by reflecting the underlying muscle with a cotton tip [29].

Two small burr holes are created on both sides of the skull by sharp dental drill bits. In general, it is easier to locate the horizontal positions for the probe once the skull is exposed. The depth of the holes should be examined carefully, and will depend on the species, strain, and age of the animals, and need to be evaluated each time when different types of animals are used. After the complete probe insertion, the muscles and skin are sutured. Following the surgery, the animal is returned to its cage and housed individually; the animal is allowed to recover from the surgery for at least 16 h before MD.

The integrity of the BBB following probe implantation is also a factor for discussion. Studies conducted using autoradiography with 14C-AIB (which does not cross the BBB under normal conditions) as well as transport characteristics of hydrophilic and moderately lipophilic drugs (following IV injection) post surgery indicate that the BBB integrity is maintained overall [30,31]. However, other studies using Cr51-EDTA transport have shown a significant effect of probe implantation on BBB permeability [32].

The MD probe, which is constantly perfused with a physiological solution at a low flow rate of 1–10 μL min^{-1} is implanted into the tissue of interest, and substances in the interstitial space fluid pass the membrane by passive diffusion along their concentration gradient resulting in a certain concentration in the perfusion medium. This dialysate is collected at timed intervals and is subjected ex vivo to different types of chemical analyses, which can be performed either in an offline or online fashion, the former of which is the most common. For offline analysis, a specified volume of sample (usually 1–20 μL) is collected in vials or tubes for later analysis. The temporal resolution that can be obtained in these experiments is usually determined by the MD flow rate, analyte recovery, and the sensitivity of the analytical method. At the typical MD flow rate of 1 μL min^{-1}, most offline experiments have temporal resolutions from 5 to 10 min [33].

Online sample analysis offers several potential advantages over offline analysis. When MD is combined with separation-based analytical method, it provides immediate feedback on treatment effects. This allows near real time detection of analyte with subminute temporal resolution, and eliminates problems related to fluid transfer and storage, including sample mislabeling or losing. It avoids problems associated with the handling of small volume samples, since nanoliter scale samples have been commonly analyzed. It also reduces the exposure of dialysate to air aimed at avoiding degradation of some unstable substance such as 5-hydroxytryptamine (5-HT), malondialdehyde (MDA) [34,35]. Therefore, sample preparation and automated analysis are simplified. Analytical information is generated while the experiment is still being processed. An online system provides higher recovery and better reproducibility.

MD has several advantages for sampling biological tissues and fluids. The resulting samples are most commonly composed of an aqueous salt solution that contains only small molecular weight analytes. In addition, it is possible to continuously monitor substances in the extracellular fluid of the brain and other tissues for several months [36,37]. The animal can also serve as its own control. This latter advantage is particularly important for tissue distribution studies where the normal protocol is to sacrifice several animals at each time point to obtain enough data to make statistically valid conclusions. Another significant advantage of MD is that studies can be performed in awake, freely moving animals. This is especially important in studies that correlate brain drug concentration and/or neurotransmitters with behavior. Because of the small size and relatively non-invasive nature of the MD probes, it is also possible to put multiple probes in a single animal. It is therefore possible to measure blood, brain, and tissue concentrations of drugs or endogenous substances simultaneously. For long-term MD studies, careful consideration should be made regarding the tissue damage associated with probe implantation. Fibrosis or gliosis can occur after several days of probe implantation [38]. A comparative description of MD and imaging techniques for the assessment of in vivo tissue drug distribution was provided in Table 1, in order to address their advantages and limitations.

4. Application in brain targeted delivery in vivo

4.1. Homogenization

Numerous experiments were performed with traditional detection methods such as homogenized and analysis systems. The tissue samples were removed, washed, and weighed immediately, then were homogenized and diluted with saline for analysis by HPLC, UV–vis, etc. For example, HPLC assay methods were established for the determination of ibuprofen and prodrugs in preparations and in plasma or brain. The detector was set to monitor the signal at

Table 1
Comparison of MD and imaging techniques for the assessment of brain drug distribution.

Analysis method	Monitored compartment	Molecular/ functional contrast	Sensitivity to contrast agents	Spatial resolution	Invasiveness	Cost	Safety	Applicability
X-ray CT	Total tissue	Poor	μmol (10^{-6})	10–500 μm scalable	Non-invasive	Medium	Medium	Pre-clinical/clinical
PET	Total tissue	Good	fmol (10^{-14})	1–5 mm	Non-invasive	High	Medium	Pre-clinical/clinical
MRI	Total tissue	Medium	nmol (10^{-9})	30–500 μm scalable	Non-invasive	High	Good	Pre-clinical/clinical
FMT	Total tissue	Good	pmol (10^{-12})	1–2 mm	Non-invasive	Low	Good	Pre-clinical
MSOT	Total tissue	Good	pmol (10^{-12})	5–200 μm scalable	Non-invasive	Low	Good	Pre-clinical/clinical
MD	Extracellular fluid of tissue concentration	Good	nmol (10^{-9})	Focal sampling	Mini-invasive	Low	Medium	Pre-clinical/clinical

219 nm corresponding to the maximum absorbance for ibuprofen and its derivatives [39]. Solid lipid nanoparticulate delivery systems of cisplatin were estimated by UV–vis spectrophotometer at 210 nm. The in vivo result of formulated solid lipid nanoparticles of cisplatin reveals that the drug is preferentially targeting to liver followed by brain and lungs [40]. To investigate the possibility of targeting, an anti-Alzheimer's drug tacrine in the brain using polymeric nanoparticles was used. Rats were killed by decapitation and the tacrine concentrations in the brain, liver, lungs, spleen and kidneys were analyzed by HPLC. A higher concentration of the drug tacrine was observed with the nanoparticles in comparison to the free drug [41]. In the study to prepare temozolomide solid lipid nanoparticles (TMZ-SLNs), and to investigate the specific drug targeting of intravenous (i.v.) injected solid lipid nanoparticles of temozolomide, the HPLC assay show that the concentrations of the temozolomide in the brain and reticuloendothelial cells-containing organs was the highest among the selected organs [42]. In summary, all of the experiments demonstrate that homogenized and analytical systems exist far and wide because of ease of use and broad applicability. However, shortcomings such as increased sacrifice and expense require non-invasive techniques.

4.2. Traditional imaging modalities

4.2.1. Microscope (fluorescence imaging)

Imaging with light has unique advantages associated with simplicity, low-cost, and small size of the equipment. Tissue sections were observed under a fluorescence microscope while plasma and urine concentrations were measured. Fluorescence showed a high accumulation of canonized bovine serum albumin (CBSA) nanoparticles (CBSA-NPs) in the brain compared to that of bovine serum albumin NPs (BSA-NPs) and uncoated NPs supported by plasma and urine profile. The significant results proved that CBSA-NPs could be a promising brain drug delivery for sulpiride [43].

Optical contrast methods offer the potential to differentiate between soft tissues, due to their distinct light absorption spectra which are otherwise indistinguishable using other modalities. Investigators have begun to probe the role of individual surface arterioles in maintaining both the structure and function of cortical regions using vessel-specific clotting by in vivo photothrombosis after craniotomy in mice [44]. In vivo video monitoring through the window revealed that the rhodamine-labeled magnetic fluid-loaded liposomes accumulated in the mouse brain microvasculature exposed to the magnet-first within superficial brain venules and then within intracerebral venules-with no significant change in blood flow ($P > 0.05$) [45]. The research tried improving the specificity and efficiency of gene transfection in gene therapy and tried making the liposome a better gene transfer vector to the brain by use of the monoclonal antibody (anti-Lex/SSEA-1)-mediated targeting of liposomes. The expression was observed under a fluorescent microscope. The results proved that the targeting liposome P-MMA-DOSPER can permeate the ependyma and can transfer genes into the nerve stem cells in vivo safely and effectively [46].

During the last decade, a large number of commercially available fluorescent probes and markers are increasingly being offered, from non-specific fluorescent dyes and fluorescent proteins to targeted or activatable photoproteins and fluorogenic-substrate-sensitive fluorochromes to enable a highly potent field for biological imaging. So far, these contrast mechanisms were proven efficient in a number of clinical and small-animal applications, including probing of tissue hemodynamics [47,48], gene expression profiling [49], and detecting protease up-regulation associated with cancer growth and inflammation [50,51]. Since many of the probes are developed to fluoresce in the near-infrared (NIR) optical window, where optical absorption is very low so that light can penetrate deeply, fluorescence imaging has been successfully translated from a microscopy level to the brain of small animal imaging and clinics [52,53]. The combination of such probes with optical imaging may yield a unique, highly sensitive technology for in vivo and real-time imaging of the expression patterns for new drug delivery. A good example of fluorescent microscopy is tested the modified PE-PEG based micellar drug delivery system loaded with the antifungal drug AmB to evaluate the efficiency of AmB accumulating into the brain [54]. Leupold et al. developed a dipalmitoylated apolipoprotein E-derived peptide named P2A2 to mediate cellular uptake of potential micellar and liposomal carriers. Confocal laser scanning microscopy and fluorescence-activated cell sorting were used to get insight into the internalization mediated by carboxyfluoresceine-labeled P2fA2 and the all D amino acid analogue P2fa2 into brain capillary endothelial cells [55]. Mice were euthanized with sodium pentobarbital. Brains were embedded in optimum cutting temperature compound and 20 μm-thick coronal tissue sections were cut onto glass slides for immunofluorescent labeling. Slides were then coverslipped with gelvatol and imaged using confocal microscopy [56].

4.2.2. X-ray

Contrast-enhanced synchrotron stereotactic radiotherapy is a radiotherapy technique leading to a differential effect that significantly improves the treatment outcome [57]. For in vivo optical imaging, 20 mice were randomly divided into four groups and injected i.v., respectively. Imaging was performed after injection by In Vivo Imaging System equipped with IR820 filter sets with 1 min. X-ray exposure time. NIR fluorescence images and X-ray images were fused together. The significant in vivo results suggest that MC-PEI is a promising brain-targeting drug delivery system, especially for gene delivery [58]. For the present study the equipment consisted of a customized CT consisting of an open multifocus X-ray tube, an amorphous silicon flat panel detector,

and a computer-navigated-control (CNC) positioning system, all installed inside a lead insulated X-ray protection cabin [59]. Curcumin, a natural antioxidant, is known to inhibit beta amyloid and beta amyloid induced oxidative stress. Formulated nanoparticles containing curcumin (ApoE3-C-PBCA) to provide photostability enhance cell uptake of curcumin by targeting. The entrapment of curcumin inside the nanoparticles was confirmed by X-ray diffraction analysis [60]. Synchrotron stereotactic radiotherapy (SSRT) is a treatment that involves the targeting of high-Z elements into tumors followed by stereotactic irradiation with monochromatic X-rays from a synchrotron source, tuned at an optimal energy. The simulated geometry was an idealized phantom representing a human head. The authors investigated the dosimetric characteristics of SSRT for various contrast agents: iodine, gadolinium, and gold; and for different beam qualities: different X-ray beams from different accelerator [61]. Craparo et al. reported the synthesis and characterization of novel amphiphilic graft copolymers based on an alpha, beta-poly(N-2-hydroxyethyl)-D,L-aspartamide(PHEA) backbone and D,L-polylactic acid (PLA) hydrophobic side chains. Polymeric micelles from PHEA-ethylenediamine-PLA and PHEA-ethylenediamine-polysorbate 80-PLA copolymers were characterized in terms of mean size, zeta potential, critical aggregation concentration (CAC), and surface composition by X-ray photoelectron spectroscopy (XPS) analysis which as a potential drug carrier for brain targeting [62]. Another example, the poly(lactide)-D-alpha-tocopheryl polyethylene glycol succinate (PLA-TPGS) of the two-copolymer blend at various component ratio were characterized by laser light scattering (LLS) for particles' size and size distribution, zeta potential analyzer for surface charge, and XPS for surface chemistry [63].

4.2.3. CT

Over the last three decades, CT has been commonly utilized for visualization of distribution and therapeutic effects of drugs. CT has emerged as a major imaging modality for imaging pharmacokinetics and treatment monitoring, mainly based on indirect tracking of morphological changes. For instance, a bilateral subthalamic DBS procedure was conducted in two patients for idiopathic Parkinson's disease. The Medtronic O-arm (R) is used to perform 2D-imaging control (frontal and lateral) as well as quick (<30 s) 3D acquisition postoperative CT. This technology allowed checking the positioning of micro-macro electrodes and definite electrodes [64]. To study the effects of cranial irradiation, Armour et al. constructed an all-plastic mouse bed equipped with an immobilizing head holder. The bed integrates with in-house Small Animal Radiation Research Platform (SARRP) for precision focal irradiation experiments and cone-beam CT. They assessed the reproducibility of the head holder to determine the need for CT-based targeting in cranial irradiation studies [65]. Chan et al. [66] describe the development of a prototype neurosurgical robotic system called NISS. The aim is to implement a robotic system capable of achieving accurate registration of robotic coordinate systems based on CT images so that it can be used in clinical application. This system has been refined sufficiently for animal trial evaluation in stereotactic biopsy of brain lesions. The interpretation of the first brain CT scan in 117 patients is indicated for ordering scans and clinically significant brain abnormalities. Medical records of patients with brain CT scans with abnormalities were reviewed for 2 weeks after the scan for changes in medical management resulting from scan findings [67].

4.3. Present imaging modalities

4.3.1. Positron emission tomography (PET)

Imaging has made important contributions in brain drug targeting, particularly in areas of pharmacokinetics and in quantifying therapeutic response. Many advances were achieved recently in present imaging modalities such as PET and MRI. It is important to appreciate the complementary nature of the various imaging techniques, and the potential of multi-modal imaging strategies to greatly accelerate brain drug development.

PET is non-invasive, has excellent sensitivity and specificity, and enables visualization of biodistribution of positron emitter-labeled compounds. It has provided quantitative spatially resolved pharmacokinetic and pharmacodynamic measurements on a wide range of small molecule brain drugs in vivo [68]. Advanced PET techniques have been used to determine pharmacokinetics of brain drugs [69,70], pharmacodynamic response following anti-cancer therapy [71–73], and even in investigations of fetal brain pharmacokinetics following maternal drug administration [74]. Indeed, since its introduction in the late 1970s, PET has become a powerful imaging modality with the ability for highly sensitive detection of molecular tracers. It is currently utilized in diagnosis, therapy monitoring, and imaging gene expression using diverse reporter genes and probes. However, high costs and other complications associated with PET and SPECT equipment limit their applicability. Moreover, the images acquired by these techniques have poor spatial resolution and hence accurate identification of regions of uptake is difficult to achieve.

4.3.2. Magnetic resonance imaging (MRI)

With the distinct advantage of functional-imaging capabilities as well as better contrast among soft tissues, MRI has emerged as a tool in oncological imaging and imaging of the diseased nervous system [75]. For instance, MRI has played an important role in evaluating new CNS therapies, notably in multiple sclerosis [76], stroke [77], and brain tumors [78,79]. It is now routinely included to provide primary or secondary outcome measures in drug trials of these disease states [80]. MRI provides exceptional soft tissue contrast and sensitivity for focal disease detection which likely will improve with ultrahigh field MRI instruments [81].

Magnetic nanoparticles (MNPs) are of considerable interest as contrast agents for MRI and carriers for drug delivery [82]. Kuo-Chen et al. trapped magnetic nanoparticles with anti-cancer drugs to form therapeutic MNPs. The technique could be used in normal brains or in those with tumors and significantly increased the deposition of therapeutic MNPs in brains with intact or compromised blood–brain barriers. Synergistic targeting and image monitoring are powerful techniques for the delivery of macromolecular chemotherapeutic agents into the CNS under the guidance of MRI [83,84]. Superparamagnetic iron oxide NPs (SPIONs), paramagnetic contrast agent (gadolinium) or perfluorocarbons have already been established as major players in tracking single or clusters of labeled cells within target tissues [85]. Iron oxide nanoparticles were utilized as a drug delivery vehicle for minimally invasive, MRI-monitored magnetic targeting of brain tumors. Accumulation of iron oxide nanoparticles in gliosarcomas can be significantly enhanced by magnetic targeting and successfully quantified by MRI [86]. Nanostructured lipid carriers (NLCs) were prepared to investigate whether the duration of brain targeting and accumulation of drugs in the brain can be improved by intravenous delivery. NLCs were developed using cetyl palmitate as the lipid matrix, squalene as the cationic surfactant, and Pluronic F68, polysorbate 80 and polyethylene glycol as the interfacial additives. An anti-Parkinson's drug, apomorphine, was used as the model drug. The base form of apomorphine was successfully entrapped by NLCs with an entrapment percentage of >60% detected by MRI. The results indicated that NLCs with moderate additives are a promising controlled-release and drug-targeting system [87].

Quantitative MRI techniques such as relaxography and diffusion based measurements continue to advance and provide excellent sensitivity for detecting occult diseases. These techniques provide a

more complete assessment of total brain disease and will also benefit from improved signal-to-noise associated with higher magnetic field MRI instruments.

4.3.3. Diffuse optical tomography (DOT)

DOT has practical potential for human brain mapping, as well as in the diagnostic imaging of brain diseases. It differentiates physiologic and molecular signatures of both malignant and benign tissues, as they relate to the area of cancer research [88]. Much effort was done to optimize the number of sources and detectors as well as mesh size that can be used for image reconstruction in reflectance mode through a series of numerical simulations and tissue-like phantom experiments with both the absorption and scattering images. The system's ability to image a target with small size as well as with low contrast relative to the background medium was tested and quantitatively analyzed [89].

Near-infrared optical imaging is a newer imaging technique that, coupled with sensitive enzymatically specific fluorescent beacons, shows much promise for earlier detection of many cancers and their in situ characterization. On the basis of animal studies demonstrating visualization of micrometastasis-sized tumors in brain and the ability to evaluate therapeutic enzyme inhibition real-time, such imaging may be incorporated in the clinical imaging paradigm in the future, both to improve cancer screening as well as for monitoring therapy in individual patients [90].

4.3.4. Fluorescence-mediated molecular tomography (FMT)

This invention relates to a fluorescence-mediated molecular tomographic imaging system designed to detect near-infrared fluorescence activation in deep tissues [23]. The system can use targeted fluorescent molecular probes or highly sensitive fluorescence molecular probes. Such probes add molecular specificity and yield high fluorescence contrast, to allow early detection and molecular target assessment of diseased tissue, such as cancers, in vivo. The new tomographic imaging system enables three-dimensional localization in deep tissues and quantitation of molecular probes [91]. FMT systems were so far successfully used in molecular imaging studies of brain disease. In one of the studies [4], using near-infrared fluorescent molecular beacons and inversion techniques that take into account the diffuse nature of photon propagation in tissue, three-dimensional in vivo images of protease activity in orthopic gliomas were obtained. In another study, a versatile delivery module based on a myristoylated polyarginine backbone was prepared as an imaging probe. The result indicated that it could be used as potentially targeted therapeutics across the BBB of mouse brain using near-infrared fluorescence imaging [92]. Whole-body fluorescence tomography of small animals works optimally in the near-IR region where the lower tissue attenuation allows the penetration of photons over several centimeters [93,23], but provides low spatial resolution.

4.3.5. Others

With the development of new contrast agents for optoacoustic imaging applications, other imaging modalities including optoacoustic tomography (MSOT) microscopy/tomography, 3D light microscopy and gamma scintigraphy imaging have begun to be applied in drug delivery. Even though optoacoustic imaging methods like MSOT are in their infancy from both technical and application standpoints, it is a rapidly emerging field in the imaging sciences that can overcome major limitations of optical imaging while retaining its contrast and sensitivity advantages [94]. In fact, many widely adopted optical contrast agents, such as fluorochromes, can be readily used by applying MSOT [7]. In one study, gamma scintigraphy imaging of rat brain was performed to ascertain the localization of risperidone in brain following intranasal and intravenous administrations. Nanoemulsion containing risperidone (RSP) was prepared to accomplish the delivery of drug to the brain via the nose. The study indicated high effective and brain targeting of RSP among the prepared nanoemulsions [95]. Therefore, it is expected to drastically expand the capabilities of photonic imaging in the field of in vivo imaging of drug delivery markers.

4.4. Microdialysis

4.4.1. In neurotransmitter research

Measurement of the in vivo dynamics of neurotransmitters in the extracellular space of the CNS has been an important tool for studies. Brain MD is the only technique that permits sampling of brain interstitial fluid (ISF) in conscious animals as well as measuring the concentration of administered neuroactive substance in this compartment. It is also possible to measure the concentration of chemical messengers that change in response to the action of a neuroactive compound on its molecular target [96,97]. Ungerstedt and Pycock [173] initially started with investigating dopamine (DA) neurotransmission in rat brain. Subsequently, this neurotransmitter was the subject of various other studies. Recent investigations using DA measurements with MD in brain targeting include the studies of the ability of noradrenergic-targeting drugs to modulate DA release in medial prefrontal cortex (mPFC) and nucleus accumbens (NAc), with the aim of selectively increasing mesocortical DA [98], the combination of rotational behavior and MD for revealing the mechanisms of action on dopamine synapses induced by drugs administrated to lesioned rats [99] or the activity of dopaminergic in neostriatum and nucleus accumbens enhanced by intranasal administration of testosterone [100], progesterone [101].

In all neurotransmitter studies with MD including ACh, DA, 5-HT, noradrenaline (NA) and gamma aminobutyric acid (GABA), the issue of the validity of the obtained results has to be kept in mind [102]. The validity depends on many different factors such as the composition of the perfusate. An analyte-free perfusion fluid will lead to a large concentration gradient from extracellular space to perfusate. This general aspect is of high relevance especially in the case of neurotransmitter studies because they involve sampling from a limited volume. Thus, the MD procedure itself could lead to a change in the composition of the extracellular space by reducing the neurotransmitter around the dialysis membrane. This by itself might already lead to increased baseline neurotransmitter levels due to possible stimulation of neurotransmitter release. Additionally, although MD is able to detect substances directly in the tissue, in the case of neurotransmitters the area around the MD membrane is not the site of action. It reflects a compartment where the neurotransmitter diffuses after release from nerve terminals. Therefore, as the density of nerve terminals differs according to the brain area, absolute changes in different brain areas have to be corrected for basal dialysate concentrations as determined with previous MD experiments [103].

In order to determine whether the analytical signal in MD is the analyte of interest, a pharmacological validation can be applied. This approach was used by Sauvinet et al. for the validation of an analytical method for the determination of the neurotransmitters glutamate (Glu), aspartate (Asp) and GABA [104]. They administered either a GABA uptake inhibitor or a Glu/Asp uptake inhibitor by retrodialysis and compared the neurotransmitter release against a control with artificial CSF. They proved that each measured peak exhibiting the same migration time as the analytical reference standard corresponded to the neurotransmitter of interest. The same technique was applied by Benturquia et al. [105]. In order to verify a MD experiment it would be desirable to establish independent evidence in addition to MD results. Further research is necessary in the field of neurotransmitter experiments. Several examples for

Table 2
Reported in vivo dialysate concentrations of neurotransmitters as measured by microdialysis in rats unless otherwise noted.

Neurotransmitter	Brain region	Ref.
Glutamate, aminobutyric acid, glycine, aspartate, Taurine, L-serine, D-serine	Striatum	[106,107]
Dopamine	Nucleus accumbens, striatum	[108,109]
Serotonin	Striatum	[108,110]
Met-enkephalin, Leu-enkephalin, dynorphin, β-endorphin	Striatum	[111,112]
Vasopressin, corticotrophin releasing hormone	Anterior pituitary	[113]
Growth hormone releasing hormone	Hypothalamus	[113,114]
Somatostatin	Striatum	[115]
Substance P	CSF (human)	[116]
Neurokinin	CSF (human)	[117]
Neuropeptide tyrosin, neurotensin	Ventral striatum	[118]
Vasoactive intestinal polypeptide	Cerebral cortex tissue	[119]
Nociceptin/orphanin FQ	Hippocampus/thalamus	[120]
Hypocretins/orexins	Nucleus accumbens core, Basal forebrain, perifornical hypothalamus, and locus ceruleus	[121,122]
Angiotensin	Globus pallidus/ventral pallidum	[123]
Acetylcholine	Hippocampus, prefrontal cortex	[124,125]

reported in vivo dialysate concentrations of neurotransmitters as measured by MD in rats were mentioned in Table 2.

4.4.2. In pre-clinical brain-targeting drug research

An important field of application is certainly the use of MD in drug disposition in brain. For CNS drugs, although the relationship between total brain concentrations and drug action has been and is being investigated widely, recent developments have put the focus on unbound brain concentrations [126–130]. In most cases, the drug has to be transported across membranes in the body to reach the site of action. However, the brain offers opportunities for testing the hypothesis that active site concentrations are better predictors of the drug effect than plasma or total tissue concentrations, because the BBB with its tight junctions and active efflux and influx transporters strictly controls the brain microenvironment.

For extracellular targets, the introduction of MD has made it possible to measure unbound tissue concentrations in vivo. This has been especially revealing for increasing our understanding of brain pharmacokinetics [128,131,132], and it has also resulted in the development of other methodologies in this area [133–135]. Unbound concentrations can be either measured directly with MD or estimated from a combination of total concentration measurements at steady state and brain tissue binding studied using the slice technique [133,134] or brain homogenates [135].

In this way, MD has been adopted for the measurement of drugs (analgesic drug, antiepileptic drug, antidepressant drug, and antineoplastic drug) in the brain. Recent investigations compared the pharmacokinetics and brain distribution of lidocaine, racemic bupivacaine (bupivacaine), and levobupivacaine in awake, spontaneously breathing rats. Tissue-to-plasma partition coefficients calculated from the total (protein-bound and unbound) and unbound concentrations in plasma and brain as well as pharmacokinetic parameters in plasma and cerebral extracellular fluid were compared among the three anesthetics. Concentrations of anesthetics in the cerebral extracellular fluid were measured by MD using the retrodialysis calibration method [136]. Similarly, a method using liquid chromatography–mass spectrometry coupled with MD and an auto-blood sampling system was developed to determine rosiglitazone and glucose concentration in the brain and blood of gerbils subjected to treatment with rosiglitazone [137]. Another study conducted on rat brain involved cefazolin [138], omeprazole [139], naringin [140], and metronidazole [141]. All of these studies sampled different tissues simultaneously (blood, brain and blood, brain and bile, respectively). This way, the penetration of the drug through the blood–brain barrier and its hepatobiliary excretion could be investigated. The blood–brain barrier transport of morphine has been studied in rats sampled by MD

and analyzed by LC–MS/MS and accelerator MS [142], as well as in pigs [143], and in patients with severe brain trauma [144,145], demonstrating an active efflux of morphine across the blood–brain barrier. Studies conducted in brain tissue only include measurements of sparfloxacin in mouse brain [146], mannitol [147] and norfloxacin [148] in rat brain and rifampicin in patients undergoing craniotomy for resection of primary brain tumors [149]. The distribution of topotecan into cerebrospinal fluid was studied in mice [150]. This study presents the basis for further studies concerning CNS pharmacokinetics with camptothecin analogs. Recently, a review assessing intratumoral drug disposition with MD in brain cancers has been published [151]. In summary, brain MD investigations of drugs are very helpful to improve our knowledge about the underlying physiology of the disposition of drugs in the brain and might in the future lead to a more targeted drug therapy.

4.4.3. In clinical research

Intracerebral MD in humans was first described in 1987 in patients with surgically treated Parkinson's disease [152]. In clinical practice, intracerebral MD is being used in the neurointensive care unit [153], although it has to be mentioned that it is still not widely available. Some concerns were raised which restrict its widespread use. These include the significant requirements for nursing and technical support and the inability to perform continuous monitoring as well as technical surgical issues that need to be resolved (optimal length for the catheters used, perfusate rates and location for catheter placement) to obtain optimal functioning of the system [154].

Previous clinical studies have shown its safety and usefulness as a monitoring method in several pathologic conditions including traumatic brain injury (TBI) [155–157], subarachnoid hemorrhage [158–160], and stroke [161]. Clinical data and imaging studies currently available do not yield reliable prognostic criteria, and MD has emerged as a monitoring system for early warning for impending complications. MD has also been used as a means of providing insight into the physiology of the brain and pathophysiology of brain injuries [155,162] as well as in elucidating the effect of drugs or other therapeutic interventions. MD is usually being used in conjunction with other established methods of cerebral monitoring [intracranial pressure (ICP), neurophysiological monitoring, PET scans, transcranial Doppler and brain tissue pO_2] so that the results can be compared and validated.

Applications in patients measuring drug concentrations in brain have been scarce so far. Blakeley et al. investigated the use of MD to assess intratumoral drug distribution in patients with recurrent high grade gliomas (HGG). It was investigated for determining whether potentially therapeutic drug exposure is achieved within

brain tumors in an exploratory clinical investigation which might provide a rational basis for selecting agents for evaluation in phase II trials [163]. Portnow et al. studied the feasibility of using intracerebral MD to examine the neuropharmacokinetics of temozolomide in brain interstitium following oral administration. Patients with primary or metastatic brain tumors had a MD catheter placed in peritumoral brain tissue at the time of surgical debulking. Concentrations of temozolomide in brain interstitium obtained by MD are consistent with published data obtained in a pre-clinical MD model, as well as from clinical studies of cerebrospinal fluid [164]. Lindberger et al. [165] studied the distribution of valproate to subdural cerebrospinal fluid in comparison to subcutaneous extracellular fluid and plasma under steady state conditions in humans. As valproate enters the cerebrospinal fluid in concentrations only marginally lower than in subcutaneous tissue, this sampling method has the potential to be used for monitoring of valproate concentrations. The same group studied the distribution of carbamazepine and phenobarbital in human subdural cerebrospinal fluid [166], yielding similar results.

Cerebral MD is a valuable tool for neurochemical monitoring of acute brain injury. Tholance et al. [167] performed an independent analytical validation of glucose, lactate and pyruvate methods by cerebral MD for clinical application. They proved that cerebral MD has the qualities required for clinical application in neurointensive care. Correct clinical interpretation of data requires the implementation of a strict quality control program and strong cooperation between clinicians and biologists. Hutchinson et al. [168] describe the role of cerebral MD as an adjunct to the management of a 49-year-old woman with hepatic encephalopathy secondary to a paracetamol overdose. The application of the MD technique, by detecting a very low cerebral glucose concentration in the presence of normal plasma glucose, assisted in clinical decision making. Cerebral MD, by enabling continuous online monitoring of substrate delivery and metabolism, may have a role in the management of patients with fulminant hepatic failure. One paper described the monitoring of different inhibitory and excitatory neurotransmitters during cerebral ischemia after head injury [169]. The authors reported that acute cerebral ischemia is accompanied by an increase in neurotransmitter amino acids such as GABA, aspartate and glutamate. These results were confirmed by Sarrafzadeh et al. [170], who observed an increase of glutamate and lactate and by Hlatky et al. [162], detecting an increase of glucose, lactate and glutamate in patients with traumatic brain injury. An overview over some earlier trauma studies also covering the application in high-flow and low-flow bypass surgery and during aneurysm operations was published a few years ago by Mendelowitsch [171]. It also focuses on technical aspects describing instrumentation needed for brain MD. In summary, further research in clinical fields might lead to the division of subgroups of patients who might in the future benefit from more tailored therapy. Additionally, a major factor preventing efficacy of antibrain cancer drugs is limited access to the tumor. Intracerebral MD allows sampling of drug in the brain extracellular fluid. The resulting pharmacokinetics–pharmacodynamics data can aid in the rational selection of drugs for investigation in brain tumor clinical trials [172].

5. Conclusion

In this review, we have discussed published examples in the area of drug delivery into brain in the context of detecting methods to increase the strength of the delivery system. Homogenization, imaging modalities, and MD are the three main techniques used for the measurement of neurotransmitters and drug delivery. Developments in imaging modalities tend to focus on improvements in

selectivity and sensitivity. New methods for sampling, such as MD, have demonstrated resolution of specific combinations of analyses, improvements in detector performance, and preservation of information from the sampling site to the analysis device. We have demonstrated that these optimized methods could significantly reduce the harm to the healthy brain when compared to tissue homogenate.

Advancements in our ability to perform analytical methods with greater control over drug delivery and bioactive properties have led to new analytical methods for imaging modalities and microdialysis. High level and sustained detection in brain targeting remains a great challenge for drug therapy. It might also be desirable for certain applications to analyze such imaging modalities and microdialysis that detect drug delivery in an inducible manner in response to temporal or pathophysiological signals. To this end, development of targeting delivery with nanoparticles would allow methods such as microdialysis to be tailored to meet desired detection needs, thus harnessing the full potential of brain targeting.

Acknowledgement

References

[1] L. Juillerat-Jeanneret, The targeted delivery of cancer drugs across the blood–brain barrier: chemical modifications of drugs or drug nanoparticles? Drug Discov. Today 13 (2008) 1099–1106.
[2] K.N. Schultz, R.T. Kennedy, Time-resolved microdialysis for in vivo neurochemical measurements and other applications, Annu. Rev. Anal. Chem. 1 (2008) 627–661.
[3] D.P. Taggart, B. Choudhary, K. Anastasiadis, et al., Preliminary experience with a novel intraoperative fluorescence imaging technique to evaluate the patency of bypass grafts in total arterial revascularization, Ann. Thorac. Surg. 75 (2003) 870–873.
[4] J. Chen, C.H. Tung, J.R. Allport, et al., Near-infrared fluorescent imaging of matrix metalloproteinase activity after myocardial infarction, Circulation 111 (2005) 1800–1805.
[5] D.E. Sosnovik, E.A. Schellenberger, M. Nahrendorf, et al., Magnetic resonance imaging of cardiomyocyte apoptosis with a novel magnetooptical nanoparticle, Magn. Reson. Med. 54 (2005) 718–724.
[6] V. Ntziachristos, C.H. Tung, C. Bremer, et al., Fluorescence molecular tomography resolves protease activity in vivo, Nat. Med. 8 (2002) 757–761.
[7] D. Razansky, M. Distel, C. Vinegoni, et al., Multispectral opto-acoustic tomography of deep-seated fluorescent proteins in vivo, Nat. Photonics 3 (2009) 412–417.
[8] Y.F. Pan, J. Feng, Q.Y. Cheng, F.Z. Li, Intracerebral microdialysis technique and its application on brain pharmacokinetic–pharmacodynamic study, Arch. Pharm. Res. 30 (2007) 1635–1645.
[9] D.J. Begley, Delivery of therapeutic agents to the central nervous system: the problems and the possibilities, Pharmacol. Ther. 104 (2004) 29–45.
[10] Y. Persidsky, S. Ramirez, J. Haorah, G. Kanmogne, Blood–brain barrier: structural components and function under physiologic and pathologic conditions, J. Neuroimmune Pharmacol. 1 (2006) 223–236.
[11] Y. Chen, G. Dalwadi, H. Benson, Drug delivery across the blood–brain barrier, Curr. Drug Deliv. 1 (2004) 361–376.
[12] J.C. Olivier, Drug transport to brain with targeted nanoparticles, NeuroRx 2 (2005) 108–119.
[13] W.M. Pardridge, CNS drug design based on principles of blood–brain barrier transport, J. Neurochem. 70 (2002) 1781–1792.
[14] B.T. Hawkins, T.P. Davis, The blood–brain barrier/neurovascular unit in health and disease, Pharmacol. Rev. 57 (2005) 173–185.
[15] M.W. Brightman, T.S. Reese, Junctions between intimately apposed cell membranes in the vertebrate brain, J. Cell Biol. 40 (1969) 648–677.
[16] N.R. Saunders, C.J. Ek, M.D. Habgood, et al., Barriers in the brain: a renaissance? Trends Neurosci. 31 (2008) 279–286.
[17] N. Saunders, M.D. Habgood, K. Dziegielewska, Barrier mechanisms in the brain, II. Immature brain, Clin. Exp. Pharmacol. Physiol. 26 (1999) 85–91.
[18] N. Saunders, M.D. Habgood, K. Dziegielewska, Barrier mechanisms in the brain, I. Adult brain, Clin. Exp. Pharmacol. Physiol. 26 (1999) 11–19.
[19] S. Giovagnoli, P. Blasi, A. Schoubben, et al., Preparation of large porous biodegradable microspheres by using a simple double-emulsion method for capreomycin sulfate pulmonary delivery, Int. J. Pharm. 333 (2007) 103–111.

[20] I. Jovanovic, B. Jordovic, M. Petkovic, et al., Preparation of smallest microparticles of poly-D,L-lactide by modified precipitation method: influence of the process parameters, Microsc. Res. Tech. 71 (2008) 86–92.

[21] A. Noda, H. Takamatsu, Y. Murakami, et al., Measurement of brain concentration of FK960 for development of a novel antidementia drug: a PET study in conscious rhesus monkeys, J. Nucl. Med. 44 (2003) 105–108.

[22] Y. Tan, H. Jiang, DOT guided fluorescence molecular tomography of arbitrarily shaped objects, Med. Phys. 35 (2008) 5703–5707.

[23] V. Ntziachristos, C. Bremer, R. Weissleder, Fluorescence imaging with near-infrared light: new technological advances that enable in vivo molecular imaging, Eur. Radiol. 13 (2003) 195–208.

[24] A.L. Freed, J.D. Cooper, M.I. Davies, et al., Investigation of the metabolism of substance P in rat striatum by microdialysis sampling and capillary electrophoresis with laser-induced fluorescence detection, J. Neurosci. Methods 109 (2001) 23–29.

[25] K.L. Kostel, S.M. Lunte, Evaluation of capillary electrophoresis with post-column derivatization and laser-induced fluorescence detection for the determination of substance P and its metabolites, J. Chromatogr. B: Biomed. Sci. Appl. 695 (1997) 27–38.

[26] K.J. McLaughlin, A.A. Faibushevich, C.E. Lunte, Microdialysis sampling with online microbore HPLC for the determination of tirapazamine and its reduced metabolites in rats, Analyst 125 (2000) 105–110.

[27] H. Benveniste, P.C. Huttemeier, Microdialysis – theory and application, Prog. Neurobiol. 35 (1990) 195–215.

[28] L. Groth, P. García Ortiz, E. Benfeldt, Microdialysis methodology for sampling in the skin, in: J. Serup, G.B.E. Jemec, G.L. Grove (Eds.), Handbook of Non-Invasive Methods and the Skin, Taylor & Francis, Boca Raton, 2006, pp. 443–454.

[29] J. Borjigin, T. Liu, Application of long-term microdialysis in circadian rhythm research, Pharmacol. Biochem. Behav. 90 (2008) 148–155.

[30] H. Benveniste, J. Drejer, A. Schousboe, et al., Elevation of the extracellular concentrations of glutamate and aspartate in rat hippocampus during transient cerebral ischemia monitored by intracerebral microdialysis, J. Neurochem. 43 (1984) 1369–1374.

[31] E.C. de Lange, M. Danhof, A.G. de Boer, D.D. Breimer, Critical factors of intracerebral microdialysis as a technique to determine the pharmacokinetics of drugs in rat brain, Brain Res. 666 (1994) 1–8.

[32] O. Major, T. Shdanova, L. Duffek, Z. Nagy, Continuous monitoring of blood–brain barrier opening to Cr51-EDTA by microdialysis following probe injury, Acta Neurochir. Suppl. (Wien.) 51 (1990) 46–48.

[33] P. Nandi, S.M. Lunte, Recent trends in microdialysis sampling integrated with conventional and microanalytical systems for monitoring biological events: a review, Anal. Chim. Acta 651 (2009) 1–14.

[34] B.H. Westerink, T.I. Cremers, Evidence for activation of histamine H3 autoreceptors during handling stress in the prefrontal cortex of the rat, Synapse 43 (2002) 238–243.

[35] C.S. Yang, P.J. Tsai, On-line, continuous and automatic monitoring of extracellular malondialdehyde concentration in anesthetized rat brain cortex, J. Chromatogr B: Biomed. Sci. Appl. 752 (2001) 33–38.

[36] M. Orlowska-Majdak, W.Z. Traczyk, D. Szymanski, Hippocampal vasopressin release evoked by N-methyl D-aspartate (NMDA) microdialysis, Physiol. Res. 52 (2003) 373–382.

[37] J.M.R. Delgado, J. Lerma, R. Martin del Rio, J.M. Solis, Dialytrode technology and local profiles of amino acids in the awake cat brain, J. Neurochem. 42 (1984) 1218–1228.

[38] M. Brunner, H. Derendorf, Clinical microdialysis: current applications and potential use in drug development, TrAC, Trends Anal. Chem. 25 (2006) 674–680.

[39] Q. Chen, T. Gong, J. Liu, et al., Synthesis, in vitro and in vivo characterization of glycosyl derivatives of ibuprofen as novel prodrugs for brain drug delivery, J. Drug Target 17 (2009) 318–328.

[40] R.C. Doijad, F.V. Manvi, D.M. Godhwani, et al., Formulation and targeting efficiency of cisplatin engineered solid lipid nanoparticles, Ind. J. Pharm. Sci. 70 (2008) 203–207.

[41] B. Wilson, M. Samanta, K. Santhi, et al., Targeted delivery of tacrine into the brain with polysorbate 80-coated poly(n-butylcyanoacrylate) nanoparticles, Eur. J. Pharm. Biopharm. 70 (2008) 75–84.

[42] G. Huang, N. Zhang, X.L. Bi, et al., Solid lipid nanoparticles of temozolomide: potential reduction of cardial and nephric toxicity, Int. J. Pharm. 355 (2008) 314–320.

[43] T. Parikh, M. Bommana, E. Squillante, et al., Efficacy of surface charge in targeting pegylated nanoparticles of sulpiride to the brain, Eur. J. Pharm. Biopharm. 74 (2010) 442–450.

[44] A. Sigler, A. Goroshkov, T.H. Murphy, Hardware and methodology for targeting single brain arterioles for photothrombotic stroke on an upright microscope, J. Neurosci. Methods 170 (2008) 35–44.

[45] C. Riviere, M. Martina, Y. Tomita, et al., Magnetic targeting of nanometric magnetic fluid loaded liposomes to specific brain intravascular areas: a dynamic imaging study in mice, Radiology 244 (2007) 439–448.

[46] S.N. Tang, Z.H. Liu, L.X. Zhao, et al., Transfection of pEGFP-C2 in brain mediated by targeting liposome P-MMA-DOSPER, Sheng Wu Yi Xue Gong Cheng Xue Za Zhi 25 (2008) 1170–1174.

[47] R. Weissleder, M.J. Pittet, Imaging in the era of molecular oncology, Nature 452 (2008) 580–589.

[48] V. Ntziachristos, A.G. Yodh, M.D. Schnall, B. Chance, MRI-guided diffuse optical spectroscopy of malignant and benign breast lesions, Neoplasia 4 (2002) 347–354.

[49] J. Grimm, D.G. Kirsch, S.D. Windsor, et al., Use of gene expression profiling to direct in vivo molecular imaging of lung cancer, Proc. Natl. Acad. Sci. U.S.A. 102 (2005) 14404–14409.

[50] V. Ntziachristos, C.H. Tung, C. Bremer, R. Weissleder, Fluorescence molecular tomography resolves protease activity in vivo, Nat. Med. 8 (2002) 757–760.

[51] D.E. Sosnovik, M. Nahrendorf, N. Deliolanis, et al., Fluorescence tomography and magnetic resonance imaging of myocardial macrophage infiltration in infarcted myocardium in vivo, Circulation 115 (2007) 1384–1391.

[52] A. Corlu, R. Choe, T. Durduran, et al., Three-dimensional in vivo fluorescence diffuse optical tomography of breast cancer in humans, Opt. Express 15 (2007) 6696–6716.

[53] E. Graves, J. Ripoll, R. Weissleder, V. Ntziachristos, A submillimeter resolution fluorescence molecular imaging system for small animal imaging, Med. Phys. 30 (2003) 901–911.

[54] L. Andreas, F. Albrecht, B. Kiderlen, et al., Delivery of amphotericin B nanosuspensions to the brain and determination of activity against *Balamuthia mandrillaris* amebas, Nanomedicine 6 (2010) 597–603.

[55] E. Leupold, H. Nikolenko, M. Beyermann, et al., Insight into the role of HSPG in the cellular uptake of apolipoprotein E-derived peptide micelles and liposomes, Biochim. Biophys. Acta 1778 (2008) 2781–2789.

[56] E.J. Kwon, J. Lasiene, B.E. Jacobson, et al., Targeted nonviral delivery vehicles to neural progenitor cells in the mouse subventricular zone, Biomaterials 31 (2010) 2417–2424.

[57] J.F. Adam, M.C. Biston, J. Rousseau, et al., Heavy element enhanced synchrotron stereotactic radiotherapy as a promising brain tumour treatment, Phys. Med. 24 (2008) 92–97.

[58] Q.G. Meng, M. Yu, B. Gu, et al., Myristic acid-conjugated polyethylenimine for brain-targeting delivery: in vivo and ex vivo imaging evaluation, J. Drug Target. 18 (2010) 438–446.

[59] S.J. Schambach, S. Bag, C. Groden, et al., Vascular imaging in small rodents using micro-CT, Methods 50 (2010) 26–35.

[60] R.S. Mulik, J. Monkkonen, R.O. Juvonen, et al., ApoE3 mediated poly(butyl) cyanoacrylate nanoparticles containing curcumin: study of enhanced activity of curcumin against beta amyloid induced cytotoxicity using in vitro cell culture model, Mol. Pharm. 7 (2010) 815–825.

[61] M. Edouard, D. Broggio, Y. Prezado, et al., Treatment plans optimization for contrast-enhanced synchrotron stereotactic radiotherapy, Med. Phys. 37 (2010) 2445–2456.

[62] E.F. Craparo, M.C. Ognibene, M.P. Casaletto, Biocompatible polymeric micelles with polysorbate 80 for use in brain targeting, Nanotechnology 19 (2008) 1–12.

[63] J. Pan, S.S. Feng, Targeted delivery of paclitaxel using folate-decorated poly(lactide) – vitamin E TPGS nanoparticles, Biomaterials 29 (2008) 2663–2672.

[64] F. Caire, C. Gantois, F. Torny, Intraoperative use of the Medtronic O-arm for deep brain stimulation procedures, Stereotact. Funct. Neurosurg. 88 (2010) 109–114.

[65] M. Armour, E. Ford, I. Iordachita, CT guidance is needed to achieve reproducible positioning of the mouse head for repeat precision cranial irradiation, Radiat. Res. 173 (2010) 119–123.

[66] F. Chan, Meng, I. Kassim, et al., Image-guided robotic neurosurgery—an in vitro and in vivo point accuracy evaluation experimental study, Surg. Neurol. 71 (2009) 640–648.

[67] L.A. Hirano, S.T. Bogardus, S. Saluja, et al., Clinical yield of computed tomography brain scans in older general medical patients, J. Am. Geriatr. Soc. 54 (2006) 587–592.

[68] J.S. Fowler, N.D. Volkow, G.J. Wang, et al., PET and drug research and development, J. Nucl. Med. 40 (1999) 1154–1163.

[69] S.J. Gatley, N.D. Volkow, G.J. Wang, et al., PET imaging in clinical drug abuse research, Curr. Pharm. Des. 11 (2005) 3203–3219.

[70] N.D. Volkow, G.J. Wang, J.S. Fowler, et al., Imaging the effects of methylphenidate on brain dopamine: new model on its therapeutic actions for attention-deficit/hyperactivity disorder, Biol. Psychiatry 57 (2005) 1410–1415.

[71] K.J. Langen, K. Hamacher, M. Weckesser, et al., O-(2-[18F]fluoroethyl)-L-tyrosine: uptake mechanisms and clinical applications, Nucl. Med. Biol. 33 (2006) 287–294.

[72] P. Price, The role of PET scanning in determining pharmacoselective doses in oncology drug development, Ernst. Schering Res. Found Workshop (2007) 185–193.

[73] N. Oku, M. Yamashita, Y. Katayama, et al., PET imaging of brain cancer with positron emitter-labeled liposomes, Pharm. Nanotechnol. 403 (2011) 170–177.

[74] H. Benveniste, J.S. Fowler, W. Rooney, et al., Maternal and fetal 11C-cocaine uptake and kinetics measured in vivo by combined PET and MRI in pregnant nonhuman primates, J. Nucl. Med. 46 (2005) 312–320.

[75] R. Alonzi, P. Hoskin, Functional imaging in clinical oncology: magnetic resonance imaging- and computerised tomography-based techniques, Clin. Oncol. 18 (2006) 555–570.

[76] J.Y. Li, R.J. Boado, W.M. Pardridge, Blood–brain barrier genomics, J. Cereb. Blood Flow Metab. 21 (2001) 61–68.

[77] M. Chopp, Z.G. Zhang, Q. Jiang, Neurogenesis, angiogenesis, and MRI indices of functional recovery from stroke, Stroke 38 (2007) 827–831.

[78] S.J. Nelson, S. Cha, Imaging glioblastoma multiforme, Cancer J. 9 (2003) 134–145.

[79] R.J. Young, E.A. Knopp, Brain MRI: tumor evaluation, J. Magn. Reson Imaging 24 (2006) 709–724.

[80] D.K. Li, M.J. Li, A. Traboulsee, et al., The use of MRI as an outcome measure in clinical trials, Adv. Neurol. 98 (2006) 203–226.

[81] T.C. William, G.A. Christoforidis, R.M. Koch, et al., Clinical magnetic resonance imaging of brain tumors at ultrahigh field: a state-of-the-art review, Top. Magn. Reson. Imaging 17 (2006) 53–61.

[82] C. Sun, J. Lee, M. Zhang, Magnetic nanoparticles in MR imaging and drug delivery, Adv. Drug Deliv. Rev. 60 (2008) 1252–1265.

[83] H.L. Liu, M.Y. Hua, H.W. Yang, et al., Magnetic resonance monitoring of focused ultrasound/magnetic nanoparticle targeting delivery of therapeutic agents to the brain, Proc. Natl. Acad. Sci. U.S.A. 107 (2010) 15205–15210.

[84] O. Veiseh, F.M. Kievit, C. Fang, et al., Chlorotoxin bound magnetic nanovector tailored for cancer cell targeting, imaging, and siRNA delivery, Biomaterials 31 (2010) 8032–8042.

[85] W. Liu, J.A. Frank, Detection and quantification of magnetically labeled cells by cellular MRI, Eur. J. Radiol. 70 (2009) 258–264.

[86] B. Chertok, B.A. Moffat, A.E. David, et al., Iron oxide nanoparticles as a drug delivery vehicle for MRI monitored magnetic targeting of brain tumors, Biomaterials 29 (2008) 487–496.

[87] S.H. Hsu, C.J. Wen, S.A. AI-Suwayeh, et al., Physicochemical characterization and in vivo bioluminescence imaging of nanostructured lipid carriers for targeting the brain: apomorphine as a model drug, Nanotechnology 40 (2010) 405101.

[88] R.X. Xu, S.P. Povoski, Diffuse optical imaging and spectroscopy for cancer, Expert Rev. Med. Devices 4 (2007) 83–95.

[89] Q. Wang, Z. Liu, H.B. Jiang, Optimization and evaluation of a three-dimensional diffuse optical tomography system for brain imaging, J. X-ray Sci. Technol. 15 (2007) 223–234.

[90] U. Mahmood, R. Weissleder, Near-infrared optical imaging of proteases in cancer, Mol. Cancer Ther. 2 (2003) 489–496.

[91] V. Ntziachristos, R. Weissleder, Fluorescence-mediated molecular tomography, United States Patent US 6615063B1, 2008.

[92] W. Pham, B.Q. Zhao, E.H. Lo, et al., Crossing the blood–brain barrier: a potential application of myristoylated polyarginine for in vivo neuroimaging, Neuroimage 28 (2005) 287–292.

[93] E.E. Graves, J.J. Ripoll, R. Weissleder, et al., A submillimeter resolution fluorescence molecular imaging system for small animal imaging, Med. Phys. 30 (2003) 901–911.

[94] D. Razansky, J. Baeten, V. Ntziachristos, Sensitivity of molecular target detection by multispectral optoacoustic tomography (MSOT), Med. Phys. 36 (2009) 939–945.

[95] M. Kumar, A. Misra, A.K. Babbar, et al., Intranasal nanoemulsion based brain targeting drug delivery system of risperidone, Int. J. Pharm. 358 (2008) 285–291.

[96] C.S. Chaurasia, M. Muller, E.D. Bashaw, et al., AAPS-FDA workshop white paper: microdialysis principles, application and regulatory perspectives, Pharm. Res. 24 (2007) 1014–1025.

[97] E.C. de Lange, P.G. Ravenstijn, D. Groenendaal, T.J. van Steeg, Toward the prediction of CNS drug-effect profiles in physiological and pathological conditions using microdialysis and mechanism-based pharmacokinetic–pharmacodynamic modeling, AAPS J. 7 (2005) E532–E543.

[98] M. Masana, A. Bortolozzi, F. Artigas, Selective enhancement of mesocortical dopaminergic transmission by noradrenergic drugs: therapeutic opportunities in schizophrenia, Int. J. Neuropsychopharmacol. 14 (2011) 53–68.

[99] M. Herrera-Marschitz, G. Arbuthnott, U. Ungerstedt, The rotational model and microdialysis: significance for dopamine signalling, clinical studies, and beyond, Prog. Neurobiol. 90 (2010) 176–189.

[100] M.A. de Souza Silva, C. Mattern, B. Topic, et al., Dopaminergic and serotonergic activity in neostriatum and nucleus accumbens enhanced by intranasal administration of testosterone, Eur. Neuropsychopharmacol. 19 (2009) 53–63.

[101] M.A. de Souza Silva, B. Topic, J.P. Huston, C. Mattern, Intranasal administration of progesterone increases dopaminergic activity in amygdala and neostriatum of male rats, Neuroscience 157 (2008) 196–203.

[102] N. Plock, C. Kloft, Microdialysis—theoretical background and recent implementation in applied life-sciences, Eur. J. Pharm. Sci. 25 (2005) 1–24.

[103] G. Di Chiara, G. Tanda, E. Carboni, Estimation of in-vivo neurotransmitter release by brain microdialysis: the issue of validity, Behav. Pharmacol. 7 (1996) 640–657.

[104] V. Sauvinet, S. Parrot, N. Benturquia, et al., In vivo simultaneous monitoring of gamma-aminobutyric acid, glutamate, and L-aspartate using brain microdialysis and capillary electrophoresis with laser-induced fluorescence detection: analytical developments and in vitro/in vivo validations, Electrophoresis 24 (2003) 3187–3196.

[105] N. Benturquia, S. Parrot, V. Sauvinet, et al., Simultaneous determination of vigabatrin and amino acid neurotransmitters in brain microdialysates by capillary electrophoresis with laser-induced fluorescence detection, J. Chromatogr. B: Analyt. Technol. Biomed. Life Sci. 806 (2004) 237–244.

[106] Y. Yu, Q. Sun, T. Zhou, et al., On-line microdialysis system with poly(amidoamine)-encapsulated Pt nanoparticles biosensor for glutamate sensing in vivo, Bioelectrochemistry 81 (2011) 53–57.

[107] C.C. Klinker, M.T. Bowser, 4-Fluoro-7-nitro-2,1,3-benzoxadiazole as a fluorogenic labeling reagent for the in vivo analysis of amino acid neurotransmitters using online microdialysis-capillary electrophoresis, Anal. Chem. 79 (2007) 8747–8754.

[108] W. Zhu, D. Wang, J. Zheng, et al., Effect of (R)-salsolinol and N-methyl-(R)-salsolinol on the balance impairment between dopamine and acetylcholine in rat brain: involvement in pathogenesis of Parkinson disease, Clin. Chem. 54 (2008) 705–712.

[109] H. Kako, Y. Kobayashi, H. Yokogoshi, Effects of n-hexanal on dopamine release in the striatum of living rats, Eur. J. Pharmacol. 651 (2011) 77–82.

[110] Y. Kitaichi, T. Inoue, S. Nakagawa, et al., Sertraline increases extracellular levels not only of serotonin, but also of dopamine in the nucleus accumbens and striatum of rats, Eur. J. Pharmacol. 647 (2010) 90–96.

[111] Q. Li, J.K. Zubieta, R.T. Kennedy, Practical aspects of in vivo detection of neuropeptides by microdialysis coupled off-line to capillary LC with multistage MS, Anal. Chem. 81 (2009) 2242–2250.

[112] H.M. Baseski, C.J. Watson, N.A. Cellar, et al., Capillary liquid chromatography with MS3 for the determination of enkephalins in microdialysis samples from the striatum of anesthetized and freely-moving rats, J. Mass Spectrom. 40 (2005) 146–153.

[113] Z. Merali, S. Hayley, P. Kent, et al., Impact of repeated stressor exposure on the release of corticotropin-releasing hormone, arginine-vasopressin and bombesin-like peptides at the anterior pituitary, Behav. Brain Res. 198 (2009) 105–112.

[114] T. Hashizume, E. Kasuya, Methodology for the study of the hypothalamic–pituitary hormone secretion in cattle, Anim. Sci. J. 80 (2009) 1–11.

[115] A. Marazioti, P.M. Pitychoutis, Z. Papadopoulou-Daifoti, et al., Activation of somatostatin receptors in the globus pallidus increases rat locomotor activity and dopamine release in the striatum, Psychopharmacology (Berl.) 201 (2008) 413–422.

[116] Z. Liu, M. Welin, B. Bragee, et al., A high-recovery extraction procedure for quantitative analysis of substance P and opioid peptides in human cerebrospinal fluid, Peptides 21 (2000) 853–860.

[117] A.A. Mathe, M.V. Rudorfer, C. Stenfors, et al., Effects of electroconvulsive treatment on somatostatin, neuropeptide Y, endothelin, and neurokinin a concentrations in cerebrospinal fluid of depressed patients: a pilot study, Depression 3 (2008) 250–256.

[118] S.H. Gruber, G.G. Nomikos, A.A. Mathé, Effects of acute and subchronic D-amphetamine on ventral striatal concentrations of neurotensin and neuropeptide Y in rats treated with antipsychotic drugs, Eur. Neuropsychopharmacol. 16 (2006) 592–600.

[119] J. Soucheleau, L. Denoroy, Determination of vasoactive intestinal peptide in rat brain by high-performance capillary electrophoresis, J. Chromatogr. 608 (1992) 181–188.

[120] L.C. Aparicio, S. Candeletti, A. Binaschi, et al., Kainate seizures increase nociceptin/orphanin FQ release in the rat hippocampus and thalamus: a microdialysis study, J. Neurochem. 91 (2004) 30–37.

[121] R.A. España, J.R. Melchior, D.C. Roberts, et al., Hypocretin 1/orexin A in the ventral tegmental area enhances dopamine responses to cocaine and promotes cocaine self-administration, Psychopharmacology (Berl.) 214 (2011) 415–426.

[122] L.I. Kiyashchenko, B.Y. Mileykovskiy, N. Maidment, et al., Release of hypocretin (orexin) during waking and sleep states, J. Neurosci. 22 (2002) 5282–5286.

[123] K. Lanckmans, S. Sarre, I. Smolders, et al., Use of a structural analogue versus a stable isotope labeled internal standard for the quantification of angiotensin IV in rat brain dialysates using nano-liquid chromatography/tandem mass spectrometry, Rapid Commun. Mass Spectrom. 21 (2007) 1187–1195.

[124] J. Ihalainen, T. Sarajärvi, S. Kemppainen, et al., A novel delayed non-match to sample object recognition task that allows simultaneous in vivo microdialysis, J. Neurosci. Methods 189 (2010) 210–215.

[125] K. Takase, F. Kimura, T. Yagami, et al., Sex-specific 24-h acetylcholine release profile in the medial prefrontal cortex: simultaneous measurement of spontaneous locomotor activity in behaving rats, Neuroscience 159 (2009) 7–15.

[126] M. Hammarlund-Udenaes, Active-site concentrations of chemicals – are they a better predictor of effect than plasma/organ/tissue concentrations? Basic Clin. Pharmacol. Toxicol. 106 (2010) 215–220.

[127] R. Clinckers, I. Smolders, K. Vermoesen, et al., Prediction of antiepileptic drug efficacy: the use of intracerebral microdialysis to monitor biophase concentrations, Expert Opin. Drug Metab. Toxicol. 5 (2009) 1267–1277.

[128] M. Hammarlund-Udenaes, M. Friden, S. Syvanen, A. Gupta, On the rate and extent of drug delivery to the brain, Pharm. Res. 25 (2008) 1737–1750.

[129] J.C. Kalvass, T.S. Maurer, G.M. Pollack, Use of plasma and brain unbound fractions to assess the extent of brain distribution of 34 drugs: comparison of unbound concentration ratios to in vivo p-glycoprotein efflux ratios, Drug Metab. Dispos. 35 (2007) 660–666.

[130] J. Watson, S. Wright, A. Lucas, et al., Receptor occupancy and brain free fraction, Drug Metab. Dispos. 37 (2009) 753–760.

[131] M. Hammarlund-Udenaes, The use of microdialysis in CNS drug delivery studies. Pharmacokinetic perspectives and results with analgesics and antiepileptics, Adv. Drug Deliv. Rev. 45 (2000) 283–294.

[132] M. Hammarlund-Udenaes, L.K. Paalzow, E.C. de Lange, Drug equilibration across the blood–brain barrier–pharmacokinetic considerations based on the microdialysis method, Pharm. Res. 14 (1997) 128–134.

[133] M. Friden, F. Ducrozet, B. Middleton, et al., Development of a high-throughput brain slice method for studying drug distribution in the central nervous system, Drug Metab. Dispos. 37 (2009) 1226–1233.

[134] M. Friden, A. Gupta, M. Antonsson, et al., In vitro methods for estimating unbound drug concentrations in the brain interstitial and intracellular fluids, Drug Metab. Dispos. 35 (2007) 1711–1719.
[135] J.C. Kalvass, T.S. Maurer, Influence of nonspecific brain and plasma binding on CNS exposure: implications for rational drug discovery, Biopharm. Drug Dispos. 23 (2002) 327–338.
[136] Y. Ikeda, Y. Oda, T. Nakamura, et al., Pharmacokinetics of lidocaine, bupivacaine, and levobupivacaine in plasma and brain in awake rats, Anesthesiology 112 (2010) 1396–1403.
[137] W.H. Sheu, H.C. Chuang, S.M. Cheng, et al., Microdialysis combined blood sampling technique for the determination of rosiglitazone and glucose in brain and blood of gerbils subjected to cerebral ischemia, J. Pharm. Biomed. Anal. 54 (2011) 759–764.
[138] T.H. Tsai, Y.F. Chen, Simultaneous determination of cefazolin in rat blood and brain by microdialysis and microbore liquid chromatography, Biomed. Chromatogr. 14 (2000) 274–278.
[139] F.C. Cheng, Y.F. Ho, L.C. Hung, et al., Determination and pharmacokinetic profile of omeprazole in rat blood, brain and bile by microdialysis and high-performance liquid chromatography, J. Chromatogr. A 949 (2002) 35–42.
[140] T.H. Tsai, Determination of naringin in rat blood, brain and bile using microdialysis and its interaction with cyclosporin a, a P-glycoprotein modulator, J. Agric. Food Chem. 50 (2002) 6669–6674.
[141] T.H. Tsai, Y.F. Chen, Pharmacokinetics of metronidazole in rat blood, brain and bile studied by microdialysis coupled to microbore liquid chromatography, J. Chromatogr. A 987 (2003) 277–282.
[142] M.W. Sadiq, M. Salehpour, N. Forsgard, et al., Morphine brain pharmacokinetics at very low concentrations studied with accelerator mass spectrometry and liquid chromatography–tandem mass spectrometry, Drug Metab. Dispos. 39 (2011) 174–179.
[143] K. Tunblad, P. Ederoth, A. Gärdenfors, et al., Altered brain exposure of morphine in experimental meningitis studied with microdialysis, Acta Anaesthesiol. Scand. 48 (2004) 294–301.
[144] P. Ederoth, K. Tunblad, R. Bouw, et al., Blood–brain barrier transport of morphine in patients with severe brain trauma, Br. J. Clin. Pharmacol. 57 (2004) 427–435.
[145] K. Tunblad, Blood–brain barrier transport of drugs across species with the emphasis on health, disease and modelling, Thesis, Uppsala, 2004.
[146] E.C. de Lange, S. Marchand, D. van den Berg, et al., In vitro and in vivo investigations on fluoroquinolones; effects of the P-glycoprotein efflux transporter on brain distribution of sparfloxacin, Eur. J. Pharm. Sci. 12 (2000) 85–93.
[147] M. Hoistad, K.C. Chen, C. Nicholson, et al., Quantitative dual-probe microdialysis: evaluation of [3H]mannitol diffusion in agar and rat striatum, J. Neurochem. 81 (2002) 80–93.
[148] S. Marchand, M. Chenel, I. Lamarche, et al., Dose ranging pharmacokinetics and brain distribution of norfloxacin using microdialysis in rats, J. Pharm. Sci. 92 (2003) 2458–2465.
[149] T. Mindermann, W. Zimmerli, O. Gratzl, Rifampin concentrations in various compartments of the human brain: a novel method for determining drug levels in the cerebral extracellular space, Antimicrob. Agents Chemother. 42 (1998) 2626–2629.
[150] M. Leggas, Y. Zhuang, J. Welden, et al., Microbore HPLC method with online microdialysis for measurement of topotecan lactone and carboxylate in murine CSF, J. Pharm. Sci. 93 (2004) 2284–2295.
[151] J. Blakeley, J. Portnow, Microdialysis for assessing intratumoral drug disposition in brain cancers: a tool for rational drug development, Expert Opin. Drug Metab. Toxicol. 6 (2010) 1477–1491.
[152] B.A. Meyerson, B. Linderoth, H. Karlsson, et al., Microdialysis in the human brain: extracellular measurements in the thalamus of Parkinsonian patients, Life Sci. 46 (1990) 301–308.
[153] U. Ungerstedt, E. Rostami, Microdialysis in neurointensive care, Curr. Pharm. Des. 10 (2004) 2145–2152.
[154] C. Charalambides, S. Sgouros, D. Sakas, Intracerebral microdialysis in children, Childs Nerv. Syst. 26 (2010) 215–220.
[155] B. Alessandri, E. Doppenberg, R. Bullock, et al., Glucose and lactate metabolism after severe human head injury: influence of excitatory neurotransmittersand injury type, Acta Neurochir. Suppl. 75 (1999) 21–24.
[156] J.C. Goodman, A.B. Valadka, S.P. Gopinath, et al., Extracellular lactate and glucose alterations in the brain after head injury measured by microdialysis, Crit. Care Med. 27 (1999) 1965–1973.
[157] L. Hillered, L. Persson, P. Nilsson, et al., Continuous monitoring of cerebral metabolism in traumatic brain injury: a focus on cerebral microdialysis, Curr. Opin. Crit. Care 12 (2006) 112–118.
[158] M.H. Maurer, D. Haux, O.W. Sakowitz, et al., Identification of early markers for symptomatic vasospasm in human cerebral microdialysate after subarachnoid hemorrhage: preliminary results of a proteome-wide screening, J. Cereb. Blood Flow Metab. 27 (2007) 1675–1683.
[159] J. Skjøth-Rasmussen, M. Schulz, S.R. Kristensen, et al., Delayed neurological deficits detected by an ischemic pattern in the extracellular cerebral metabolites in patients with aneurysmal subarachnoid hemorrhage, J. Neurosurg. 100 (2004) 8–15.
[160] F. Schlenk, D. Graetz, A. Nagel, et al., Insulin-related decrease in cerebral glucose despite normoglycemia in aneurysmal subarachnoid hemorrhage, Crit. Care 12 (2008) R9.
[161] S. Schneweis, M. Grond, F. Staub, et al., Predictive value of neurochemical monitoring in large middle cerebral artery infarction, Stroke 32 (2001) 1863–1867.
[162] R. Hlatky, A.B. Valadka, J.C. Goodman, et al., Patterns of energy substrates during ischemia measured in the brain by microdialysis, J. Neurotrauma 21 (2004) 894–906.
[163] J.O. Blakeley, J. Olson, S.A. Grossman, et al., Consortium. Effect of blood brain barrier permeability in recurrent high grade gliomas on the intratumoral pharmacokinetics of methotrexate: a microdialysis study, J. Neurooncol. 91 (2009) 51–58.
[164] J. Portnow, B. Badie, M. Chen, et al., The neuropharmacokinetics of temozolomide in patients with resectable brain tumors: potential implications for the current approach to chemoradiation, Clin. Cancer Res. 15 (2009) 7092–7098.
[165] M. Lindberger, T. Tomson, L. Wallstedt, et al., Distribution of valproate to subdural cerebrospinal fluid, subcutaneous extracellular fluid, and plasma in humans: a microdialysis study, Epilepsia 42 (2001) 256–261.
[166] M. Lindberger, T. Tomson, S. Lars, Microdialysis sampling of carbamazepine, phenytoin and phenobarbital in subcutaneous extracellular fluid and subdural cerebrospinal fluid in humans: an in vitro and in vivo study of adsorption to the sampling device, Pharmacol. Toxicol. 91 (2002) 158–165.
[167] Y. Tholance, G. Barcelos, I. Quadrio, et al., Analytical validation of MD analyzer for monitoring glucose, lactate and pyruvate in cerebral MDs, Clin. Chim. Acta 412 (2011) 647–654.
[168] P.J. Hutchinson, A. Gimson, P.G. Al-Rawi, et al., MD in the management of hepatic encephalopathy, Neurocrit. Care 5 (2006) 202–205.
[169] P.J. Hutchinson, M.T. O'Connell, P.G. AI-Rawi, et al., Increases in GABA concentrations during cerebral ischaemia: a microdialysis study of extracellular amino acids, J. Neurol. Neurosurg. Psychiatry 72 (2002) 99–105.
[170] A.S. Sarrafzadeh, K.L. Kiening, T.A. Callsen, et al., Metabolic changes during impending and manifest cerebral hypoxia in traumatic brain injury, Br. J. Neurosurg. 17 (2003) 340–346.
[171] A. Mendelowitsch, Microdialysis: intraoperative and posttraumatic applications in neurosurgery, Methods 23 (2001) 73–81.
[172] J. Blakeley, J. Portnow, MD for assessing intratumoral drug disposition in brain cancers: a tool for rational drug development, Expert Opin. Drug Metab. Toxicol. 6 (2010) 1477–1491.
[173] U. Ungerstedt, C. Pycock, Functional correlates of dopamine neurotransmission, Bull. Schweiz. Akad. Med. Wiss. 30 (1974) 44–55.

High resolution magic angle spinning NMR to investigate ligand–receptor binding events for mass-limited samples in liquids

Fabio Ziarelli [a], Ling Peng [b], Cheng-Cai Zhang [c], Stéphane Viel [d],*

[a] *Fédération des Sciences Chimiques de Marseille FR CNRS 1739, av. Escadrille Normandie Niémen, Case 511, 13013 Marseille, France*
[b] *Centre Interdisciplinaire de Nanoscience de Marseille UPR CNRS 3118, Département de Chimie, 163 Avenue de Luminy, 13288 Marseille Cedex 09, France*
[c] *Laboratoire de Chimie Bactérienne UPR CNRS 9043, 31 Chemin Joseph Aiguier, 13402 Marseille Cedex 20, France*
[d] *Aix-Marseille Université, Laboratoire Chimie Provence UMR CNRS 6264, av. Escadrille Normandie Niémen, Case 512, 13013 Marseille, France*

ARTICLE INFO

ABSTRACT

This work shows that high resolution magic angle spinning (HR-MAS) can be used to elucidate ligand–receptor binding phenomena for mass-limited samples in liquid solution. With respect to conventional 5 mm liquid-state NMR probe heads, HR-MAS allows for a considerable reduction (about one order of magnitude) in sample volume requirement, which represents a considerable advantage when working with biological samples present in low amount. More specifically, using a 20-μL active volume HR-MAS probe head, NMR experiments typically used to describe binding events (e.g. Saturation Transfer Difference, WaterLOGSY, Diffusion Ordered Spectroscopy) were successfully recorded. In fact, contrary to other NMR experiments (e.g. TOCSY), which require special care when performed on liquid samples by HR-MAS, no interferences due to fast sample spinning were observed here. Collectively, the results indicate that HR-MAS allows for a significant mass sensitivity enhancement (a 3-fold increase in signal-to-noise ratio per unit of measuring time and mass was obtained here), hereby improving correspondingly the detection limit of the previously mentioned NMR experiments. More importantly, because MAS removes magnetic susceptibility broadenings in the sample, a good spectral resolution can be easily achieved in HR-MAS even for slightly heterogeneous samples, such as those arising from incomplete purification.

© 2011 Elsevier B.V. All rights reserved.

1. Introduction

The characterization of binding events involving biomacromolecules (e.g. proteins, polysaccharides, nucleic acids, etc.) is of fundamental importance for understanding relevant biological processes and plays a key role in drug discovery [1]. As such, ligand–receptor binding investigations currently represent an active field of research [2]. In this context, Nuclear Magnetic Resonance (NMR) spectroscopy is an extremely powerful tool [3] because it provides various methods not only for detecting and quantifying ligand affinities to specific receptors, but also for elucidating the corresponding binding sites (epitope mapping) [4]. The main advantage of NMR over other techniques lies in its ability to study both low and high affinity ligands, by detecting and analyzing either the ligand or the receptor [5]. One of the most sensitive and versatile NMR techniques available to date for elucidating binding events is the Saturation Transfer Difference (STD) technique [6], which is based on ligand detection as opposed to receptor detection. Roughly speaking, the rationale behind the STD technique is to

compare the NMR spectra of the ligand recorded in the presence of a receptor in two different conditions, by saturating alternatively a selected set of NMR resonances due to the studied receptor. In this way, the saturation spreads throughout the entire receptor by a process known as *spin diffusion*, and is in turn transferred to the bound ligand which, by exchange, is moved into the solution where it is detected. The so-obtained spectra are then subtracted (directly inside the NMR receiver), and the resulting NMR spectrum only shows the resonances of the interacting ligand. In other words, because of the absence of saturation transfer, the NMR signals of all the non-interacting species in a mixture will cancel out, which makes the STD technique perfectly adapted for screening investigations. Moreover, because STD most often relies on ^{1}H observation, it is rather sensitive (as compared to other NMR observable nuclei, such as ^{13}C). The high sensitivity of the experiment also results from the high ligand concentration that is typically used (in large excess with respect to the investigated receptor). In addition, experimental refinements involving isotope filtering and editing schemes [7] as well as two-dimensional heteronuclear correlations acquisition modes [8], have been introduced for improving the resolution of the experiment, while other technical improvements have been dedicated to increase the sensitivity [9]. As a matter of fact, sensitivity is key to achieving optimal detection limits. As outlined before,

only the NMR signals of the interacting ligands are observed in the STD spectrum, provided of course that the signal-to-noise ratio (S/N) is high enough. In other words, the lowest levels of ligand (and hence receptor) will be detected as long as the S/N is optimized. This becomes critical when analyzing mass-limited samples (e.g. when very small amounts of the receptor and/or the ligand are available), especially on traditional liquid-state NMR setups. Indeed, liquid-state NMR experiments are typically performed on 5 mm probe heads, which require the use of 5 mm external diameter (e.d.) sample tubes. In this case, a solution volume of about 600 μL is necessary to guarantee an optimal spectral resolution after shimming the sample. In fact, this configuration places the air/solution interface away from the receiver coil, hereby avoiding the associated magnetic field distortions that would otherwise be extremely difficult to remove by shimming. However, the active volume of the probe in this case, namely the volume of solution that is actually 'seen' by the NMR receiver coil, is usually much lower (about 200 μL). Clearly, when the amount of sample is limited, this protocol will correspondingly reduce the sensitivity of the NMR experiments due to the unavoidable dilution.

To circumvent this difficulty, the ideal protocol would be to place the whole sample within the active volume of the probe without perturbing the spectral resolution. To this end, susceptibility matched NMR sample tubes, such as those provided by Shigemi Inc. (Pennsylvania, USA), can be used. However, to achieve optimal resolution, different types of tubes must be used depending on the type of solvent (CDCl$_3$, D$_2$O, DMSO, etc.) in order to properly match the magnetic susceptibility contrast due to the solution/air interface. Overall, these tubes still require significant shimming, are rather fragile and may hence be difficult to handle or clean, which could make them rather unsuitable for high-throughput NMR analysis. Alternatively, NMR probe heads designed for tubes of smaller diameter can be used [10]. In this way, the size of the NMR coil is reduced and capillary NMR tubes of varying diameters are used, hereby enhancing the mass sensitivity correspondingly. Although the resulting capillary tubes are likely to be fragile, due to the low thickness of the glass wall, they can still be used for high-throughput NMR analysis. A nice demonstration along these lines has recently been provided by Bourry et al. [11], who have proposed a titration protocol based on the use of a 1-mm room temperature probe head to investigate intermolecular interactions in the liquid-state. However, this setup still requires cylindrically shaped NMR capillary tubes, which implies that the whole sample is not placed entirely within the coil active volume, with a corresponding loss of signal strength due to the dilution. Again, susceptibility matched sample tubes could be used in this case (though there are currently available for 2.5 mm probe heads only), but the above-mentioned drawbacks would still apply.

Here, we propose to use HR-MAS as an alternative to both of these options. The use of HR-MAS for the analysis of heterogeneous media has already been largely documented [12]. Indeed, it has been shown that spinning the sample sufficiently fast at the so-called magic angle (~54.7°) with respect to the external magnetic field, removes the spectral broadenings due to susceptibility gradients. This yields NMR spectra for heterogeneous materials which spectral resolution is of comparable quality to that of liquid-state NMR spectra [13]. As such, HR-MAS has become an invaluable tool in the field of biomedical analysis [14,15]. When analyzing liquid samples, the main advantage of the HR-MAS technology (sometimes referred to as nanoprobe technology, depending upon the manufacturer) lies in the ability to place the whole sample within the coil active volume of the NMR probe head [16], without suffering from magnetic field distortions because they are removed by MAS. This makes sample shimming in HR-MAS a relatively straightforward task [17]. One major point of concern, however, is that not all liquid-state NMR experiments can be readily adapted

to this setup. For instance, the combination of radiofrequency field inhomogeneity with MAS has already been shown to prevent exploitable TOCSY spectra to be recorded when specific mixing sequences are used [18–20]. Perturbations may also be encountered for other types of liquid-state NMR experiments, such as Diffusion Ordered Spectroscopy (DOSY), especially if the experimental parameters are not optimized [21]. In this respect, although STD NMR spectra recorded with HR-MAS probe heads have already been reported in the literature, these studies exclusively focused on semi-solid samples (e.g. mixtures of a solution with a solid, being either controlled pore glass beads [22] or chromatographic supports [23]). They did not clearly assess the potential complications arising from sample spinning when analyzing liquid samples by HR-MAS. Instead, the present study shows that such interferences can be safely neglected when recording NMR experiments dedicated to the investigation of intermolecular interactions.

2. Materials and methods

2.1. Chemicals and reagents

The following compounds: 4-trifluoromethylbenzoic acid (TFBA), 2,2,2-trifluoroethanol, glucose and Human Serum Albumine (HSA) were supplied by Sigma–Aldrich and were used without further purification. The deuterated water (D$_2$O) was provided by Eurisotop (Saint-Aubin, France). In addition, a 20 mM phosphate buffer (pH 7) was prepared by mixing proper amounts of NaH$_2$PO$_4$ and Na$_2$HPO$_4$ (also supplied as monohydrate salts by Sigma–Aldrich).

2.2. Instrumentation

All NMR experiments were performed at 300 K using a BRUKER AVANCE spectrometer (Bruker BioSpin GmbH, Rheinstetten, Germany) operating at 400.2 MHz and 376.5 MHz for the ^{1}H and ^{19}F Larmor frequency, respectively. Two commercial NMR probe heads were used: a 5 mm double-resonance broadband inverse (BBI) probe head from BRUKER (Bruker BioSpin AG, Fällanden, Switzerland) and a triple-resonance 4 mm HR-MAS probe head optimized for ^{19}F detection from DOTY (Doty Scientific Inc., South Carolina, USA). Both of these probes were equipped with a magnetic field gradient coil (aligned along the z-axis and the spinning axis, respectively). The HR-MAS spinning rate was 4 kHz. The 4 mm Zirconia HR-MAS rotors were equipped with Teflon inserts. This ensured that the active coil volume of the HR-MAS probe head was the same as the sample volume (i.e. the volume of solution that is analyzed) and equaled 20 μL. In contrast, for the 5 mm BBI probe head, the sample volume was ~600 μL, which corresponded to a recommended tube filling height of 40 mm. Note that a slightly lower value of ~500 μL could have been used as well, but at the expense of more demanding shimming. Moreover, the active coil volume was ~200 μL (calculated considering an internal tube diameter of 4.2 mm and an active region height of 15 mm). Importantly, note that this value for the active coil volume is strictly probe-dependent.

2.3. NMR experiments

Typical acquisition parameters were used for both conventional and HR-MAS liquid-state NMR experiments. The presence in both cases of a gradient coil allowed us to use them for coherence selection and solvent signal suppression. The proton 90° RF pulse was 9 μs and 12 μs for the BBI and HR-MAS probes, respectively, while the fluorine 90° RF pulse was 11 μs (HR-MAS probe only). The WATERGATE spectra were acquired using a selective 180° RF pulse applied on the water resonance (4 ms, BRUKER shape file:
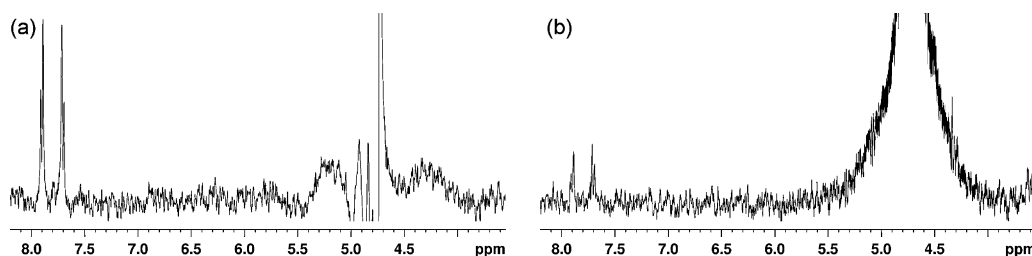
Fig. 1. Expanded view of the 400 MHz ^{1}H WATERGATE NMR spectra obtained on a sample of TFBA (2 μg) dissolved in a H_2O/D_2O (90/10, v/v) phosphate buffer (20 mM) at 300 K. The spectra shown in (a) and (b) were obtained using a HR-MAS and a conventional 5 mm liquid-state NMR probe head, respectively. The respective sample volumes were 20 and 600 μL, giving a TFBA concentration of (a) 525 μM and (b) 17.5 μM. In both cases, 128 transients were acquired and a 2-Hz exponential line broadening was applied prior to Fourier Transform (FT). The aromatic ^{1}H signals due to TFBA are located within the 7.5–8.0 spectral range. The residual water signal is shown at around 4.7 ppm.

Squa100.100). The saturation of the receptor resonances in the STD spectrum was ensured by using a train of 40 selective 90° RF pulses (50 ms, BRUKER shape file: Gaus10.1000), separated by a delay of 1 ms. The offset of the saturation pulses was alternatively switched between 0 ppm and +250 ppm, being on- and off-resonance with the receptor signals, respectively. A $T_{1\rho}$-filter was also used to remove the broad signals due to the fast relaxing species (the receptor). The WaterLOGSY spectrum was acquired by setting the carrier frequency on resonance with the water signal (∼4.7 ppm) and using a selective 180° RF pulse to inverse the water magnetization (10 ms, BRUKER shape file: Gaus10.1000). The mixing time was set to 1 s. Both the STD and WaterLOGSY experiments were combined with the WATERGATE solvent suppression scheme. The ^{19}F DOSY spectra were recorded using the bipolar gradient longitudinal eddy current delay pulse sequence proposed by Wu et al. [24]. The gradient coil of the HR-MAS probe head was calibrated to be 23 G cm^{-1} A^{-1} [21]. The diffusion time and gradient pulse duration were set to 80 ms and 1.6 ms, respectively, and 16 gradient values were used from 2% to 30% of the maximum gradient strength. Additional acquisition and processing parameters can be found in the captions to the figures.

3. Results and discussion

To illustrate the potential of HR-MAS for the analysis of mass-limited samples, the following protocol was applied. A sample containing 2 μg of TFBA, a ligand that is known to interact with HSA, was analyzed [25]. No HSA was used in this case. Fig. 1 compares the ^{1}H WATERGATE spectra of the experiments recorded on this sample with the same experimental conditions using HR-MAS (Fig. 1a) and conventional 5 mm liquid-state (Fig. 1b) NMR probe heads. While both spectra display a similar noise level, the TFBA signals are more intense in the former than in the latter case. A closer inspection of these spectra indicates that the S/N, as measured over a 200 Hz noise spectral region, equals 16.1 and 5.3 (Fig. 1a and b, respectively), which represents a 3-fold increase in S/N. This suggests that, with respect to the conventional liquid-state NMR probe head, the detection limit of the HR-MAS technique for mass-limited samples is improved by a factor of 3 or, equivalently, that the experimental time required for achieving a given S/N value can be reduced by almost one order of magnitude, which represents a significant advantage in case screening investigations ought to be performed.

At this point, it may be interesting to discuss the origin of the so-obtained 3-fold sensitivity enhancement. The difference in signal strength is among other things related to the difference in the absolute amount of spins that are detected. Considering the sample volumes of the HR-MAS (20 μL) and BBI (600 μL) probe heads, as well as their corresponding active coil volumes, 20 μL and 200 μL (see Section 2.2), one would expect a 600/200 difference in signal strength in favor of the HR-MAS probe head, which is very close indeed to that experimentally observed. Obviously,

other (probe-dependent) values for the sample and the active coil volumes would yield slightly different calculations, but the overall signal strength advantage of the HR-MAS probe head observed for mass-limited samples would still remain. However, other parameters influence the actual probe sensitivity. While sensitivity of NMR probe heads usually scale inversely with coil diameter [10], which again should favor the HR-MAS probe head, the truly significant parameter that determines the probe head sensitivity is the quality (Q) factor, which is indirectly revealed by the length of the 90° RF excitation pulse for a given amplifier power level. Experimentally, we used 12 μs and 9 μs for the HR-MAS and BBI probe heads, respectively, which indicates that the Q factor of the former was lower than that of the latter, in agreement with the fact the triple-resonance HR-MAS probe head used here was not optimized for ^{1}H but for ^{19}F detection. Clearly, higher Q probes would yield even higher sensitivity, but at the expense of possible radiation damping artifacts, which have been shown to arise even for small-volume probe heads [26]. In addition, note the slightly improved water signal suppression for the HR-MAS setup (Fig. 1a), as illustrated by the reduced line width of the residual water ^{1}H NMR signal at ∼4.7 ppm. This is due to the higher radiofrequency field homogeneity of HR-MAS probe heads, as the whole sample can be placed within the most homogeneous region of the coil.

Having demonstrated the sensitivity advantage of HR-MAS for the analysis of mass-limited samples, the next step was to verify that typical NMR experiments used to investigate intermolecular interactions could be readily performed in HR-MAS. To do so, another sample was prepared, which consisted of TFBA, glucose and another fluorine-bearing molecule (trifluoroethanol) in the presence of HSA. Literature data shows that glucose does not interact with HSA [25,27]. Higher concentrations were used in this case (10 mM for TFBA instead of 0.5 mM in Fig. 1) merely to avoid wasting experimental machine time. Totally equivalent results would be obtained with samples of lower concentrations, but at the expense of longer acquisition times. The HSA concentration was set to 0.1 mM (130 μg only for our HR-MAS setup), giving rise to a ligand/receptor ratio of 100:1, in agreement with previously reported data. More generally, note that the ligand/receptor ratio depends on the value of the association constant and the method used [4].

Two types of NMR experiments were recorded, namely Saturation Transfer Difference and WaterLOGSY, which currently represent the most versatile NMR techniques for the investigation of intermolecular interactions [3,4]. In contrast to STD, which is based on the saturation of the receptor NMR resonances, the Water-LOGSY experiment relies on the bulk water to detect the binding of ligands to proteins. Among the various WaterLOGSY experimental protocols that are available, the one chosen here relies on a selective inversion of the water magnetization, which is then transferred to the receptor and to the interacting ligands, whose signals thus appear out of phase with respect to those due to the non-interacting species. Fig. 2 shows the spectra obtained in both cases
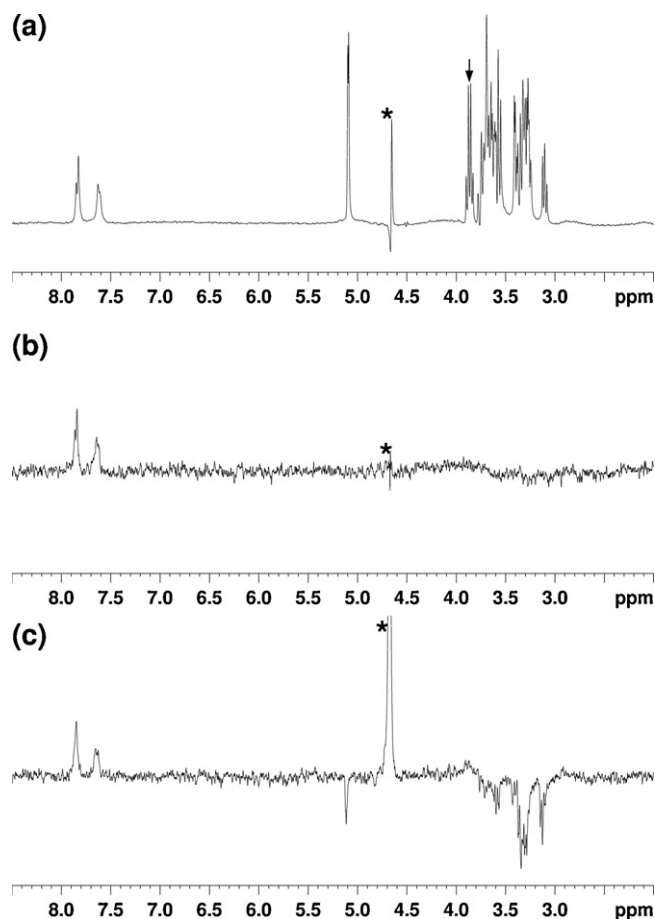
Fig. 2. Series of 400 MHz ^{1}H HR-MAS NMR spectra obtained on a liquid sample containing a mixture of TFBA (10 mM), glucose (30 mM), trifluoroethanol (10 mM) and HSA (0.1 mM) dissolved in a H_2O/D_2O (90/10, v/v) phosphate buffer (20 mM) at 300 K; (a) ^{1}H WATERGATE spectrum; (b) ^{1}H STD spectrum; (c) [1]H WaterLOGSY spectrum. The residual water signal at 4.7 ppm is indicated with a star (*), while the quadruplet signal (at ∼3.8 ppm) due to the CH_2 of trifluoroethanol (CF_3CH_2OH) is shown with a downward pointing arrow in (a). The ^{1}H signals of glucose (used as a control for non-interacting species) are located within the 3.0–4.0 spectral region, plus the anomeric ^{1}H signal at around 5.1 ppm. In (b), the glucose signals are eliminated whereas, in (c), they appear out of phase with respect to the TFBA signals, as expected for a non-interacting species in the WaterLOGSY experiment. Note that both of these last 2 experiments are intrinsically less sensitive than a simple pulse-acquire experiment (such as WATERGATE), which explains the large difference in S/N observed. As such, 128 transients were used in (a) whereas 256 were accumulated in (b) and (c). In all cases, a 2-Hz exponential line broadening was applied prior to FT.

(Fig. 2b and c, respectively), and compare them with the ^{1}H WATER-GATE spectrum used as a reference (Fig. 2a). In the STD spectrum, only the aromatic signals due to TFBA are observable. All the other signals due to glucose and trifluoroethanol were suppressed by phase cycling because these compounds did not interact with HSA. Again, note the almost perfect water signal suppression afforded by the HR-MAS probe head. In Fig. 2c, as expected, the phase of the TFBA signals (interacting ligand) appears positive while that of the glucose and trifluoroethanol signals (non-interacting species) is negative. Collectively, these results show that STD and Water-LOGSY spectra can be readily recorded in HR-MAS on liquid-state samples.

DOSY NMR experiments can also be performed to investigate intermolecular interactions, as illustrated in Fig. 3. It has already been shown in the literature that accurate self-diffusion coefficients could be measured for liquid samples in HR-MAS [21]. As such, ^{19}F DOSY were recorded on a third sample, containing TFBA (10 mM) and trifluoroethanol (10 mM) in the presence of HSA (2 mM) in
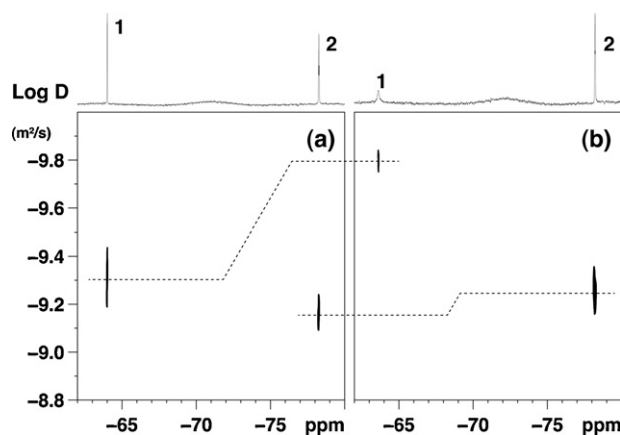

Fig. 3. ^{19}F DOSY HR-MAS NMR spectra recorded on a mixture of TFBA (10 mM) and CF_3CH_2OH (10 mM) dissolved in a H_2O/D_2O (90/10, v/v) phosphate buffer (20 mM) at 300 K in the absence (a) and presence (b) of HSA (2 mM). The corresponding ^{19}F spectra are reported on top. Signals **1** and **2** refer to TFBA (−64 ppm) and CF_3CH_2OH (−78 ppm), respectively. Chemical shifts are referenced with respect to $CFCl_3$ used as an external standard. The dashed grey lines on the DOSY maps are reported to illustrate the changes in the diffusion coefficient values observed between the two experimental setups (with and without HSA). 32 transients were accumulated for each of the 16 gradient values. In both cases, a 4-Hz exponential line broadening was applied prior to FT in the frequency dimension.

a phosphate buffer (20 mM, pH 7). The advantage of ^{19}F over ^{1}H detection is clear here, as no water suppression scheme is required. As can be seen, in the presence of HSA, the correlation spot due to TFBA is shifted toward lower diffusion coefficient values (Fig. 3b), indicating that TFBA interacts with HSA. This agrees with the significant exchange broadening observed for the ^{19}F TFBA resonance (top spectrum in Fig. 3b), revealing the presence of an intermediate exchange regime on the NMR timescale. In contrast, fast exchange was observed on the diffusion timescale [28], leading to the observation of an exchange-averaged diffusion coefficient, which value lies between those of the free and bound TFBA (assuming a two-site exchange model). Diffusion data can then be used to estimate the association constant, as described in Refs. [2,28]. In this experiment, a higher HSA concentration was used to ensure that the binding would induce a detectable change in the TFBA diffusion coefficient [2,28]. One important point to note in this case is the possible change in viscosity brought about by the presence of the protein in solution, as can be evidenced with the DOSY correlation cross-peak of the non-interacting species (CF_3CH_2OH), which is shifted slightly toward lower diffusion coefficient values in the presence of HSA, hereby revealing the corresponding increase in solution viscosity. All together, the diffusion coefficients reported in Fig. 3 allowed us to calculate the molar fraction of bound ligands (∼0.76), which agreed satisfactorily with the value that can be derived from literature data [28].

4. Conclusion

This work has shown that HR-MAS can be used with liquid solutions to analyze mass-limited samples. With respect to conventional 5 mm liquid-state NMR probe heads, HR-MAS offers a large reduction in sample volume requirement (at least one order of magnitude). This represents an important point, as biological macromolecules are not always easy to obtain in bulky quantity. In addition, typical NMR experiments used to investigate intermolecular interactions (STD, WaterLOGSY, DOSY) could be readily performed in HR-MAS, without any specific optimization of the acquisition parameters. Overall, the results indicate that the HR-MAS sensitivity for mass-limited samples can be significantly enhanced (a 3-fold increase in S/N was achieved in this

study). Equally important benefits of HR-MAS are the simplicity of the shimming procedure and the increased RF excitation field homogeneity (which allows for solvent signal suppression of higher quality). Collectively, these results suggest that HR-MAS is perfectly suited for high-throughput analysis because it allows one to work with stiff and easy-to-clean zirconia rotors, as opposed to fragile, glass capillary tubes. This point has been reinforced lately with the commercial availability of automatic sample changers. Finally, and most importantly in the framework of screening investigations, slightly heterogeneous samples, such as those resulting from the presence of semi-solid matters in the sample solution (as typically observed in the case of incomplete purification), can be readily analyzed in HR-MAS without deploring any significant loss of spectral resolution.

Acknowledgments

References

[1] M. Pellecchia, I. Bertini, D. Cowburn, C. Dalvit, E. Giralt, W. Jahnke, T.L. James, S.W. Homans, H. Kessler, C. Luchinat, B. Meyer, H. Oschkinat, J. Peng, H. Schwalbe, G. Siegal, Perspectives on NMR in drug discovery: a technique comes of age, Nat. Rev. Drug Discov. 7 (2008) 738–745.
[2] L. Fielding, NMR methods for the determination of protein-ligand dissociation constants, Prog. Nucl. Magn. Reson. Spectrosc. 51 (2007) 219–242.
[3] C. Dalvit, NMR methods in fragment screening: theory and a comparison with other biophysical techniques, Drug Discov. Today 14 (2009) 1051–1057.
[4] B. Meyer, T. Peters, NMR spectroscopy techniques for screening and identifying ligand binding to protein receptors, Angew. Chem. Int. Ed. 42 (2003) 864–890.
[5] R. Campos-Olivas, NMR screening and hit validation in fragment based drug discovery, Curr. Top. Med. Chem. 11 (2011) 43–67.
[6] M. Mayer, B. Meyer, Characterization of ligand binding by saturation transfer difference NMR spectroscopy, Angew. Chem. Int. Ed. 38 (1999) 1784–1788.
[7] K. Feher, P. Groves, G. Batta, J. Jimenez-Barbero, C. Muhle-Goll, K.E. Kover, Competition saturation transfer difference experiments improved with isotope editing and filtering schemes in NMR-based screening, J. Am. Chem. Soc. 130 (2008) 17148–17153.
[8] J.L. Wagstaff, S. Vallath, J.F. Marshall, R.A. Williamson, M.J. Howard, Two-dimensional heteronuclear saturation transfer difference NMR reveals detailed integrin alpha v beta 6 protein–peptide interactions, Chem. Commun. 46 (2010) 7533–7535.
[9] Y.L. Xia, Q. Zhu, K.Y. Jun, J.C. Wang, X.L. Gao, Clean STD-NMR spectrum for improved detection of ligand–protein interactions at low concentration of protein, Magn. Reson. Chem. 48 (2010) 918–924.
[10] G.E. Martin, Small-volume and high-sensitivity NMR probes, Annu. Rep. NMR Spectrosc. 56 (2005) 1–96.
[11] D. Bourry, D. Sinnaeve, K. Gheysen, B. Fritzinger, G. Vandenborre, E.J.M. Van Damme, J.M. Wieruszeski, G. Lippens, C. Ampe, J.C. Martins, Intermolecular interaction studies using small volumes, Magn. Reson. Chem. 49 (2011) 9–15.
[12] W.P. Power, High-resolution magic angle spinning-enabling applications of NMR spectroscopy to semi-solid phases, in: G. Webb (Ed.), Annu. Rep. NMR Spectrosc., London, 2011, pp. 111–156.
[13] G. Lippens, M. Bourdonneau, C. Dhalluin, R. Warrass, T. Richert, C. Setharaman, C. Boutillon, M. Piotto, Study of compounds attached to solid supports using high resolution magic angle spinning NMR, Curr. Org. Chem. 3 (1999) 147–169.
[14] J.C. Lindon, O.P. Beckonert, E. Holmes, J.K. Nicholson, High-resolution magic angle spinning NMR spectroscopy: application to biomedical studies, Prog. Nucl. Magn. Reson. Spectrosc. 55 (2009) 79–100.
[15] M. Malet-Martino, U. Holzgrabe, NMR techniques in biomedical and pharmaceutical analysis, J. Pharm. Biomed. Anal. 55 (2011) 1–15.
[16] S. Sanchez, F. Ziarelli, S. Viel, C. Delaurent, S. Caldarelli, Improved solid-state NMR quantifications of active principles in pharmaceutical formulations, J. Pharm. Biomed. Anal. 47 (2008) 683–687.
[17] M. Piotto, K. Elbayed, J.-M. Wieruszeski, G. Lippens, Practical aspects of shimming a high resolution magic angle spinning probe, J. Magn. Reson. 173 (2005) 84–89.
[18] M. Delepierre, A. Prochnicka-Chalufour, J. Boisbouvier, L.D. Possani, Pi7, an orphan peptide from the scorpion pandinus imperator: a 1H NMR analysis using a nano-NMR probe, Biochemistry 38 (1999) 16756–16765.
[19] E. Kupce, P.A. Keifer, M. Delepierre, Adiabatic TOCSY MAS in liquids, J. Magn. Reson. 148 (2001) 115–120.
[20] K. Elbayed, B. Dillmann, J. Raya, M. Piotto, F. Engelke, Field modulation effects induced by sample spinning: application to high-resolution magic angle spinning NMR, J. Magn. Reson. 174 (2005) 2–26.
[21] S. Viel, F. Ziarelli, G. Pages, C. Carrara, S. Caldarelli, Pulsed field gradient magic angle spinning NMR self-diffusion measurements in liquids, J. Magn. Reson. 190 (2008) 113–123.
[22] J. Klein, R. Meinecke, M. Mayer, B. Meyer, Detecting binding affinity to immobilized receptor proteins in compound libraries by HR-MAS STD NMR, J. Am. Chem. Soc. 121 (1999) 5336–5337.
[23] S. Schauff, V. Friebolin, M.D. Grynbaum, C. Meyer, K. Albert, Monitoring the interactions of tocopherol homologues with reversed-phase stationary HPLC phases by H-1 suspended-state saturation transfer difference high-resolution/magic angle spinning NMR spectroscopy, Anal. Chem. 79 (2007) 8323–8326.
[24] D. Wu, A. Chen, C.S. Johnson Jr., An improved diffusion-ordered spectroscopy experiment incorporating bipolar-gradient pulses, J. Magn. Reson., Ser. A 115 (1995) 260–264.
[25] M.L. Liu, J.K. Nicholson, J.C. Lindon, Analysis of drug–protein binding using nuclear magnetic resonance based molecular diffusion measurements, Anal. Commun. 34 (1997) 225–228.
[26] V.V. Krishnan, Radiation damping in microcoil NMR probes, J. Magn. Reson. 179 (2006) 294–298.
[27] A. Chen, M.J. Shapiro, NOE pumping. 2. A high-throughput method to determine compounds with binding affinity to macromolecules by NMR, J. Am. Chem. Soc. 122 (2000) 414–415.
[28] L.H. Lucas, C.K. Larive, Measuring ligand–protein binding using NMR diffusion experiments, Concepts Magn. Reson. A 20A (2004) 24–41.

Evaluation of laser diode thermal desorption (LDTD) coupled with tandem mass spectrometry (MS/MS) for support of in vitro drug discovery assays: Increasing scope, robustness and throughput of the LDTD technique for use with chemically diverse compound libraries

Iain Beattie [a,*], Aaron Smith [a], Daniel J. Weston [a], Peter White [a,1], Simon Szwandt [b], Laura Sealey [c]

[a] Discovery DMPK, AstraZeneca R&D Charnwood, Bakewell Road, Loughborough LE11 5RH, UK
[b] Thermo Fisher Scientific, Boundary Way, Hemel Hempstead HP2 7GE, UK
[c] Department of Chemistry, Loughborough University, Loughborough LE11 3TU, UK

ABSTRACT

Within the drug discovery environment, the key process in optimising the chemistry of a structural series toward a potential drug candidate is the design, make and test cycle, in which the primary screens consist of a number of in vitro assays, including metabolic stability, cytochrome P450 inhibition, and time-dependent inhibition assays. These assays are often carried out using multiple drug compounds with chemically diverse structural features, often in a 96 well-plate format for maximum time-efficiency, and are supported using rapid liquid chromatographic (LC) sample introduction with a tandem mass spectrometry (MS/MS) selected reaction monitoring (SRM) endpoint, taking around 6.5 h per plate. To provide a faster time-to-decision at this critical point, there exists a requirement for higher sample throughput and a robust, well-characterized analytical alternative. This paper presents a detailed evaluation of laser diode thermal desorption (LDTD), a relatively new ambient sample ionization technique, for compound screening assays. By systematic modification of typical LDTD instrumentation and workflow, and providing deeper understanding around overcoming a number of key issues, this work establishes LDTD as a practical, rapid alternative to conventional LC–MS/MS in drug discovery, without need for extensive sample preparation or expensive, scope-limiting internal standards. Analysis of both the five and three cytochrome P450 competitive inhibition assay samples by LDTD gave improved sample throughput (0.75 h per plate) and provided comparable data quality as the IC_{50} values obtained were within 3 fold of those calculated from the LC–MS/MS data. Additionally when applied generically to a chemically diverse library of over 250 proprietary compounds from the AstraZeneca design, make and test cycle, LDTD demonstrated a success rate of 98%.

© 2011 Elsevier B.V. All rights reserved.

1. Introduction

The overriding goal of the pharmaceutical industry is to develop new or improved treatment for disease, the cost of which has been slowly escalating over the last decade and was recently estimated to be in the region of one billion (US) dollars per product-to-market [1]. To sustain the critical research and development (R&D) process, the key requirements across the pharmaceutical industry have been earlier compound attrition and shorter time-to-market, to help bring concomitant cost savings and recover revenue. In the early 1990s, one of the main causes of attrition was poor

pharmacokinetic (PK) performance, accounting for around 40% of all compound failures [2]. With the introduction of in vitro assays and early determination of in vivo PK properties in the drug discovery phase, this figure decreased to around 10% within 10 years [2], suggesting that high-throughput ADME (absorption, distribution, metabolism and elimination) screens resulted in selection of compounds with optimised properties to have a better chance of success in man.

The desire to design out other potential liabilities, borne out of continual early stage improvements, has resulted in an increased number of in vitro screens; some common ADME assays include metabolic stability, cytochrome P450 (CYP) inhibition, CYP induction, permeability and hepatic uptake to name a few of the ADME assays, in addition to physicochemical assays such as solubility, log D, parallel artificial membrane permeation assay (PAMPA) and plasma protein binding (PPB). These assays are used to screen

---

* Corresponding author. Tel.: +44 0 1625 582828; fax: +44 0 1625 230614.
 E-mail address: iain.beattie@astrazeneca.com (I. Beattie).
[1] Current address: BASi, Abbey Park, Kenilworth, Warwickshire CV8 2LY, UK.

compounds synthesized by medicinal chemists and identify possible candidate drugs, in liaison with a cross-function project team, for progression toward resource-intensive in vivo assays. Currently within AstraZeneca, the front-line ADME screening assays of metabolic stability, cytochrome P450 (CYP) inhibition, and CYP induction are run weekly with a three-day turnaround time, allowing medicinal chemists to act rapidly on the data provided and shape future synthesis or provide ongoing refinement of a chemical series. Around 200 new (proprietary) compounds are screened each week in these 96 well-plate format assays, which have conventional liquid chromatography (LC) separation with tandem mass spectrometry (MS/MS) analytical end-points, taking nearly 2 days (instrument time) to analyze. Key technologies underpinning this achievement are the development of automated liquid handlers, programmed to carry out a variety of different assays with minimal human intervention; LC–MS/MS to provide robust and selective analytical methods to analyze the large number of samples generated by the assays; and intelligent software to process and interrogate the data generated [3–5]. When running a tight timeline such as this, the two-day sample turnaround is only manageable if there are no problems, such as with instrumentation, for example – otherwise the deadline for delivery is missed for that week, having a detrimental impact on time-to-decision and drug project progression. To meet the weekly assay cycle time for over 200 compounds requires significant (dedicated) LC–MS/MS resource, however actual analysis has always been the rate-limiting step, in terms of making advances in sample turnaround times. Reducing analytical run time means higher sample capacity, faster response-to-query and the need for fewer dedicated instruments. A number of methods have been published to increase the turnaround time, including cassette analysis, cassette incubations for CYP inhibition assays, fast chromatography using monolithic columns [6], staggered chromatography [7] and ultra-performance liquid chromatography (UPLC) [8,9] with columns capable of operating at very high pressure, providing higher resolution, sensitivity and throughput (lower run time) than conventional high performance liquid chromatography (HPLC). That said, however, the time scale for all of these approaches is still measured in minutes per sample, not seconds. To provide a step-change in faster delivery of data to projects at this critical point, there exists a requirement for higher sample throughput and a robust, well-characterized analytical alternative to conventional LC–MS/MS methodologies.

Recent disclosure of the laser diode thermal desorption (LDTD) interface [10] presents a number of possibilities for meeting this demand, and forms part of the wider field of ambient sampling and ionization MS which has grown rapidly in the last 7 years [11–13]. In keeping with many of the seminal ambient MS technologies, such as desorption electrospray ionization (DESI) [14,15], direct analysis in real-time (DART) [16], and extractive electrospray (EESI) [17], the LDTD technique requires little-to-no sample preparation and provides rapid sample desorption and subsequent ionization, both of which are temporally and spatially decoupled from one another. Indeed, it is true to say that these new ambient MS techniques have already begun challenging convention in many areas of analytical science [18] and the pharmaceutical industry, including the process development [19]. The LDTD instrument can be retro-fitted to multiple vendor ion-source housings and relies upon thermal desorption followed by sample ionization in the gas-phase. Briefly, a liquid sample is deposited in to a metal well insert of a proprietary LazWell sample plate (Phytronix Technologies Inc., Quebec, Canada) and allowed to dry. A laser heats the underside of the metal sample well, increasing laser power over a number of seconds to thermally desorb the sample into the mass spectrometer ion source, where subsequent ionization is effected using atmospheric pressure chemical ionization (APCI). This produces a LDTD sample desorption profile of a few seconds in width, akin to the

shape of a LC peak, which can be captured and interrogated using existing MS software. Typical run times are in the region of 10–20 s per sample.

Although this approach has shown potential to increase throughput for various in vitro assays in drug discovery, there have been a limited number of applications disclosed in the literature; most have been for ADME assays targeting the same analytes each time, such as CYP inhibition [10] and plasma samples [20,21], largely with carryover-free analytical performance [9]. In these cases, however, costly isotopically labeled internal standards or structural analogues were used to compensate for the high variability (% CV) of the response by LDTD, often limiting analytical scope. Initial thoughts from the global AstraZeneca DMPK community, following initial evaluation of the LDTD system, were that it could be used for some assays but only using an internal standard, primarily due to the poor reproducibility (% CV) across the sample plate, and different considerations for sample preparation would be required depending on the sample matrix. Of equal concern, it was noticed that there were a significant percentage of proprietary compounds which did not perform well using the LDTD technique, which precluded using the LDTD for the metabolic stability assay, which was by far the largest (in terms of numbers of samples) and most chemically diverse assay. As a result, it was decided to carry out a long-term evaluation of the LDTD system, interfaced to a Quantum Ultra triple quadrupole MS (Thermo Fisher Scientific, San Jose, CA, USA) to determine how and why these limitations existed on a fundamental level, whether they could be overcome, and if LDTD could be used instead of LC–MS for a range of in vitro ADME assays used in drug discovery at AstraZeneca. The results of this evaluation are presented herein with frank assessment of how the systematic modification of typical LDTD instrumentation and workflows has improved the performance of LDTD–MS/MS within the drug discovery environment.

2. Experimental

2.1. Chemicals, reagents and materials

Gradient quality methanol was sourced from Romil Ltd. (Cambridge, UK); HPLC grade acetonitrile and DMSO from Thermo Fisher Scientific (Loughborough, Leicestershire, UK). Diclofenac, 4-hydroxydiclofenac, bufuralol, hydroxybufuralol, phenacetin, acetaminophen, mephenytoin, 4-hydroxymephenytoin, midazolam, 1-hydroxymidazolam, bupropion, 1-hydroxybupropion, amodiaquine, N-desmethylamodiaquine, erythromycin and clomiphene were obtained from Sigma–Aldrich (Dorset, UK). Pitavastatin was obtained from Sequoia Research Products (Pangbourne, UK). A selection of 250 proprietary AstraZeneca compounds, covering a wide range of physicochemical properties, was sourced from the in-house compound management bank (AstraZeneca R&D Charnwood). All chemicals and reagents were used as received without further purification.

2.2. Instrumentation

The LDTD source (Phytronix Technologies Inc., Quebec, Canada) utilized proprietary LazWell[TM] 96 well-plates (Phytronix Technologies Inc., Quebec, Canada) for sample introduction, and was mounted on a TSQ Quantum Ultra tandem quadrupole mass spectrometer (Thermo Fisher Scientific, San Jose, CA, USA), operated in selected reaction monitoring (SRM) mode and controlled using Xcalibur (v2.1) and QuickQuan (v2.3) (both Thermo Fisher Scientific). The LDTD source was held at 270 °C with an initial sweep gas flow of 0.3 (arbitrary units) with air as the carrier gas, which was controlled via the auxilliary gas setting and bubbled through

a water reservoir. This ensured increased water vapour in-source to aid the atmospheric chemical ionization (APCI) process. Laser power and pattern were varied dependant on the type of samples being analyzed (see next section). QuickQuan software was used to determine the appropriate source conditions for each compound (i.e. tube lens voltage, collision energy and resultant product ion for SRM). Samples were spiked onto the Lazwell plates, initially using an eight channel multi-pipette and later on a Hamilton Micro-lab STAR Automation platform (Hamilton Bonaduz AG, Bonaduz, Switzerland).

2.3. Preparation of solutions

Stock solutions of the CYP inhibition compounds were made up in 3:1 (v/v) methanol:water. Solutions for optimisation were prepared at 100 μmol/L in 3:1 (v/v) methanol:water and 10 μL spiked into each well. Clomiphene was prepared at 10 ng/mL in 3:1 (v/v) methanol:water. Erythromycin was prepared at 5 μg/mL in acetonitrile and all AstraZeneca compounds were prepared in DMSO at 5 mmol/L.

2.4. Cytochrome P450 competitive inhibition assays

Two cocktail cytochrome P450 competitive inhibition assays which are currently used within AstraZeneca with an LC–MS end point were the first assays to determine whether LDTD could be used instead. The methodology behind both of these assays have already been published; the first assay including five cytochrome P450s – 1A2, 2C9, 2C19, 2D6 and 3A4 [22]; the second including three cytochrome P450s – 2B6, 2C8 and 3A5 [23].

3. Results and discussion

3.1. Linearity and reproducibility

Prior to running real samples, the reproducibility and linearity of the LDTD source were evaluated using clomiphene, which is recommended by the manufacturer (Phytronix Technologies Inc.) as a system suitability test (SST) and should generate a coefficient of variance (% CV) within 7%. Reproducibility was one of the issues highlighted as being poor when analyzing the CYP inhibition compounds or standard compounds, both within AstraZeneca and in the literature [10,20,21], thus necessitating use of expensive, scope-limiting internal standards. The reproducibility was tested by measuring the % CV across 12 wells by spotting 2 μL of a 10 ng/mL solution of clomiphene. A laser pattern of a 2 s ramp up to 40% maximum power with a 2 s hold was used for this work. A % CV of 7% was obtained for clomiphene on the system and it was decided to run this every day prior to running samples to confirm the system performance. Linearity was assessed using the same laser pattern over two ranges, 10–1000 ng/mL and 1–75 ng/mL. The calibration curves generated are shown in Fig. 1(A) and (B) with R^2 values of 0.9876 and 0.9970, respectively. These data demonstrate that the
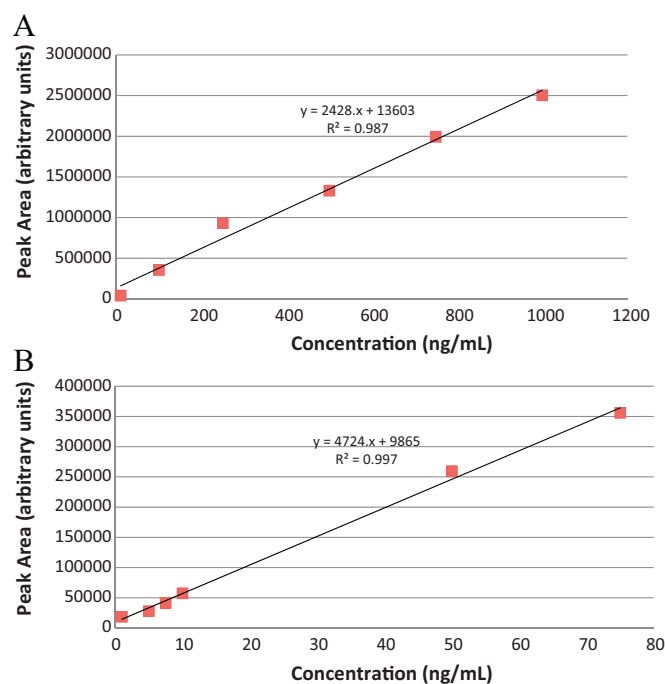

Fig. 1. Calibration curves showing the linearity of the LDTD experiment – (A) 10–1000 ng/mL; (B) 1–75 ng/mL.

system is capable of generating low % CVs and is linear over 3 orders of magnitude for clomiphene. The objective is to try and replicate this for other compounds.

3.2. Sample desorption: optimising laser pattern

Evaluation of the laser patterns for pure samples was completed using a 200 ng/mL cassette of 3 clinically relevant compounds in 3:1 (v/v) MeOH:H$_2$O. The compounds used were 1-hydroxybupropion, 1-hydroxymidazolam, and N-desmethylamodiaquine, which were the metabolites for three of the CYP inhibition assays. 2 μL of the solution was spiked into 12 wells for each laser pattern. The results are summarized in Table 1 and, although there was only a few percent variation for the average of the three compounds, the 2 s ramp to 40% maximum laser power with a 2 s hold was selected as it gave the lowest % CV for each of the three compounds as well as producing the best peak shape, important for easier peak integration.

As the assays for which the LDTD was intended to support would involve biological matrix, the next step was to determine what effect the matrix would have on the peak shape and sensitivity. A cassette of four AstraZeneca compounds at a concentration of 500 ng/mL were spiked into a blank rat hepatocyte incubation sample which was then quenched 4:1 (v/v) with methanol and 2 μL of sample spiked into the wells and analyzed initially using the optimal laser pattern obtained for pure standards (vide infra). The peaks

Table 1
Showing the average % CVs for 1-hydroxybupropion, 1-hydroxymidazolam and N-desmethylamodiaquine using a variety of laser patterns.

| Laser pattern	Average % CV (intra-compound, inter-compound)			
	1-Hydroxybupropion	1-Hydroxymidazolam	N-Desmethylamodiaquine	Average % CV
2 SecRamp_30%	13.77	25.70	22.58	20.68
3SecRamp_30%	11.73	42.60	44.56	32.96
2SecRamp_40%	9.82	23.68	23.47	18.99
3SecRamp_40%	11.74	30.76	24.09	22.20
2SecRamp_50%	15.62	32.60	19.98	22.73
3SecRamp_50%	15.17	32.43	18.62	22.07
4Sec_40%_NOHOLD	12.71	28.59	31.54	24.28
4Sec_50%_NOHOLD	10.61	24.24	22.26	19.04
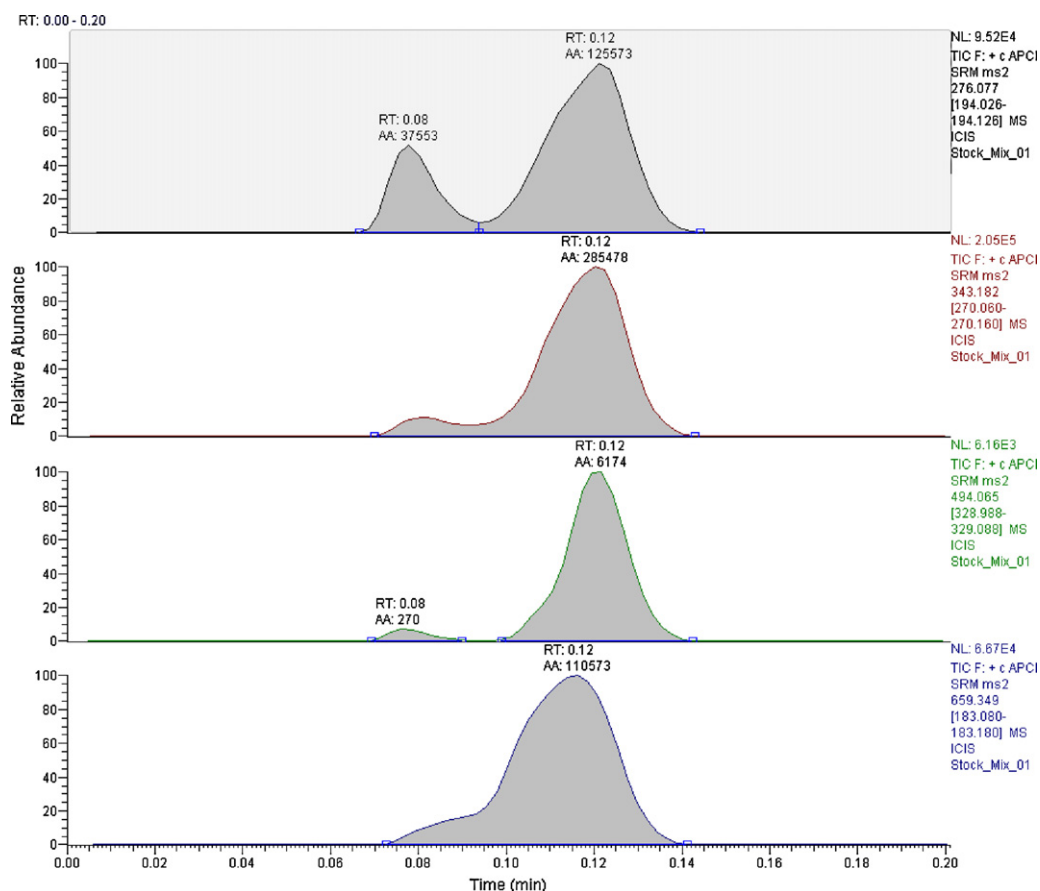
Fig. 2. LDTD peak shapes obtained for 4 AstraZeneca compounds in rat hepatocytes using a 2 s ramp to 40% maximum laser power with a 2 s hold.

obtained using this laser pattern (Fig. 2) were of poor quality, being broad and in three of the traces forming two peaks. This is most likely due to the quenched sample containing high levels of protein or buffer salts from the cell media which results in a thicker layer in the centre of the dried spot on drying, tapering off to a thin layer at the well edges (Fig. 3). When the metal surface of the well is heated by the laser, the thinner outer part of the dried sample desorbs first, resulting in the first peak, followed closely by the larger second peak as the thicker part of the dried sample is desorbed. This peak shape is not acceptable for good integration and there is some concern as to whether the dried sample is fully desorbed from the plate.

To improve this, the sample was further diluted and the laser pattern changed to ensure more complete desorption of the sample and minimize the formation of two (split) peaks. The effect of using a faster laser ramp with a longer hold is shown in Fig. 4, where the faster ramp has virtually removed the two peaks observed before
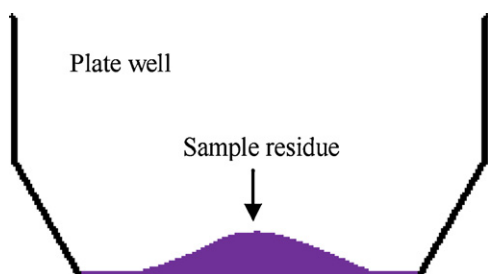

Fig. 3. Diagram representing the likely shape of the dried spot residue in the base of the LazWell plate sample well.

and the longer hold has resulted in a slight increase in peak area. As a result, it is clear that optimal sample dilution conditions and laser profile has to be determined for each type of sample matrix.

3.3. Sample ionization: LDTD and MS source optimisation

Source conditions were another area that could have an effect on LDTD performance; primarily the sweep gas and transfer line temperature, but also the water vapour content of the air used as the carrier gas which is required to aid the APCI process. Initial work was carried out using a sweep gas setting of 0.3 (arbitrary units) with a transfer line temperature of 270 °C, as recommended by the manufacturer, with air as the carrier gas plumbed directly into the LDTD source. It was suggested that using a lower temperature in the region of 150 °C with no sweep gas would increase the response and lower the % CV. This was tested out by using the same four compounds used to optimise the laser pattern in rat hepatocyte matrix, using pure solutions at 500 ng/mL in 3:1 (v/v) methanol:water. The results, shown in Table 2, indicated that running with the sweep gas turned off generally reduced % CVs at both high and low temperatures. Running at the lower temperature did improve peak area in some cases, but % CVs were much higher. The set of optimised conditions were chosen as no sweep gas with the higher temperature (270 °C), as they gave the best combination of low % CV and higher peak areas.

When trying to optimise a wide range of compounds using QuickQuan, it was noticed that a number of compounds failed to optimise. Examination of the QuickQuan optimisation reports showed that most of the compounds had a weak molecular ion but a strong fragment ion 18 Da less than the expected molecular ion, indicating a loss of water, which was consistent with their
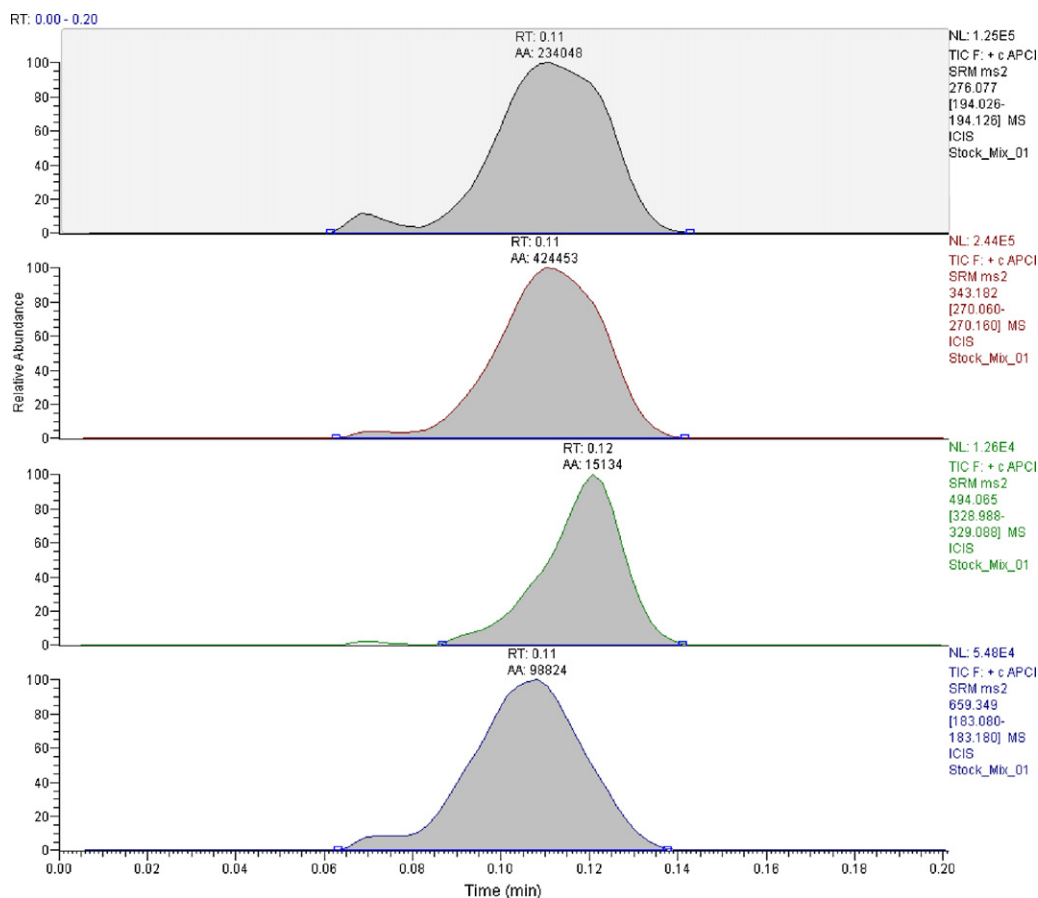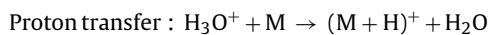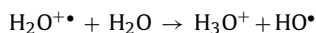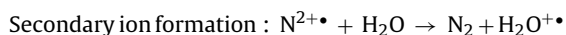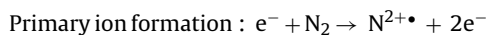
Fig. 4. Improved LDTD peak shapes obtained for 4 AstraZeneca compounds in rat hepatocytes using a 1 s ramp to 40% maximum laser power with a 3 s hold.

structures having a labile hydroxyl group that would result in a net loss of H_2O. On further discussion with Thermo Fisher Scientific, it was suggested that if the water content of the gas flowing into the source fell below 5 parts-per-million (ppm), the LDTD sensitivity could be significantly reduced. The reason for this is that the APCI reaction process consists of a series of reactions culminating in ionization of the analyte by means of proton transfer from a secondary ion, as shown below:

Primary ion formation : $e^- + N_2 \rightarrow N^{2+\bullet} + 2e^-$

Secondary ion formation : $N^{2+\bullet} + H_2O \rightarrow N_2 + H_2O^{+\bullet}$

$H_2O^{+\bullet} + H_2O \rightarrow H_3O^+ + HO^{\bullet}$

Proton transfer : $H_3O^+ + M \rightarrow (M + H)^+ + H_2O$

In conventional APCI, when LC is the sample inlet method, there would be an excess of solvent vapour, such as methanol and water from the LC eluent, which would be available for the secondary ion process. On entering the source, the analyte would most likely undergo proton transfer, which would be less energetic, resulting in primarily a protonated molecular ion. In the absence of sufficient solvent vapour, such as with a solvent-free ionization source like LDTD, the analyte would be ionized as part of the secondary ion process which, being more energetic, would result in cleavage of the more labile bonds – as shown in Fig. 5 for a pitavastatin standard in 3:1 (v/v) methanol:water at 5 μg/mL. The spectrum shows a very weak molecular ion at m/z 422, with much stronger fragment ions at m/z 404 and 358 corresponding to a loss of H_2O and CH_2O_2, respectively. The carrier gas was bubbled through water and allowed to equilibrate before running pitavastatin; the results

Table 2
Effect of transfer capillary temperature and sweep-gas flow on % CV and average MS peak area for four AstraZeneca compounds.

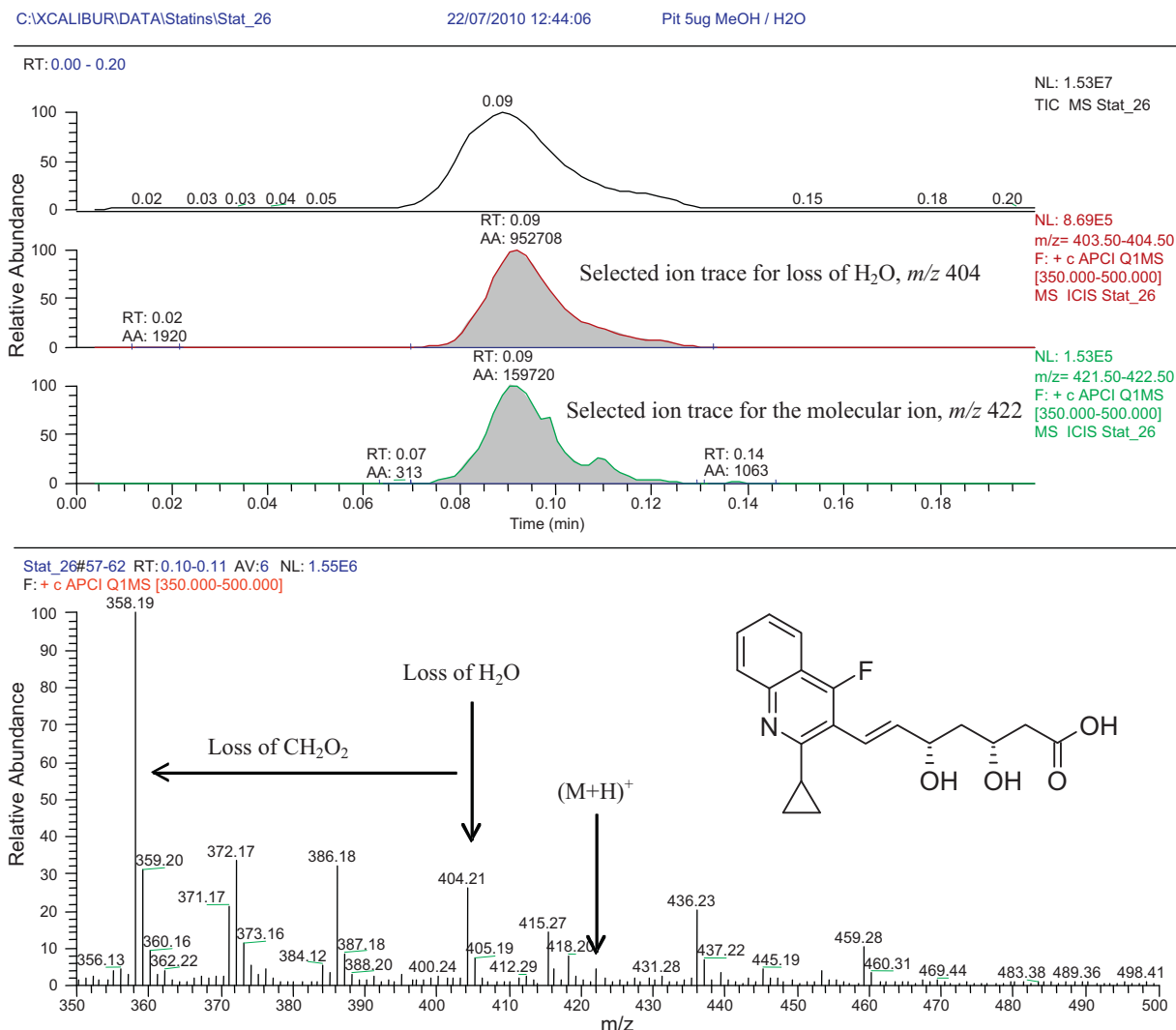| Transfer capillary temperature (°C)	Sweep gas		Compound name			
			AZ–1	AZ–2	AZ–3	AZ–4
150	On	Average peak area	108,453	12,717	35,318	32,292
		% CV	14.98	47.40	41.76	35.64
150	Off	Average peak area	127,847	4890	21,824	9949
		% CV	8.10	26.85	11.36	27.57
270	On	Average peak area	361,592	6220	29,114	23,519
		% CV	16.96	9.44	28.63	3.75
270	Off	Average peak area	347,413	5939	31,419	17,777
		% CV	7.36	24.36	6.63	7.64

Fig. 5. APCI–MS spectrum of pitavastatin obtained *via* LDTD without water vapour added to the carrier gas, demonstrating the significant fragmentation occurring (molecular ion *m/z* 422).

(Fig. 6) were markedly different with a 20-fold increase in response for the molecular ion, whilst the fragment ions remained largely unchanged. Although water content of the carrier gas will vary across different laboratories, clearly the one used here was quite low. Furthermore, as adding the water vapour did not have a detrimental effect on other compounds, it was decided to continue using this revised set-up for future work.

3.4. Pre-coating the LazWell plate

It was observed that when spiking low levels of compounds on to the plate surface as standard solutions in 1:1 (v/v) methanol/water at around 0.1 µg/mL, which would be around the top concentrations used for the main assays, the responses were often very low

and the variability of response very high. It was suspected that the compounds were binding to the metal foil surface, which forms the base of the well-plate. An investigation into the effect of pre-coating the metal surface with a sacrificial compound was carried out. A number of high-molecular weight compounds were evaluated to minimize isobaric interferences for small molecules (data not shown) and the one selected was erythromycin, which was spiked onto a clean plate (10 µL of a 5 µg/mL solution in acetonitrile). This ensured that the drop spread evenly over the plate coating the whole surface and, as it dried so quickly, the sample solution (2 µL) could be added on top as normal. This was tried initially for five commercially available compounds and significantly improved both the % CV and intensity of response. The effect on % CV is shown in Table 3 where it is clear that coating the plate with

Table 3
% CV for five commercially available compounds comparing treated and uncoated plate.

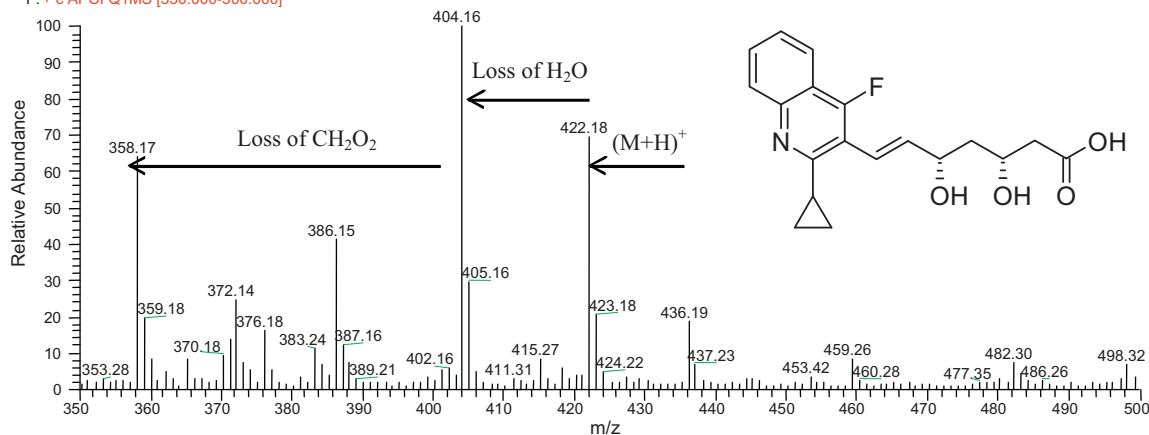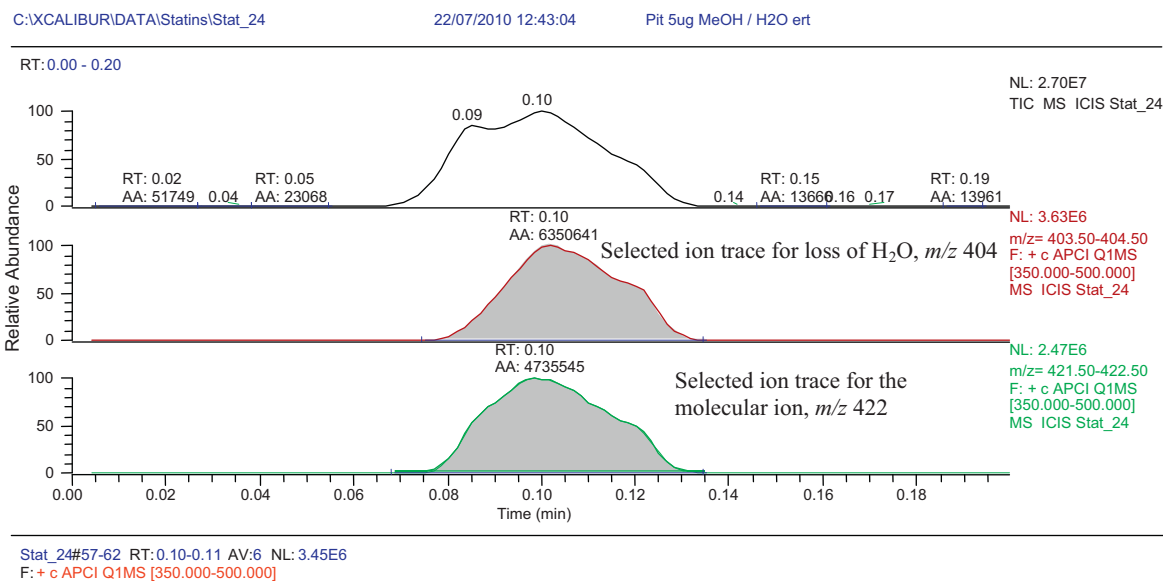|	% CV					
	Paracetamol	Hydroxybufuralol	1-Hydroxymidazolam	4-Hydroxymephenytoin	4-Hydroxydiclofenac	Average
Clean plate	10.85	12.90	61.91	18.77	15.41	23.97
Erythromycin	6.30	4.57	4.68	6.27	15.24	7.41

Fig. 6. APCI–MS spectrum of pitavastatin obtained *via* LDTD with the carrier gas bubbled through water to increase the water vapour content of the carrier gas demonstrating the reduced fragmentation occurring (molecular ion *m/z* 422).

erythromycin dramatically reduced the variability of the response. The effect of coating the plate on the response is equally dramatic with gains of up to 20-fold gain in peak area, graph shown in Fig. 7. Ten AstraZeneca compounds covering a range of physical chemical properties were also compared for their response, graph shown
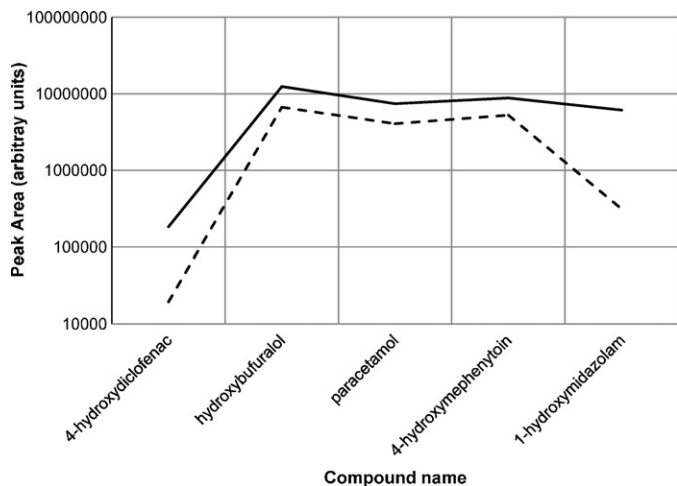
in Fig. 8, and the result was the same with gains of between 4 and 1000-fold in response due to the erythromycin coating on the metal surface. It is clear that the metal surface has a significant capacity for adsorbing compounds and in order to be able to run standard compounds effectively then the plate surface needs to be treated prior to spotting the sample on. This may not be so much of an issue

Fig. 7. Graph comparing LDTD response for coated (solid line) and uncoated plates (dotted line) for five commercially available compounds.
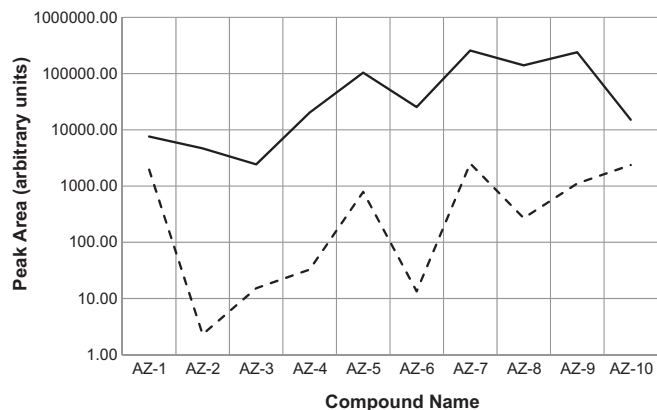

Fig. 8. Graph comparing LDTD response for coated (solid line) and uncoated (dotted line) plates for ten AstraZeneca compounds covering a wide range of physicochemical properties.

with biological matrices which will contain an excess of proteins, peptides and other compounds from the matrix that will compete with the analyte for the binding sites.

3.5. LDTD and SRM (MS/MS) optimisation

As the LDTD approach is targeted at high-throughput in vitro assays, which are normally run on triple quadrupole (LC–MS) instruments using SRM methods, there needs to be an efficient method to optimise a large number of new compounds at a time. To that end, the QuickQuan software (Thermo Fisher Scientific) used for LC–MS optimisation was modified for the LDTD workflow. The optimisation process requires five laser shots of the same compound to identify the parent ion, optimise the tube lens in positive ion mode, optimise the tube lens in negative ion mode, obtain a product ion scan in the most sensitive ion mode and finally optimises collision energy and determines the most intense product ion and creates the selected reaction monitoring (SRM) method. Traditionally this required spiking 5 different wells with the same compound, which would only allow 19 compounds to be optimised per plate, requiring 5 plates for a run of approx. 100 compounds for a typical metabolic stability assay, which would result in an excessive (costly) use of plates. By spiking each well with 10 µL of a 100 µmol/L solution into a single well, and using a 2 s ramp to 40% maximum laser power with a 2 s hold, it was found there was

enough drug material for five shots from one well. This allowed 96 compounds to be optimised from a single plate in a single LDTD run taking 3 h. This method has been tested using over 250 proprietary AstraZeneca compounds, covering a wide range of chemistries and properties, with a 98% success rate. For optimisation runs it was found that used plates could be washed and re-used with no impact on performance, thus saving on buying new plates. One of the issues which had been observed within AstraZeneca of only a limited range of chemistries working with LDTD initially, may well have been due to a combination of a dry carrier gas and sample adsorption on to the plate. In this work, by using 10 µL of a 100 µmol/L solution to optimise, adsorption appeared minimal and of little detriment. It is worth noting the QuickQuan software, proprietary to Thermo Fisher instrumentation, was key in providing successful automated optimisation (98% success) for such a large number of compounds in an expedient manner.

3.6. Five cytochrome P450 competitive inhibition assay

Having resolved a number of the issues and now having a much better understanding of the system, the next step was to replicate the assays currently being run by conventional LC–MS/MS methods. If successful then LDTD could run the assays in a significantly shorter time period. The first assay to concentrate on was the five cytochrome P450 competitive inhibition assay currently used
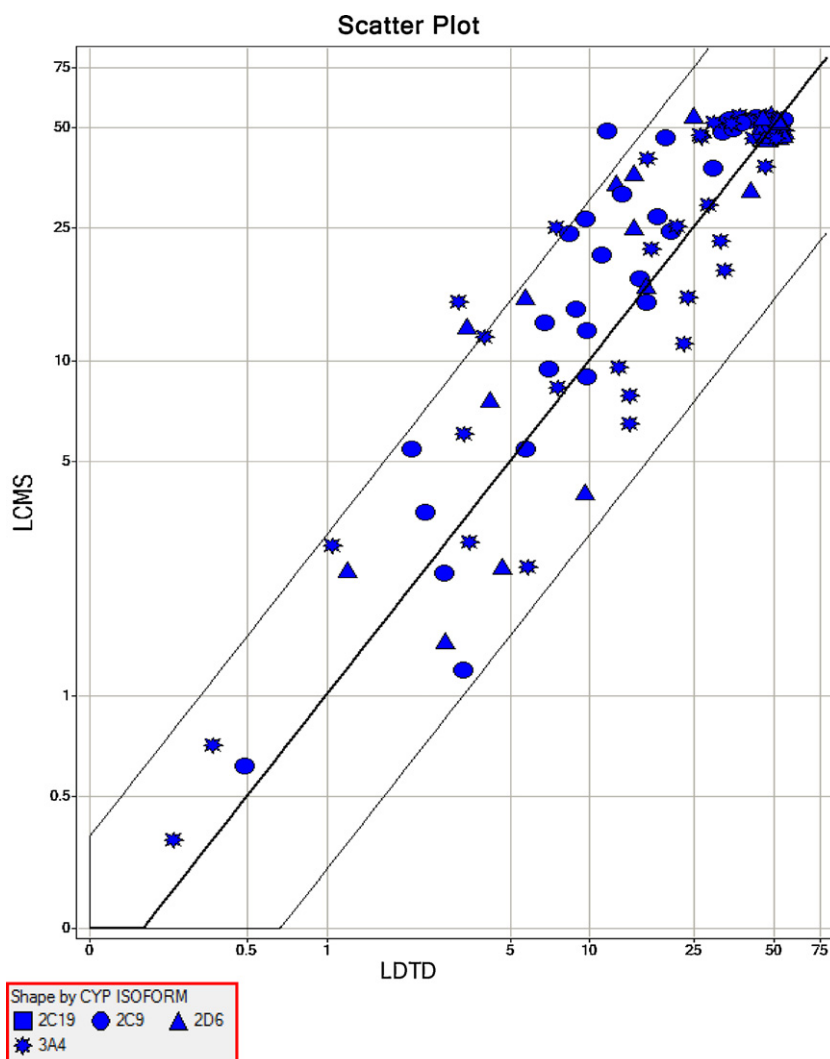

Fig. 9. Comparison of IC50 values obtained through analysis using LDTD versus LC–MS for 4 of the 5 CYP 450s (3-fold error lines shown).

Table 4
Substrates and metabolites for the five CYP inhibition assay using LDTD without internal standard.

Substrate	Metabolite	Isoform	CV
Bufuralol	Hydroxybufuralol	2D6	4.7
Mephenytoin	4-Hydroxymephenytoin	2C19	7.8
Midazolam	1-Hydroxymidazolam	3A4	3.3
Diclofenac	4-Hydroxydiclofenac	2C9	7.1
Phenacetin	Paracetamol	1A2	–

Table 5
Substrates and metabolites for the three CYP inhibition assay using LDTD without internal standard.

Substrate	Metabolite	Isoform	% CV
Bupropion	1-Hydroxybupropion	2B6	5.8
Midazolam	1-Hydroxymidazolam	3A5	10.4
Amodiaquine	N-Desmethylamodiaquine	2C8	11.2

within AstraZeneca which is run as a cocktail incubation with an LC–MS end point, where the same analytes are screened for every time so should be relatively straightforward for LDTD. However as stated previously, groups that have tried these on LDTD have had to use isotopically labeled internal standards to account for the high CVs. The aim of this work was to be able to use LDTD without the use of any internal standard.

The five substrates used for each isoform are listed in Table 4 along with the % CV obtained for four of the metabolites from DMSO control samples which also contain the same matrix as the test samples. For this work only four of the five metabolites will be reported as the current LC/MS assay used at AstraZeneca uses phenacetin as a probe substrate for CYP isoform 1A2, which is metabolized to paracetamol. Under LDTD conditions, phenacetin degraded to paracetamol in-source, which is not a problem in the LC-based assay where they are separated by retention time, but with LDTD there is no temporal or spatial separation so an alternative substrate such as tacrine, for example, would have to be used.

As recommended earlier, method development was carried out to determine the optimal quench for the samples and also the best laser pattern for this matrix. The best results were obtained using a 4:1 (v/v) quench with methanol and a laser pattern of a 1 s ramp to 40% maximum power with a 3 s hold. The % CV for the DMSO

control samples which contained matrix are very reproducible, with all being less than 10% and negating need for an internal standard. Plates from the assay were then quenched 4:1 (v/v) with methanol, centrifuged and aliquots taken for the LC–MS and LDTD analyses. Resultant data were compared for 36 compounds and are summarized in Fig. 9, showing 95% of the results were within 3 fold of the LC–MS assay, which is acceptable. Repeating the same set of samples on the LC–MS assay generated the same variability, but the largest gain was in analysis time; with comparative sample sets taking 6.5 h by LC–MS and 0.75 h by LDTD.

3.7. Three CYP competitive inhibition assay

The next assay to be attempted was a three CYP inhibition assay covering 2B6, 3A5 and 2C8. The CVs for each of these from the DMSO controls are shown in Table 5. These values were around 10% or lower and were obtained using a 4:1 (v/v) quench with methanol but a slightly different laser pattern (2 s ramp to 40% maximum power with a 2 s hold). Comparison of these data with those from the LC–MS assay (Fig. 10) showed them to be within an acceptable 3-fold error margin. However, these were only for 2C8 and 3A5 as there were problems with the LDTD analysis of 2B6, in the form of a strong isobaric interference coming from the plate surface at the same SRM transition (m/z 255–238) as the molecular ion of 1-hydroxybupropion, making it impossible to
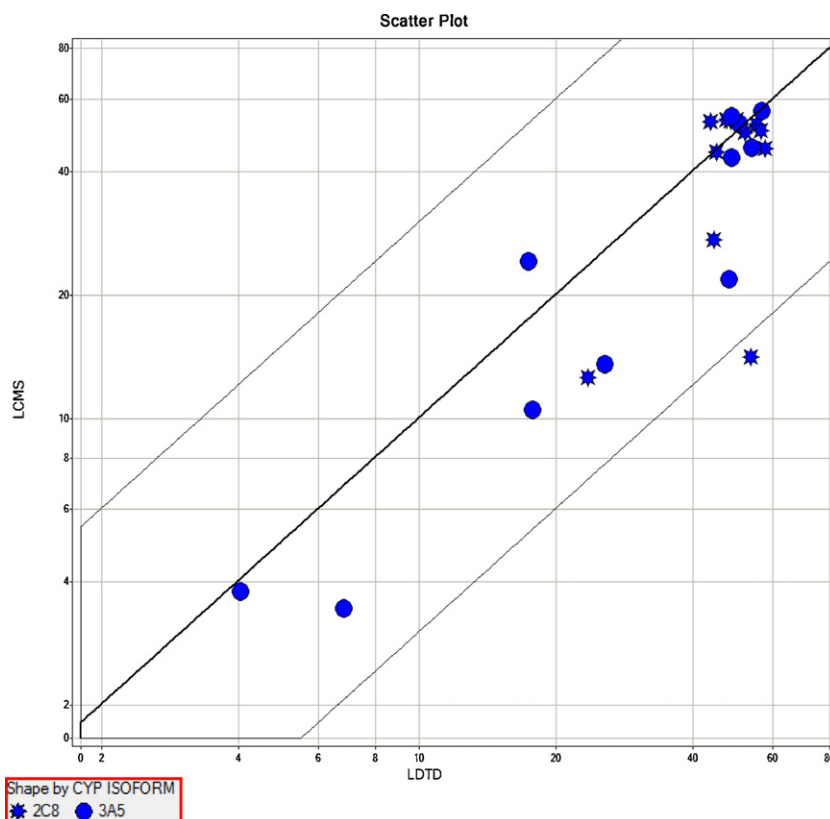

Fig. 10. Comparison of IC50 values obtained through analysis using LDTD versus LC–MS for 2C8 and 3A5 (3-fold error lines shown).
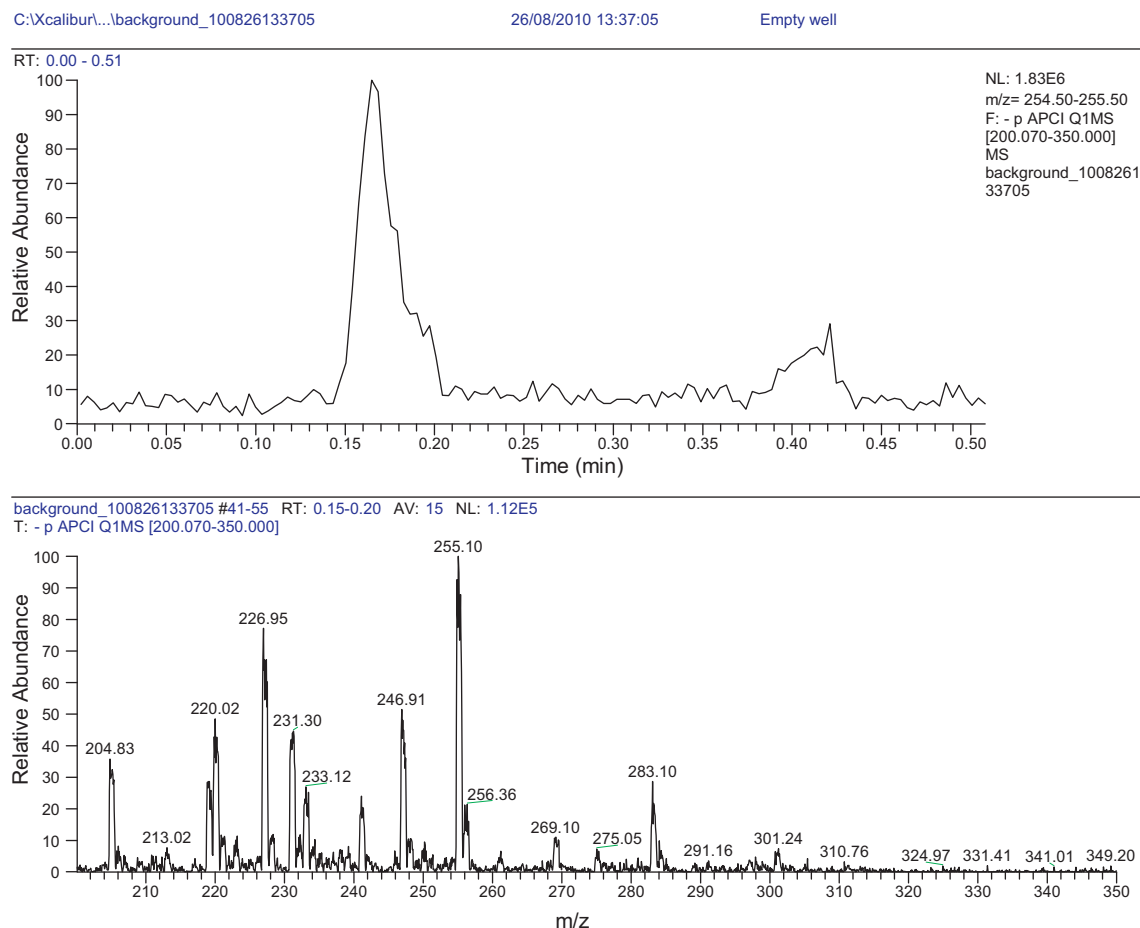
Fig. 11. Selected ion trace for *m/z* 255 (top) showing the response from two laser shots of the same unused well resulting in a strong response in the first shot (spectrum shown in lower pane) with much reduced response for the second shot.

perform meaningful quantification. This interference was confirmed as being plate-derived by running several new plates (from different boxes and batches) in full scan MS, to assess what came off the plate under LDTD desorption conditions. The resultant spectrum and selected ion trace (*m/z* 255) shows the response for two laser shots from the same unused well (Fig. 11), where the first laser shot clearly removes the bulk of the interference as the response for the second shot is reduced significantly. These data demonstrate that it should not be assumed the LazWell plates have little-to-no chemical background, but may still have some uncharacterized contaminants that may cause interference. This particular problem was resolved by using a different SRM transition for LDTD analysis of 1-hydroxybupropion (data not shown) with no further issues.

4. Conclusion

A number of issues had been highlighted with LDTD that made it difficult to use as a frontline analytical tool to replace LC–MS, such as high variability requiring the use of internal standards and not being able to analyze a reasonably wide range of chemistries, despite the promise of huge gains in throughput. However from the results reported here, it is clear that once the reasons for those issues are understood and resolved then the system is capable of running a much wider range of chemistries than first thought without the need for an internal standard, with the observed variability of the LDTD no worse than would be observed with LC–MS methodology.

The key factors identified that impacted on variability were the plate surface and the source conditions. Once these had been optimised then the degree of variability dropped down to more or less single figure values and allowed the next step to proceed. This was to carry out some simple method development to determine the optimal conditions for preparing the samples from each different matrix and the best laser pattern to ensure complete desorption of the sample. The two assays presented in this paper are a five and three cytochrome P450 competitive inhibition assay carried out at AstraZeneca as a cassette incubation and was felt to be a good starting point for LDTD as the analytes are always the same and the samples would be in the same format. From comparative analyses, it was clear the quality of the LDTD data was comparable to the conventional LC–MS assay but was obtained in 0.75 h (45 min) compared to 6.5 h for LC–MS. In the current climate of trying to reduce time scales and maximizing the use of high capital equipment, LDTD certainly has that potential to make a big impact in both these areas.

Financial and competing interests

Acknowledgements

References

[1] W. Korfmacher, Bioanalytical assays in a drug discovery environment, in: W. Korfmacher (Ed.), Using Mass Spectrometry for Drug Metabolism Studies, Boca Raton, FL, 2005, pp. 1–34.

[2] R.A. Boyd, R.L. Lalonde, Nontraditional approaches to first-in-human studies to increase efficiency of drug development: will microdose studies make a significant impact? Clin. Pharmacol. Ther. 81 (2007) 24–26.

[3] S.A. Roberts, High-throughput screening approaches for investigating drug metabolism and pharmacokinetics, Xenobiotica 31 (2001) 557–589.

[4] P.V. Kaplita, H. Hu, L. Liu, T.M. Farrell, H. Grbic, D.M. Spero, Automatable formats of higher throughput ADMET profiling for drug discovery support, J. Assoc. Lab. Autom. 10 (2005) 140–148.

[5] H. Wan, A.G. Holmén, High throughput screening of physicochemical properties and in vitro ADME profiling in drug discovery, Comb. Chem. High Throughput Screen 12 (2009) 315–329.

[6] S.X. Peng, A.G. Barbone, D.M. Ritchie, High-throughput cytochrome P450 inhibition assays by ultrafast gradient liquid chromatography with tandem mass spectrometry using monolithic columns, Rapid Commun. Mass Spectrom. 17 (2003) 509–518.

[7] Y. Hsieh, W.A. Korfmacher, Increasing speed and throughput when using HPLC–MS/MS systems for drug metabolism and pharmacokinetic screening, Curr. Drug Metab. 7 (2006) 479–489.

[8] R. Xu, M. Manuel, J. Cramlett, D.B. Kassel, A high throughput metabolic stability screening workflow with automated assessment of data quality in pharmaceutical industry, J. Chromatogr. A 1217 (2010) 1616–1625.

[9] O. Heudi, High-throughput quantitative analysis of pharmaceutical compounds in biological matrices, Bioanalysis 3 (2011) 819–821.

[10] J. Wu, C.S. Hughes, P. Picard, S. Letarte, M. Gaudreault, J.-F. Lévesque, D.A. Nicoll-Griffith, K.P. Bateman, High-throughput cytochrome P450 inhibition assays using laser diode thermal desorption-atmospheric pressure chemical ionization–tandem mass spectrometry, Anal. Chem. 79 (2007) 4657–4665.

[11] G.A. Harris, A.S. Galhena, F.M. Fernandez, Ambient sampling/ionization mass spectrometry: applications and current trends, Anal. Chem. 83 (2011) 4508–4538.

[12] D.J. Weston, Ambient ionization mass spectrometry: current understanding of mechanistic theory analytical performance and application areas, Analyst 135 (2010) 661–668.

[13] G.J. Van Berkel, S.P. Pasilis, O. Ovchinnikova, Established and emerging atmospheric pressure surface sampling/ionization techniques for mass spectrometry, J. Mass Spectrom. 43 (2008) 1161–1180.

[14] Z. Takats, J.M. Wiseman, B. Gologan, R.G. Cooks, Mass spectrometry sampling under ambient conditions with desorption electrospray ionization, Science 306 (2004) 471–473.

[15] D.R. Ifa, C. Wu, Z. Ouyang, R.G. Cooks, Desorption electrospray ionization and other ambient ionization methods: current progress and preview, Analyst 135 (2010) 669–681.

[16] R.B. Cody, J.A. Laramee, H.D. Durst, Versatile new ion source for the analysis of materials in open air under ambient conditions, Anal. Chem. 77 (2005) 2297–2302.

[17] H. Chen, A. Venter, R.G. Cooks, Extractive electrospray ionization for direct analysis of undiluted urine, milk and other complex mixtures without sample preparation, Chem. Commun. 42 (2006) 2042–2044.

[18] D.J. Weston, A.R. Ray, A.W.T. Bristow, Commentary: challenging convention using ambient ionization and direct analysis mass spectrometric techniques, Rapid Commun. Mass Spectrom. 25 (2011) 821–825.

[19] R. Helmy, W. Schafer, L. Buhler, S. Marcinko, B. Musselman, E. Guidry, H. Jenkins, F. Fleitz, C.J. Welch, Ambient pressure desorption ionization mass spectrometry in support of preclinical pharmaceutical development, Org. Process Res. Dev. 14 (2010) 386–392.

[20] J.G. Swales, R. Gallagher, R.M. Peter, Determination of metformin in mouse, rat, dog and human plasma samples by laser diode thermal desorption/atmospheric pressure chemical ionization tandem mass spectrometry, J. Pharm. Biomed. Anal. 53 (2010) 740–744.

[21] O. Heudi, S. Barteau, P. Picard, P. Tremblay, F. Picard, O. Kretz, Laser diode thermal desorption-positive mode atmospheric pressure chemical ionization tandem mass spectrometry for the ultra-fast quantification of a pharmaceutical compound in human plasma, J. Pharm. Biomed. Anal. 54 (2011) 1088–1095.

[22] R. Weaver, K. Graham, I.G. Beattie, R. Riley, Cytochrome P450 inhibition using recombinant proteins and mass spectrometry/multiple reaction monitoring technology in a cassette incubation, Drug Metab. Dispos. 31 (2003) 955–966.

[23] C.J. O'Donnell, K. Grime, P. Courtney, D. Slee, R. Riley, The development of a cocktail CYP2B6, CYP2C8 and CYP3A5 inhibition assay and a preliminary assessment of utility in a drug discovery setting, Drug Metab. Dispos. 35 (2007) 381–385.

Comparison of high-resolution ultrasonic resonator technology and Raman spectroscopy as novel process analytical tools for drug quantification in self-emulsifying drug delivery systems

Cordula Stillhart [a,b], Martin Kuentz [a,*]

[a] *University of Applied Sciences Northwestern Switzerland, Institute of Pharmaceutical Technology, Gründenstrasse 40, 4132 Muttenz, Switzerland*
[b] *University of Basel, Institute of Pharmaceutical Technology, Klingelbergstrasse 50, 4056 Basel, Switzerland*

ABSTRACT

Self-emulsifying drug delivery systems (SEDDS) are complex mixtures in which drug quantification can become a challenging task. Thus, a general need exists for novel analytical methods and a particular interest lies in techniques with the potential for process monitoring. This article compares Raman spectroscopy with high-resolution ultrasonic resonator technology (URT) for drug quantification in SEDDS. The model drugs fenofibrate, indomethacin, and probucol were quantitatively assayed in different self-emulsifying formulations. We measured ultrasound velocity and attenuation in the bulk formulation containing drug at different concentrations. The formulations were also studied by Raman spectroscopy. We used both, an in-line immersion probe for the bulk formulation and a multi-fiber sensor for measuring through hard-gelatin capsules that were filled with SEDDS. Each method was assessed by calculating the relative standard error of prediction (RSEP) as well as the limit of quantification (LOQ) and the mean recovery.

Raman spectroscopy led to excellent calibration models for the bulk formulation as well as the capsules. The RSEP depended on the SEDDS type with values of 1.5–3.8%, while LOQ was between 0.04 and 0.35% (w/w) for drug quantification in the bulk. Similarly, the analysis of the capsules led to RSEP of 1.9–6.5% and LOQ of 0.01–0.41% (w/w). On the other hand, ultrasound attenuation resulted in RSEP of 2.3–4.4% and LOQ of 0.1–0.6% (w/w). Moreover, ultrasound velocity provided an interesting analytical response in cases where the drug strongly affected the density or compressibility of the SEDDS. We conclude that ultrasonic resonator technology and Raman spectroscopy constitute suitable methods for drug quantification in SEDDS, which is promising for their use as process analytical technologies.

1. Introduction

The American Food and Drug Administration (FDA) initiative on process analytical technologies (PAT) has notably increased the interest in novel analytical methods for pharmaceutical product analysis (US FDA PAT Guidance, 2004). A variety of methods for drug quantification in pharmaceutical formulations, such as infrared (IR) spectroscopy or high-performance liquid chromatography (HPLC), require extensive manual sample preparation, are time-consuming, and usually destructive. This is in contrast to the main PAT requirements asking for rapid and non-destructive analytical methods. Today we know about a couple of analytical techniques that are used for process monitoring [1]. However, some processes and drug delivery systems are particularly challenging, so

that applied research is needed for the implementation of existing techniques and the evaluation of novel methods.

A highly promising technique is based on ultrasound analytics since sound waves can propagate through turbid media of liquid and semi-solid pharmaceutical formulations. Ultrasound technology has evolved over time and two main applications have been established: acoustic resonance spectroscopy and high-resolution ultrasonic resonator technology (URT). In spectroscopic analysis, ultrasound velocity and attenuation are measured over a large frequency range. In contrast, URT utilizes a specific ultrasound frequency to determine high-resolution ultrasound velocity and attenuation. Recently, Medendorp et al. pioneered the use of acoustic resonance spectroscopy as a PAT tool for drug quantification in semi-solids [2]. Similarly, Chen et al. measured the concentration of a model drug and an excipient in acetone solution with this technique [3]. URT was also applied in process analytics [4,5], but to the best of our knowledge real-time monitoring of drug concentration in pharmaceutical formulations has never been assessed. However,

---

* Corresponding author. Tel.: +41 61 467 46 88; fax: +41 61 467 47 01.
  E-mail address: martin.kuentz@fhnw.ch (M. Kuentz).
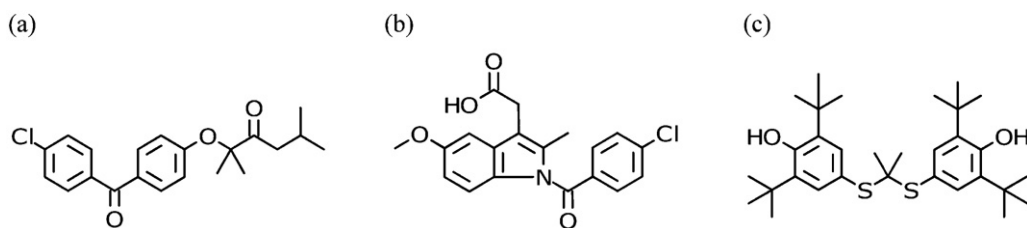
(a)　　　　　　　　　　　(b)　　　　　　　　　　　(c)

Fig. 1. Chemical structures of (a) fenofibrate, (b) indomethacin, and (c) probucol.

this technology bears great potential as a PAT tool for drug quantification due to the rapid data collection without additional sample preparation, the relative low-cost instrumentation, the fast computing time, and the possibility of flow-through measurement.

In contrast to the ultrasound-based method, Raman spectroscopy has already gained some importance in several process analytical applications [6]. The high chemical specificity of Raman spectroscopy is one of the key advantages over other tools, such as IR spectroscopy. An increasing number of Raman applications have been reported in recent years. Many quantitative Raman methods focused on solid dosage forms such as tablets, capsules, and powders [7–12]. In addition, Gotter et al. [13] described the use of Raman spectroscopy for the quantification of a drug suspended in a simple semi-solid formulation consisting of paraffin. More complex solid pharmaceutical formulations were analyzed by Hargreaves et al. [7], who established Raman spectroscopy for quantitative analysis of multi-component pharmaceutical capsules. Along with the quantification of an active pharmaceutical ingredient (API), this study demonstrated the method suitability for the quantification of three low-level excipients in the formulation. To the best of our knowledge, more complex semi-solid formulations such as self-emulsifying drug delivery systems (SEDDS) have not been investigated yet.

SEDDS are typically mixtures of up to five excipients (triglyceride oils, mixed glycerides, lipophilic surfactants, hydrophilic surfactants, and water-soluble cosolvents) [14] that undergo self-emulsification if they are exposed to water. Their ability to enhance oral absorption of poorly water-soluble drugs led to a growing interest in formulation research [14]. Some formulations, e.g. ritonavir (Norvir®), saquinavir (Fortovase®), and cyclosporine (Sandimmun Neoral®) have already reached the market.

Since SEDDS provide complex matrices, we aimed to use such formulations to evaluate URT as well as Raman spectroscopy for API quantification. Particular emphasis was placed on comparing the two methods with respect to their analytical performance in the different systems. Moreover, we considered two optical Raman configurations: one was intended for in-line measurement in the bulk solution and the other, a multi-fiber sensor, was foreseen for drug quantification through hard-gelatin capsules filled with SEDDS.

2. Materials and methods

2.1. Materials

Polysorbate 80 and Miglyol® 812 were purchased from Hänseler AG (Herisau, Switzerland), Imwitor® 742 and Imwitor® 988 were supplied by Sasol Germany GmbH (Witten, Germany), and Cremophor® RH 40 by BASF SE (Ludwigshafen, Germany). Fenofibrat, indomethacin, and probucol were all obtained from Sigma–Aldrich Chemie GmbH (Buchs, Switzerland). Uncolored hard-gelatin capsules Licaps® (size 1) were received from Capsugel (Bornem, Belgium).

For the preparation of the simulated gastric media we obtained sodium chloride from Carl Roth GmbH (Karlsruhe, Germany),

pepsin from Hänseler AG (Herisau, Switzerland), sodium taurocholate from Prodotti chimici ed alimentari S.p.A. (Basaluzzo, Italy), phosphatidylcholine from Lipoid GmbH (Ludwigshafen, Germany), and hydrochloric acid (1 N) from Sigma–Aldrich Chemie GmbH (Buchs, Switzerland).

2.2. Samples and analytics

Two different SEDDS consisting of polysorbate 80, Imwitor® 988, Miglyol® 812 (50/15/35; PO), and Cremophor® RH 40, Imwitor® 742, Miglyol® 812 (40/30/30; CO) were selected as model formulations [15,16]. For both formulations we prepared a concentration series with each of the three APIs fenofibrate (Fen), indomethacin (Ind), and probucol (Pro), separately (Fig. 1). Therefore a total of six concentration series, each including 33 samples, were studied.

The oils (Miglyol® 812, Imwitor® 742, Imwitor® 988) and the surfactant (Cremophor® RH 40 and polysorbate 80, respectively) were mixed on a magnetic stirrer at 40 °C until a clear solution was obtained. Samples of different API concentrations were then prepared by dissolving the drugs in the vehicle at room temperature using a magnetic stirrer.

In the analytical part of the experiment, the drug content was first determined in each bulk formulation by Raman spectroscopy and URT. The formulations were then manually filled into hard-gelatin capsules (∼70% volumetric filling degree). A multi-fiber Raman probe was subsequently used for API quantification through the capsule to compare in-line bulk analytics with a drug assay through the capsule material. Finally, HPLC was used as the reference method for API quantification. A detailed description of each analytical method is given in the following sections.

2.2.1. Solubility study

The solubility of the three APIs in PO and CO was determined in triplicate at room temperature. An excess amount of API was added to the formulations and then the suspensions were continuously mixed on a magnetic stirrer. To ensure that the equilibrium was reached, the solubility was determined after 24 h, 48 h, and 72 h. Then, samples were centrifuged at 2000 rpm for 30 min using an Eppendorf centrifuge (model 5415 C) to separate non-dissolved API from the vehicle. Finally, the drug concentration in the supernatant was assessed by HPLC.

2.2.2. Characterization of diluted SEDDS

The model systems were characterized with respect to their self-emulsification behavior upon dilution under physiological conditions. Therefore, formulations with and without API were diluted at 37 °C (1:200, w/w) in a medium simulating the stomach in the fasted state (FaSSGF). This medium had a pH of 1.6 and contained minor concentrations of phosphatidylcholine (20 μM) and bile salts (80 μM) according to Vertzoni et al. [17]. The diluted samples were gently shaken for a few seconds to mimic the limited mixing stress that occurs physiologically. We measured the particle size on a Zeta Sizer Nano ZS (Malvern Instruments, Malvern, UK), equipped with a 4 mW He–Ne Laser operating at a wavelength of

Table 1
Overview of HPLC methods used for API quantification.

API	Mobile phase	Injection volume	UV detection
Fen	Acetonitrile–ammoniumacetate buffer (pH 3.5; 25 mM) (65:35, v/v)	20 μL	287 nm
Ind	Phosphoric acid (50 mM)–acetonitrile (40:60, v/v)	5 μL	260 nm
Pro	Acetonitrile–water (96:4, v/v)	10 μL	241 nm

633 nm. The scattering signal was detected at an angle of 173° and each sample was measured for 10 min. The result was expressed as intensity averaged particle diameter (nm) and as polydispersity index (PDI).

2.3. Instrumental and analytical conditions

2.3.1. Raman spectroscopy

Raman spectra were recorded in the backscattering modus using a Raman RXN1 analyzer (Kaiser Optical Systems, Inc., Ann Arbor, MI) equipped with a charge-coupled device (CCD camera) and a diode laser operating at a wavelength of 785 nm. Measurements were carried out with a laser power of 400 mW and background Rayleigh scattering was removed by a holographic filter during spectra acquisition.

We recorded the Raman spectra of the bulk formulations with a single-fiber optic probe (spot size 0.007 mm^2) by direct immersion of the probe head into the formulation. The vials were wrapped in aluminum foils to avoid the influence of external light on the detection of Raman scattering. To collect Raman spectra through the capsules, a multi-fiber P^{h}AT probe was used. This sensor had a non-contact sampling optic device with a laser spot diameter of 6 mm. Scattered radiation was then collected by an array of 50 optical fibers and delivered to the CCD detector. Capsules were positioned on an iris holder to locate each capsule at the same position and to avoid displacement during the measurement. A sample holder consisting of a black metal block shielded the samples from external light.

The reference spectra of the pure drugs in powder form and of the empty hard-gelatin capsule were recorded with a non-contact probe. This optics utilized a single fiber for excitation and another for collection, and provided a sampling area of 0.007 mm^2 such as the immersion probe.

Spectra were acquired at a resolution of 4 cm^{-1} and processed for subsequent data analysis using the iC Raman Instrument software (Version 3.0, Mettler-Toledo AutoChem Inc., Columbia, MD).

2.3.2. Ultrasonic resonator technology

High-resolution URT is based on the calculation of the attenuation, A (s^2/m) and velocity, U (m/s) of a sound wave propagating through a sample [18]. In a homogenous ideal liquid, the velocity of a sound wave is determined by the density, ρ and the adiabatic compressibility, κ of the fluid. The mathematical relationship is described by the Newton–Laplace equation:

$$U = \frac{1}{\sqrt{\kappa \rho}} \tag{1}$$

Urick [19] generalized this relation to mixtures of different components. Therefore, sound velocity in the mixture U_{12} can be described as (using the subscripts 1 and 2 for the pure components):

$$\frac{1}{U_{12}^2 \rho_{12}} = \frac{\phi_1}{U_1^2 \rho_1} + \frac{\phi_2}{U_2^2 \rho_2} \tag{2}$$

where ϕ is the volume fraction and ρ is the density of the two components with the labeled subscripts.

In the ultrasonic experiments we measured sound velocity U as well as acoustic attenuation A. The latter parameter summarized several contributions to energy loss during sound propagation. It is inversely proportional to the square of sound frequency f, as described by the following equation:

$$A = \frac{\alpha}{f^2} \tag{3}$$

The term α refers to the acoustical attenuation factor that describes the absorption of a sound wave with amplitude a travelling a distance x through a medium (a_0 = initial amplitude):

$$\alpha = -\frac{1}{x}\ln\left(\frac{a}{a_0}\right) \tag{4}$$

Ultrasonic velocity and attenuation were measured using the ResoScan® System (TF Instruments Inc., Monmouth Junction, NJ). The ResoScan® was equipped with two identical parallel resonator cells having a path length of 7.0 mm (ground wave λ_0 = 14 mm) with a fundamental frequency of approximately 10 MHz. Since ultrasonic velocity is strongly temperature-dependent, a Peltier-element-controlled thermostat ensured a highly stable temperature in the resonator cavities (resolution 1 mK, stability ≤±5 mK). Ultrasound velocity was measured in a range of 1100–1900 m/s and ultrasonic attenuation was measured between 10^{-14} and 10^{-13} s^2/m.

To remove air bubbles, we centrifuged all samples prior to the ultrasonic analysis. Thus, an Eppendorf centrifuge (model 5415 C) was employed for 2 min at 2000 rpm. A sample of about 200 μL was then carefully transferred to the resonator cavities. Since we measured the difference in ultrasound velocity (ΔU) and attenuation (ΔA) between active formulations and placebo formulations, the API-containing formulation was injected into one of the cells, while the placebo formulation was filled in the other. Once thermal equilibrium was reached in both cells, we started the measurement. The analysis was done in triplicate at room temperature.

2.3.3. Reference measurements

The drug content of each sample was determined by HPLC. HPLC (Agilent Technologies 1200 Series) analysis was assessed with an isocratic pump (G1310A), an autosampler (G1329A) and a variable wavelength detector (G1314B). All measurements were performed on a LiChrospher 60, RP select B 125-4 (5 μm) column (Merck, Darmstadt, Germany) at a flow rate of 1 mL/min. Before measuring, the samples were diluted with water at a ratio of 1:200, except CO/Pro samples, which were diluted with acetonitrile:water (96:4). The HPLC conditions are detailed in Table 1.

2.3.4. Density measurement using Coriolis mass flow technology

Density of the six formulations (Fen/CO, Ind/CO, Pro/CO, Fen/PO, Ind/PO, and Pro/PO) at five different drug concentrations (0.5, 1, 2, 3, and 4%, w/w) was measured. We used the Mass Sense Density Meter (Integrated Sensing Systems Inc., Ypsilanti, MI, USA) which was equipped with a microelectromechanical system (MEMS) density sensor. This technology used a micromachined tube which was driven into resonance electrostatically while its motion was sensed capacitively by two metal electrodes. The density ρ of the liquid was deduced from the Coriolis force as described by the following equation:

$$\rho = \frac{1}{V}\left[\left(\frac{K_s}{4\pi^2 f^2}\right) - m_t\right] \tag{5}$$

where V is the internal volume of the resonant tube, m_t is the tube mass, K_s is the spring constant of the tube, and f is the resonance frequency of the tube [20]. The density was measured in the range from 0.6 to 1.3 g/mL with an accuracy of ± 0.001 g/mL and values were determined in triplicate at room temperature.

2.4. Data analysis

Raman spectra were analyzed by partial least square (PLS) regression. This method establishes a relationship between a set of dependent variables Y and a set of independent variables X (in our case the reference concentration obtained by HPLC and the Raman spectra, respectively). The method performs a principal component analysis based on the independent variable matrix and maximizes the correlation with the dependent variable matrix at the same time. This multivariate analysis was performed using the software iC Quant (Version 1.0, Mettler-Toledo AutoChem Inc., Columbia, MD). All spectral data were mean-centered. Further pre-processing steps comprised baseline correction and normalization to unit length.

URT data were analyzed by univariate regression plotting of ΔU and ΔA, separately, versus the reference concentrations obtained by HPLC.

The limit of quantification, LOQ (%, w/w) was calculated according to the International Conference of Harmonization (ICH) guidelines [21]. Thus, a calibration curve was modeled using a set of 6–10 samples containing API within an order of magnitude of the estimated quantification limit. Based on the standard deviation σ and the slope S of the calibration curve, the LOQ was expressed as:

$$\text{LOQ} = \frac{10 \times \sigma}{S} \tag{6}$$

Samples with an API concentration above the calculated LOQ were used for model calibration and validation. Simple and time-saving quantification methods are preferred for process analytical applications. Therefore, we aimed to assess the predictive power of the calibration models that were constructed with a small number of calibration points. We used calibration sets comprising 5–7 samples, while the remaining samples were used to validate the models. This division between calibration and validation samples was maintained for all models.

Relative standard error of prediction, RSEP (%) was calculated according to the equation:

$$\text{RSEP} = \sqrt{\frac{\sum_{i=1}^{n}(c_i^p - c_i^a)^2}{\sum_{i=1}^{n}(c_i^a)^2}} \times 100 \tag{7}$$

where n is the number of samples, c^a the actual concentration (detected by HPLC) and c^p the predicted concentration (by the model).

Mean recovery (%) was established for each model according to the equation:

$$\text{Mean recovery} = \frac{1}{n}\sum_{i=1}^{n}\frac{c^p}{c^a} \times 100 \tag{8}$$

3. Results and discussion

3.1. SEDDS characterization

We studied two model SEDDS with different drugs for the evaluation of URT and Raman spectroscopy. The model systems were named according to the surfactant so that for the formulation with polysorbate 80, PO was assigned and for the formulations with Cremophor® RH 40, the label CO was given. In both systems, a concentration series of the drugs fenofibrate, indomethacin, and
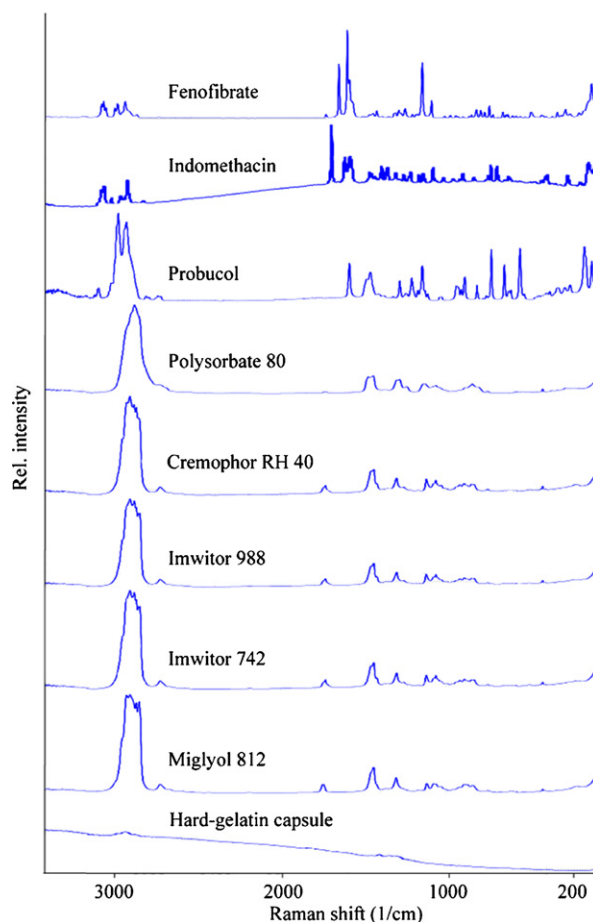

Fig. 2. Raman spectra of pure APIs and excipients.

probucol was prepared. Table 2 shows the main characteristics of the test systems.

The model compounds demonstrated different solubilities in the formulations, but in all cases a wide range of concentrations was enabled, which was beneficial considering the aim of the study. Furthermore, the presence of drug did not strongly alter the dilution characteristics of the SEDDS. This anticipated self-emulsification of the lipid-based formulations (PO and CO), both with and without API, was verified. We analyzed the samples diluted in FaSSGF by dynamic laser light scattering. The mean particle diameter of all formulations was in the range of typical SEDDS [14], as seen in Table 2. The CO formulations even formed rather small particles, so that these systems were basically self-microemulsifying drug delivery systems (SMEDDS). Larger swollen micelles were obtained from the dilution of the polysorbate formulations. Furthermore, PO systems were generally more polydisperse upon dilution as opposed to the CO formulations. However, such differences were not considered to be of relevance for the scope of the current analytical research.

3.2. Raman spectroscopy

Fig. 2 shows the Raman spectra of pure APIs (Fen, Ind, and Pro) and excipients (polysorbate 80, Cremophor® RH 40, Imwitor® 988, Imwitor® 742, Miglyol® 812, and the empty capsule). We analyzed these APIs in powder form as well as the empty gelatin capsule with a single-fiber non-contact optic probe. The spectra of the different excipients were subsequently collected using the immersion probe. All API spectra had some distinct Raman bands in the ranges of 1000–1500 cm^{-1} and 2700–3200 cm^{-1}. In some of these ranges,

Table 2
Characterization of lipid formulations used in the study.

Formulation	Concentration range measured [%, w/w] (number of samples)	Solubility[a] ± SD [%, w/w]	Particle diameter[b] (PDI) [nm]
PO	–	–	123.1 (0.269)
PO/Fen	0.01–8.00 (33)	8.58 ± 0.02	138.6 (0.219)
PO/Ind	0.01–4.00 (33)	5.63 ± 0.02	93.3 (0.252)
PO/Pro	0.01–8.00 (33)	11.34 ± 0.01	135.0 (0.192)
CO	–	–	31.2 (0.078)
CO/Fen	0.01–8.00 (33)	14.14 ± 0.11	35.9 (0.069)
CO/Ind	0.01–4.00 (33)	4.61 ± 0.02	34.9 (0.063)
CO/Pro	0.01–8.00 (33)	11.90 ± 0.14	34.8 (0.054)

[a] API concentration measured after 72 h (25 °C).
[b] Dilution ratio: 1:200 (w/w) in FaSSGF; temperature: 37 °C; API concentration: 8% (w/w) for formulations with Fen and Pro, 4% (w/w) for formulations with Ind.

the different excipients exhibited a comparatively lower Raman activity.

To evaluate Raman spectroscopy as a method for drug quantification, we first recorded the spectra of the six concentration series, each with 33 samples, directly from the bulk formulation. Subsequently, following manual filling of the formulation into hard-gelatin capsules, additional spectra were determined through the capsules using the P^hAT probe. Despite the partially overlapping spectral ranges of pure APIs and excipients, each formulation revealed at least one region where the signal intensity was highly specific for the API. In these regions, increasing drug concentrations showed peaks with increasing heights as well as areas. This was observed for both measurements in the bulk and through the capsules, as seen in Figs. 3 and 4. Based on these preliminary observations, backscatter Raman spectroscopy appeared to be promising for quantitative determination of the model drugs in SEDDS.

PLS analysis was then performed on the complete data set, while the number of PLS components was determined by cross-validation. Different calibrations constructed on API-specific spectral ranges did not greatly affect the obtained models. Therefore, we always considered the entire spectral ranges of 500–3300 cm^{-1} (bulk formulation) and 500–1800 cm^{-1} (capsules) for multivariate analysis.

Table 3 lists the values of LOQ, RSEP, and mean recovery of drug quantification in the different formulations. Interestingly, the LOQ values obtained from drug quantification in the capsules were in the range of values obtained from the measurements in the bulk solution. This similar sensitivity was mainly due to the optical devices

specifically used for these two analytical tasks. Drug quantification in the capsules required the use of the P^hAT probe. This system, having 50 collected optical fibers, provided a sampling area (28.3 mm^2) that was about 40–900 times larger than that present in conventional dispersive and FT-Raman, so that it had higher sensitivity to scattered radiation than the single-fiber probe. On the other hand, the prediction errors of the calibration models were equal or even smaller for the drug assays in the bulk formulation compared to the capsules. This result can also be inferred from the plots of actual vs. predicted concentrations (Figs. 5 and 6). There was a tendency of slightly higher R^2 for drug quantification in the bulk as compared to the capsule (0.9973–0.9995 vs. 0.9732–0.9991). Such a subtle effect was likely to contribute to some increase in prediction error of drug quantification in the capsules, which was mostly attributable to the experimental setup. Since the laser beam diameter of the P^hAT probe slightly exceeded the capsule width, there was some signal noise resulting in an undulating baseline as seen on the spectra in (Figs. 3 and 4, spectra on the right side). This effect was further enhanced by the transparency of the samples coupled with the short distance covered by the laser beam, leading to a signal noise coming from the background of the sample.

Regarding the different SEDDS types, drug quantification in PO formulations led to clearly higher prediction errors than those based on CO. This tendency was particularly pronounced for the quantification in capsules, where the predictive ability in PO systems was up to three times lower compared to CO-based formulations (RSEP 3.5–6.5% vs. 1.9–2.4%). Even though the type of SEDDS affected RSEP, all values were sufficiently low to fulfill the
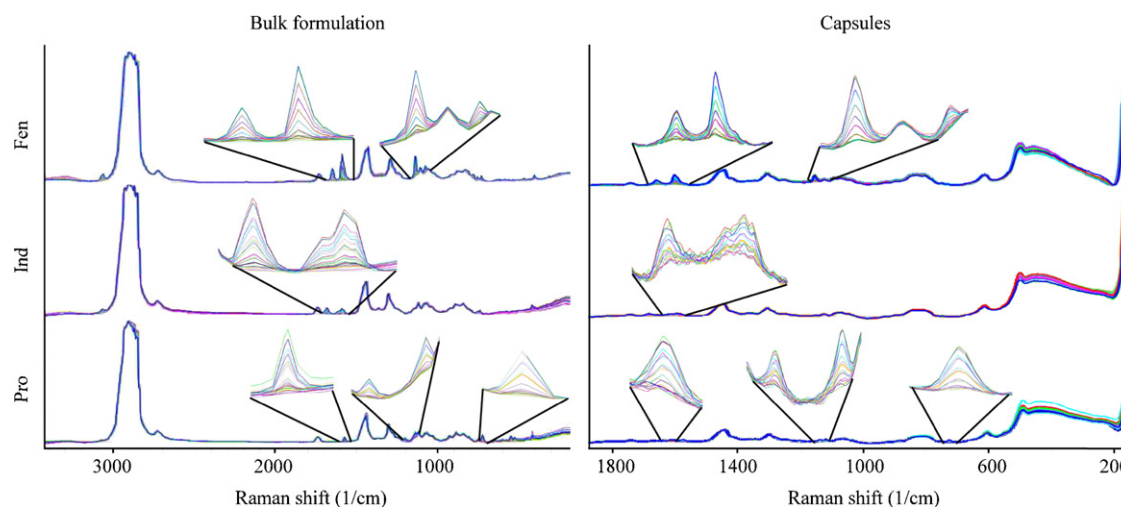

Fig. 3. Raman spectra of CO formulations collected in the bulk (left) and through the capsules (right). The 33 spectra of each concentration series are combined in each illustration, Raman signals generated from APIs are highlighted.

Fig. 4. Raman spectra of PO formulations collected in the bulk (left) and through the capsules (right). The 33 spectra of each concentration series are combined in each illustration, Raman signals generated from APIs are highlighted.
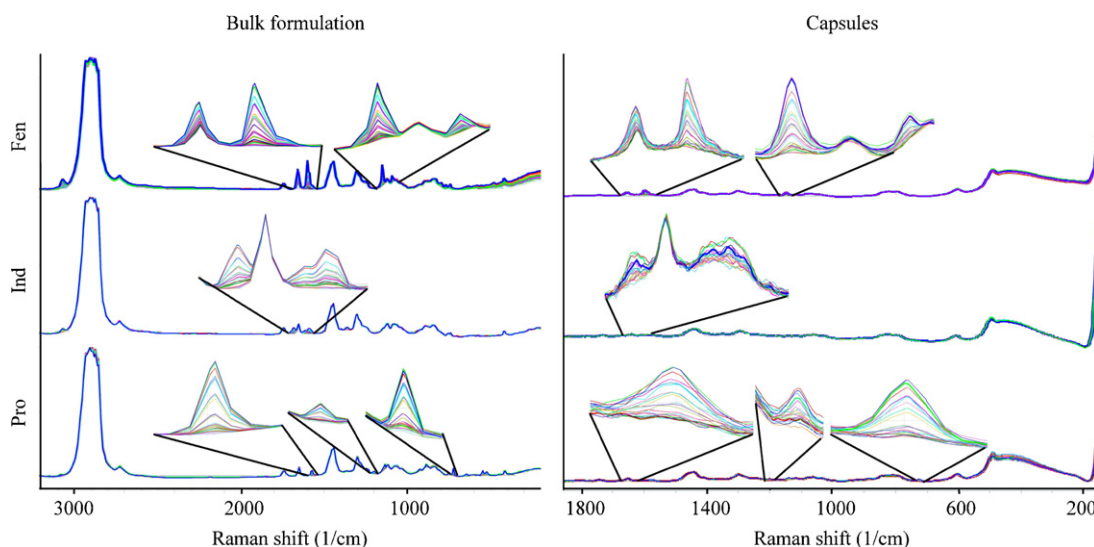
general acceptance criteria of performance parameters in analytical validation [22]. The obtained results encouraged the use of Raman spectroscopy as an accurate method for API quantification in complex semi-solid formulations. Together with the intrinsic Raman activity of the analyzed substance, it was the type of lipid mixture that apparently influenced the predictive ability of the method.

With respect to the PAT feasibility, the immersion probe can be directly employed as in-line setup for real-time monitoring of the intermediate product (i.e. the capsule fill mass). Raman spectroscopy was very promising for drug quantification through the capsules as well. However, optimization of the instrument setup might even improve its usefulness as a PAT method. Despite the advantages of the large sampling area, the laser beam area should not exceed the capsule size to reduce background noise within Raman backscattering. Moreover, the analytical procedure was not as fast as the manufacturing of the capsules. Since only a defined portion of the capsules can be transferred to the sample holder, the analysis of the final product was performed at-line.

A similar approach was adopted by Johansson et al. [9], where the transmission and the backscatter mode of Raman spectroscopy were compared for the quantitative analysis of tablets and capsules. Spectra were recorded with the P^{h}AT probe. This study demonstrated that transmission Raman leads to even more robust calibration models for solid pharmaceutical formulations as compared to backscatter Raman. In fact, the transmission setup allowed the entire tablet thickness to be analyzed, which was an

improvement when compared to the backscatter mode, where only about 10% of a typical tablet was sampled (sampling depth of approximately 5 mm) [9]. The homogenous drug mixtures and transparent capsules used in our study provided an advantageous situation for the backscattering setup so that only limited improvement could be expected from a Raman transmission mode. This expectation was supported by the relatively low RSEP obtained from our experiments. Backscatter Raman demonstrated robust models for this type of drug delivery systems.

3.3. URT

In addition to using Raman spectroscopy, we analyzed the six concentration series by ultrasound velocimetry. However, since the ResoScan® system was only suitable for analyzing liquid samples, API quantification in capsules was not performed. We determined ultrasound velocity and attenuation as relative values. Thus, two sample cells were always filled, whereby the placebo formulation was filled in the first cell (cell 1) and the drug-containing formulation in the second cell (cell 2). The differences in ultrasound velocity ΔU and attenuation ΔA between the two samples were obtained by subtracting the values measured in cell 1 from the values measured in cell 2, and used for univariate analysis.

Generally, there was a linear relationship for both acoustic responses as a function of API concentration (Fig. 7). We noticed the tendency of ΔA to be more sensitive to drug concentration

Table 3
Prediction of API concentration in capsules and in the bulk formulation using Raman spectroscopy.

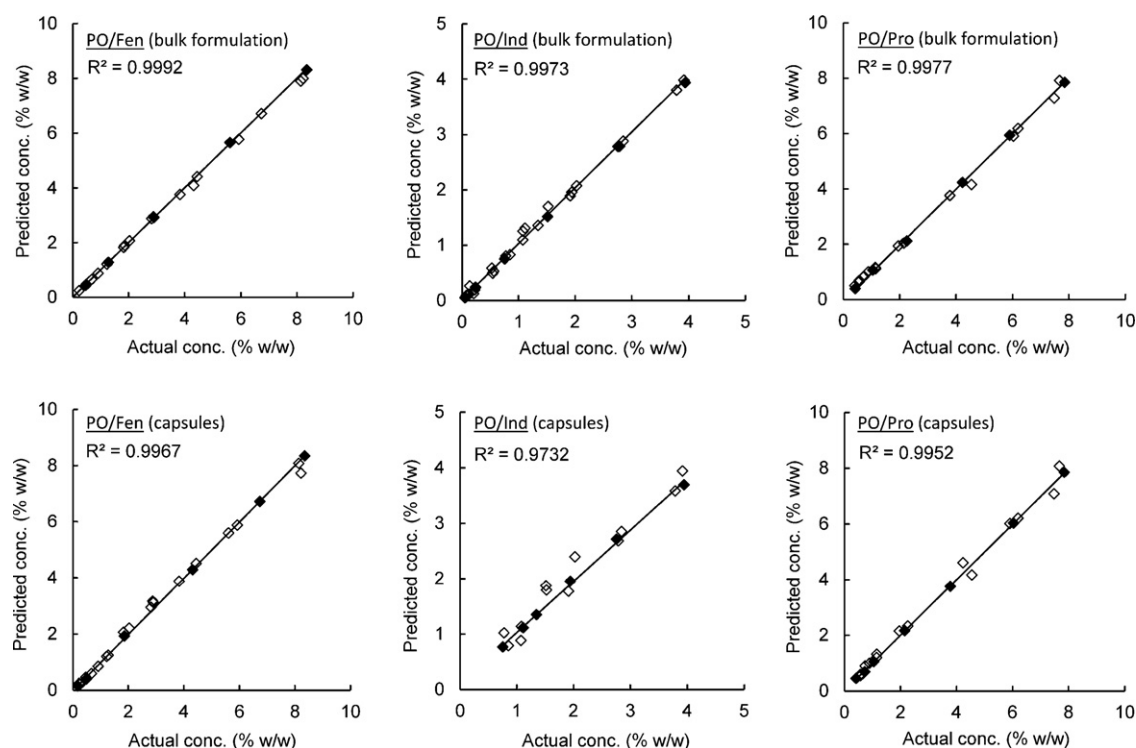| Formulation	Bulk formulation			Capsules		
	LOQ [%, w/w]	RSEP [%, nominal]	Recovery ± 95% CI [%, nominal]	LOQ [%, w/w]	RSEP [%, nominal]	Recovery ± 95% CI [%, nominal]
PO						
Fen	0.20	2.32	99.1 ± 1.3	0.05	3.55	99.8 ± 3.3
Ind	0.04	3.83	101.6 ± 2.9	0.41	6.54	99.6 ± 4.8
Pro	0.35	3.18	102.0 ± 3.6	0.06	4.52	102.7 ± 2.8
CO						
Fen	0.10	1.99	99.5 ± 2.7	0.34	1.87	100.5 ± 2.1
Ind	0.09	2.96	100.2 ± 1.7	0.01	2.05	100.0 ± 1.1
Pro	0.25	1.48	100.9 ± 1.6	0.02	2.40	99.2 ± 2.8

Fig. 5. Calibration plots of PO formulations obtained for measurements in the bulk formulation (top) and through the capsules (bottom). ◆ = calibration data set, ◇ = validation data set.

compared to ΔU. The drugs fenofibrate and probucol exhibited smaller quantification limits and prediction errors with ΔA as response, when compared to calibration models built on ΔU (Table 4). Indomethacin was different, and the special character of this drug was further underlined by the results of ΔU calibration.

Fig. 7 shows the double plots of ΔU and ΔA as a function of drug concentration. The values of ΔA were generally higher with increasing drug concentrations. The extent of increase and thus the slope of the linear models were mainly affected by the drug type, while there was barely any difference between the formulation types.

The largest ΔA variation was induced by indomethacin and probucol, and this was likely to result in lower LOQs, as observed with these formulations when compared with systems with fenofibrate (Table 4). Nevertheless, the analytical performance of ΔA was in a similar range as that of Raman spectroscopy. This was a remarkable result in the context of ultrasound attenuation as a monitoring parameter in complex lipid-based formulations.

With both, fenofibrate and probucol, ΔU decreased with increasing drug concentrations. Furthermore, ΔU calibration models of these two drugs led to particularly high values of LOQ and RSEP. Interestingly, analytical performance was different in the case of indomethacin where ultrasound velocity even increased with drug load. For better understanding of this finding, consider Eqs. (1) and (2). Thus, any change in ultrasound speed is attributed to differences in apparent density or compressibility of the mixture. It was therefore of interest to study how the density of the formulations was affected by different drug amounts.

Five drug concentrations (range 0.5–4%, w/w) were compared with respect to density changes (Fig. 8). The results indicated that density in the mixture increased with drug load. As inferred from the slopes m, the density increase was particularly pronounced for SEDDS containing indomethacin (0.027 [m_{Ind}] vs. 0.005–0.015 [m_{Pro}, m_{Fen}]). Increasing density would theoretically lead to decreasing values of ΔU, provided that the drug concentration does not change the apparent bulk compressibility in the mixture. The unusual finding for indomethacin could therefore only

Table 4
Prediction of API concentration in the bulk formulation using URT: evaluation based on ΔU and ΔA.

Formulation	ΔU			ΔA		
	LOQ [%, w/w]	RSEP [%, nominal]	Recovery ± 95% CI [%, nominal]	LOQ [%, w/w]	RSEP [%, nominal]	Recovery ± 95% CI [%, nominal]
PO						
Fen	1.48	5.43	98.5 ± 6.4	0.40	2.33	101.4 ± 1.9
Ind	0.14	1.08	100.6 ± 1.6	0.20	3.26	101.8 ± 3.5
Pro	2.05	5.43	98.5 ± 3.6	0.13	4.42	103.9 ± 4.2
CO						
Fen	2.29	5.34	98.0 ± 4.3	0.64	3.51	97.0 ± 2.9
Ind	0.80	1.35	99.4 ± 1.6	0.48	2.36	97.9 ± 1.8
Pro	1.24	3.44	100.6 ± 2.9	0.39	3.00	101.9 ± 3.7
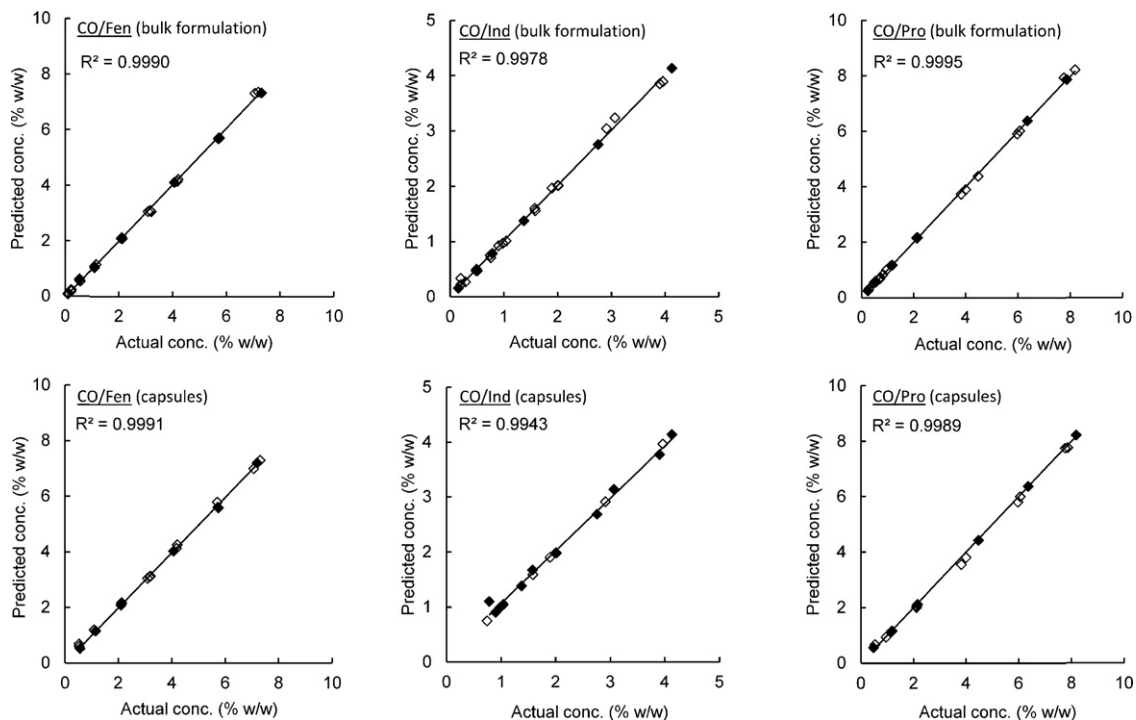
Fig. 6. Calibration plots of CO formulations obtained for measurements in the bulk formulation (top) and through the capsules (bottom). ♦ = calibration data set, ◊ = validation data set.

be explained with a dominating drug effect on the apparent bulk compressibility which appears to have outweighed the increasing density induced by indomethacin. This drug strongly affected the structure of the lipid mixture, and reduced compressibility originated from a perturbation of the liquid-crystalline structure by the drug. Drugs with a strong effect on the structuring of SEDDS are suitable candidates for analytics based on ultrasound velocity.

Fig. 7. Variation of ΔU (○) and ΔA (△) with drug concentration.

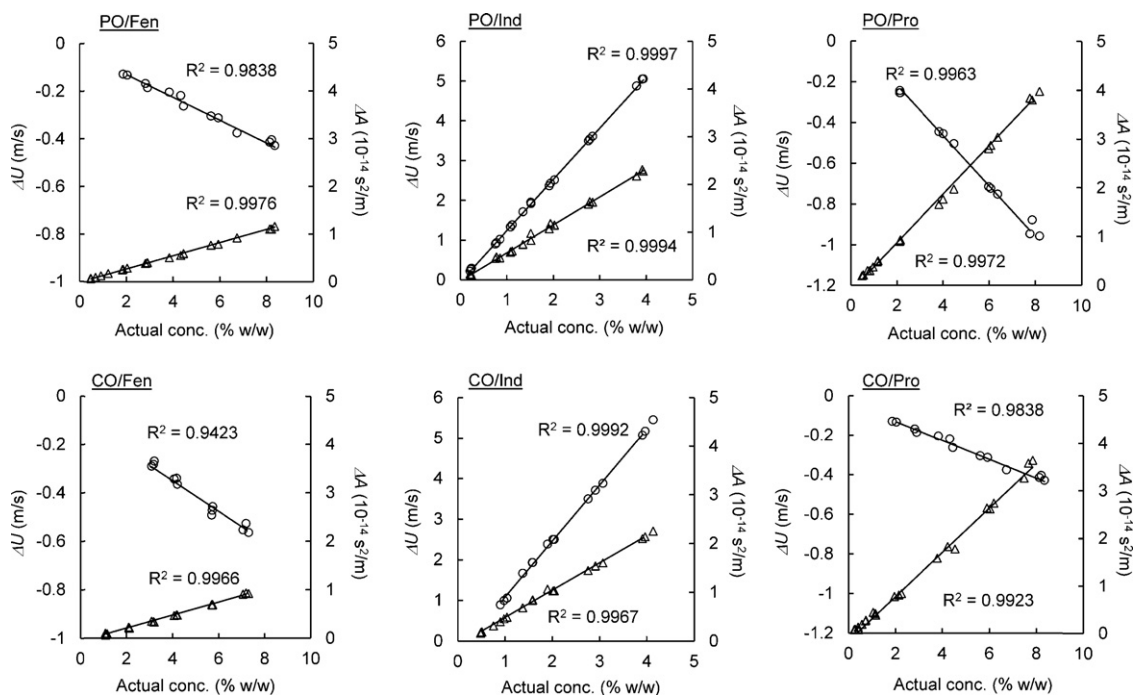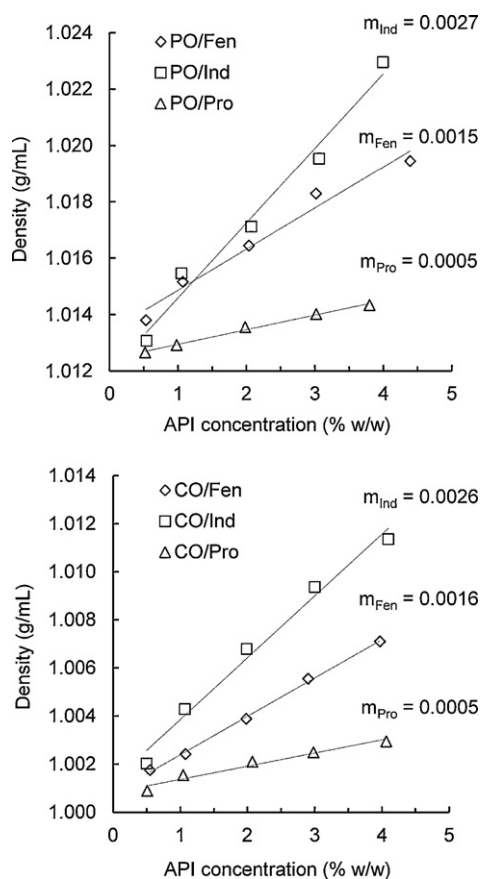**Fig. 8.** Variation of density with drug concentration.

4. Conclusion

Raman spectroscopy and URT were well suited for rapid and non-destructive drug quantification in complex lipid-based formulations. Therefore both methods have a high potential for implementation as PAT tools in real-time monitoring the production of SEDDS or other lipid mixtures. These methods are not only useful in process analysis, but may also be used when simple and rapid calibration is required. This is the case, for example, during formulation development where the composition of the formulations is changing many times. Since the development of a formulation-specific method is time-consuming, rapid calibration is clearly advantageous.

Due to the ability of detecting even impurities and degradation products, Raman spectroscopy currently has an advantage over URT. However, the modern ultrasound method has proven to be simple and fast, while showing excellent calibration performance with API quantification in SEDDS. Specifically, the response of ultrasound attenuation resulted in high sensitivity and good predictability. Therefore, ΔA bears the advantage of broad application as a parameter for drug quantification, while ΔU is particularly suitable for predicting drug concentrations if a pronounced influence of the drug is exerted on the apparent compressibility or density of the mixture.

References

[1] K.A. Bakeev, Process Analytical Technology, 2nd ed., Wiley, Chichester, 2010.
[2] J. Medendorp, R.G. Buice, R.A. Lodder, Acoustic-resonance spectrometry as a process analytical technology for the quantification of active pharmaceutical ingredient in semi-solids, AAPS PharmSciTech 7 (2006) E22–E29.
[3] R.R. Chen, T. Zelesky, N. Ilasi, S.S. Sekulic, Simultaneously measuring concentrations of a model drug and a model excipient in solution using ultrasonic spectrometry, J. Pharm. Biomed. Anal. 37 (2005) 239–247.
[4] R.B. Shah, A.S. Zidan, T. Funck, M.A. Tawakkul, A. Nguyenpho, M.A. Khan, Quality by design: characterization of self-nano-emulsified drug delivery systems (SNEDDs) using ultrasonic resonator technology, Int. J. Pharm. 341 (2007) 189–194.
[5] M. Cavegn, R. Douglas, G. Akkermans, M. Kuentz, Study of an ultrasound-based process analytical tool for homogenization of nanoparticulate pharmaceutical vehicles, J. Pharm. Sci. 100 (2011) 3374–3385.
[6] J. Rantanen, Process analytical applications of Raman spectroscopy, J. Pharm. Pharmacol. 59 (2007) 171–177.
[7] M.D. Hargreaves, N.A. Macleod, M.R. Smith, D. Andrews, S.V. Hammond, P. Matousek, Characterisation of transmission Raman spectroscopy for rapid quantitative analysis of intact multi-component pharmaceutical capsules, J. Pharm. Biomed. Anal. 54 (2011) 463–468.
[8] S. Mazurek, R. Szostak, Quantitative determination of diclofenac sodium in solid dosage forms by FT-Raman spectroscopy, J. Pharm. Biomed. Anal. 48 (2008) 814–821.
[9] J. Johansson, A. Sparen, O. Svensson, S. Folestad, M. Claybourn, Quantitative transmission Raman spectroscopy of pharmaceutical tablets and capsules, Appl. Spectrosc. 61 (2007) 1211–1218.
[10] T.M. Niemczyk, M. Delgado-Lopez, F.S. Allen, J.T. Clay, D.L. Arneberg, Quantitative assay of bucindolol in gel capsules using infrared and Raman spectroscopy, Appl. Spectrosc. 52 (1998) 513–518.
[11] C. Eliasson, N.A. Macleod, L.C. Jayes, F.C. Clarke, S.V. Hammond, M.R. Smith, P. Matousek, Non-invasive quantitative assessment of the content of pharmaceutical capsules using transmission Raman spectroscopy, J. Pharm. Biomed. Anal. 47 (2008) 221–229.
[12] A. Szep, G. Marosi, B. Marosfoi, P. Anna, I. Mohammed-Ziegler, M. Viragh, Quantitative analysis of mixtures of drug delivery system components by Raman microscopy, Polym. Advan. Technol. 14 (2003) 784–789.
[13] B. Gotter, W. Faubel, St. Heissler, J. Hein, R.H.H. Neubert, Determination of drug content in semisolid formulations by non-invasive spectroscopic methods: FTIR-ATR, -PAS, -Raman and PDS, J. Phys.: Conf. Ser. 214 (2010) 1–5.
[14] C.W. Pouton, Lipid formulations for oral administration of drugs: non-emulsifying self-emulsifying and 'self-microemulsifying' drug delivery systems, Eur. J. Pharm. Sci. 11 (2000) 93–98.
[15] K. Mohsin, M.A. Long, C.W. Pouton, Design of lipid-based formulations for oral administration of poorly water-soluble drugs: precipitation of drug after dispersion of formulations in aqueous solution, J. Pharm. Sci. 98 (2009) 3582–3595.
[16] C. Ditner, R. Bravo, G. Imanidis, M. Kuentz, A systematic dilution study of self-microemulsifying drug delivery systems in artificial intestinal fluid using dynamic laser light backscattering, Drug Dev. Ind. Pharm. 35 (2009) 199–208.
[17] M. Vertzoni, J. Dressman, J. Butler, J. Hempenstall, C. Reppas, Simulation of fasting gastric conditions and its importance for the in vivo dissolution of lipophilic compounds, Eur. J. Pharm. Biopharm. 60 (2005) 413–417.
[18] F. Eggers, Ultrasonic velocity and attenuation measurements in liquids with resonators, extending the MHz frequency-range, Acustica 76 (1992) 231–240.
[19] R.J. Urick, A sound velocity method for determining the compressibility of finely divided substances, J. Appl. Phys. 18 (1947) 983–987.
[20] R. Smith, D.R. Sparks, D. Riley, N. Najafi, A MEMS-based Coriolis mass flow sensor for industrial applications, IEEE Trans. Ind. Electron. 56 (2009) 1066–1071.
[21] Guidance for Industry, Q2B Validation of Analytical Procedures: Methodology, U.S. Department of Health and Human Services, Food and Drug Administration, Center for Drug Evaluation and Research (CDER), 1996.
[22] J. Ermer, J.H. Miller, Method Validation in Pharmaceutical Analysis: A Guide to Best Practice, Wiley-VCH Verlag GmbH, Weinheim (D), 2005.

A validated Ultra High Pressure Liquid Chromatographic method for the characterisation of confiscated illegal slimming products containing anorexics

E. Deconinck, K. Verlinde, P. Courselle, J.O. De Beer*

Division of food, Medicines and Consumer Safety, Section Medicinal Products, Scientific Institute of Public Health (IPH), J. Wytmansstraat 14, B-1050 Brussels, Belgium

A B S T R A C T

A fully validated UHPLC–DAD method for the identification and quantification of pharmaceutical prepa-
rations, containing molecules frequently found in illegal slimming products (sibutramine, modafinil,
ephedrine, nor-ephedrine, metformin, theophyllin, caffeine, diethylpropion and orlistat) was developed.
The proposed method uses a Vision HT C18-B column (2 mm × 100 mm, 1.5 μm) with a gradient using
an ammonium acetate buffer pH 5.0 as aqueous phase and acetonitrile as organic modifier. The obtained
method was fully validated based on its measurement uncertainty (accuracy profile). Calibration lines
for all components were linear within the studied ranges. The relative bias and the relative standard
deviations for all components were respectively smaller than 3.0% and 1.5%, the β-expectation tolerance
limits did not exceed the acceptance limits of 10% and the relative expanded uncertainties were smaller
than 3% for all of the considered components.

A UHPLC–DAD method was obtained for the identification and quantification of these kind of pharma-
ceutical preparations, which will significantly reduce analysis times and workload for the laboratories
charged with the quality control of these preparations and which can, if necessary, be coupled to a
MS-detector for a more thorough characterisation.

© 2011 Elsevier B.V. All rights reserved.

1. Introduction

Slimming products are some of the most sold over the counter products in local pharmacies in Belgium and in most West-European countries. The increasing problem of obesity in the Western world as well as the "ideal figure" promoted in the West-ern culture makes slimming products very popular, which results in the fact that slimming products are big business. In Belgium most medicines designed for weight loss are only available on medical prescription when the condition of a patient justifies their use. This is one of the reasons why these products are bought through inter-net and enter the market in an illegal way. Since these products are not regulated they can be misleading and the patient can be con-fronted with counterfeit medicines or food supplements to which medicines, like sibutramin and diethylpropion, are added without any indication of their presence on package or leaflet [1–4].

Patients are not always aware that this kind of preparations can cause serious health problems like psychosis [3] and cardio-vascular problems [4], when not used under medical supervision. The most dangerous here are the food supplements to which medicines are added as adulterants, since the patient believes he is taking a supplement, mostly herbal based [1]. De Carvalho et al. [5] reviewed the aldulteration cases concerning phytother-apeutic slimming formulations, which represent the major class of slimming products bought through internet and seized by European customs. The reported adulterants can mainly be cate-gorized in six pharmacological classes: the anorexics (sibutramin, orlistat, diethylpropion, rimonabant) the anxiolytics (mainly ben-zodiazepines), the antidepressants (e.g. fluoxetine, sertraline), the diuretics (e.g. furosemide, hydrochlorothiazide, and the laxatives (e.g. phenolphtaleïne) [5,6]. Also the counterfeit medicines can cause serious health problems since their quality and composition is not guaranteed.

Since the number of slimming products entering Europe through the internet increases rapidly, it is important for the reg-ulatory instances to check these products for their quality and composition in order to evaluate the health risk for the population.

Different papers describe analytical methods for the detection and the quantification of adulterants in these kind of preparations. The majority of the papers uses LC–MS methods for the identifica-tion [6–10] and the quantification [7–10] of the adulterants. There are a few disadvantages using only LC–MS methods. Off course it is the method of choice for the identification of the adulterants in pharmaceutical preparations, but the quantification is often com-plex and necessitates in most cases an internal standard. The more not all quality control laboratories in the world are equipped with

* Corresponding author. Tel.: +32 2 642 51 70; fax: +32 2 642 53 27.
 E-mail address: Jacques.Debeer@wiv-isp.be (J.O. De Beer).

Table 1
Concentration levels for the samples used for method validation.

Concentration level (mg/ml)	Sibutramin	Modafinil	Ephedrine	Norefedrine	Metformine
Level 1	1.00	0.50	1.51	1.49	0.20
Level 2	0.50	0.37	1.01	1.00	0.10
Level 3	0.25	0.25	0.50	0.50	0.05

expensive LC–MS instruments. An LC–DAD method for the quantification of sibutramine hydrochloride in capsules was reported by Diefenbach et al. [11]. Other techniques as UV–Vis and IR spectroscopy and voltammetry were also reported [5].

This article describes a validated Ultra High Pressure Liquid Chromatography method with diode area detection for the identification and the quantification of nine components regularly found in illegal slimming products. The selection of the nine components was based on the components regularly found in the samples analysed in routine in our lab. The general procedure at the lab is the identification of the adulterants with a LC–MS screening method followed by a confirmation of identity and quantification method, chosen according to the found pharmacological class. The method presented here is a method for the identification and quantification of anorexics and some additives that are found regularly in preparations containing this kind of drugs. The method was validated according to the requirements of the ISO 17025 guideline [12], applying the total error approach [13,14].

2. Methods and materials

2.1. Standards and reagents

The reference standard for sibutramin. HCl monohydrate was kindly donated by Abbott (Wavre, Belgium). Modafinil was donated by Cephalon (Frazer, USA) and Metformine was donated by Germania Pharmaceutika (Wien, Austria). The reference standards for Orlistat and DL-Norephedrine HCL were purchased from Sigma–Aldrich (St. Louis, USA). Ephedrin sulphate was purchased from Acros (Geel, Belgium). Theophyllin was purchased from Certa (Braine-L'Alleud, Belgium) and caffeine from Fagron (Waregem, Belgium).

Ammonium acetate, acetic acid, ammonium solution and boric acid were purchased from Merck (Darmstadt, Germany), formic acid from VWR Prolabo (Fontenay-Sous-Bois, France), ammonium formate was purchased from Alfa Aesar (Karlsruhe, Germany) and MeOH and acetonitrile from Biosolve (Valkenswaard, The Netherlands).

2.2. Equipment and chromatographic conditions

Method development and validation was performed on an Acquity UPLC^{TM} system (Waters, Milford, USA). The system consisted of a binary solvent manager, a sample manager and a photo diode array detector. The output signal was monitored and processed using the Waters Empower2 software.

Initial screenings were performed on three stationary phases an Acquity BEH C18 column 2.1 mm × 100 mm, 1.7 μm (Waters, Milford, USA), a Grace Vision HT^{TM} C18-P 2 mm × 100 mm, 1.5 μm (Grace Davision Discovery Sciences, Lokeren, Belgium) and a Grace Vision HT^{TM} C18-B 2 mm × 100 mm, 1.5 μm. For the screenings mobile phases were used consisting of combinations of three buffers: an ammonium formate buffer of pH 3, an ammonium acetate buffer of pH 5 and a borate buffer of pH 9, and two organic modifiers: acetonitrile or methanol. The screenings were performed under gradient conditions with a gradient starting at 95% buffer and 5% organic modifier, going to a plateau of 2 min of 50% buffer and 50% organic modifier in 8 min at a flow of 0.5 ml/min

and detection wavelengths of 230 and 254 nm. Column temperature was set at 50 °C and the injection volume on 5 μl.

Method optimisation and validation were performed on the Grace Vision HT^{TM} C18-B 2 mm × 100 mm, 1.5 μm under gradient conditions using a mobile phase composed of a 0.025 M ammonium acetate buffer of pH 5 and acetonitrile.

2.3. Sample preparation

2.3.1. Preparation of standards

For screening purposes stock solutions of 1 mg/ml were prepared for all compounds, except for diethylpropion, where a sample, in which it was identified was used (1 capsule/20 ml methanol).

Validation tests for quantification were performed for 5 components: sibutramin, metformin, modafinil, ephedrine and nor-ephedrine. Caffein and theophyllin were not tested since they are not illegally present in such, generally plant based, products. Orlistat was not quantified since the used detection method is not appropriate for sensitive quantification, due to the lack of UV absorption by the molecule. Diethylpropion was not taken into account during validation since the practical fact that no reference standards could be purchased.

Calibration standards were prepared starting from separated stock solutions for each of the five components for which validation tests were performed. The respective stock solutions contained 5 mg/ml sibutramin, 5 mg/ml modafinil, 10 mg/ml ephedrine, 10 mg/ml nor-ephedrine and 1 mg/ml metformin.

Starting from these solutions standards were prepared by making dilutions of respectively 0.125, 0.250, 0.375, 0.500, 0.625, 0.750 and 1.0 ml in 5 ml. All solutions were prepared in methanol.

2.3.2. Preparation of samples

In order to validate the method following, the "total error" approach, blank spiked samples were prepared starting from stock solutions with the same concentrations as the ones used for the preparation of the standards. Stock solutions for sample preparation were prepared separately from the ones used for the standards. Starting from these stock solutions three samples were prepared with different concentration levels. As blank matrix an herbal sample, found to be negative for medicinal molecules was used. For each concentration level an amount of 30 mg herbal matrix was spiked. The concentration levels of the different components were chosen in function of the concentrations occurring in pharmaceutical preparations previously analysed at our laboratory. Attention was paid to the fact that in all three samples the different components were present in concentrations showing the same proportions as the solutions obtained with samples from practice. Table 1 shows the concentration levels chosen for each of the analytes.

2.4. Method validation

The method validation was performed in accordance with the requirements of the ISO17025 guideline using the total error approach [12–15].
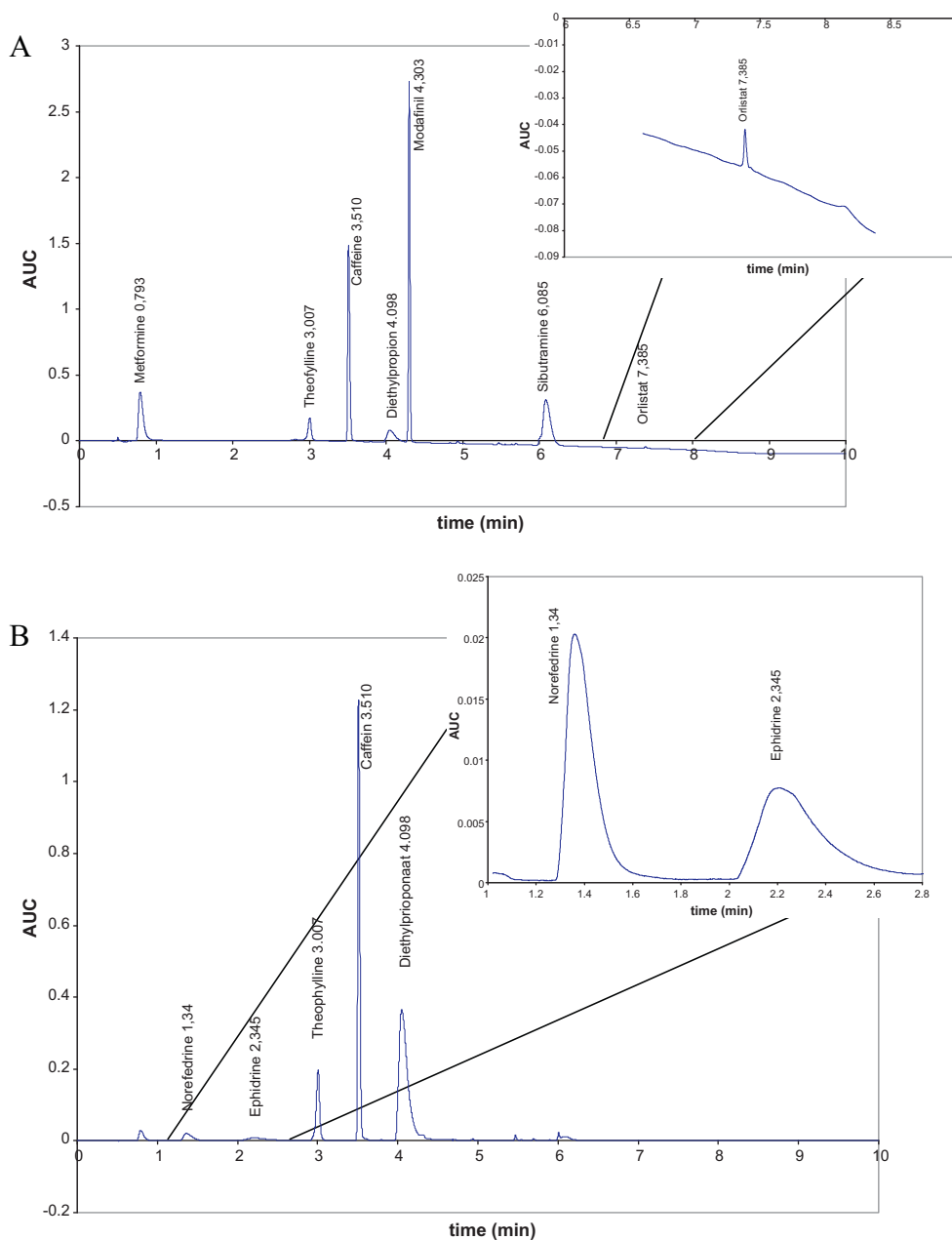
Fig. 1. Chromatogram obtained with the optimised gradient conditions for a mixture containing 0.1 mg/ml of each substance. (a) Chromatogram at 230 nm; (b) chromatogram at 254 nm.

2.5. Statistics

The statistical analysis was performed using Microsoft Excel 2003.

3. Results

3.1. Selection and optimisation of the method

Initial screenings were performed as described in Section 2.2.

Based on the visual inspection (retention times, resolution and peak symmetry), it was concluded that the best initial separation was obtained using the Vision HT C18-B column as stationary phase, the ammonium acetate buffer pH 5.0 as aqueous phase and acetonitrile as organic modifier. This method gave the separation of the majority of the compounds, though ephedrine and

nor-ephedrine were not separated and orlistat was not eluted from the column.

Based on this information the gradient was adapted. The initial conditions were changed to 98% buffer and 2% organic modifier and were kept for 2 min in order to separate ephedrine and nor-ephedrine. To elute orlistat from the column the plateau was brought to 100% organic modifier. This adaption led to a method that was able to separate all nine molecules in a run of 10 min. It has to be said that orlistat, due to its physicochemical properties, does not absorb enough in UV and therefore cannot be quantified with this method. Quantification may be possible when the instrument is coupled to ELSD or mass spectrometry. The method is suitable to confirm that no interference of orlistat will occur during the quantification of the other compounds.

The final gradient starts at 98% buffer and 2% organic modifier. After 2 min a linear gradient is started to reach 100% organic
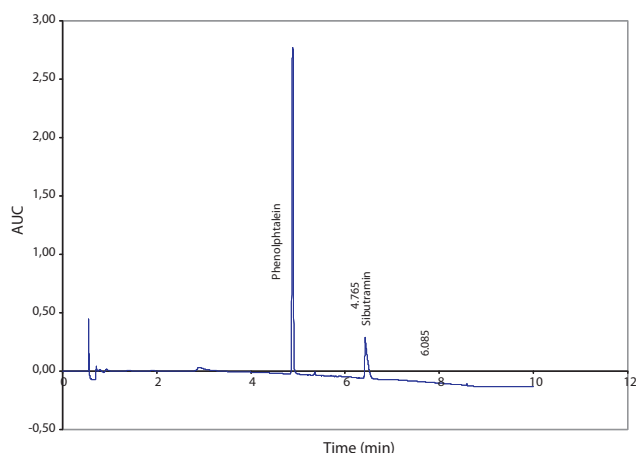
Fig. 2. Chromatogram obtained with the optimised gradient for a real sample containing 5.90 mg sibutramin per unit in a plant based matrix.

modifier after 8 min of run. The plateau is kept for 2 min. The flow was 0.5 ml/min, the injection volume 5 μl and detection of ephedrine, nor-ephedrine and diethylpropion was performed at 254 nm, while the other molecules were detected at 230 nm. Column temperature was set at 50 °C. Fig. 1 shows the corresponding chromatogram at 230 and 254 nm.

As an example Fig. 2 shows the chromatogram of a real sample containing 5.90 mg of sibutramin in a plant based matrix. The chromatogram was taken using a methanol extraction of 10 mg sample in 10 ml methanol. Phenolphtaleine was also found to be present as active ingredient, used as a laxative in slimming preparations. Phenolphtaleïne did not interfere with the identification. It was clearly separated from the nine molecules, used for method development.

3.2. Validation

3.2.1. Selectivity

The selectivity of detection was ensured by determining the retention time of each component separately and by monitoring the UV-spectra of the different components during the different analyses.

Table 2
Summary of the quality of the calibration curves for the different components.

Component	Concentration range (mg/ml)	R^2 value	Quality coefficient (%)
Sibutramine	0.10–1.00	0.9984	2.551
Modafinil	0.125–1.00	0.9998	0.913
Ephedrine	0.25–2.00	0.9975	3.200
Norefedrine	0.25–2.00	1.0000	0.301
Metformin	0.03–0.25	0.9994	1.519

3.2.2. Linearity of the calibration lines

For the five components used in the validation six calibration standards were prepared in order to evaluate the relationship between the area under the curve and the concentration. The linearity of the relationship was evaluated for each of the components in a concentration range, covering the normal range of concentrations obtained when analyzing pharmaceutical preparations.

The calibration curves were obtained using ordinary least-square linear regression and the linearity was confirmed with the R^2 values and the quality coefficient [16]. Table 2 summarizes for the five components the concentration ranges of the calibration curves, the R^2 values and the quality coefficients. From this table it can clearly been concluded that the calibration curve for all components is linear within the chosen concentration ranges.

3.2.3. Trueness, precision, accuracy and uncertainty assessment

A statistical approach based on the "total error" profiles was applied to validate the method.

As explained in Section 2.3.2 spiked blank samples were prepared at three concentration levels. Every sample was prepared in triple and analysed for three consecutive days.

The concentrations of the spiked samples were back-calculated using the calibration lines, prepared as described in Section 2.3.1 to determine the linearity between theoretical and measured concentrations, the mean relative bias, the repeatability, the intermediate precision and the β-expectation tolerance or total error intervals at the 5% level. All results are shown in Table 3.

The relationships between calculated and theoretical values are clearly linear with R^2-values from 0.9997 to 1.000.

Trueness refers to the closeness of agreement between the average of the obtained values and the known exact concentration of the spiked samples and is a measure for the systematic errors of the method [17]. It is expressed in terms of relative bias. From Table 3 it

Table 3
Trueness, precision, accuracy and uncertainty.

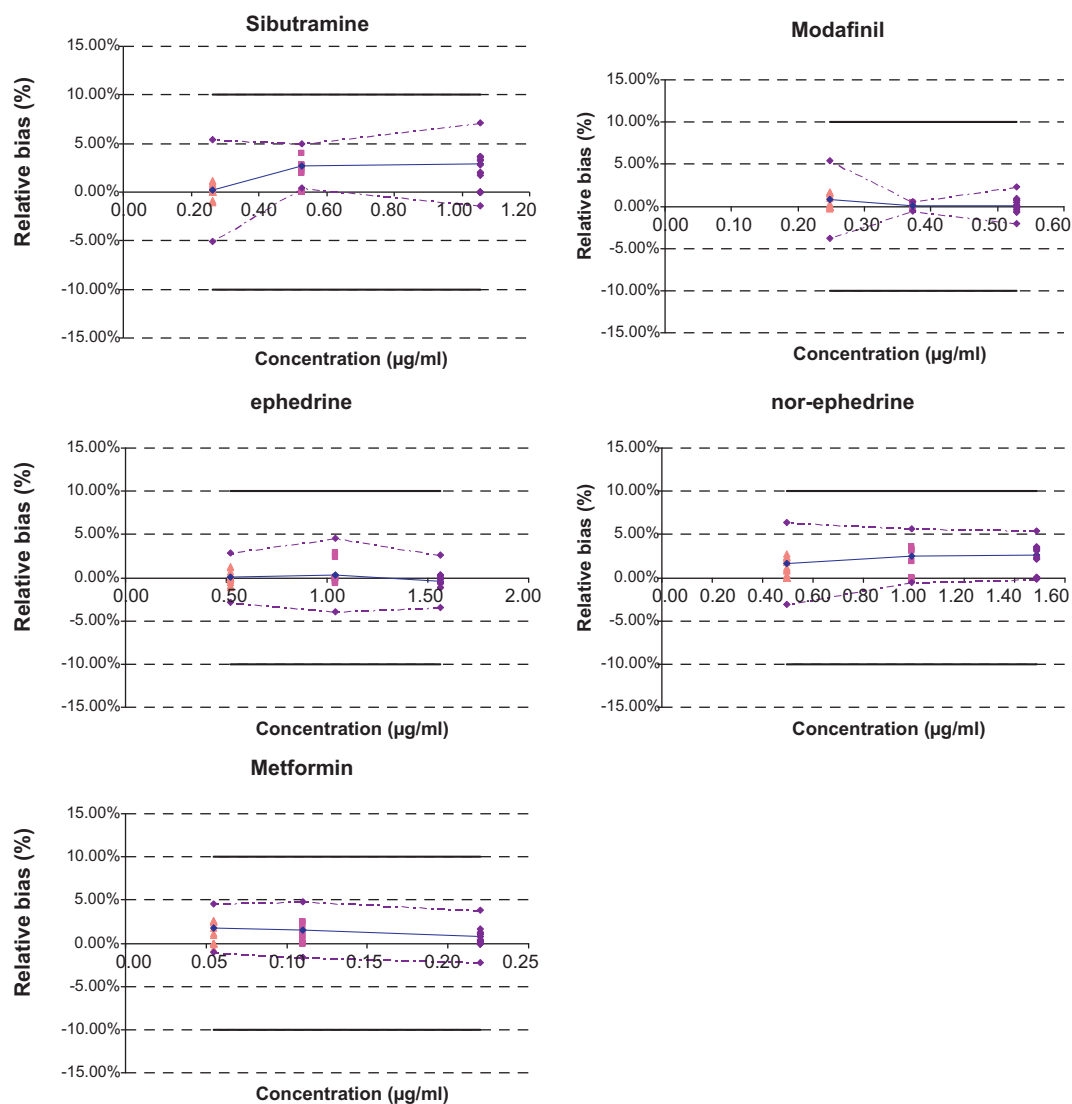|	Level	Sibutramin	Modafinil	Ephedrine	Norephedrine	Metformin
Trueness						
	1	2.90	0.12	-0.42	2.62	0.76
Relative bias (%)	2	2.76	0.03	0.32	2.54	1.57
	3	0.20	0.76	0.01	1.63	1.77
Intra-assay precision						
	1	0.256	0.393	0.72	1.086	0.311
Repeatability (RSD %)	2	0.424	0.252	1.076	1.199	0.513
	3	0.227	0.421	0.680	0.351	1.053
Between-assay precision						
	1	0.842	0.617	0.614	1.080	0.617
Intermediate precision (RSD %)	2	0.627	0.252	1.380	1.199	0.884
	3	1.056	0.940	0.948	0.940	1.097
Accuracy						
	1	[−1.37;7.17]	[−2.06;2.30]	[−3.40;2.57]	[−0.15;5.40]	[−2.26;3.79]
β-Expectation tolerance limits (%)	2	[−0.40;4.95]	[−0.56;0.61]	[−3.89;4.53]	[−0.52;5.61]	[−1.64;4.77]
	3	[−5.04;5.44]	[−3.86;5.38]	[−2.90;2.91]	[−3.06;6.32]	[−1.03;4.58]
Uncertainty						
	1	1.984	1.371	1.388	2.350	1.406
Relative expanded uncertainty (%)	2	1.430	0.524	3.031	2.593	2.014
	3	2.435	2.146	2.093	2.189	2.373

Fig. 3. Accuracy profile of the five components. The plain line is the relative bias, the dashed lines are the β-expectation tolerance limits, the bold plain line are the acceptance limits (10%) and the dots represent the relative back-calculated concentrations, plotted with respect to their targeted concentration.

can be concluded that the trueness for all components is acceptable since the relative bias is always smaller than 3%.

The precision is a measure for the relative errors of the method and is expressed as the relative standard deviations (RSD) for repeatability and intermediate precision. From Table 3 it can be seen that an acceptable precision is obtained for all components. The maximal RSD is obtained for efedrine and is 1.380%.

Accuracy takes into account the total error of the test results and is represented by the β-expectation tolerance intervals. The acceptance limits for the bias were set at 10%. This is based on the fact that the general acceptance limits for the content of pharmaceutical preparations, made by a pharmacist, are from 90 to 110% and that it is considered that the quality of illegal/counterfeit preparations is not higher than those preparations. As shown in Table 3 and Fig. 3 the relative β-expectation tolerance intervals, obtained from the ordinary least-squares regression, did not exceed the acceptance limits, which mean that each future measurement of unknown samples will be included in the tolerance limits for the relative bias at the 5% level. When looking at Fig. 3 the β-expectation tolerance intervals are much better than the 10% limits and, with exception for sibutramine, they fall almost in the 5% limits.

The uncertainty represents the dispersion of the values that could reasonably be attributed to the analyte. The expanded uncertainty represents an interval around the results where the unknown true value can be observed with a confidence level of 95%. The relative expanded uncertainties (%) are obtained by dividing the corresponding expanded uncertainties with the corresponding concentrations. Results are shown in Table 3. Since all uncertainties are below 5% percent the method is considered to have acceptable uncertainties for all components.

3.2.4. Recovery

The absolute recoveries of the five components were determined at the three concentration levels used to construct the accuracy profile. The recoveries were determined by analysing spiked blank samples and calculating their concentrations using calibration lines in analogy with what was done for the accuracy profile. Table 4 summarizes the mean recoveries obtained for the five components at each concentration level. All recoveries are within acceptable limits, indicating that the method is suited for the analysis of these active substances in pharmaceutical preparations.

Table 4
Summary of the recoveries obtained for the five components.

Concentration level	Sibutramin (%)	Modafinil (%)	Ephedrine (%)	Nor-ephedrine (%)	Metformin (%)
Level 1	102.1	98.9	99.4	100.0	101.1
Level 2	102.1	100.4	100.0	101.9	101.6
Level 3	100.9	99.6	100.7	102.1	102.5

4. Conclusions

An ultra fast liquid chromatography method with diode area detection was developed and validated for the qualitative and quantitative analysis of pharmaceuticals preparations containing active ingredients frequently found in illegal slimming products. The validation was performed following the ISO17025 requirements and proved that the method was suited for purpose and can be used in the routine analysis of these pharmaceutical preparations.

The method is a gradient method using an ammonium acetate buffer of pH 5 as aqueous phase, acetonitrile as organic modifier and a Vision HT C18-B column as stationary phase. The gradient starts at 98% of aqueous phase which is kept for 2 min. After 2 min a linear gradient is started to reach 100% of organic phase at 8 min. The plateau of 100% organic phase is hold for 2 min before returning to the start conditions. The flow was 0.5 ml/min, the injection volume was 5 μl and the column temperature was set on 50 °C.

The method was applied in the routine analysis of illegal slimming products at our lab and showed a good performance. It was also shown that phenolphthalein, a molecule not taken into account during method development was separated from the other molecules and did not interfere with the analysis.

The presented method is able to fully characterise illegal samples, suspected to contain slimming drugs, in runs of only 10 min. The more the use of an ammonium acetate buffer combined with acetonitrile allows the transfer to a mass spectrometer, allowing even a more thorough investigation, for example if unknown molecules are present or if there is a doubt about the presence of a certain compound. The application of this method in routine analysis at our lab represented a gain of time and solvent consumption in comparison with the more traditional HPLC methods, focussing on one molecule at the time.

References

[1] M.H.Y. Tang, S.P.L. Chen, S.W. Ng, A.Y.W. Chan, T.W.L. Mak, Case series on a diversity of illicit weight-reducing agents: from the well known to the unexpected, Br. J. Clin. Pharmacol. 71 (2011) 250–253.

[2] D. Müller, W. Weinmann, M. Hermanns-Clausen, Chinese slimming capsules containing sibutramine sold over the internet: a case series, Dtsch. Arztebl. Int. 106 (2009) 218–222.

[3] S.P. Chen, M.H. Tang, S.W. Ng, W.Y. Poon, A.Y. Chan, T.W. Mak, Psychosis associated with usage of herbal slimming products adulterated with sibutramine: a case series, Clin. Toxicol. (Phila.) 48 (2010) 832–838.

[4] Y.P. Yuen, C.K. Lai, W.T. Poon, S.W. Ng, A.Y. Chan, T.W. Mak, Adulteration of over-the-counter slimming products with pharmaceutical analogue – an emerging threat, Hong Kong Med J. 13 (2007) 216–220.

[5] L.M. de Carvalho, M. Martini, A.P.L. Moreira, A.P.S. de Lima, D. Correia, T. Falcao, S.C. Garcia, A.V. de Bairros, P.C. do Nascimento, D. Bohrer, Presence of synthetic pharmaceuticals as adulterants in slimming phytotherapeutic formulations and their analytical determination, Forensic Sci. Int. 204 (2011) 6–12.

[6] B.J. Venhuis, M.V. Vredenbregt, N. Kaun, J.K. Mauri, Z. Fijalek, D. de Kaste, The identification of rimonabant polymorphs, sibutramine and analogues of both in counterfeit Acomplia bought on the internet, J. Pharm. Biomed. Anal. 54 (2011) 21–26.

[7] Y. Chen, L. Zhao, F. Lu, Y. Chai, Y. Wu, Determination of synthetic drugs used to adulterate botanical dietary supplements using QTRAP LC–MS/MS, Food Addit. Contam. Part A: Chem. Anal. Control Expo. Risk Assess. 26 (2009) 595–603.

[8] J. Wang, B. Chen, S. Yao, Analysis of six synthetic adulterants in herbal weight-reducing dietary supplements by LC electrospray ionization–MS, Food Addit. Contam. Part A: Chem. Anal. Control Expo. Risk Assess. 25 (2008) 822–830.

[9] J.W. Bae, C.I. Choi, S.Y. Lee, Simultaneous determination of sibutramine and its active metabolites in human plasma by LC–MS/MS and its application to a pharmacokinetic study, Biomed. Chromatogr., doi:10.1002/bmc.1587, in press.

[10] S.H. Kim, J. Lee, T. Yoon, J. Choi, D. Choi, D. Kim, S. Won Kwon, Simultaneous determination of anti-diabetes/anti-obesity drugs by LC/PDA, and targeted analysis of sibutramine analog in dietary supplements by LC/MS/MS, Biomed. Chromatogr. 23 (2009) 1259–1265.

[11] I.C. Diefenbach, M. Friedrich, M.R. Dos Santos, C.F. Bittencourt, Development and validation of a column high-performance liquid chromatographic method for determination of sibutramine in capsules, J. AOAC Int. 92 (2009) 148–151.

[12] EN ISO/IEC 17025 General requirements for the competence of testing and calibration laboratories, 2005, www.iso.org.

[13] M. Fienberg, Validation of analytical methods based on accuracy profiles, J. Chromatogr. A 1158 (2007) 174–183.

[14] M. Feinberg, M. Laurentie, A global approach to method validation and measurement uncertainty, Accredit. Qual. Assur. 11 (2006) 3–9.

[15] B. De Backer, B. Debrus, P. Lebrun, L. Theunis, N. Dubois, L. Decock, A. Verstraete, P. Hubert, C. Charlier, Innovative development and validation of an HPLC/DAD method for the qualitative and quantitative determination of major cannabinoids in cannabis plant material, J. Chromatogr. B 877 (2009) 4115–4124.

[16] J.O. De Beer, T.R. De Beer, L. Goeyens, Assessment of quality performance parameters for straight line calibration curves related to the spread of the abscissa values around their mean, Anal. Chim. Acta 584 (2007) 57–65.

[17] D.L. Massart, B.G.M. Vandeginste, L.M.C. Buydens, S. De Jong, P.J. Lewi, J. Smeyers-Verbeke, Handbook of Chemometrics and Qualimetrics-Part A, Elsevier Science, Amsterdam, 1997.

Rapid discrimination and quantification of alkaloids in *Corydalis Tuber* by near-infrared spectroscopy

Hai-yan Lu[a], Shi-sheng Wang[a], Rui Cai[a], Yu Meng[a], Xin Xie[b], Wei-jie Zhao[a],*

[a] *School of Pharmaceutical Science and Technology, Dalian University of Technology, Linggong Road 2, Dalian 116023, PR China*
[b] *Pfizer Inc, Daqing Road 22, Dalian 116600, PR China*

ARTICLE INFO

ABSTRACT

With the application of near-infrared spectroscopy (NIRS), a convenient and rapid method for determination of alkaloids in *Corydalis Tuber* extract and classification for samples from different locations have been developed. Five different samples were collected according to their geographical origin, 2-Der with smoothing point of 17 was applied as the spectral pre-treatment, and the 1st to scaling range algorithm was adjusted to be optimal approach, classification model was constructed over the wavelength range of 4582–4270 cm^{-1}, 5562–4976 cm^{-1} and 7000–7467 cm^{-1} with a great recognition rate. For prediction model, partial least squares (PLS) algorithm was utilized referring to HPLC-UV reference method, the optimum models were obtained after adjustment. Pre-processing methods of calibration models were COE for protopine and min–max normalization for palmatine and MSC for tetrahydropalmatine, respectively. The root mean square errors of cross-validation (RMSECV) for protopine, palmatine, tetrahydropalmatine were 0.884, 1.83, 3.23 mg/g. The correlation coefficients (R^2) were 99.75, 98.41 and 97.34%. *T* test was applied, in the model of tetrahydropalmatine; there is no significant difference between NIR prediction and HPLC reference method at 95% confidence interval with $t = 0.746 < t_{(0.05,20)} = 2.086$, therefore NIRS is a reliable analytical tool in establishing prediction models.

© 2011 Elsevier B.V. All rights reserved.

1. Introduction

Corydalis Tuber (named *Yanhusuo* in Chinese) of the family Papaveraceae is a perennial herb that is widely distributed in the Zhejiang, Hubei, Sichuan, Jiangsu province and Northeast of China. It is a traditional Chinese medicine (TCM) that shows therapeutic effects of promoting blood circulation, reinforcing vital energy and alleviating pain, for instance headache/chest pain, epigastric pain, abdominal pain, backache, arthralgia or trauma [1,3], cardiac arrhythmia, gastric and duodenal ulcer and menorrhalgia [4,5]. Tertiary and quaternary alkaloids are the main chemical ingredients of *C. Tuber* [2]. Nearly 20 alkaloids of these two types have been isolated. An HPLC method using unmodified silica with reversed-phase eluents was developed for the determination of DL-tetrahydropalmatine in *Corydalis Yanhusuo* W.T. Wang and its set prescription preparations [6], and a high-performance liquid chromatography (HPLC) method with MS and UV-detection was developed for the qualitative and quantitative

determination of alkaloids in *C. yanhusuo* [7]. The content of most alkaloids varies with the geographic position and growing environment etc. Consequently, to compare the quality and efficacy and facilitate discrimination of *C. Tuber*, a reliable analytical technique should be developed. NIR qualitative model establishment had been applied to *C. Tuber* from two different origins in a previous study [8], but no literature has been reported to determine the contents of alkaloids in *C. Tuber* and various species have not been identified with the application of near-infrared reflectance spectroscopy.

Near-infrared spectroscopy analysis is suitable for different state of samples and a wide range of analytical applications. It is a rapid, highly sensitive, nondestructive method with minimal or no sample preparation, suitable for on-line analysis. Conventional analysis is time consuming while near infrared spectral scanning just needs a few seconds. With these advantageous features, NIRS has been extensively used as a qualitative and quantitative analysis tool in the chemical [9] pharmaceutical [10] and food [11,12] industries.

In this work, NIR spectroscopy and chemometric techniques were applied for quantitative determination of protopine, palmatine and tetrahydropalmatine in *C. Tuber*, using PLS regression for

the calibration and validation. The precision and accuracy of the new NIR method and the standard HPLC method were compared. On the basis of the NIR qualitative model the source of five *C. Tuber* samples of different origin was also identified.

2. Materials and methods

2.1. Samples and reagents

For the classification model, samples of raw *C. Tuber* were collected from five main growing localities in China (Zhejiang, Sichuan, Northeast, Anhui, Jiangsu), respectively. For the quantitative analysis model 70 samples were used while 30 were used as calibration set, 20 as validation set, and the rest formed the prediction set.

All samples were first milled into powder with a high-speed medicinal herb grinder (AK-1000A, 1000 W, Aoli Medicine Manufactory, China) and then passed through a 100-mesh sieve. In order to minimize the effect of moisture, the samples were dried at 60 °C for 1 h prior to analysis.

Protopine, palmatine and tetrahydropalmatine were bought from the National Institute for the Control of Pharmaceutical and Biological Products (Beijing, PR China). HPLC-grade acetonitrile was obtained from Tianjin Concord Chemical Reagent Company (Tianjin, PR China). Water was purified by Milli-Q water system (Millipore Corp., MA, USA). All other reagents were of analytical grade.

2.2. HPLC analysis

About 1 g of dried *C. Tuber* was dissolved in 30 ml of 70% ethanol in an Erlenmeyer flask for 1 h using the ultrasonic wave technique; the pH of the solution was set to 3.5 with acetic acid and filtered. After filtration, the extract was evaporated to 10 ml by rotary evaporation at 50 °C under reduced pressure to yield the crude extract. Then the pH value of the filtrate was raised to 12 with NaOH (5%, w/v) and extracted with diethyl ether three times (15, 10, 10 ml). The combined extract was evaporated to dryness with a rotary evaporator at 30 °C .The dry residue was then dissolved in 10 ml methanol and filtered through 0.45 mm membrane filter before HPLC analysis.

A Waters HPLC system (Waters Technologies Inc., USA) consisting of Waters Pump 600, UV Detector486 and 717 Auto Sampler was used to separate and analyze 10 μl sample injections at 280 nm over a Phenomenex Luna C18 column (250 mm × 4.6 mm, i.d., 5 μm). A linear gradient elution of A (0.2% acetic acid solution, adjusted with triethylamine to pH 5.0) and B (acetonitrile) was used according to the following profile: 0–15 min, 20% B; 15–35 min linear increase to 80% B; 35–37 min linear decrease to 20% B [8]. The solvent flow rate was 1.0 ml/min and the column temperature was set at 25. The injection volume was 10 μl. Chromatographic peaks were identified by comparing the retention times with those of standards.

2.3. NIR spectra collection

The NIR spectra of *C. Tuber* samples were recorded using a Bruker Matrix-I FT-NIR spectrometer (Bruker Optik, Ettlingen, Germany) equipped with a PbS detector, an integrating sphere, sample cup and rotary tables. The system was operated by OPUS spectral acquisition and processing software (Bruker Optik, Ettlingen, Germany). The spectra were obtained with a 8 cm^{-1} resolution over a wavelength range of 12,500–4000 cm^{-1} with 64 scans per spectrum, both sample and background scan time were 32 s. The temperature was kept at 29 °C [13], and the air absorption is recorded as a reference standard. Powder samples were weighed precisely (1 g) and put in glass bottles with cover. A slight tap was needed to make the powder in the glass more uniform and dense before the measurements.

2.4. Spectra preprocessing

In addition to important chemical information, the collected sample spectra also contain other irrelevant information and noise. In the original near-infrared spectra of *C. Tuber* samples in Fig. 1 the bands overlap severely. For this reason spectral preprocessing reducing the effects of systematic noise, baseline variation, light scattering, and path length differences is a critical step [14]. Several different types of pretreatment have been applied, including the first-derivative (1-Der), second-derivative (2-Der), multiplicative scatter correction (MSC), vector normalization (VN), min–max normalization (MMN), constant offset elimination (COE) and wavelet transform (WT) with the application of the Wavelet Toolbox, Matlab7.1.

2.5. NIR data treatment

While establishing the NIR quantitative model, the real content of protopine, palmatine and tetrahydropalmatine were obtained with reference to HPLC results, which were uniformly distributed over the entire concentration range in both calibration and test sets. The capability of the partial least squares (PLS) regression model was estimated by series parameters. A leave-one-sample-out cross-validation was used, and dimension factor was determined by correlation coefficient (R^2) of calibration and root mean square error of cross-validation (RMSECV). The R^2 values give an indication of the percentage variation in Y attributable to the variation in X; models with values of 0.92–0.96 are suitable for most application including quality control and those above 0.98 for all applications. Model prediction accuracy was evaluated with RPD: values above 3 are considered to be good and excellent predictive models. The bias (average difference between predicted and measured values) was based on the *t*-test to find any significant difference. Computing formula of above mentioned parameters can be found in Ref [15].

Selectivity (S) is the key factor that determines whether the qualitative model is applicable or not. Identification is achieved by comparing a sample spectrum to a reference spectrum or a library of reference spectra; qualitative applications of NIR spectroscopy typically involve establishing a mathematical relationship between NIR spectral response and a physical or chemical property of interest. Demonstrating specificity against a physical or chemical property of interest is based on interpreting both NIR spectral attributes and chemometric parameters in terms of the intended application [16]. The identification model was established by utilizing algorithms such as factorization, standardization, scaling to 1st range. As an elementary method, factorization spectrum is expressed as a linear combination of spectral factor, $a = T_1 af_1 + T_2 af_2 + T_3 af_3 + \ldots$, where f_i is the factor spectrum which is orthogonal, T_i is the coefficient of each factor spectrum, characterized by its contribution of corresponding f_i to spectrum. Then acquire

spectrum distance: D.

$$D = \sqrt{\sum_i [T_i a - T_i b]^2} \tag{1}$$

$$D_T = Max(Hit) + XS_{Dev} \tag{2}$$

$$S = \frac{D}{T_1 + T_2} \tag{3}$$

Calculate the distance spectrum (*Hit*) of each sample to the average spectrum in the training set, and accordingly gain the threshold
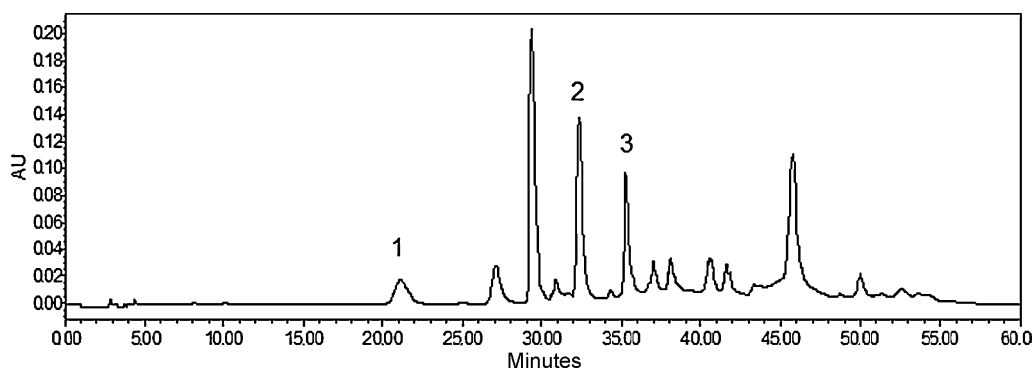
Fig. 1. HPLC chromatogram of *C. Tuber* extract (the peaks marked with 1–3 were Protopine, Palmatine, Tetrahydropalmatne, respectively).

calculated for each sample (DT). *Max*(*Hit*) is the maximum distance of the sample spectrum to the average spectrum; XS_{Dev}: the standard deviation of *Hit*; *X* is a coefficient, usually selected based on experience 0.25, using the above formula to compare the matching of spectra. Finally get the selectivity: *S*. Exceeding the value of 2, selectivity (*S*) means every class can be completely separated. So the larger is *S*, the greater distinction between different classes we can get, and the better is accuracy of the prediction model we can construct. Formulae (1), (2), (3) can be found in Ref. [17].

3. Results and discussion

3.1. HPLC studies of C. Tuber

Fig. 1 shows a typical HPLC-UV chromatogram of *C. Tuber* extract solution. Since the National Institute for the Control of Pharmaceutical and Biological Products (Beijing, PR China) can only supply three reference standards: protopine, palmatine, tetrahydropalmatine, we dealt with the quantitative analysis of these three alkaloids. Criteria for assessing the suitability of the system are described in the chapter on chromatographic separation techniques. The results are listed in Table 1. The calibration curves of three standards show good linearity ($R^2 > 0.9998$) covering the range recorded for the test. LODs (S/N > 3) of three standards are in the range of 0.2–0.5 µg/ml. It can be concluded that the method had a good repeatability and is accurate with recoveries of more than 97%.

The results (Table 2) verify the suitability of laboratory method for choosing the validation set, due to similar values for mean, SD, standard error, range displayed by calibration and validation set. The precision of the reference method illustrated as the SEL, and the ranges for the validation set lay within the range recorded for the calibration set.

3.2. Classification of C. Tuber

Herbal medicines from different geographical origin containing various types and concentration of alkaloids, obviously show diverse efficacy. Consequently, this chapter is dealing with NIR spectroscopy techniques to identify samples from five different locations.

Table 2
Statstical analysis of calibration and validation sets: data range, mean and standard deviation(SD), stand error of laboratory (SEL).

Parameter	Item	Calibration set (*n*=30)	Validation set (*n*=20)
Protopine	Range	42.21–48.79	43.07–46.97
	Mean	44.74	43.65
	SD	1.80	2.31
	SEL	1.03	1.01
Palmatine	Range	63.40–69.12	63.57–66.85
	Mean	66.09	65.53
	SD	1.48	1.62
	SEL	1.84	1.73
Tetrahydropalmatine	Range	120.32–129.11	122.64–129.06
	Mean	123.37	125.53
	SD	2.01	3.75
	SEL	3.32	3.65

100 samples were collected while 75 of them were used for identification model and the rest were utilized as validation set. Spectra of *C. Tuber* samples from five locations over the 12,500–4000 cm^{-1} range are shown in Fig. 2a. As a result of intense band overlapping, difference between various samples in the spectra is hard to uncover, so pretreatment is needed. Comparison of diverse spectra pretreatments such as 1-Der, 2-Der, and Savitsky-Golay (S.G.), MSC, VN, MMN, COE, 1Der + MSC and WT were acquired, of which 2-Der with smoothing point of 17 as illustrated in Fig. 2b were demonstrated as optimum pretreatment. 2-Der was used to eliminate the baseline shift and enhance spectral differences and resolution. After treatment with 2-Der, there was no distinct change over the wavelength range of 12,500–7700 cm^{-1} which mostly includes baseline information. Further effort was taken over the wavelength range of 7700–4000 cm^{-1} containing abundant chemical information for component content of the samples.

The average spectra of the samples from five different locations (Fig. 2b) have similar profiles, the bands were interpreted as overtones and combinations of fundamental vibrations of the –CH, –NH, and –OH groups. The peaks around 7234 cm^{-1} and 5874 cm^{-1} arise from 1st overtone of C–H. Other characteristic absorbance peaks can be interpreted as: 2nd overtone of C–H–O (5346 cm^{-1}), combination N–H and O–H banding (4466 cm^{-1}, 4380 cm^{-1}),

Table 1
The methodology parameters and the calibration curve of the reference method.

Compounds	t_R (min)	Calibration curves	R^2	Linearity ranges (µg/ml)	Test ranges (µg/ml)	LOD (µg/ml)	Repeatability (RSD%, *n*=6)	Recovery (%, *n*=3)
Protopine	20.38	$Y = 240552X - 171549$	1.0000	42–420	42.21–48.79	0.02	0.78446	97.94
Palmatine	26.75	$Y = 652557X - 312939$	0.9999	40–400	63.40–69.12	0.04	0.26506	100.76
Tetrahydropalmatine	30.86	$Y = 371167X - 240640$	0.9998	86–860	120.32–129.11	0.05	0.13199	98.54

Y: the peak area of chromatogram; *X*: the concentration of each active compound.
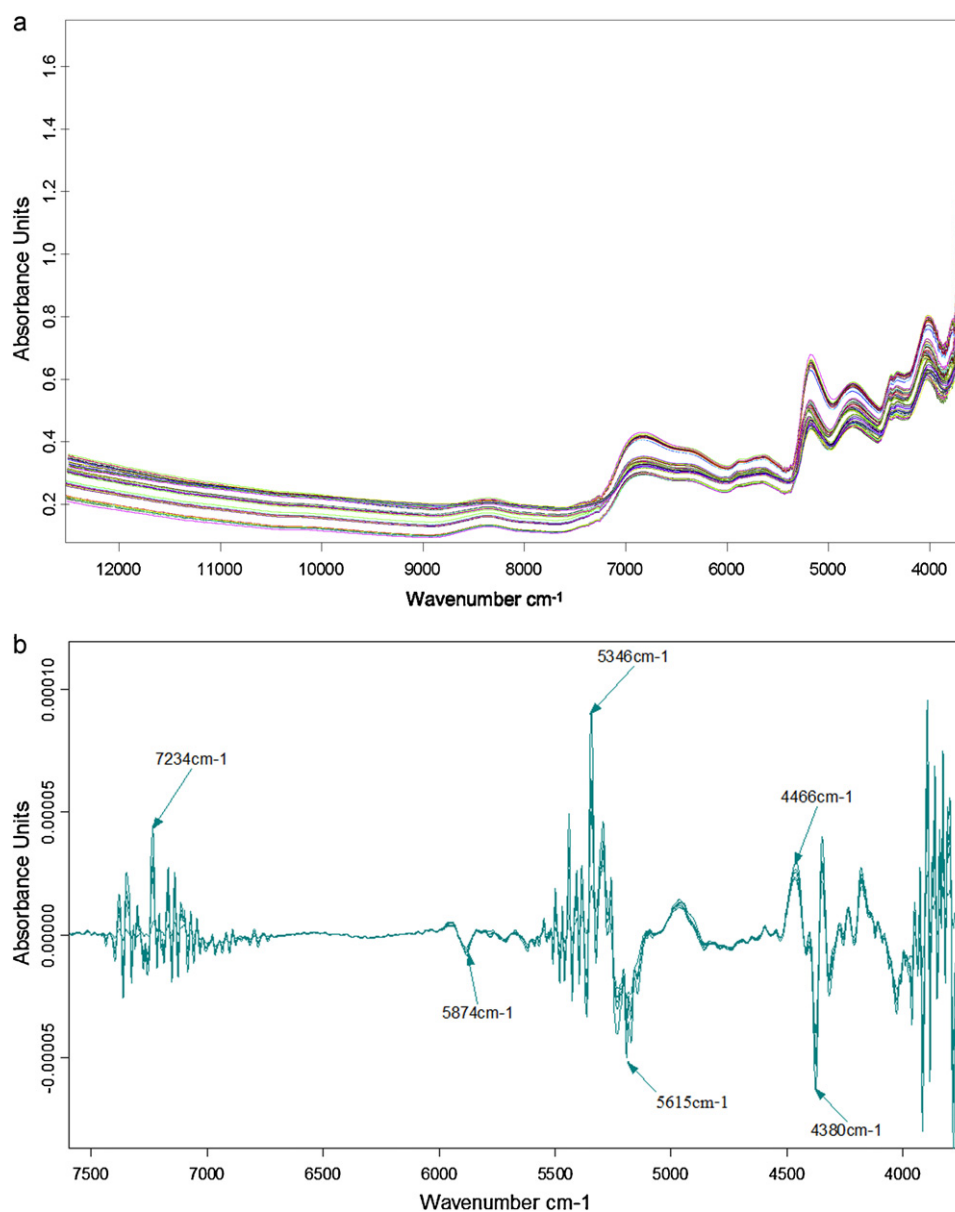
Fig. 2. (a) Sixctra of Corydabs Tuber samples from five locations. (b) Spectra pre-treated with second deriative.

combination OH stretching and OH banding ($5165\,\text{cm}^{-1}$) [18]. The areas of 4582–$4270\,\text{cm}^{-1}$, 5562–$4976\,\text{cm}^{-1}$ and 7000–$7467\,\text{cm}^{-1}$ were chosen to build classification model. The 1st to scaling range algorithm was confirmed highest efficiency in discriminating.

The detailed outcome is shown in Table 3, all the selectivities of discriminant model have exceeded 2. 25 samples were precisely distinguished with a 100% recognized rate, indicating that NIR spectroscopy techniques can be used to differentiate samples accurately. Construction over the area of $12{,}500$–$4000\,\text{cm}^{-1}$ displayed 88% recognition rate.

3.3. Quantification of alkaloids content with PLSR algorithm

3.3.1. Spectra investigation

In this study, 70 samples were collected and divided into three sets: calibration (30), validation (20), prediction (20), in order to construct robust PLS models. It can be observed from Fig. 1a that the region of 4000–$7500\,\text{cm}^{-1}$ contains abundant chemical information which is caused by the stretch or deformation vibration of C–H, O–H and C–H groups. NIR spectra in the region of 4000–$4600\,\text{cm}^{-1}$ exhibiting much noise should be excluded from further study. Taking tetrahydropalmatine as example the wavelength range of 5420.2–$4597.7\,\text{cm}^{-1}$ was chosen for building quantitative model after abundant adjustment.

3.3.2. Calibration of models

PLS regression model for tetrahydropalmatine content with various pretreatments is presented in Table 3. The performance of models was evaluated by the parameters of RMSECV, RMSEP, R^2, RPD and the standard error of prediction corrected for bias. Higher R^2 values improve discrimination. The optimum model should be determined by the lowest RMSECV (using the leave-one-out cross-validation technique), RMSEP and highest R^2, which could be significantly affected by the dimension factor (D) of PLS regression and spectral pretreatment methods. As illustrated in Table 4, MSC has revealed as optimum pre-processing approach. While MSC was used to correct the light scattering effects due to particle size distribution and packing density by adjusting the spectra based on ranges of wavelengths carrying no specific chemical information [19].

Table 3
The selectivity report of qualitative model.

Group1	Group2	S	T_1	T_2	D
Northeast	Zhejiang	4.31075	0.346075	0.470450	3.519829
Jiangsu	Sichuan	2.372921	0.359916	0.085967	1.058044
Sichuan	Jiangsu	3.453831	0.085967	0.359916	1.540003
Zhejiang	Sichuan	3.709749	0.470450	0.085967	2.064166
Anhui	Jiangsu	6.569718	0.771981	0.359916	7.436241

Table 4
PLS regression model for tetrahydropalmatine content with various pretreatment.

Pre-treated methods	Calibration		validation	
	$R^2\%$	RMSECV(10^{-5}g/g)	$R^2\%$	RMSEP(10^{-5}g/g)
1Der+MSC	91.17	0.59	90.75	0.65
VN	94.7	0.457	95.53	0.412
1-Der	95.05	0.442	94.42	0.523
2-Der	93.38	0.511	94.04	0.498
WT	81.23	2.434	84.62	1.758
MSC	**97.34**	**0.323**	**96.32**	**0.365**

Results from models with best capability are marked in bold.

In the same spectral pretreatment method, every PLS model has an optimum dimension factor (D). The case of 'overfitting' or 'underfitting' would appear if the factor applied in the calibration is too big or small, and the information from the spectrum would be misrepresented or obtained not sufficiently, which reveals that neither of them could acquire good performance of model prediction. The OPUS was able to recommend the appropriate factor, as the value of D increases, RMSECV decreases gradually and R^2 increased by degrees, Furthermore, if D exceeds the optimum ($D=9$), the value of RMSECV and R^2 incline to unchanged.

3.3.3. Results of calibration

Three separate PLS calibrations were developed corresponding to contents of palmatine, protopine, tetrahydropalmatine. Fig. 3 demonstrates the relations of values measured by HPLC with the results predicted by optimized NIR models. All models with low bias displayed excellent predictive capacity in term of the criteria outlined by Williams [20] who suggests that an R^2 value greater than 0.9 and RPD values greater than 3 indicate excellent quantitative information. The bias adjustment time after time has gained parameters of optimal models of the *C. Tuber* powder in Table 5.

3.4. Results of validation model

With their optimal parameters, the PLSR models were used to predict the content of 20 samples in the validation set, achieving good prediction accuracy with overall R^2 exceeding 96.33%; no outliers and RMSEP below 0.00764 mg/g. The standard error of calibration (RMSECV) in Table 5 was close to the laboratory
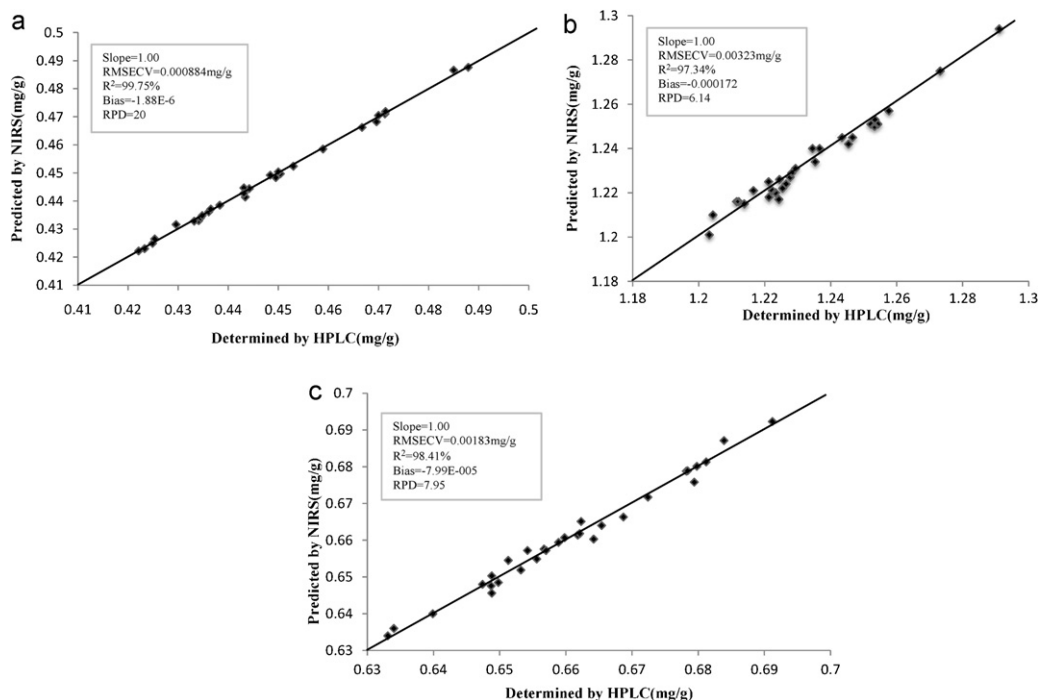

Fig. 3. (a) Relation of values measured by HPLC and the Protopine model, (b) relation of values measured by HPLC and the Tetrahydropalmatine model and (c) relation of values measured by HPLC and the Palmatine model.

Table 5
Parameters of optimal calibrations of the *C. Tuber* powder.

	Protopine	Palmatine	Tetrahydropalmatine
Spectral pretreatment method	COE	min–max normalization	MSC
Range of wavelength (cm^{-1})	7502.2–6098.2; 5450.2–4597.7	7502.2–5446.3; 5207.2–4728.9	5450.2–4597.7
Rank	9	4	9
RMSECV (μg/g)	0.884	1.83	3.23
R^2 (the calibration) (%)	99.75	98.41	97.34
RMSEP (μg/g)	1.64	7.64	4.73
R^2 (the validation) (%)	98.42	96.33	97.23

standard error SEL (Table 3), being within the acceptable limits for NIRS calibration procedures [21].

Exploration on results obtained by HPLC and NIR method has been validated by *t*-test. Taking tetrahydropalmatine as an example, the value statistics *t* is 0.746 less than $t_{(0.05,20)} = 2.086$ with a significant level of 0.05, which implies the accuracy of the established NIR method.

4. Conclusion

A NIR spectroscopic method was developed to analyze a complex TCM, *C. Tuber*, and a qualitative and quantitative model was successfully constructed. Five samples of *C. Tuber* from different locations were collected and distinguished showing that NIR method can be used as an efficient analytical tool for classification of similar samples. The prediction results for PLSR method with different pre-processing were investigated to produce optical calibration model, while true content of three parameters was measured by HPLC. The comparison between HPLC and NIR method showed no significant difference at 95% confidence interval, therefore NIR spectra method provide accurate and rapid analysis of alkaloid content of *C. Tuber* samples.

References

[1] F.Y. Tang, A.G. Nie, Qualitative and quantitative determination of ten alkaloids in traditional Chinese medicine *C. yanhusuo* W.T. Wang by LC–MS/MS and LC–DAD, J. Clin. Exp. Med. 5 (2006) 185–186.
[2] S. Tong, J. Yan, J. Lou, Preparative Isolation, Purification of Alkaloids from *C. yanhusuo* W. T. Wang by High Speed Counter-Current Chromatography, J. Liq. Chromatogr. Relat. Technol. 28 (2005) 2979–2989.
[3] W.C. Lenung, H. Zheng, Anxiolytic-like action of orally administered DL-tetrahydropalmatine in elevated plus-maze, Neuropsychopharmacol. Biol. Psychiatry 27 (2003) 775–779.
[4] A.P. Sagare, Y.L. Lee, T.C. Lin, C.C. Chen, Cytokinin-induced somatic embryogenesis and plant regeneration in *C. yanhusuo* (Fumariaceae) — a medicinal plant, Plant Sci. 160 (2000) 139–147.
[5] L.Z. Zhang, J. Guiyang, Two methods of preparing the total alkaloids of *C. yanhusuo*, Med. Coll. 31 (2006) 280–282.
[6] Y.F. Yuan, Z.L. Liu, X.L. Li, Use of silica gel with reversed-phase eluents for the separation and determination of alkaloids in *C. Yanhusuo* W. T. Wang and its preparations, Biomed. Chromatogr. 10 (1996) 11–14.
[7] B. Ding, T.T. Zhou, G.R. Fan, Z.Y. Hong, Y.T. Wu, Qualitative and quantitative determination of ten alkaloids in traditional Chinese medicine *C. yanhusuo* W.T. Wang by LC–MS/MS and LC–DAD, J. Pharm. Biomed. Anal. 45 (2007) 219–226.
[8] Y. Lai, Y. Ni, S. Kokot, Discrimination of *Rhizoma Corydalis* from two sources by near-infrared spectroscopy supported by the wavelet transform and least-squares support vector machine methods, Vib. Spectrosc. 56 (2011) 154–160.
[9] J. Xue, C. Wu, L. Wang, S. Jiang, G. Huang, J. Zhang, S. Wen, L. Ye, Dynamic prediction models for alkaloid content using NIR technology for the study and online analysis of parching in Areca Seed, Food Chem. 126 (2011) 725–730.
[10] I.C. Wang, M.J. Lee, D.Y. Seo, H.E. Lee, Y. Choi, W.S. Kim, C.S. Kim, M.Y. Jeong, G.J. Choi, Polymorph transformation in paracetamol monitored by in-line nir spectroscopy during a cooling crystallization process, AAPS Pharm. Sci. Tech. 12 (2011) 764–770.
[11] J.S. Ribeiro, M.M.C. Ferreira, T.J.G. Salva, Talanta 83 (2011) 1352–1358.
[12] Y. Huang, T.M. Rogers, M.A. Wenz, Detection of sodium chloride in cured Salmon Roe by SW-NIR spectroscopy, J. Agric. Food Chem. 49 (2001) 4161–4167.
[13] Z.-H. Jiang, Z. Yang, C.-L. So, C.-Y. Hse, Rapid prediction of wood crystallinity in Pinus elliotii plantation wood by near-infrared spectroscopy, J. Wood Sci. 53 (2007) 449–453.
[14] T. Naes, T. Isaksson, T. Fearn, T. Davies, NIR Publications, Chichester, 2002, p.105.
[15] Y. Liu, X. Sun, A. Ouyang, Nondestructive measurement of soluble solid content of navel orange fruit by visible–NIR spectrometric technique with PLSR and PCA-BPNN, LWT - Food Sci. Technol. 43 (2010) 602–607.
[16] K.H. Norris, G.E. Ritchie, Assuring specificity for a multivariate near-infrared (NIR) calibration: the example of the Chambersburg Shoot-out 2002 data set, J. Pharm. Biom. Anal. 48 (2008) 1037–1041.
[17] Spectroscopic Software, Reference Manual, Version 5,I 26039.
[18] L.E. Rodriguez-Saona, F.S. Fry, M.A. McLaughlin, E.M. Calvey, Carbohydrate Res. 336 (2001) 63–74.
[19] A. Candolfi, R. De Maesschalck, D. Jouan-Rimbaud, P.A. Hailey, D.L. Massart, The influence of data pre-processing in the pattern recognition of excipients near-infrared spectra, J. Pharm. Biomed. Anal. 21 (1999) 115–132.
[20] P.C. Williams, Implementation of near-infrared technology, in: P.C. Williams, K.H. Norris (Eds.), In Near-Infrared Technology in the Agricultural and Food Industries, AACC, Inc., St. Paul, MN, U. S. A., 2001, pp. 145–169.
[21] E.R. Leite, J.W. Stuth, Fecal NIRS, equations to assess diet quality of free-ranging goats, Small Rum. Res. 15 (1995) 223–230.

Isolation and structural characterization of two tadalafil analogs found in dietary supplements

Valerie M. Toomey, Jonathan J. Litzau, Cheryl L. Flurer *

U.S. Food and Drug Administration, Forensic Chemistry Center, 6751 Steger Drive, Cincinnati, OH 45237, USA

ABSTRACT

During routine screenings of two "libido enhancer" dietary supplements using LC–MS^n, two compounds were detected that displayed structural similarities to tadalafil. These compounds were isolated from the supplements using high-performance liquid chromatography with fraction collection, and were characterized further using accurate mass determination and NMR. "Compound 1" had an m/z of 434 for the [M+H]$^+$ ion, with a corresponding chemical formula of $C_{24}H_{24}N_3O_5$. "Compound 2" had an m/z of 432 for the [M+H]$^+$ ion, with a corresponding chemical formula of $C_{25}H_{26}N_3O_4$. Although mass spectrometry indicated that these modifications occurred in place of the $-CH_3$ found on the pyrazinopyridoindole-1,4-dione of tadalafil, NMR was required to elucidate the correct configurations of these substitutions. The data obtained using NMR indicated that the structure of the $-C_3H_7O$ moiety found in Compound 1 was 2-hydroxypropyl, and the $-C_4H_9$ in Compound 2 was n-butyl. These new analogs were given the names 2-hydroxypropylnortadalafil and n-butylnortadalafil, respectively.

Published by Elsevier B.V.

1. Introduction

For the past several years, synthetic phosphodiesterase type-5 (PDE-5) inhibitors such as sildenafil, tadalafil and vardenafil have been identified routinely in "all natural" herbal supplements that are marketed for "male enhancement" [1–5]. More recently, the trend has shifted toward the introduction of analogs of the approved PDE-5 inhibitors. These compounds exhibit minor structural alterations compared to their approved or commercial counterparts. The presence of analogs in herbal supplements or in unapproved drug products could pose a significant risk to public health, because these analogs are not declared on the labeling. In many cases, there is no information available to the public with regard to their toxicological or pharmacological effects.

Several analogs of tadalafil, found in dietary supplements and other herbal products, have been reported in the literature. Aminotadalafil was first described in 2006, and has been characterized extensively using MS [6–8], NMR and Fourier-transform infrared spectroscopy [6]. Other analogs that have been detected include N-octylnortadalafil [9] and chloropretadalafil [10], which is a precursor in the synthesis of tadalafil or related compounds [11–13]. Another compound found in a supplement was characterized as a condensation product between aminotadalafil and 5-hydroxymethylfuraldehyde [14].

This article describes the structural characterization of 2-hydroxypropylnortadalafil ("Compound 1") and n-butylnortadalafil ("Compound 2"), analogs of tadalafil (Fig. 1). These compounds were detected during routine screening of "libido enhancer" dietary supplements using LC–ESI-MS^n. The compounds were isolated from the supplement matrices using HPLC followed by fraction collection. Determination of the accurate mass of the isolated compounds further supported the proposed modifications, and NMR analyses elucidated the structures of those modifications. Although no chiral analyses were conducted, it is believed that the n-butylnortadalafil is equivalent to "Compound 13" [11], first described in 2003 in a discussion of various substituted piperazinediones that were evaluated during the development of tadalafil.

2. Experimental

2.1. Samples and chemicals

The two dietary supplement products were obtained during an inspection at a distribution warehouse, and were submitted to the laboratory for analysis. Both products were supplied as single-serving foil packages, each containing one capsule. The product containing Compound 1 was composited by combining the contents of 15 capsules, having an average capsule content weight of 0.93 g. The product containing Compound 2 was composited using the contents of 4 capsules, having an average capsule content weight of 0.95 g.

* Corresponding author. Tel.: +1 513 679 2700; fax: +1 513 679 2761.
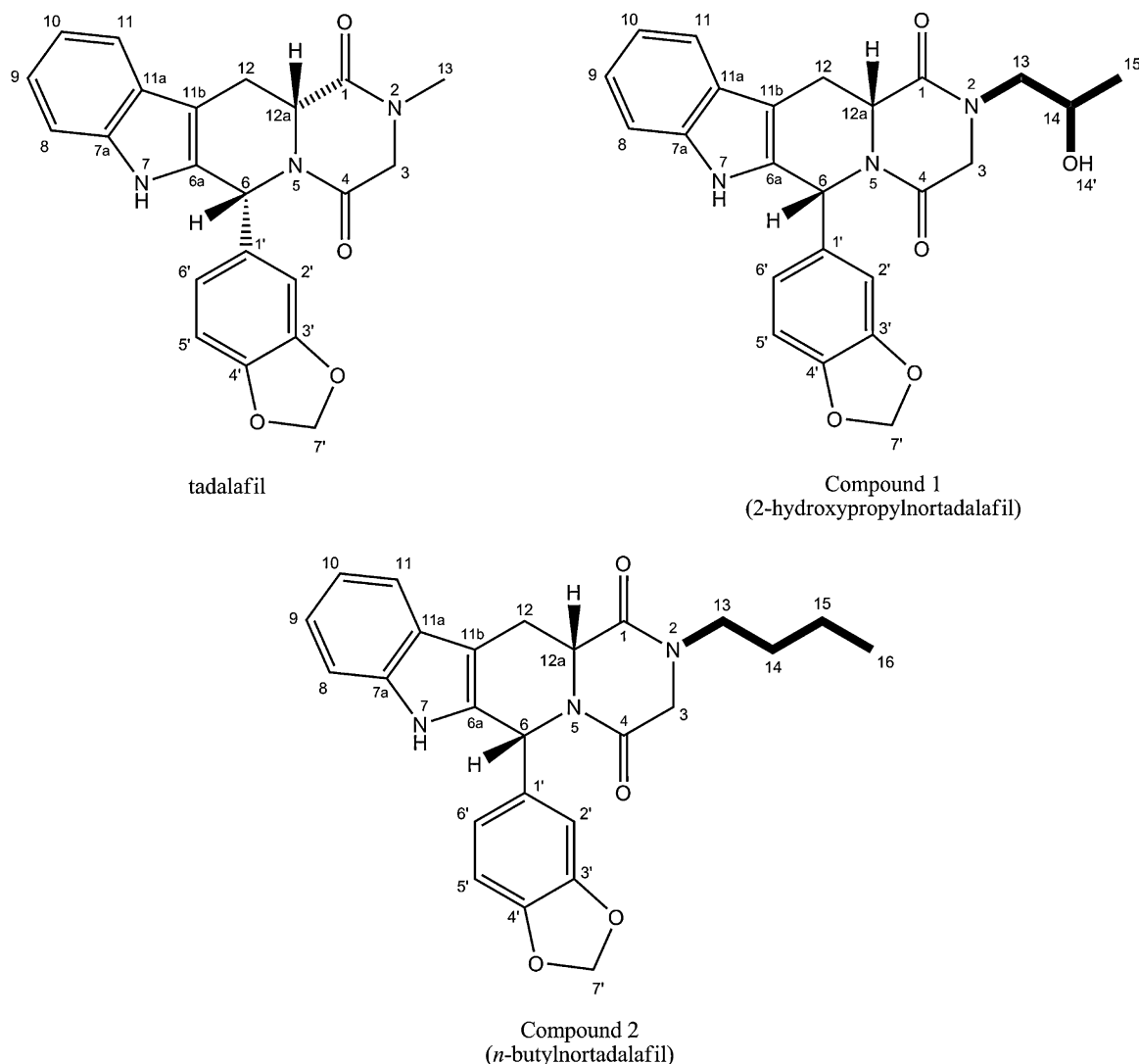 *E-mail address:* cheryl.flurer@fda.hhs.gov (C.L. Flurer).

Fig. 1. Structures of tadalafil, Compound 1 (2-hydroxypropylnortadalafil) and Compound 2 (*n*-butylnortadalafil). Structural differences are emphasized in bold.

Tadalafil was provided by Eli Lilly and Company (Indianapolis, IN, USA). The following HPLC grade solvents were purchased from Fisher Scientific (St. Louis, MO, USA): CH_3OH, CH_3CN, 0.1% (v/v) formic acid in water, 0.1% (v/v) formic acid in CH_3CN, 0.1% (v/v) trifluoroacetic acid (TFA) in water, and 0.1% TFA (v/v) in CH_3CN. Dimethylsulfoxide (DMSO-d_6) + 0.05% (v/v) tetramethylsilane (TMS) used for NMR analysis was purchased from Cambridge Isotope Laboratories, Inc. (Andover, MA, USA). The 18 MΩ cm deionized H_2O was generated using a Milli-Q Académic system (Millipore, Bedford, MA, USA).

2.2. LC–MS^n analyses

Samples were prepared for initial screening experiments by extracting 0.1 g composite in 5 mL 50:50 (v/v) CH_3CN:DIH$_2O$ and shaking. The extracts were filtered through 0.2 μm PTFE syringe filters, and were diluted further, 10 μL and 990 μL extraction solvent, prior to analysis.

LC–MS^n analyses were performed using a Thermo-Finnigan LTQ ion trap mass spectrometer equipped with an Ion Max source (ThermoElectron Corp., San Jose, CA, USA) coupled to an Agilent 1100 Series HPLC system (Agilent Technologies, Santa Clara, CA, USA). The column used was a Zorbax SB-C18, 2.1 mm × 150 mm, 3.5 μm column, maintained at 40 °C. Solvent A consisted of 0.1% formic acid

in water, and Solvent B was 0.1% formic acid in CH_3CN. The gradient employed, at a flow rate of 0.2 mL/min, was linear from 5% B to 95% B in 15 min, and was held at 95% B for 10 min, with a post-run equilibration of 7 min. The autosampler was maintained at 15 °C, with an injection volume of 1 μL.

Data acquisition and analysis were accomplished using Xcalibur software. The instrument parameters for the mass spectrometer were as follows: ionization = positive, electrospray; sheath gas flow = 50 arbitrary units; auxiliary gas flow = 15 arbitrary units; sweep gas flow = 15 arbitrary units; spray voltage = 3.5 kV; capillary temperature = 300 °C. Three scan events were used to collect the MS^n data. The first scan event collected the full scan MS data over the range m/z 80–650. The second was a data-dependent scan to collect MS/MS data on the most intense full scan ions, using a collision energy of 45%, with helium as the collision gas. The third was a data-dependent scan to collect MS^3 data on the most intense product ion from the second scan event, using a collision energy of 35%.

2.3. HPLC analyses

Sample extracts were prepared by mixing 0.25 g of each matrix and 25 mL 50:50 (v/v) CH_3CN:DIH$_2O$ with shaking. Aliquots were filtered through 0.45 μm nylon syringe filters prior to injection.
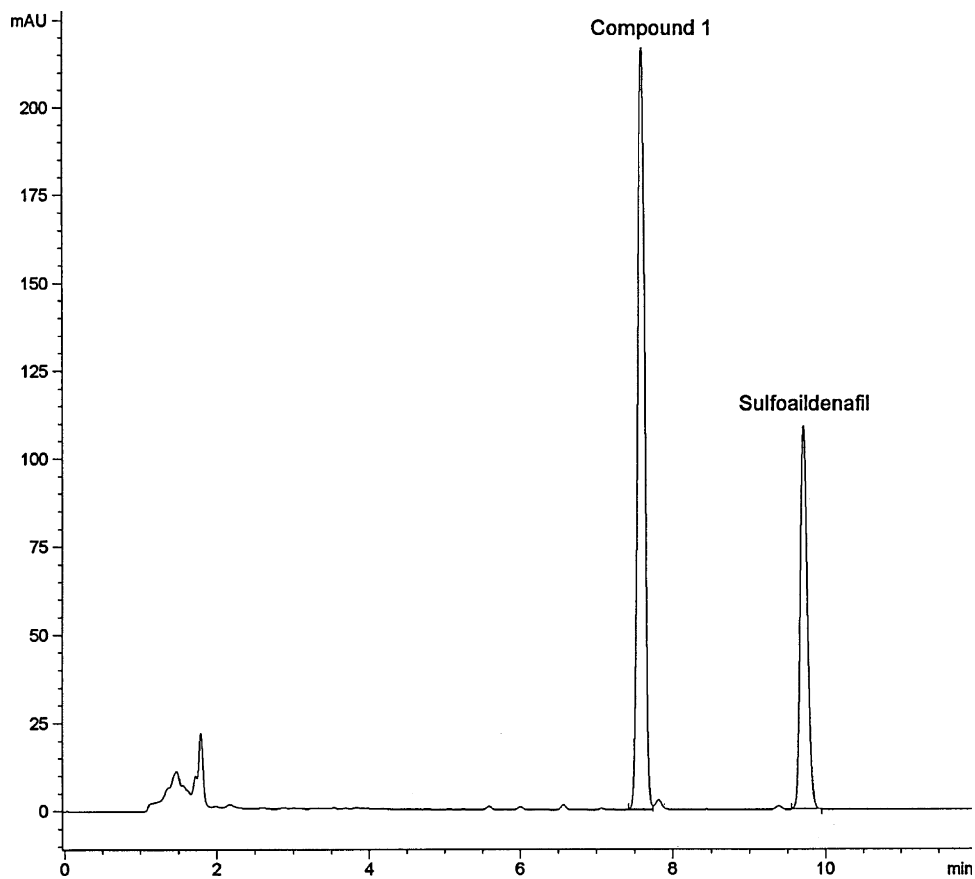
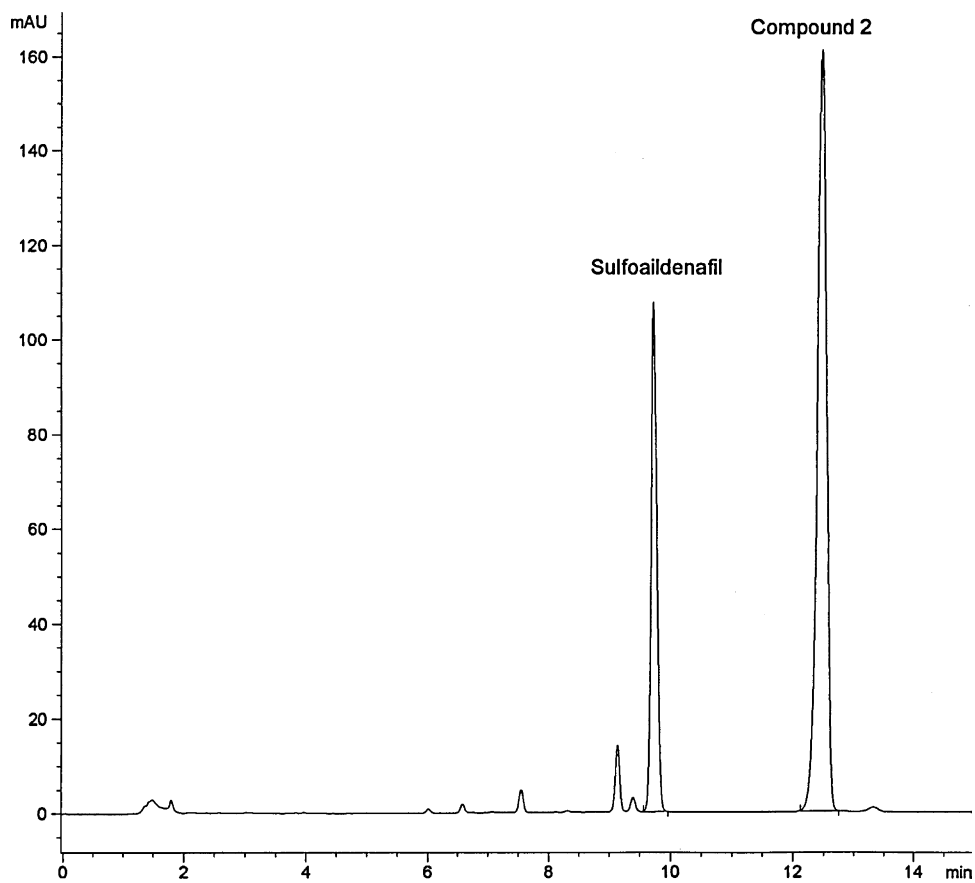**Fig. 2.** Chromatogram of product containing sulfoaildenafil and Compound 1.

Fig. 3. Chromatogram of product containing sulfoaildenafil and Compound 2.
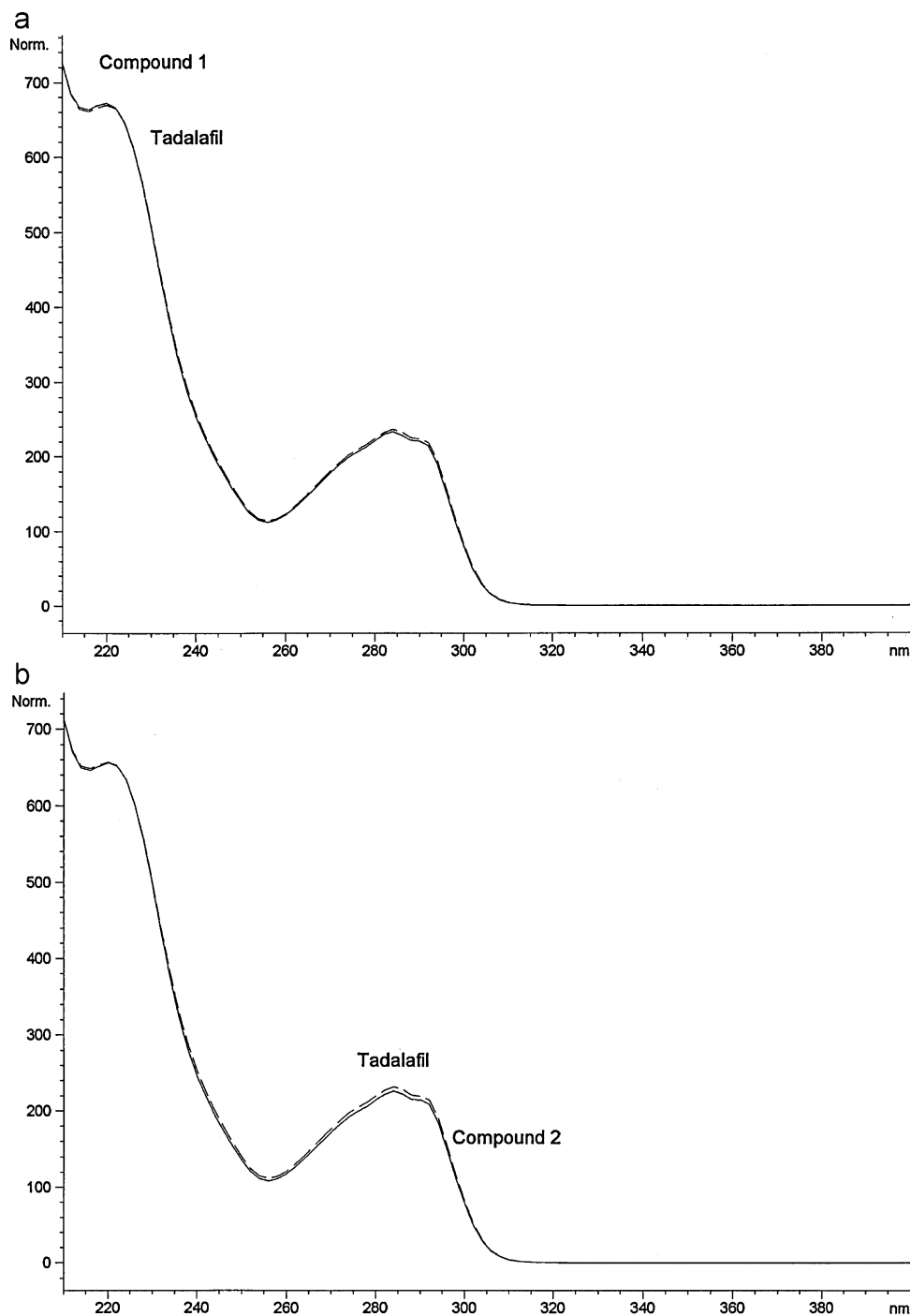
Fig. 4. (a) UV spectra of tadalafil and Compound 1. (b) UV spectra of tadalafil and Compound 2. Spectra were obtained using the chromatographic conditions indicated in the text. Compounds 1 and 2 are represented by the solid lines, and tadalafil by the dashed lines.

Experiments were conducted on an Agilent 1200 Series HPLC. Separation of matrix components was accomplished using a Zorbax SB-C8, 4.6 mm × 150 mm, 5 μm column maintained at 25 °C and a flow rate of 1 mL/min. Solvent A consisted of 0.1% TFA in water, and Solvent B consisted of 0.1% TFA in CH_3CN. The mobile phase was programmed with an initial composition of 25% B for 1 min, followed by a linear gradient to 50% B in 7 min. The hold time at 50% B varied, 4 min for Compound 1, and 7 min for Compound 2, with a post-run equilibration time of 5 min. The injection volume was 10 μL, with detection at 285 nm and spectral collection from 190 to 400 nm. The spectrum of each peak in the chromatogram was compared to the spectrum obtained from a tadalafil reference standard, in order to determine which component was most closely related to tadalafil.

Once the peaks corresponding to the compounds of interest were identified, the HPLC was coupled to an Agilent 1200 Series analytical scale fraction collector. The injection volume was increased to 100 μL, and peak collection occurred using a time-based trigger. The collected fractions were consolidated and taken to dryness using a Labconco CentriVap concentrator and cold trap (Fisher), programmed at 80 °C in 60-min periods as necessary. To test for purity, the residues were reconstituted in 50:50 (v/v)
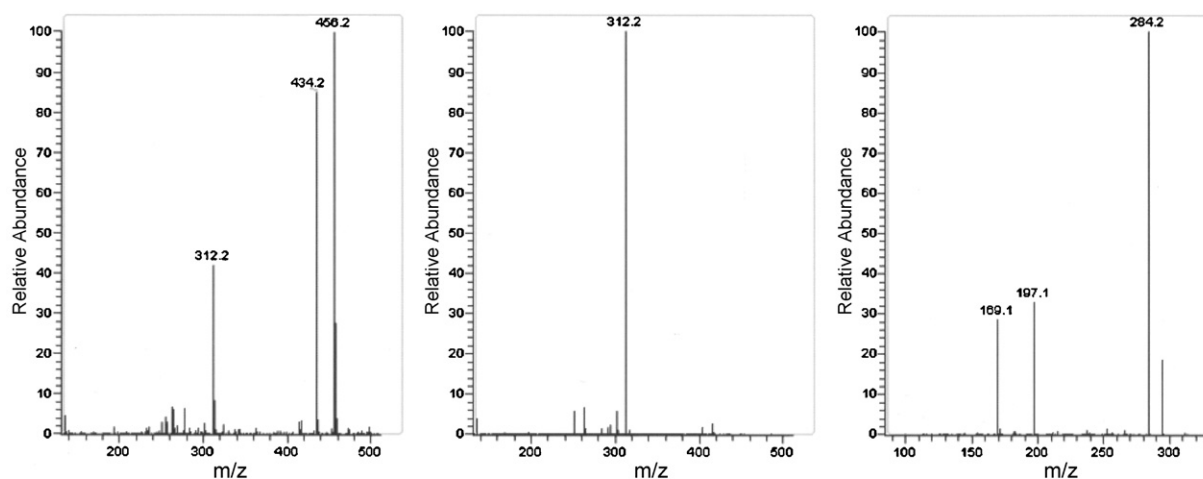
Fig. 5. Mass spectra of Compound 1. From left to right, the full scan event yielding m/z 434 ([M+H]$^+$), the MS/MS of m/z 434, and the MS^3 of m/z 434 → 312.

CH$_3$OH:DIH$_2$O, diluted as necessary, and re-analyzed using LC–MS. Mass spectra were acquired using direct infusion, with the syringe pump at 5 μL/min. Due to the presence of a second component, Compound 2 was subjected to a second purification step, utilizing an isocratic mobile phase of 45% B and an injection volume of 10 μL of the concentrated sample solution. The resulting fractions were treated as above.

2.4. Accurate mass analyses

Accurate mass measurements on the isolated compounds were acquired using an Agilent 1200 series UHPLC system and Exactive Orbitrap mass spectrometer equipped with an Ion Max source (Thermo Scientific, Waltham, MA). The column used was a Zorbax SB-C18, 2.1 mm × 50 mm, 1.8 μm column, which was maintained at 40 °C. Solvent A was 0.1% formic acid in water, and Solvent B was CH$_3$CN. The flow rate was 0.35 mL/min, and the gradient was linear from 5% B to 95% B in 3.5 min, and was held at 95% B for 3 min, with a post-run equilibration time of 3 min. The autosampler was maintained at 15 °C, with an injection volume of 1 μL. Data acquisition and analysis were accomplished using Xcalibur software. The instrument parameters for the mass spectrometer were as follows: ionization = positive, electrospray; sheath gas flow = 55 arbitrary units; auxiliary gas flow = 25 arbitrary units; sweep gas flow = 2 arbitrary units; spray voltage = 3.25 kV; capillary temperature = 275 °C; capillary voltage = 50 V; tube lens voltage = 120 V; skimmer voltage = 35 V; resolution = 25,000; automatic gain control (AGC) target = 1,000,000; scan range m/z 100–500. The instrument was calibrated per manufacturer's specifications.

2.5. NMR analyses

^{1}H and ^{13}C NMR spectra were recorded at 25 °C on a Bruker AVANCE III 500 spectrometer equipped with a 5 mm BBFO probe (Bruker BioSpin Corp., Billerica, MA, USA). All NMR experiments were conducted using DMSO-d_6 containing 0.05% (v/v) TMS as an internal reference. Chemical shifts are reported in δ (ppm) values relative to the internal reference and coupling constants (J) are reported in Hz. Two-dimensional NMR experiments were used to assign the chemical shifts of Compounds 1 and 2. Distortionless enhancement by polarization transfer (DEPT), ^{1}H–^{1}H correlated spectroscopy (^{1}H–^{1}H COSY), heteronuclear single quantum coherence (HSQC), and heteronuclear multiple-bond correlation (HMBC) were employed using conventional pulse sequences.

3. Results and discussion

3.1. HPLC analyses

The isolation of the compounds of interest utilized retention time as the trigger for fraction collection, so the peaks were characterized by their UV spectra in comparison to the spectrum obtained from tadalafil. The chromatogram for the product containing Compound 1 is shown in Fig. 2, and indicates that it was not as strongly retained as tadalafil (t_R 8.5 min) under these conditions. Conversely, Compound 2, shown in Fig. 3, was more strongly retained, and required an extended isocratic hold at 50% B in order to ensure complete elution of matrix components. Their UV spectra, compared to that of tadalafil, displayed almost identical characteristics (Fig. 4A and B). Both products also contained the compound sulfoaildenafil, as observed in Figs. 2 and 3.

Based on comparisons of the peak areas to those obtained from tadalafil standard solutions, Compound 1 was present at approximately 30 mg per capsule, and Compound 2 at approximately 35 mg per capsule.

3.2. Mass spectrometry

Tadalafil, having a molecular weight of 389, generates an [M+H]$^+$ ion at m/z 390, and product ions of m/z 268, 240, 197 and 169 [6–8]. The mass spectra for Compounds 1 and 2, obtained on the LTQ, are shown in Figs. 5 and 6, respectively. Compound 1 had an [M+H]$^+$ ion at m/z 434, an [M+Na]$^+$ ion at m/z 456, and a product ion at m/z 312. The MS^3 (434 → 312) spectrum contained ions at m/z 284, 197 and 169. Compound 2 had an [M+H]$^+$ ion at m/z 432, and a product ion at m/z 310. The MS^3 (432 → 310) spectrum contained ions at m/z 282, 197 and 169. Due to the commonality of the fragment ions that resulted from the loss of the alkyl group from the nitrogen in the pyrazinopyridoindole-1,4-dione [6–8], it was postulated that the substitutions occurred in that portion of the molecule.

Based on the accurate mass determinations, Compound 1 has a chemical formula for the [M+H]$^+$ ion of C$_{24}$H$_{24}$N$_3$O$_5$ (error −0.68260 ppm). Compared to tadalafil, the differences in formulae can be explained by the exchange of the –CH$_3$ on the piperazine-dione for a –C$_3$H$_7$O group. Compound 2 has a chemical formula for the [M+H]$^+$ ion of C$_{25}$H$_{26}$N$_3$O$_4$ (error 0.03337 ppm), which could correlate to the exchange of the –CH$_3$ group for a –C$_4$H$_9$. Unfortunately, mass spectrometry cannot elucidate the configurations of the substitutions. If the –C$_3$H$_7$O in Compound 1 were a
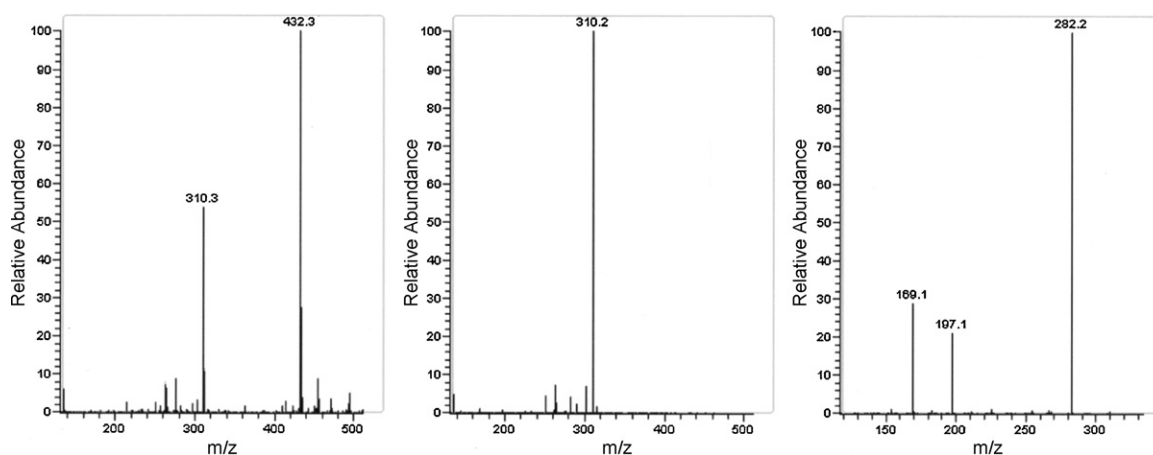
Fig. 6. Mass spectra of Compound 2. From left to right, the full scan event yielding m/z 432 ([M+H]$^+$), the MS/MS of m/z 432, and the MS^3 of m/z 432 → 310.

hydroxypropyl group, it could be either 1- or 2-hydroxy. Similarly, the $-C_4H_9$ modification found on Compound 2 could take the form of *n*-, *iso*-, or *tert*-butyl. The compounds were subjected to NMR for the final step in their structural characterization.

3.3. NMR spectroscopy

For both Compounds 1 and 2, exchange of the *N*-methyl group on the piperazinedione ring of tadalafil (position 13, Fig. 1) was evidenced by disappearance of the ^{1}H and ^{13}C NMR methyl group signals present in pure tadalafil at δ_H 2.93 (3H, s) and δ_C 32.8, respectively. Table 1 summarizes the NMR data for pure tadalafil and Compound 1. The similarity of the NMR spectra gave clear evidence that Compound 1 was structurally related to tadalafil. ^{13}C NMR and DEPT spectra of Compound 1 indicated the presence of 24

carbons, including a methine carbon at δ_C 64.5, a methylene carbon at δ_C 52.8, and a methyl carbon at δ_C 21.0, that were not observed in pure tadalafil. These signals are consistent with exchange of the *N*-methyl group of tadalafil with $-C_3H_7O$ as established from the accurate mass analysis. Interpretation of the DEPT, ^{1}H–^{1}H COSY and HSQC data indicated the configuration of the $-C_3H_7O$ group to be 2-hydroxypropyl, as illustrated in Fig. 1. Specifically, the methyl group (δ_C 21.0) exhibited connectivity to the deshielded methine carbon (δ_C 64.5) which appears at the characteristic chemical shift of an oxygenated moiety. The final two non-exchangeable protons are accounted by the methylene group (δ_C 52.8), showing ^{1}H–^{1}H COSY correlation to the methine proton (δ_H 3.88) but to no other signals. The connectivity of the 2-hydroxypropyl group was established from the HMBC data (Table 1). The methylene protons at ca. δ_H 3.35 (H-13) of the 2-hydroxypropyl group showed long-range

Table 1
NMR data of pure tadalafil and Compound 1 (DMSO-d_6).

Pos.[a]	Tadalafil		Compound 1				
	^{1}H (δ_H)[b]	^{13}C (δ_C)	^{1}H (δ_H)	^{13}C (δ_C)	DEPT[c]	COSY	HMBC
1		166.9		166.8	0		H-13/H-12a/H-3/H-12
3	3.95 (1H, d, J = 17.2)	51.4	4.03 (1H, m)	51.4	2	H-3	H-13
	4.17 (1H, dd, J = 17.1, 1.3)		4.29 (1H, m)			H-3	H-13
4		166.5		167.3	0		H-3
6	6.13 (1H, s)	55.1	6.18 (1H, s)	54.8	1		
6a		136.2		136.8	0		H-6/H-12/H-7
7	11.02 (1H, s)		11.08 (1H, s)				
7a		136.9		136.1	0		H-11/H-9
8	7.30 (1H, d, J = 7.9)	111.3	7.31 (1H, d, J = 8.0)	111.3	1	H-9	H-10/H-11
9	7.06 (1H, m)	121.2	7.06 (1H, m)	121.2	1	H-8/H-10	H-8/H-11
10	6.99 (1H, m)	118.8	7.00 (1H, m)	118.8	1	H-9/H-11	H-8
11	7.54 (1H, d, J = 7.7)	118.1	7.54 (1H, d, J = 7.7)	118.1	1	H-10	H-9
11a		125.7		125.7	0		H-7/H-11/H-8/H-10
11b		104.7		104.6	0		H-6/H-7/H-11/H-12
12	2.97 (1H, ddd, J = 15.8, 11.7, 0.7)	23.1	2.96 (1H, m)	22.5	2	H-12/H-12a	
	3.52 (1H, dd, J = 15.8, 4.5)		3.48 (1H, m)			H-12/H-12a	
12a	4.40 (1H, dd, J = 11.7, 4.2)	55.4	4.44 (1H, dd, J = 11.6, 4.1)	55.3	1	H-12	
13	2.93 (3H, s)	32.8	3.49–3.21 (2H, m)	52.8	2	H-14	H-3/H-14/H-15
1′		133.9		133.9	0		H-6
2′	6.87 (1H, s)	106.9	6.85 (1H, s)	106.8	1		H-6/H-6′
3′		147.0		147.1	0		H-2′/H-5′/H-7′
4′		146.0		146.1	0		H-6′/H-7′
5′, 6′	6.78 (2H, d, J = 1.2)	108.0	6.77 (2H, m)	108.0	1		H-6/H-6′
		119.3		119.1	1		H-6/H-2′
7′	5.92 (2H, s)	100.9	5.92 (2H, s)	100.9	2		
14			3.88 (1H, br m)	64.5	1	H-13/H-15	
14′			3.35 (1H, s)				
15			1.04 (3H, d, J = 6.3)	21.0	3	H-14	H-13/H-14

[a] See Fig. 1 for atom numbering.
[b] d: doublet; dd: doublet of doublet; ddd: doublet of doublet of doublet; s: singlet; m: multiplet; br: broad.
[c] Number in DEPT is the number of attached protons.

Table 2
NMR data of pure tadalafil and Compound 2 (DMSO-d_6).

Pos.[a]	Tadalafil		Compound 2				
	^{1}H (δ_H)[b]	^{13}C (δ_C)	^{1}H (δ_H)	^{13}C (δ_C)	DEPT[c]	COSY	HMBC
1		166.9		166.6	0		H-13/H-12a/H-3/H-12
3	3.95 (1H, d, J = 17.2)	51.4	3.91 (1H, d, J = 16.9)	49.7	2	H-3	H-13
	4.17 (1H, dd, J = 17.1, 1.3)		4.21 (1H, dd, J = 16.9, 0.9)			H-3	H-13
4		166.5		167.3	0		H-3
6	6.13 (1H, s)	55.1	6.18 (1H, s)	54.8	1		
6a		136.2		136.8	0		H-6/H-12/H-7
7	11.02 (1H, s)		11.09 (1H, s)				
7a		136.9		136.1	0		H-11/H-9
8	7.30 (1H, d, J = 7.9)	111.3	7.31 (1H, d, J = 8.0)	111.3	1	H-9	H-10/H-11
9	7.06 (1H, m)	121.2	7.06 (1H, m)	121.2	1	H-8/H-10	H-8/H-11
10	6.99 (1H, m)	118.8	7.00 (1H, m)	118.8	1	H-9/H-11	H-8
11	7.54 (1H, d, J = 7.7)	118.1	7.54 (1H, d, J = 7.8)	118.1	1	H-10	H-9
11a		125.7		125.7	0		H-7/H-11/H-8/H-10
11b		104.7		104.6	0		H-6/H-7/H-11/H-12
12	2.97 (1H, ddd, J = 15.8, 11.7, 0.7)	23.1	2.95 (1H, dd, J = 15.6, 11.7)	22.5	2	H-12/H-12a	
	3.52 (1H, dd, J = 15.8, 4.5)		3.48 (1H, m)			H-12/H-12a	
12a	4.40 (1H, dd, J = 11.7, 4.2)	55.4	4.43 (1H, dd, J = 11.7, 4.6)	55.3	1	H-12	
13	2.93 (3H, s)	32.8	3.48–3.34 (2H, m)	44.8	2	H-14	H-3/H-14/H-15
1'		133.9		133.8	0		H-6
2'	6.87 (1H, s)	106.9	6.84 (1H, s)	106.7	1		H-6/H-6'
3'		147.0		147.1	0		H-2'/H-5'/H-7'
4'		146.0		146.1	0		H-6'/H-7'
5', 6'	6.78 (2H, d, J = 1.2)	108.0	6.76 (2H, m)	108.0	1		H-6/H-6'
		119.3		119.0	1		H-6/H-2'
7'	5.92 (2H, s)	100.9	5.92 (2H, s)	100.9	2		
14			1.49 (2H, m)	28.6	2	H-13/H-15	H-13/H-15/H-16
15			1.26 (2H, m)	19.3	2	H-14/H-16	H-13/H-14
16			0.90 (3H, t, J = 7.4)	13.6	3	H-15	H-14/H-15

[a] See Fig. 1 for atom numbering.
[b] d: doublet; dd: doublet of doublet; ddd: doublet of doublet of doublet; s: singlet; m: multiplet; br: broad.
[c] Number in DEPT is the number of attached protons.

correlations to the carbonyl carbon at δ_C 166.8 (C-1) and to the methylene carbon at δ_C 51.4 (C-3), supporting the 2-hydroxypropyl group being bonded to the piperazinedione ring at the *N2*-position. The HMBC data also provided confirmation of the 2-hydroxypropyl configuration with indicative correlations of δ_H 1.04/δ_C 52.8, 64.5 (H-15/C-13, C-14), ca. δ_H 3.35/δ_C 166.8, 51.4, 64.5, 21.0 (H-13/C-1, C-3, C-14, C-15), and the absence of any long-range correlations for H-14. The δ values for the remaining NMR signals and associated correlations of Compound 1 were in agreement with those of pure tadalafil from published data [9–11] and data collected for the tadalafil reference standard.

Determination of the configuration of the –C$_4$H$_9$ moiety of Compound 2 was analogous to that of Compound 1. ^{1}H and ^{13}C NMR assignments for pure tadalafil and Compound 2 are summarized in Table 2. Given the similarity of the NMR spectra, characterization was focused on signals appearing in Compound 2 that were not present in tadalafil. ^{13}C NMR and DEPT spectra of Compound 2 indicated the presence of 25 carbons, including methylene carbons at δ_C 44.8, δ_C 28.6, and δ_C 19.3, and a methyl carbon at δ_C 13.6, that were not observed in pure tadalafil. These signals are consistent with exchange of the *N*-methyl group of tadalafil with –C$_4$H$_9$ as established from the accurate mass analysis. The assignment of the –C$_4$H$_9$ substitution as *n*-butyl was determined by DEPT, ^{1}H–^{1}H COSY, and HSQC data. Specifically, the methyl group (δ_C 13.6) exhibited connectivity to the methylene carbon (δ_C 19.3) which showed connectivity to both the terminal methyl group as well as the methylene carbon at 28.6 ppm. The methylene carbon (δ_C 28.6) was also correlated to the more deshielded methylene group (δ_C 44.8) and vice versa, thereby establishing the linear configuration of the butyl group. The HMBC data (Table 2) showed correlations of the methylene protons of the *n*-butyl group at ca. δ_H 3.41 (H-13) to the carbonyl carbon at δ_C 166.6 (C-1) and to the methylene carbon at δ_C 49.7 (C-3), establishing that the substitution of the *n*-butyl group occurred at the *N2*-position of the piperazinedione ring. The

HMBC data also provided confirmation of the n-butyl configuration with indicative correlations of δ_H 0.90/δ_C 28.6, 19.3 (H-16/C-14, C-15), δ_H 1.26/δ_C 44.8, 28.6 (H-15/C-13, C-14), δ_H 1.49/δ_C 44.8, 19.3, 13.6 (H-14/C-13, C-15, C16), and ca. δ_H 3.41/δ_C 166.6, 49.7, 28.6, 19.3 (H-13/C-1, C-3, C-14, C-15). With the exception of the value for the exchangeable amine proton (H-7), the δ_H values obtained for Compound 2 are in agreement with those of "Compound 13" (equivalent to *n*-butylnortadalafil) reported by Daugan et al. [11]. The absolute configurations of Compounds 1 and 2 were not determined.

4. Conclusion

In the present study, the structures of two compounds similar to tadalafil, detected in dietary supplements, were determined using LC–ESI-MS^n, accurate mass, and NMR. Based on the data obtained, the differences in structures were confined to substitutions of the *N*-methyl group on the piperazinedione ring, the first a 2-hydroxypropyl substitution, and the second an *n*-butyl. These compounds were given the names 2-hydroxypropylnortadalafil and *n*-butylnortadalafil, respectively. Although it is likely that the *n*-butylnortadalafil is comparable to "Compound 13" [11], we believe that this is the first report for the analog 2-hydroxypropyl-nortadalafil.

References

[1] M.-C. Tseng, J.-H. Lin, Determination of sildenafil citrate adulterated in a dietary supplement capsule by LC/MS/MS, J. Food Drug Anal. 10 (2002) 112–119.
[2] S.R. Gratz, C.L. Flurer, K.A. Wolnik, Analysis of undeclared synthetic phosphodiesterase-5 inhibitors in dietary supplements and herbal matrices by LC–ESI-MS and LC–UV, J. Pharm. Biomed. Anal. 36 (2004) 525–533.
[3] X. Zhu, S. Xiao, B. Chen, F. Zhang, S. Yao, Z. Wan, D. Yang, H. Han, Simultaneous determination of sildenafil, vardenafil and tadalafil as forbidden components in natural dietary supplements for male sexual potency by high-performance

liquid chromatography–electrospray ionization mass spectrometry, J. Chromatogr. A 1066 (2005) 89–95.

[4] P. Zou, S.S.-Y. Oh, P. Hou, M.-Y. Low, H.-L. Koh, Simultaneous determination of synthetic phosphodiesterase-5 inhibitors found in a dietary supplement and pre-mixed bulk powders for dietary supplements using high-performance liquid chromatography with diode array detection and liquid chromatography–electrospray ionization tandem mass spectrometry, J. Chromatogr. A 1104 (2006) 113–122.

[5] S. Singh, B. Prasad, A.A. Savaliya, R.P. Shah, V.M. Gohil, A. Kaur, Strategies for characterizing sildenafil, vardenafil, tadalafil and their analogues in herbal dietary supplements, and detecting counterfeit products containing these drugs, Trends Anal. Chem. 28 (2009) 13–28.

[6] P. Zou, P. Hou, M.-Y. Low, H.-L. Koh, Structural elucidation of a tadalafil analogue found as an adulterant of a herbal product, Food Addit. Contam. 23 (2006) 446–451.

[7] S.R. Gratz, B.M. Gamble, R.A. Flurer, Accurate mass measurement using Fourier transform ion cyclotron resonance mass spectrometry for structure elucidation of designer drug analogs of tadalafil, vardenafil and sildenafil in herbal and pharmaceutical matrices, Rapid Commun, Mass Spectrom. 20 (2006) 2317–2327.

[8] P. Zou, P. Hou, S.S.-Y. Oh, M.-Y. Low, H.-L. Koh, Electrospray tandem mass spectrometric investigations of tadalafil and its analogue, Rapid Commun. Mass Spectrom. 20 (2006) 3488–3490.

[9] T. Hasegawa, K. Takahashi, M. Saijo, T. Ishii, T. Nagata, M. Kurihara, Y. Haishima, Y. Goda, N. Kawahara, Isolation and structural elucidation of cyclopentynafil and N-octylnortadalafil found in a dietary supplement, Chem. Pharm. Bull. 57 (2009) 185–189.

[10] T. Hasegawa, M. Saijo, T. Ishii, T. Nagata, Y. Haishima, N. Kawahara, Y. Goda, Structural elucidation of a tadalafil analogue found in a dietary supplement, J. Food Hyg. Soc. Jpn. 49 (2008) 311–315.

[11] A. Daugan, P. Grondin, C. Ruault, A.-C. Le Monnier de Gouville, H. Coste, J.M. Linget, J. Kirilovsky, F. Hyafil, R. Labaudinière, The discovery of tadalafil: a novel and highly selective PDE5 inhibitor. 2: 2,3,6,7,12,12a-hexahydropyrazino[1′,2′:1,6]pyrido[3,4-b]indole-1,4-dione analogues, J. Med. Chem. 46 (2003) 4533–4542.

[12] T. Beghyn, C. Hounsou, B.P. Deprez, PDE5 inhibitors: an original access to novel potent arylated analogues of tadalafil, Bioorg. Med. Chem. Lett. 17 (2007) 789–792.

[13] X.-X. Shi, S.-L. Liu, W. Xu, Y.-L. Xu, Highly stereoselective Pictet–Spengler reaction of D-tryptophan methyl ester with piperonal: convenient syntheses of Cialis (tadalafil), 12a-epi-Cialis, and their deuterated analogues, Tetrahedron: Asymmetry 19 (2008) 435–442.

[14] A. Häberli, P. Girard, M.-Y. Low, X. Ge, Isolation and structure elucidation of an interaction product of aminotadalafil found in an illegal health food product, J. Pharm. Biomed. Anal. 53 (2010) 24–28.

Identification of a novel sildenafil analogue in an adulterated herbal supplement

Julie Vaysse, Véronique Gilard, Stéphane Balayssac, Chantal Zedde, Robert Martino, Myriam Malet-Martino *

Groupe de RMN Biomédicale, Laboratoire SPCMIB (UMR CNRS 5068), Université Paul Sabatier, 118 route de Narbonne, 31062 Toulouse cedex, France

A B S T R A C T

iErect, a new dietary supplement marketed as "100% natural" and sold over the Internet, was analyzed. It contains thiosildenafil, a sildenafil analogue already reported as an adulterant in herbal formulations, and a new compound whose structure was elucidated after isolation using NMR, MS and IR. It was named depiperazinothiosildenafil as it results from the hydrolytic cleavage of the S–N bond of the sulfonamide group of thiosildenafil. A capsule of iErect contains a very high amount ($\approx$220 mg) of thiosildenafil and $\approx$30 mg of depiperazinothiosildenafil, which places consumers at risk for potentially serious side-effects.

© 2011 Elsevier B.V. All rights reserved.

1. Introduction

Adulterants are frequently detected in dietary supplements or herbal medicines aimed at increasing sexual function. In addition to the approved phosphodiesterase-5 (PDE-5) inhibitors, sildenafil (Viagra®), tadalafil (Cialis®) and vardenafil (Levitra®) in Europe and USA, udenafil (Zydena®) in South Korea and Malaysia, mirodenafil (Mvix®) in South Korea, and lodenafil carbonate (Helleva®) in Brazil, it has been reported that "natural" herbal products were also adulterated with unapproved analogues in which most often minor modifications were brought to the parent structure. To our knowledge, 29 analogues have been described so far in the literature as illegal additives in herbal drugs [1–31].

In this study, a new sildenafil analogue was isolated from iErect, a new "100% natural enhance formula", which was claimed to contain plant extracts, vitamins, zinc and arginine. Thiosildenafil and the new analogue called depiperazinothiosildenafil were detected in the preparation and their chemical structures elucidated using NMR, MS and IR.

2. Experimental

2.1. Commercial herbal drug

Four different boxes of iErect (Fig. 1A) containing either 1 or 4 capsules (batches 7164 and 8164) were purchased at different dates between December 2010 and June 2011 on the Internet from a Lituanian site and two French sites. The claimed composition for a net weight of 585 mg/capsule was as follows: arginine 150 mg, Rosenroot *Rhodiola rosea* 100 mg, Mallow *Malva sylvestris* 50 mg, Ginger *Zingiber officinale* 50 mg, *Tribulus terrestris Trigonella foenum-graecum* 50 mg, Stinging Nettle *Urtica dioica* 50 mg, Pumpkin *Cucurbita pepo* 25 mg, Cinnamon *Cinnamomum zeylanicum* 25 mg, zinc 30 mg, vitamin E 30 mg, niacin (vitamin B3) 25 mg. The capsules were analyzed before expiry date (12/2012).

2.2. NMR analysis

2.2.1. Preparation of samples for NMR analysis

The capsule was emptied and 10 mg were dissolved in 1.5 mL of the chosen solvent (CD$_3$CN, CD$_3$OD or CD$_3$CN:D$_2$O (80:20)) under vortex agitation during 10 min and then sonication for 10 min. The suspension was then centrifuged (5 min, 4000 rpm) and 500 µL of the supernatant was analyzed.

For the quantitative analysis, the capsule was emptied and 10% of the powder ($\approx$58 mg) was dissolved in 10 mL of methanol under magnetic stirring during 40 min, then sonicated for 5 min. After centrifugation (5 min, 4000 rpm), an aliquot of 1 mL was evaporated to dryness and the residue dissolved in 1 mL of methanol-d4. The experiments were done in triplicate on each batch. The quantification was performed on the ^{1}H NMR signals of aromatic protons 15 and 18 (Fig. 1B). The solid residue from the first extraction was re-extracted using the same protocol. The supernatants of the three extracts from the same batch were pooled, then lyophilized and the
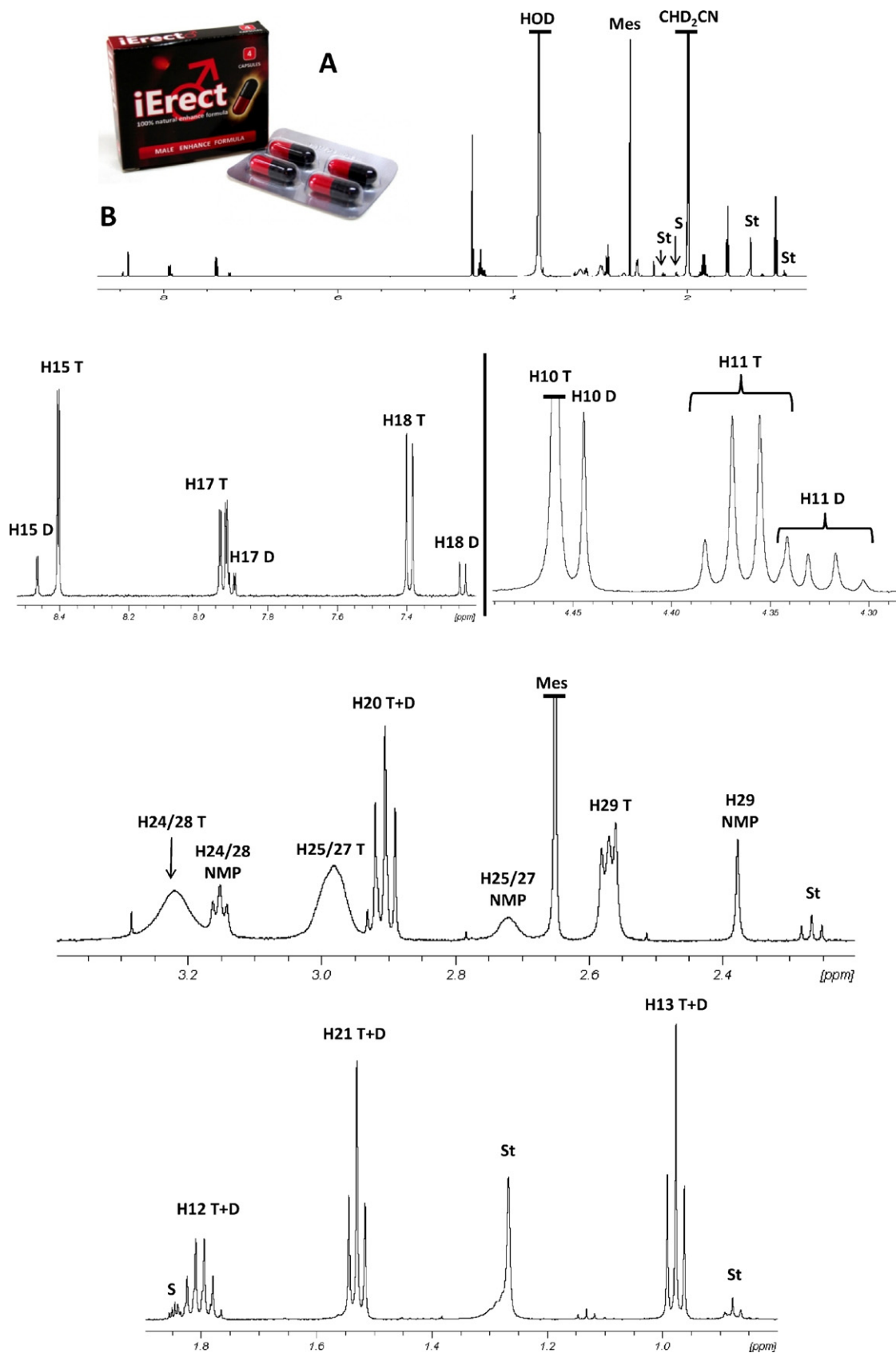
Fig. 1. (A) Photography of iErect box and capsules; (B) ^{1}H NMR spectrum of a CD$_3$CN:D$_2$O (80:20) extract of a iErect capsule content. T: thiosildenafil; D: depiperazinoth-iosildenafil; NMP: N-methylpiperazine; Mes: mesylate; St: stearate; S: satellite signal of CHD$_2$CN. The CH$_3$ 29 resonance of thiosildenafil usually appears as a singlet. The multiplicity observed for this signal in the spectrum shown results most probably from a coupling with ^{14}N nucleus.

residue dissolved in 1 mL of methanol-d4. The quantification was performed on the ^{1}H NMR singlet of CH$_3$ 10 (Fig. 1B).

2.2.2. Stability of thiosildenafil

Three experiments were carried out in order to check the stability of thiosildenafil. In the first one, the supernatants obtained as described in Section 2.2.1 were analyzed by ^{1}H NMR immediately after their preparation and after 24 h at $37 \pm 0.2\,^{\circ}$C in a water bath. In the second experiment, 30 mg of commercial powder was dissolved in 1.5 mL of CD$_3$CN:D$_2$O (80:20) under vortex agitation during 20 min and then sonicated for 10 min. The suspension was then centrifuged (5 min, 4000 rpm). 500 µL of the supernatant was transferred into a NMR tube and the solution was analyzed immediately. The tube was then placed in an ultrasonic bath for 2 additional hours and a second ^{1}H NMR spectrum was recorded. Finally, an authentic sample of thiosildenafil obtained after purification of the commercial preparation (see below) was submitted to the same extraction protocol in CD$_3$CN:D$_2$O (80:20) than that used for the commercial powder.

2.2.3. NMR recording conditions

The NMR experiments were performed on a Bruker Avance 500 spectrometer (Bruker BioSpin AG, Fällanden, Switzerland) equipped with a 5 mm dual ^{1}H–^{13}C TCI cryoprobe. Sodium 2,2,3,3-tetradeutero-3-trimethylsilylpropionate (TSP; Sigma–Aldrich, St. Louis, MO, USA) was used as an internal reference for chemical shift (δ) measurement and quantification. A solution of TSP (10 µL) was added before the NMR analysis at a final concentration of 0.2 mM in all the samples analyzed. The recording and processing conditions for ^{1}H NMR, quantitative ^{1}H NMR and 2D DOSY ^{1}H NMR spectra have already been described [22,32].

For structural characterization of thiosildenafil and the unknown compound in the crude extracts and after purification, 1D (^{1}H and ^{13}C) and 2D (gCOSY, gHSQC and gHMBC) NMR spectra were recorded in two different solvent systems, CD$_3$OD and CD$_3$CN:D$_2$O (80:20).

2.3. LC–MS analysis of iErect methanolic extracts

The HPLC system used consisted of an Agilent 1100 series apparatus (Agilent Technologies, Santa Clara, CA, USA). An Applied System QTRAP triple quadrupole mass spectrometer, equipped with a Turbo Ion Spray (TIS) interface, was used for detection. Both were controlled by an Agilent Analyst software (version 1.4). The analytical column was a reversed-phase column Luna C18 (100 mm × 3 mm i.d.; 3 µm particle size; Phenomenex Inc., Torrance, CA, USA). The mobile phase consisted of a mixture of (A) a buffer solution (ammonium acetate 10 mmol L^{-1}, pH 7) and (B) acetonitrile. The starting mobile phase was 70% A–30% B during 1 min, then a linear gradient was run up to 20% A–80% B in 5 min, then to 10% A–90% B in 1 min, followed by isocratic elution at the same ratio during 3 min. The flow rate was 0.6 mL min^{-1} and the volume injected 10 µL. The unknown compound and thiosildenafil eluted respectively at 4.6 and 8.1 min.

The mass spectrometer was operated in positive ionization mode with TIS heater set at 440 °C. Nitrogen served both as auxiliary, collision gas and nebulizer gas. The operating conditions for TIS interface were: mass range 100–1000 u (1 s), step size 0.1 u; Q1 TIS MS spectra were recorded in profile mode, IS 5000 V, DP 80 V.

2.4. Isolation of thiosildenafil and new analogue

The content from two capsules was suspended in methanol, vortexed for 10 min and then sonicated for 10 min. After filtration, the solid phase was washed twice with dichloromethane.

The liquid phases were pooled and evaporated to dryness. Purification was carried out using a Waters Delta Prep 4000 system (Waters Corporation, Milford, MA, USA) equipped with a 486 tunable absorbance detector set at 300 nm. 100 mg of powder was put on 10 g of silica (50 µm). The mobile phase was a mixture of ethyl acetate:dichloromethane:methanol (45:45:10) with a flow rate of 8 mL min^{-1}.

The eluted fractions were collected and analyzed with a Waters Acquity UPLC-DAD system controlled by Waters Empower 2 software. The analysis conditions were: Acquity UPLC BEH C18 column (50 mm × 2.1 mm i.d.; 1.7 µm particle size); mobile phase: (A) demineralized water and (B) acetonitrile (HPLC grade) both containing 0.1% (v/v) trifluoroacetic acid; flow rate: 0.3 mL min^{-1}; detection wavelength: 254 nm. The gradient condition was as follows: 0–0.5 min, isocratic elution with a 90:10 A:B mixture; 0.5–6 min, linear increase to 20:80 A:B ratio; re-equilibration for 0.5 min with a 90:10 A:B mixture before the start of the next run. The unknown compound and thiosildenafil eluted respectively at 3.6 and 4.5 min.

2.5. MS, MS/MS and high resolution MS analyses

The methanolic extract of the capsule content and the purified compounds dissolved in methanol were directly infused in an Applied Biosystems API 365 triple-quadrupole mass spectrometer (Applied Biosystems Inc., Foster City, CA, USA), equipped with a TIS interface and controlled by the Analyst software (version 1.4). The mass spectrometer was operated in positive ionization mode. Nitrogen served both as auxiliary and collision gas and oxygen served as nebulizer gas. The operating conditions for TIS interface were as follows: (1) in MS mode: mass range 100–600 u (1 s), step size 0.1 u; Q1 TIS MS spectra were recorded in profile mode, IS 4700 V, DP 50 V; and (2) in MS–MS mode: precursor mass 491 u for thiosildenafil and 409 u for the new analogue; mass range 30–500 u for thiosildenafil and 50–500 for the new analogue, step size 0.1 u; MS–MS spectra were recorded in profile mode, IS 4700 V for thiosildenafil and 5000 V for the unknown compound, DP 50 V, CE 50 V for thiosildenafil and 45 V for the unknown compound.

The accurate mass of the new analogue was determined on a Waters GCT Premier time-of-flight (TOF) mass spectrometer equipped with a Desorption Chemical Ionization (DCI) probe employing methane as the reagent gas and controlled by the MassLynx 4.1 software. The TOF-MS was operated between m/z 100 and 600 in positive ionization mode. The sample was dissolved in methanol and analyzed after direct infusion.

2.6. IR spectroscopy

Samples were prepared in KBr pellets and spectra were recorded on a Thermo Nicolet Nexus 670 FTIR spectrophotometer (Thermo Nicolet Corporation, Madison, WI, USA) over the spectral range 4000–400 cm^{-1}.

3. Results and discussion

3.1. NMR and LC–MS of iErect extracts

The herbal dietary supplement iErect was extracted with CD$_3$OD, CD$_3$CN or CD$_3$CN:D$_2$O (80:20) and the extracts were subjected to ^{1}H and ^{13}C NMR analysis. The three spectra were quite similar. As an illustration, we present in Fig. 1B the ^{1}H NMR spectrum in CD$_3$CN:D$_2$O. It showed characteristic signals of the lubricant agent stearate (0.88 ppm, t, 7.1 Hz; 1.27 ppm, broad s; 2.27 ppm, t, 7.5 Hz), and of methanesulfonate (2.65 ppm, s), a non-toxic acid often used to form salts of active pharmaceutical ingredients containing basic centers. Their attributions were confirmed by spiking with authentic standards. Some other resonances
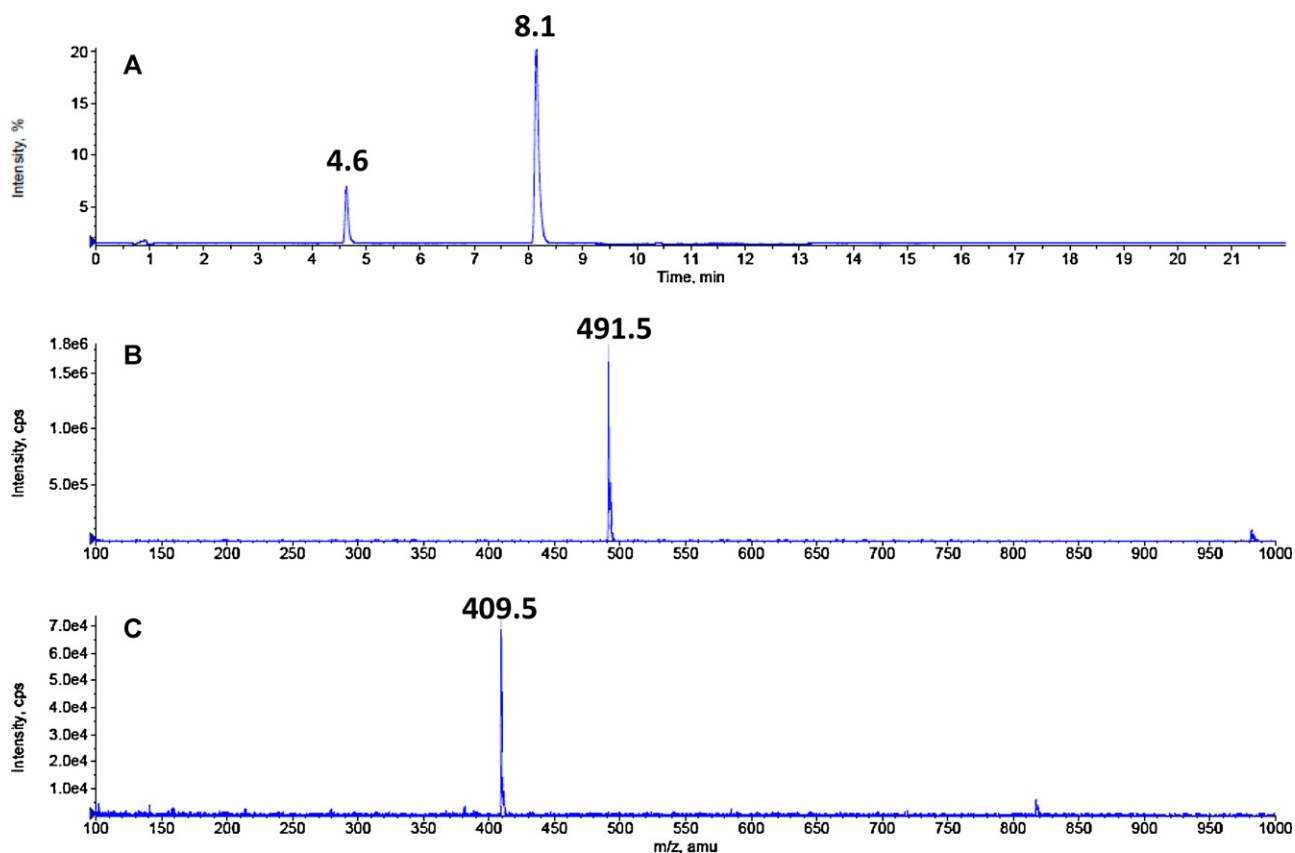
Fig. 2. (A) HPLC chromatogram of a acetonitrile:H_2O (80:20) extract of a iErect capsule content; (B) and (C) mass spectra of the compounds eluting at 8.1 and 4.6 min, respectively.

could correspond to protons from two PDE-5 inhibitors with one in a greater amount. The LC–MS analysis of the extract showed the presence of two major peaks at RT 4.6 min and 8.1 min with protonated molecular ions at m/z 409.5 and 491.5, respectively (Fig. 2) and a very minor peak with a RT at 6.0 min and m/z 475.5 (not shown in Fig. 2). Among the PDE-5 inhibitors and their analogues described in the literature, only thiosildenafil and sildenafil have molecular weights (490.6 and 474.6 Da) corresponding to the observed ions. These data suggest that iErect could contain thiosildenafil, a very low quantity of sildenafil (not detected in ^{1}H NMR) and an unknown PDE-5 inhibitor analogue with a molecular weight of 408.5 Da.

3.2. Characterization of thiosildenafil and unknown compound after isolation

^{1}H and ^{13}C NMR data of isolated compounds are listed in Table 1. The NMR resonances were assigned by 2D NMR experiments (gCOSY, gHSQC and gHMBC) and comparison with published data for thiosildenafil [15]. The strong resemblance of ^{1}H and ^{13}C NMR spectra of the unknown analogue with those of thiosildenafil would indicate that this compound is a thiosildenafil derivative. The fact that the proton and carbon signals at positions 24/28, 25/27, and 29 are not present and the 10.2 ppm deshielding of quaternary carbon 16 relative to thiosildenafil suggest the cleavage of the sulfonamide SO_2–N bond, generating a sulfonic acid function. The unknown compound was thus identified as 4-ethoxy-3-(1-methyl-7-thio-3-propyl-1*H*-pyrazolo[4,3-*d*]pyrimidin-5(6*H*)-yl)benzenesulfonic acid, hereinafter referred to as depiperazinothiosildenafil (Fig. 3). Spiking the iErect extracts with these two products after their isolation and purification enabled unambiguous attribution of their respective proton resonances.

To confirm the structures of both compounds, a MS study was conducted. The MS and MS–MS spectra of thiosildenafil (Fig. 4A) were in agreement with literature data [15,33]. Compared to thiosildenafil, the MS–MS spectrum of the unknown analogue (Fig. 4B) showed the absence of all the peaks corresponding to the N-methylpiperazine (NMP) ions at m/z 100 ([NMP]$^+$), 99 ([CH_2=N–CH_2–CH_2–N(CH_3)=CH_2]$^+$), and fragments at 85 (loss of CH_2 from the fragment ion at m/z 99) and 58 ([(CH_3)$_2$N=CH_2]$^+$) or resulting from NMP methyl transfer on the S atom of the C=S bond at m/z 407, 343 and 341 [33]. Two common peaks were observed in MS–MS spectra of thiosildenafil and the unknown compound at m/z 327 (loss of NMP-SO_2H for thiosildenafil and of sulfonic acid for the unknown compound), and 299 resulting from an additional neutral loss of C_2H_4. Moreover, the MS–MS spectrum of the new analogue displayed a strong peak at m/z 381 due to the loss of C_2H_4. The accurate mass of the protonated molecular ion of the unknown compound was found at m/z 409.1003 in agreement with the calculated mass 409.1004 of $C_{17}H_{21}N_4O_4S_2$ within −0.2 ppm, which corresponds to the atomic composition of depiperazinothiosildenafil $C_{17}H_{20}N_4O_4S_2$.
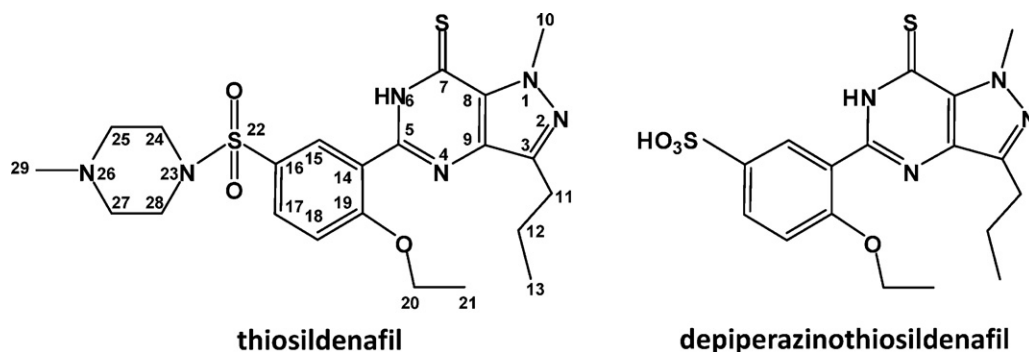
The UV spectra of thiosildenafil and depiperazinothiosildenafil are similar and show two absorption bands at 295 and 354 nm, the last one being characteristic of conjugated heterocyclic thiones [15].

The IR spectra of isolated thiosildenafil and depiperazinothiosildenafil revealed common absorption bands characteristic of an amine moiety (ν_{NH} at 3271 and 3251 cm^{-1}, respectively) and a thiocarbonyl group directly attached to a nitrogen atom which leads to 3 bands at 1498, 1253 and 928 cm^{-1} for thiosildenafil, and 1498, 1258 and 927 cm^{-1} for depiperazinothiosildenafil, all of them being associated at least partly with the C=S stretching vibration as a consequence of the strong coupling between the C=S

Table 1
^{1}H and ^{13}C NMR characteristics of thiosildenafil and unknown analogue (depiperazinothiosildenafil) detected in the herbal dietary supplement iErect. Spectra were recorded in CD$_3$OD.

Atom	Group	Thiosildenafil			Depiperazinothiosildenafil		
		δ [1]H (ppm)	Multiplicity[a]	δ [13]C (ppm)	δ [1]H (ppm)	Multiplicity[a]	δ [13]C (ppm)
3	Cq C=N			147.9			147.9
5	Cq C=N			149.8			150.5
7	Cq C=S			175.7			175.2
8	Cq C=C			134.7			134.7
9	Cq C=C			135.4			135.4
10	N–CH$_3$	4.48	s	40.6	4.46	s	40.5
11	CH$_2$	2.88	t, J = 7.5 Hz	29.1	2.89	t, J = 7.4 Hz	29.1
12	CH$_2$	1.81	sext, J = 7.45 Hz	24.2	1.82	sext, J = 7.4 Hz	24.2
13	CH$_3$	0.99	t, J = 7.4 Hz	15.1	0.98	t, J = 7.4 Hz	15.1
14	Cq Ar			124.1			121.7
15	CH Ar	8.32	d, J = 2.45 Hz	132.4	8.55	d, J = 2.3 Hz	130.45
16	Cq Ar			130.2			140.4
17	CH Ar	7.96	dd, J = 2.45 and 8.85 Hz	134.3	7.89	dd, J = 2.3 and 8.8 Hz	132.5
18	CH Ar	7.41	d, J = 8.85 Hz	115.4	7.23	d, J = 8.8 Hz	115.6
19	Cq Ar			162.9			160.3
20	O–CH$_2$	4.34	q, J = 7.0 Hz	67.9	4.31	q, J = 6.95 Hz	67.6
21	CH$_3$	1.52	t, J = 7.0 Hz	15.9	1.55	t, J = 6.95 Hz	15.7
24/28	N–CH$_2$ piperazine	3.06	Broad signal	47.8			
25/27	N–CH$_2$ piperazine	2.52	Broad signal	56.0			
29	N–CH$_3$ piperazine	2.27	s	46.7			

[a] s: singlet; d: doublet; dd: doublet of doublet; t: triplet; q: quadruplet; sext: sextuplet.

Fig. 3. Chemical structures of the PDE-5 inhibitor analogues, thiosildenafil and depiperazinothiosildenafil, contained in the dietary supplement iErect.

and C–N groups [34]. In the spectrum of thiosildenafil, medium intensity bands at 2856 and 2806 cm^{-1} were attributed to asymmetric and symmetric ν_{CH_3} of the N-methyl group of piperazine, and two strong absorption bands at 1352 and 1171 cm^{-1} corresponded to the asymmetric and symmetric stretching vibrations of SO$_2$ in the sulfonamide group [34]. All these absorption bands were not present in the IR spectrum of depiperazinothiosildenafil, whereas two very strong bands were observed at 1190 (broad band with shoulders) and 1034 cm^{-1} characteristic of the asymmetric and symmetric stretching vibrations of a SO$_3$ group [34]. These data were consistent with the cleavage of the S–N sulfonamide bond of thiosildenafil leading to the formation of a sulfonic acid compound.

3.3. 2D DOSY ^{1}H NMR

The fact that the new analogue was a cleavage product of thiosildenafil led us to look for the presence of NMP in the commercial dietary supplement iErect. 2D DOSY ^{1}H NMR is an attractive method as the virtual separation of a mixture is based on the differences in self-diffusion coefficients D of the various components and D generally decrease with increasing molecular weight. The 2D DOSY ^{1}H NMR spectrum presented in Fig. 5 clearly demonstrated the presence of thiosildenafil and depiperazinothiosildenafil on the same line (D = 937 μm^2 s^{-1}), stearate (D = 1139 μm^2 s^{-1}), and methanesulfonate and NMP also aligned (D = 1264 μm^2 s^{-1}). The presence of NMP in iErect extracts was confirmed by careful

Table 2
^{1}H NMR chemical shift ranges of piperazine moieties in CD$_3$CN:D$_2$O and CD$_3$OD extract solutions of iErect.

Proton numbering[a]	Thiosildenafil (ppm)	NMP (ppm)[b]
24/28	3.33–3.05	3.33–2.87
25/27	3.28–2.47	3.05–2.44
29	2.88–2.18	2.61–2.30

[a] cf. Fig. 3.
[b] NMP: N-methylpiperazine.

spiking with an authentic sample. Indeed, the ^{1}H NMR chemical shifts of the protons from the piperazine ring and from the methyl group linked to the nitrogen atom of piperazines in NMP and thiosildenafil are very concentration-dependent being upfield shielded with decreasing concentrations (Table 2). The broad signals of the N–CH$_2$ protons are often overlapped whereas the singlets of N–CH$_3$ are often well resolved and their quantification easily performed. COSY, HSQC, HMBC and even DOSY experiments are thus necessary for an unambiguous attribution of all the resonances of the piperazine moieties in iErect extract solutions.

3.4. Origin of depiperazinothiosildenafil

As already stated above, the extraction of the content of iErect capsules in three different solvents gave identical ^{1}H NMR spectra
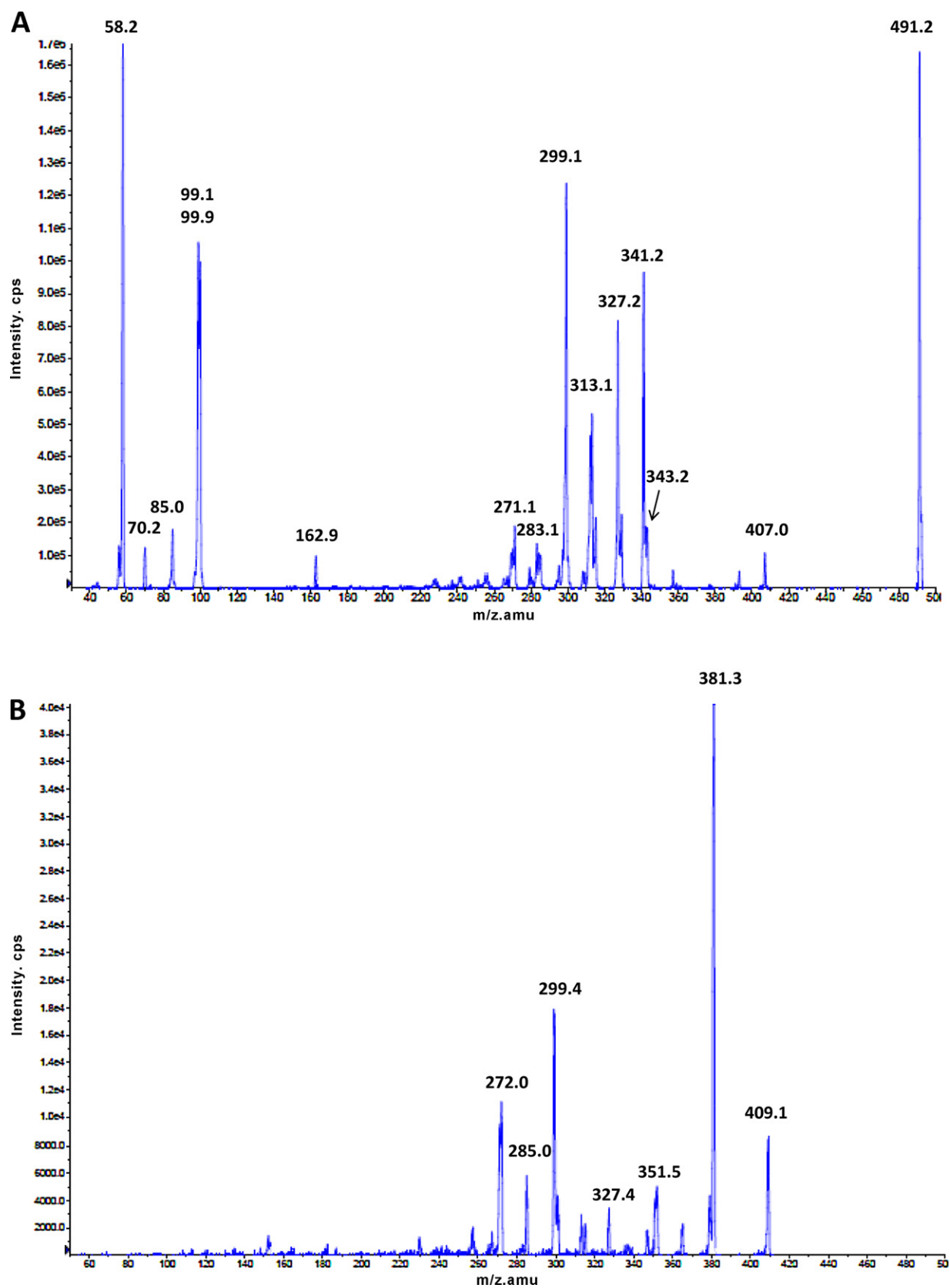
Fig. 4. MS–MS spectra of pure (A) thiosildenafil (product ion spectrum of the molecular peak at *m/z* 491.2) and (B) depiperazinothiosildenafil (product ion spectrum of the molecular peak at *m/z* 409.1).
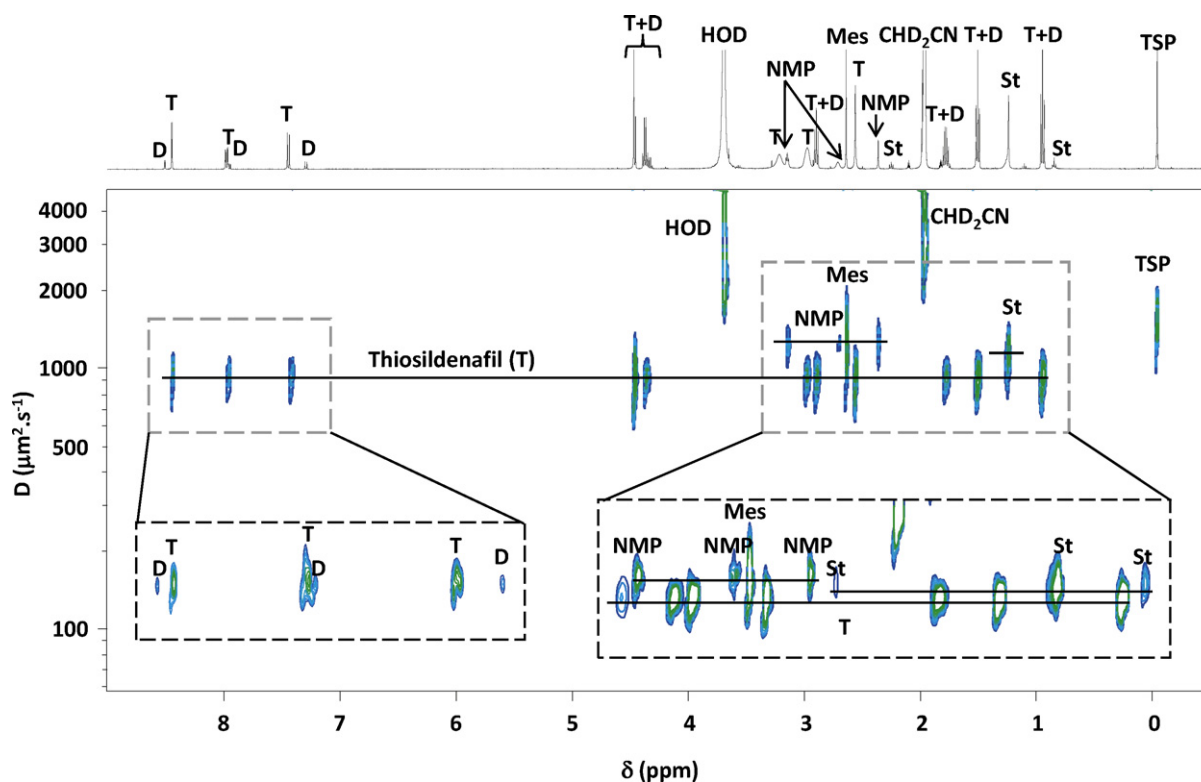
Fig. 5. 2D DOSY ^{1}H NMR spectrum of a $CD_3CN:D_2O$ (80:20) extract of a iErect capsule content. Deeper sections of some signals are shown in the boxes presented in the lower part of the figure. T: thiosildenafil; D: depiperazinothiosildenafil; NMP: N-methylpiperazine; Mes: mesylate; St: stearate; TSP: sodium 2,2,3,3-tetradeutero-3-trimethylsilylpropionate (internal reference).

in terms of relative percentage of depiperazinothiosildenafil with respect to thiosildenafil. Three experiments were nevertheless performed to check the stability of thiosildenafil in order to confirm that the cleavage of the sulfonamide bond did not occur during the preparation of the extracts from commercial iErect. Pure thiosildenafil was subjected to the same extraction protocol in $CD_3CN:D_2O$ (80:20) than that used for the commercial powder. No degradation could be observed on the ^{1}H NMR spectrum. The effect of an extended duration of sonication (2 additional hours) on a $CD_3CN:D_2O$ (80:20) extract of the commercial product was also verified. The ^{1}H NMR spectra before and after the additional sonication period were identical. A last verification consisting in heating for 24 h at 37 °C the CD_3CN, CD_3OD or $CD_3CN:D_2O$ (80:20) extract of the commercial powder did not show any change in the relative intensities of the ^{1}H NMR signals, which is consistent with the fact that the breakdown of the sulfonamide bond of thiosildenafil was obtained after heating at 105 °C for 21 h in a 6.1 mol L^{-1} solution of HCl [23]. All these experiments demonstrate that depiperazinothiosildenafil was not formed in our experimental extraction conditions and was indeed present in the commercial formulation. The identical relative proportions of depiperazinothiosildenafil and NMP with respect to thiosildenafil (respectively $18.3 \pm 1.0\%$ and $18.8 \pm 1.4\%$ ($n = 6$) in CD_3OD and $CD_3CN:D_2O$ (80:20) extracts) could suggest that the hydrolytic cleavage of the S–N bond of the sulfonamide group of thiosildenafil occurred during its synthesis.

Kim et al. [35] patented two different ways to prepare thiosildenafil (Fig. 6). The first one involved three steps: (i) conversion of the C=O of compound A into C=S (compound B) by P_2S_5 treatment, (ii) chlorosulfonation of the benzene ring in the para position relative to the ethoxy group of compound B leading to a benzenesulfonyl chloride (compound C), and (iii) reaction of the latter compound with NMP in a 3.6-fold molar excess of amine. Even if the column chromatographic purification described in the patent at this stage

was not thoroughly performed, this synthetic route cannot explain the presence in equimolar amounts of NMP and depiperazinothiosildenafil resulting from compound C hydrolysis. The second way consisted in a direct thionation of sildenafil with P_2S_5 in a quasi-stoechiometric ratio (1/1.1) of sildenafil/sulfur atom. The subsequent work-up to get pure thiosildenafil involves a treatment with dichloromethane and 6 mol L^{-1} aqueous sodium hydroxide, which is unlikely to provoke the breakdown of the SO_2–N bond as base-catalyzed hydrolysis of arenesulfonamides is unusual [36]. The only remaining possibility to explain the presence of depiperazinothiosildenafil and NMP in equimolar amounts might be that sildenafil used to prepare thiosildenafil was partially degraded into NMP and a sulfonic acid moiety whose ketone function in position 7 is thionated during the treatment with P_2S_5. However, one cannot exclude the degradation of thiosildenafil during the formulation process of commercial iErect preparations, which is unknown.

3.5. Quantification of thiosildenafil and depiperazinothiosildenafil in iErect commercial formulations

The contents of thiosildenafil and depiperazinothiosildenafil were measured by ^{1}H NMR in both batches 7164 and 8164 of iErect. They were identical and amounted to 217 ± 5 and 31 ± 2 mg/capsule for thiosildenafil and depiperazinothiosildenafil, respectively. A second extraction of the previously extracted powder resulted in additional 2 mg of thiosildenafil and 0.5 mg of depiperazinothiosildenafil. The amount of thiosildenafil in iErect was very high compared to those reported by Uchiyama et al. [17] and Reepmeyer and d'Avignon [23] who found respectively 0.4 mg in a 400 mg tablet and 35 mg in a ≈320 mg capsule. The "herbal" dietary supplement iErect thus places consumers at risk for potentially serious side-effects. Indeed, the unapproved analogue thiosildenafil has an inhibitory activity against the isolated enzyme
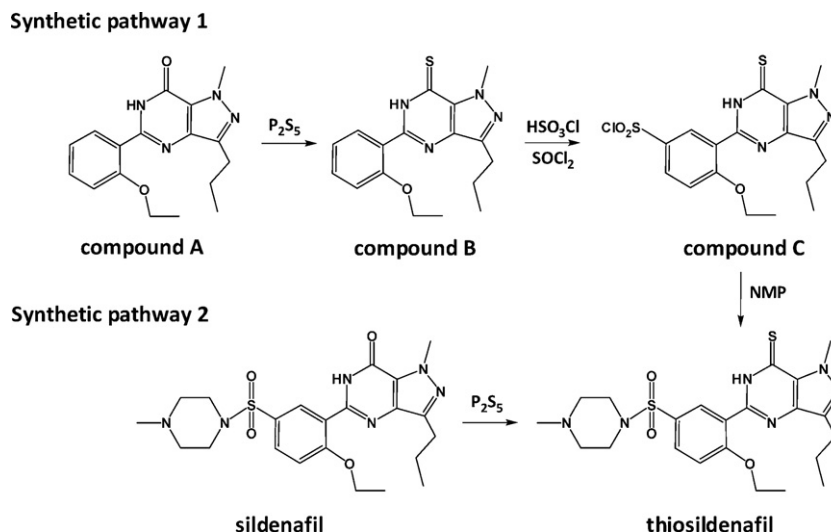
Fig. 6. Synthetic pathways of thiosildenafil described in Ref. [35]. P2S5: phosphorus pentasulfide; HSO3Cl: chlorosulfonic acid; SOCl2: thionyl chloride; NMP: N-methylpiperazine.

PDE-5 more than ten-fold higher than that of sildenafil (IC$_{50}$ = 0.59 and 6.86 nM, respectively) [35]. Moreover, each capsule of iErect contains more than 200 mg of thiosildenafil whereas the maximum recommended human dose of sildenafil is 100 mg/day [37]. To our knowledge, depiperazinothiosildenafil was not reported in the literature. However, acetilacid which is the benzoic acid derived from acetildenafil is active against isolated PDE-5 and displays an IC$_{50}$ of 5.5 nM [38]. A PDE-5 inhibitory activity of depiperazinothiosildenafil that would add to that of thiosildenafil cannot thus be excluded.

4. Conclusion

The dietary supplement iErect, sold over the Internet, marketed as 100% natural and advertised as a sexual performance enhancer for men, was found to contain two analogues of sildenafil. After isolation, their structures were elucidated using NMR, MS and IR. One of them is thiosildenafil already described in the literature [15] and the second one, named depiperazinothiosildenafil, results from the hydrolytic cleavage of the S–N bond of the sulfonamide group of thiosildenafil. To our knowledge, it is the first time that this compound is detected in a commercial formulation.

Acknowledgements

References

[1] M.H. Shin, M.K. Hong, W.S. Kim, Y.J. Lee, Y.C. Jeoung, Identification of a new analogue of sildenafil added illegally to a functional food marketed for penile erectile dysfunction, Food Addit. Contam. 20 (2003) 793–796.

[2] C. Shin, M. Hong, D. Kim, Y. Lim, Structure determination of a sildenafil analogue contained in commercial herb drinks, Magn. Reson. Chem. 42 (2004) 1060–1062.

[3] L. Blok-Tip, B. Zomer, F. Bakker, K.D. Hartog, M. Hamzink, J. ten Hove, M. Vredenbregt, D. de Kaste, Structure elucidation of sildenafil analogues in herbal products, Food Addit. Contam. 21 (2004) 737–748.

[4] P. Zou, P. Hou, M.Y. Low, H.L. Koh, Structure elucidation of a tadalafil analogue found as an adulterant of a herbal product, Food Addit. Contam. 23 (2006) 446–451.

[5] J.C. Reepmeyer, J.T. Woodruff, Use of liquid chromatography–mass spectrometry and a hydrolytic technique for the detection and structure elucidation of a novel synthetic vardenafil designer drug added illegally to a "natural" herbal dietary supplement, J. Chromatogr. A 1125 (2006) 67–75.

[6] P. Hou, P. Zou, M.Y. Low, E. Chan, H.L. Koh, Structural identification of a new acetildenafil analogue from pre-mixed bulk powder intended as a dietary supplement, Food Addit. Contam. 23 (2006) 870–875.

[7] S.R. Gratz, B.M. Gamble, R.A. Flurer, Accurate mass measurement using Fourier transform ion cyclotron resonance mass spectrometry for structure elucidation of designer drug analogs of tadalafil, vardenafil and sildenafil in herbal and pharmaceutical matrices, Rapid Commun. Mass Spectrom. 20 (2006) 2317–2327.

[8] J.C. Reepmeyer, J.T. Woodruff, Use of liquid chromatography–mass spectrometry and a chemical cleavage reaction for the structure elucidation of a new sildenafil analogue detected as an adulterant in an herbal dietary supplement, J. Pharm. Biomed. Anal. 44 (2007) 887–893.

[9] P. Zou, S.S.Y. Oh, K.H. Kiang, M.Y. Low, H.L. Koh, Liquid chromatography ion trap/time-of-flight mass spectrometric study on the fragmentation of an acetildenafil analogue, Eur. J. Mass Spectrom. 13 (2007) 233–238.

[10] J.C. Reepmeyer, J.T. Woodruff, D.A. d'Avignon, Structure elucidation of a novel analogue of sildenafil detected as an adulterant in an herbal dietary supplement, J. Pharm. Biomed. Anal. 43 (2007) 1615–1621.

[11] M. Dusek, M. Sanda, P. Cuhra, S. Barsova, Simultaneous LC–MS/MS determination of sildenafil and related analogues added illegally to herbal products intended for the treatment of erectile dysfunction, in: Proc. 3rd International Symposium on Recent Advances in Food Analysis, Prague, November 7–9, 2007, p. 238.

[12] P. Zou, P. Hou, S.S.Y. Oh, X. Ge, B.C. Bloodworth, M.Y. Low, H.L. Koh, Identification of benzamidenafil, a new class of phosphodiesterase-5 inhibitor, as an adulterant in a dietary supplement, J. Pharm. Biomed. Anal. 47 (2008) 255–259.

[13] K. Kumazaka, N. Kawahara, K. Doi, T. Kojima, Y. Goda, Determination of (R)-xanthoanthrafil, a phosphodiesterase-5 inhibitor, in a dietary supplement promoted for sexual enhancement, Chem. Pharm. Bull. 56 (2008) 227–230.

[14] B.J. Venhuis, G. Zomer, D. de Kaste, Structure elucidation of a novel synthetic thiono analogue of sildenafil detected in an alleged herbal aphrodisiac, J. Pharm. Biomed. Anal. 46 (2008) 814–817.

[15] P. Zou, P. Hou, S.S.Y. Oh, Y.M. Chong, B.C. Bloodworth, M.Y. Low, H.L. Koh, Isolation and identification of thiohomosildenafil and thiosildenafil in health supplements, J. Pharm. Biomed. Anal. 47 (2008) 279–284.

[16] Y.H. Lam, W.T. Poon, C.K. Lai, A.Y.W. Chan, T.W.L. Mak, Identification of a novel vardenafil analogue in herbal product, J. Pharm. Biomed. Anal. 46 (2008) 804–807.

[17] N. Uchiyama, K. Saisho, R. Kikura-Hanajiri, Y. Haishima, Y. Goda, Determination of a new type of phosphodiesterase-5 inhibitor, thioquinapiperifil, in a dietary supplement promoted for sexual enhancement, Chem. Pharm. Bull. 56 (2008) 1331–1334.

[18] X. Ge, M.Y. Low, P. Zou, L. Lin, S.O.S. Yin, B.C. Bloodworth, H.L. Koh, Structural elucidation of a PDE-5 inhibitor detected as an adulterant in a health supplement, J. Pharm. Biomed. Anal. 48 (2008) 1070–1075.

[19] T. Hasegawa, M. Saijo, T. Ishii, T. Nagata, Y. Haishima, N. Kawahara, Y. Goda, Structural elucidation of a tadalafil analogue found in a dietary supplement, J. Food Hyg. Soc. Jpn. 49 (2008) 311–315.

[20] M.C. Lin, Y.C. Liu, Y.L. Lin, J.H. Lin, Isolation and identification of a novel sildenafil analogue adulterated in dietary supplements, J. Food Drug Anal. 16 (2008) 15–20.

[21] D.M. Choi, S. Park, T.H. Yoon, H.K. Jeong, J.S. Pyo, J. Park, D. Kim, S.W. Kwon, Determination of analogs of sildenafil and vardenafil in foods by column

liquid chromatography with a photodiode array detector, mass spectrometry, and nuclear magnetic resonance spectrometry, J. AOAC Int. 91 (2008) 580–588.

[22] S. Balayssac, S. Trefi, V. Gilard, M. Malet-Martino, R. Martino, M.A. Delsuc, 2D and 3D DOSY ^{1}H NMR, a useful tool for analysis of complex mixtures: application to herbal drugs or dietary supplements for erectile dysfunction, J. Pharm. Biomed. Anal. 50 (2009) 602–612.

[23] J.C. Reepmeyer, D.A. d'Avignon, Structure elucidation of thioketone analogues of sildenafil detected as adulterants in herbal aphrodisiacs, J. Pharm. Biomed. Anal. 49 (2009) 145–150.

[24] L. Li, M.Y. Low, F. Aliwarga, J. Teo, X.W. Ge, Y. Zeng, B.C. Bloodworth, H.L. Koh, Isolation and identification of hydroxythiohomosildenafil in herbal dietary supplements sold as sexual performance enhancement products, Food Addit. Contam. 26 (2009) 145–151.

[25] T. Hasegawa, K. Takahashi, M. Saijo, T. Ishii, T. Nagata, M. Kurihara, Y. Haishima, Y. Goda, N. Kawahara, Isolation and structural elucidation of cyclopentynafil and N-octylnortadalafil found in a dietary supplement, Chem. Pharm. Bull. 57 (2009) 185–189.

[26] H. Goker, M. Coskun, M. Alp, Isolation and identification of a new acetildenafil analogue used to adulterate a dietary supplement: dimethylacetildenafil, Turk. J. Chem. 34 (2010) 157–163.

[27] C.S. Ng, T.Y. Law, Y.K. Cheung, P.C. Ng, K.K. Choi, Development of a screening method for the detection of analogues of sildenafil and vardenafil by the use of liquid chromatography coupled with triple quadrupole linear ion trap mass spectrometer, Anal. Methods 2 (2010) 890–896.

[28] B.J. Venhuis, G. Zomer, H.D. Meiring, Y. Aubin, D. de Kaste, The identification of a nitrosated prodrug of the PDE-5 inhibitor aildenafil in a dietary supplement: a Viagra with a pop, J. Pharm. Biomed. Anal. 54 (2011) 735–741.

[29] H.M. Lee, C.S. Kim, Y.M. Jang, S.W. Kwon, B.J. Lee, Separation and structural elucidation of a novel analogue of vardenafil included as an adulterant in a dietary supplement by liquid chromatography–electrospray ionization mass spectrometry, infrared spectroscopy and nuclear magnetic resonance spectroscopy, J. Pharm. Biomed. Anal. 54 (2011) 491–496.

[30] X. Ge, L. Li, H.L. Koh, M.Y. Low, Identification of a new sildenafil analogue in a health supplement, J. Pharm. Biomed. Anal. 56 (2011) 491–496.

[31] U. Wollein, W. Eisenreich, N. Schramek, Identification of novel sildenafil-analogues in an adulterated herbal food supplement, J. Pharm. Biomed. Anal. (2011), doi:10.1016/j.jpba.2011.07.012.

[32] S. Trefi, C. Routaboul, S. Hamieh, V. Gilard, M. Malet-Martino, R. Martino, Analysis of illegally manufactured formulations of tadalafil (Cialis®) by ^{1}H NMR 2D DOSY ^{1}H NMR and Raman spectroscopy, J. Pharm. Biomed. Anal. 47 (2008) 103–113.

[33] J. Lee, H.H. Yoo, M.Y. Kang, D.H. Kim, Low-energy collision-induced dissociation of sildenafil thiono analogues: gas-phase intramolecular nucleophilic substitution through ion-neutral complexes between a cationic substrate and a thione-containing neutral nucleophile, Rapid Commun. Mass Spectrom. 19 (2005) 1767–1770.

[34] G. Socrates, Infrared and Raman Characteristic Group Frequencies, third ed., John Wiley & Sons, Chichester, 2001.

[35] J.H. Kim, Y. Kim, K.I. Choi, D.H. Kim, G. Nam, J.H. Seo, Novel pyrazolopy-rimidinethione derivatives, preparation methods thereof and their use as therapeutics for erectile dysfunction, US Patent 0176371A1 (2004).

[36] S. Searles, S. Nukina, Cleavage and rearrangement of sulfonamides, Chem. Rev. 59 (1959) 1077–1103.

[37] Data Sheet, Viagra®, 2008. www.medsafe.govt.nz/profs/datasheet/v/viagratab.pdf.

[38] A.S. Bell, K.N. Terrett, Pyrazolopyrimidinone antianginal agents, European Patent 0526004A1 (1993).

Target separation of a new anti-tumor saponin and metabolic profiling of leaves of *Panax notoginseng* by liquid chromatography with eletrospray ionization quadrupole time-of-flight mass spectrometry

Qian Mao[a], Jie Yang[a], Xiu-Ming Cui[a], Jing-Jing Li[a], Yin-Tao Qi[a], Ping-Hu Zhang[b,*], Qiang Wang[a,*]

[a] *State Laboratory of Modern Chinese Medicines, China Pharmaceutical University, Nanjing 210009, PR China*
[b] *Jiangsu Center for New Drug Screening & National New Drug Screening Laboratory, China Pharmaceutical University, Nanjing 210009, PR China*

ABSTRACT

A method coupling high-performance liquid chromatography (HPLC) with quadrupole time-of-flight mass spectrometers (QTOF-MS) using an eletrospray ionization (ESI) source was firstly developed for detection, characterization and guiding target separation of variants of protopanaxdiol saponin from leaves of *Panax notoginseng*. Under the guidance of LC–QTOF-MS, a new trace saponin was probed according to the precise elemental compositions of molecular ions and the fragmentation behavior, and then separated from the ethanol extract of the plant by a set of chromatographic methods. It was further confirmed by NMR experiments as 3-*O*-β-D-glucopyranoside-3β,l2β,23β-triol-20-ene-dammar (Pn-1). The cytotoxic assay showed that Pn-1 had relatively stronger anti-tumor effects against three tumor cell lines (NCI-H460, HepG2 and SGC-7901) than Rg₃, an approved clinical agent for cancer therapy. Meanwhile, based on accurate mass measurements within 5 ppm for each molecular ions and subsequent product ions, 48 saponins, including 40 protopanaxadiol saponins, 7 protopanaxatriol saponins and 1 oleanane saponin were identified. It is noted that the knowledge of the presence of abundant protopanaxadiol saponins in leaves of *P. notoginseng* may provide tools for a full understanding of the chemical diversity of secondary metabolites from the different parts of *P. notoginseng*. From the points of time consuming and accurate mass measurement capability, the LC–QTOF-MS is a highly powerful tool for screening and guiding target separation of new compounds in herbal extract, and thus benefits the speed of new drug discovery progress.

© 2011 Elsevier B.V. All rights reserved.

1. Introduction

The root of *Panax notoginseng* (Burk.) F.H. Chen (Araliaceae) has been widely used for activation of blood circulation to dissipate blood stasis, treatment of inflammation and different body pains [1]. The constituents isolated and characterized in root of *P. notoginseng* include ginsenosides, polysaccharides, peptides, polyacetylenic alcohols, and fatty acids. The main bioactive ingredients are thought to be the dammarane-type saponins, including the protopanaxadiol (PPD) group, the protopanaxatriol (PPT) group and other low-abundant group [2]. Although the root of *P. notoginseng* is more frequently used than other parts of the plant, saponins are found in all parts of the plant and their compositions and concentrations vary greatly depending on the tissues. The leaves of *P. notoginseng* (PNL) possess abundant protopanaxadiol type saponins, which are known to have stronger anti-tumor activity than protopanaxtriol group [1–3].

Recent structural–function relationship of ginsenosides studies showed that their anti-tumor activities increase with the decrease of sugar number. Furthermore, cancer cell inhibition by saponins is also influenced by the number and location of polar hydroxyl groups [2]. Such as ginsenoside Rg₃, a PPD group saponin with two glucoses, has been approved for clinical use as an anticancer agent in China. According to these structure–function relations, our group has been interested in detailed detection and isolation of PPD group ginsenosides with less or no sugars moieties for new oncology drug discovery. However, due to low sensitivity, low abundance and non-chromophoren, it is difficult to extract, isolate and purify new bioactive saponins by traditional strategies. Although improved separation techniques are applied, the isolation procedure of new bioactive saponins is very time-consuming and costly without analytical guidance. Hence, it is desirable to develop rapid and sensitive methods for the detection, characterization and target isolation of novel anti-tumor saponins in PNL.

Although introduced several years ago, coupling of high-performance liquid chromatography (HPLC) and quadrupole

Type	Name	R₁	R₂	R₃
	Pn-1			
PPD group	Ginsenoside Rb₁	-Glc²-¹Glc	-Glc⁶-¹Glc	
	Ginsenoside Rc	-Glc²-¹Glc	-Glc⁶-¹Ara(f)	
	Ginsenoside Rb₂	-Glc²-¹Glc	-Glc⁶-¹Ara(p)	
	Ginsenoside Rb₃	-Glc²-¹Glc	-Glc⁶-¹Xyl	
	Ginsenoside Rd	-Glc²-¹Glc	-Glc	
	Ginsenoside F₂	-Glc	-Glc	
	20 (R)-ginsenoside Rg₃	-Glc²-¹Glc	H	
PPT group	Notoginsenoside R₁	H	-Glc	-Glc²-¹Xyl
	Ginsenoside Rg₁	H	-Glc	-Glc
Oleanane group	Scoposides E	-Xyl³-¹Rha³-¹Ara	H	
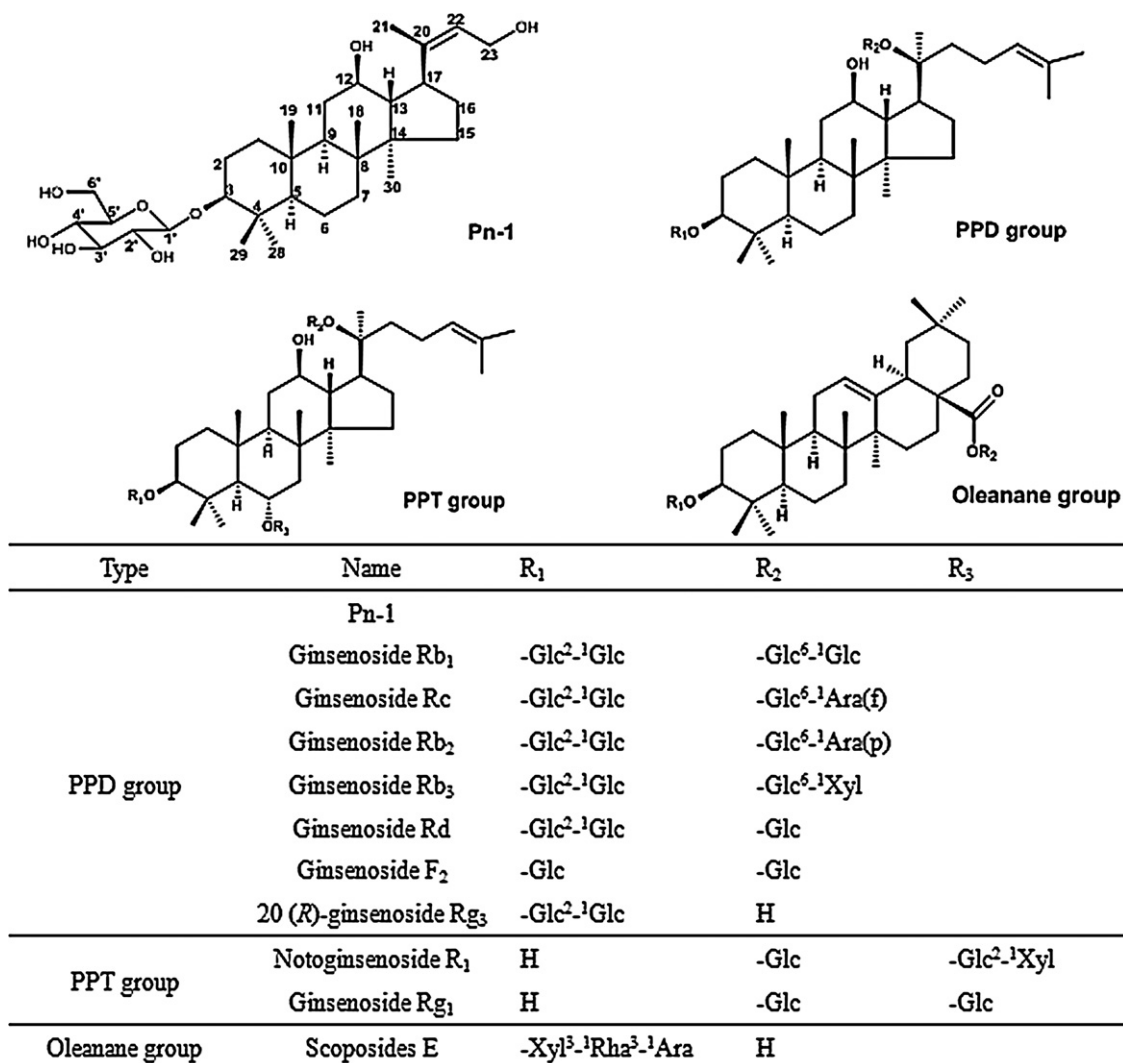
Fig. 1. Structures of Pn-1 and reference compounds.

time-of-flight mass spectrometers (QTOF-MS) has been embraced by researchers as a powerful and robust tool with high sensitivity, high mass accuracy, and abundant fragments ions [4]. To our best knowledge, many analytical techniques have been developed for analysis of constituents in *P. notoginseng*, including HPLC–ELSD, MEKC, HSCCC, LC–MS^n, UPLC–ESI-MS, and UPLC–QTOF [5–10]. However, LC–QTOF-MS has not been reported for detection and guiding target separation of new bioactive saponins and systematic study of structural characterization of chemical constituents in PNL.

This paper marks the first report on HPLC coupled with QTOF-MS technique for screening, characterization and guiding target isolation of a new anti-tumor compound in PNL. Furthermore, a total of 48 saponins (marked as P1–P48), including 40 PPD group saponins, 7 PPT group saponins, and 1 oleanane saponin were characterized and identified from the ethanol extract of PNL by LC–QTOF-MS.

2. Materials and methods

2.1. Chemicals and materials

Reference compounds were isolated previously from leaves of *P. notoginseng* by a series of chromatographic procedures in our laboratory, including notoginsenoside R₁, ginsenoside Rg₁, Rc, Rb₁, Rb₂, Rb₃, Rc, Rd, F₂, and 20 (R)-Rg₃. The structures of reference compounds were elucidated and unequivocally identified by spectroscopic methods such as UV, IR, MS, ^{1}H NMR and ^{13}C NMR. The purity of each standard compound was determined to be higher than 95% by normalization of the peak area detected by HPLC-DAD. Herein, a new compound Pn-1, was characterized for the first time as 3-O-β-D-glucopyranoside-3β,l2β,23β-triol-20-ene-dammar by a set of 1D and 2D NMR spectroscopic techniques. Their structures were shown in Fig. 1.

The HPLC grade acetonitrile was purchased from Merck (Darmstadt, Germany). Deionized water (18 MV) was prepared by passing distilled water through a Milli-Q system (Millipore, Milford, MA, USA). Formic acid (purity 96%) was purchased from Tedia (Fairfield, OH, USA). Other reagents and chemicals were of analytical grade.

The PNL were collected in Wenshan County, Yunnan Province, China, and identified by Dr. Xiu-Ming Cui, Department of Natural Medicinal Chemistry, China Pharmaceutical University, where a voucher specimen (No.110330) has been deposited.

2.2. Sample preparation

The dried leaves of *P. notoginseng* were powdered to a homogeneous size in a mill, sieved through a 40-mesh sieve. The accurately weighed powder (1.0 g) was suspended in 30 mL 70% (v/v) methanol, ultrasonically extracted for 60 min, and then cooled at room temperature. 70% methanol was added to compensate

for the lost weight. The methanolic solution was centrifuged at 15 000 rpm for 10 min, and the supernatants were transferred to an autosampler vial for LC–QTOF-MS analysis.

2.3. LC–QTOF-MS conditions

Analyses were performed on an Agilent Series 1100 liquid chromatograph (Agilent Technologies, Palo Alto, CA, USA), consisting of a binary pump, an online degasser, an autosampler and a thermostatically controlled column compartment. The chromatographic separation was performed on an Alltima C_{18} column (3 μm, 53 mm, 7 mm) at 30 °C. A linear gradient elution of water–formic acid (100:0.1, v/v) (A) and acetonitrile–formic acid (100:0.1, v/v) (B) was used for the separation of samples. The gradient programmer was as follows: 10–25% B at 0–25 min; 25% B at 25–35 min; 25–31% B at 35–45 min; 31% B at 45–65 min; 31–45% B at 65–85 min; 45–51% B at 85–95 min; 51–56% B at 95–100 min; 56–100% B at 100–105 min.

The TOF-MS analysis worked in negative mode and mass range was set at m/z 300–1700. The conditions of ESI source were as follows: gas temperature, 330 °C; drying gas (N_2) flow rate, 5 L/min; nebulizer, 45 psig; sheath gas temperature, 400 °C; sheath gas flow, 10 L/min; capillary voltage, 3000 V; fragmentor, 60 V; skimmer voltage, 65 V; OCT 1 RF Vpp, 750 V. All the operations, acquisition, and analysis of data were controlled by Agilent LC-MS-QTOF MassHunter Data Acquisition Software Ver. A.01.00 (Agilent Technologies) and Agilent MassHunter Qualitative Analysis Software B.02.00, respectively.

2.4. Isolation of a new protopanaxadiol saponin

The leaves of *P. notoginseng* (approximately 10 kg) collected in Yunnan province of China were extracted with 75% (v/v) ethanol. The ethanolic extract was partitioned into an ethyl acetate (EtOAc)-water mixture to furnish an EtOAc-soluble fraction and an aqueous phase. The aqueous phase was further extracted with *n*-butanol (*n*-BuOH) to give an *n*-BuOH-soluble fraction and H_2O soluble fraction. The *n*-BuOH-soluble fraction (so-called saponin fraction) was subjected to macroporous resin HPD100 and eluted with 25%, 50% and 85% (v/v) ethanol in water. The 85% ethanolic fraction (100 g) was subjected to normal-phase and reversed-phase column chromatography and finally semi-preparative HPLC to afford one new saponin Pn-1 [8 mg, yield 0.0008%, t_R 25 min, 45% (v/v) acetonitrile in water].

2.5. Chromatographic semi-preparative separation of Pn-1

Semi-preparative HPLC separation was carried out with a Shimadzu (Japan) LC-10A system equipped with a binary pump (LC-10A), a Rheodyne injector (California, USA) provided with 200 μL loop, a column temperature controller (CTO 10 AV), a diode array detector (SPD-M10A) and a Hedra C_{18} reverse phase column (10 mm × 250 mm, 5 μm). The column temperature was maintained at room temperature. The mobile phase was acetonitrile/water (45:55, v/v). The flow rate was 2.25 mL/min and the UV detection wavelength was set at 210 nm. The structure of the Pn-1 was elucidated by spectroscopic methods including extensive 1D and 2D NMR experiments, and compared with literature publications. 1D and 2D NMR spectra were recorded on a Bruker AVANCE III AV-500 spectrometer (^{1}H 500 MHz, ^{13}C 125 MHz), using pyridine (C_5D_5N) as solvent and TMS as internal standard.

2.6. Cytotoxicy assay

The anti-tumor effect of Pn-1 and other 3 major ginsenosides from PNL, including 20(R)-ginsenoside Rg$_3$, ginsenoside Rc and ginsenoside Rb$_2$, on NCI-H460 cells (human lung cancer),

HepG2 cells (human hepatocellular cancer), SGC-7901 (human gastric adenocarcinoma) were examined by MTT (methylthiazoleyl-diphenyl-tetrazolium bromide) assays. The three tumor cell lines (1×10^5) were incubated in 96-well assay plates for 24 h. Ginsenoside Rh$_2$, exhibiting activity against a variety of cancer cells [11], was used as positive control. After treatment with various concentrations of Pn-1 and other 4 ginsenosides for 72 h, plates were incubated with 20 μL of MTT solution (5 mg/mL in PBS) for 4 h at 37 °C. DMSO 120 μL was then added to solubilize the formazan crystals in viable cells, and 4 h later absorbances were read at 570 nm using a Safire 2 microplate reader (Tecan, Switzerland). The cell survival percentages were calculated by dividing the mean OD of compound-containing wells by that of control wells.

3. Results and discussion

3.1. Optimum conditions for LC–QTOF-MS analysis

Since the chromatographic conditions (the compositions of mobile phase, the column temperature and the flow rate) have signification impacts on the separation of the saponins, several preliminary experiments were performed for good separation of saponins. Different mobile phases, including methanol/water, acetonitrile/water, acetonitrile/formic acid in water and acetonitrile containing formic acid/formic acid in water system, were investigated firstly. The gradient elution with methanol/water induced the baseline drift at 203 nm when the saponins in PNL were detected. The acetonitrile/water system showed more powerful separation for the major saponins in PNL than the methanol/water system. When formic acid was added into both of the mobile phases, the symmetries of most chromatographic peaks were improved remarkably. Thus, a solvent system consisting of 0.1% formic acid in acetonitrile and 0.1% formic acid in water was eventually selected. Furthermore, column temperature and flow rate were also investigated. The flow rate of 0.8 mL/min was adopted in this method based on a compromise between the speed, separation efficiency, peak width and column backpressure. In addition, the high column temperature of 30 °C was set due to the decrease in the column pressure and improvement in the separation of compounds compared with 25 °C and 30 °C.

As for QTOF-MS, previous studies have shown that negative ion mode has higher sensitivity, clearer mass spectra and lower background noise than positive ion mode to confirm molecular ions of ginsenosides [12]. Therefore, negative ion mode was applied for the compound detection and characterization. In addition, fragmentor voltage plays a vital role for obtaining extensive fragmentation information and sensitive detection of the molecular ions. We varied the fragmentor voltage values at 55, 60, 68, and 75 V, observing the relative abundance of the molecular ions and maximal fragmentation information. Finally, considering sensitivity and fragmentation information, the value at 60 V was applied. Fig. 2 shows the typical total ion chromatograms (TIC) of PNL. More than 50 peaks in all were separated and detected according to the spectrum of each peak in the TIC.

3.2. Strategy for screening and target separation of the new bioactive saponin

As described before, PPD group saponins with lower polarity imply higher anti-tumor activity [2]. For detection and isolation of new bioactive saponins, we proposed a strategy for screening and guiding target separation of new anti-tumor saponins from PNL. Firstly, according to the guidance of structure–function relationship, we paid a lot of attention to the minor peaks of low-polarity fraction. We determined the molecular formulas for compounds
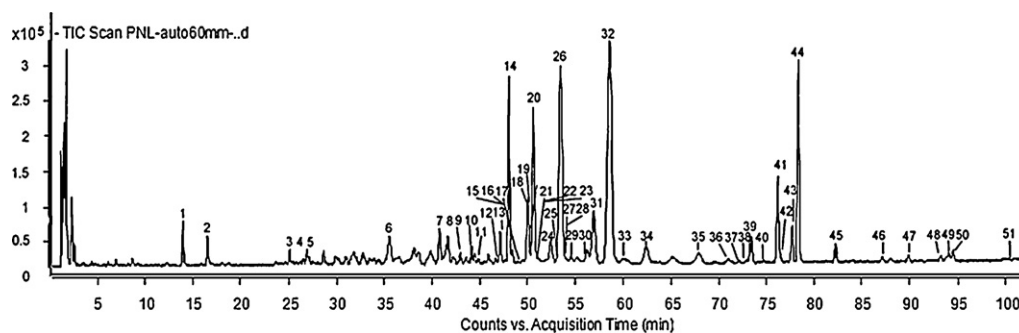
Fig. 2. Total ion chromatogram of PNL by LC–QTOF-MS in negative mode.

by accurate mass measurement. After checking the proposed fragmentation pathways and searching databases, the most possible structure could be determined. Among the compounds, the compounds with less sugar, which belonged to PPD group and did not hit any record in databases, could be assigned as target compounds. The next step was to enrich the target compounds by means of macroporous resin. Under the same condition of LC–QTOF-MS, we compared the HPLC chromatography of enriched fractions from macroporous resin. The fraction with higher content of target compounds was submitted to different column chromatography until the purification of target compounds was achieved. Finally, the anti-tumor activities of target compounds could be evaluated by cytotoxic assay.

3.3. Screening and target separation of Pn-1

When we screened the peaks appearing during 85–90 min, noteworthy 2 peaks (P49 and P50) showed base peaks of $[M-H]^-$ at 565.3749 and 795.4642 in spectrum, respectively. The molecular formulas of the two compounds were determined as $C_{32}H_{53}O_8$ and $C_{50}H_{63}O_6$ with error of -0.54 and -1.56 ppm, respectively. It was astonishing to find that the two compounds did not correspond to any compounds found in *Panax* species. Due to lack of enough fragment ions, the identity of P50 needs further confirmation. We

identified P49 and proposed the possible fragmentation pathways according to its fragment ions.

As seen in Scheme 1, P49 produced a $[M+COOH]^-$ ion with high intensity at m/z 611.3795 ($C_{33}H_{55}O_{10}$) and $[M-H]^-$ at m/z 565.3749 ($C_{32}H_{53}O_8$). The moderately abundant product ion at m/z 403.3219 ($C_{26}H_{43}O_3$), formed by the neutral loss of a glucose unit (162 Da) from the precursor ion, did not correspond to any of the known aglycone moiety by comparison with literature publication. Moreover, P49 had a Mr 56 Da less than that of ginsenoside Rh$_2$ [11], which indicated the compound might loss 4 methylenes on sidechain or have some change in rings. The abundant fragment ion at m/z 161.0458 ($C_6H_9O_5$) was a glucose by loss of a H_2O. The obvious fragment ion at m/z 101.0244 ($C_4H_5O_2$) resulted from successive neutral loss of $C_2H_4O_2$. Deduced from these fragmentation features, we assumed the peak might be a new variant of protopanaxadiol saponin with modified position in the side-chain. Scheme 1 shows the accurate mass measurements of fragment ions observed in mass spectra and proposed pathways.

To confirm this assumption, the isolation of constituents from the low polarity fraction by several chromatographic methods was performed. Macroporous resin HPD100 was employed to enrich the low polarity part. Under the same analytical condition of LC–QTOF-MS, we compared the chromatography of 3 enriched elutions (by 25%, 50% and 85% ethanol). The 85% elution contained relatively higher content of target compounds than that of other
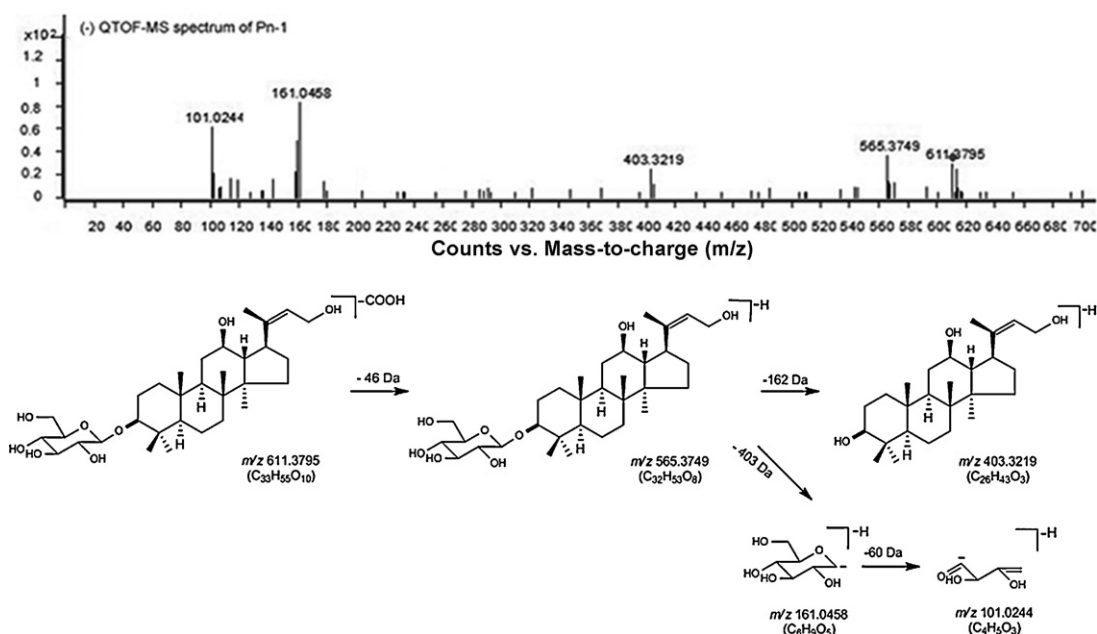
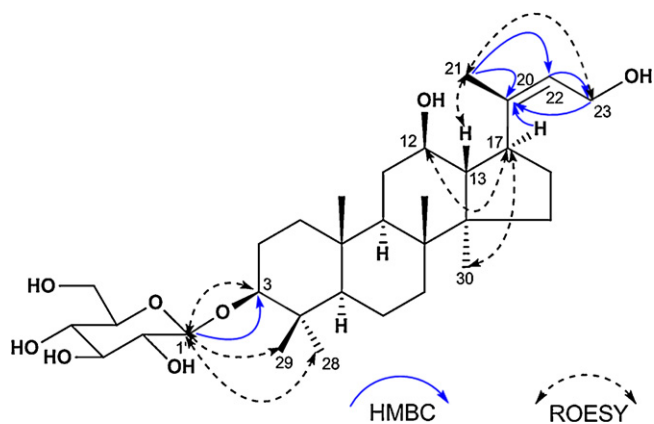**Scheme 1.** The negative QTOF-MS spectra and proposed fragmentation pathways of Pn-1.

Fig. 3. Key HMBC and ROESY correlations of Pn-1.

two elutions. Thus, the 85% elution was subjected to normal-phase column, reverse-phase column chromatography repeatedly and semi-preparative HPLC. Owing to low quantity of P50, we just obtained 0.5 mg, which was not enough for spectroscopic experiment of unequivocal structural determination (^{1}H NMR, ^{13}C NMR and 2D NMR). However, enrichment and purification of P49, named Pn-1, was achieved.

For further determination and elucidation of the compound, HRESIMS, IR, DEPT, 1D and 2D NMR (including ^{1}H–^{1}H COSY, HSQC, HMBC, ROESY) experiments were applied to confirm the proposed structure. The HRESIMS of the compound exhibited a pseudo-ion [M−H]$^-$ at m/z 565.3788 compatible with the molecular formula $C_{32}H_{53}O_8$ with six degrees of unsaturation. The IR spectrum showed the presence of hydroxyl (3417 cm^{-1}) and olefinic (1639 cm^{-1}) groups. The ^{13}C NMR, ^{1}H NMR, HMBC, and ROESY (Table 1) spectrum of Pn-1 showed a doublet proton signal assignable to one β-D-glucopyranosyl moieties [δ 4.98 (1H, d, J = 7.5 Hz)], correlated with a methine carbon signal at δ 107.4 (d), characteristic of an acetal carbon, in the HSQC spectrum. The carbon signals of the aglycone part in the ^{13}C NMR of Pn-1 were found to nearly superimposable on those of ginsenoside Rh$_2$ [13]. However, the aglycone molecular weight of Pn-1 was 56 Da less than that of ginsenoside Rh$_2$, which was in good agreement with absence of four carbons in ^{13}C NMR. To our best knowledge, absence of any carbon in the side-chain has not been reported previously. In addition, protopanaxadiol, which had a side-chain common in ginsenosides, showed resonances at δ 126.4 (d) and 130.8 (s) for C-24 and C-25, respectively, while Pn-1 had double-bond carbons resonating at δ 126.5 (d) and 142.2 (s). A comparison of the chemical shifts of the two olefinic carbons of Pn-1 with those of reported ginsenosides, such as notoginsenoside R$_8$ [14], suggested that the double bond in the side-chain of Pn-1 was located between C-20 and C-22. The observed characteristic double doublet proton signals at δ 4.49 and 4.54, and the methylene carbon signal at δ 59.5 (t) for C-23 of Pn-1 confirmed the presence of a hydroxy connected to it in the terminal of the side-chain. The complete planar structure of Pn-1 was established by the analysis of its long range HMBC correlations, in which the key HMBC correlations from H-1′ to C-3, indicating the only one β-D-glucopyranosyl moiety linked to C-3, from both H-21 and H-23 to C-20, from H-21 to C-22, and from H-22 to C-23, confirming the side-chain was a butyl alcohol-2-en group, which connected to C-17 by the HMBC correlation between H-17 and C-20. The relative configuration of Pn-1 was mainly determined by a ROESY spectrum, in which the correlations of H-17/H-12, and H-17/H-30 indicated that they were co-facial and were arbitrarily assigned α-orientation. Thus, the structure of Pn-1 was elucidated as shown in Fig. 3.

3.4. Structural characterization of major glycosides

The major saponins in PNL generally contained the PPD group, the PPT group, and the oleanane group, which displayed characteristic ions at m/z 459, 475, and 455, respectively. The PPD group had sugar moieties attached to the β-OH at C-3 or C-20, while the PPT group had sugar moieties attached to the α-OH at C-6 or β-OH at C-20 and the oleanane group had a five membered epoxy ring at C-20. Major saponins in PNL were screened from ethanol extract of PNL rapidly by extracting those characteristic ions. Table 2 summarizes the QTOF-MS data of 48 saponins screened and identified from PNL. 10 saponins were unambiguously assigned by comparison their retention times, characteristic fragment ions with those of standards. Other saponins were determined by the molecular ions based on [M−H]$^-$ or [M+COOH]$^-$ firstly. Then the accurate molecular formulas of each compound were calculated and their chemical formulas were searched by against chemical databases including Scifinder and Dictionary of Natural Products [15]. The most probable molecular formulas of the saponins were determined with different criteria including mass accuracy <5 ppm, the nitrogen rule, the double-bond equivalent index (DBE), the isotopic pattern [16]. The others were tentatively identified by matching molecular formulas with known saponins and by elucidating the fragment ions. Moreover, abundant literatures of chromatographic behavior of saponins offered complementary data for identification of saponins, especially isomeric saponins. Totally, 47 known saponins were identified or tentatively characterized. Of these known saponins, 15 typical saponins were described to demonstrate details of the elucidation procedure, while other saponins were shown in Tables 3 and 4.

3.4.1. PPD group

P24, P31, P32 and P33 were a group of isomeric saponins. As listed in Table 3, they yielded intensive molecular ion peaks at m/z 1077.5865–1077.5888, which corresponded to the molecular formula of $C_{53}H_{89}O_{22}$. They shared the same characteristic fragment ion m/z 459 and almost identical fragment ions, indicating that they were a group of PPD saponins. Another group of fragment ions of P24 at m/z 945.5438 ($C_{48}H_{81}O_{18}$), 783.4847 ($C_{42}H_{71}O_{13}$), 621.4364 ($C_{36}H_{61}O_8$), 459.3804 ($C_{30}H_{51}O_3$) originated from [M−H−(Ara−H$_2$O)]$^-$, [M−H−(Ara−H$_2$O)−(Glc−H$_2$O)]$^-$, [M−H−(Ara−H$_2$O)−2(Glc−H$_2$O)]$^-$, [M−H−(Ara−H$_2$O)−3(Glc−H$_2$O)]$^-$, respectively. By comparison their retention times and MS data with those of reference compounds, P24, P31 and P32 were then unequivocally identified as ginsenoside Rc, ginsenoside Rb$_2$, and ginsenoside Rb$_3$. Due to limited information, P33 was tentatively identified as notoginsenoside L.

When applying a mass window of 1163.5880–1163.5891 ($C_{56}H_{91}O_{25}$), three peaks were screened and marked with P30, P34, P36. Product ions at m/z 459 indicated the presence of PPD moiety. It was noticed that P30 generated the same fragments ions as those of P24. Moreover, its fragmentation pathways were also quite similar to those of P24. The difference between P24 and P30 was that the characteristic product ion at m/z 1163.5890, which was formed by an addition of 86 Da corresponding to one malonyl. As seen from Table 3, fragment ions generated by P34 and P36 were the same as those of P30. It was proposed that P30, P34 and P36 belonged to a group of isomeric saponins. They were tentatively supposed to be malonate saponins related to P24. Owing to the unavailability of reference standards of the malonyl saponins, they were tentatively ascribed as malonyl-ginsenoside Rc and its two isomers. For further structural information of these saponins, NMR experiments are needed.

P35 had the elemental composition of $C_{48}H_{81}O_{18}$, and their molecular masses were 132 Da less than that of ginsenoside Rc,

Table 1
1D and 2D NMR data for Pn-1 (C_5D_5N, δ in ppm, 500 MHz).

Position	δ_C	δ_H (multi, J in Hz)	HMBC	ROSEY
Aglycone				
1α	39.8 (t)	0.81 m	C-2, 3, 5, 10, 19	H-2α, 3
1β		1.57 m		H-2β, 19
2α	27.2 (t)	1.81 m	C-1, 3	H-1α, 3
2β		2.25 m		H-1β, 19
3	89.2 (d)	3.40 dd (11.5, 4.3)	C-4, 28, 29	H-1′, 2α, 28
4	40.1 (s)			
5	56.9 (d)	0.78 m	C-1, 4, 6, 7, 10, 28, 29	H-9, 28
6α	18.9 (t)	1.53 m	C-5, 7, 8, 10	H-5, 9, 28
6β		1.40 m		H-18, 19, 29
7α	35.8 (t)	1.53 m	C-5, 6, 8, 9	H-5, 9
7β		1.25 m		H-18, 19, 29
8	40.7 (s)			
9	51.3 (d)	1.46 m	C-1, 5, 7, 11, 12	H-5, 30
10	37.5 (s)			
11α	29.6 (t)	1.96 m	C-8, 9, 12, 13	H-9, 12
11β		1.56 m		H-18, 19
12	72.4 (d)	3.94 m	C-9, 11, 13, 14, 17	H-9. 17, 30
13	51.7 (d)	2.25 m	C-11, 12, 14, 16, 17	H-18, 21
14	51.5 (s)			
15α	28.6 (t)	1.11 m	C-13, 14, 16, 17, 30	H-16α,17, 30
15β		1.53 m		H-13, 16β
16α	32.9 (t)	1.54 m	C-13, 14, 16, 17, 20	H-15α, 17, 30
16β		1.96 m		H-13, 15β
17	50.7 (d)	2.86 m	C-12, 14, 20, 21	H-12, 16α, 30
18	16.3 (q)	1.01 s	C-7, 8, 9, 14	H-13, 19, 11β
19	17.2 (q)	1.01 s	C-1, 5, 9, 10	H-13, 18, 11β
20	142.2 (s)			
21	14.0 (q)	1.85 s	C-17, 20, 22	H-13, 23b
22	126.5 (d)	6.03, t (6.5)	C-17, 20, 21	H-21, 23b
23a	59.5 (t)	4.49 dd (12.5, 6.5)	C-20, 22	H-15α, 16α, 17
23b		4.54 dd (12.5, 6.5)		H-15β, 16β, 21
28	33.1 (q)	1.33 s	C-3, 4, 5, 29	H-3, 5, 6α
29	17.5 (q)	1.01 s	C-3, 4, 5, 28	H-2β, 18, 19
30	16.9 (q)	0.83 s	C-8, 13, 14, 15	H-5, 9, 15α
Glucosyl				
1′	107.4 (d)	4.98 d (7.5)	C-3	H-2α, 3, 28
2′	76.3 (d)	4.05 m		
3′	78.8 (d)	4.28 m		
4′	79.2 (d)	4.33 m		
5′	72.9 (d)	3.95 m		
6′a	62.6 (t)	4.63 dd (11.2, 2.4)		
6′b		4.98 d (7.5)		

corresponding to the loss of one xylose or arabinose. P35 possessed similar fragmentation mechanisms as ginsenoside Rc. It produced a predominant $[M-H]^-$ ions at m/z 945.5426 and other abundant characteristic fragment ions including m/z 783.4832, 621.4304, 459.3866, resulting from successive or simultaneous neutral losses of glucoses. P35 and P39 yielded identical $[M-H]^-$ ions, as well as the same fragment ions, indicating that they were another group of isomeric saponins. As shown in Table 3, P35 was unequivocally identified as ginsenoside Rd by comparison with an authentic standard. Compound K was considered to be the most appropriate candidate corresponding to P39 by comparison with literature information [12].

P37 and P38 were also a team of isomeric saponins. The group shared the same molecular ions and almost identical fragment ions. They formed the molecular ion at m/z 1031.5423 ($C_{51}H_{83}O_{21}$). Their fragment pathways were similar to those of ginsenoside Rd, while their molecular ions were 86 Da more than that of ginsenoside Rd. The addition of 86 Da suggested the presence of malonate saponin. P37 and P38 were thus assigned as malonyl-ginsenoside Rd and malonyl-compound K.

3.4.2. Oleanane group

As shown in Fig. 4, P48 produced a high-abundant molecular ion peak at m/z 865.4951 for $[M-H]^-$ in negative ion mode, which corresponded to the molecular formula of $C_{46}H_{73}O_{15}$ with error

of 0.46 ppm. Successive losses of arabinose, rhamnose and arabinose from the protonated ion at m/z 865.4951 lead to the product ions at m/z 733.4527 ($C_{41}H_{67}O_{11}$), 587.3848 ($C_{35}H_{55}O_7$), 455.3525 ($C_{30}H_{47}O_3$), indicating the presence of three sugar moieties. The sugar moiety fragment ion at m/z 145.0484 ($C_6H_9O_5$) was generated from $[Rha-H]^-$. By further comparison the t_R and MS data with those of reference compounds, P48 was unequivocally identified as Scoposide E [17], which was firstly found in *Panax* species to our best knowledge.

3.4.3. PPT group

P5 produced abundant $[M-H]^-$ peaks at m/z 945.5426 corresponding to the formula $C_{48}H_{81}O_{18}$ with 0.25 ppm. The product ions at m/z 783.4963 ($C_{42}H_{71}O_{13}$), 637.4352 ($C_{36}H_{61}O_9$) and 475.3770 ($C_{30}H_{51}O_4$), were proposed to be $[M-H-(Glc-H_2O)-CO_2]^-$, $[M-H-(Glc-H_2O)-(Rha-H_2O)-CO_2]^-$ and $[M-H-2(Glc-H_2O)-(Rha-H_2O)-CO_2]^-$. Based on those accurate elemental compositions, it was assigned as ginsenoside Re according to the literature [18]. Table 4 shows the accurate mass measurements of major fragment ions observed in spectra of the group compounds.

3.4.4. Other compounds

It was interesting that two major peaks: P1 and P2 gave abundant ions $[M-H]^-$ at m/z 625.1657 ($C_{42}H_{25}O_6$) and 609.1707

Table 2
LC–QTOF-MS accurate mass measurements for the major constituents in leaves of *Panax notoginseng*.

No.	t_R (min)	Compound	Formula [M−H]$^-$	Experimental m/z [M−H]$^-$	Theoretical m/z [M−H]$^-$	Error (ppm)	Reference
1	13.93	Unknown	$C_{42}H_{25}O_6$	625.1664	625.1651	−1.18	–
2	16.52	Unknown	$C_{42}H_{25}O_5$	609.1716	609.1707	−1.40	–
3	25.03	Notoginsenoside R$_1$[a]	$C_{47}H_{79}O_{18}$	931.5299	931.5272	0.63	[12]
4	26.94	Ginsenoside Rg$_1$[a]	$C_{42}H_{71}O_{14}$	799.4864	799.4849	−1.84	[12]
5	27.09	Ginsenoside Re	$C_{48}H_{81}O_{18}$	945.5428	945.5428	0.25	[25]
6	35.61	Yesanchinoside H	$C_{53}H_{89}O_{23}$	1093.5789	1093.5800	0.52	[20]
7	40.77	Floralginsenoside Tc/Td/isomer	$C_{53}H_{89}O_{24}$	1109.5755	1109.5744	−1.01	[20]
8	41.64	Floralginsenoside Tc/Td/isomer	$C_{53}H_{89}O_{24}$	1109.5748	1109.5744	−0.38	[20]
9	44.14	Floralginsenoside Tc/Td/isomer	$C_{53}H_{89}O_{24}$	1109.5752	1109.5744	−0.74	[20]
10	44.50	Yesanchinoside G	$C_{53}H_{87}O_{23}$	1091.5641	1091.5644	0.51	[20]
11	44.84	Notoginsenoside T/Notoginsenoside D	$C_{64}H_{107}O_{31}$	1371.6780	1371.6802	1.59	[23,24]
12	47.31	Ginsenoside RAo/Quinquenoside V	$C_{60}H_{101}O_{28}$	1269.6431	1269.6485	4.24	[20]
13	47.65	Quinquenoside L$_{17}$/Ginsenoside Re$_4$/isomer	$C_{47}H_{79}O_{18}$	931.5275	931.5272	−0.33	[19,21]
14	47.93	Notoginsenoside T/Notoginsenoside D	$C_{64}H_{107}O_{31}$	1371.6783	1371.6802	1.37	[23,24]
15	48.10	Notoginsenoside R$_4$/Fa	$C_{59}H_{99}O_{27}$	1239.6398	1239.6379	−1.51	[20]
16	48.17	Notoginsenoside Q	$C_{63}H_{105}O_{30}$	1341.6662	1341.6696	2.54	[25]
17	48.44	Quinquenoside L$_{17}$/Ginsenoside Re$_4$/isomer	$C_{47}H_{79}O_{18}$	931.5286	931.5272	−1.51	[19,21]
18	50.01	Notoginsenoside Fc/Ra$_1$/Ra$_2$	$C_{58}H_{97}O_{26}$	1209.6292	1209.6274	−1.52	[21,22]
19	50.38	Yesanchinoside E	$C_{54}H_{91}O_{23}$	1107.5963	1107.5957	−0.57	[21]
20	50.62	Ginsenoside Rb$_1$[a]	$C_{54}H_{91}O_{23}$	1107.5985	1107.5957	−2.56	[12]
21	50.80	Quinquenoside L$_{17}$/Ginsenoside Re$_4$/isomer	$C_{47}H_{79}O_{18}$	931.5287	931.5272	−1.62	[19,21]
22	51.17	Malonyl-notoginsenoside R$_4$/Fa	$C_{62}H_{101}O_{30}$	1325.6339	1325.6383	3.33	[21]
23	52.12	Notoginsenoside R$_4$/Fa	$C_{59}H_{99}O_{27}$	1239.6321	1239.6379	4.69	[20]
24	52.31	Ginsenoside Rc[a]	$C_{53}H_{89}O_{22}$	1077.5887	1077.5851	−3.34	[25]
25	52.33	Notoginsenoside Fc/Ra$_1$/Ra$_2$	$C_{58}H_{97}O_{26}$	1209.6298	1209.6274	−2.02	[21]
26	52.72	Malonyl-ginsenoside Rb$_1$	$C_{57}H_{93}O_{26}$	1193.5989	1193.5961	−2.38	[21,22]
27	53.61	Notoginsenoside Fc/Ra$_1$/Ra$_2$	$C_{58}H_{97}O_{26}$	1209.6283	1209.6274	−0.78	[21]
28	54.08	Malonyl-ginsenoside Rb$_1$/isomer	$C_{57}H_{93}O_{26}$	1193.5989	1193.5961	−2.38	[21,22]
29	54.60	Notoginsenoside S	$C_{63}H_{105}O_{30}$	1341.6640	1341.6696	4.18	[23]
30	56.03	Malonyl-ginsenoside Rb$_2$/Rb$_3$/Rc	$C_{56}H_{91}O_{25}$	1163.5890	1163.5855	−3.01	[21,22]
31	56.98	Ginsenoside Rb$_2$[a]	$C_{53}H_{89}O_{22}$	1077.5883	1077.5851	−2.97	[12]
32	58.75	Ginsenoside Rb$_3$[a]	$C_{53}H_{89}O_{22}$	1077.5888	1077.5851	−3.43	[12]
33	60.12	Notoginsenoside L/R$_7$	$C_{53}H_{89}O_{22}$	1077.5865	1077.5851	−1.30	[21]
34	62.43	Malonyl-ginsenoside Rb$_2$/Rb$_3$/Rc	$C_{56}H_{91}O_{25}$	1163.5888	1163.5855	−2.84	[21,22]
35	68.27	Ginsenoside Rd[a]	$C_{48}H_{81}O_{18}$	945.5426	945.5428	0.25	[12]
36	71.08	Malonyl-ginsenoside Rb$_2$/Rb$_3$/Rc	$C_{56}H_{91}O_{25}$	1163.5891	1163.5855	−3.10	[22]
37	71.40	Malonyl-ginsenoside Rd	$C_{51}H_{83}O_{21}$	1031.5423	1031.5432	0.90	[22]
38	72.91	Malonyl-compound K	$C_{51}H_{83}O_{21}$	1031.5423	1031.5432	0.90	[21]
39	73.25	Compound K	$C_{48}H_{81}O_{18}$	945.5467	945.5428	−4.08	[21]
40	74.50	Notoginsenoside P/O	$C_{52}H_{87}O_{21}$	1047.5754	1047.5745	−0.83	[23]
41	76.18	Notoginsenoside Fe/Notoginsenoside Fd/Vinaginsenoside R$_{18}$	$C_{47}H_{79}O_{17}$	915.5325	915.5323	−0.25	[20]
42	76.31	Ginsenoside F$_3$/Notoginsenoside R$_2$	$C_{41}H_{69}O_{13}$	769.4782	769.4744	−3.68	[21]
43	77.01	Notoginsenoside Fe/Notoginsenoside Fd/Vinaginsenoside R$_{18}$	$C_{47}H_{79}O_{17}$	915.5320	915.5323	0.30	[20]
44	78.29	Notoginsenoside Fe/Notoginsenoside Fd/Vinaginsenoside R$_{18}$	$C_{47}H_{79}O_{17}$	915.5330	915.5323	−0.29	[20]
45	82.10	Ginsenoside F$_2$[a]	$C_{42}H_{71}O_{13}$	783.4899	783.4895	0.15	[12]
46	87.06	20(R)-Ginsenoside Rg$_3$[a]	$C_{42}H_{71}O_{13}$	783.4876	783.4900	3.08	[12]
47	88.04	20(S)-Ginsenoside Rg$_3$	$C_{42}H_{71}O_{13}$	783.4865	783.4900	4.48	[12]
48	93.59	Scoposide E[a]	$C_{46}H_{73}O_{15}$	865.4951	865.4900	0.46	[17]
49	94.10	Pn-1	$C_{32}H_{53}O_8$	565.3749	565.3746	−0.54	[13]
50	94.54	Unknown	$C_{50}H_{63}O_6$	795.4642	795.4630	−1.56	–
51	101.61	Gynosaponin M	$C_{41}H_{69}O_{12}$	753.4768	753.4795	3.51	[21]

[a] Further confirmation in comparison with authentic standards.

Table 3
Retention times (t_R) and MS data for identification of PPD group saponins by LC–QTOF-MS.

No.	t_R (min)	[M−H]$^-$	Fragment ions (m/z)	Identification
6	35.61	1093.5789 ($C_{53}H_{89}O_{23}$)	781.5083/[M−H−(Xyl−H$_2$O)−(Glc−H$_2$O)−H$_2$O]$^-$ 619.3924/[M−H−(Xyl−H$_2$O)−2(Glc−H$_2$O)−H$_2$O]$^-$	Yesanchinoside H
7	40.77	1109.5755 ($C_{53}H_{89}O_{24}$)	797.4697/[M−H−(Ara−H$_2$O)−(Glc−H$_2$O)−H$_2$O]$^-$	Floralginsenoside Tc or
8	41.64			Floralginsenoside Td or
9	44.14			Isomer
10	44.50	1091.5641 ($C_{53}H_{87}O_{23}$)	473.3650/[M−H−(Xyl−H$_2$O)−3(Glc−H$_2$O)−H$_2$O]$^-$	Yesanchinoside G
11	44.84	1371.6780 ($C_{64}H_{107}O_{31}$)	1239.6341/[M−H−(Xyl−H$_2$O)]$^-$ 1107.5944/[M−H−2(Xyl−H$_2$O)]$^-$ 945.5431/[M−H−2(Xyl−H$_2$O)−(Glc−H$_2$O)]$^-$ 783.4881/[M−H−2(Xyl−H$_2$O)−2(Glc−H$_2$O)]$^-$	Notoginsenoside T
14	47.93		459.3883/[M−H−2(Xyl−H$_2$O)−4(Glc−H$_2$O)]$^-$	Notoginsenoside D
18	50.01	1209.6292 ($C_{54}H_{91}O_{23}$)	1077.5864/[M−H−(Xyl−H$_2$O)]$^-$ 945.5463/[M−H−(Xyl−H$_2$O)−(Ara−H$_2$O)]$^-$	Notoginsenoside Fc or
25	52.33		783.4897/[M−H−(Xyl−H$_2$O)−(Ara−H$_2$O)−(Glc−H$_2$O)]$^-$	Notoginsenoside Ra$_1$ or
27	53.61		621.4340/[M−H−(Xyl−H$_2$O)−(Ara−H$_2$O)−2(Glc−H$_2$O)]$^-$ 459.3874/[M−H−(Xyl−H$_2$O)−(Ara−H$_2$O)−3(Glc−H$_2$O)]$^-$	Notoginsenoside Ra$_2$
19	50.38	1107.5963 ($C_{54}H_{91}O_{23}$)	945.5422/[M−H−(Glc−H$_2$O)]$^-$ 783.4850/[M−H−2(Glc−H$_2$O)]$^-$	Yesanchinoside E
20	50.62		621.4344/[M−H−3(Glc−H$_2$O)]$^-$ 459.3869/[M−H−4(Glc−H$_2$O)]$^-$	Ginsenoside Rb$_1$
31	56.98	1077.5883 ($C_{53}H_{89}O_{22}$)	945.5438/[M−H−(Xyl−H$_2$O)]$^-$ 783.4807/[M−H−(Xyl−H$_2$O)−(Glc−H$_2$O)]$^-$	Ginsenoside Rb$_2$
32	58.75		621.4354/[M−H−(Xyl−H$_2$O)−2(Glc−H$_2$O)]$^-$ 459.3814/[M−H−(Xyl−H$_2$O)−3(Glc−H$_2$O)]$^-$	Ginsenoside Rb$_3$
24	52.31		945.5438/[M−H−(Ara−H$_2$O)]$^-$ 783.4847/[M−H−(Ara−H$_2$O)−(Glc−H$_2$O)]$^-$	Ginsenoside Rc
33	60.12		621.4364/[M−H−(Ara−H$_2$O)−2(Glc−H$_2$O)]$^-$ 459.3804/[M−H−(Ara−H$_2$O)−3(Glc−H$_2$O)]$^-$	Notoginsenoside L
30	56.03	1163.5880 ($C_{56}H_{91}O_{25}$)	1077.5886 [M−H−Ma]$^-$ 945.5438/[M−H−(Ara−H$_2$O)]$^-$	Malonyl-ginsenoside Rc
34	62.43		783.4807/[M−H−(Ara−H$_2$O)−(Glc−H$_2$O)]$^-$ 621.4364/[M−H−(Ara−H$_2$O)−2(Glc−H$_2$O)]$^-$ 459.3804/[M−H−(Ara−H$_2$O)−3(Glc−H$_2$O)]$^-$ 1077.5877/[M−H−Ma]$^-$ 945.5423/[M−H−(Xyl−H$_2$O)]$^-$	Malonyl-ginsenoside Rb$_2$ or
36	71.08		783.4817/[M−H−(Xyl−H$_2$O)−(Glc−H$_2$O)]$^-$ 621.4354/[M−H−(Xyl−H$_2$O)−2(Glc−H$_2$O)]$^-$ 459.3809/[M−H−(Xyl−H$_2$O)−3(Glc−H$_2$O)]$^-$	Malonyl-ginsenoside Rb$_3$
35	68.27	945.5426 ($C_{48}H_{81}O_{18}$)	783.4832/[M−H−(Glc−H$_2$O)]$^-$ 621.4304/[M−H−2(Glc−H$_2$O)]$^-$	Ginsenoside Rd
39	73.25		459.3866/[M−H−3(Glc−H$_2$O)]$^-$	Compound K
37	71.40	1031.5423 ($C_{51}H_{83}O_{21}$)	945.5496 [M−H−Ma]$^-$ 783.4891 [M−H−Ma−(Glc−H$_2$O)]$^-$	Malonyl-ginsenoside Rd
38	72.91		621.4304/[M−H−Ma−2(Glc−H$_2$O)]$^-$ 459.3896 [M−H−Ma−3(Glc−H$_2$O)]$^-$	Malonyl-compound K
12	47.31	1269.6431 ($C_{60}H_{101}O_{28}$)	1107.5946/[M−H−(Glc−H$_2$O)]$^-$ 945.5487/[M−H−2(Glc−H$_2$O)]$^-$ 783.4879[M−H−3(Glc−H$_2$O)]$^-$ 621.4336[M−H−4(Glc−H$_2$O)]$^-$	Ginsenoside Rao or Quinquenoside V
15	48.10	1239.6379 ($C_{59}H_{99}O_{27}$)	1107.5960/[M−H−(Xyl−H$_2$O)]$^-$ 945.5413/[M−H−(Xyl−H$_2$O)−(Glc−H$_2$O)]$^-$	Notoginsenoside R$_4$ or
23	52.12		783.4881/[M−H−(Xyl−H$_2$O)−2(Glc−H$_2$O)]$^-$ 621.4339/[M−H−(Xyl−H$_2$O)−3(Glc−H$_2$O)]$^-$	Notoginsenoside Fa
16	48.17	1341.6696 ($C_{63}H_{105}O_{30}$)	1209.6267/[M−H−(Xyl−H$_2$O)]$^-$ 1077.6377/[M−H−2(Xyl−H$_2$O)]$^-$	Notoginsenoside Q
29	54.60		945.5454/[M−H−2(Xyl−H$_2$O)−(Glc−H$_2$O)]$^-$ 783.4874/[M−H−2(Xyl−H$_2$O)−2(Glc−H$_2$O)]$^-$ 621.4369/[M−H−2(Xyl−H$_2$O)−3(Glc−H$_2$O)]$^-$ 459.3898/[M−H−2(Xyl−H$_2$O)−4(Glc−H$_2$O)]$^-$	Notoginsenoside S

Table 3 (*Continued*)

No.	t_R (min)	$[M-H]^-$	Fragment ions (m/z)	Identification
26	52.72	1193.5989 ($C_{57}H_{93}O_{26}$)	1107.5951/$[M-H-Ma]^-$ 945.3812/$[M-H-Ma-(Glc-H_2O)]^-$	Malonyl-ginsenoside Rb$_1$ or
28	54.08		783.4850/$[M-H-Ma-2(Glc-H_2O)]^-$ 621.4344/$[M-H-Ma-3(Glc-H_2O)]^-$ 459.3869/$[M-H-Ma-4(Glc-H_2O)]^-$	Malonyl-ginsenoside Rb$_1$ isomer
40	74.50	1047.5754 ($C_{52}H_{87}O_{21}$)	621.4317/$[M-H-2(Glc-H_2O)]^-$ 459.3897/$[M-H-3(Glc-H_2O)]^-$	Notoginsenoside P or Notoginsenoside O
41	76.18	915.5325 ($C_{47}H_{79}O_{17}$)	783.4896/$[M-H-(Ara-H_2O)]^-$ 621.4348/$[M-H-(Ara-H_2O)-(Glc-H_2O)]^-$ 459.3860/$[M-H-(Ara-H_2O)-2(Glc-H_2O)]^-$	Notoginsenoside Fe or
43	77.01			Notoginsenoside Fd
44	78.29	915.5330 ($C_{47}H_{79}O_{17}$)	783.4890/$[M-H-(Xyl-H_2O)]^-$ 621.4348/$[M-H-(Xyl-H_2O)-(Glc-H_2O)]^-$ 459.3860/$[M-H-(Xyl-H_2O)-2(Glc-H_2O)]^-$	Vinaginsenoside R18
45	82.10	783.4899 ($C_{42}H_{71}O_{13}$)	621.4398/$[M-H-(Glc-H_2O)]^-$ 459.3852/$[M-H-2(Glc-H_2O)]^-$	Ginsenoside F$_2$
46	87.06			20(R)-Ginsenoside Rg$_3$
47	88.04			20(S)-Ginsenoside Rg$_3$
22	51.17	1325.6378 ($C_{62}H_{101}O_{30}$)	1239.6365/$[M-H-Ma]^-$ 1107.5965/$[M-H-Ma-(Xyl-H_2O)]^-$ 945.3898/$[M-H-(Xyl-H_2O)-(Glc-H_2O)]^-$ 621.4313/$[M-H-(Xyl-H_2O)-3(Glc-H_2O)]^-$	Malonyl-notoginsenoside R$_4$ or Malonyl-notoginsenoside Fa
51	101.61	753.4785 ($C_{41}H_{69}O_{12}$)	459.3830/$[M-H-(Xyl-H_2O)-(Glc-H_2O)]^-$	Gynosaponin M

Table 4
Retention times (t_R) and MS data for identification of PPT group by LC–QTOF-MS.

No.	t_R (min)	$[M-H]^-$	Fragment ions (m/z)	Identification
3	25.03	931.5299 ($C_{47}H_{79}O_{18}$)	637.4347/$[M-H-(Glc-H_2O)-(Xyl-H_2O)-CO_2]^-$ 475.3795/$[M-H-2(Glc-H_2O)-(Xyl-H_2O)-CO_2]^-$	Notoginsenoside R$_1$
13	47.65			Quinquenoside L$_{17}$ or
17	48.44			Ginsenoside Re$_4$ or
21	50.08			Isomer
4	26.94	799.4864 ($C_{42}H_{71}O_{14}$)	637.4347/$[M-H-(Glc-H_2O)-CO_2]^-$, 475.3784/$[M-H-2(Glc-H_2O)-CO_2]^-$	Ginsenoside Rg$_1$
5	27.09	945.5426 ($C_{48}H_{81}O_{18}$)	783.4963 $[M-H-(Glc-H_2O)-CO_2]^-$ 637.4352/$[M-H-(Glc-H_2O)-(Rha-H_2O)-CO_2]^-$ 475.3770/$[M-H-2(Glc-H_2O)-(Rha-H_2O)-CO_2]^-$	Ginsenoside Re
42	76.31	769.4782 ($C_{41}H_{69}O_{13}$)	475.3796/$[M-H-(Xyl-H_2O)-(Glc-H_2O)]^-$	Ginsenoside F$_3$ or Notoginsenoside R$_2$

($C_{42}H_{25}O_5$), respectively. By comparing the fragment ions with references, both of them were not saponins. With the help of Scifinder Database, their formulas did not match any possible compounds, which were assumed to be flavone or other types according to their UV wavelength of maximum absorbance. The structural identities need further NMR methods to confirmation.

3.5. Anti-tumor effects of Pn-1

The cell survival percentages were calculated by dividing the mean OD of compound-containing wells by that of control wells. As seen in Table 5, after 72 h treatment, Pn-1 showed cytotoxic activity on NCI-H460, HepG2 and SGC-7901 with IC$_{50}$ value of 52.2 ± 4.2, 121.6 ± 2.2 and $79.7 \pm 5.0 \,\mu M$, respectively. Ginsenoside Rc and ginsenoside Rb$_2$ showed no cytotoxic activity up to $200.0 \,\mu M$. It was interesting that 20(R)-ginsenoside Rg$_3$, an approved clinical agent for cancer therapy, just showed weak cytotoxic activities ($200.0 \,\mu M$) on these three cell lines. Compared with 20(R)-ginsenoside Rg$_3$, the anti-tumor effects of Pn-1 on these cell lines was stronger than it. Ginsenoside Rh$_2$, used as the positive

Table 5
Cytotoxicity data for Pn-1 and other four compounds in selected human cancer cell lines.[a]

Compound	Cell line		
	NCI-H460	HepG2	SGC-7901
Pn-1	52.2 ± 4.2	121.6 ± 2.2	79.7 ± 5.0
Ginsenoside Rc	>200	>200	>200
Ginsenoside Rb$_2$	>200	>200	>200
20(R)-Ginsenoside Rg$_3$	$\geq$200	$\geq$200	$\geq$200
Ginsenoside Rh$_2$ [b]	35.8 ± 3.2	55.9 ± 3.5	32.9 ± 1.3

[a] All compounds are expressed as IC$_{50}$ values in μM, and results are the means $\pm$ SD of three independent experiment in triplicate,.
[b] Positive control.

control, had cytotoxic activities on NCI-H460, HepG2 and SGC-7901 cells with IC$_{50}$ value of 35.8 ± 3.2, 55.9 ± 3.5 and $32.9 \pm 1.3 \,\mu M$, respectively. These data suggested that the anti-tumor activity of Pn-1 on NCI-H460 cells was more similar to Rh$_2$ than other two cell lines. Further investigations are needed to increase insight into anti-tumor mechanisms of Pn-1. Whatever, the results
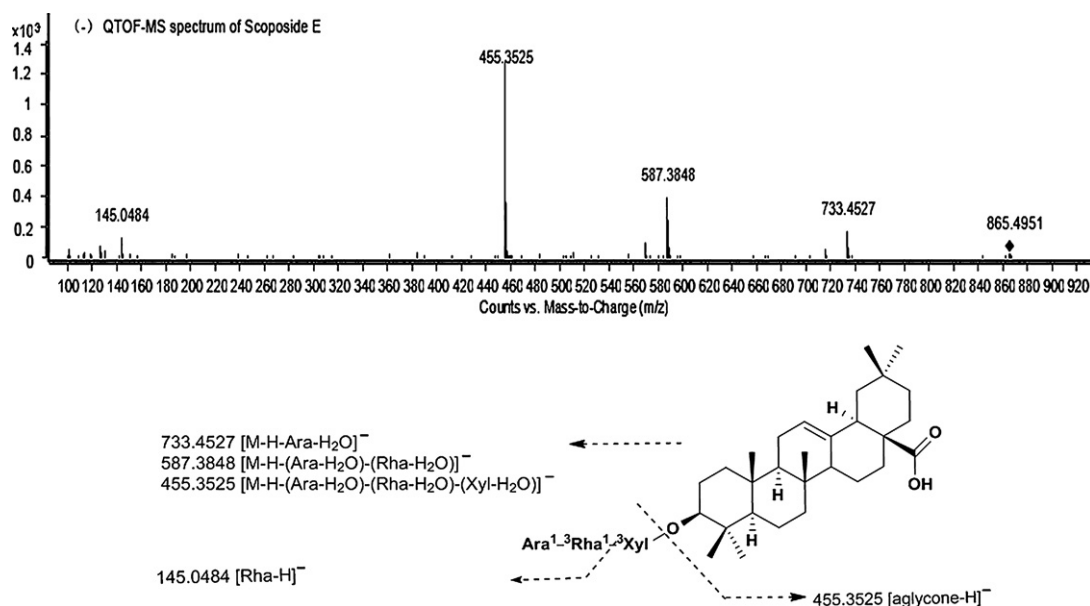
Fig. 4. The negative MS spectra and proposed fragmentation pathways of Scoposide E.

indicated Pn-1 might be a potential novel compound for use in medical oncology.

4. Conclusions

For the first time, in this study, LC–QTOF-MS was successfully applied in *Panax* species to probe novel compounds and to guide the isolation process. Under the guidance of structure–function relationship, PPD group saponins with low polarity in PNL were detected and characterized by LC–QTOF-MS. With the help of analytical guidance, Pn-1, a new saponin with one sugar molecular, was enriched and target isolated by different chromatographic methods. It was characterized as 3-O-β-D-glucopyranoside-3β,l2β,23β-triol-20-ene-dammar by 1D and 2D NMR technique, with a new skeleton never found before. The result of cytotoxic assay demonstrated that the anticancer effects of Pn-1 was more powerful than Rg_3, a clinical anti-tumor agent for cancer therapy, which implied that Pn-1 might be a promising candidate for further development as a novel anti-tumor agent. Moreover, the LC–QTOF-MS method provided valuable structural information about the glycosyl and aglycone moieties of the major constituents in PNL. A total of 48 major saponins, including 40 PPD saponins, 7 PPT saponins and 1 oleanane saponin, were screened out and identified in this complex extract without any further sample pre-treatment by the LC–QTOF-MS method. The results of this study clearly demonstrated the potential of LC–QTOF-MS for the rapid and sensitive detection and guiding of new bioactive compounds, and opened perspectives for similar studies on other medicinal herbs. It can be foreseen that the application of LC–QTOF-MS as an analytical guidance to probe new compounds will be a robust tool for characterization predicting and guiding target separating of bioactive novel components in complex natural extract, and thus accelerate the progress of drug discovery.

Acknowledgements

References

[1] W.G. Ma, M. Mizutani, K.E. Malterud, S.L. Lu, B. Ducrey, S. Tahara, Saponins from the roots of *Panax notoginseng*, Phytochemistry 52 (1999) 1133–1139.
[2] L.W. Qi, C.Z. Wang, C.S. Yuan, American ginseng: potential structure–function relationship in cancer chemoprevention, Biochem. Pharmacol. 80 (2010) 947–954.
[3] J.B. Wan, F.Q. Yang, S.P. Li, Y.T. Wang, X.M. Cui, Chemical characteristics for different parts of *Panax notoginseng* using pressurized liquid extraction and HPLC-ELSD, J. Pharm. Biomed. Anal. 41 (2006) 1596–1601.
[4] I.V. Chernushevich, A.V. Loboda, B.A. Thomson, An introduction to quadrupole-time-of-flight mass spectrometry, J. Mass Spectrom. 36 (2001) 849–865.
[5] J. Guan, C.M. Lai, S.P. Li, A rapid method for the simultaneous determination of 11 saponins in *Panax notoginseng* using ultra performance liquid chromatography, J. Pharm. Biomed. Anal. 44 (2007) 996–1000.
[6] S.F. Wang, S. Ye, Y.Y. Cheng, Separation and on-line concentration of saponins from *Panax notoginseng* by micellar electrokinetic chromatography, J. Chromatogr. A 1109 (2006) 279–284.
[7] Q.Z. Dua, G. Jerzc, R. Waibelb, P. Winterhalterc, Isolation of dammarane saponins from *Panax notoginseng* by high-speed counter-current chromatography, J. Chromatogr. A 1008 (2003) 173–180.
[8] Y.Y. Liu, J.B. Li, J.M. He, Z. Abliz, J. Qu, S.S. Yu, S.G. Ma, J. Liu, D. Du, Identification of new trace triterpenoid saponins from the roots of *Panax notoginseng* by high-performance liquid chromatography coupled with electrospray ionization tandem mass spectrometry, Rapid Commun. Mass Spectrom. 23 (2009) 667–679.
[9] M. Dan, M. Su, X.F. Gao, T. Zhao, A. Zhao, G.X. Xie, Y.P. Qiu, M.M. Zhou, Z. Liu, W. Jia, Metabolite profiling of *Panax notoginseng* using UPLC–ESI-MS, Phytochemistry 69 (2008) 2237–2244.
[10] G.X. Xie, R. Plumb, M.M. Su, Z.H. Xu, A. Zhao, M.F. Qiu, X.B. Long, Z. Liu, W. Jia, Ultra-performance LC–TOF-MS analysis of medicinal *Panax* herbs for metabolomicresearch, J. Sep. Sci. 31 (2008) 1015–1026.
[11] C.C. Cheng, S.M. Yang, C.Y. Huang, J.C. Chen, W.M. Chang, S.L. Hsu, Molecular mechanisms of ginsenoside Rh_2-mediated G_1 growth arrest and apoptosis in human lung adenocarcinoma A549 cells, Cancer Chemother. Pharmacol. 55 (2005) 531–540.
[12] S.L. Li, S.F. Lai, J.Z. Song, C.F. Qiao, X. Liu, Y. Zhou, H. Cai, B.C. Cai, H.X. Xu, Decocting-induced chemical transformations and global quality of Du-Shen-Tang, the decoction of ginseng evaluated by UPLC–QTOF-MS/MS based chemical profiling approach, J. Pharm. Biomed. Anal. 53 (2010) 946–957.
[13] W. Wang, Y.Q. Zhao, E.R. Rayburn, D.L. Hill, H. Wang, R.W. Zhang, In vitro anticancer activity and structure–activity relationships of natural products isolated from fruits of *Panax ginseng*, Cancer Chemother. Pharmacol. 59 (2007) 589–601.
[14] P. Zhao, Y.Q. Liu, C.R. Yang, Minor dammarane saponins from *Panax notoginseng*, Phytochemistry 41 (1996) 1419–1422.
[15] L.W. Qi, C.Y. Chen, P. Li, Structural characterization and identification of iridoid glycosides, saponins, phenolic acids and flavonoids in Flos Lonicerae Japonicae by a fast liquid chromatography method with diode-array detection and

time-of-flight mass spectrometry, Rapid Commun. Mass Spectrom. 23 (2009) 3227–3242.

[16] C.Y. Li, L.W. Qi, P. Li, X.D. Wen, Y.F. Zhu, E.H. Liu, Z. Gong, X.L. Yang, M.T. Ren, Y.J. Li, X.X. Ge, Identification of metabolites of Danggui Buxue Tang in rat urine by liquid chromatography coupled with electrospray ionization time-of-flight mass spectrometry, Rapid Commun. Mass Spectrom. 23 (2009) 1977–1988.

[17] N.B. Sarıkahya, S. Kırmızıgul, Antimicrobial triterpenoid glycosides from Cephalaria scoparia, J. Nat. Prod. 73 (2010) 825–830.

[18] G.Y. Zhu, Y.W. Li, D.K.P. Hau, Z.H. Jiang, Z.L. Yu, W.F. Fong, Protopanaxatriol-type ginsenosides from the root of Panax ginseng, J. Agric. Food Chem. 59 (2011) 200–205.

[19] G.Y. Li, Y.M. Zeng, H. Meng, X. Li, J.H. Wang, A new triterpenoid saponin from the leaves and stems of Panax quinquefolium L, Chin. Chem. Lett. 20 (2009) 1207–1210.

[20] L.P. Christensen, Ginsenosides chemistry, biosynthesis, analysis, and potential health effects, Adv. Food Nutr. Res. 55 (2009) 1–99.

[21] N. Fuzzati, B. Gabetta, K. Jayakar, R. Pace, F. Peterlongo, Liquid chromatography–electrospray mass spectrometric identification of ginsenosides in Panax ginseng roots, J. Chromatogr. A 854 (1999) 69–79.

[22] X.Q. Ma, X.M. Liang, Q. Xu, X.Z. Zhang, H.B. Xiao, Identification of ginsenosides in roots of Panax ginseng by HPLC–APCI/MS, Phytochem. Anal. 16 (2005) 181–187.

[23] M. Yoshikawa, T. Morikawa, Y. Kashima, K. Ninomiya, H. Matsuda, Structures of new dammarane-type triterpene saponins from the flower buds of Panax notoginseng and hepatoprotective effects of principal ginseng saponins, J. Nat. Prod. 66 (2003) 92–927.

[24] M. Yoshikawa, T. Murakami, T. Ueno, K. Yashiro, N. Hirokawa, N. Murakami, J. Yamahara, H. Matsuda, R. Saijoh, O. Tanaka, Bioactive saponins and glycosides. VIII. Notoginseng (1), new dammaranes-type triterpene oligoglycosides, notoginsenosides-A, -B, -C, and -D from the dried root of Panax notoginseng (Burk.) F.H. Chen, Chem. Pharm. Bull. 45 (1997) 1039–1045.

[25] B.S. Sun, L.J. Cu, Z.M. Fang, C.Y. Wang, Z. Wang, M.R. Lee, Z. Li, J.J. Li, C.K. Sung, Simultaneous quantification of 19 ginsenosides in black ginseng developed from Panax ginseng by HPLC-ELSD, J. Pharm. Biomed. Anal. 50 (2009) 15–22.

NMR analysis and site-specific protonation constants of streptomycin

Gábor Orgován, Béla Noszál *

Department of Pharmaceutical Chemistry, Semmelweis University, Research Group of Drugs of Abuse and Doping Agents, Hungarian Academy of Sciences, Budapest H-1092, Hőgyes Endre u. 9, Hungary

ARTICLE INFO

ABSTRACT

Streptomycin, the classical aminoglycoside antibiotic, generally considered the most basic drug compound was characterized in terms of protonation macro- and microconstants.

^{1}H NMR–pH and ^{1}H–^{13}C HSQC–pH titrations were carried out on streptomycin and streptidine, a symmetrical constituent compound of reduced complexity to monitor the proton-binding processes of the basic sites. Accurate, undistorted, electrodeless pH measurement was ensured by a new set of in tube indicators.

The microscopic protonation constants of the two guanidino groups of streptomycin were calculated by evaluating the various NMR–pH data and transferring the pair-interactivity parameter from streptidine to streptomycin. Inherent guanidino basicities fall in the range of 13.03–13.39 $\log k$ units, which drop to 12.48–12.85 upon protonation of the other site. pH-dependent distribution of the major microspecies and charge-related biological consequences are provided.

© 2011 Elsevier B.V. All rights reserved.

1. Introduction

Streptomycin is the most widely known member in the aminoglycoside antibiotic class of drugs, and also, the first effective remedy for tuberculosis [1]. Due to its ototoxicity, the therapeutic use of streptomycin has gradually been replaced by less toxic compounds, but it is still used as a second-line treatment of tuberculosis and nosocomial infections.

Streptomycin inhibits the protein synthesis of bacteria, by binding to the 30S subunit of the ribosomes [2,3], causing an error in translation [4].

A streptomycin review has recently been published as a book chapter [5].

Streptomycin, the tricyclic, tribasic molecule consists of an aminocyclitol base: streptidine (1,3-diguanido-2,4,5,6-tetrahydroxycyclohexane) and a nitrogen-containing carbohydrate: streptobiosamine, which consists of streptose (5-deoxy-3-C-formyl-L-lyxose) and N-methyl-2-deoxy-2-aminoglucose (Fig. 1).

Streptidine, the constituent compound is an important molecule in its own right, too. It can inhibit some of the aminoglycoside-modifying enzymes, mainly O-adenyl transferases, which are responsible for the bacterial resistance against aminoglycosides [6].

The two guanidino and the secondary amino sites make the molecule of streptomycin peculiar: it has long been known to be the most basic antibiotic drug. Its site-specific basicity, however,

has only been reported by Nys et al. [7]. The protonation microconstants of the two guanidino groups were considered identical and independent: $k^{G1} = k^{G3} = k_{G3}^{G1} = k_{G1}^{G3}$. This assumption is certainly false. The two basic sites have different chemical environments (G1 guanidino group is sterically less hindered, than G3 group), and are separated only by three carbons, thus the logarithm of the interactivity parameter must differ from 0.

Despite its pharmaceutical importance no data have been published on the protonation constants of streptidine.

As a triprotic molecule, the microspeciation scheme of streptomycin comprises 8 microspecies and 12 microconstants [8]. The guanidino and amino basicities differ by at least 3 orders of magnitude, therefore the first two protonation steps can be overwhelmingly assigned to the two guanidino groups, which simplifies the microspeciation scheme (Fig. 2).

Difficulties of the streptomycin microspeciation lie in the following facts:

- The first two protonation steps take place at high pH, where an undistorted pH cannot be measured by glass electrode.
- Because of the vicinity of the protonation sites, none of the spectroscopic signals is site-specific.
- Streptomycin rapidly decomposes in those basic solutions where its protonation processes actually take place. (The main product is maltol [9].)

In this work ^{1}H NMR–pH and ^{1}H–^{13}C HSQC–pH titrations were done to characterize the protonation equilibria. To improve the accuracy of pH measurement in highly basic solutions, a new

* Corresponding author. Tel.: +36 1 217 0891; fax: +36 1 217 0891.
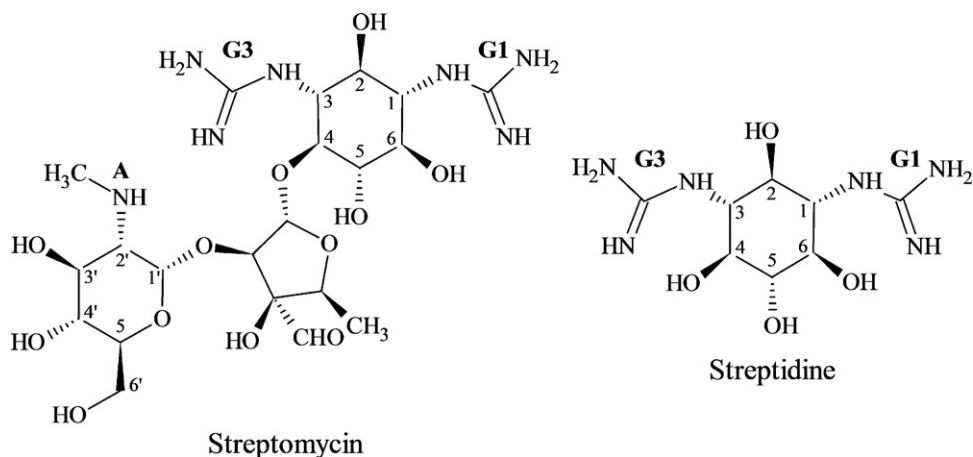E-mail address: nosbel@gytk.sote.hu (B. Noszál).

Fig. 1. Formulae and numbering of streptomycin and streptidine.

set of *in situ* NMR–pH indicator molecules were introduced and a least-distorted pH-determination method was elaborated [10]. Protonation macroconstants were determined from the various NMR–pH titrations. Due to the symmetry in streptidine, its site-specific basicities and the related interactivity parameter could be calculated. The macroconstants of streptomycin and the guanidino–guanidino interactivity parameter could be combined to calculate the streptomycin major protonation pathway microconstants.

2. Experimental

2.1. Chemicals

Streptomycin sulfate was purchased from Merck, the indicator molecules, sodium 3-(trimethylsilyl)-1-propanesulfonate (DSS), D_2O were purchased from Sigma–Aldrich. All chemicals were of analytical grade. The solutions were prepared with bidistilled water.

Streptidine sulfate was prepared by the method of Latorre *et al.* [6]: 5 g streptomycin sulfate was dissolved in 40 ml methanol containing 1.5 ml H_2SO_4. After 72 h streptidine sulfate was isolated as a white solid by filtration.

2.2. NMR titrations

All measurements were carried out on a Varian Inova spectrometer (600 MHz for ^1H). Spectra were recorded at 25 °C, and referenced to internal DSS (0.1 mM). The titrations were carried out in a medium of 95% (v/v) H_2O and 5% (v/v) D_2O. Such a small amount of D_2O shifts the pH scale only by 0.02 unit, according to the Gross–Butler–Purlee theory [11,12]. The ionic strength was 1 M. The water signal was suppressed by double pulse field gradient spin echo pulse sequence [13], while presaturation was applied during the HSQC and HMBC experiments. Spectra were processed with VNMRj 2.2C software.

"Electrodeless" titrations were carried out: basic and neutral stock solutions were prepared, each contained 7 different
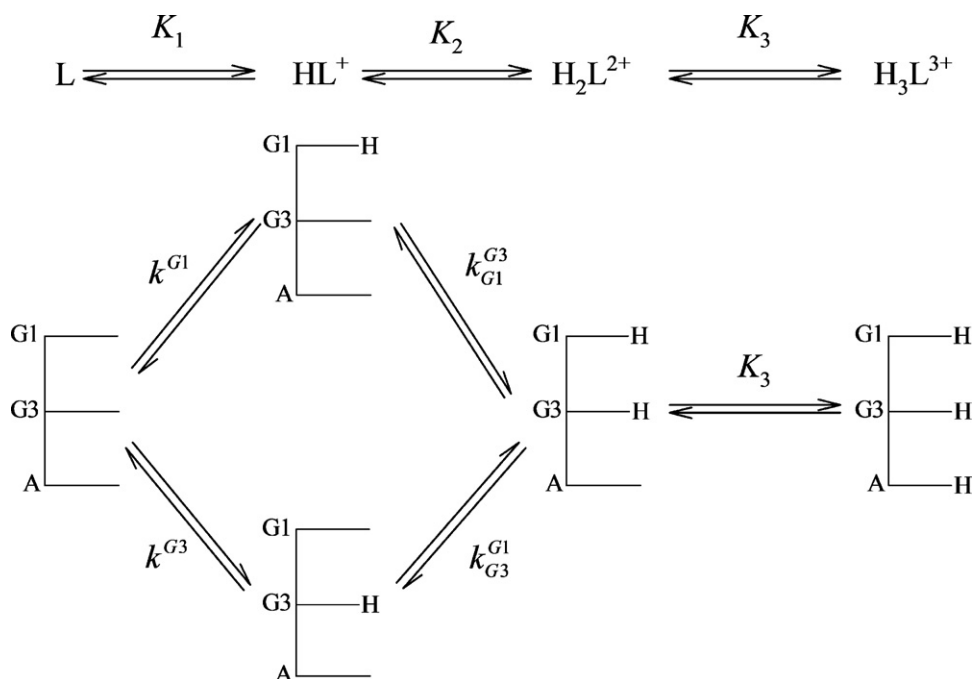
Fig. 2. Microspeciation scheme of streptomycin, in terms of K_1, K_2, K_3 stepwise macroconstants and $k^{G1}, \ldots, k^{G3}_{G1}$ microconstants. Superscripts of the microconstants indicate the site of protonation, whereas subscript (if any) show the site already protonated. G1, G3 and A stand for 1-guanidino, 3-guanidino and amino groups, respectively.
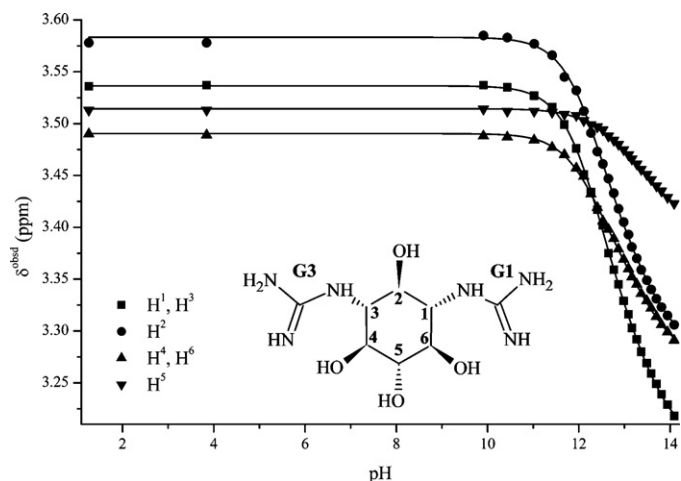
Fig. 3. ^{1}H NMR–pH titration curves of streptidine. The computer fits are the solid lines.

pH indicator molecules (methylguanidine, acetone oxime, *tert*-butylamine, sarcosine, TRIS, imidazole and acetic acid). Concentration of the indicator molecules were 0.5–2 mM. The samples were prepared by mixing the basic (1 M NaOH) and neutral (1 M KCl) stock solutions. In case of streptomycin titration streptomycin sulfate was dissolved in the solutions right before recording the NMR spectra. Since streptidine sulfate is stable in alkaline medium, it was dissolved in both stock solutions.

The pH of each solution was calculated from the chemical shifts of the indicators, using Eq. (1), where $\log K_{\text{Ind}}$ is the protonation constant, δ_{HInd} and δ_{Ind} are the limiting chemical shifts of the deprotonated and protonated forms, respectively, and $\delta_{\text{Ind}}^{\text{obsd}}$ is the observed chemical shift.

$$\text{pH} = \log\ K_{\text{ind}} + \log \frac{\delta_{\text{Ind}}^{\text{obsd}} - \delta_{\text{HInd}}}{\delta_{\text{Ind}} - \delta_{\text{Ind}}^{\text{obsd}}} \tag{1}$$

3. Results and discussion

The microspeciation of streptomycin was done as follows:

- NMR–pH titrations of streptomycin and streptidine.
- Determination of the macroconstants.
- Determination of the pair-interactivity parameter for the guanidino groups in streptidine.
- Calculation of the microconstants of streptomycin.

3.1. NMR analysis of streptidine and streptomycin

Assignments in the ^{1}H and HSQC spectra of streptidine and streptomycin were based on chemical shifts, multiplicity patterns and HMBC experiments. The proton signals are highly overlapping, therefore HSQC spectra were used to determine the chemical shifts of the protons.

During the course of NMR–pH titrations all the four carbon-bonded protons of streptidine were followed (Fig. 1), while 13 such protons were observed to follow streptomycin chemical shifts: the six protons on the streptidine ring and 7 protons on the N-methyl-glucosamine moiety (H^2, H^3, H^4, H^5, H^6 a and b, and the N-methyl signal) (Figs. 3 and 4).

3.2. Determination of the macroconstants

The macroconstants were determined by simultaneous nonlinear least-square parameter fitting, using OriginPro 8 software.

Table 1
Macroscopic protonation constants of streptidine and streptomycin.

	Streptidine	Streptomycin
$\log K_1$	13.53 ± 0.04	13.55 ± 0.06
$\log K_2$	12.39 ± 0.02	12.33 ± 0.02
$\log K_3$		8.29 ± 0.01

The macroconstants were calculated from chemical shift changes as a function of pH [14]:

$$\delta^{\text{obsd}} = \frac{\delta_{\text{L}} + \delta_{\text{HL}^+}K_1[\text{H}^+] + \delta_{\text{H}_2\text{L}^{2+}}K_1 K_2[\text{H}^+]^2 + \delta_{\text{H}_3\text{L}^{3+}}K_1 K_2 K_3[\text{H}^+]^3}{1 + K_1[\text{H}^+] + K_1 K_2[\text{H}^+]^2 + K_1 K_2 K_3[\text{H}^+]^3} \tag{2}$$

where δ^{obsd} is the observed chemical shift, δ_{L}, δ_{HL^+}, $\delta_{\text{H}_2\text{L}^{2+}}$ and $\delta_{\text{H}_3\text{L}^{3+}}$ are the chemical shifts of the non-protonated, mono-, di- and triprotonated species, respectively. In case of streptidine, which has only two basic sites $K_3 = 0$.

The stepwise protonation constants are listed in Table 1.

The second and third protonation steps take place in a highly separated manner, near pH 12.3 and 8.3, as the secondary amino group is far less basic than the guanidinos. Those microspecies in which the amino groups are protonated while the guanidino(s) are deprotonated are heavily inferior ones in concentration, and were therefore neglected.

3.3. Determination of the interactivity parameter between the two guanidino groups

Since the two guanidino groups of streptomycin are positioned in their close vicinity, none of the carbon-bound protons are selective for their protonation. Thus, in order to elucidate the microconstants, a deductive method had to be used, in which streptidine, a symmetrical constituent of streptomycin served as a model compound. Being symmetrical, not only the macro-, but also the microconstants and the interactivity parameter could be determined. Latter could be transferred into the microspeciation scheme of streptomycin, since the pair interactivity parameter has been shown to be the most invariant quantity. In fact, it is more invariant than the microconstant itself [15–17].

The pair interactivity parameter quantitates the basicity-reducing effect at site A upon protonation of site B and vice verse. This parameter is mainly influenced by the connecting bonds between the two sites, and it is least influenced by the solution circumstances, which makes this parameter best transferable between molecules of analogous moieties.

Due to its symmetry, the two basic sites in streptidine are equivalent, thus the microconstants can be determined from the macroconstants, as follows [8]:

$$K_1 = k^{\text{G1}} + k^{\text{G3}} = 2 \cdot k^{\text{G1}}, \qquad K_1 K_2 = k^{\text{G1}} k_{\text{G1}}^{\text{G3}} = k^{\text{G3}} k_{\text{G3}}^{\text{G1}} \tag{3}$$

The interactivity parameter is the basicity ratio of a site in two protonation states of the molecule:

$$E^{\text{G1G3}} = \frac{k_{\text{G3}}^{\text{G1}}}{k^{\text{G1}}}, \qquad pE^{\text{G1G3}} = \log k^{\text{G1}} - \log k_{\text{G3}}^{\text{G1}} \tag{4}$$

The values of the streptidine microconstants are:

$\log k^{\text{G1}} = \log k^{\text{G3}} = 13.23 \pm 0.04;$

$\log k_{\text{G3}}^{\text{G1}} = \log k_{\text{G3}}^{\text{G1}} = 12.69 \pm 0.02; \tag{5}$

The interactivity parameter for streptidine is: $pE^{\text{G1-G3}} = \log k^{\text{G1}} - \log k_{\text{G3}}^{\text{G1}} = 0.54 \pm 0.04$
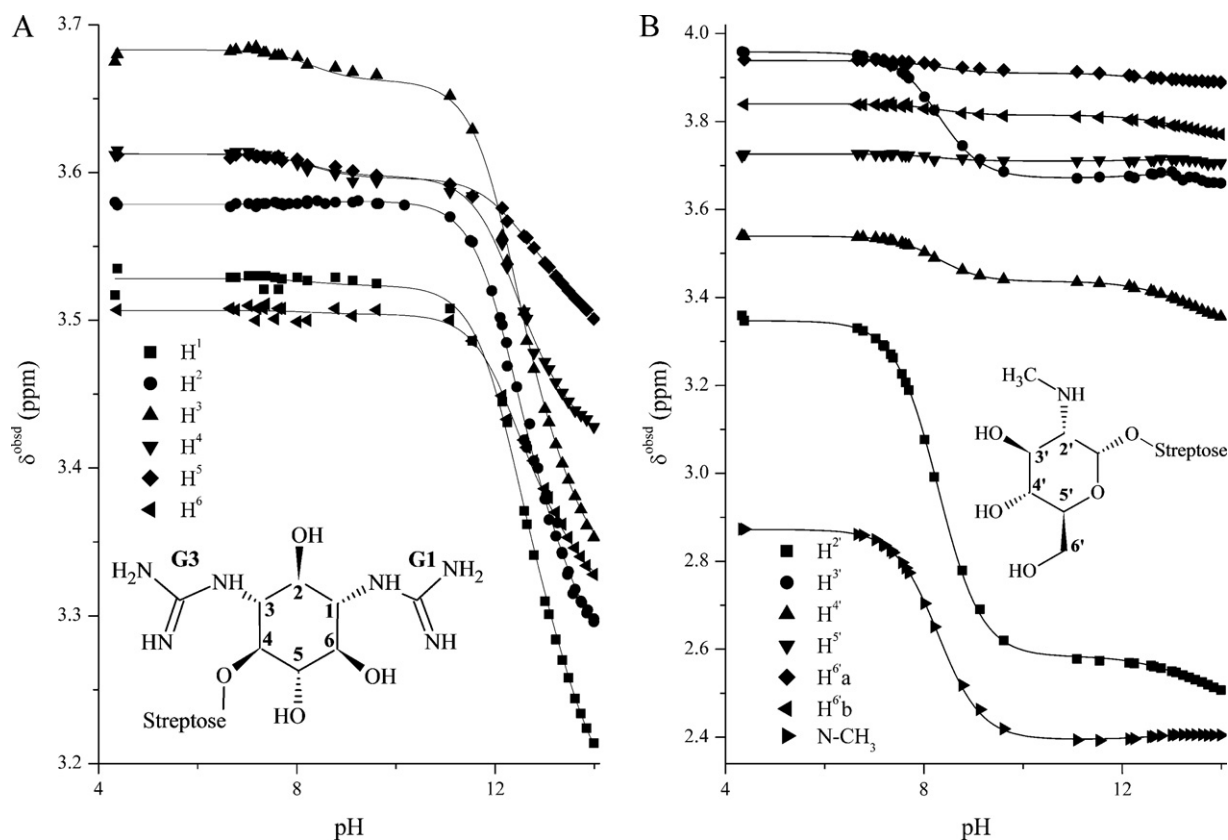
Fig. 4. ^{1}H NMR–pH titration curves of the protons on the streptidine (A) and glucosamine (B) rings of streptomycin. Computer fits are solid lines.

Table 2
Chemical shift differences ($\Delta\delta$, ppm) between the nonprotonated and monoprotonated forms of streptomycin.

	$\Delta\delta$ (ppm)
H[1]	0.137
H[2]	0.102
H[3]	0.098
H[4]	0.046
H[5]	0.054
H[6]	0.063

3.4. Calculation of streptomycin microconstants

A combination of the streptomycin macroconstants and the G1–G3 interactivity parameter provide an appropriate mathematical system to calculate the major microconstants. It is a further task, however, to select whether G1 or G3 is the more basic site.

In order to assign the higher basicity to G1 or G3, the chemical shift differences between the non-protonated and monoprotonated forms of the streptidine ring ($\Delta\delta = \delta_{HL^+} - \delta_L$) in streptomycin were ranked. The larger difference in the vicinity indicated the more basic site. The results are listed in Table 2.

It can be seen that the G1 guanidino group is more basic, which is in good agreement with the structure of the molecule, since it is sterically less hindered than the G3 guanidino group.

The microconstants can be calculated from the macroconstants and interactivity parameters, as follows:

$$K_1 = k^{G1} + k^{G3} \tag{6}$$

$$K_1 K_2 = k^{G1} k^{G3} E^{G1-G3} = k^{G1} k_{G1}^{G3} = k^{G3} k_{G3}^{G1} \tag{7}$$

The errors of the microconstants were calculated by the error propagation rule of Gauss [18]. The error of $\log k^{G1}$ is:

$$\sigma_{\log k^{G1}}^2 = \left(\frac{\partial \log k^{G1}}{\partial \log K_1} \right)^2 \sigma_{\log K_1}^2 + \left(\frac{\partial \log k^{G1}}{\partial \log K_2} \right)^2 \sigma_{\log K_2}^2$$
$$+ \left(\frac{\partial \log k^{G1}}{\partial p E^{G1G3}} \right)^2 \sigma_{p E^{G1-G3}}^2 \tag{8}$$

After algebraic transformations Eq. (8) can be rearranged to:

$$\sigma_{\log k^{G1}}^2 = \frac{\left(\sqrt{10^{2 \cdot \log K_1} - 4 \times 10^{\log K_1 + \log K_2 + p E^{G1-G3}}} - 2 \times 10^{\log K_2 + p E^{G1-G3}} + 10^{\log K_1} \right)^2 \sigma_{\log K_1}^2}{\sqrt{10^{2 \cdot \log K_1} - 41 \times 10^{\log K_1 + \log K_2 + p E^{G1-G3}}} - 4 \times 10^{\log K_2 + p E^{G1-G3}} + 10^{\log K_1}} + \cdots$$
$$+ \frac{\left(2 \times 10^{\log K_2 + p E^{G1-G3}} \right)^2 (\sigma_{\log K_2}^2 \sigma_{p E^{G1-G3}}^2)}{\sqrt{10^{2 \cdot \log K_1} - 4 \times 10^{\log K_1 + \log K_2 + p E^{G1-G3}}} - 2 \times 10^{\log K_2 + p E^{G1-G3}} + 10^{\log K_1}} \tag{9}$$

The microconstants are listed in Table 3.

Table 3
The microconstants of the streptomycin guanidino groups.

Microconstant	Value
$\log k^{G1}$	13.39 ± 0.11
$\log k^{G3}$	13.03 ± 0.10
$\log k_{G1}^{G3}$	12.48 ± 0.13
$\log k_{G3}^{G1}$	12.85 ± 0.11
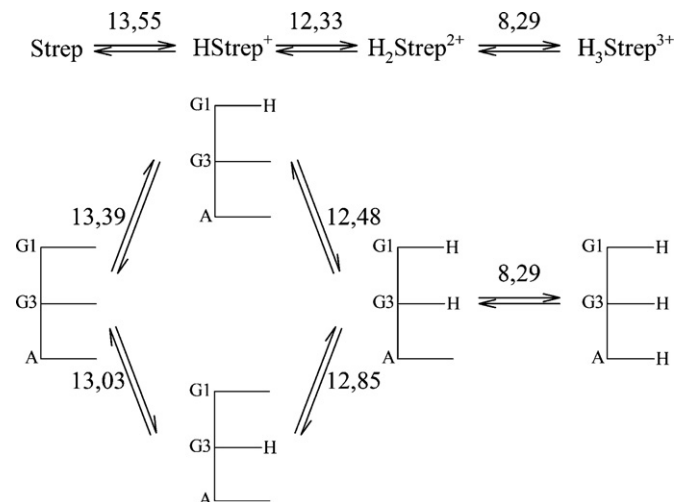
Fig. 5. The macro- and microspeciation scheme and the assigned protonation constants of streptomycin.
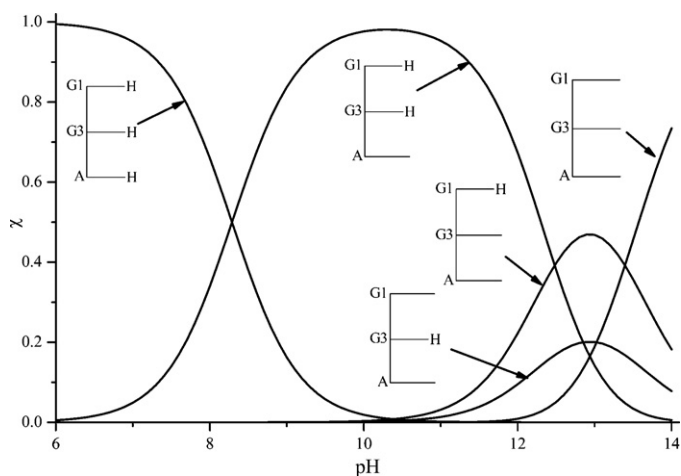
Fig. 6. The pH-dependent distribution of the major microspecies of streptomycin.

A summary diagram including all the assigned micro- and macroconstants is depicted in Fig. 5.

4. Conclusions

Protonation constants of streptomycin, the most basic antibiotic and streptidine, its aminocyclitol component were quantified by using unbiased, undistorted NMR–pH measurements and appropriate evaluation methods. Microspeciation of any compound containing two guanidino groups was also achieved for the first time.

Using the determined micro- and macroconstants, the pH-dependent distribution of the major microspecies could be calculated (Fig. 6).

Fig. 6 shows that even at 1 M NaOH solution 25% of the streptomycin molecules are still protonated. At physiological pH (pH 7.4) the vast majority of streptomycin is triprotonated.

The constants determined also indicate the hydrogen-bonding acceptor propensity of streptomycin at the site-specific level, an important property in the highly selective biochemical processes.

Concerning the well-known ototoxic side-effect and the concomitant presence of streptomycin in the central nervous system, allows another important conclusion on its biological behavior in light of its charge. The fact, that the molecule exists in every aqueous biological medium in a tricationic form, implies that it presumably enters the central nervous system by means of transporter protein system(s).

References

[1] A. Schatz, E. Bugie, S.A. Walkman, Streptomycin, a substance exhibiting antibiotic activity against Gram-positive and Gram-negative bacteria, Proc. Soc. Exp. Biol. Med. 55 (1944) 66–69.
[2] E.C. Cox, J.R. White, J.G. Flaks, Streptomycin action and the ribosome, Proc. Natl. Acad. Sci. 51 (1964) 703–709.
[3] J.E. Davies, Studies on the ribosomes of streptomycin sensitive and resistant streins of Escherichia coli, Proc. Natl. Acad. Sci. 51 (1964) 659–664.
[4] J. Davies, W. Gilbert, L. Gorini, Streptomycin, suppression, and the code, Proc. Natl. Acad. Sci. 51 (1964) 883–890.
[5] J. Davies, In the beginning there was streptomycin, in: D.P. Arya (Ed.), Aminoglycoside Antibiotics, John Wiley & Sons, Inc., Hoboken, NJ, USA, 2007, pp. 1–13.
[6] M. Latorre, P. Peñalver, J. Revuelta, J.L. Asensio, E. García-Junceda, A. Bastida, Rescue of the streptomycin antibiotic activity by using streptidine as a "decoy acceptor" for the aminoglycoside-inactivating enzyme adenyl transferase, Chem. Commun. (2007) 2829–2831.
[7] P.S. Nys, E.M. Savitskaya, T.S. Kolygina, Determination of ionization constants of streptomycin by the indicator method, Pharm. Chem. J. 5 (1971) 576–579.
[8] Z. Szakács, B. Noszál, Protonation microequilibrium treatment of polybasic compounds with any possible symmetry, J. Math. Chem. 26 (1999) 139–155.
[9] J.R. Schenck, M.A. Spielman, The formation of maltol by the degradation of streptomycin, J. Am. Chem. Soc. 67 (1945) 2276–2277.
[10] G. Orgován, B. Noszál, Electrodeless, accurate pH determination in highly basic media using a new set of ^{1}H NMR pH indicators, J. Pharm. Biomed. Anal. 54 (2011) 958–964.
[11] P.K. Glasoe, F.A. Long, Use of glass electrodes to measure acidities in deuterium oxide, J. Phys. Chem. 64 (1960) 188–190.
[12] E.L. Purlee, On the solvent isotope effect of deuterium in aqueous acid solutions, J. Am. Chem. Soc. 81 (1959) 263–272.
[13] T.L. Hwang, A.J. Shaka, Water suppression that works. Excitation sculpting using arbitrary wave-forms and pulsed-field gradients, J. Magn. Reson. A 112 (1995) 275–279.
[14] Z. Szakács, M. Kraszni, B. Noszál, Determination of microscopic acid–base parameters from NMR–pH titrations, Anal. Bioanal. Chem. 378 (2004) 1428–1448.
[15] D.L. Rabenstein, Nuclear magnetic resonance studies of the acid–base chemistry of amino acids and peptides. I. Microscopic ionization constants of glutathione and methylmercury-complexed glutathione, J. Am. Chem. Soc. 95 (1973) 2797–2803.
[16] K. Mernissi-Arifi, L. Schmitt, G. Schlewer, B. Spiess, Complete resolution of the microscopic protonation equilibria of D-myo-inositol 1,2,6-Tris (phosphate) and related compounds by ^{31}P NMR and potentiometry, Anal. Chem. 67 (1995) 2567–2574.
[17] A.M. Santos, A.M. Esteves, C.M. Vaz, J.J.R. Frausto da Silva, B. Noszal, E. Farkas, Microscopic acid–base equilibria of a synthetic hydroxamate siderophore analog, piperazine-1,4-bis(N-methylacetohydroxamic acid), J. Chem. Soc., Perkin Trans. 2 (1997) 1977–1983.
[18] M. Drosg, Basics on uncertainties, in: M. Drosg (Ed.), Dealing with Uncertainties, Springer Berlin, Heidelberg, 2009, pp. 17–48.

Antioxidant activity-guided phytochemical investigation of *Artemisia gmelinii* Webb. ex Stechm.: Isolation and spectroscopic challenges of 3,5-*O*-dicaffeoyl (epi?) quinic acid and its ethyl ester

Árpád Könczöl[a], Zoltán Béni[b], Márta Meszlényi Sipos[a], Attila Rill[a], Viktor Háda[b], Judit Hohmann[c], Imre Máthé[c], Csaba Szántay Jr.[b], György Miklós Keserű[a], György Tibor Balogh[a,*]

[a] *Compound Profiling Laboratory, Gedeon Richter Plc., Gyömrői u. 19-21., H-1475 Budapest, Hungary*
[b] *Spectroscopic Research, Gedeon Richter Plc., Gyömrői u. 19-21., H-1475 Budapest, Hungary*
[c] *Department of Pharmacognosy, University of Szeged, Eötvös u. 6., H-6720 Szeged, Hungary*

ARTICLE INFO

ABSTRACT

Although *Artemisia gmelinii* Webb. ex Stechm. has long been used in south and south-east Asia to treat many kinds of inflammatory diseases, up until now its bioactivity-coupled phytochemical characterization has not been reported. We identified one fraction of the methanolic extract of *A. gmelinii* as a hit in our antioxidant screening (DPPH) campaign. In order to identify the active radical scavenger components of the extract, a DPPH-HPLC spiking assay was carried out. Out of six detected known compounds caffeic acid (**1**) and scopoletin (**4**) had already been identified in the plant, but four of them, namely chlorogenic acid (**2**), 4-*O*-caffeoylquinic acid (**3**), luteolin-7-*O*-glucoside (**5**), and apigenin-7-*O*-glucoside (**6**) are first described here. Moreover, the two most active compounds of the mixture, 3,5-*O*-dicaffeoylquinic acid (**7**) and its ethyl ester derivative (**8**) were isolated with preparative HPLC. The spectroscopic identification of **7** and **8** presented a surprising challenge due to literature ambiguities. These questions are discussed in detail.

© 2011 Elsevier B.V. All rights reserved.

1. Introduction

Artemisia gmelinii Webb. ex Stechm. (Asteraceae), also known as Gmelin's wormwood, is a perennial herb widespread in south and south-east Asia with several ethnopharmacological applications, however its phytochemical composition is not well studied. The leaf and stem are used in Korea to treat inflammatory liver conditions [1]; "tablets" made from flowers are taken in India to overcome cold, cough and fever [2]; pastes made from the fresh plant are used externally to cure headache, boils and pimples in Nepal [3,4]. In contrast, the literature data regarding the chemical composition of *A. gmelinii* is limited only to three studies: caffeic acid, scopoletin, 4′,7-di-*O*-methylapigenin, 4′,5,7-trihydroxy-3′,6-dimethoxyflavone, acacetin and velutin as phenolic compounds were isolated from the ethanol extract [5], and some ubiquitous monoterpenes and sesquiterpenes (e.g. guaianolides) were identified in the petrol ether extract [6,7], but no data regarding the bioactivity of the plant extracts has been reported.

We found one fraction of the methanolic extract of *A. gmelinii* as a hit in our antioxidant screening campaign (1,1-diphenyl-2-picryl-hydrazyl (DPPH)). An LC–MS method was developed to separate and characterize the major constituents of the extract. Moreover, the LC method was coupled offline with the DPPH assay, based on the work of Tang et al. [8], to indicate the free radical scavenger molecules in the mixture. The two most active compounds were tentatively identified as dicaffeoylquinic acid (DCQA) derivatives and were isolated with preparative HPLC. During the detailed structure elucidation of the two species based on NMR and molecular modelling, we were faced however with difficulties regarding the unambiguous "resolvability" of these structures because of their inherent structural dynamics as well as due to ambiguities in the relevant literature data.

This article describes the activity-guided identification and isolation as well as the problems surrounding the structure elucidation of 3,5-DCQA and its ethyl ester, as the two most active antioxidative compounds in the methanolic extract of *A. gmelinii*.

2. Materials and methods

2.1. Plant material and chemicals

Aerial parts of *A. gmelinii* were collected before full blooming from the experimental field of the Institute of Ecology and Botany of the Hungarian Academy of Sciences, Vácrátót, Hungary. The plant

material was identified by Dr. Vilmos Miklósi. A voucher specimen (No. L8275) has been deposited in the Herbarium of the Institute.

All solvents were LC-grade, acetonitrile, ethanol, methanol, chloroform, trifluoroacetic acid, acetic acid were purchased from Merck (Darmstadt, Germany). Purified water (18 mΩ) was obtained from a Millipore (Bedford, MA, USA) Milli-Q water-purification system. Apigenin-7-O-glucoside, luteolin-7-O-glucoside and cynarin were purchased from PhytoLab (Vestenbergsgreuth, Germany). 4-O-Caffeoylquinic acid was purchased from Biopurify Phytochemicals Ltd. (Chengdu, Sichuan, China). All other standards and reagents were analytical grade and purchased from Sigma–Aldrich (St Louis, MO, USA). Fresh DPPH stock solution was prepared by dissolving DPPH in ethanol on each day of analysis and kept at 4 °C in a refrigerator.

2.2. Sample preparation and extraction

Dried and ground aerial parts of A. gmelinii (50 g) were first extracted with 1× 200 ml and 1× 100 ml of CHCl$_3$–MeOH, 9:1 (v/v) using an ultrasonic bath for 2× 15 min (this procedure yielded the CHCl$_3$ extract). After filtration the residual plant material was dried and extracted with 1× 200 ml and 1× 100 ml of 70% (v/v) aqueous MeOH at room temperature in an ultrasonic bath for 2× 15 min. The filtered and combined aqueous methanolic extracts were evaporated to dryness in vacuo to yield 3.7 g of brown oily material. This extract was fractionated by open column chromatography on silica gel (Kieselgel 60, 0.063–0.200 mm, 1.07734.100 Merck, Germany) (sorbent: 83 g, column size: 30 cm × 3 cm ⌀) using a gradient system of CHCl$_3$/MeOH/H$_2$O (90:10:1, 90:15:1.5, 90:25:2.5, 90:35:3.5, 90:45:4.5, and 90:60:6 (v/v), each 200 ml). The last fraction (VI) was obtained in a yield of 705 mg. 60 mg of the obtained sample was dissolved in dimethyl sulfoxide, filtered through a 0.45-μm Millipore (Billerica, MA, USA) filter and stored at −19 °C in a deep-well plate until required for screening experiments.

2.3. Isolation of compounds 7 and 8

The employed chromatographic system comprised of the following parts: a Gilson 305/306 (Middleton, WI, USA) pump, a Shimadzu SPD-10A (Columbia, MD, USA) UV–vis detector and a Büchi 684 (New Castle, DE, USA) fraction collector. Preparative separations were carried out on a Waters (Milford, MA, USA) X-Terra Prep RP18 (300 mm × 30 mm, 10 μm) column using water acidified with 0.1% (v/v) acetic acid as eluent A and acetonitrile acidified with 0.1% (v/v) acetic acid as eluent B in an optimized gradient program (5–50% B in 160 min) at a flow rate of 15 ml/min. The detection wavelengths were 220 nm and 320 nm.

The last fraction (VI) obtained from column chromatography (620 mg) was dissolved in the 1:1 (v/v) mixture of eluents A and B, and injected into HPLC. The effluent containing the solute corresponding to the observed peaks of 7 and 8 was collected in the fraction collector. The collected fractions were concentrated and dried under vacuum to yield purified 7 (78 mg, t_R = 102 min) and 8 (25 mg, t_R = 122 min).

2.3.1. Compound 7

(1s,3R,4s,5S)-1,3-Bis({[(2E)-3-(3,4-dihydroxyphenyl)prop-2-enoyl]oxy})-4,5-dihydroxycyclohexane-1-carboxylic acid. Pale yellow, waxy crystalline solid. UV–vis (CH$_3$CN) λ_{max}: 218, 240, 296sh, 325 nm; ^{1}H and ^{13}C NMR (Table 2, Table S1); [M+H]$^+$ (ESI): m/z 517.13457, calculated value for C$_{25}$H$_{25}$O$_{12}$: 517.13405 (delta: 1.0 ppm). Adduct ions of [M+Na]$^+$, [2M+H]$^+$ and [2M+Na]$^+$ can be detected at m/z 539.11654, 1033.26313 and 1055.24460, respectively. The mass accuracy was between 1.0 and 2.2 ppm for the adduct ions.

2.3.2. Compound 8

Ethyl(1s,3R,4s,5S)-1,3-bis({[(2E)-3-(3,4-dihydroxyphenyl)prop-2-enoyl]oxy})-4,5-dihydroxycyclohexane-1-carboxylate. Pale yellow, waxy crystalline solid. UV–vis (CH$_3$CN) λ_{max}: 218, 240, 300sh, 325 nm; ^{1}H and ^{13}C NMR (Table 2, Table S1); [M+H]$^+$ (ESI): m/z 545.16607, calculated value for C$_{27}$H$_{29}$O$_{12}$: 545.16535 (delta: 1.3 ppm). Adduct ions of [M+Na]$^+$, [2M+H]$^+$ and [2M+Na]$^+$ can be detected at m/z 567.14793, 1089.32514 and 1111.30706, respectively. The mass accuracy was between 1.1 and 1.6 ppm for the adduct ions.

2.4. DPPH-HPLC assay

2.4.1. HPLC-DAD-ESI-MS conditions

Experiments were performed on an Agilent 1200 liquid chromatography system equipped with a diode array detector and coupled with an Agilent 6120 MSD (Agilent Technologies, Palo Alto, CA, USA). Analyses were carried out at 40 °C on an Ascentis Express C$_{18}$ column (50 mm × 3.0 mm, 2.7 μm) with a mobile phase flow rate of 1.1 ml/min. The composition of eluent A was 0.1% (v/v) trifluoroacetic acid in water, eluent B was the mixture of acetonitrile and water in 95:5 (v/v) with 0.1% (v/v) trifluoroacetic acid. A linear gradient of 2–25% B was applied at a range of 0–8 min, then 25% B held for 1 min. This was followed by a 2 min equilibration period prior to the next injection. The UV–vis spectra were recorded between 200 and 400 nm and chromatographic profiles were registered at 320 nm. The injection volume was set to 10 μl. The MSD operating parameters were as follows: negative and positive ionization mode, scan spectra from m/z 100 to 800, drying gas temperature 350 °C, nitrogen flow rate 13 l/min, nebuliser pressure 50 psi, quadrupole temperature 100 °C, capillary voltage 3000 V, fragmentors were in the range 60–180 V.

2.4.2. DPPH spiking assay

The modified method of Tang et al. [8] was applied to characterize the active constituents in the methanolic extract of A. gmelinii. Briefly, 0.5 ml of A. gmelinii methanolic extract dissolved in DMSO, and 0.5 ml of 1.5 mM DPPH stock solution were mixed and allowed to react for 30 min. The reaction mixture was then filtered through a 0.45 μm filter and injected for HPLC analysis. Ethanol was added to the extract to provide the unreacted control sample.

2.5. DPPH radical scavenging capacity

The antioxidant activities of the chloroform extract, methanol extract, semi-purified fractions and the two, isolated compounds were tested according to the method described by Blois [9] and modified by Hu and Kitts [10] for microplate format. The purple-coloured DPPH is a stable free radical, which is reduced to the yellow 2,2-diphenyl-1-picrylhidrazine when allowed to react with an antioxidant. 250 μl of DMSO solution of samples in six concentrations, ranging from 0.5 to 300 μg/ml, and 50 μl of 0.3 mM DPPH ethanolic solution were mixed in a 96 well microtiter plate. Absorbance of each well was measured at 517 nm after 30 min incubation at room temperature by an UV–visible plate reader (Multiskan Spektrum, Thermo Labsystem). The degree of scavenging activity was determined by the following formula: Inhibition (%) = [(Abs$_{control}$ − Abs$_{sample}$)/Abs$_{control}$] × 100. IC$_{50}$ values, the concentrations of the samples required to scavenge 50% of DPPH radical, were calculated by Prism 4 for Windows (Graph Pad Software, San Diego, USA) after sigmoidal dose–response curve fitting and expressed as the mean of three determinations.

2.6. Spectroscopic methods

2.6.1. HRMS analysis

High-resolution MS measurements were carried out on a Thermo LTQ FT Ultra mass spectrometer (ESI, 4.0 kV spray voltage, 295 °C capillary temperature, solvent: MeOH:H_2O 1:1 + 1% (v/v) cc. acetic acid, direct infusion).

2.6.2. NMR analysis and spectral simulations

All NMR measurements were performed on a Varian 800 MHz spectrometer equipped with a $^1H\{^{13}C/^{15}N\}$ Triple Resonance ^{13}C Enhanced Salt Tolerant Cold Probe operating at 800 MHz for ^1H and 201 MHz for ^{13}C. Chemical shifts were referenced to TMS used as an internal standard. ^1H–^1H, direct ^1H–^{13}C, long-range ^1H–^{13}C spin–spin connectivities were established from ^1H, 2D-GHSQCAD, GCOSY and 2D-GHMBCAD experiments, respectively. All pulse sequences were used as available in the VNMRJ 3.1 pulse sequence library. All NMR measurements were performed in DMSO-d_6 as solvent.

Spectral simulations were performed using a gNMR 5.1 freeware package. (Peter H.M. Budzelaar, available at http://home.cc.umanitoba.ca/~budzelaa/gNMR/gNMR.html).

2.6.3. CD spectroscopy

CD spectrum of **7** was collected on a Chirascan CD spectrometer (Applied Photophysics Ltd., Leatherhead, UK).

2.7. Molecular modelling

Spartan 4′01 (Wavefunction Inc.) and Gaussian 03 [11] software packages were used for geometry optimizations and for coupling constant calculations, respectively. Geometry optimizations were performed at the DFT level using B3LYP functional and standard 6-31G basis sets. Optimized geometries together with the calculated coupling constants are presented in Supplementary material.

2.8. Statistical analysis

Statistical calculations were carried out with the Statistica 9.0 software (StatSoft). Results are expressed as the mean ± S.E.M. of 3 parallel experiments. Student's *t*-test was used for statistical analysis; *p* values > 0.05 were considered to be significant.

3. Results and discussion

3.1. Phytochemical and antioxidant characterization

Six compounds (**1**–**6**) were identified on the chromatogram of the extract (Fig. 1a) by comparing the retention time, the UV and MS spectra of the major peaks with those of authentic reference compounds. Caffeic acid (**1**) and scopoletin (**4**) as ubiquitous secondary plant metabolites were described earlier [5], but chlorogenic acid (**2**), 4-O-caffeoylquinic acid (cryptochlorogenic acid) (**3**), luteolin-7-O-glucoside (**5**) and apigenin-7-O-glucoside (**6**) are reported here for first time in *A. gmelinii*. After spiking (i.e. overdosing) the sample with the DPPH radical solution (Fig. 1b) the peak areas of compounds **7** and **8** exhibited the most pronounced decrease, therefore the preparative HPLC purification was targeted to isolate **7** and **8** (see Section 3.2. for the structure elucidation of **7** and **8**).

The decreasing trend of the IC$_{50}$ values in Table 1 shows clearly that the radical scavenger components of *A. gmelinii* were enriched in the methanolic extract, especially in the last (VI) eluting fraction obtained by column chromatography. The isolated DCQAs (**7**, **8**) possess great antioxidant capacities, which indirectly verified the efficiency of the DPPH-HPLC spiking assay. The IC$_{50}$ values of
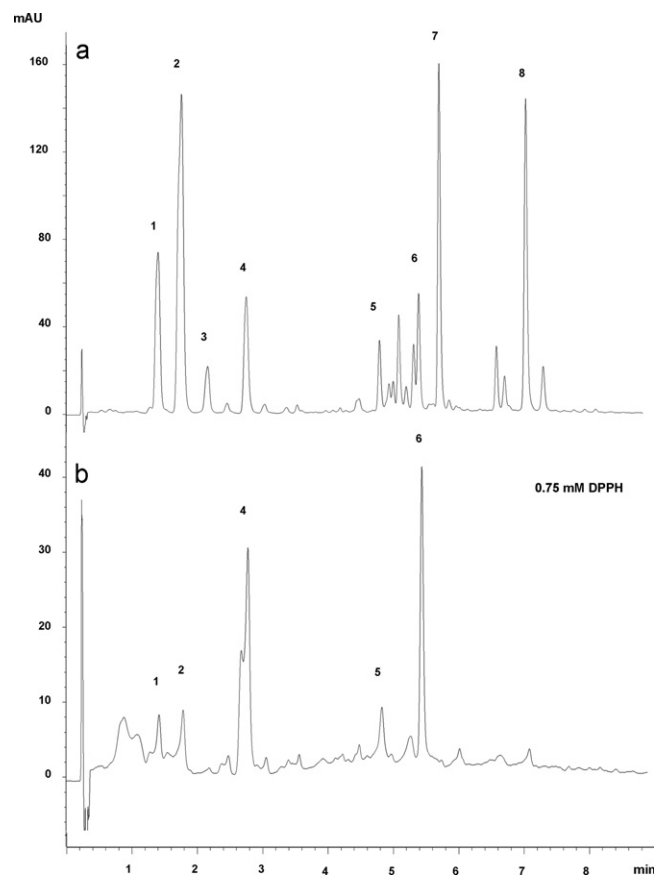

Fig. 1. (a) HPLC-DAD chromatogram, obtained at 320 nm, of fraction VI of the methanolic extract of *Artemisia gmelinii* before and (b) after allowing it to react with 0.75 mM DPPH radical. **1**, caffeic acid (1.43 min); **2**, chlorogenic acid (1.80 min); **3**, 4-O-caffeoylquinic acid (2.21 min); **4**, scopoletin (2.81 min); **5**, luteolin-7-O-glucoside (4.88 min); **6**, apigenin-7-O-glucoside (5.49 min); **7**, compound 7 (5.81 min); **8**, compound 8 (7.16 min).

compounds **7** and **8** were significantly lower than those of the positive control trolox, and were at a similar level as the outstanding activity of quercetin. The observed superior reactivity of the two DCQA derivatives towards the DPPH radical is in accordance with the findings of Saito et al. [12], describing the contribution of an intramolecular interaction of the two caffeoyl residues. Moreover, after comparing the IC$_{50}$ values of compounds **7** and **8** to the value of cynarin could be supposed that the radical scavenging potential of these species are not affected by the difference in the observed stereochemistry of the quinic acid core moiety.

Finally, the identified constituents of *A. gmelinii*, namely caffeic acid, chlorogenic acid, luteolin-7-O-glucoside (cynaroside),

Table 1
DPPH radical scavenging activities of *A. gmelinii* extracts and isolated compounds.

Sample	IC$_{50}$ (μg/ml)
CHCl$_3$ extract	>300
70% (v/v) aqueous MeOH extract	76.6 ± 4.9
Fraction I of 70% (v/v) aqueous methanol extract	>300
Fraction II of 70% (v/v) aqueous methanol extract	>300
Fraction III of 70% (v/v) aqueous methanol extract	109.9 ± 9.85
Fraction IV of 70% (v/v) aqueous methanol extract	53.71 ± 7.41
Fraction V of 70% (v/v) aqueous methanol extract	49.9 ± 4.07
Fraction VI of 70% (v/v) aqueous methanol extract	38.12 ± 4.19
Compound **7**	8.74 ± 0.86
Compound **8**	10.63 ± 1.14
Cynarin	10.14 ± 1.05
Trolox	17.92 ± 1.13
Quercetin	9.40 ± 0.62

and caffeoyl derivatives were described previously as the major hepatoprotective compounds of artichoke (*Cynara scolymus* L.) [13]. This similitude suggests that the identified phenylpropanoids and flavonoids may contribute *via* their free radical scavenging potential to the pharmacological effect of *A. gmelinii*, especially in inflammatory liver conditions.

3.2. Structure elucidation

The structural identification of a natural product, be it a known or an unknown substance, is typically practiced according to the following protocol. After chromatographic separation and/or isolation (HPLC)-(HR)–MS and ^{1}H NMR spectra are recorded, serving as the basis for the rapid identification of known compounds by comparison with the literature data. Should a given compound turn out to be a suspect of being a new natural product, further one- (1D) and two dimensional (2D) (HPLC)-NMR data are collected so as to undertake a full *ab initio* structure elucidation, possibly by comparing the structural features deduced from the NMR data for the unknown to those already reported or observed for related known compounds. This approach is commonly believed to yield precise structures in a relatively straightforward manner, especially when using today's ultra-effective NMR and MS capabilities. However, in practice the structure elucidation process may be burdened with ambiguities, as already pointed out by Pauli et al. [14] in connection with the structure determination of various caffeoylquinic acid derivatives.

Problems in that regard include, firstly, the phenomenon that for a given configuration the observed chemical shifts and the *J* coupling pattern of the quinic acid ring protons sometimes exhibit a significant sensitivity to solvent, temperature and concentration, resulting in a subtle variability in the data so that they may not necessarily be diagnostic of the configuration at hand. Loosely speaking, we may say that there is an element of "indeterminism" in the measured couplings in these molecular systems. The reason for this seems to stem from the fact that the H–H vicinal coupling values are well known to depend sensitively on the dihedral bond angle. The six-membered ring of the quinic acid moiety is expected to show fast conformational mobility on the ^{1}H NMR chemical shift timescale at room temperature, with each conformational species being associated with its unique set of dihedral angles. Therefore the *J* coupling measured between any given two vicinal protons will be the weighted average of all dihedral angles sampled on the conformational potential energy surface by that proton pair during acquisition of the NMR spectrum. Clearly, the most important conformers that are expected to have the highest influence on the measured coupling constant will be the two chair, or nearly chair-shaped geometries. Overall, we have a complex system where any medium-induced change in the conformational dynamics or in the geometry of the low-energy conformers (i.e., in the shape of the conformational potential energy surface) can potentially influence the measured coupling pattern of a given quinic acid derivative. Although there are discussions in the literature aimed at rationalizing the measured quinic acid ring proton coupling constants as well as their empirical solvent dependence for various quinic acid caffeoyl derivatives, these focus mostly on a static twisted-chair or twisted-boat model [14,15] with only scarce mentioning of the possibility of a dynamic effect [14]. However, one should conceptually view the "*J*-indeterminism" problem in terms of the variability of conformational energy surface as a whole, i.e., as potentially resulting from a combination of static geometrical effects (small changes in the geometry of the predominant or dominant species) and dynamic conformational effects (the averaging of couplings due to equilibrating conformers). Clearly, differently substituted quinic acid derivatives are expected to show different degrees of "*J*-indeterminism". For example, as can be expected
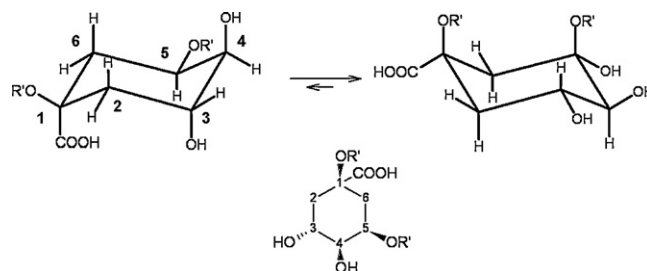

Fig. 2. Conformational preference of cynarin in DMSO (R′: caffeoyl).

from an intuitive consideration of the bulkiness of the various substituents, 3 (or 5) monocaffeoyl, or 4,3- (or 4,5-), or 1,3- (or 1,5-) dicaffeoyl quinic acids (cynarin – see Fig. 2) tend to exist predominantly in one chair-like conformation [15,16], and are therefore expected to exhibit relatively little *J*-variability. However, for 3,5-Odicaffeoylquinic acids one would expect that the minor chair conformation should have a non-negligible population. Indeed, Flores-Parra et al. showed that in quinic acid itself, which is a structurally relevant analogy for the 3,5-dicaffeoyl quinic acid derivative, the two chair conformers are present in a 73:27 ratio at room temperature in DMSO [17].

Additionally to the above difficulties, in practice the structural identification of natural quinic acid derivatives is also complicated by the fact that there are inconsistencies in the NMR data reported in the literature, as was also pointed out by Pauli et al. [16], making it difficult to use some of that data as a solid reference.

For the above reasons the structure elucidation of compounds **7** and **8** turned out to present a particular challenge. Although **7** and the C(4) epimer of **8** were already reported in the literature (see discussion of the available literature data below), and in that sense our finding of these structures in *A. gmelinii* may not be regarded as surprising, we wish to point out below that, under the realistic conditions in which one typically has to infer their structure (limited amounts of not entirely pure sample, gradual degradation in time, etc.. . .), there remains a certain degree of structural ambiguity which cannot be resolved in practice, and this aspect of the problem has received little attention in the literature.

After isolating **7** and **8**, HR-MS and standard 1D and 2D NMR data were collected for both compounds in DMSO-d_6 as solvent. Based on the HR-MS data and the ^{1}H and ^{13}C NMR assignments listed in Table 2 (complete assignments are presented in the Supplementary material, together with those observed for cynarin) the constitution of **7** and **8** could be readily identified as shown in Fig. 3.

In order to determine the relative stereochemistry of these compounds a coupling constant analysis of the quinic acid ring protons
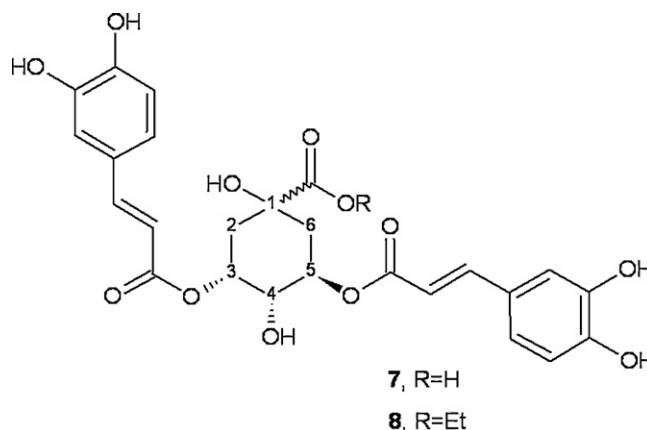

7, R=H

8, R=Et

Fig. 3. Proposed structures and numbering of compounds **7** and **8**.

Table 2
^{1}H and ^{13}C chemical shifts for the quinic acid like core in **7**, **8**, and cynarin in DMSO-d_6.

Position	7		8		Cynarin	
	^{1}H (ppm)	^{13}C (ppm)	^{1}H (ppm)	^{13}C (ppm)	^{1}H (ppm)	^{13}C (ppm)
1	–	72.4	–	72.4		79.3
2	1.97 m	34.6	2.00 m	34.4	2.27 m	31.7
2	2.15 m		2.20 m		2.50 m	
3	5.12 m	70.9	5.08 m	70.9	5.29 ddd	71
4	3.84 ddd	67.4	3.84 dd	66.5	3.49 ddd	72.8
5	5.20 ddd	70.5	5.18 ddd	69.9	4.00 ddd	65.8
6	1.98 m	34.6	2.00 m	34.4	1.71 m	
6	2.15 m		2.20 m		2.29 m	39.4
7	–	175.2	–	173.2		172.4

was then performed. J coupling values were determined by simulation of the ^{1}H NMR spectrum of **7** and **8** together with that observed for the commercially available quinic acid dicaffeinate isomer, cynarin, as a model system (Table 2 and Figs. S1–S3 in Supplementary material). We compared the obtained NMR data of **7** and **8** with those published in the literature. In 1992 Wang et al. reported the isolation of 3,5-DCQA and its ethyl ester derivative from the MeOH extract of *Psiadia trinervia* [18], referring to 3,5-DCQA as an already known compound from a prior synthetic work [19] and characterizing the ethyl ester derivative of 3,5-DCQA as an artificial product. Their structural conclusion regarding these components was based on ^{1}H and ^{13}C NMR data obtained in DMSO-d_6 and on CD spectroscopic data. Comparing our own data obtained in the same media for compound **7**, neither the chemical shifts nor the coupling constants were identical with those given for 3,5-DCQA, thus at this point **7** could be plausibly identifed as 3,5-epi-DCQA (Table 3).

Searching for the NMR properties of 3,5-epi-DCQA we found that in 2005 Kim and Lee reported [20] an isolate from *Chrysanthemum morfolium* to be the "new" dicaffeoylquinic acid derivative, 3,5-epi-DCQA. Their structural conclusion was based on ^{1}H and ^{13}C NMR chemical shift and coupling constant data obtained in MeOD as solvent, as compared to those published by Pauli et al. [16]) for 3,5-DCQA. Furthermore, the spectral data obtained in DMSO-d_6 (presented in their paper as a figure but not reported numerically) for both 3,5-epi-DCQA and for 3,5-DCQA (isolated from the same species as well) were compared. The absolute configuration given for 3,5-epi-DCQA was based on CD data. A comparison of our NMR data for **7** to those reported for 3,5-epi-DCQA by Kim et al. indicated that, in contrast to our earlier conclusion, **7** cannot be 3,5-epi-DCQA. However, this comparison also revealed that practically identical NMR data and analogous CD curves were reported for the substance in question, but while Wang et al. identified it as 3,5-DCQA, Kim and Lee concluded that it is 3,5-epi-DCQA. This contradiction shows that one of the conclusions must be erroneous, and also introduces an element of uncertainty regarding the structure of the C(4) epimer of **8** reported by Wang et al. [18], since that structure was inferred on the premise that it must originate from an unintended esterification during the isolation procedure of the component believed to be 3,5-epi-DCQA.

At this point further analysis of the reference data given by Pauli et al. [16] and Tolonen et al. [15] was undertaken. Both studies reported in detail the NMR spectral properties of the compound postulated to be 3,5-DCQA in different media. Pauli et al. used MeOD, while Tolonen et al. used D_2O as solvent for the NMR measurements. A comparison of the reported NMR data (together with those presented by Kim and Lee [20] in a figure) to those observed for **7** indicated that **7** is not identical to the compound described as 3,5-DCQA in those papers, again suggesting that it is in fact 3,5-epi-DCQA. We must note however that neither of these publications gave any direct indication or evidence on the relative configuration of C(1) and C(4), i.e. on the problem of whether the substance has been proven to be 3,5-DCQA or 3,5-epi-DCQA.

Furthermore, our analysis of the coupling constants available in three different media clearly showed that in MeOD or in DMSO both chair invertomers have a non-negligible contribution to the ring conformational equilibrium, while in D_2O this equilibrium is shifted towards the conformer having both H4 and H5 in axial positions, explaining the "J-indeterminisim" of the system as discussed earlier.

Although both Wang et al. and Kim et al. have deduced the absolute configuration of 3,5-(epi-)DCQA from CD spectroscopy, in fact the CD spectra can only distinguish between (−) and (+) quinic acid cores. However, it cannot distinguish decisively between 3,5-DCQA and 3,5-epi-DCQA (for an exhaustive discussion of the relevant stereochemistries see Ref. [21]). The CD spectrum of **7** is identical to that reported by Wang, showing that both compounds have negative exciton chirality (with negative first and positive second Cotton effects) which is in accordance with a (3R,5R) configuration in both cases.

In conclusion, in the absence of an X-ray structure, on the basis of the above data the two possible epimeric structures (3,5-*O*-dicaffeoylquinic acid and 3,5-*O*-dicaffeoylepiquinic acid in the case of **7** and ethyl-3,5-*O*-dicaffeoylquinate and ethyl-3,5-*O*-dicaffeoylepiquinate in the case of **8**) cannot be distinguished with absolute exactness, and the structural conclusions appearing in the literature regarding these compounds should be handled with care. (In principle a methodical comparison of the pertinent stereoisomers, if they were available in pure form and in adequate quantities for detailed NMR studies, would probably resolve these issues.) At present, a tentative structural conclusion can be given on the basis of the aforementioned conformational preference of **7** in different media together with a molecular modelling of the possible conformers at the DFT level (optimized geometries, calculated energies and coupling constants are presented in Supplementary material). As has been mentioned, the coupling constants given by Tolonen et al. for 3,5-DCQA [15] indicate that the conformational equilibrium is shifted in D_2O towards the conformer having both H4 and H5 in axial positions. Geometry optimization at the DFT level of model systems (phenolic hydroxyls were not included so as to

Table 3
Simulated spin–spin coupling constants of cynarin, **7** and **8**.

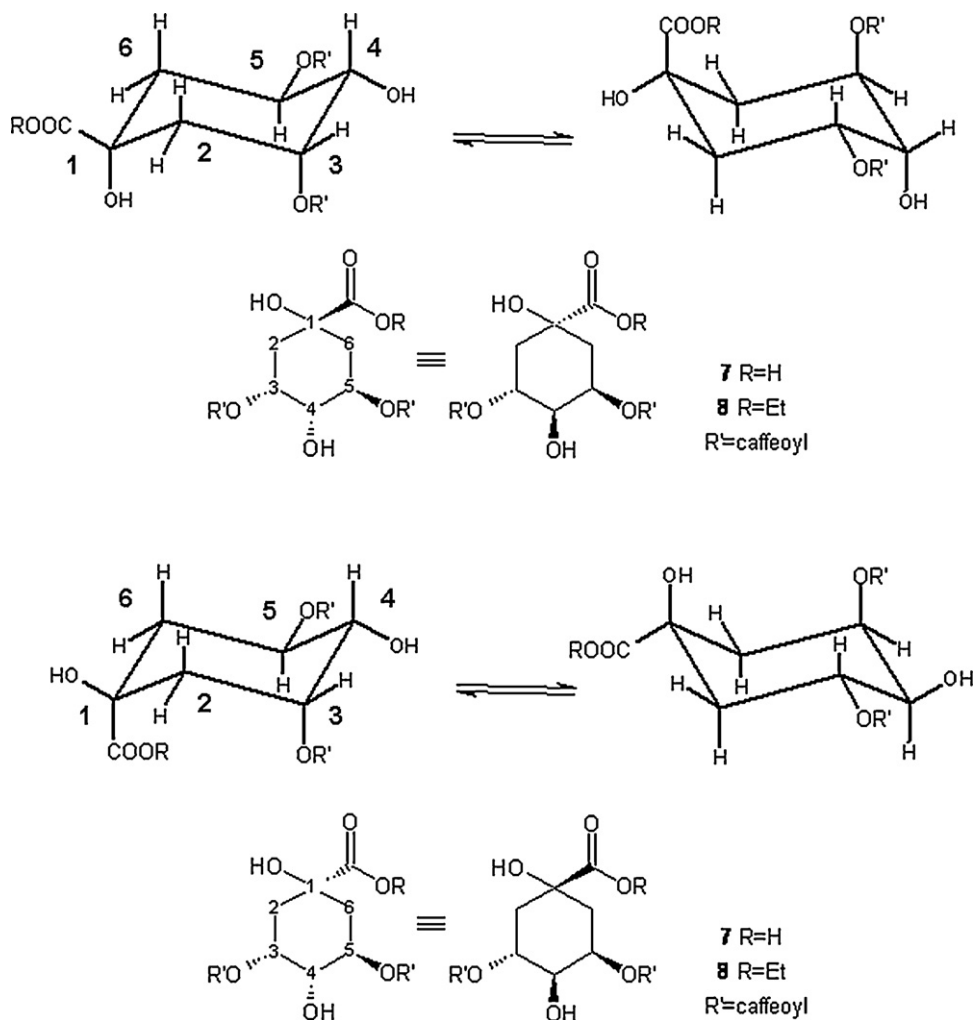|	Cynarin	7	8
$^2J_{6e-6a}$	−13.43	−14.09	−13.8
$^2J_{2e-2a}$	−14.96	−12.72	−12.8
$^3J_{4OH-4}$	4.91	4.97	–
$^3J_{3-2}$	10.55	8.58	9.75
$^3J_{3-2}$	4.60	2.26	4.25
$^3J_{3-4}$	8.80	3.16	3.00
$^3J_{4-5}$	3.05	6.45	5.88
$^3J_{5-6}$	4.28	7.56	3.9
$^3J_{5-6}$	3.58	3.93	3.00

Fig. 4. Conformational preference of 3,5-O-dicaffeoylquinic acid (top) and 3,5-O-dicaffeoyl-epi-quinic acid (bottom).

reduce the computational cost) show that the conformer having the desired arrangement is energetically (ca. 10.6 kJ/mol) more favored in the case of 3,5-DCQA while ca. 7.0 kJ/mol less favored in the case of its epi analogue (see Supplementary material). Based on these considerations, and taking into account the close similarities of the chemical shift values observed for **7** and **8**, we conclude that **8** is the ethyl ester derivative of **7**, where the latter is tentatively identified as 3,5-O-dicaffeoylquinic acid (Fig. 4).

4. Conclusions

We have firstly identified chlorogenic acid (**2**), 4-O-caffeoylquinic acid (**3**), luteolin-7-O-glucoside (**5**), apigenin-7-O-glucoside (**6**), 3,5-O-dicaffeoylquinic acid (**7**) and its ethyl ester derivative (**8**) in the extracts of *A. gmelinii*. The structural identification of **2–6** was straightforward on the basis of their chromatographic retention times and UV and MS spectra. However, compounds **7** and **8** had to be isolated and subjected to detailed NMR studies and molecular modelling for identification. This turned out to be an unexpectedly difficult task due to the inherent structural dynamics of these molecules as well as ambiguities in the relevant literature data. The identified phenylpropanoids and flavonoids may contribute *via* their free radical scavenging potential to the beneficial pharmacological effects of *A. gmelinii*, especially in inflammatory liver conditions.

Appendix A. Supplementary data

Supplementary data associated with this article can be found, in the online version, at doi:10.1016/j.jpba.2011.10.012.

References

[1] Medicinal Plants in the Republic of Korea Complied by Natural Products Research Institute Seoul National University, World Health Organization, Regional Office for the Western Pacific, Manila, 1998, p. 37.
[2] B. Ballabh, O.P. Chaurasia, Traditional medicinal plants of cold desert Ladakh-used in treatment of cold, cough and fever, J. Ethnopharmacol. 112 (2007) 341–349.
[3] S.K. Ghimire, Y.C. Lama, G.R. Tripathi, S. Schmitt, Y. Aumeeruddy-Thomas, Conservation of Plant Resources, Community Development and Training in Applied Ethnobotany at Shey-Phoksundo National Park and its Buffer Zone. Dolpa. Report Series No. 41, WWF Nepal Program, Kathmandu, Nepal, 2001.
[4] N.P. Manandhar, Plants and People of Nepal, Timber Press Inc., Portland, Oregon, 2002.
[5] I.I. Chemesova, L.M. Belenovskaya, L.P. Markova, Phenolic compounds of *Artemisia gmelinii*, Chem. Nat. Compd. 19 (1987) 364–365.

[6] H. Greger, C. Zdero, F. Bohlmann, Eudesman-12,8-β-olides and other terpenes from *Artemisia* species, Phytochemistry 25 (1986) 891–897.

[7] M.A. Khanina, E.A. Serykh, L.M. Pokrovsky, A.V. Tkachev, Results of chemical study of *Artemisia gmelinii* Web. et Stechm. from Siberia, Chem. Plant Raw Mater. 3 (2000) 77–84.

[8] D. Tang, H.J. Li, J. Chen, C.W. Guo, P. Li, Rapid and simple method for screening of natural antioxidants from Chinese herb *Flos Lonicerae Japoicae* by DPPH-HPLC-DAD-TOF/MS, J. Sep. Sci. 31 (2008) 3519–3526.

[9] M.S. Blois, Antioxidant determination by the use of a stable free radical, Nature 181 (1958) 1199–1200.

[10] C. Hu, D.D. Kitts, Dandelion (*Taraxacum officinale*) flower extract suppresses both reactive oxygen species and nitric oxide and prevents lipid oxidation *in vitro*, Phytomedicine 12 (2005) 588–597.

[11] M.J. Frisch, G.W. Trucks, H.B. Schlegel, G.E. Scuseria, M.A. Robb, J.R. Cheeseman, J.A. Montgomery Jr., T. Vreven, K.N. Kudin, J.C. Burant, J.M. Millam, S.S. Iyengar, J. Tomasi, V. Barone, B. Mennucci, M. Cossi, G. Scalmani, N. Rega, G.A. Petersson, H. Nakatsuji, M. Hada, M. Ehara, K. Toyota, R. Fukuda, J. Hasegawa, M. Ishida, T. Nakajima, Y. Honda, O. Kitao, H. Nakai, M. Klene, X. Li, J.E. Knox, H.P. Hratchian, J.B. Cross, C. Adamo, J. Jaramillo, R. Gomperts, R.E. Stratmann, O. Yazyev, A.J. Austin, R. Cammi, C. Pomelli, J.W. Ochterski, P.Y. Ayala, K. Morokuma, G.A. Voth, P. Salvador, J.J. Dannenberg, V.G. Zakrzewski, S. Dapprich, A.D. Daniels, M.C. Strain, O. Farkas, D.K. Malick, A.D. Rabuck, K. Raghavachari, J.B. Foresman, J.V. Ortiz, Q. Cui, A.G. Baboul, S. Clifford, J. Cioslowski, B.B. Stefanov, G. Liu, A. Liashenko, P. Piskorz, I. Komaromi, R.L. Martin, D.J. Fox, T. Keith, M.A. Al-Laham, C.Y. Peng, A. Nanayakkara, M. Challacombe, P.M.W. Gill, B. Johnson, W. Chen, M.W. Wong, C. Gonzalez, J.A. Pople, Gaussian 03, Revision B. 05, Gaussian, Inc., Pittsburgh, PA, 2003.

[12] S. Saito, S. Kurakane, M. Seki, E. Takai, T. Kasai, J. Kawabata, Radical scavenging activity of dicaffeoylcyclohexanes: Contribution of an intramolecular interaction of two caffeoyl residues, Bioorg. Med. Chem. 13 (2005) 4191–4199.

[13] R. Gebhardt, M. Fausel, Antioxidant and hepatoprotective effects of artichoke extracts and constituents in cultured rat hepatocytes, Toxicol. In Vitro 11 (1997) 669–672.

[14] G.F. Pauli, U. Kuczkowiak, A. Nahrstedt, Solvent effects in the structure dereplication of caffeoyl quinic acids, Magn. Reson. Chem. 37 (1999) 827–836.

[15] A. Tolonen, T. Joutsamo, S. Mattlla, T. Kämäräine, J. Jalonen, Identification of isomeric dicaffeoylquinic acids from *Eleutherococcus senticosus* using HPLC-ESI/TOF/MS and ^{1}H-NMR methods, Phytochem. Anal. 13 (2002) 316–328.

[16] G.F. Pauli, F. Poetsch, A. Nahrstedt, Structure assignment of natural quinic acid derivatives using proton nuclear magnetic resonance techniques, Phytochem. Anal. 9 (1998) 177–185.

[17] A. Flores-Parra, D.M. Gutiérrez-Avella, R. Contreras, F. Khuong-Huu, ^{13}C and ^{1}H NMR investigation of quinic acid derivatives: complete spectral assignment and elucidation of preferred conformations, Magn. Reson. Chem. 27 (1989) 544–555.

[18] Y. Wang, M. Hamburger, J. Guebo, K. Hostettmann, Cylohexaecarboxylic-acid derivatives from *Psiadia trinervia*, Helv. Chim. Acta 75 (1992) 269–275.

[19] M.L. Scarpati, M. Guiso, Structure of the three dicaffeoyl-quinic acids of coffees (isochlorogenic acid), Tetrahedron Lett. 39 (1964) 2851–2853.

[20] H.J. Kim, Y.S. Lee, Identification of new dicaffeoylquinic acids from *Chrysanthemum morifolium* and their antioxidant activities, Planta Med. 71 (2005) 871–876.

[21] E.L. Eliel, M.B. Ramirez, (−)-Quinic acid: configurational (sterochemical) descriptors, Tetrahedron-Asymmetr. 8 (1997) 3551–3554.

Simultaneous quantification of polymethoxylated flavones and coumarins in *Fructus aurantii* and *Fructus aurantii immaturus* using HPLC–ESI-MS/MS

Hai-Fang Chen [a], Wu-Gang Zhang [b], Jin-Bin Yuan [a], Yan-Gang Li [a], Shi-Lin Yang [b], Wu-Liang Yang [a],*

[a] *The Key Laboratory of Modern Preparation of TCM of Ministry of Education, Jiangxi University of Traditional Chinese Medicine, Nanchang, Jiangxi Province 330004, China*
[b] *National Pharmaceutical Engineering Center for Solid Preparation in Chinese Herbal Medicine, Jiangxi University of Traditional Chinese Medicine, Nanchang, Jiangxi Province 330004, China*

ABSTRACT

The major lipid-soluble constituents in *Fructus aurantii* (*zhiqiao*) and *Fructus aurantii immaturus* (*zhishi*) are polymethoxylated flavones (PMFs) and coumarins. In the present study, a high-performance liquid chromatography with electrospray ionization tandem mass spectrometry method was developed to quantify PMFs (nobiletin, tangeretin, 5-hydroxy-6,7,8,4′-tetramethoxyflavone, and natsudaidai) and coumarins (marmin, meranzin hydrate, and auraptene) simultaneously. PMFs and coumarins were detected by electrospray ionization tandem mass spectrometry in positive ion mode and quantified with multiple reaction monitor. Samples were separated on a Diamonsil C_{18} (150 mm × 4.6 mm, 5 μm) column using acetonitrile and formic acid–water solution as a mobile phase in gradient mode with a flow rate at 0.5 mL/min. All calibration curves showed good linearity ($r^2 > 0.9977$) within the test ranges. Variations of the intraday and interday precisions were less than 4.07%. The recoveries of the components were within the range of 95.79%–105.04% and the relative standard deviations were less than 3.82%. The method developed was validated with acceptable accuracy, precision, and extraction recoveries and can be applied for the identification and quantification of four PMFs and three coumarins in citrus herbs.

© 2011 Elsevier B.V. All rights reserved.

1. Introduction

Fructus aurantii (*zhiqiao*) and *Fructus aurantii immaturus* (*zhishi*) are the dried unripe fruit and young fruit of *Citrus aurantium* L. or its cultivated variety, respectively. *Zhiqiao* and *zhizhi* are used as drugs for regulating Qi flow in Chinese clinical applications and for strengthening the spleen and stomach; they have been used in Traditional Chinese Medicine since ancient times [1].

Numerous bioactive compounds, particularly characteristic lipid-soluble constituents, such as polymethoxylated flavones (PMFs) and coumarins, have been isolated and identified from *zhiqiao* and *zhishi*, as well as flavonoid glycosides and alkaloids in the hydrophilic fractions. Nobiletin and tangeretin are the representative constituents of PMFs [2]. Coumarins, such as meranzin hydrate, marmin, auraptene, are present in the citrus herbs [3–5]. According to several studies reported in the literature, these components show exceptional pharmacologic activity, including anticarcinogenic [2,6,7], antioxidant and antimicrobial [8], and gastric mucosal protective properties [9], as well as a neuroprotective effect [10–12]. These have recently attracted the

attention of many scholars, and the study of *zhiqiao* and *zhishi* has gradually become a popular topic domestically and overseas.

Numerous studies in the literature have mainly focused on the quantification of PMFs and flavonoid glycosides or the qualitative analysis of coumarins alone using various methods. Four flavonoid glycosides, with naringenin, hesperitin, and two PMFs (tangeretin, nobiletin) of sour orange, were simultaneously determined through high-performance liquid chromatography with electrospray ionization tandem mass spectrometry (HPLC–ESI-MS) [13]. Some oxygen heterocyclic compounds (PMFs and coumarins) of citrus essential oils in different citrus cultivars were qualitatively analyzed through HPLC with diode array detectors (HPLC–DAD) and HPLC with atmospheric pressure chemical ionization tandem mass spectrometry (HPLC–APCI-MS) [14,3]. The PMFs in *Fructus aurantii* were identified through APCI-MS and ultra-performance liquid chromatography with electrospray ionization quadrupole time-of-flight tandem mass spectrometry (UPLC/Q-TOF MS/MS) [15,16]. Hydroxylated PMFs had been quantified with HPLC with ultraviolet detection and HPLC with electrochemical detection [17,18].

Based on the aforementioned studies, few reports have focused on the simultaneous quantification on PMFs and coumarins in *zhiqiao* and *zhishi*. The synergistic action of multiple components and multiple target sites is characteristic of Traditional Chinese

---

* Corresponding author. Tel.: +86 791 7118659; fax: +86 791 7118658.
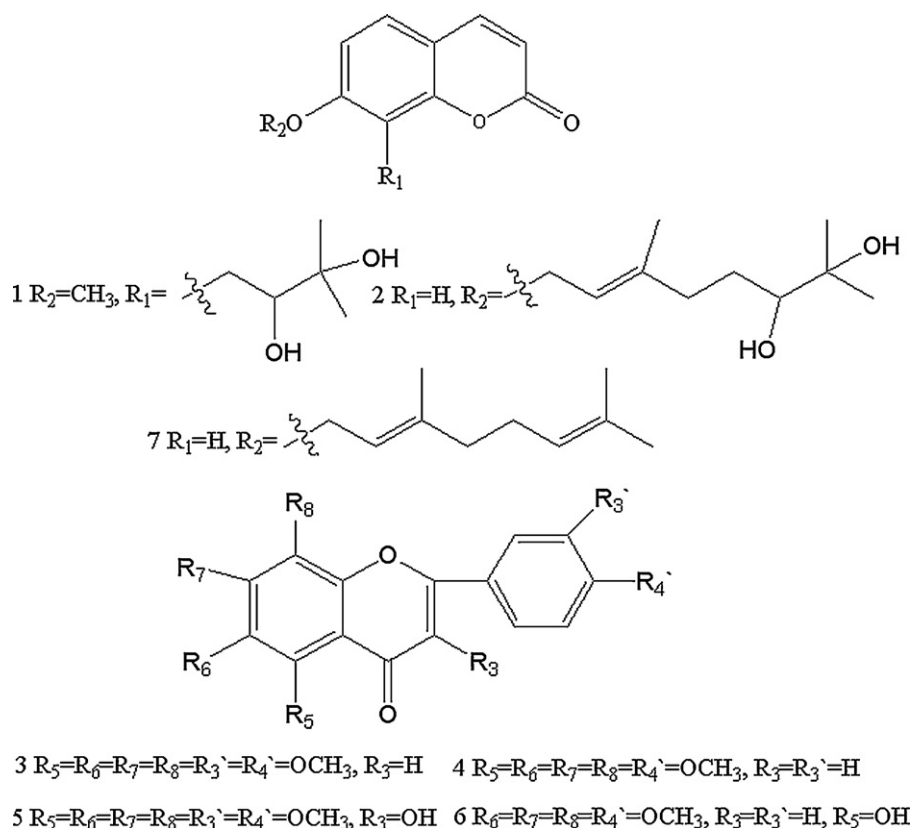*E-mail address:* yangwuliang@163.com (W.-L. Yang).

Fig. 1. Chemical structures of the four PMFs and three coumarins. Meranzin hydrate (1), marmin (2), nobiletin (3), tangeretin (4), natsudaidai (5), 5-hydroxy-6,7,8,4′-tetramethoxyflavone (6), and auraptene (7).

Medicine. Therefore, identifying and quantifying the aforementioned constituents (PMFs and coumarins) is necessary because of the numerous lipid-soluble constituents present in citrus herbs. Furthermore, simultaneous analysis of these constituents would be equally significant for controlling the quality of *zhiqiao* and *zhishi*, as well as other citrus herbs. HPLC–ESI-MS is sensitive in detecting trace constituents and it could obtain better responses to some trace components. Moreover, for some components with similar retention behavior, which are not easily separated, the quantification according to precursor/product ion information at short analysis time using HPLC–ESI-MS/MS could be accurately accomplished. For this reason, HPLC–ESI-MS/MS in multiple reaction monitoring (MRM) mode was applied during the simultaneous quantification of seven lipid-soluble constituents in the present study.

2. Experimental

2.1. Chemicals, reagents and materials

Seven constituents, including meranzin hydrate (1), marmin (2), nobiletin (3), tangeretin (4), natsudaidai (3-hydroxy-5,6,7,8,3′,4′-hexamethoxyflavone) (5), 5-hydroxy-6,7,8,4′-tetramethoxyflavone (6), and auraptene (7) were isolated from *Fructus aurantii* in our laboratory. These compounds were identified using ESI-MS, ^{1}H NMR, and ^{13}C NMR, and further confirmed according to data reported in the literature [2,4]; their structures are shown in Fig. 1. The purity of all the constituents exceeded 98% by HPLC analysis.

HPLC-grade acetonitrile was purchased from Tedia (Tedia Company, Inc., USA). The methanol used for extraction was supplied by Zhenxing Chemical Reagent Corporation (Shanghai, China). Reverse osmosis Milli-Q water was prepared using a Millipore Purification System (AKKL-UP-IV-5; Millipore, Taiwan, China) and filtered through a 0.22 μm membrane filter before use. All other chemicals were of analytical grade.

The *zhiqiao* and *zhishi* samples of different varieties and places of production are listed in Table 1. The material origin was identified by Professor Wuliang Yang.

2.2. Instrumentation and conditions

The HPLC–MS/MS system was an Agilent 1200 liquid chromatograph and a 6410 triple quadrupole mass spectrometer, equipped with ESI ion source. The HPLC system used was an Agilent Series 1200 (Agilent Technologies, Santa Clara, CA, USA) liquid chromatograph, equipped with a vacuum degasser, quaternary pump, and an autosampler. Separation was performed on a 150 mm × 4.6 mm, 5 μm particle size LC-C_{18} column (Diamonasil C_{18}) with the column temperature set at 30 °C. The mobile phase was composed of acetonitrile (A) and 0.1% formic acid (B), with a gradient elution as follows: 0 min, 45% (A); 6 min, 50% (A); 10 min, 90% (A); 12 min, 100% (A); and 18 min, 100% (A). The flow rate was 0.5 mL/min and the injection volume was 10 μL.

The MS conditions were as follows: drying gas temperature, 350 °C; drying gas flow, 8 L/min; nebulizer pressure, 40 psi; corona current, 10 nA; and capillary voltage, 4000 V. MRM mode was applied for quantitative analysis using precursor/product ion information. Data acquisition was performed with MassHunter Workstation (Agilent Technologies, USA).

Table 1
Summary of the tested samples of *zhiqiao* and *zhishi*.

Sample	Variety		Origin	Source
1	*Zhiqiao*	*Citrus aurantium* "Daidai"	Jinhua, Zhejiang Province, China	Collected from the field
2	*Zhiqiao*	*Citrus aurantium* "Daidai"	Lanxi, Zhejiang Province, China	Collected from the field
3	*Zhiqiao*	*Citrus aurantium* L.	Yuanjiang, Hunan Province, China	Collected from the field
4	*Zhiqiao*	*Citrus aurantium* L.	Huaihua, Hunan Province, China	Collected from the field
5	*Zhiqiao*	*Citrus aurantium* L.	Qijiang, Sichuan Province, China	Collected from the field
6	*Zhiqiao*	*Citrus aurantium* L.	Jiangjin, Sichuan Province, China	Collected from the field
7	*Zhiqiao*	*Citrus aurantium* "Xiangcheng"	Huanggang, Jiangxi Province, China	Collected from the field
8	*Zhiqiao*	*Citrus aurantium* "Xiucheng"	Huanggang, Jiangxi Province, China	Collected from the field
9	*Zhiqiao*	*Citrus aurantium* "Xiangcheng"	Xingan, Jiangxi Province, China	Collected from the field
10	*Zhiqiao*	*Citrus aurantium* "Xiucheng"	Xingan, Jiangxi Province, China	Collected from the field
11	*Zhiqiao*	*Citrus aurantium* "Xiangcheng"	Changfu, Jiangxi Province, China	Collected from the field
12	*Zhiqiao*	*Citrus aurantium* "Xiucheng"	Changfu, Jiangxi Province, China	Collected from the field
13	*Zhiqiao*	*Citrus aurantium* "Xiucheng"	Xingan, Jiangxi Province, China	Purchased from a local drug store
14	*Zhishi*	*Citrus aurantium* "Xiangcheng"	Xingan, Jiangxi Province, China	Purchased from a local drug store
15	*Zhishi*	*Citrus aurantium* "Xiangcheng"	Zhangshu, Jiangxi Province, China	Purchased from a local drug store
16	*Zhishi*	*Citrus aurantium* "Daidai"	Zhejiang Province, China	Purchased from drug store in Bozhou, Anhui Province
17	*Zhishi*	*Citrus aurantium* L.	Hubei Province, China	Purchased from a local drug store
18	*Zhishi*	*Citrus aurantium* L.	Shanxi Province, China	Purchased from a local drug store

2.3. Standard solution preparation

The PMFs and coumarins were accurately weighed, respectively, dissolved in methanol, and further diluted to a certain concentration. Then, a stock solution containing meranzin hydrate (96.9 μg/mL), marmin (257.5 μg/mL), nobiletin (115.1 μg/mL), tangeretin (49.7 μg/mL), 5-hydroxy-6,7,8,4′-tetramethoxyflavone (12.7 μg/mL), natsudaidai (45.2 μg/mL), and auraptene (65.3 μg/mL) was prepared and stored at 4 °C before use.

2.4. Preparation of samples

The dry material powder (0.5 g) was accurately weighed and reflux-extracted with 25 mL 100% methanol for 1 h, and then the solution was adjusted to the original weight. An aliquot of the supernate was aspirated, diluted twice, and then filtered through a 0.22 μm membrane before injection.

2.5. Method validation

The method was validated by determination of linearity, limit of detection (LOD), limit of quantification (LOQ), precision, recovery, and stability. Linearity of calibration curve was tested by analyzing the reference compounds at six stock solution concentrations. The stock solution was diluted to a series of concentrations (0.5/100, 1/100, 2/100, 4/100, 4/50, and 8/50) from the original concentration to establish calibration curves, and each level of the concentration was analyzed in duplicate. The LOD and LOQ were evaluated at signal-to-noise ratios of 3 and 10, respectively.

The precision of the developed method was evaluated using intraday and interday variations. Approximately 0.5 g of the sample was prepared as described in Section 2.4. In the intraday variability test, the sample was analyzed for six replicates within 1 day, whereas in the interday variability test, the sample was tested in duplicate over three consecutive days. The relative standard deviations (RSDs) were calculated as measurements of precision.

To evaluate the accuracy of the analytical method, the recovery study was measured by analyzing spiked samples. A certain amount of reference substances (low, medium, and high concentrations) were added into a certain amount of *zhiqiao* samples (sample 13, Jiangxi Province; 0.25 g), respectively and were then extracted and analyzed under the proposed method. Three replicate extractives

at each level were used to determine the extraction recovery rates and the RSDs were calculated.

To investigate the stability of the sample, the sample solution was stored in a refrigerator at 4 °C and analyzed at different time points (0, 2, 4, 6, 8, 12, 16, and 24 h).

3. Results and discussion

3.1. Optimization of extraction conditions

To obtain satisfactory extraction efficiency, the extraction conditions, including extraction method, extraction solvent, extraction solvent volume, and extraction time, were optimized. The results suggest that reflux extraction is better than ultrasonic extraction. Furthermore, 70% methanol, 90% methanol, and 100% methanol were investigated, respectively, and 100% methanol was the preferred extraction solvent. Different solvent volumes were examined, and an extraction efficiency of 25 mL solvent volume was equivalent to that of 50 and 75 mL. The samples were extracted with 25 mL of 100% methanol using different extraction times (0.5, 1.0, 1.5, 2, 2.5, and 3 h). The results indicate that the extraction efficiency at 1 h has no significant difference with that at 1.5 h, or even at 3 h.

3.2. Optimization of LC-MS/MS conditions

The HPLC conditions were optimized to improve the separation of the PMFs and coumarins. Different mobile phases (methanol–water, acetonitrile–water, aqueous methanol–formic acid solution, aqueous acetonitrile–formic acid solution) and flow rates (0.4, 0.5, and 0.6 mL/min) were examined and compared. Aqueous acetonitrile–formic acid solution at a flow rate of 0.5 mL/min achieved satisfactory separation and it saved analysis time.

In the current study, each standard solution of seven analytes was infused into the chromatograph, and the APCI and ESI source parameters were investigated using two detection modes (positive ion and negative ion modes). The results show that ESI in positive ion mode is better and has excellent signal sensitivity. Then, in single ion monitoring mode and product ion scan mode, the maximum signal intensity was achieved by adjusting the fragmentor energy and collision energy, and the precursor/product ion information was acquired. Finally, MRM scanning mode was established

to quantify the target constituents in the samples. The typical chromatograms are shown in Fig. 2.

3.3. Identification of PMFs and coumarins from citrus herbs

To confirm the structure of these investigated compounds further, the mass spectral data of the PMFs and coumarins under ESI positive ion mode were recorded and the quasi-molecular ions and major fragment ions of these compounds were examined. The PMFs and coumarins exhibited quasi-molecular ions $[M + H]^+$, $[M + Na]^+$, and $[M + K]^+$ and fragment ions $[M - CH_3 + H]^+$, $[M - 2CH_3 + H]^+$, $[M - 2CH_3 - H_2O + H]^+$, $[M - 2CH_3 - CO + H]^+$, $[M - C_{10}H_{18}O_2 + Na]^+$, and $[M - C_{10}H_{16} + H]^+$. The characteristic fragmentation patterns of some compounds were in accordance with the data reported in a previous study [16]. Mass parameters including MS, MS^n fragmentation ions, and product ion, are summarized in Table 2.

3.4. Linearity, LOD and LOQ

The calibration curves were obtained by plotting the peak areas versus the concentration of the standards. In a relatively wide concentration range, all the standards show good linearity ($r^2 > 0.9977$), as shown in Table 2. A known concentration of standard solution was used to test the sensitivity of the method. The LOD and LOQ were less than 1.28 and 2.6, respectively. The data are summarized in Table 2.

3.5. Precision, accuracy and stability

The intraday and interday variations in precision were less than 4.07% (RSD). The results are shown in Table 3. The recovery rates of all the components ranged from 95.79% to 105.04%, and the RSDs were less than 3.82%, which indicates that the developed method is reproducible, with good accuracy for all the constituents. The details are shown in Table 4. The result of the stability study demonstrates that the sample is very stable in methanol solution and the RSDs of the seven compounds were all within permissible ranges (less than 2.7%).

3.6. Quantification of PMFs and coumarins in citrus herbs

Fructus aurantii (*zhiqiao*) is widely distributed in different places of China, including Hunan, Jiangxi, Sichuan, and Zhejiang Provinces; the first three provinces are considered genuine production places in China. The results in Table 5 show that the PMF and coumarin content varies dramatically among different origins. The total content of all the investigated constituents in samples from Hunan Province was high, especially the five constituents meranzin hydrate, nobiletin, tangeretin, 5-hydroxy-6,7,8,4′-tetramethoxyflavone, and auraptene, the contents of which were the highest among all *zhiqiao* samples collected from field. In contrast, the total content of all the constituents in the samples from other provinces were relatively low. In addition, the total content of the constituents in sample 13, which was purchased from a drug store, was surprisingly high.

The content of the investigated constituents in samples from Jiangxi Province (samples 7–12) varied with the variety and the production region. The data in Table 5 show that meranzin hydrate is the most abundant constituent, followed by nobiletin in most cases. In the same production region, differences in the content were less among the varieties *Citrus aurantium* "Xiucheng" and *Citrus aurantium* "Xiangcheng" except samples from Xingan County. However, significant differences in the total content of the samples were observed among different production regions.
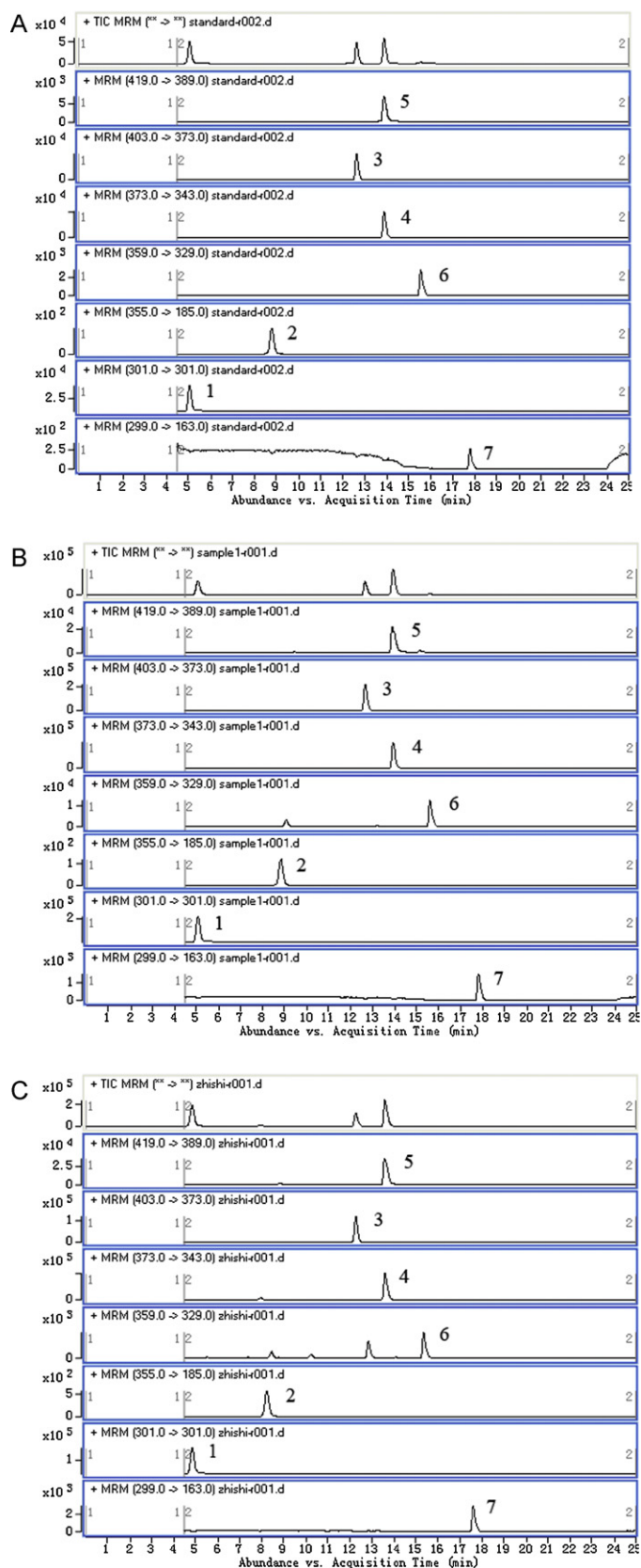

Fig. 2. Total ion MRM chromatograms of the standard solution (A), the *zhiqiao* sample (B), and the *zhishi* sample (C) obtained in positive mode. Meranzin hydrate (1), marmin (2), nobiletin (3), tangeretin (4), natsudaidai (5), 5-hydroxy-6,7,8,4′-tetramethoxyflavone (6), and auraptene (7).

Table 2
Mass spectral data and calibration curves of the seven constituents.

Compounds	MS (m/z)	MS^n (m/z)	Precursor ion/product ion	Regression equation	r^2	Test range (ng/mL)	LOD (ng)	LOQ (ng)
Meranzin hydrate	301[M + Na]$^+$	301[M + Na]$^+$	301 → 301	$Y = 320.82X + 240131$	0.9989	484.5–15,504	0.06	0.16
Marmin	355[M + Na]$^+$	185[M − C$_{10}$H$_{18}$O$_2$ + Na]$^+$	355 → 185	$Y = 0.47X + 959$	0.9994	1287.5–41,200	1.28	2.5
Nobiletin	403[M + H]$^+$	388[M − CH$_3$ + H]$^+$, 373[M − 2CH$_3$ + H]$^+$	403 → 373	$Y = 272.18X + 123636$	0.9990	575.5–18,416	0.035	0.12
Tangeretin	373[M + H]$^+$	343[M − 2CH$_3$ + H]$^+$	373 → 343	$Y = 869.77X + 84970$	0.9984	248.5–7952	0.02	0.08
Natsudaidai	419[M + H]$^+$, 441[M + Na]$^+$, 457[M + K]$^+$	404[M − CH$_3$ + H]$^+$, 389[M − 2CH$_3$ + H]$^+$, 361[M − 2CH$_3$-CO + H]$^+$	419 → 389	$Y = 141.63X + 59963$	0.9996	226–7232	0.11	0.52
5-Hydroxy-6,7,8,4′-tetramethoxyflavone	359[M + H]$^+$, 381[M + Na]$^+$, 397[M + K]$^+$	344[M − CH$_3$ + H]$^+$, 329[M − 2CH$_3$ + H]$^+$, 311[M − 2CH$_3$-H$_2$O + H]$^+$	359 → 329	$Y = 214.77X + 1246$	0.9998	63.5–2032	0.008	0.03
Auraptene	299[M + H]$^+$, 321[M + Na]$^+$	163[M − C$_{10}$H$_{16}$ + H]$^+$	299 → 163	$Y = 3.05X + 954$	0.9977	326.5–10,488	0.9	2.6

Table 3
Intraday and interday precision of seven analytes.

Compounds	Intraday ($n = 6$)		Interday ($n = 3$)	
	Content (μg/g)	RSD (%)	Content (μg/g)	RSD (%)
Meranzin hydrate	2412.52 ± 22.93	0.95	2430.18 ± 15.49	0.64
Marmin	418.44 ± 17.05	4.07	430.76 ± 13.84	3.21
Nobiletin	1964.22 ± 24.26	1.23	1985.57 ± 22.02	1.11
Tangeretin	1049.58 ± 16.79	1.60	1055.71 ± 7.31	0.69
Natsudaidai	317.85 ± 7.35	2.31	319.01 ± 4.44	1.39
5-Hydroxy-6,7,8,4′-tetramethoxyflavone	123.11 ± 1.78	1.45	121.66 ± 2.05	1.68
Auraptene	1440.53 ± 34.44	2.39	1446.27 ± 13.62	0.94

The data presented in Table 5 (samples 14–18) also show that the content of the target components in *zhishi* varies with production region. Compared with that of *zhiqiao*, the total content of the constituents in *zhishi* was relatively low in most provinces, particularly in samples from Zhejiang, Shanxi, and Hubei Provinces. This could be accounted for by the differences in the growth stage of *zhishi* and *zhiqiao*, causing differences in the accumulation of secondary metabolites in *zhishi* and *zhiqiao*.

The total content of the components in *zhishi* from Jiangxi Province was significantly higher, which might indicate that regional difference is one of the main causes for the differences in the content of the constituents. Moreover, a distinguishing feature of *zhishi* from Jiangxi Province was the significant abundance of marmin, up to seven times that of *zhiqiao* from Jiangxi Province (sample 13).

In summary, PMFs and coumarins are abundant in most citrus herbs, and significant differences in their content are present in *zhiqiao*, which can be attributed to differences in production origins and varieties, as well as genuine production place. This is also true for the constituents in *zhishi*.

Table 4
Recoveries of seven analytes.

Compounds	Original (μg)	Added (μg)	Detected (μg)	Recovery rate (%)	RSD (%)
Meranzin hydrate	601.96	493.00	1085.92	98.16	2.13
		609.00	1198.98	98.03	1.59
		739.50	1310.37	95.79	1.41
Marmin	103.83	82.40	186.73	100.61	2.39
		103.00	209.15	102.25	3.82
		123.60	222.49	96.00	0.98
Nobiletin	487.47	395.94	891.42	102.02	2.56
		488.02	973.03	99.49	2.00
		589.31	1056.03	96.47	1.24
Tangeretin	261.63	212.04	471.82	99.13	1.19
		259.16	533.85	105.04	1.24
		306.28	577.93	103.27	1.85
Natsudaidai	80.64	65.09	146.70	101.48	3.21
		79.55	159.45	99.06	1.50
		97.63	175.89	97.56	2.07
5-Hydroxy-6,7,8,4′-tetramethoxyflavone	29.86	23.37	54.24	104.35	1.87
		29.46	60.31	103.35	3.34
		35.56	65.48	100.17	2.78
Auraptene	361.21	301.68	672.49	103.18	2.34
		368.72	735.90	101.61	1.71
		435.76	795.39	99.63	3.59

Table 5
Content (μg/g) of the seven constituents in citrus herbs ($n = 3$).

Sample	Meranzin hydrate	Marmin	Nobiletin	Tangeretin	Natsudaidai	5-Hydroxy-6,7,8,4'-tetramethoxyflavone	Auraptene	Total (μg/g)
1	469.75 ± 15.73[a]	191.70 ± 8.49	336.96 ± 7.03	274.09 ± 4.59	51.12 ± 2.52	2.58 ± 0.10	378.86 ± 11.13	1705.06
2	1438.18 ± 33.99	–[c]	481.04 ± 9.22	171.92 ± 2.09	92.16 ± 2.48	0.66 ± 0.02	29.91 ± 0.58	2213.87
3	1743.47 ± 40.77	435.00 ± 26.03	1623.68 ± 42.22	1001.66 ± 36.70	341.04 ± 14.06	120.69 ± 5.39	595.29 ± 9.70	5860.83
4	1734.03 ± 83.02	483.94 ± 6.28	1236.07 ± 39.79	829.20 ± 26.38	289.40 ± 5.76	154.23 ± 4.93	1719.18 ± 47.49	6446.05
5	91.61 ± 3.54	+[b]	91.57 ± 4.38	56.15 ± 3.84	438.48 ± 16.65	0.58 ± 0.02	355.55 ± 9.10	1033.94
6	305.59 ± 6.47	169.57 ± 6.49	124.52 ± 3.22	90.58 ± 3.26	565.68 ± 15.28	1.10 ± 0.02	450.79 ± 21.77	1707.83
7	1371.66 ± 30.69	226.59 ± 9.61	588.10 ± 14.90	422.59 ± 6.53	401.84 ± 5.99	5.64 ± 0.27	64.65 ± 3.98	3081.07
8	1184.94 ± 46.37	451.81 ± 16.83	449.65 ± 16.22	256.20 ± 8.96	380.11 ± 19.33	4.90 ± 0.25	131.44 ± 4.75	2859.05
9	425.12 ± 6.62	183.29 ± 6.76	+[b]	+[b]	+[b]	8.36 ± 0.35	111.47 ± 2.72	719.88
10	881.14 ± 64.16	239.89 ± 6.75	430.86 ± 5.09	305.70 ± 3.27	488.85 ± 17.22	8.36 ± 0.35	+[b]	2354.80
11	1076.54 ± 37.79	370.63 ± 15.95	706.77 ± 24.42	320.31 ± 11.30	495.57 ± 12.46	7.64 ± 0.36	148.63 ± 2.36	3126.09
12	1478.98 ± 43.54	341.27 ± 11.17	834.38 ± 34.91	525.80 ± 21.41	442.29 ± 11.11	10.03 ± 0.37	86.19 ± 3.12	3718.94
13	2420.73 ± 40.85	425.10 ± 17.45	1989.49 ± 33.33	1058.16 ± 14.57	320.89 ± 7.25	122.07 ± 1.17	1457.52 ± 7.90	7793.96
14	1568.47 ± 36.81	3009.25 ± 134.22	1005.62 ± 32.38	625.52 ± 15.37	643.96 ± 20.92	20.71 ± 0.91	785.82 ± 14.38	7659.35
15	1348.44 ± 14.70	2941.91 ± 76.41	771.98 ± 19.36	484.11 ± 6.34	604.51 ± 8.06	16.22 ± 0.41	2056.67 ± 94.30	8223.84
16	30.00 ± 0.98	+[b]	661.31 ± 21.25	369.14 ± 6.46	+[b]	12.30 ± 0.41	25.80 ± 1.15	1098.55
17	287.97 ± 4.40	+[b]	388.68 ± 7.52	251.01 ± 2.20	+[b]	11.51 ± 0.44	111.38 ± 4.16	1050.55
18	+[b]	+[b]	714.57 ± 8.46	442.06 ± 10.77	+[b]	17.88 ± 0.75	105.13 ± 3.94	1279.64

[a] Mean ± S.D. ($n = 3$).
[b] Less than the quantifiable limit.
[c] Not detected.

4. Conclusion

To our knowledge, this is the first report on the simultaneous quantification of PMFs and coumarins in *Fructus aurantii* and *Fructus aurantii immaturus*. The HPLC–ESI-MS method described in this paper is suitable for the qualitative and quantitative analysis of PMFs and coumarins in citrus herbs. The method is simple and reliable, and it can be applied for PMFs and coumarins in relative pharmaceutical studies.

Acknowledgements

References

[1] The Pharmacopoeia of the People's Republic of China, Part I: The Pharmacopoeia Commission of PRC, China Medical Science Press, 2010.
[2] S. Li, M.H. Pan, C.S. Lai, C.Y. Lo, S. Dushenkov, C.T. Ho, Isolation and syntheses of polymethoxyflavones and hydroxylated polymethoxyflavones as inhibitors of HL-60 cell lines, Bioorg. Med. Chem. 15 (2007) 3381–3389.
[3] P. Dugo, L. Mondello, L. Dugo, R. Stancanelli, G. Dugo, LC-MS for the identification of oxygen heterocyclic compounds in citrus essential oils, J. Pharm. Biomed. Anal. 24 (2000) 147–154.
[4] Y. Satoh, S. Tashiro, M. Satoh, Y. Fujimoto, J.Y. Xu, T. Ikekawa, Studies on the bioactive constituents of *Aurantii fructus immaturus*, Yakugaku Zasshi. 116 (1996) 244–250.
[5] Y. Yamada, N. Nakatani, H. Fuwa, Epoxyaurapten and marmin from juice oil in hassaku (citrus hassaku) and the spasmolytic activity of 7-geranyloxycoumarin-related compounds, Agric. Biol. Chem. 51 (1987) 1105–1110.
[6] J.A. Manthey, N. Guthrie, Antiproliferative activities of citrus flavonoids against six human cancer cell lines, J. Agric. Food Chem. 50 (2002) 5837–5843.
[7] T. Tanaka, K. Kawabata, M. Kakumoto, H. Makita, A. Hara, H. Mori, K. Satoh, A. Hara, A. Murakami, W. Kuki, Y. Takahashi, H. Yonei, K. Koshimizu, H. Ohigashi, Citrus auraptene inhibits chemically induced colonic aberrant crypt foci in male F344 rats, Carcinogenesis 18 (1997) 2155–2161.
[8] M.S. Mokbel, Y. Watanabe, F. Hashinaga, T. Suganuma, Purification of the antioxidant and antimicrobial substance of ethyl acetate extracts from Buntan (Citrus grandis Osbeck) fruit peel, Pak. J. Biol. Sci. 9 (2006) 145–150.
[9] H. Takase, K. Yamamoto, H. Hirano, Y. Saito, A. Yamashita, Pharmacological profile of gastric mucosal protection by marmin and nobiletin from a traditional herbal medicine, *Aurantii fructus immaturus*, Jpn. J. Pharmacol. 66 (1994) 139–147.
[10] Y. Akao, T. Itoh, K. Ohguchi, M. Iinuma, Y. Nozawa, Interactive effects of polymethoxy flavones from citrus on cell growth inhibition in human neuroblastoma SH-SY5Y cells, Bioorg. Med. Chem. 16 (2008) 2803–2810.
[11] A. Nakajima, T. Yamakuni, M. Haraguchi, N. Omae, S.Y. Song, C. Kato, O. Nakagawasai, T. Tadano, A. Yokosuka, Y. Mimaki, Y. Sashida, Y. Ohizumi, Nobiletin, a citrus flavonoid that improves memory impairment, rescues bulbectomy-induced cholinergic neurodegeneration in mice, J. Pharmacol. Sci. 105 (2007) 122–126.
[12] F. Epifano, G. Molinaro, S. Genovese, R.T. Ngomba, F. Nicoletti, M. Curini, Neuroprotective effect of prenyloxycoumarins from edible vegetables, Neurosci. Lett. 443 (2008) 57–60.
[13] X.G. He, L.Z. Lian, L.Z. Lin, W.M. Bernart, High-performance liquid chromatography–electrospray mass spectrometry in phytochemical analysis of sour orange (Citrus aurantium L.), J. Chromatogr. A. 791 (1997) 127–134.
[14] I.L. Bonaccorsi, H.M. McNair, L.A. Brunner, P. Dugo, G. Dugo, Fast HPLC for the analysis of oxygen heterocyclic compounds of citrus essential oils, J. Agric. Food Chem. 47 (1999) 4237–4239.
[15] D.Y. Zhou, D.L. Chen, Q. Xu, X.Y. Xue, F.F. Zhang, X.M. Liang, Characterization of polymethoxylated flavones in *Fructus aurantii* by liquid chromatography with atmospheric pressure chemical ionization combined with tandem mass spectrometry, J. Pharm. Biomed. Anal. 43 (2007) 1692–1699.
[16] D.Y. Zhou, X.L. Zhang, Q. Xu, X.Y. Xue, F.F. Zhang, X.M. Liang, UPLC/Q-TOF MS/MS as a powerful technique for rapid identification of polymethoxylated flavones in *Fructus aurantii*, J. Pharm. Biomed. Anal. 50 (2009) 2–8.
[17] S. Li, Y. Wang, Z. Wang, H. Xiao, C.Y. Lo, N. Rawson, C.T. Ho, Quantitative analysis of hydroxylated polymethoxyflavones by high-performance liquid chromatography, Biomed. Chromatogr. 24 (2010) 838–845.
[18] P. Dong, P. Qiu, Y. Zhu, S. Li, C.T. Ho, D.J. McClements, H. Xiao, Simultaneous determination of four 5-hydroxy polymethoxyflavones by reversed-phase high performance liquid chromatography with electrochemical detection, J. Chromatogr. A 1217 (2010) 642–647.

Characterization of compounds and potential neuraminidase inhibitors from the n-butanol extract of *Compound Indigowoad Root Granule* using ultrafiltration and liquid chromatography–tandem mass spectrometry

Shu Liu [a,c], Jun Yan [b], Junpeng Xing [a], Fengrui Song [a], Zhiqiang Liu [a,*], Shuying Liu [a]

[a] *Changchun Center of Mass Spectrometry, Changchun Institute of Applied Chemistry, Chinese Academy of Sciences, Changchun 130022, PR China*
[b] *College of Pharmacy, Jilin University, Changchun 130021, PR China*
[c] *Graduate School of Chinese Academy of Sciences, Beijing 100039, PR China*

A B S T R A C T

The liquid chromatography–tandem mass spectrometry (LC–MS/MS) methods were used to identify the pharmacologically active n-butanol extract from *Compound Indigowoad Root Granule.* As a result, eighteen compounds belonging to various structural classes such as nucleosides, purines, flavonoids and amino acid were unambiguously identified. Then an in vitro neuraminidase (NA) inhibition assay was carried out to examine the inhibitory activity of the standard samples and extracts on NA. After which, ultrafiltration liquid chromatography with photodiode array detection coupled to electrospray ionization tandem mass spectrometry (ultrafiltration LC–MS/MS) was used to study NA inhibitory activity of standard flavones and n-butanol extract of *Compound Indigowoad Root Granule.* This method is highly selective and sensitive, and it could be used for characterization of bioactive compounds and botanical extracts. The result provides some enlightenment for the explanation of the antiviral activity of *Compound Indigowoad Root Granule* and some guidance for natural anti-influenza medicine development.

© 2011 Elsevier B.V. All rights reserved.

1. Introduction

NA is an enzyme present in the surface of the influenza virus, it is recognized as an attractive target for developing agents against influenza infection and its inhibitors have been widely used in the treatment of influenza infection [1–4]. Although synthetic NA inhibitors exemplified by oseltamivir and zanamivir have been designed to halt the spread of the virus in the body, adverse side effects such as nausea, vomiting, diarrhea, abdominal pain were observed [5]. Hence, naturally existing NA inhibitors have attracted considerable interest for treating influenza.

The *Compound Indigowoad Root Granule* is composed of two kinds of Chinese herbal medicines: banlangen (Isatis root) and daqingye (Isatis leaf). It is one of the most well-known approved prescription remedy and frequently used as anti-leukemia, antipyretic, anti-inflammatory and anti-virus agents [6–8]. In addition, *Compound Indigowoad Root Granule* has been accredited as antiviral agent against influenza virus [9]. For the investigation on the potential use of the *Compound Indigowoad Root Granule* for lead compound discovery to treat Influenza, this prescription was selected as the potential NA inhibitors.

In vitro methods applied in the fractionated extracts of medicinal herbs have been commonly used to screen the NA inhibitors. However, the assays based on fractionation required multiple-step isolations of active compounds and needed to accompany with conventional structure elucidation analyses, which are time-consuming and labor-intensive [10]. In addition, most of the in vitro screening techniques are based on optical or radioactive detection [11–13], which may be affected by matrix interference, especially when complex samples are analyzed.

To overcome the limitations of the in vitro screening assays and enhance the throughput of the drug discovery, an ultrafiltration–LC–MS/MS was used. This method has been proved to be a powerful tool for screening biologically active compounds from botanical extracts because the ultrafiltration step facilitates the separation of ligand–receptor complexes from unbound compounds, followed by LC–MS/MS identification of the ligands. Low sample consumption, no need for immobilization and reuse of enzymes can be considered as most important advantages of ultrafiltration–LC–MS/MS for high throughput screening and identification of active compounds [14–17].

In this study, firstly, the LC–MS/MS methods was used to identify the pharmacologically active compounds in n-butanol extract of *Compound Indigowoad Root Granule.* Secondly, an in vitro model was carried out to examine the inhibitory activity of the standard samples and extracts on NA, After which, ultrafiltration–LC–MS/MS

method was used to screen a mixture of flavonoid glycosides in order to determine their relative binding affinity to NA. The results showed that flavonoid aglycones had higher affinity for NA than glycans, which is consistent with the inhibitory activity data obtained from the in vitro model. The ultrafiltration–LC–MS/MS method was also used to study the binding affinity between the n-butanol extract of *Compound Indigowad Root Granule* and NA, The result provides some enlightenments for the explanation of the antiviral activity of *Compound Indigowad Root Granule*.

2. Materials and methods

2.1. Plant materials and standard substances

Banlangen (*Isatis root*) and daqingye (*Isatis leaf*) were purchased from drugstore (Tongrentang, Changchun, PR China).

Apigenin, luteolin, catechin, genistin, genistein, isorhamnetin, baicalein and baicalin standards were purchased from the National Institute for the Control of Pharmaceutical and Biological Products (Beijing, China). Isoorientin and isovitexin were purchased from Shanghai Tauto Biotech Co., Ltd. (Shanghai, China). Cytidine, Guanine, Adenine and Adenosine were purchased from Sigma (St. Louis, MO, USA). Guanosine and Uridine were obtained from Aladdin-Reagent Co., Ltd. (Beijing, China). Neuraminidase from *Clostridium perfringens* (*C. welchii*) was obtained from Sigma (St. Louis, MO, USA). 2-(N-Morpholino) ethanesulfonic acid hydrate (MES), calcium chloride and ammonium acetate were also obtained from Sigma (St. Louis, MO, USA). HPLC grade methanol was purchased from Fisher Scientific (Loughborough, UK); HPLC grade acetic acid was purchased from TEDIA (Fairfield, OH). Water was obtained from Milli-Q water purification system (Milford, MA). Solvents and all other chemicals not mentioned, were of Analytical grade and purchased from Beijing Shiji (Beijing, China).

2.2. Neuraminidase inhibitors screen kit

Neuraminidase Inhibitors Screen Kit was purchased from Beyotime Institute of Biotechnology Co., Ltd. (Shanghai, China), which contains 10 ml buffer, 1 ml neuraminidase, 1 ml fluorescent substrate and 1.2 ml Milli-Q water.

2.3. Preparation of plant extracts

The preparation of plant extracts was performed according to *Drug Standard of Ministry of Public Health of the People's Republic of China* [18] or referred to reported literature [19], this literature contains more information on the extraction methodology. 600 g Banlangen powder and 900 g daqingye powder were refluxed twice in 4500 ml water for 1 h and filtered. The filtrate was concentrated to 200 ml, and 600 ml ethanol was added. The mixtures were filtrated after precipitated by ethanol for 24 h and the filtrate was concentrated by rotary evaporation at 50 °C. The final extracts were partitioned with n-butanol for three times to give n-butanol extract. The n-butanol extract was passed through a 0.45 μm filter and 10 μL of the filtrate was injected into the HPLC–MS system directly.

2.4. LC–MS/MS analysis of n-butanol extracts

The n-butanol extract of *Compound Indigowad Root Granule* was analyzed using LC–MS/MS, which consisted of a Waters (Milford, MA) 2695 HPLC system coupled to an ion trap mass spectrometer with an electrospray ionization source (Finnigan MAT, San Jose, CA). HPLC separations were carried out using a C18 analytical column (4.6 mm × 250 mm, 5 μm, Kromasil) and an injection volume of 10 μL. The column temperature was kept at 25 °C. The flow rate

was set to 0.8 ml/min and the eluting gradient was as follows: [methanol (A) and 0.5% acetic acid in water (B)]: 0–10 min, 5% A; 10–20 min, 5–20% A; 20–30 min, 20–30% A; 30–50 min, 30–35% A; 65 min, 55% A. The mass spectrometer was operated in the positive and negative ion modes with source voltage of 5.0 kV. The metal capillary voltage was set to 4.5 V and temperature at 250 °C, the sheath gas (N_2) flow rate was 60 arb and the scan range was m/z 100–1500 Da; the maximum injection time was 200 millisecond.

2.5. LC–MS/MS analysis of ultrafiltration samples

The released ligands were redissolved in 40 μL of methanol/water (50:50; v/v). Aliquots (20 μL) of this reconstituted ligand solution were analyzed using LC–MS/MS. HPLC separations were carried out using a C18 column (150 mm × 4.6 mm, 5 μm, Dikma, Beijing, China) and a C18 guard column (Dikma). The column temperature was kept at 25 °C. The flow rate was set to 0.5 ml/min and the eluting gradient for six flavone standards was as follows: [methanol (A) and 0.5% acetic acid in water (B)]: 0–9 min, 30–73% A; 9–15 min, 73–74% A; 15–20 min, 74% A; 20–25 min, 74–74.5% A.; 25–28 min, 74.5–90% A. Mobile phase used for flavone compounds from extracts was as follows: [methanol (A) and 0.5% acetic acid in water (B)]: 0–5 min, 55% A; 5–10 min, 55–70% A; 10–15 min, 70–100% A; 15–25 min, 100% A. The mass spectrometer was operated in the negative ion mode with source voltage of 5.0 kV. The metal capillary voltage was set to 4.5 V and temperature at 250 °C, the sheath gas (N_2) flow rate was 60 arb, the scan range was m/z 100–1500 Da; the maximum injection time was 200 millisecond.

2.6. Neuraminidase inhibition assay

The NA inhibition studies were carried out in a 96-well microplate reader using a procedure given by Kit instruction and this method was also reported by Gubareva et al. [20,21]. A reaction mixture containing 70 μL of reaction buffer solution, 10 μL of NA, and 10 μL of standard samples in 10% methanol were added to each well. Vibration mixing was carried out for about 1 min and incubation at temperature 37 °C for 2 min so that the NA and standard samples can fully interacted. After which, 10 μL of fluorescent substrate was added to give a total of 100 μL reaction mixture. The entire mixture was thoroughly mixed by vibration for about 1 min and the plate was incubated at 37 °C for 20 min. The fluorescence was read on a Tecan GENios multifunctional microplate reader (Männedorf, Switzerland), with an excitation wavelength at 360 nm and an emission wavelength at 440 nm. The Controls contained the same reaction mixture and water of the same volume as the standard samples. The inhibition (%) was calculated using the formula: $(A1 − A2)/A1 × 100$, where A1 is the absorbance of the control, and A2 is the absorbance of the sample. IC50 was determined by plotting the percentage of NA activity against inhibitor concentration using software that came with the microplate reader.

2.7. Screening protocol

Each incubation mixture was prepared by mixing 55 μL of 16 μM standard samples and 55 μL of 16 μM NA in buffer solution to give a total volume of 110 μL. The buffer solution contained 0.33 M MES, 4 mM $CaCl_2$ at pH 3.5. The mixture was incubated for 30 min at 37 °C and an aliquot of 100 μL of the mixture was injected into the ultrafiltration chamber and filtered through a Microcon (Millipore, Bedford, MA) YM-100 centrifugal filter containing a regenerated cellulose ultrafiltration membrane with a 100,000 MW cutoff by centrifugation at 7000 × g for 5 min at room temperature. The filter was washed three times by centrifugation using 100 μL aliquots of the buffer solution at room temperature
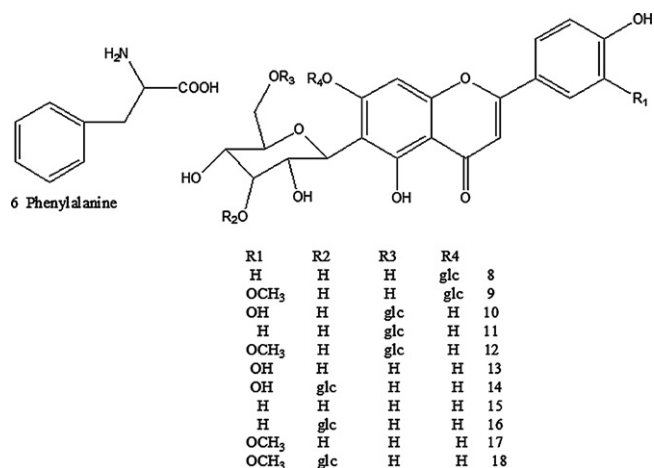
Fig. 1. Structures of compounds 6, 8–18. Consecutive numbering is according to their chromatographic retention.
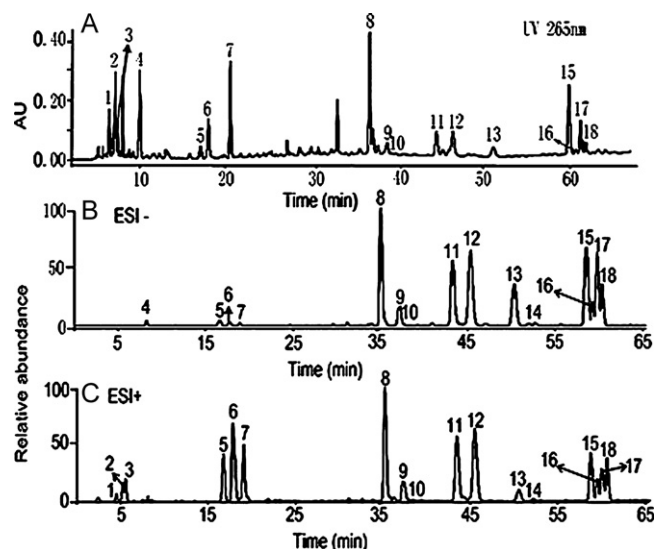

Fig. 2. HPLC profiles of n-butanol extract of *Compound Indigowoad Root Granule* with UV (a), ESI-MS detectors in negative ion modes (b) and ESI-MS detectors in positive ion modes (c).

so as to remove the unbound compounds. The bound ligands were released by adding 100 μL of methanol followed by centrifugation at $7000 \times g$ for 7 min and this process was repeated three times. The solvent in the ultrafiltrate was removed under vacuum, and the released ligands were used for LC–MS/MS analysis. A control experiment in which no enzyme was used was also carried out before each screening experiment.

3. Results and discussion

3.1. Structural characterization of compounds from n-butanol extract of Compound Indigowoad Root Granule

LC–MS/MS method was used to analyze the n-butanol extract of *Compound Indigowoad Root Granule* that has strong antiviral activity. An overview of identified compounds is given in Fig. 1. Fig. 2 shows the HPLC and electrospray mass spectrometry (negative and positive ion modes) profiles of extract of *Compound Indigowoad Root Granule*. Compounds 1, 4–7, 13 and 15 were identified on the basis of their on-line spectroscopic data in combination with MS/MS data, and the subsequent confirmation by co-chromatography with reference compounds. The compounds 2 and 3 were identified by comparing their λ_{max} and retention time with reference compounds. According to the liquid chromatography with photodiode array detection data the compounds 8–18 could be classified into three groups: compound 8 had two λ_{max} at 270 and 325 nm;

compounds 9, 10, 12–14, 17, 18 had nearly the same UV spectra with their λ_{max} at around 269 and 347 nm; and compounds 11, 15, 16 had nearly the same UV spectra with their λ_{max} at around 269 and 335 nm. All these compound's UV data were consistent with the flavonoids, indicating that compounds 8–18 were flavonoids. The flavonoids in the extract were all flavonoid glycosides, but their corresponding flavonoid aglycones which are only three types: Apigenin, luteolin and 4′,5,7-trihydroxy-5′-methoxyflavone were identified using the ESI-MS^n data and literature data [22–24]. An overview of all compounds identified in the n-butanol extract of *Compound Indigowoad Root Granule*, MS/MS and UV data of compounds is given in Table 1.

3.2. The inhibition activity of standard samples and extracts by an in vitro enzyme assay

The in vitro NA Inhibition assay was conducted as a comparative experiment to the ultrafiltration LC–MS/MS based assay. Apigenin, which is a strong NA inhibitor was used as a positive control [10,25]. The result of the enzyme inhibition assay showed that the flavonoid aglycones had strong inhibitory activity while the inhibitory activity of the glycans except the baicalin was very low

Table 1

The LC–MS^2 and UV data of compounds identified from n-butanol extract of *Compound Indigowoad Root Granule*.

No.	t_R (min)	UVλ_{max} (nm)	[M+H]$^+$	[M−H]$^-$	MS^2	Compounds
1	4.41	276	244	242	244: 112	Cytidine
2	5.16	260	136	134	–	Guanine
3	5.49	246, 273	152	150	–	Adenine
4	8.38	260	245	243	245: 113	Uridine
5	16.64	252	284	282	284: 152	Guanosine
6	17.70	257	166	164	164: 147, 118	Phenylalanine
7	18.94	255	268	266	268: 136	Adenosine
8	35.05	270, 325	595	593	593: 473, 431, 341, 311	Saponarin
9	37.07	269, 347	625	623	623: 503, 461, 371, 341	Isoscoparin-7-O-glucopyranoside
10	37.25	269, 347	611	609	609: 357, 327	Isoorientin-6″-O-glucopyranoside
11	43.21	269, 335	595	593	593: 341, 311	Isovitexin-6″-O-glucopyranoside
12	45.25	269, 347	625	623	623: 371, 341	Isoscoparin-6″-O-glucopyranoside
13	50.33	268, 351	449	447	447: 357, 327	Isoorientin
14	52.13	269, 349	611	609	609: 519, 429, 339	Isoorientin-3″-O-glucopyranoside
15	58.50	270, 337	433	431	431: 341, 311	Isovitexin
16	59.24	269, 335	595	593	593: 503, 413, 323	Isovitexin-3″-O-glucopyranoside
17	59.75	269, 345	463	461	461: 371, 341	Isoscoparin
18	60.37	269, 348	625	623	623: 533, 443, 353	Isoscoparin-3″-O-glucopyranoside

Table 2
Inhibition activity of standard compounds and extract against neuraminidase.

Samples	Inhibition[a],[b] (%)	IC50[a],[c] (μM)
ECIRG	3.02[d]	>100
Catechin	0	>100
Baicalein	40.31	30.52
Baicalin	23.02	49.34
Genistien	25.54	43.25
Genistin	8.48	92.51
Isorhamnetin	42.58	28.67
Apigenin	51.33	18.98
Luteolin	48.72	21.41
Isovitexin	4.01	>100
Isoorientin	3.55	>100
Nucleosides[e]	0	>100

[a] The result was an average of three determinations.

[b] Inhibition by 20 μM standard compounds.

[c] Concentration required for 50% inhibition of the enzyme activity under the assay conditions.

[d] Inhibition by 25 μg/ml n-butanol extract of *Compound Indigowood Root Granule* (ECIRG).

[e] Nucleosides contain Cytidine, Guanine, Adenine, Adenosine, Guanosine and Uridine.

also the nucleosides and catechin possessed no NA inhibition activities (as shown in Table 2).

3.3. Ultrafiltration–LC–MS analysis

The ultrafiltration LC–MS/MS screening is an affinity screening method based on MS. The ultrafiltration chamber which was used as a solution-phase extraction device, is very important in this method. When a mixture of target compounds is injected into the ultrafiltration chamber containing a macromolecular receptor, such as NA, the macromolecules and the ligand–receptor form complexes. In this study the complex was retained by the ultrafiltration membrane, while unbound and low molecular weight compounds were washed away by centrifugation with aliquots of buffer solution. Then, the ligand–receptor complex was disrupted by the addition of organic solvent or changing pH value, and then the released components were identified by LC–MS/MS analysis.

The receptor and ligand concentration ratio also determine the number of potentially active compounds that would be obtained, so the first step in development of the screening assay was to establish a suitable concentration ratio of receptor and ligand that would maximize chances of screening out potential active ingredients and minimize emergence of false-positive results. To validate the assay, six flavonoid glycosides were chosen as the positive controls, which can inhibit NA activity at different degrees as shown by an in vitro enzyme assay and in previous studies [10,25]. The chromatographic conditions were optimized to achieve complete separation of the six compounds, the LC–MS/MS data was also a concern to identify the compounds in each peak, the chromatogram of the six compounds is shown in Fig. 3(a).

Incubations of equimolar concentrations 10 μM of compounds were carried out with two different concentrations of the NA (5 and 10 μM). After the incubation with NA and ultrafiltration affinity purification, the trapped ligands are analyzed by LC–MS/MS. The LC-chromatograms for these experiments are shown in Fig. 3(b) and (c). Enhancement of HPLC peak areas in the experimental incubations (solid lines) indicated specific binding of ligands to NA. Based on these chromatograms and the standard curves, enrichment factors which represent the specific binding of each ligand to NA were obtained. The enrichment factors were calculated according to equation 1: $(A1 - A2)/A3 \times 100\%$, where A1 is the area of the experiment with NA, A2 is the area of the control without NA and A3 is the area of the compounds without experimental process. The enrichment factors are shown in Table 3. These
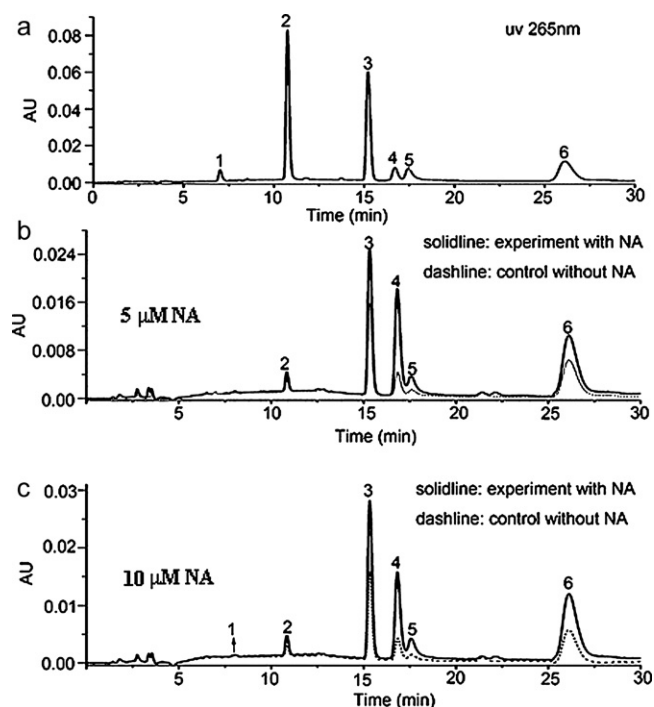
Fig. 3. The UV chromatogram of ultrafiltration LC–MS/MS screening of six flavonoid glycosides for binding to NA. (a) The UV chromatogram of six flavonoid glycosides. (b) The UV chromatogram of ultrafiltration screening experiment with 5 μM NA. (c) The UV chromatogram of ultrafiltration screening experiment with 10 μM NA.

enrichment factors can be used to rank the relative binding affinities of these flavonoid glycosides. The results acquired by using ultrafiltration LC–MS/MS methods were similar to the in vitro enzyme assay's results. The results further proved that flavonoid aglycone possessed higher affinity for NA than glycan. This shows that the ultrafiltration LC–MS/MS method is a feasible and reliable method to screen the inhibitors of NA from the compounds mixture.

Subsequently, the validated ultrafiltration LC–MS/MS method was used to screen the inhibitors of NA from the *Compound Indigowood Root Granule*. When the extract was screened directly, no compound was found to interact with NA, possibly because the metabolites of the compounds in the extract were responsible for the inhibition recorded in vivo. As mentioned earlier, the flavonoid glycosides had weak NA inhibitory activity, and the main constituents in extracts of the *Compound Indigowood Root Granule* were flavonoid glycosides with one or more sugar moiety, so there was a weak or complete absence of interaction between extract and enzyme. The flavonoid glycosides can be metabolized into their corresponding aglycones in vivo as reported in previous literature [26,27], so we choose the corresponding flavonoid aglycones of the flavonoid glycosides or the flavonoid glycosides with one sugar in the extracts which we able to obtain as the research objects. The LC-chromatograms for these experiments are shown in Fig. 4.

Table 3
The enrichment factors of flavones binding to NA.

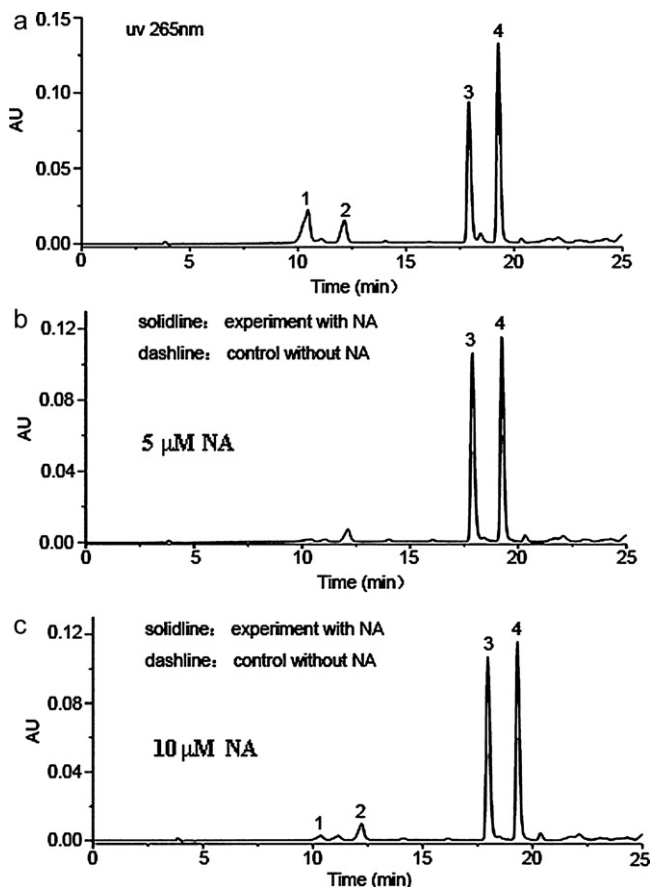| Samples	Enrichment of factors in different concentrations of NA	
	5 μM	10 μM
Catechin	–	0.15 ± 1.21
Baicalein	7.23 ± 0.53	14.11 ± 0.42
Baicalin	3.54 ± 0.89	9.05 ± 0.78
Genistien	3.45 ± 0.62	8.01 ± 0.56
Genistin	0.71 ± 1.02	1.65 ± 0.98
Isorhamnetin	8.12 ± 0.48	14.41 ± 0.55

Fig. 4. The UV chromatogram of ultrafiltration LC–MS/MS screening of four flavonoid glycosides from the n-butanol extract of *Compound Indigowoad Root Granule* for binding to NA. (a) The UV chromatogram of four flavonoid glycosides. (b) The UV chromatogram of ultrafiltration screening experiment with 5 μM NA. (c) The UV chromatogram of ultrafiltration screening experiment with 10 μM NA.

At 5 μM NA, only the flavonoid aglycones: apigenin and luteolin possessed NA binding activities but when NA concentration was increased to 10 μM, the other four ligands were observed (Fig. 4(c)) because weak ligands can also be identified with the increase in NA concentration. The results further proved that real inhibitors of NA in *Compound Indigowoad Root Granule* were the metabolites of the compounds in extract and not the unmetabolized extracts.

4. Conclusions

In this study, eighteen compounds from the n-butanol extract of *Compound Indigowoad Root Granule* were identified by liquid chromatography–tandem mass spectrometry (LC–MS/MS). The ultrafiltration LC–MS/MS method used to test for n-butanol extract of *Compound Indigowoad Root Granule* and standard flavones binding activities on NA was reliable and reproducible. The results showed that flavonoid aglycones had strong NA binding activities, while the flavonoid glycosides possessed weak or no NA binding activities. Based on the results of this study, the real inhibitors of NA in *Compound Indigowoad Root Granule* are the metabolites of the compounds in the extract rather than the unmetabolized extract. The experimental results explained the antiviral mechanism of *Compound Indigowoad Root Granule* to some extent, which also provided some guidance for the discovery of potential anti-influenza virus medicine from natural products.

References

[1] N.A. Meanwell, M. Krystal, Taking aim at a moving target-inhibitors of influenza virus part 1: virus adsorption, entry and uncoating, Drug Discovery Today 1 (1996) 316–324.

[2] M. von Itzstein, W.Y. Wu, G.B. Kok, M.S. Pegg, J.C. Dyason, B. Jin, T. van Phan, M.L. Smythe, H.F. White, S.W. Oliver, P.M. Colman, J.N. Varghese, D. MichaelRyan, J.M. Woods, R.C. Bethell, V.J. Hotham, J.M. Cameron, C.R. Penn, Rational design of potent sialidase-based inhibitors of influenza virus replication, Nature 363 (1993) 418–423.

[3] P. Palese, K. Tobita, M. Ueda, R.W. Compans, Characterization of temperature sensitive influenza virus mutants defective in neuraminidase, Virology 61 (1974) 396–410.

[4] C. Liu, M.C. Eichelberger, R.W. Compans, G.M. Air, Influenza type A virus N does not play a role in viral entry, replication, assembly, or budding, J. Virol. 69 (1995) 1099–1106.

[5] A. Kitching, A. Roche, S. Balasegaram, R. Heathcock, H. Maguire, Oseltamivir adherence and side effects among children in three London schools affected by influenza A (H1N1) v, May 2009 – an internet-based cross-sectional survey, EuroSurveillance 30 (2009) 1–4.

[6] T. Kunikata, T. Tatefuji, H. Aga, K. Iwaki, M. Ikeda, M. Kurimoto, Indirubin inhibits inflammatory reactions in delayed-type hypersensitivity, Eur. J. Pharmacol. 410 (2000) 93–100.

[7] N.K. Mak, C.Y. Leung, X.Y. Wei, X.L. Shena, R.N.S. Wonga, K.N. Leungd, M.C. Funge, Inhibition of RANTES expression by indirubin in influenza virus infected human bronchial epithelial cells, Biochem. Pharmacol. 67 (2004) 167–174.

[8] J.J. Liu, R.W. Huang, D.J. Lin, X.Y. Wu, Q. Lin, Antiproliferation effects of ponicidin on human myeloid leukemia cells in vitro, Oncol. Rep. 13 (2005) 653–657.

[9] H.Y. Tang, D. Yan, S.F. Zhang, H.B. Li, R.H. Liu, X.H. Xiao, Agglutinated activity bioassay method for the determination of antivirus potency of *Banlangen granula*, Acta Pharmacol. Sin. 45 (2010) 479–483.

[10] T. Nagai, R. Moriguchi, Y. Suzuki, T. Tomimori, H. Yamada, Mode of action of the anti-influenza virus activity of plant flavonoid, 5,7,4'-trihydroxy-8-methoxyflavone, from the roots of *Scutellaria baicalensis*, Antivir. Res. 26 (1995) 11–25.

[11] M.E. Schurdak, M.J. Voorbach, L. Gao, X. Cheng, K.M. Comess, S.M. Rottinghaus, U. Warrior, H.N. Truong, D.J. Burns, B.A. Beutel, Complex gel permeation assays for screening combinatorial libraries, J. Biomol. Screen. 6 (2001) 313–323.

[12] L.M. von Itzstein, W.Y. Wu, T.V. Phen, J. Betty, Antiviral 4-substituted-2-deoxy-2,3-didehydro derivatives of alpha D neuraminic acid, EP Appl. 92309684.6, 1993.

[13] T. Nagai, Y. Miyaichi, T. Tomimori, H. Yamada, Inhibitor of mouse liver sialidase by plant flavonoids, Biochem. Biophys. Res. Commun. 163 (1989) 25–31.

[14] B.M. Johnson, D. Nikolic, R.B. van Breemen, Applications of pulsed ultrafiltration–mass spectrometry, Mass Spectrom. Rev. 21 (2002) 76–86.

[15] Y.K. Sun, C.G. Gu, X.M. Liu, W.Z. Liang, P. Yao, J.L. Bolton, R.B. van Breemen, Ultrafiltration tandem mass spectrometry of estrogens for characterization of structure and affinity for human estrogen receptors, J. Am. Soc. Mass Spectrom. 16 (2005) 271–279.

[16] D.T. Liu, J. Guo, Y. Luo, D.J. Broderick, M.I. Schimerlik, J.M. Pezzuto, R.B. van Breemen, Screening for ligands of human retinoid X receptor using ultrafiltration mass spectrometry, Anal. Chem. 79 (2007) 9398–9402.

[17] H. Li, F.R. Song, J.P. Xing, R. Tsao, Z.Q. Liu, S.Y. Liu, Screening and structural characterization of α-glucosidase inhibitors from Hawthorn leaf flavonoids extract by ultrafiltration LC-DAD-MSn and SORI-CID FTICR MS, J. Am. Soc. Mass Spectrom. 20 (2009) 1496–1503.

[18] Editorial Committee of Pharmacopoeia of People's Republic of China, Drug Standard of Ministry of Public Health of the People's Republic of China, People's Medical Publishing House, Beijing, China, Volume 12 [M], 1977.

[19] J. Yan, Studies on Chemical Composition's Isolation Analysis and Activity's Evaluation of Compound Indigowoad Root Granule, Jilin University, Changchun, 2008.

[20] L.V. Gubareva, R.G. Webster, F.G. Hayden, Detection of influenza virus resistance to neuraminidase inhibitors by an enzyme inhibition assay, Antivir. Res. 53 (2002) 47–61.

[21] M. Potier, L. Mameli, M. Belisle, L. Dallaire, S.B. Melancon, Fluorometric assay of neuraminidase with a sodium (4-methylumbelliferyl-α-D-N-acetylneuraminate) substrate, Anal. Biochem. 94 (1979) 287–296.

[22] T. Mohn, I. Plitzko, M. Hamburger, A comprehensive metabolite profiling of *Isatis tinctoria* leaf extracts, Phytochemistry 70 (2009) 924–934.

[23] X.Y. Deng, G.H. Gao, S.N. Zheng, F.M. Li, Qualitative and quantitative analysis of flavonoids in the leaves of *Isatis indigatica* Fort. by ultra-performance liquid chromatography with PDA and electrospray ionization tandem mass spectrometry detection, J. Pharm. Biomed. Anal. 48 (2008) 562–567.

[24] F. Ferreres, P.B. Andrade, P. Valentão, A. Gil-Izquierdo, Further knowledge on barley (*Hordeum vulgare* L.) leaves O-glycosyl-C-glycosyl flavones by liquid chromatography–UV diode-array detection-electrospray ionisation mass spectrometry, J. Chromatogr. A 1182 (2008) 56–64.

[25] T. Nagai, Y. Miyaicht, T. Tomimori, Y. Suzuki, H. Yamada, Inhibition of influenza virus sialidase and anti-influenza virus activity by plant flavonoids, Chem. Pharm. Bull. 38 (1990) 1329–1332.

[26] Y. Zhang, X.W. Tie, B.L. Bao, X.Q. Wu, Y. Zhang, Metabolism of flavone C-glucosides and p-coumaric acid from antioxidant of bamboo leaves (AOB) in rats, Br. J. Nutr. 97 (2007) 484–494.

[27] Y. Liu, M. Hu, Absorption and metabolism of flavonoids in the CACO-2 cell culture model and a perused rat intestinal model, Drug Metab. Dispos. 30 (2002) 370–377.

The effect of anti-tubercular drug, ethionamide on the secondary structure of serum albumins: A biophysical study☆

Umesha Katrahalli, Veerendra Kumar A. Kalalbandi, Seetharamappa Jaldappagari*

Department of Chemistry, Karnatak University, Dharwad 580 003, India

ARTICLE INFO

ABSTRACT

Serum albumin (SA) is the principal extra cellular protein with higher concentration in the blood plasma and acts as a carrier for many drugs to different molecular targets. The present work is designed to investigate the mechanism of interaction between the protein and an anti-tubercular drug, ethionamide (ETH) at the physiological pH by different molecular spectroscopic techniques viz., fluorescence, UV absorption, CD and FTIR. The interaction of SA with ETH was studied by following the quenching of intrinsic fluorescence of protein by ETH at different temperatures. The Stern–Volmer quenching constant, binding constant and the binding site numbers were calculated from fluorescence results. The results indicated the presence of static quenching mechanism in both HSA–ETH and BSA–ETH systems. The distances of separation between the acceptor and donor were calculated based on the theory of fluorescence resonance energy transfer and were found to be 2.35 nm and 2.18 nm for HSA–ETH and BSA–ETH systems, respectively. The conformational changes in protein were confirmed from UV absorption, CD and FTIR spectral data. Displacement experiments with different site probes revealed that the site I was the main binding site for ETH in protein. Effect of some metal ions was also investigated.

© 2011 Elsevier B.V. All rights reserved.

1. Introduction

Spectroscopic techniques such as fluorescence, UV absorption, FTIR and circular dichroism are useful in the study of interactions of small molecules with protein [1]. Binding of a drug with the albumin affects its pharmacological effect since only the free fraction of drug exhibits therapeutic activity. In the body of an animal, serum albumin is the main transporting protein which has the ability to bind and transport the various exogenous and endogenous ligands by forming complexes. A great deal of attention has been paid to investigate the interaction of SA with a number of active natural or synthetic ligands because it has its own importance in clinical and pharmaceutical fields [2]. Among serum albumins, bovine serum albumin (BSA) and human serum albumin (HSA) are involved in transportation of small ligands including drugs. The structure of BSA has 76% similarity with that of HSA [3]. HSA has only one tryptophan (Trp-214) which is located in sub domain IIA, where as BSA has two tryptophans moieties (Trp-135 and Trp-214), located in sub-domain IA and IIA, respectively [4].

Tuberculosis continues to be a major worldwide epidemic disease and drugs such as isoniazid (INH) and rifampicin have historically been successful in the treatment of this disease [5]. Ethionamide (ETH, Fig. 1), 2-ethylpyridine-4-carbothioamide, a commonly used antibiotic, is used in the treatment of tuberculosis. This drug presents strong bacteriostatic properties against some mycobacteria and is rather more active against isoniazid-resistant mutants [6]. Like INH, this drug is thought to be a prodrug, which must be converted to its active form by the bacterial cell. In the present study, we have investigated the mechanism of interaction of ETH with protein (HSA and BSA) employing different spectroscopic methods.

2. Materials and methods

2.1. Materials

HSA (fatty acid free), BSA (Fraction V, approximately 99%; protease free and essentially γ-globulin free), warfarin, ibuprofen and digitoxin were purchased from Sigma–Aldrich Chemical Co., St. Louis, USA. Pure sample of ethionamide was gifted by Medopharm, Bengalooru, India. All the investigations were carried out in 0.1 M phosphate buffer solution of pH 7.4. All the chemicals used were of analytical reagent grade and Millipore water was used throughout the experiment.
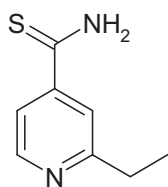
Fig. 1. Structure of ethionamide (ETH).

2.2. Methods

2.2.1. Fluorescence studies

The fluorescent measurements were carried out on a Hitachi Instrument F-7000 spectrofluorometer provided with a 1 cm quartz cell equipped with a 150 W Xenon lamp at 301 K. The fluorescence intensity of both HSA and BSA at increasing molar ratios of ETH to SA was recorded upon excitation at 280 nm for HSA and at 296 nm for BSA keeping 5 nm as excitation and emission slit widths. For this, the concentration of protein was fixed at 2.5 μM while that of the drug was varied from 5 to 50 μM. Fluorescence measurements were carried out at 294 K, 301 K and 310 K. For this, the instrument was thermostatically controlled by a Cyberlab CB2000 circulating water bath.

2.2.2. Energy transfer between ETH and protein

The emission spectrum of protein (each of 2.5 μM) upon excitation at 280 nm for HSA and at 296 nm for BSA was recorded. The absorption spectrum of 2.5 μM ETH was also recorded in the wavelength range similar to that of emission spectrum. The overlap of these two spectra was used to calculate the energy transfer based on the Förster's theory.

2.2.3. Absorption studies

The absorption measurements of protein were recorded on a CARY BIO-50 double beam spectrophotometer with a 1 cm quartz cell equipped with a 150 W Xenon lamp at 301 K. Absorbance values of protein in the absence and presence of ETH were recorded in the range of 250–350 nm. The concentration of HSA/BSA was fixed at 2.5 μM while that of the drug was varied from 5 to 50 μM.

2.2.4. Circular dichroism studies

Circular dichroism measurements were made on a JASCO-810 spectropolarimeter (Tokyo, Japan) using a quartz cell of 0.1 cm with three scans averaged for each CD spectrum in the range of 200–250 nm. The molar ratios of protein to drug concentrations were maintained at 1:2, 1:4 and 1:6 and CD spectra were recorded.

2.2.5. FTIR spectroscopic measurements

The infrared spectra of protein solutions were obtained on a Thermo Nicolet-5700 FTIR spectrophotometer via the attenuated total reflection (ATR) method with resolution of 4 cm^{-1} and 60 scans.

Spectra processing procedure: IR spectra of protein and buffer solutions were recorded separately under similar conditions. The absorbance of buffer solution was then subtracted from that of protein solution (to get the FTIR spectrum of the protein alone). Later, the spectrum of drug, and protein–drug system (along with buffer solution) was noted down under similar conditions. Further, the absorbance of drug solution was subtracted from that of protein–drug solution to get the FTIR spectrum of protein–ETH complex. The subtraction criterion was that the original spectrum of protein solution between 2200 and 1800 cm^{-1} was not depicted any significant signal in this region [7].
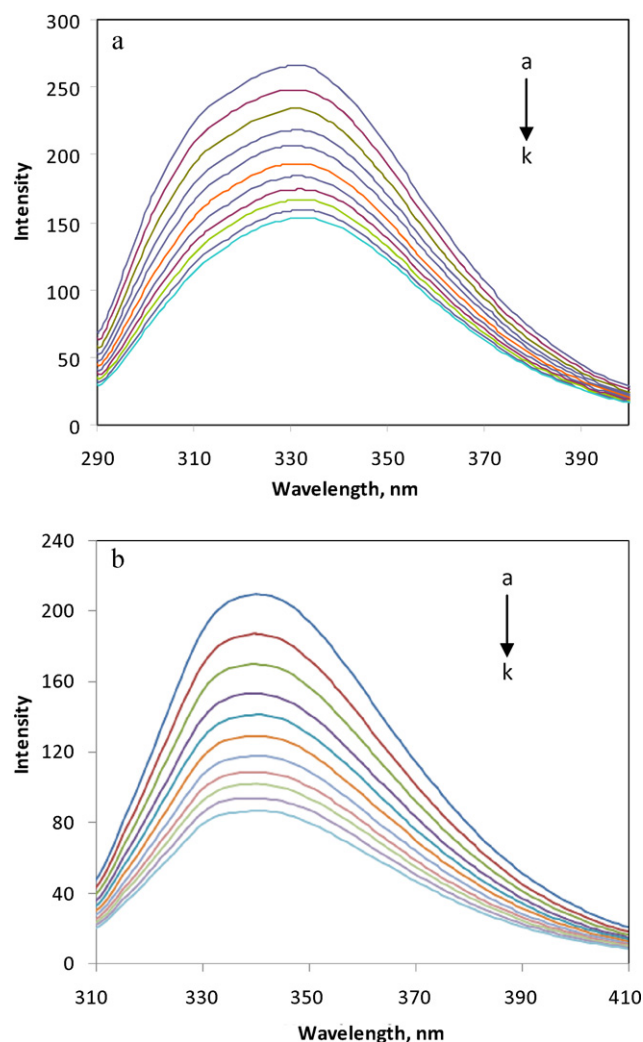
Fig. 2. Fluorescence spectra of HSA (a) and BSA (b) (2.5 μM) in presence of ETH: (a) 0, (b) 5, (c) 10, (d) 15, (e) 20, (f) 25, (g) 30, (h) 35, (i) 40, (j) 45 and (k) 50 μM.

2.2.6. Competitive binding studies

The competitive binding studies were performed using different competitors, warfarin for site I, ibuprofen for site II and digitoxin for site III by keeping the concentration of protein and the competitor, constant (each of 2.5 μM). The fluorescence quenching titration was performed as before to determine the binding constant of ETH–protein in the presence of the above said site probes.

3. Results and discussion

3.1. Fluorescence quenching studies

In order to understand the quenching mechanism operating between ETH and protein, the fluorescence quenching experiments were performed. The fluorescence spectra of HSA (Fig. 2a) and BSA (Fig. 2b) were recorded in the presence of increasing amounts of ETH, separately. In these spectra, we noticed that the fluorescence intensity of protein decreased regularly with increasing concentrations of ETH indicating the interaction between the drug and protein.

The fluorescence results were preliminarily analyzed using the Stern–Volmer equation [8] shown below:

$$(1)\quad \frac{F_0}{F} = 1 + K_{SV}[Q] = 1 + k_q\tau_0[Q]$$

where F and F_0 are the fluorescence intensities with and without the quencher, respectively, k_q is the bimolecular quenching rate constant, K_{SV} is the Stern–Volmer quenching constant, τ_0 is

Table 1
Stern–Volmer quenching constants and modified Stern–Volmer association constants for HSA–ETH and BSA–ETH systems at different temperatures.

System	T (K)	$K_{SV} \times 10^{-4}$ (L mol^{-1})	$K_q \times 10^{-12}$ (L mol^{-1} s^{-1})	R^2	$K_a \times 10^{-4}$ (L mol^{-1})	R^2
HSA	294	2.13 ± 0.041	4.26 ± 0.041	0.997	1.01 ± 0.031	0.999
	301	1.90 ± 0.024	3.80 ± 0.024	0.999	1.33 ± 0.026	0.999
	310	1.49 ± 0.034	2.98 ± 0.034	0.999	1.54 ± 0.028	0.991
BSA	294	2.72 ± 0.011	5.44 ± 0.011	0.999	1.03 ± 0.022	0.999
	301	2.31 ± 0.036	4.62 ± 0.036	0.999	2.01 ± 0.041	0.999
	310	2.14 ± 0.023	4.28 ± 0.023	0.999	3.15 ± 0.027	0.999

the average life time of biomolecule without the quencher and its value was reported to be 5 ns [9] and [Q] is the concentration of the quencher. The quenching rate constant, k_q could be calculated using the equation shown below:

$$K_{SV} = k_q \tau_0 \tag{2}$$

The Stern–Volmer plots (Fig. 3a and b) revealed the presence of static quenching as evident from decreased K_{SV} values (Table 1) with increase in temperature [10,11]. Further, the higher values of k_q compared to that reported for the maximum quenching rate constant of bimolecular diffusion collision (2.0×10^{10} L mol^{-1} s^{-1}) supported the static quenching mechanism between the drug and protein [12–14]. Therefore, the quenching data were further analyzed using the modified Stern–Volmer equation shown below [8,15]:

$$\frac{F_0}{F_0 - F} = \frac{1}{f_a K_a [Q]} + \frac{1}{f_a} \tag{3}$$

where F and F_0 are the fluorescence intensities of protein with and without ETH, respectively; K_a is the Stern–Volmer quenching constant of the accessible fraction, [Q] is the concentration of quencher and f_a is the fraction of the initial fluorescence of protein that is accessible to the quencher. The plot of $F_0/(F_0 - F)$ versus $1/[Q]$ (figures not shown) yielded f_a^{-1} as the intercept on y axis and $(f_a K_a)^{-1}$ as the slope. The values of f_a for ETH–HSA and ETH–BSA were found to be 1.25 and 1.27, respectively, indicating that only 80.31% and

78.88% of the initial fluorescence of HSA and BSA was accessible for quenching. The results are listed in Table 1.

The fluorescence data was also used to evaluate the binding constant, K and the number of binding sites, n for drug–protein complex using the equation shown below [16]:

$$\frac{\log(F_0 - F)}{F} = \log K + n \; \log[Q] \tag{4}$$

From the intercept and slope of the graph of $\log[(F_0 - F)/F]$ versus $\log[Q]$ (figures not shown), the values of K were found to be $(3.95 \pm 0.052) \times 10^4$, $(2.72 \pm 0.035) \times 10^4$ and $(2.42 \pm 0.032) \times 10^4$ M^{-1} for HSA–ETH and $(1.30 \pm 0.024) \times 10^5$, $(6.43 \pm 0.054) \times 10^4$ and $(5.06 \pm 0.046) \times 10^4$ M^{-1} for BSA–ETH at 294, 301 and 310 K, respectively. The values of n (1.04–1.16) were found to be close to unity indicating the presence of single class of binding site for ETH in both HSA and BSA. The decreased K values with increase in temperature suggested the lesser stability of ETH–protein complex at higher temperature.

3.2. Binding mode

Thermodynamic parameters, ΔH^0 and ΔS^0 were evaluated using the van't Hoff's equation shown below:

$$\log K = \frac{-\Delta H^0}{2.303RT} + \frac{\Delta S^0}{2.303R} \tag{5}$$

where K is the binding constant and R is the gas constant. The values of ΔH^0 and ΔS^0 were calculated from the slope and intercept, respectively, of the plot of $\log K$ versus $1/T$ (figures not shown). The value of free energy change was evaluated using the Gibbs–Helmholtz equation given below [17]:

$$\Delta G^0 = \Delta H^0 - T\Delta S^0 \tag{6}$$

The corresponding values for ETH–HSA and ETH–BSA are summarized in Table 2. Both processes were found to be spontaneous as evident from negative ΔG^0 values. The negative ΔH^0 and positive ΔS^0 values indicated that both hydrogen bonding and hydrophobic forces played a major role in the formation of ETH–HSA complex. Where as the negative values of both ΔH^0 and ΔS^0 for ETH–BSA revealed that the van der Waals forces and hydrogen bonding played a significant role in the formation of ETH–BSA complex [18].

Fig. 3. The Stern–Volmer curves for quenching of ETH with HSA (a) and BSA (b) at different temperatures.

Table 2
The relative thermodynamic parameters of HSA–ETH and BSA–ETH systems at different temperatures.

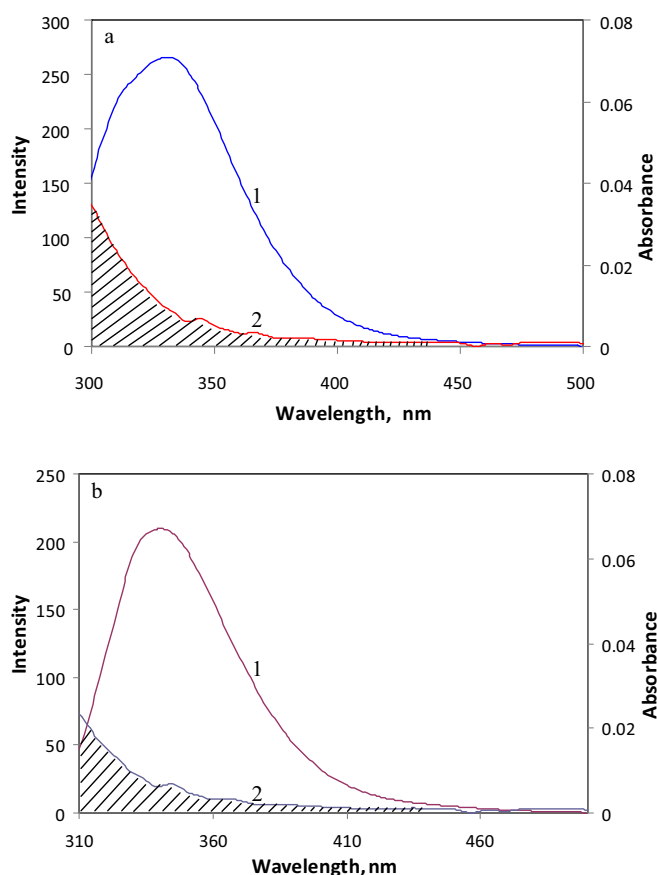| System	T (K)	ΔG^0 (kJ mol^{-1})	ΔH^0 (kJ mol^{-1})	ΔS^0 (J mol^{-1} K^{-1})
HSA	294	-25.88 ± 0.008		
	301	-25.85 ± 0.014	-23.11 ± 0.012	9.27 ± 0.016
	310	-26.02 ± 0.011		
BSA	294	-28.80 ± 0.022		
	301	-28.33 ± 0.008	-44.80 ± 0.022	-54.5 ± 0.014
	310	-27.92 ± 0.016		

Fig. 4. The overlap of fluorescence spectrum of (a) HSA/BSA (1) with the absorption spectrum of ETH (2); {[HSA/BSA]:[ETH] = 1:1}.

3.3. Fluorescence resonance energy transfer

The spectral studies revealed that both HSA and BSA formed complexes with ETH. The distance r between the protein residue and acceptor was calculated based on fluorescence resonance energy transfer [19]. This distance of separation and the extent of spectral overlap determine the extent of energy transfer. The overlap of fluorescence emission spectrum of protein and the absorption spectrum of ETH is shown in Fig. 4a and b. The efficiency of energy transfer, E is related to r as shown below:

$$E = 1 - \frac{F}{F_0} = \frac{R_0^6}{R_0^6 + r^6} \tag{7}$$

where R_0 is the critical distance when the efficiency of energy transfer is 50%, which is calculated using the equation given below:

$$R_0^6 = 8.8 \times 10^{-25} k^2 \eta^{-4} \Phi J \tag{8}$$

where k^2 is the spatial orientation factor of the dipole, η is the refractive index of the medium, Φ is the fluorescence quantum yield of the donor and J is the overlap integral of the fluorescence emission spectrum of the donor and the absorption spectrum of the acceptor. The value of J was evaluated using the equation shown below:

$$J = \frac{\sum F(\lambda)\varepsilon(\lambda)\lambda^4 \Delta\lambda}{\sum F(\lambda)\Delta\lambda} \tag{9}$$

where $F(\lambda)$ is the fluorescence intensity of the fluorescent donor of wavelength, λ and $\varepsilon(\lambda)$ is the molar absorption co-efficient of the acceptor at wavelength, λ. In the present case, $K^2 = 2/3$, $\eta = 1.36$ and $\Phi = 0.118$ for HSA–ETH system [20] and $K^2 = 2/3$, $\eta = 1.336$ and $\Phi = 0.15$ for BSA–ETH system [10]. From Eqs. (7) to (9), we were
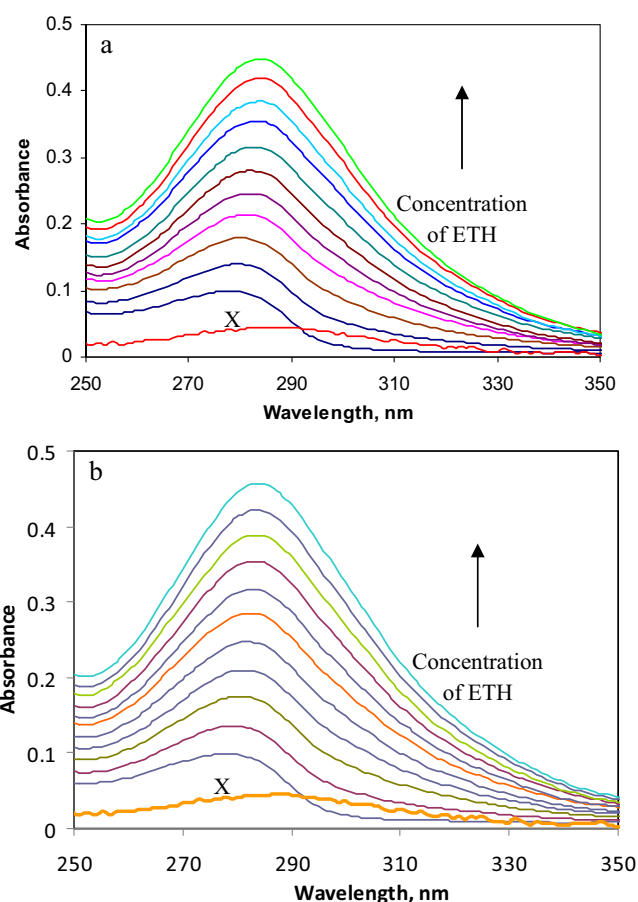
Fig. 5. Absorption spectra of HSA (a), BSA (b), ETH and HSA/BSA–ETH system. Protein concentration was maintained at 2.5 μM and that of ETH at 5 μM. (x) refers to ETH only.

able to calculate that $J = 2.33 \times 10^{-15}$ and 2.14×10^{-15} cm^3 L mol^{-1}, $R_0 = 2.86$ and 3.11 nm, $E = 0.23$ and 0.28 and $r = 3.50$ and 3.40 nm for HSA–ETH and BSA–ETH systems, respectively. The value of $r < 8$ nm [21,22] observed in the present study revealed the presence of static quenching mechanism [20] and the transfer of energy between the protein and drug.

3.4. UV absorption studies

UV absorption spectra of protein in the presence of increasing amounts of ETH are shown in Fig. 5a and b. It could be noticed from the figure that the intensity of absorption of HSA/BSA increased with successive addition of ETH. Further, a red shift in the maximum peak of protein was observed probably due to the formation of complex between ETH and HSA/BSA [10,23].

3.5. Conformational changes in protein upon interaction with ETH

3.5.1. Circular dichroism (CD) analysis

Circular dichroism, a sensitive technique to monitor the conformational changes in the protein [24], was employed in the present study. For this, the CD spectra of HSA and BSA in the absence and presence of different concentrations of ETH were recorded (Fig. 6a and b, respectively). The CD spectra of protein (HSA/BSA) showed two minima at 208 nm and 222 nm, characteristics of an α-helical structure of the protein. The negative peaks at 208–209 nm and 222–223 nm were attributed $n \rightarrow \pi^*$ transition for peptide bond of the α-helix [25]. The helical content of free and bound protein was
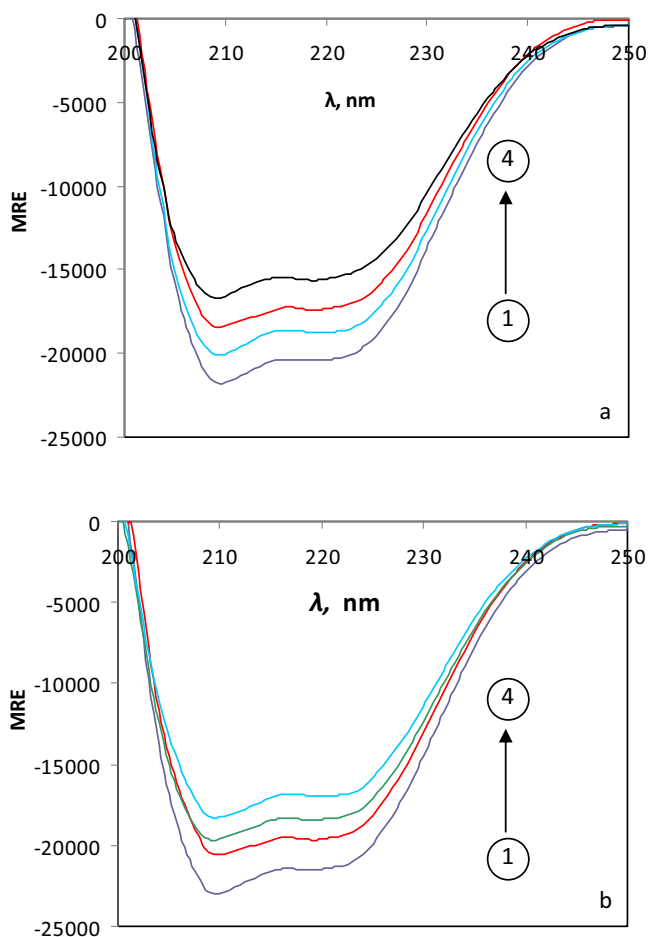
Fig. 6. CD spectra of HSA–ETH (a) and BSA–ETH (b) systems. HSA/BSA concentration was fixed at 2.5 μM (1). In HSA/BSA–ETH system, the ETH concentration was kept at 5 (2), 10 (3), and 15 μM (4).

calculated from the mean residue elipticity (MRE) values at 208 nm using the equation shown below [26]:

$$MRE = \frac{\theta_{obs}}{C_p n l \times 10} \quad (\text{in units of } deg\, cm^2\, dmol^{-1}) \qquad (10)$$

θ_{obs} is the observed CD (in milli degrees), C_p is the concentration of the protein, n is the number of amino acid residues and l is the path length of the cell (in cm).

$$\alpha\text{-Helix}(\%) = \frac{-MRE_{208} - 4000}{33,000 - 4000} \times 100 \qquad (11)$$

where MRE_{208} is the observed MRE value at 208 nm, 4000 is the MRE of α-form and random coil conformation cross at 208 nm and 33,000 is the MRE value of a pure α-helix at 208 nm.

The α-helicity decreased gradually from $(58.9 \pm 0.9)\%$ in free HSA to $(42.7 \pm 0.5)\%$ in bound HSA and from $(62.6 \pm 0.8)\%$ in free BSA to $(47.1 \pm 0.4)\%$ in bound BSA thereby indicating that the ETH has altered the hydrogen bonding networks of protein. Further, it also revealed the changes in secondary structure of the respective protein. The shapes of CD spectra of HSA and BSA in the absence and presence of ETH were observed to be similar indicating that the structure of protein was predominantly α-helical even after binding with ETH [27].

3.5.2. FTIR analysis

In order to get more information on binding mechanism and changes in conformation of the protein upon interaction with ETH, FTIR spectra of protein alone and protein–drug systems were recorded. Amide I band is generally more sensitive compared to amide II band for the changes in secondary structure of the protein [28]. The amide I band occurs in the region of 1600–1700 cm^{-1} (mainly C=O stretching vibrations of amide groups) while amide II occurs around 1500–1600 cm^{-1} (mainly C–N stretch couple with N–H bending frequency). Fig. 7a and b shows that the peak position of amide I and amide II bands are shifted from 1648.5 to 1644.1 cm^{-1} and from 1561.3 to 1552.8 cm^{-1} in HSA–ETH system, and from 1651.2 to 1647.4 cm^{-1} and from 1558.5 to 1551.7 cm^{-1} in BSA–ETH system, respectively. This indicated that
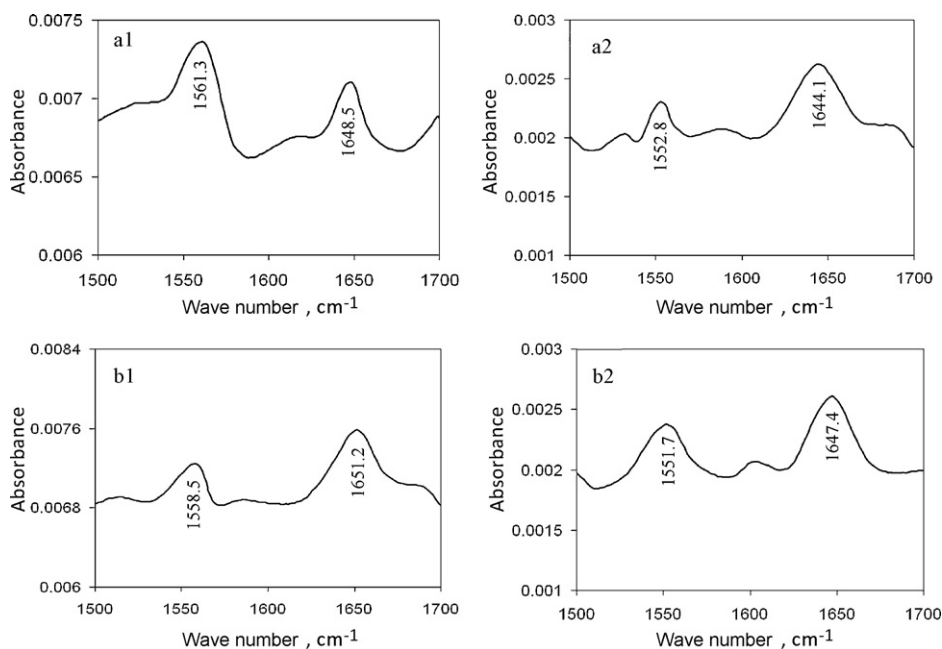
Fig. 7. FTIR spectra and difference spectra of HSA/BSA; the FTIR spectra of free HSA (a1)/BSA (b1) (subtracting the absorption of buffer solution from the absorption of protein solution) and the FTIR difference spectra of HSA (a2)/BSA (b2) (subtracting the absorption of ETH-free form from that of ETH–HSA/BSA bound form) in phosphate buffer; $C_{HSA/BSA} = 5$ μM and $C_{ETH} = 5$ μM.

Table 3
Binding constant values of HSA–ETH and BSA–ETH systems in presence of site probes at 301 K.

System	K (M^{-1}) without site probe	K (M^{-1}) with warfarin	K (M^{-1}) with ibuprofen	K (M^{-1}) with digitoxin
HSA + ETH	$2.72 \times 10^4 \pm 0.022$	$1.67 \times 10^3 \pm 0.028$	$2.70 \times 10^4 \pm 0.034$	$2.72 \times 10^4 \pm 0.012$
BSA + ETH	$6.43 \times 10^4 \pm 0.012$	$5.16 \times 10^3 \pm 0.023$	$6.40 \times 10^4 \pm 0.014$	$6.42 \times 10^4 \pm 0.018$

the secondary structure of protein was changed upon interaction with ETH. The ETH has interacted with C=O and C–N groups in protein polypeptides and resulted in rearrangement of polypeptide carbonyl hydrogen bonding network [29].

3.6. Site specific probe

In order to locate the binding site of ETH in protein, the competitive binding experiments were performed using different site competitors viz. warfarin, ibuprofen and digitoxin for sites I, II and III respectively as per Sudlow et al. [30] and Sjoholm et al. [31] classification of binding sites. For this, emission spectra of ETH–protein and ternary mixtures of protein–ETH-site probe were recorded, separately. The corresponding binding constant values were evaluated and are shown in Table 3. In both cases (ETH–HSA and ETH–BSA systems), the binding constant values decreased remarkably in the presence of warfarin while this value remained almost same in the presence of ibuprofen and digitoxin. These results revealed that the warfarin displaced ETH from the binding site while ibuprofen and digitoxin had a little effect on the binding of ETH to HSA/BSA. Hence, we concluded that the ETH bound to site I of HSA/BSA, which is located in the hydrophobic pocket of subdomain IIA.

3.7. Effect of metal ions

In plasma, there are some of the metal ions which can affect the binding of drugs to serum albumins. Hence, the effects of some of common metal ions viz., K$^+$, Mn^{2+}, Ni^{2+}, Co^{2+}, Zn^{2+}, and Cu^{2+} on the binding of ETH to protein was investigated at 301 K by fluorescence technique. For this, the concentration of both protein and metal ion was kept constant (2.5 µM) while that of the drug solution was varied (5–50 µM). The corresponding results are given in Table 4. The decreased binding constant of ETH–HSA in the presence of Cu^{2+}, Co^{2+}, Ni^{2+} and K$^+$ might cause the drug to be quickly cleared from the blood [32]. This might lead to the need of higher doses of ETH to achieve the desired therapeutic effect. However, the binding constant increased in the presence of Zn^{2+} and Mn^{2+} thereby making the ETH to be retained for longer time in the blood [33]. This would lead to lesser doses of drug to achieve the intended therapeutic effect. Further, it was noticed that the binding constant of ETH–BSA decreased in the presence of all of the above ions thereby causing ETH to be quickly cleared from the blood. This might necessitate for higher doses of ETH in the presence of above metal ions.

Table 4
The effect of metal ions on the binding of ETH to protein at 301 K.

Metal ions	Binding constant (M^{-1})	
	HSA + ETH	BSA + ETH
Without metal ion	$2.72 \times 10^4 \pm 0.022$	$6.43 \times 10^4 \pm 0.022$
With Cu^{2+}	$2.22 \times 10^4 \pm 0.012$	$1.93 \times 10^4 \pm 0.026$
With Co^{2+}	$2.14 \times 10^4 \pm 0.018$	$4.59 \times 10^4 \pm 0.014$
With Zn^{2+}	$3.85 \times 10^4 \pm 0.027$	$3.48 \times 10^4 \pm 0.031$
With Ni^{2+}	$2.52 \times 10^4 \pm 0.011$	$2.44 \times 10^4 \pm 0.024$
With Mn^{2+}	$3.73 \times 10^4 \pm 0.017$	$2.13 \times 10^4 \pm 0.015$
With K$^+$	$1.51 \times 10^4 \pm 0.032$	$5.29 \times 10^4 \pm 0.033$

4. Conclusions

In this paper, the interaction between ethionamide and serum albumin was investigated employing different spectroscopic techniques. The results revealed that the secondary structure of protein was affected upon interaction with the drug. Fluorescence results indicated the presence of static quenching mechanism in the binding of ETH to protein. Based on spectral data we have concluded that the ETH bound to site I of protein, which is located in the hydrophobic pocket of subdomain IIA.

References

[1] V. Anbazhagan, R. Renganathan, Study on the binding of 2,3-diazabicyclo[2.2.2]oct-2-ene with bovine serum albumin by fluorescence spectroscopy, J. Lumin. 128 (2008) 1454–1458.
[2] Q. Lu, C. Ba, D. Chen, Investigating noncovalent interactions of rutin–serum albumin by capillary electrophoresis-frontal analysis, J. Pharma. Biomed. Anal. 47 (2008) 888–891.
[3] B.X. Huang, H.Y. Kim, C. Dass, Probing three-dimensional structure of bovine serum albumin by chemical cross-linking and mass spectrometry, J. Am. Soc. Mass Spectrom. 15 (2004) 1237–1247.
[4] D.C. Carter, J.X. Ho, Structure of serum albumin, Adv. Protein Chem. 45 (1994) 153–203.
[5] T.A. Vannelli, A. Dykman, P.R. Ortiz de Montellano, The antituberculosis drug ethionamide is activated by a flavoprotein monooxygenase, J. Biol. Chem. 277 (2002) 12824–12829.
[6] A. Quemard, G. Laneelle, C. Lacave, Mycolic acid synthesis: a target for ethionamide in mycobacteria? Antimicrob. Agents Chemother. 36 (1992) 1316–1321.
[7] A. Dong, P. Huang, W.S. Caughey, Protein secondary structure in water from second derivative amide I infra red spectra, Biochemistry 29 (1990) 3303–3308.
[8] J.R. Lakowicz, Principles of Fluorescence Spectroscopy, 3rd ed., Plenum Press, New York, NY, USA, 2006, pp. 277, 278, 289.
[9] N. Tayeh, T. Rungassamy, J.R. Albani, Fluorescence spectral resolution of tryptophan residues in bovine and human serum albumins, J. Pharm. Biomed. Anal. 50 (2009) 107–116.
[10] F.L. Cui, J. Fan, J.P. Lib, Z.D. Hu, Interactions between 1-benzoyl-4-p-chlorophenyl thiosemicarbazide and serum albumin: investigation by fluorescence spectroscopy, Bioorg. Med. Chem. 12 (2004) 151–157.
[11] F.L. Cui, J.L. Wang, Y.R. Cui, J.P. Li, Fluorescent investigation of the interactions between N-(p-chlorophenyl)-N′-(1-naphthyl) thiourea and serum albumin: synchronous fluorescence determination of serum albumin, Anal. Chim. Acta 571 (2006) 175–183.
[12] J.R. Lakowicz, G. Weber, Quenching of fluorescence by oxygen. A probe for structural fluctuations in macromolecules, Biochemistry 12 (1973) 4161–4170.
[13] W.R. Ware, Oxygen quenching of fluorescence in solution: an experimental study of the diffusion process, J. Phys. Chem. 66 (1962) 455–458.
[14] G.Z. Chen, X.Z. Huang, J.G. Xu, Z.Z. Zheng, Z.B. Wang, The Methods of Fluorescence Analysis, 2nd ed., Science Press, Beijing, 1990, p. 2.
[15] X. Wu, J. Liu, H. Huang, W. Xue, X. Yao, J. Jin, Interaction studies of aristolochic acid I with human serum albumin and the binding site of aristolochic acid I in subdomain IIA, Int. J. Biol. Macromol. 49 (2011) 343–350.
[16] F. Ge, C. Chen, D. Liu, B. Han, X. Xiong, S. Zhao, Study on the interaction between theasinesin and human serum albumin by fluorescence spectroscopy, J. Lumin. 130 (2010) 168–173.
[17] Q. Zhanga, Y. Nia, S. Kokot, Molecular spectroscopic studies on the interaction between ractopamine and bovine serum albumin, J. Pharm. Biomed. Anal. 52 (2010) 280–288.
[18] D.P. Ross, S. Subramanian, Thermodynamics of protein association reactions: forces contributing to stability, Biochemistry 20 (1981) 3096–3102.

[19] A. Sharma, S.G. Schulman, Introduction to Fluorescence Spectroscopy, John Wiley & Sons, Inc., New York, 1999.
[20] G. Hong, L. Liandi, L. Jiaqin, Q. Kong, C. Xingguo, Z. Hu, The study on the interaction between human serum albumin and a new reagent with antitumour activity by spectrophotometric methods, J. Photochem. Photobiol. A 167 (2004) 213–221.
[21] Y.J. Hu, Y. Liu, J.B. Wang, X.H. Xiao, S.S. Qu, Study of the interaction between monoammonium glycyrrhizinate and bovine serum albumin, J. Pharm. Biomed. Anal. 36 (2004) 915–919.
[22] B. Valeur, J.C. Brochon, New Trends in Fluorescence Spectroscopy, 6th ed., Springer Press, Berlin, 1999, p. 25.
[23] S. Bi, D. Song, Y. Tian, X. Zhou, Z. Liu, H. Zhang, Molecular spectroscopic study on the interaction of tetracyclines with serum albumins, Spectrochim. Acta Part A 61 (2005) 629–636.
[24] K.H. Ulrich, Molecular aspects of ligand binding to serum albumin, Pharmacol. Rev. 33 (1981) 17–53.
[25] T.L. Lilianna, A. Karaczyn, B.K. Keppler, H. Kozøowski, Studies on the interactions between human serum albumin and trans-indazolium (bisindazole) tetrachlororuthenate(III), J. Inorg. Biochem. 78 (2000) 341–346.
[26] Z.X. Lu, T. Cui, Q.L. Shi, Applications of circular dichroism (CD) and optical rotatory dispersion (ORD), in: Molecular Biology, Science Press, Beijing, China, 1987.
[27] Y.J. Hu, Y. Liu, X.S. Shen, X.Y. Fang, S.S. Qu, Studies on the interaction between 1-hexylcarbamoyl-5-fluorouracil and bovine serum albumin, J. Mol. Struct. 738 (2005) 143–147.
[28] K. Rahmelow, W. Hubner, Secondary structure determination of proteins in aqueous solution by infrared spectroscopy: a comparison of multivariate data analysis methods, Anal. Biochem. 241 (1996) 5–13.
[29] H. Cheng, H. Liu, Y. Zhang, G. Zou, Interaction of the docetaxel with human serum albumin using optical spectroscopy methods, J. Lumin. 129 (2009) 1196–1203.
[30] G. Sudlow, D.J. Birkett, D.N. Wade, Further characterization of specific drug binding sites on human serum albumin, Mol. Pharmacol. 12 (1976) 1052–1061.
[31] I. Sjoholm, B. Ekman, A. Kober, I.L. Pahlman, B. Seiving, T. Sjodin, Binding of drugs to human serum albumin. XI. The specificity of three binding sites as studied with albumin immobilized in microparticles, Mol. Pharmacol. 16 (1979) 767–777.
[32] L. Ying, H. Wenying, L. Jiaqin, S. Fenling, H. Zhide, C. Xingguo, Binding of the bioactive component jatrorrhizine to humanserum albumin, Biochim. Biophys. Acta 1722 (2005) 15–21.
[33] G. Wang, D. Wang, X. Li, Y. Lu, Exploring the binding mechanism of dihydropyrimidinones to human serum albumin: spectroscopic and molecular modeling techniques, Colloids Surf. B 84 (2011) 272–279.

HPLC–MS method for the simultaneous quantification of the antileukemia drugs imatinib, dasatinib and nilotinib in human peripheral blood mononuclear cell (PBMC)

Antonio D'Avolio [a,*], Marco Simiele [a], Silvia De Francia [b], Alessandra Ariaudo [b], Lorena Baietto [a], Jessica Cusato [a], Carmen Fava [b], Giuseppe Saglio [b], Francesco Di Carlo [b], Giovanni Di Perri [a]

[a] Laboratory of Clinical Pharmacology and Pharmacogenetics[1], Department of Infectious Diseases, University of Torino, Amedeo di Savoia Hospital, Turin, Italy
[b] Department of Biological and Clinical Sciences, University of Torino, S. Luigi Gonzaga Hospital, Regione Gonzole 10, 10043 Orbassano, Turin, Italy

ARTICLE INFO

ABSTRACT

A new method using high performance liquid chromatography coupled with electrospray mass spectrometry is described for the quantification of PBMC concentration of tyrosine kinase inhibitors imatinib, dasatinib and nilotinib. A simple PBMC isolation and extraction procedure were applied on 10–14 mL of blood aliquots. Chromatographic separation of drugs and Internal Standard (quinoxaline) was achieved with a gradient (acetonitrile and water + formic acid 0.05%) on a C18 reverse phase analytical column with 25 min of analytical run, at flow rate of 0.25 mL/min. Mean intra- and inter-day precision for all compounds were 8.76 and 12.20%; mean accuracy was −3.86%; extraction recovery ranged within 79 and 91%. Calibration curves ranged from 50.0 to 0.25 ng. The limit of quantification was set at 0.25 ng for all the analyzed drugs.

This novel developed methodology allows a specific, sensitive and reliable simultaneous intracellular determination of the three tyrosine kinase inhibitors imatinib, dasatinib and nilotinib in a single chromatographic run, useful for drugs estimation in PBMC of patients affected by chronic myeloid leukemia.

1. Introduction

Chronic myeloid leukemia (CML) is a myeloproliferative disorder, characterized by the presence of the Philadelphia chromosome, consequence of a translocation 9–22, producing a fusion oncogene referred to as BCR-ABL, encoding for a BCR-ABL kinase [1]. Thus, the use of BCR-ABL-targeted therapy is the standard of care for this disease. Current frontline therapy for CML is imatinib (Gleevec™, STI-571), a 2-phenylaminopyrimidine-type inhibitor of the BCR-ABL kinase [2], that competitively inhibits the binding of ATP to the ATP binding pocket of BCR-ABL [3,4]. In the International Randomized Study of Interferon and STI571 (IRIS; ClinicalTrials.gov number, NCT00006343), imatinib has been associated with a superior response rate and improved progression-free survival, as compared with the previous standard therapy, interferon alfa plus low-dose cytarabine [5–7]. Eight-year follow-up of IRIS revealed that responses to imatinib were durable and had an

acceptable adverse-event profile, with an estimated rate of overall survival of 85% [8]. Although most patients show excellent responses to imatinib treatment, nearly 20% of patients who take the drug do not have a complete cytogenetic response, and others may have intolerable side effects or drug resistance over time [8]. Resistance, mainly caused by point mutations, leads to a reduced affinity of imatinib for the ATP binding domain of the BCR-ABL protein and to a reactivation of the BCR-ABL kinase activity [9,10]. Loss of response and transformation to advanced disease occur mainly in the first 3 years of imatinib therapy, inducing a rate of overall survival often poor in these patients [8]. To overcome imatinib resistance and intolerance, more potent tyrosine kinase inhibitors (TKIs), such as dasatinib and nilotinib, have been developed for the treatment of CML. Dasatinib (Sprycel™, BMS-354825) is a structurally distinct drug which has a more potent activity than imatinib [11,12]. It also inhibits Src kinases, proteins that play a critical role in the development, growth, progression, and metastasis of a number of human cancers [13]. Dasatinib offers a new treatment option for patients with CML or Ph-positive acute lymphoblastic leukemia who are either unable to tolerate or resistant to previous therapy, including imatinib. Dasatinib has been found to be more effective in eliciting a cytogenetic or hematologic response and better tolerated than high-dose imatinib. However, many factors play a role

in determining whether dasatinib may provide benefit to patients. Some of these factors are known, such as BCR-ABL-sensitive mutations, whereas other mechanisms of CML not related to BCR-ABL are unknown or unclear [14]. Another second generation TKI is nilotinib (Tasigna[TM], AMN107). It is a close analog of imatinib with higher potency and selectivity for BCR-ABL kinase inhibition *in vitro* and *in vivo* than imatinib [15,16]. Nilotinib was first approved in the United States and elsewhere in 2007 for patients with CML in the chronic or accelerated phase who had resistance to or could not tolerate imatinib [17,18]. In a phase 3 study, randomized, open-label, multicenter trial, authors compared the efficacy and safety of nilotinib with that of imatinib. Analysis was done for patients with newly diagnosed Philadelphia chromosome–positive CML in the chronic phase, with the rate of major molecular response at 12 months as the primary end point. Study showed more efficacy for nilotinib [19].

Due to the large TKIs proposal in CML treatment, imatinib-resistant patients may find the right path to reach clinical effectiveness. A good help may be also offered to this purpose by employing of therapeutic drug monitoring (TDM), essential tool, today, for the management of CML patients. Sub-inhibitory drug concentrations and sequential treatment with multiple TKIs can promote, in fact, the selection of BCR-ABL kinase domain mutations in CML patients. Measurement of antileukemia drugs plasma concentrations reached by treated patients, then, can be useful to monitor CML patients over time, leading the evaluation of patient adherence to daily oral therapy, potential drug–drug interactions, treatment efficacy, and severe drug-related adverse events [20,21].

In recent years, numerous laboratories have reported the use of high-throughput bioanalytical procedures for the single and simultaneous quantification of plasma concentrations of antileukemia drugs [22–35]. Based on validated high performance liquid chromatography (HPLC) methods, the plasma pharmacokinetics (PK) of imatinib has been well investigated, while only few paper on the PK of dasatinib and nilotinib are available to date [11–21,36–39]. If data miss about plasmatic PK, no literature exist at all related to intracellular quantification of all TKIs, included imatinib. Topic that should be deeply investigated, instead, in order to have a better indication about ongoing treatment efficacy. Measurement of TKIs plasma concentrations, in fact, is a reliable tool to perform TDM; however, only the drugs fraction reaching the intracellular compartment is expected to exert action. Then a convenient correlation should be done, also, between clinical outcome and intracellular drug levels reached in treated patients. As variability in drug PK and inadequate patient compliance, also poor penetration of drugs into body compartments, particularly in leukocytes or peripheral blood mononuclear cell (PBMC), may contribute to the occurrence of sub-therapeutic drug level, leading loss of treatment efficacy. By the way the mechanisms by which TKIs drugs accumulate within cells remain generally unknown and it should be further investigated, because very few data are published to date [26,40–42]. Moreover, a number of transmembrane transport proteins, such as P-glycoprotein, the gene product of *ABCB*1 (*MDR*1), and related ABC (ATP binding cassette) B1 (ABCB1), ABCG2, such as solute carrier 22A1 (SLC22A1), solute carrier organic anion transporter family members 1B1 (SLCO1B1) and SLCO1B3 transporters are known to actively mediate the efflux and uptake of drugs from cells. The genes coding for these transport and regulatory proteins are polymorphic in humans, with consequences on the expression and function, potentially influencing the intracellular levels of TKIs drugs. In particular it was observed in CML patients an association of SLCO1B3 polymorphism with intracellular accumulation of imatinib in leukocytes [42]. Thus, as intracellular concentrations of TKIs drugs are influenced by both their physico-chemical properties and host genetic factors, an assay enabling the monitoring of TKIs levels at the site of their pharmacological action, appears to be an

essential tool for the ongoing investigations aimed at preventing TKIs therapy failure or toxicity.

Herein, aim of our study was to develop and validate an HPLC method coupled with electrospray mass spectrometry (HPLC–MS) detection for the simultaneous quantification of imatinib, dasatinib and nilotinib in human PBMC.

2. Experimental

2.1. Chemicals

Imatinib (Glivec[TM], STI-571) and nilotinib (Tasigna[TM], AMN-107) were kindly supplied by Novartis Pharma AG (Basel, Switzerland); dasatinib (Sprycel[TM], BMS-354825) was purchased from Sequoia Research (Pangbourne, United Kingdom). Acetonitrile HPLC grade and methanol HPLC grade were purchased from J.T. Baker (Deventer, Holland). HPLC grade water was produced with Milli-DI system coupled with a Synergy 185 system by Millipore (Milan, Italy). Quinoxaline (QX) and formic acid were obtained from Sigma–Aldrich (Milan, Italy). Lymphoprep was purchased from Sentinel Diagnostics (Milan, Italy). Blank cells (PBMCs) were isolated from the blood of healthy donors, kindly supplied by the Blood Bank of the Maria Vittoria Hospital (Turin, Italy).

2.2. Stock solutions, standards (STD) and quality controls (QC)

The stock solutions of imatinib, dasatinib and nilotinib were prepared by dissolving an accurately weighed amount of drug in methanol to obtain a final concentration of 1 mg/mL; all stock solutions were then stored at −20 °C. The stock solutions were stored maximum for 3 months.

The Internal Standard (IS) working solution was prepared with QX [1 μg/mL] in methanol and HPLC grade water (50:50, v/v) and stored at 4 °C until use. The six calibration standards and three quality controls (QCs) were prepared adding a determined volume of stock solutions, or diluted stock solution, to each blank PBMCs aliquots before storage at −80 °C, during no more than three months, in a manner similar to that described in other publications [43,44].

Calibration ranges, from STD 6 to STD 1, and QC amount for all drugs are listed in Table 1.

2.3. PBMC isolation

Clinical samples were collected, after obtaining written informed consent according to local Ethics Committee indications, from patients treated with TKIs. Blood samples were collected in two EDTA tubes (2 × 7 mL).

PBMCs were isolated from 10 to 14 mL of blood using lymphoprep density gradient centrifugation (700 × *g*, 25 min, 4 °C with a Jouan Centrifuge [Model BR4i, Saint-Herblain, France]) at each sampling, as described previously [44]. PBMCs were then fast washed twice in 40 mL cold-ice phosphate-buffered saline and centrifuged (750 × *g*, 6 min, 4 °C).

The resulting pellet of washed PBMCs was dissolved with 1 mL extraction solution (methanol:water, 70:30 (v/v)), switched in two criovials (500 μL each) and then stored at −80 °C until analyses, and for no longer than three months.

The time taken to process PBMCs from phlebotomy to methanol extraction solution was less than 1 h, ensuring that sampling conditions were ice cold to prevent drug loss [45,46]. Blank PBMCs isolated from the blood of healthy donors, as previously described, were stored in aliquots of around 5×10^6 cells.

The cell number were afterwards determined by absorbance with a new procedure (paper in progress). This method used 10 μL of stored unknown number PBMC aliquots versus 10 μL of known

Table 1
Detected mass (Da), cone voltage used (V) and retention time (RT, in min) used to quantify Internal Standard and each drug, and absolute amounts from STD6 to STD1 (LOQ), QCs (QC high, QC medium and QC low) and LOD.

Drugs data					Amounts (ng)								
Drugs	RT (min)	Mass (Da)	Cone voltage (V)	STD 6	STD 5	STD 4	STD 3	STD 2	LOQ/STD 1	QC high	QC medium	QC low	LOD
Imatinib	9.6	493.80	45	50	10	5	2	0.5	0.25	8	4	1	0.06
Dasatinib	10.6	487.50	35	50	10	5	2	0.5	0.25	8	4	1	0.06
Nilotinib	12.0	529.50	35	50	10	5	2	0.5	0.25	8	4	1	0.06
IS	14.8	313.30	50	–	–	–	–	–	–	–	–	–	–

numbers of PBMC reference aliquots. The known number of the reference aliquots were obtained by a Bekman Coulter Z2 (Instrumentation Laboratory, Milan, Italy), and managed by Z2 AccuComp Software (Version 3.01), without the use of the trypan blue exclusion.

The cellular volume used to calculate intracellular concentrations of TKIs was 285 fL, as described previously [47].

2.4. STD, QC and samples preparation

The stored aliquots of STDs, QCs and patient samples PBMCs were defrosted at room temperature. Fifty microliters of IS working solution was added to each tube and the samples were vortexed for 10 s. STDs, QCs and patient tube samples were sonicated in an ice-water bath three time (Cycle 0,75; Amplitude 80%), to fully lyse PBMCs, using a sonicator UP-50 H (Dr. Hielscher GmbH, Teltow, Germany). After a centrifugation at (7000 × g, 10 min at 4 °C), 10 μL of supernatant were used for the cell count, and the remainder supernatant were collected into glass tubes. The remaining pellets were then washed by vortex for 10 s with 200 μL of acetonitrile:metanol solution (50:50, v/v), centrifuged (7000 × g, 10 min at 4 °C) and each supernatant was collected in the indicated glass tubes to be treated by vortex-vacuum evaporation to dryness at 60 °C.

Each extract was reconstituted with 60 μL of HPLC-grade water and acetonitrile solution (60:40, v/v) and 20 μL were injected into the column. For validation purposes, all samples were extracted and analyzed in duplicate. All procedure steps were carried out at room temperature, excluding that of sonication.

2.5. Chromatographic and MS conditions

The HPLC–MS instrument used was a Waters system (Milan, Italy), with binary pump model 1525, AF degaser, 717-plus autosampler, and Micromass ZQ mass detector. LC–MS Empower Pro software (version year 2002, Waters; Milan, Italy) was used.

The chromatographic separation was performed at 35 °C using a column oven, on Atlantis T3 C-18 3 μm column (150 mm × 2.1 mm I.D.) (Waters; Milan, Italy), protected by a Security Guard with C18 (4.0 mm × 3.0 mm I.D.) pre-column (Phenomenex; CA, USA). The chromatographic run was performed with a gradient (Table 2), and the mobile phase was composed by HPLC grade water containing 0.05% formic acid, for mobile phase A, and HPLC grade acetonitrile containing 0.05% formic acid, for mobile phase B.

Detector settings were ESI, positive polarity ionization; capillary voltage 3.5 kV; source temperature 110 °C; desolvation temperature 350 °C; nitrogen desolvation flow 800 L/h; and nitrogen cone flow 100 L/h. Ions detected, in single ion recording (SIR) mode, were m/z 493.8 with a cone voltage of 45 V for imatinib, m/z 487.5 with a cone voltage of 35 V for dasatinib, m/z 529.5 with a cone voltage of 35 V for nilotinib and m/z 313.0 with a cone voltage of 50 V for QX (IS).

2.6. Specificity and selectivity

Interference from endogenous compounds was investigated by analysis of six different blank PBMC samples. Moreover interference from some potentially co-administered drugs were evaluated for: zidovudine, didanosine, stavudine, lamivudine, abacavir, tenofovir, emtricitabine, ethambutol, isoniazid, ribavirin, voriconazole, posaconazole and itraconazole (some of many drugs routinely analyzed in our laboratory). An "interfering drug" has been considered as a molecule which exhibits a retention time close to 0.3 min from the analytes, and with the potential capability to cause ion suppression.

2.7. Matrix effect

"Matrix effect" was investigated using six different blank PBMC samples and comparing peak areas obtained from standard solutions of a solution of water and acetonitrile (60:40), containing all our analytes at three different concentrations, and peak areas obtained from blanks post-extraction solution with the same amount of analytes, as described by Taylor [48]. Possible "matrix effect" was calculated, as deviation %, comparing the peak area obtained from the PBMC extract with the peak area obtained from the standard solution.

2.8. Accuracy, precision, calibration and limit of quantification

Intra-day and inter-day accuracy and precision were determined by assaying ten spiked PBMC samples at three different concentrations (QCs) for each drug. Accuracy was calculated as the percent deviation from the nominal concentration. Inter-day and intra-day precision were expressed as the standard deviation at each QC concentration. Each calibration curve was obtained using six calibration points in duplicate, and the ranges are listed in Table 1. Calibration curves were created by plotting the peak area ratios of each drugs relative to the IS against the various drugs concentrations in the spiked PBMC standards. A quadratic regression was used for all curves in order to obtain the best fit for all calibration points. The limit of detection (LOD) in PBMC was defined

Table 2
Chromatographic condition (gradient): mobile phase A (HPLC grade water + 0.05% formic acid) and mobile phase B (HPLC grade acetonitrile + 0.05% formic acid). The flow was 0.25 ml/min.

Time (min)	% Mobile phase A	% Mobile phase B
0.0	74	26
0.1	73	27
2.0	55	45
4.0	50	50
9.0	40	60
9.5	30	70
9.6	5	95
14.0	5	95
14.1	95	5
15.1	95	5
25.0	75	25

as the concentration that yields a signal-to-noise ratio of 3/1. The lowest concentration levels that could determined with a percent deviation from the nominal concentration and relative standard deviation < 20%, was considered the lowest limit of quantification (LOQ), as requested by international guidelines [49].

2.9. Recovery

Recovery from PBMC, using the extraction procedures, was assessed by comparing the peak area obtained from multiple analyses ($n = 3$) of spiked samples (QCs) with the peak area from standard solution of all analytes in a solution of water and acetonitrile (60:40) at the same concentrations, as described by international guidelines [49].

2.10. Stability

The stability of antileukemia drugs at different conditions has been previously assayed in many articles [3,25,32,34,50]. For this reason stability assays were not performed.

2.11. Patients PBMC samples

Patients receiving standard dosing of imatinib, dasatinib or nilotinib, underwent blood sampling after obtaining their informed consent for the measurement of PBMC drugs concentrations. Blood samples were collected in EDTA tube (2×7 mL) and processed as described above (see Section 2.3).

3. Results

Time of analytical run was chosen as 25 min, according to the retention times of substances, their good separation and with the use of a wash column step and its re-equilibration, that allows to reduce potential ghost-peak interferences highlighted without the washing step. Our analyte retention times were 9.6 ± 0.2 min for imatinib, 10.6 ± 0.2 min for dasatinib, 12.0 ± 0.2 min for nilotinib, 14.8 ± 0.2 min for QX. Representative chromatograms of a blank PBMC extracted and STD1 of imatinib, dasatinib and nilotinib are shown in Fig. 1A–C, respectively. Representative chromatogram of a imatinib, dasatinib and nilotinib STD6 PBMC extracted and QX is shown in Fig. 2. Mean regression coefficient (r^2) of all calibration curves was higher than 0.99 for all analytes.

3.1. Specificity and selectivity

The assay did not show any significant interference with other potentially concomitant drugs (see Section 2.6). The tested six blank PBMC samples did not show any interference in the retention times analytes windows for each specified ion detected (Fig. 1A–C).

3.2. Accuracy, precision, limit of quantification

Results of the validation of the method are listed in Table 3 for all analytes. All observed data (intra-day and inter-day precision [R.S.D.%]) were all below 15.0%, as request for FDA guidelines [49]. LOQ and LOD are listed in Table 1.

3.3. Recovery

Multiple aliquots ($n = 3$) at each of the three QCs amounts were assayed and mean recovery of drugs were 79% for imatinib, 82% for nilotinib and 91% for dasatinib (mean CV, for all drugs, 6.8%). Mean IS recovery was 89% (mean CV 2.0%).

3.4. Matrix effect

The deviation % of the peak area at the three amounts for all analytes is comparable, ranging from −13.5% to −1.4% (mean −6.4%), showing the absence of the "matrix effect".

3.5. Analysis of plasma samples from treated patients

Method developed was applied for assaying of 52 PBMC samples, corresponding to different points of time–concentration curve, obtained from 40 patients treated with TKI drugs (28 with imatinib, 4 with dasatinib, 8 with nilotinib). Values obtained resulted in the expected range of concentrations, previously defined in our laboratory (unpublished data) and close to published results by different procedure and kind of analyzed cell [26,40,42]. The mean ratios (PBMC/plasma) of C_{trough} concentrations were 7.8, 35.3 and 5.7 for imatinib, dasatinib and nilotinib, respectively.

4. Discussion and conclusion

Targeted therapies using imatinib, dasatinib and nilotinib, based on the inhibition of protein tyrosine kinases, represent currently the therapeutic strategies for treatment of CML. TDM, recently, has become an essential tool for the management of CML patients, particularly for patients taking imatinib [21,39], which efficacy threshold in terms of plasma concentrations is clearly defined. In order to manage primary or acquired resistance to imatinib, clinical studies using dasatinib or nilotinib as second line therapy or combination of therapies with different TKIs, in sequential or simultaneous administration, are currently under evaluation [21,39]. Sub-inhibitory intracellular drug concentrations, probably, and sequential treatment with multiple tyrosine kinase inhibitors promote the selection of BCR-ABL kinase domain mutations in CML patients [51,52]. Poor penetration of drugs into leukocytes or PBMC, inadequate treatment adherence, and variability in drug PK may also contribute to the occurrence of sub-therapeutic drug level. In fact, only the fraction reaching the intracellular compartment is reasonably expected to exert a therapeutic action. Very few data are published to date [26,40–42], probably due to the difficult to develop, validate and use, a reliable method to quantify intracellular drug concentration. In this context, the aim of our study, an HPLC–MS method setting for the simultaneous quantification of TKIs in human PBMC, has encountered current need, because no methods for this simultaneous intracellular determination of these drugs, are available up to now.

The method we have developed and validated, based on a very close PBMC isolation and drug extraction procedure published by our group for antiretroviral drugs [44]. This method can be used everywhere, because require instruments available in all laboratories. These procedures were then coupled to HPLC instrument with single mass detector.

For this purpose we have chosen as our internal standard quinoxaline, as it is easy to purchase, inexpensive (compared with deuterated drug isotopes) and reliable in its chemical behavior. This xenobiotic was fully used as IS in our other validated method [25,44,53–60], with UV and mass detectors. Moreover it is not a potential coadministred drug as was the case in other studies [41,42].

The method developed is suitable to be used in clinical studies due to its high extraction efficiency, its high sensitivity, its good reproducibility and due to the simultaneous quantification of the three drugs using a small volumes of blood (10–14 mL).

In fact, since no therapeutic window has been clearly defined for the imatinib, dasatinib and nilotinib in PBMC, as in plasma
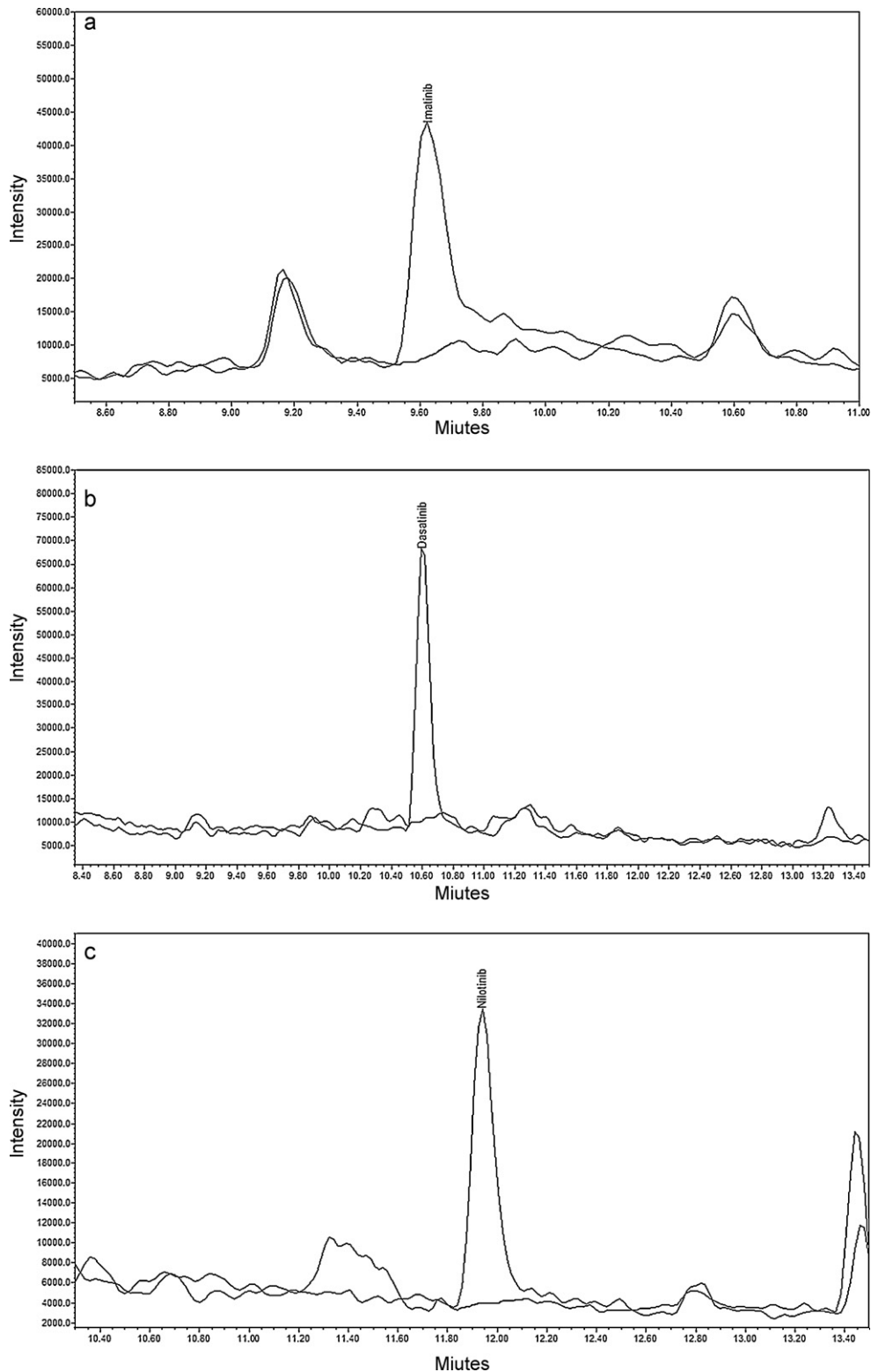
Fig. 1. Overlapping of STD1 and blank PBMC extracted ions detection (A, imatinib; B, dasatinib; and C, nilotinib).

(excluding imatinib [36,38,39]), it could be interesting try to quantify intracellular concentrations of the three drugs and assess at first potential correlation with plasma concentrations, then a concentration-response relationship. At present no reports showed data related to intracellular levels. Moreover, measurement of antileukemia intracellular concentrations, even if more elaborated than TKIs plasma determination, can be useful, as plasma concentration, to evaluate patient adherence to daily oral therapy, treatment efficacy, severe drug-related adverse events, and potential drug–drug interactions, especially in patients who must take drugs interfering with cytochrome P450 [20].

Moreover, TKIs are substrate of transmembrane transport proteins encoded by ABCB1, SLCO1B1 and SLCO1B3 gene [42]. The genes coding for these transport are polymorphic with
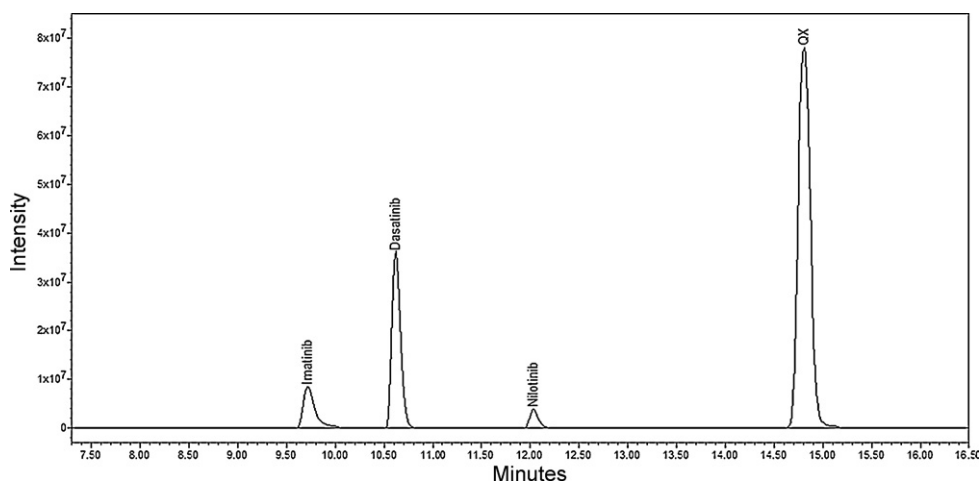
Fig. 2. STD6 extracted chromatogram.

Table 3
Accuracy (CV%), intra-day and inter-day precision, as relative standard deviation (RSD%), assayed for all drugs ($n = 10$).

Drugs	QC high			QC medium			QC low		
	Accuracy %	Precision R.S.D. %		Accuracy %	Precision R.S.D. %		Accuracy %	Precision R.S.D. %	
		Intra-day	Inter-day		Intra-day	Inter-day		Intra-day	Inter-day
Imatinib	−5.72	7.57	11.04	−4.56	8.54	13.01	−6.63	10.69	14.12
Dasatinib	2.68	7.98	10.73	−4.22	8.98	11.28	−3.60	9.53	12.28
Nilotinib	2.05	7.60	10.61	−5.77	7.99	12.56	−8.96	9.94	14.18

consequences on the expression and function, potentially influencing the intracellular levels of TKI drugs.

The LOQ (0.25 ng) and calibration curves included a wide range of imatinib, dasatinib and nilotinib concentrations/amounts, optimized according to expected and founded ranges of drug concentrations in PBMC patients. Choice of limits of these ranges was based on the values available in the clinical reports, too [26,40,42].

Data of the developed assay makes our method suitable, then, to perform imatinib, dasatinib and nilotinib quantification in PBMC CML patients. Reliability of our method has been demonstrated for all drug concentrations; relative error at QCs concentrations, intra-day and inter-day precision (Table 3) indicate the good performances of our method. Absence of interference peaks at the analyte retention times, without a "matrix effect", coupled with an experienced collection procedure and treatment of PBMC [44] allowed accurate measurement of drugs intracellular levels.

5. Conclusion

We report a new method using HPLC–MS for the simultaneous intracellular determination of imatinib, dasatinib and nilotinib in a single chromatographic run. The selectivity of the assay described could be exploited optimally when monitoring all the three substances in PBMC and/or tissues during animal and clinical PK studies of single or concomitant administration. The described HPLC–MS method allows the rapid, simple, sensitive, and selective simultaneous intracellular quantification of the three major antileukemia drugs. This method could be currently used for the clinical study (or monitoring) of PBMC TKIs concentrations in patients treated with imatinib, dasatinib and/or nilotinib.

References

[1] C.L. Sawyers, Chronic myeloid leukemia, N. Engl. J. Med. 340 (1999) 1330–1340.
[2] B.J. Druker, M. Talpaz, D.J. Resta, B. Peng, E. Buchdunger, J.M. Ford, N.B. Lydon, H. Kantarjian, R. Capdeville, S. Ohno-Jones, C.L. Sawyers, Efficacy and safety of a specific inhibitor of the BCR-ABL tyrosine kinase in chronic myeloid leukemia, N. Engl. J. Med. 344 (2001) 1031–1037.
[3] R. Bakhtiar, L. Khemani, M. Hayes, T. Bedman, F. Tse, Quantification of the antileukemia drug STI571 (Gleevec) and its metabolite (CGP 74588) in monkey plasma using a semi-automated solid phase extraction procedure and liquid chromatography–tandem mass spectrometry, J. Pharm. Biomed. Anal. 28 (2002) 1183–1194.
[4] B.J. Druker, Imatinib as a paradigm of targeted therapies, Adv. Cancer. Res. 91 (2004) 1–30.
[5] B.J. Druker, F. Guilhot, S.G. O'Brien, I. Gathmann, H. Kantarjian, N. Gattermann, M.W. Deininger, R.T. Silver, J.M. Goldman, R.M. Stone, F. Cervantes, A. Hochhaus, B.L. Powell, J.L. Gabrilove, P. Rousselot, J. Reiffers, J.J. Cornelissen, T. Hughes, H. Agis, T. Fischer, G. Verhoef, J. Shepherd, G. Saglio, A. Gratwohl, J.L. Nielsen, J.P. Radich, B. Simonsson, K. Taylor, M. Baccarani, C. So, L. Letvak, R.A. Larson, Five-year follow-up of patients receiving imatinib for chronic myeloid leukemia, N. Engl. J. Med. 355 (2006) 2408–2417.
[6] T.P. Hughes, J. Kaeda, S. Branford, Z. Rudzki, A. Hochhaus, M.L. Hensley, I. Gathmann, A.E. Bolton, I.C. van Hoomissen, J.M. Goldman, J.P. Radich, Frequency of major molecular responses to imatinib or interferon alfa plus cytarabine in newly diagnosed chronic myeloid leukemia, N. Engl. J. Med. 349 (2003) 1423–1432.
[7] S.G. O'Brien, F. Guilhot, R.A. Larson, I. Gathmann, M. Baccarani, F. Cervantes, J.J. Cornelissen, T. Fischer, A. Hochhaus, T. Hughes, K. Lechner, J.L. Nielsen, P. Rousselot, J. Reiffers, G. Saglio, J. Shepherd, B. Simonsson, A. Gratwohl, J.M. Goldman, H. Kantarjian, K. Taylor, G. Verhoef, A.E. Bolton, R. Capdeville, B.J. Druker, Imatinib compared with interferon and low-dose cytarabine for newly diagnosed chronic-phase chronic myeloid leukemia, N. Engl. J. Med. 348 (2003) 994–1004.
[8] T.P. Hughes, A. Hochhaus, S. Branford, M.C. Muller, J.S. Kaeda, L. Foroni, B.J. Druker, F. Guilhot, R.A. Larson, S.G. O'Brien, M.S. Rudoltz, M. Mone, E. Wehrle, V. Modur, J.M. Goldman, J.P. Radich, Long-term prognostic significance of early molecular response to imatinib in newly diagnosed chronic myeloid leukemia: an analysis from the International Randomized Study of Interferon and STI571 (IRIS), Blood 116 (2010) 3758–3765.
[9] M.E. Gorre, M. Mohammed, K. Ellwood, N. Hsu, R. Paquette, P.N. Rao, C.L. Sawyers, Clinical resistance to STI-571 cancer therapy caused by BCR-ABL gene mutation or amplification, Science 293 (2001) 876–880.
[10] N.P. Shah, C.L. Sawyers, Mechanisms of resistance to STI571 in philadelphia chromosome-associated leukemias, Oncogene 22 (2003) 7389–7395.
[11] A.V. Kamath, J. Wang, F.Y. Lee, P.H. Marathe, Preclinical pharmacokinetics and in vitro metabolism of dasatinib (BMS-354825): a potent oral multi-targeted kinase inhibitor against SRC and BCR-ABL, Cancer Chemother. Pharmacol. 61 (2008) 365–376.
[12] L.J. Lombardo, F.Y. Lee, P. Chen, D. Norris, J.C. Barrish, K. Behnia, S. Castaneda, L.A. Cornelius, J. Das, A.M. Doweyko, C. Fairchild, J.T. Hunt, I. Inigo, K. Johnston, A. Kamath, D. Kan, H. Klei, P. Marathe, S. Pang, R. Peterson, S. Pitt, G.L.

Schieven, R.J. Schmidt, J. Tokarski, M.L. Wen, J. Wityak, R.M. Borzilleri, Discovery of N-(2-chloro-6-methyl-phenyl)-2-(6-(4-(2-hydroxyethyl)-piperazin-1-yl)-2-methylpyrimidin-4-ylamino)thiazole-5-carboxamide (BMS-354825), a dual Src/Abl kinase inhibitor with potent antitumor activity in preclinical assays, J. Med. Chem. 47 (2004) 6658–6661.

[13] M.C. Frame, Src in cancer: deregulation and consequences for cell behaviour, Biochim. Biophys. Acta 1602 (2002) 114–130.

[14] M. Steinberg, Dasatinib: a tyrosine kinase inhibitor for the treatment of chronic myelogenous leukemia and philadelphia chromosome-positive acute lymphoblastic leukemia, Clin. Ther. 29 (2007) 2289–2308.

[15] H. Kantarjian, F. Giles, L. Wunderle, K. Bhalla, S. O'Brien, B. Wassmann, C. Tanaka, P. Manley, P. Rae, W. Mietlowski, K. Bochinski, A. Hochhaus, J.D. Griffin, D. Hoelzer, M. Albitar, M. Dugan, J. Cortes, L. Alland, O.G. Ottmann, Nilotinib in imatinib-resistant CML and philadelphia chromosome-positive ALL, N. Engl. J. Med. 354 (2006) 2542–2551.

[16] E. Weisberg, P.W. Manley, W. Breitenstein, J. Bruggen, S.W. Cowan-Jacob, A. Ray, B. Huntly, D. Fabbro, G. Fendrich, E. Hall-Meyers, A.L. Kung, J. Mestan, G.Q. Daley, L. Callahan, L. Catley, C. Cavazza, M. Azam, D. Neuberg, R.D. Wright, D.G. Gilliland, J.D. Griffin, Characterization of AMN107, a selective inhibitor of native and mutant Bcr-Abl, Cancer Cell 7 (2005) 129–141.

[17] M.M. Oken, R.H. Creech, D.C. Tormey, J. Horton, T.E. Davis, E.T. McFadden, P.P. Carbone, Toxicity and response criteria of the Eastern Cooperative Oncology Group, Am. J. Clin. Oncol. 5 (1982) 649–655.

[18] J.E. Sokal, E.B. Cox, M. Baccarani, S. Tura, G.A. Gomez, J.E. Robertson, C.Y. Tso, T.J. Braun, B.D. Clarkson, F. Cervantes, et al., Prognostic discrimination in "good-risk" chronic granulocytic leukemia, Blood 63 (1984) 789–799.

[19] G. Saglio, D.W. Kim, S. Issaragrisil, P. le Coutre, G. Etienne, C. Lobo, R. Pasquini, R.E. Clark, A. Hochhaus, T.P. Hughes, N. Gallagher, A. Hoenekopp, M. Dong, A. Haque, R.A. Larson, H.M. Kantarjian, Nilotinib versus imatinib for newly diagnosed chronic myeloid leukemia, N. Engl. J. Med. 362 (2010) 2251–2259.

[20] M. Baccarani, G. Saglio, J. Goldman, A. Hochhaus, B. Simonsson, F. Appelbaum, J. Apperley, F. Cervantes, J. Cortes, M. Deininger, A. Gratwohl, F. Guilhot, M. Horowitz, T. Hughes, H. Kantarjian, R. Larson, D. Niederwieser, R. Silver, R. Hehlmann, Evolving concepts in the management of chronic myeloid leukemia: recommendations from an expert panel on behalf of the European Leukemia Net, Blood 108 (2006) 1809–1820.

[21] N. Singh, L. Kumar, R. Meena, T. Velpandian, Drug monitoring of imatinib levels in patients undergoing therapy for chronic myeloid leukaemia: comparing plasma levels of responders and non-responders, Eur. J. Clin. Pharmacol. 65 (2009) 545–549.

[22] A. Awidi, Salem II, N. Najib, R. Mefleh, B. Tarawneh, Determination of imatinib plasma levels in patients with chronic myeloid leukemia by high performance liquid chromatography–ultraviolet detection and liquid chromatography–tandem mass spectrometry: methods' comparison, Leuk. Res. 34 (2010) 714–717.

[23] S. Bouchet, E. Chauzit, D. Ducint, N. Castaing, M. Canal-Raffin, N. Moore, K. Titier, M. Molimard, Simultaneous determination of nine tyrosine kinase inhibitors by 96-well solid-phase extraction and ultra performance LC/MS–MS, Clin. Chim. Acta 412 (2011) 1060–1067.

[24] A. Davies, A.K. Hayes, K. Knight, S.J. Watmough, M. Pirmohamed, R.E. Clark, Simultaneous determination of nilotinib, imatinib and its main metabolite (CGP-74588) in human plasma by ultra-violet high performance liquid chromatography, Leuk. Res. 34 (2010) 702–707.

[25] S. De Francia, A. D'Avolio, F. De Martino, E. Pirro, L. Baietto, M. Siccardi, M. Simiele, S. Racca, G. Saglio, F. Di Carlo, G. Di Perri, New HPLC–MS method for the simultaneous quantification of the antileukemia drugs imatinib, dasatinib, and nilotinib in human plasma, J. Chromatogr. B: Anal. Technol. Biomed. Life Sci. 877 (2009) 1721–1726.

[26] J. Klawitter, Y.L. Zhang, N. Anderson, N.J. Serkova, U. Christians, Development and validation of a sensitive assay for the quantification of imatinib using LC/LC–MS/MS in human whole blood and cell culture, Biomed. Chromatogr. 23 (2009) 1251–1258.

[27] K. Micova, D. Friedecky, E. Faber, A. Polynkova, T. Adam, Flow injection analysis vs. ultra high performance liquid chromatography coupled with tandem mass spectrometry for determination of imatinib in human plasma, Clin. Chim. Acta 411 (2010) 1957–1962.

[28] M. Miura, N. Takahashi, K. Sawada, High-performance liquid chromatography with solid-phase extraction for the quantitative determination of nilotinib in human plasma, Biomed. Chromatogr. 24 (2010) 789–793.

[29] M. Miura, N. Takahashi, K. Sawada, Quantitative determination of imatinib in human plasma with high-performance liquid chromatography and ultraviolet detection, J. Chromatogr. Sci. 49 (2011) 412–415.

[30] R.L. Oostendorp, J.H. Beijnen, J.H. Schellens, O. Tellingen, Determination of imatinib mesylate and its main metabolite (CGP74588) in human plasma and murine specimens by ion-pairing reversed-phase high-performance liquid chromatography, Biomed. Chromatogr. 21 (2007) 747–754.

[31] R.A. Parise, M.J. Egorin, S.M. Christner, D.D. Shah, W. Zhou, J.H. Beumer, A high-performance liquid chromatography–mass spectrometry assay for quantitation of the tyrosine kinase inhibitor nilotinib in human plasma and serum, J. Chromatogr. B: Anal. Technol. Biomed. Life Sci. 877 (2009) 1894–1900.

[32] S. Pursche, O.G. Ottmann, G. Ehninger, E. Schleyer, High-performance liquid chromatography method with ultraviolet detection for the quantification of the BCR-ABL inhibitor nilotinib (AMN107) in plasma, urine, culture medium and cell preparations, J. Chromatogr. B: Anal. Technol. Biomed. Life Sci. 852 (2007) 208–216.

[33] O. Roth, O. Spreux-Varoquaux, S. Bouchet, P. Rousselot, S. Castaigne, S. Rigaudeau, V. Raggueneau, P. Therond, P. Devillier, M. Molimard, B. Maneglier, Imatinib assay by HPLC with photodiode-array UV detection in plasma from patients with chronic myeloid leukemia: comparison with LC–MS/MS, Clin. Chim. Acta 411 (2010) 140–146.

[34] K. Titier, S. Picard, D. Ducint, E. Teilhet, N. Moore, P. Berthaud, F.X. Mahon, M. Molimard, Quantification of imatinib in human plasma by high-performance liquid chromatography–tandem mass spectrometry, Ther. Drug Monit. 27 (2005) 634–640.

[35] M. Yuki, Y. Yamakawa, T. Uchida, T. Nambu, T. Kawaguchi, A. Hamada, H. Saito, High-performance liquid chromatographic assay for the determination of nilotinib in human plasma, Biol. Pharm. Bull. 34 (2011) 1126–1128.

[36] A. Awidi, A.O. Ayed, N. Bsoul, A. Magablah, R. Mefleh, M. Dweiri, M. Ramahi, E. Arafat, M. Bishtawi, L. Marie, Relationship of serum imatinib trough level and response in CML patients: long term follow-up, Leuk. Res. 34 (2010) 1573–1575.

[37] E. Faber, D. Friedecky, K. Micova, M. Divoka, B. Katrincsakova, S. Rozmanova, M. Jarosova, K. Indrak, T. Adam, Imatinib dose escalation in two patients with chronic myeloid leukemia, with low trough imatinib plasma levels measured at various intervals from the beginning of therapy and with suboptimal treatment response, leads to the achievement of higher plasma levels and major molecular response, Int. J. Hematol. 91 (2010) 897–902.

[38] B. Peng, M. Hayes, D. Resta, A. Racine-Poon, B.J. Druker, M. Talpaz, C.L. Sawyers, M. Rosamilia, J. Ford, P. Lloyd, R. Capdeville, Pharmacokinetics and pharmacodynamics of imatinib in a phase I trial with chronic myeloid leukemia patients, J. Clin. Oncol. 22 (2004) 935–942.

[39] S. Picard, K. Titier, G. Etienne, E. Teilhet, D. Ducint, M.A. Bernard, R. Lassalle, G. Marit, J. Reiffers, B. Begaud, N. Moore, M. Molimard, F.X. Mahon, Trough imatinib plasma levels are associated with both cytogenetic and molecular responses to standard-dose imatinib in chronic myeloid leukemia, Blood 109 (2007) 3496–3499.

[40] M. Holdhoff, J.G. Supko, G.L. Gallia, C.L. Hann, D. Bonekamp, X. Ye, B. Cao, A. Olivi, S.A. Grossman, Intratumoral concentrations of imatinib after oral administration in patients with glioblastoma multiforme, J. Neurooncol. 97 (2010) 241–245.

[41] S. Roche, G. McMahon, M. Clynes, R. O'Connor, Development of a high-performance liquid chromatographic-mass spectrometric method for the determination of cellular levels of the tyrosine kinase inhibitors lapatinib and dasatinib, J. Chromatogr. B: Anal. Technol. Biomed. Life Sci. 877 (2009) 3982–3990.

[42] T. Nambu, A. Hamada, R. Nakashima, M. Yuki, T. Kawaguchi, H. Mitsuya, H. Saito, Association of SLCO1B3 polymorphism with intracellular accumulation of imatinib in leukocytes in patients with chronic myeloid leukemia, Biol. Pharm. Bull. 34 (2011) 114–119.

[43] S. Colombo, A. Beguin, A. Telenti, J. Biollaz, T. Buclin, B. Rochat, L.A. Decosterd, Intracellular measurements of anti-HIV drugs indinavir, amprenavir, saquinavir, ritonavir, nelfinavir, lopinavir, atazanavir, efavirenz and nevirapine in peripheral blood mononuclear cells by liquid chromatography coupled to tandem mass spectrometry, J. Chromatogr. B: Anal. Technol. Biomed. Life Sci. 819 (2005) 259–276.

[44] A. D'Avolio, M. Simiele, M. Siccardi, L. Baietto, M. Sciandra, V. Oddone, F.R. Stefani, S. Agati, J. Cusato, S. Bonora, G. Di Perri, A HPLC–MS method for the simultaneous quantification of fourteen antiretroviral agents in peripheral blood mononuclear cell of HIV infected patients optimized using medium corpuscular volume evaluation, J. Pharm. Biomed. Anal. 54 (2011) 779–788.

[45] J. Ford, S.H. Khoo, D.J. Back, The intracellular pharmacology of antiretroviral protease inhibitors, J. Antimicrob. Chemother. 54 (2004) 982–990.

[46] S.H. Khoo, P.G. Hoggard, I. Williams, E.R. Meaden, P. Newton, E.G. Wilkins, A. Smith, J.F. Tjia, J. Lloyd, K. Jones, N. Beeching, P. Carey, B. Peters, D.J. Back, Intracellular accumulation of human immunodeficiency virus protease inhibitors, Antimicrob. Agents Chemother. 46 (2002) 3228–3235.

[47] M. Simiele, A. D'Avolio, L. Baietto, M. Siccardi, M. Sciandra, S. Agati, J. Cusato, S. Bonora, G. Di Perri, Evaluation of the mean corpuscular volume of peripheral blood mononuclear cells of HIV patients by a coulter counter to determine intracellular drug concentrations, Antimicrob. Agents Chemother. 55 (2011) 2976–2978.

[48] P.J. Taylor, Matrix effects: the Achilles heel of quantitative high-performance liquid chromatography-electrospray–tandem mass spectrometry, Clin. Biochem. 38 (2005) 328–334.

[49] FDA, Guidance for Industry Bioanalytical Method Validation, Center for Drug Evaluation and Research of the U.S. Department of Health and Human Services Food and Drug Administration, 2001.

[50] R. Bakhtiar, J. Lohne, L. Ramos, L. Khemani, M. Hayes, F. Tse, High-throughput quantification of the anti-leukemia drug STI571 (Gleevec) and its main metabolite (CGP 74588) in human plasma using liquid chromatography–tandem mass spectrometry, J. Chromatogr. B: Anal. Technol. Biomed. Life Sci. 768 (2002) 325–340.

[51] J. Cortes, E. Jabbour, H. Kantarjian, C.C. Yin, J. Shan, S. O'Brien, G. Garcia-Manero, F. Giles, M. Breeden, N. Reeves, W.G. Wierda, D. Jones, Dynamics of BCR-ABL kinase domain mutations in chronic myeloid leukemia after sequential treatment with multiple tyrosine kinase inhibitors, Blood 110 (2007) 4005–4011.

[52] N.P. Shah, B.J. Skaggs, S. Branford, T.P. Hughes, J.M. Nicoll, R.L. Paquette, C.L. Sawyers, Sequential ABL kinase inhibitor therapy selects for compound drug-resistant BCR-ABL mutations with altered oncogenic potency, J. Clin. Invest. 117 (2007) 2562–2569.

[53] L. Baietto, A. D'Avolio, F.G. De Rosa, S. Garazzino, M. Michelazzo, G. Ventimiglia, M. Siccardi, M. Simiele, M. Sciandra, G. Di Perri, Development and validation of a

simultaneous extraction procedure for HPLC–MS quantification of daptomycin, amikacin, gentamicin, and rifampicin in human plasma, Anal. Bioanal. Chem. 396 (2010) 791–798.

[54] L. Baietto, A. D'Avolio, F.G. De Rosa, S. Garazzino, S. Patanella, M. Siccardi, M. Sciandra, G. Di Perri, Simultaneous quantification of linezolid, rifampicin, levofloxacin, and moxifloxacin in human plasma using high-performance liquid chromatography with UV, Ther. Drug. Monit. 31 (2009) 104–109.

[55] L. Baietto, A. D'Avolio, G. Ventimiglia, F.G. De Rosa, M. Siccardi, M. Simiele, M. Sciandra, G. Di Perri, Development, validation, and routine application of a high-performance liquid chromatography method coupled with a single mass detector for quantification of itraconazole, voriconazole, and posaconazole in human plasma, Antimicrob. Agents Chemother. 54 (2010) 3408–3413.

[56] A. D'Avolio, L. Baietto, M. Siccardi, M. Sciandra, M. Simiele, V. Oddone, S. Bonora, G. Di Perri, An HPLC-PDA method for the simultaneous quantification of the HIV integrase inhibitor raltegravir, the new nonnucleoside reverse transcriptase inhibitor etravirine, and 11 other antiretroviral agents in the plasma of HIV-infected patients, Ther. Drug Monit. 30 (2008) 662–669.

[57] A. D'Avolio, M. Sciandra, M. Siccardi, L. Baietto, D.G. de Requena, S. Bonora, G. Di Perri, A simple and sensitive assay for determining plasma tipranavir concentration in the clinical setting by new HPLC method, J. Chromatogr. B: Anal. Technol. Biomed. Life Sci. 848 (2007) 374–378.

[58] A. D'Avolio, M. Siccardi, M. Sciandra, L. Baietto, S. Bonora, L. Trentini, G. Di Perri, HPLC–MS method for the simultaneous quantification of the new HIV protease inhibitor darunavir, and 11 other antiretroviral agents in plasma of HIV-infected patients, J. Chromatogr. B: Anal. Technol. Biomed. Life Sci. 859 (2007) 234–240.

[59] A. D'Avolio, M. Simiele, L. Baietto, M. Siccardi, M. Sciandra, S. Patanella, S. Bonora, G. Di Perri, A validated high-performance liquid chromatography–ultraviolet method for quantification of the CCR5 inhibitor maraviroc in plasma of HIV-infected patients, Ther. Drug Monit. 32 (2010) 86–92.

[60] A. D'Avolio, M. Simiele, M. Siccardi, L. Baietto, M. Sciandra, S. Bonora, G. Di Perri, HPLC–MS method for the quantification of nine anti-HIV drugs from dry plasma spot on glass filter and their long term stability in different conditions, J. Pharm. Biomed. Anal. 52 (2010) 774–780.

Quantification of cabazitaxel in human plasma by liquid chromatography/triple-quadrupole mass spectrometry: A practical solution for non-specific binding

Peter de Bruijn*, Anne-Joy M. de Graan, Annemieke Nieuweboer, Ron H.J. Mathijssen, Mei-Ho Lam, Ronald de Wit, Erik A.C. Wiemer, Walter J. Loos

Department of Medical Oncology, Erasmus MC – Daniel den Hoed Cancer Center, University Medical Center, Rotterdam, The Netherlands

ABSTRACT

A rapid and sensitive liquid chromatography/tandem mass spectrometry (LC–MS/MS) method has been developed and validated for the quantitative determination of cabazitaxel, a novel tubulin-binding taxane, in 100 μl aliquots of human lithium heparinized plasma with deuterated cabazitaxel as internal standard. The sample extraction and cleaning-up involved a simple liquid–liquid extraction with 20 μl aliquots of 4% ammonium hydroxide, 100 μl aliquots of acetonitrile and 1 ml aliquots of n-butylchloride. Chromatographic separations were achieved on a reversed phase C_{18} column eluted at a flow-rate of 0.20 ml/min on a gradient of acetonitrile. The overall cycle time of the method was 5 min, with cabazitaxel eluting at 3.0 min. The multiple reaction monitoring transitions were set at 836 > 555 (m/z), and 842 > 561 (m/z) for cabazitaxel and the internal standard, respectively. The calibration curves were linear over the range of 1.00–100 ng/ml with the lower limit of quantitation validated at 1.00 ng/ml. The within-run and between-run precisions, also at the level of the LLQ, were within 8.75%, while the accuracy ranged from 88.5 to 94.1%. As dilution of samples prior to extraction resulted in a loss of cabazitaxel of approximately 6.5% per dilution step, a second calibration curve ranging from 40.0 to 4000 ng/ml was validated and was also linear. The within-run and between-run precisions in this range were within 4.99%, while the accuracy ranged from 95.8 to 100.3%. The method was successfully applied to samples derived from a clinical study.

© 2011 Elsevier B.V. All rights reserved.

1. Introduction

Acquired and intrinsic resistance to docetaxel and paclitaxel (i.e., the two approved first generation taxanes) is still an important concern in daily clinical practice. Therefore, the intravenously available semi-synthetic taxanes, cabazitaxel (Jevtana®; XRP6258; TXD258; RPR116258A) and larotaxel (RPR109881A) were selected for clinical development as a result of their efficacy in a broad range of cell-lines and tumor models of mouse and human origin. Also, both compounds showed greater potency than docetaxel in cell lines expressing the drug transporter p-glycoprotein (reviewed in [1–3]).

While larotaxel is currently still under clinical evaluation, cabazitaxel has been approved in the US by the Food and Drug Administration (FDA) in June 2010 [3] and in Europe by the European Medicines Agency (EMA) in January 2011 [4] in combination with prednisone for the treatment of patients with castration-resistant metastatic prostate cancer whose disease progresses after docetaxel treatment, based on the results of the TROPIC trail investigating cabazitaxel plus prednisone versus mitoxantrone plus prednisone following docetaxel failure [5]. Cabazitaxel is currently being investigated in the setting of metastatic breast cancer progressing after taxane or anthracycline based chemotherapeutic regimens [6,7].

A population pharmacokinetic model was developed using pharmacokinetic data from five different studies [4], from which two currently have been published as peer reviewed manuscripts [7,8]. The pharmacokinetics of cabazitaxel are linear in the studied dose-range of 10–30 mg/m² given as 1 h infusions and are consistent with a three-compartment pharmacokinetic model with half lives in the initial, intermediate and terminal phase of approximately 4.4 min, 1.6 h, and 95 h, respectively. The drug has a fast plasma clearance estimated to be 48.5 l/h in the studied population and has a large volume of distribution of 4870 l. The *ex vivo* protein binding was 91.6%, mainly to albumin and lipoproteins, while the

* Corresponding author at: Erasmus University Medical Center – Daniel den Hoed Cancer Center, Department of Medical Oncology, Josephine Nefkens Building, Room Be-462, 's Gravendijkwal 230, 3015 CE Rotterdam, The Netherlands.
Tel.: +31 10 7041252; fax: +31 10 7041053.
E-mail address: p.debruijn@erasmusmc.nl (P. de Bruijn).

drug displays low binding to α1-acid glycoprotein. Cabazitaxel is extensively metabolized by cytochrome P450 iso-enzymes CYP3A4 and CYP3A5, with CYP2C8 playing a minor role in its metabolism. Cabazitaxel and its metabolites are mainly excreted via the feces (76% of the dose) and to a lesser extent through the urinary pathway (3.7% of the dose).

Neutropenia is the principle dose-limiting and most commonly observed toxicity in cabazitaxel treatment when administered as 1 h infusion every 3 weeks [8]. In the phase III trial comparing the efficacy of prednisone plus cabazitaxel to mitoxantrone, grade $\geq$3 neutropenia was observed in 82% of the patients in the cabazitaxel arm, with 8% of the patients experiencing febrile neutropenia [5]. Of the non-hematological toxicities diarrhea is the most commonly observed side effect seen in this regimen [5,8]. Overall, diarrhea occurred in 47% of the patients with 6% experiencing grade $\geq$3 diarrhea [5]. In a weekly schedule, diarrhea was even more pronounced and considered a dose-limited toxicity [9].

As cabazitaxel is a promising new anticancer agent for taxanes-resistant tumors, it is expected that numerous subsequent clinical studies investigating both single agent and cabazitaxel-based combinations will be initiated. For this purpose, quantitation of cabazitaxel is imperative.

To the best of our knowledge, no reports have been published describing a validated bioanalytical method for the quantitation of cabazitaxel. We have developed and validated a sensitive and selective liquid chromatography–tandem mass spectrometry (LC–MS/MS) assay for cabazitaxel in human plasma, according to the Guidance for Industry, Bioanalytical Method Validation, as specified by the FDA. In addition, we discuss the non-specific binding of cabazitaxel observed during sample preparation and provide a simple and practical solution to deal with this phenomenon during pharmacokinetic analysis.

2. Experimental

2.1. Chemicals

Cabazitaxel (purity 92.9%) and the deuterated internal standard, ^{2}H$_6$-cabazitaxel (purity 97.4%), were kindly supplied by Sanofi-Aventis (Frankfurt am Main, Germany). All chemicals were of analytical grade or higher. Acetonitrile, methanol and water were purchased from Biosolve BV (Valkenswaard, The Netherlands). Dimethyl sulfoxide, ammonium formate and n-butylchloride were from Sigma–Aldrich (Zwijndrecht, The Netherlands). Formic acid and ammonium hydroxide were obtained from J.T. Baker (Deventer, The Netherlands) and 2-propanol from Merck (Darmstadt, Germany). Blank lithium heparinized plasma was purchased from Biological Specialty Corporation (BSC, Colmar, PA, USA).

2.2. Preparation of stock solutions, calibration standards and quality control samples

Cabazitaxel stock solutions were prepared at 1 mg/ml free base in dimethyl sulfoxide. Stock solutions were aliquotted and stored at $T < -70\,^\circ$C. Separate stock solutions were prepared for the construction of the calibration curve standards and the pools of quality control samples. The internal standard stock solution was prepared at 1 mg/ml in dimethyl sulfoxide, which subsequently was aliquotted and stored at $T < -70\,^\circ$C. Internal standard working solutions were prepared at concentrations of 100 and 1000 ng/ml in acetonitrile, which were stored at $T < 8\,^\circ$C for a maximum of 3 months.

Calibration standards were prepared in duplicate on the day of analysis, by addition of 10 μl aliquots of appropriate dilutions of cabazitaxel stock solution in acetonitrile/DMSO (1:1, v/v) to 190 μl aliquots of human lithium heparinized plasma with concentrations of 1.00, 2.50, 10.0, 25.0, 50.0, 75.0, 90.0 and 100 ng/ml for quantitation of cabazitaxel in the concentration range of 1.00–100 ng/ml and 40.0, 120, 500, 1000, 2500, 3600 and 4000 ng/ml for concentrations of cabazitaxel in the range of 40.0–4000 ng/ml.

Pools of QC samples were prepared in human lithium heparinized plasma at concentrations of 1.00 ng/ml (lower limit of quantitation, LLQ), 3.00 ng/ml (QC low), 40.0 ng/ml (QC middle) and 80.0 ng/ml (QC high) for calibration standard curve in the range of 1.00–100 ng/ml and at 40.0 ng/ml (LLQ; i.e., QC middle above), 120 ng/ml (QC low), 1500 ng/ml (QC middle) and 3000 ng/ml (QC high) for calibration standard curve in the range of 40.0–4000 ng/ml. Pools of QC samples were aliquotted and stored at $T < -70\,^\circ$C and $T < -20\,^\circ$C upon processing.

2.3. Sample preparation

For both calibration ranges, aliquots of 20 μl 4% ammonium hydroxide and 100 μl of internal standard working solution (100 ng/ml for the range of 1.00–100 ng/ml and 1000 ng/ml for the range of 40.0–4000 ng/ml) were added to 100 μl of plasma samples in 2 ml microcentrifuge tubes followed by 1 ml aliquots of n-butylchloride. Hereafter, the samples were vigorously mixed for 10 min and then centrifuged at 18,000 × g at ambient temperature for 10 min. Aliquots of 1 ml of the organic phase were transferred into 4.5 ml glass tubes and evaporated under nitrogen at $T = 70\,^\circ$C. The residues were resuspended in 100-μl aliquots of acetonitrile/water/ammonium formate (40:60:0.2, v/v/v). After 5 min of centrifugation at 3000 × g, the supernatants were transferred into 350 μl 96-well plates, which were placed into the chilled ($T = 10\,^\circ$C) autosampler, from which aliquots of 50 μl were injected onto the HPLC column for the low-range method (1.00–100 ng/ml) and 10 μl for the high-range method (40.0–4000 ng/ml).

2.4. Equipment

The LC–MS/MS system was purchased from Waters Chromatography B.V. (Etten-Leur, The Netherlands) and consisted of a Waters 2795 Separation Module coupled to a Quatro micro API Mass Spectrometer. The MassLynx V4.1 SCN627 software package was used for the acquisition and processing of data. Quantification was performed using QuanLynx as implemented in the MassLynx software.

2.5. Chromatographic conditions

Analytes were separated on an Alltima HP C$_{18}$ HL column 3 μm, 50 mm × 2.1 mm, (Grace, Breda, The Netherlands) thermostatted at $T = 40\,^\circ$C. A gradient at a flow-rate of 0.20 ml/min was achieved with mobile phase A, composed of 2 mM ammonium formate and mobile phase B, composed of acetonitrile. A linear gradient was used, with 50–15% mobile phase A, from 0 to 1.5 min, followed by holding on 15% mobile phase A (i.e., 85% mobile phase B) for 1.5 min. This was succeeded by a linear gradient back to 50% mobile phase A from 3.0 to 3.1 min, which was held for 1.9 min to re-equilibrate. The overall run time of the assay was 5 min. A pre-column volume of 300 μl was applied and a parallel injection was enabled. The needle wash solvent was composed of acetonitrile/methanol/water/2-propanol/formic acid (25:25:25:25:0.1, v/v/v/v/v).

2.6. Mass spectrometry

Tandem mass spectrometry was performed in the positive ion electrospray ionization mode. Mass transitions of m/z were optimized for cabazitaxel and ^{2}H$_6$-cabazitaxel (internal standard) by infusion of the respective analytes in acetonitrile/water/formic acid (40:60:0.1, v/v/v) via a T-union. Optimal MS settings were manually adjusted. The desolvation gas was set at 800 l/h and the cone
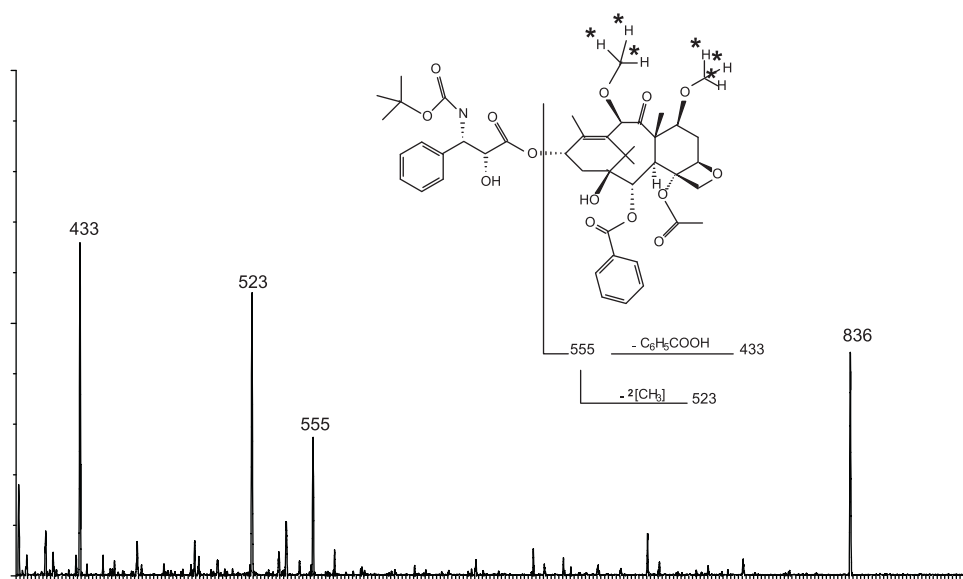
Fig. 1. Mass spectrum and chemical structure of cabazitaxel. The asterisks represent the deuterium atoms in the stable labeled internal standard $^2H_6$-cabazitaxel.

gas at 25 l/h (nitrogen). The ionspray voltage was kept at 3.50 kV and the cone voltage at 20 V for cabazitaxel and 19 V for the IS, with a source temperature of $T = 120\,^{\circ}C$ and desolvation temperature of $T = 350\,^{\circ}C$. The dwell times were set at 150 ms and the inter-channel delay at 50 ms. Multiple reaction monitoring (MRM) mode was applied for the quantitation with the following parameters: m/z 836 > 555, collision energy at 10 V for cabazitaxel and m/z 842 > 561, collision energy at 10 V for the internal standard (Fig. 1). The collision cell pirani pressure was set at $\sim 5e^{-3}$ mbar (argon). The column effluent was passed through the mass spectrometer and monitored between 2 and 4 min after start of MS method, 0–2 min and 4–5 min sent to waste.

2.7. Quantitation

Calibration curves were generated using peak area ratios of cabazitaxel to internal standard $^2H_6$-cabazitaxel versus the known cabazitaxel concentrations with a linear regression analysis with a weighting scheme of 1/concentration for the low curve and 1/concentration^2 for the high curve.

2.8. Method validation

The quantitative LC–MS/MS method was validated in accordance with the Guidance for Industry, Bioanalytical Method Validation, as specified by the FDA (http://www.fda.gov/downloads/Drugs/GuidanceComplianceRegulatoryInformation/Guidances/ucm070107.pdf).

Potential presence of endogenous contaminating compounds that may interfere with the analytical assay was determined by analyzing blank human lithium heparinized plasma samples of ten different lots. The following substances were investigated for interference with the analytical method: aprepitant, budesonide, dexamethasone, domperidon, granisetron, lorazepam, oxazepam, paracetamol and metoclopramide. All drugs have been dissolved/diluted in water to a concentration of 1 mg/ml followed by a 500-fold dilution in blank human lithium heparinized plasma. Aliquots have subsequently been diluted in plasma containing the different drugs to yield final cabazitaxel concentrations of 8.00 and 50.0 ng/ml, which have been processed and compared to equal concentrations in blank human lithium heparinized plasma.

Accuracy (ACC), within-run precision (WRP) and the between-run precision (BRP) for both calibration curve ranges were determined by analyzing 5 replicates of pools of LLQ and QC samples independently over a three-run period, with the calibration curve standards processed in duplicate. The ACC, WRP and BRP at the level of the LLQ and QC samples were calculated by one-way analysis of variance, using the run as the variable as earlier described [10,11].

For the validation of the LLQ, besides the validation of the pools as described above, blank human lithium heparinized plasma of 10 different donors were spiked at a concentration of 1.00 ng/ml and quantitated in a separate run.

The evaluation of the matrix effect was tested by comparing the MS/MS response of cabazitaxel at a concentration of 3.00 and 80.0 ng/ml (for the low curve) and at 3000 ng/ml (for the high curve) spiked in triplicate in acetonitrile/water/formic acid (40:60:0.1, v/v/v) to the MS/MS responses of the analytes spiked in triplicate into extracts of blank human lithium heparinized plasma, as described recently [10,12].

Extraction recovery was determined by comparing the MS/MS response of cabazitaxel at a concentration of 3.00 and 80.0 ng/ml (for the low curve) and at 3000 ng/ml (for the high curve) spiked in triplicate into six different lots of blank lithium heparinized plasma before extraction, to the MS/MS responses of the analytes spiked in triplicate into extracts of blank human lithium heparinized plasma after extraction, corrected for the evaporated volume of organic phase [10,12].

The stability of cabazitaxel in human lithium heparinized plasma was tested with QC low (3.00 ng/ml) and both QC high (80.0 and 3000 ng/ml) at ambient temperature for a period of 18 h as well as following 3 freeze–thaw cycles, in which the samples were thawed for at least 30 min followed by refreezing for at least 18 h. Long-term stability at $T < -20\,^{\circ}C$ and $T < -70\,^{\circ}C$ in human lithium heparinized plasma has been investigated using the same QC samples as described above. Also the storage stability of processed samples in the autosampler was tested in triplicate at the concentration of QC low and both QC high. QC samples were processed in triplicate and repeatedly injected on different time points.
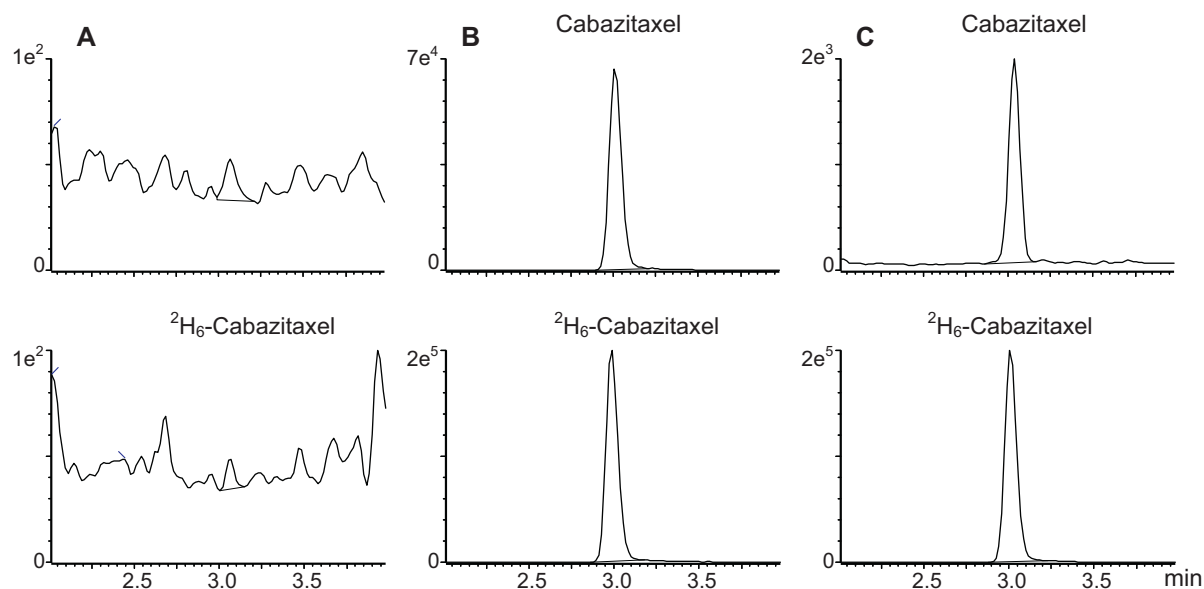
Fig. 2. Representative chromatograms of (A) double blank processed plasma sample collected prior to the administration of 25 mg/m² cabazitaxel, (B) plasma sample taken prior to the end of infusion containing 267 ng/ml cabazitaxel and (C) plasma sample collected on day 7 containing 1.03 ng/ml cabazitaxel. Samples A and C are quantitated on the calibration curve in the range of 1.00–100 ng/ml cabazitaxel and sample B on the calibration curve in the range of 40.0–4000 ng/ml.

2.9. Non-specific binding

As during the initial method validation non-specific binding of cabazitaxel was observed (see results section), an experiment was conducted to establish the potential loss of cabazitaxel during sample dilution. QC high (80.0 ng/ml) was serially diluted (in triplicate) to 40.0, 20.0, 10.0 and 5.00 ng/ml in blank plasma, subsequently processed and the individual accuracies estimated.

2.10. Application of method to clinical samples

To demonstrate the applicability of the validated bioanalytical method, blood samples were collected from seven patients enrolled in a clinical study in which cabazitaxel was administered intravenously over 60 min at a dose of 25 mg/m² (see www.trialregister.nl; NTR study number 2840). Twelve blood samples in the presence of lithium heparin as anticoagulant were obtained during the first 24 h after administration. A last blood sample was drawn between day 7 and 9. Samples were processed within 15 min of collection to isolate the plasma, which was stored at $T < -70\,°C$ before analysis as described. All patients provided written informed consent and the local institutional review boards approved the clinical protocol (MEC 2011-091).

Individual pharmacokinetic parameters were estimated using non-compartmental analysis using the software program Phoenix WinNonLin 6.1 (Pharsight, Mountain View, CA).

3. Results and discussion

3.1. LC–MS/MS conditions

Cabazitaxel belongs to the group of taxanes with a single protonation site located on the secondary amine of the side-chain. Optimal sensitivity was achieved by the addition of ammonium formate, presumably by generation of an intermediate ion [M+NH₄⁺] which may dissociate into [M+H⁺] and ammonia during the electrospray process. Therefore, for optimal signals the mobile phase was composed of 2 mM aqueous ammonium formate and acetonitrile.

The cabazitaxel product ion spectra (Fig. 1) yielded abundant product ions suitable for use in multiple reaction monitoring. Main fragment m/z 555 resulted from the baccatin III core while m/z 523 is generated by loss of the methyl groups of the baccatin III core and m/z 433 was generated by loss of the benzoic acid from the baccatin III core. The product ion at m/z 555 was selected as the MRM ion for quantitation of cabazitaxel and the product ion at m/z 561 for its stable isotope labeled internal standard ²H₆-cabazitaxel.

Cabazitaxel was separated from early eluting hydrophilic, potentially response-suppressing, matrix components by applying a step gradient. A relative short analysis time of 5 min, with cabazitaxel eluting at 3.0 min (Fig. 2) was maintained.

3.2. Non-specific binding

During the initial method validation a QC diluted spiked at a concentration of 4000 ng/ml was included on the calibration curve standards in the range of 1.00–100 ng/ml. This QC sample was 50-fold diluted in blank plasma in 2 steps prior to extraction. The accuracy was below 85% during the first two validation runs. Therefore a new pool was prepared, which also failed for the accuracy. Non-specific binding is a well-known drawback of taxanes [13], therefore, non-specific binding during sample dilution was most likely the underlying explanation of the low accuracy of the diluted QC sample. This was investigated by serial dilution of the QC sample with a spiked concentration of 80.0 ng/ml. As shown in Fig. 3, the accuracy decreases linearly by 6.5% following each sequential dilution step. Addition of polysorbate 80 or Cremophor EL up to concentrations of 1% to overcome non-specific binding [13], did not result in increased accuracies. Also, accuracy could not be improved by using pipette tips and/or laboratory tubes of different materials and brands (data not shown).

Eventually, validation of the method at a higher concentration range, to avoid additional steps in sample processing for samples in which the concentration exceeds the 100 ng/ml, was performed. The range of 40.0–4000 ng/ml was selected based on the available data of maximum concentrations of 535 ± 305 ng/ml following the administration of 25 mg/m² cabazitaxel [8].

Table 1
Calculations of the between-run and within-run precisions and the average accuracy of the LLQ and QC samples.[a]

Sample	Spiked (ng/ml)	GM (ng/ml)	ACC (%)	WRP (%)	BRP (%)	n[b] (%)
Range 1.00–100 ng/ml						
LLQ	1.00	0.885	88.5	8.75	5.98	13 of 15
Low	3.00	2.81	93.7	8.12	#[c]	13 of 15
Middle	40.0	37.3	93.3	2.94	#[c]	15 of 15
High	80.0	75.3	94.1	3.03	0.67	15 of 15
Range 40.0–4000 ng/ml						
LLQ	40.0	39.7	99.3	4.75	3.72	15 of 15
Low	120	119	99.2	4.15	3.29	15 of 15
Middle	1500	1504	100.3	4.99	#[c]	15 of 15
High	3000	2873	95.8	4.11	#[c]	15 of 15

Abbreviations: GM, grand mean; ACC, average accuracy; WRP, within-run precision; BRP, between-run precision.

[a] $n = 5$ in 3 separate runs.
[b] Number of individual samples falling within acceptable range of accuracy of 85–115% (80–120% at LLQ).
[c] No additional variation observed by performing the assay in different runs.

3.3. Assay performance

The results of the method were linear ($r \geq 0.9987$) in the concentration range of 1.00–100 ng/ml as well as in the range of 40.0–4000 ng/ml ($r \geq 0.9950$) in human lithium heparinized plasma. None of the potentially co-administrated drugs interfered with the quantitation of cabazitaxel.

The LLQ was validated at 1.00 ng/ml with the measured concentrations of cabazitaxel in nine out of ten independently spiked plasma samples falling within the acceptable range of accuracy of 80–100%. The average measured concentration in all ten samples was 0.940 ± 0.087 ng/ml. The within-run and between-run precisions and the accuracies at seven tested concentrations in human lithium heparinized plasma, including at the level of the LLQ, are summarized in Table 1. All fall within the accepted ranges as specified by the Food and Drug Administration.

The mean measured extraction efficiencies for cabazitaxel were 92%, 100% and 106% at the concentrations of 3.00, 80.0 and

Table 2
Stability of cabazitaxel.

Condition	% to concentration at the initial time point		
	3.00 ng/ml	80.0 ng/ml	3000 ng/ml
Ambient temp (18 h)	105	95.5	99.8
3 freeze/thaw cycles	100	103	100
Processed sample ($T = 10 °C$, 20 h)	112	109	105
$T < -20 °C$ (6 months)	90.5	94.9	111
$T < -70 °C$ (6 months)	90.3	93.7	107

3000 ng/ml, respectively. The values for the matrix effect were 66%, 72% and 86% at 3.00, 80.0 and 3000 ng/ml, respectively.

Cabazitaxel was stable in lithium heparinized plasma (i) at ambient temperature for at least 18 h, (ii) during three consecutive freeze–thaw cycles and (iii) at least 6 months when stored at $T < -20 °C$ and $T < -70 °C$. As processed samples, cabazitaxel was stable for at least 20 h in the chilled ($T = 10 °C$) autosampler (Table 2).
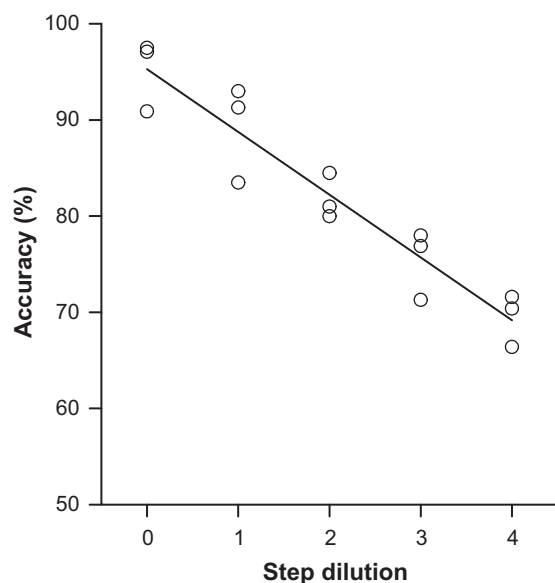
Fig. 3. Linear correlation between the number of dilution steps and the observed accuracy of QC sample high spiked with 80.0 ng/ml cabazitaxel. Dilution "0" represents the accuracy following no dilution, "1" following 2-fold dilution in one step (i.e. 40.0 ng/ml), "2" following 4-fold dilution in 2 steps (i.e. 20.0 ng/ml), "3" following 8-fold dilution in 3 steps (i.e. 40.0 ng/ml) and "4" following 16-fold dilution in 4 steps (i.e. 5.00 ng/ml). The equation of the linear curve is: $y = -6.5 \times x + 95.3$, in which the -6.5 represents the loss of 6.5% of cabazitaxel per dilution step.
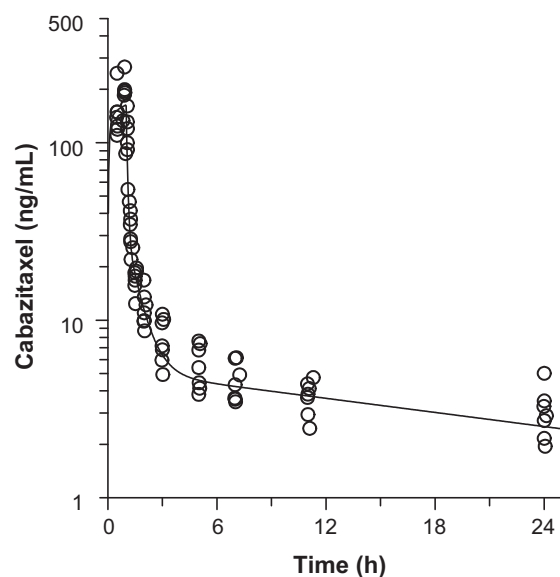
Fig. 4. Average plasma concentration-time profile of cabazitaxel in 7 patients following the administration of 25 mg/m^2 as a 1 h infusion in the first course. Open symbols represent individual concentration data. The solid line represents the fit according to a three-compartmental pharmacokinetic model (model 19 with $1/y^2$ weighting; Phoenix WinNonLin version 6.1; Pharsight, Mountain View, CA).

3.4. Clinical application

As shown in Fig. 4, plasma concentration versus time curves could be readily determined. The data indicate that the lower limit of quantitation of 1.00 ng/ml is sufficient for monitoring drug-plasma levels in samples obtained from patients treated with cabazitaxel at a dose of 25 mg/m^2. Preliminary pharmacokinetic data revealed maximum concentrations of 189 ± 14.7 ng/ml ($n = 7$) and AUC$_{(0-24\,h)}$ values of 248 ± 31.9 ng h/ml ($n = 7$). We were able to quantitate concentrations up to 7–9 days after administration with concentrations in the range of 1.03–1.25 ng/ml. The method is thus sensitive enough for pharmacokinetic analysis in clinical pharma-cokinetic studies beyond 24 h. Representative chromatograms are shown in Fig. 2.

4. Conclusion

A sensitive, selective, accurate and precise LC–MS/MS method has been developed and validated for the analysis of cabazitaxel in human heparinized plasma, which meets the current require-ments of bioanalytical method validation. As sample dilution prior to extraction results in the loss of cabazitaxel, a secondary calibra-tion range has been validated to avoid sample dilution. This method will prove to be a valuable tool for pharmacokinetic (interaction) studies with cabazitaxel.

References

[1] O. Metzger-Filho, C. Moulin, E. de Azambuja, A. Ahmad, Larotaxel: broadening the road with new taxanes, Expert Opin. Investig. Drugs 18 (2009) 1183–1189.
[2] D.P. Michielsen, J.G. Braeckman, L. Denis, Cabazitaxel for the treatment of prostate cancer, Expert Opin. Pharmacother. 12 (2011) 977–982.
[3] S. Oudard, TROPIC: phase III trial of cabazitaxel for the treatment of metastatic castration-resistant prostate cancer, Future Oncol. 7 (2011) 497–506.
[4] Assessment Report for Jevtana (Cabazitaxel), Procedure No.: EMEA/H/C/002018, European Medicines Agency, London, 2011.
[5] J.S. de Bono, S. Oudard, M. Ozguroglu, S. Hansen, J.P. Machiels, I. Kocak, G. Gravis, I. Bodrogi, M.J. Mackenzie, L. Shen, M. Roessner, S. Gupta, A.O. Sartor, Prednisone plus cabazitaxel or mitoxantrone for metastatic castration-resistant prostate cancer progressing after docetaxel treatment: a randomised open-label trial, Lancet 376 (2010) 1147–1154.
[6] X. Pivot, P. Koralewski, J.L. Hidalgo, A. Chan, A. Goncalves, G. Schwartsmann, S. Assadourian, J.P. Lotz, A multicenter phase II study of XRP6258 administered as a 1-h i.v. infusion every 3 weeks in taxane-resistant metastatic breast cancer patients, Ann. Oncol. 19 (2008) 1547–1552.
[7] C. Villanueva, A. Awada, M. Campone, J.P. Machiels, T. Besse, E. Magherini, F. Dubin, D. Semiond, X. Pivot, A multicentre dose-escalating study of cabazitaxel (XRP6258) in combination with capecitabine in patients with metastatic breast cancer progressing after anthracycline and taxane treatment: A phase I/II study, Eur. J. Cancer 47 (2011) 1037–1045.
[8] A.C. Mita, L.J. Denis, E.K. Rowinsky, J.S. Debono, A.D. Goetz, L. Ochoa, B. Forouzesh, M. Beeram, A. Patnaik, K. Molpus, D. Semiond, M. Besen-val, A.W. Tolcher, Phase I and pharmacokinetic study of XRP6258 (RPR 116258A), a novel taxane, administered as a 1-hour infusion every 3 weeks in patients with advanced solid tumors, Clin. Cancer Res. 15 (2009) 723–730.
[9] K.A. Gelmon, J. Latreille, A. Tolcher, L. Genier, B. Fisher, D. Forand, S. D'Aloisio, L. Vernillet, L. Daigneault, A. Lebecq, M. Besenval, E. Eisenhauer, Phase I dose-finding study of a new taxane, RPR 109881A, administered as a one-hour intravenous infusion days 1 and 8 to patients with advanced solid tumors, J. Clin. Oncol. 18 (2000) 4098–4108.
[10] P. de Bruijn, I.M. Moghaddam-Helmantel, M.J. de Jonge, T. Meyer, M.H. Lam, J. Verweij, E.A. Wiemer, W.J. Loos, Validated bioanalytical method for the quan-tification of RGB-286638, a novel multi-targeted protein kinase inhibitor, in human plasma and urine by liquid chromatography/tandem triple-quadrupole mass spectrometry, J. Pharm. Biomed. Anal. 50 (2009) 977–982.
[11] H. Rosing, W.Y. Man, E. Doyle, A. Bult, J.H. Beijnen, Bioanalytical liquid chro-matographic method validation. A review of current practices and procedures, J. Liq. Chromatogr. RT 23 (2000) 329–354.
[12] B.K. Matuszewski, M.L. Constanzer, C.M. Chavez-Eng, Strategies for the assessment of matrix effect in quantitative bioanalytical methods based on HPLC–MS/MS, Anal. Chem. 75 (2003) 3019–3030.
[13] W.J. Loos, W.C. Zamboni, F.K. Engels, P. de Bruijn, M.H. Lam, R. de Wit, J. Verweij, E.A. Wiemer, Pitfalls of the application of microdialysis in clinical oncology: controversial findings with docetaxel, J. Pharm. Biomed. Anal. 45 (2007) 288–294.

Validated LC–MS/MS method for the quantitative determination of the glucosylceramide synthase inhibitor miglustat in mouse plasma and human plasma and its application to a pharmacokinetic study

Elke Spieker[a], Winfried Wagner-Redeker[a,*], Jasper Dingemanse[b]

[a] Swiss BioAnalytics AG, Sternenfeldstrasse 14, 4127 Birsfelden, Switzerland
[b] Actelion Pharmaceuticals Ltd., Gewerbestrasse 16, 4123 Allschwil, Switzerland

ABSTRACT

A sensitive liquid chromatography–tandem mass spectrometry method has been developed to quantify miglustat in mouse plasma and in human plasma. The method involved simple protein precipitation with methanol. N-(n-nonyl)deoxynojirimycin was used as internal standard. Separation was performed on a Gemini C_{18} column (2.1 mm × 50 mm, particle size 5 μm) with a binary gradient at a flow rate of 600 μl/min. The mobile phases were methanol and water both containing 0.01% of a 25% ammonium hydroxide solution. The triple stage quadrupole mass spectrometer was operated in APCI mode using the transitions m/z 220.1 ≥ 158.0 for miglustat and m/z 290.1 ≥ 228.0 for the internal standard. The method was linear over a range of 10–10,000 ng/ml. The intra-day coefficients of variation for mouse plasma were equal to or smaller than 14.1%. The intra- and inter-day accuracies were 84.5–107.2% and 90.9–104.0%, respectively. For human plasma the intra-day coefficients of variation were equal to or smaller than 13.5%, while accuracies ranged between 93.6% and 100.0%. The validated method offered increased sensitivity (10 times higher) and decreased cycle times compared to other methods. It was successfully applied to the pharmacokinetic assessment of miglustat during treatment of patients with cystic fibrosis.

© 2011 Elsevier B.V. All rights reserved.

1. Introduction

Miglustat (OGT 918, N-butyl-deoxynojirimycin, trade name Zavesca™) is an imino sugar [1] (molecular mass: 219 u) registered for the treatment of Gaucher disease and Niemann-Pick type C disease [2]. Miglustat is an orally administered drug that crosses the blood–brain barrier. The primary pharmacological activity of miglustat is inhibition of the enzyme glucosylceramide synthase, catalyzing the first step in the biosynthesis of glycosphingolipids (GSLs), i.e., the formation of glucosylceramide (GlcCer). Reduced formation of GlcCer will lead to decreased biosynthesis of more complex GSLs. This therapeutic principle, called substrate reduction therapy, may be useful in treatment of disorders of intracellular (predominantly lysosomal) accumulation of GSLs either due to their deficient breakdown or intracellular transport/trafficking [3–5].

Following oral administration, miglustat is rapidly absorbed with a median time to reach maximum concentration (t_{max}) at approximately 2.5 h. A minor route of metabolism is glucuronidation, but excretion as unchanged compound into urine is predominant.

Quantification of miglustat in human plasma by coupling of liquid chromatography with tandem mass spectrometry has been reported by Guitton et al. [6]. The authors employed electrospray (ESI) as ionization method and used miglitol as internal standard. The method covered a range of 125–2500 ng/ml, although the authors reported the ability to analyze plasma concentrations down to 25 ng/ml [6].

We have analyzed miglustat in plasma samples since 2006 and our first validated method for human plasma employed reversed phase HPLC/MS/MS with ESI as ionization mode. When using this method routinely, however, we faced unwanted effects. The ESI-method could not be easily transferred from analysis of human samples to analysis of samples from toxicology species. We also aimed at maximizing sensitivity of the assay. Detection limits of 10 ng/ml or lower may be required if pharmacokinetic profiles are to be investigated for 48 h or more or if small-volume samples from pediatric populations are to be analyzed. We therefore decided to improve the method. Goal was to develop a simple, sensitive, and rapid assay for the quantification of miglustat in mouse plasma and in human plasma as well as in plasma from other species with minimum modifications necessary. The method employed atmospheric pressure chemical ionization (APCI) MS/MS coupled to reversed phase HPLC. It has been fully validated for mouse plasma. Partial validation was performed for human plasma. The method was successfully applied to plasma samples from cats as well.

* Corresponding author. Fax: +41 61 317 2310.
E-mail address: w.redeker@swissbioanalytics.com (W. Wagner-Redeker).

2. Experimental

2.1. Materials

Methanol (MeOH) was purchased from Avantor (Deventer, The Netherlands), ammonium hydroxide solution (NH$_4$OH (aq.)) from Riedel-de Haën (Seelze, Germany), miglustat and N-(n-nonyl)deoxynojirimycin, for use as internal standard (IS) from TRC Toronto Research Chemicals Inc. (North York, ON, Canada). A Milli-Q plus system from Millipore AG (Volketswil, Switzerland) was used to produce HPLC grade water. Mouse plasma with K$_3$-EDTA as anticoagulant was obtained from Harlan Laboratories Ltd. (Füllinsdorf, Switzerland). Human blank plasma with K$_3$-EDTA as an anticoagulant was obtained from the Blutspendezentrum SRK, beider Basel (Basel, Switzerland) from healthy volunteers. Captiva filter plates (pore size 0.2 μm) were purchased from Agilent Technologies (Basel, Switzerland).

2.2. Sample preparation

2.2.1. Preparation of standard solutions

For the preparation of calibration (CAL) samples miglustat was dissolved in MeOH to a concentration of 1.00 mg/ml. A separate stock solution was used for the preparation of quality control (QC) samples at a concentration of 2.50 mg/ml. Further dilutions were done with H$_2$O/MeOH (50:50, v/v). For preparation of CAL and QC samples, seven and four working solutions, respectively, of miglustat were prepared. The concentrations were in the range of 500–500,000 ng/ml for the CAL samples and 500–375,000 ng/ml for the QC samples. These working solutions were prepared by serial dilutions and had concentrations 50 times higher than those of the respective plasma standards. All concentrations were calculated considering the purity of the test items.

2.2.2. Preparation of CAL and QC samples

CAL and QC samples were prepared with blank mouse plasma and blank human plasma. Miglustat working solutions were spiked into the respective plasma at a ratio of 2:98, yielding seven CAL samples with a final concentration of 10.0, 20.0, 50.0, 250, 1000, 5000, and 10,000 ng/ml and four QC samples with a final concentration of 10.0, 30.0, 500, and 7500 ng/ml. The concentration of the QC samples corresponded to the expected concentrations in clinical pharmacokinetic studies.

2.2.3. Sample preparation mouse plasma

Proteins were precipitated by adding 75 μl MeOH containing the IS at a concentration of 500 ng/ml to an aliquot of 25 μl plasma at room temperature. The samples were centrifuged for 30 min at approximately 3360 × g and approximately 8 °C. Because of the limited sample volume, the supernatants were not filtered but diluted with one volume equivalent of 0.0025% NH$_4$OH (aq.) in H$_2$O/MeOH (50:50, v/v). An aliquot of 10 μl of the diluted supernatant was injected into the HPLC system. During analysis, the samples were stored at 8 °C in the autosampler tray.

2.2.4. Sample preparation human plasma

Proteins were precipitated by adding 300 μl MeOH containing the IS at a concentration of 500 ng/ml to an aliquot of 100 μl plasma at room temperature. The plasma samples were filtered through a protein precipitation plate (pore size 0.2 μm) and then diluted with one volume equivalent of 0.0025% NH$_4$OH (aq.) in H$_2$O/MeOH (50:50, v/v). 10.0 μl of the diluted filtrate were injected into the HPLC system. During analysis, the samples were stored at 8 °C in the autosampler tray.

2.3. Chromatography

Liquid chromatography (LC) was performed using a Rheos 2200 HPLC pump (Thermo Fisher Scientific, San Jose, USA) and a PAL HTS autosampler (CTC Analytics, Zwingen, Switzerland), equipped with a cool stack. Injection volume was 10 μl, injected into a 20 μl loop. A Gemini C$_{18}$ column (2.1 mm × 50 mm), packed with 5 μm particles (Phenomenex, Torrance, CA, USA) was used for LC separation. LC flow rate was 600 μl/min. Eluent A consisted of water containing 0.01% of a 25% NH$_4$OH (aq.) solution, eluent B of MeOH containing 0.01% of a 25% NH$_4$OH (aq.) solution. The eluent composition was kept at 100% A for 0.3 min after injection and then changed linearly to 100% B over a period of 0.7 min. Eluent composition was kept at 100% B for another minute and then went back ballistically to 100% A. The system was ready for the next injection after an equilibration time of 1 min, giving a total cycle time of 3 min. In order to avoid unnecessary contamination of the ion source of the mass spectrometer (MS), the eluent was directed into waste for the first minute of the gradient.

2.4. Mass spectrometry

A Quantum Ultra triple quadrupole mass spectrometer (Thermo Fisher Scientific, San Jose, USA) was used for compound detection. The system was operated in positive ion mode using an APCI source, operated under standard conditions (APCI voltage 4.0 kV, vaporizer temperature 400 °C, capillary temperature 300 °C). Sheath gas and auxiliary gas pressures were set to 60 and 10 units, respectively. Collision gas pressure was 1 mTorr. Signals were detected in selected reaction monitoring (SRM) mode using the mass transition m/z 220.1 ≥ 158.0 for miglustat and m/z 290.1 ≥ 228.0 for the IS. Optimum collision energy was 20 eV for both fragmentation reactions. For each transition a scan time of 0.1 s was chosen, yielding about 20 data points across each LC peak.

2.5. Validation

A full validation was performed for mouse plasma covering specificity, matrix effects, intra-day and inter-day precision and accuracy, sample dilution integrity, analyte recovery, and analyte stability. For human plasma a partial validation was performed including investigation of intra-day precision and accuracy, matrix effects, specificity and analyte stability.

3. Results and discussion

3.1. Mass spectrometry

In Fig. 1 the MS/MS spectra of miglustat and the IS N-(n-nonyl)deoxynojirimycin are shown. The spectra of the two compounds are very similar, shifted by 70 u, which corresponds to the difference in length of the alkyl side chain (C$_4$H$_9$ vs. C$_9$H$_{19}$). The spectra show a large number of fragmentation pathways as expected for this class of compounds.

In order to investigate the fragmentation pathway of ions, accurate mass experiments may yield valuable information [7]. They often allow unequivocal assignments of sum formulas, which in turn help to differentiate between possible fragmentation reactions. We have therefore investigated the MS/MS fragmentation pattern of miglustat and the IS with our Orbitrap mass spectrometer and evaluated the data with help of Mass Frontier™, a software tool optimized to assign fragment structures generated by collision-induced dissociation (CID) from a known precursor structure (Thermo Fisher Scientific, USA). The software makes use of known fragmentation rules as well as a large database of fragmentation pathways collected from literature references.
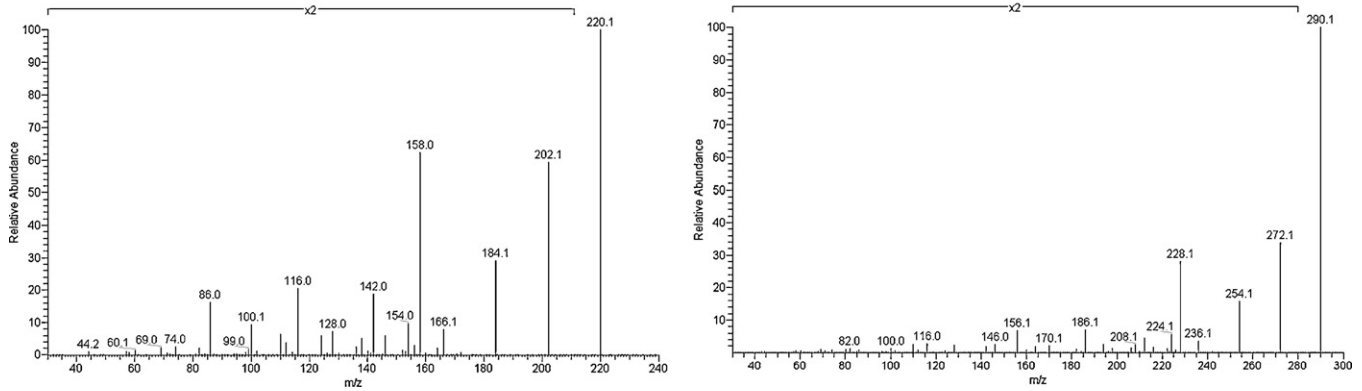
Fig. 1. MS/MS spectra of miglustat (left) and the internal standard (right); collision energy 20 eV, collision gas pressure 1 mTorr.

The Orbitrap MS/MS spectrum of miglustat is shown in Fig. 2, together with the sum formulas and some likely structures of the fragments. Mass error in these experiments is less than ±3 ppm, no internal lock mass was used. The relative intensity of fragments generated in a triple stage quadrupole (TSQ) and an ion trap are usually different for a number of reasons. Helium is used as collision gas in an ion trap, whereas Argon is the typical collision gas in a TSQ. In a TSQ one always observes consecutive fragmentation reactions which are normally not present in an ion trap. The two experiments also differ in the number of collisions and in the ion life time, all affecting the reaction rate and therefore the intensity of a given fragment. However, the underlying excitation and fragmentation mechanism is identical in both instruments. To determine the structure of fragment ions is not an easy task and very likely the reality will be more complex than proposed here. If looking at a simple loss of water from protonated miglustat, e.g. (fragment mass 202.1441), at least four fragment structures are possible, depending on which hydroxyl group is protonated during ionization. Fragment ions often represent mixtures of isomers and the assignments that have been made in Fig. 2 describe one of several possibilities.

Consecutive losses of water, as present in the CID spectra of miglustat and N-(n-nonyl)deoxynojirimycin, may show limited specificity, therefore we have selected m/z 158 and m/z 228 as daughter ions.

3.2. Liquid chromatography

Polar compounds often exhibit little retention on C_{18} columns potentially giving rise to ion suppression effects. However, fast chromatographic methods will allow high sample throughput and narrow peak shapes, enabling the scientist to report results quickly and to achieve superior assay sensitivity. If such methods are employed, special care must be taken to verify the selectivity of the method and to characterize and exclude potential matrix effects.

Using the gradient system described in the experimental section, miglustat elutes in a very sharp peak after approximately 1.35 min (peak width at half height: 2.5 s), the IS has a retention time of approximately 1.70 min (Fig. 3).
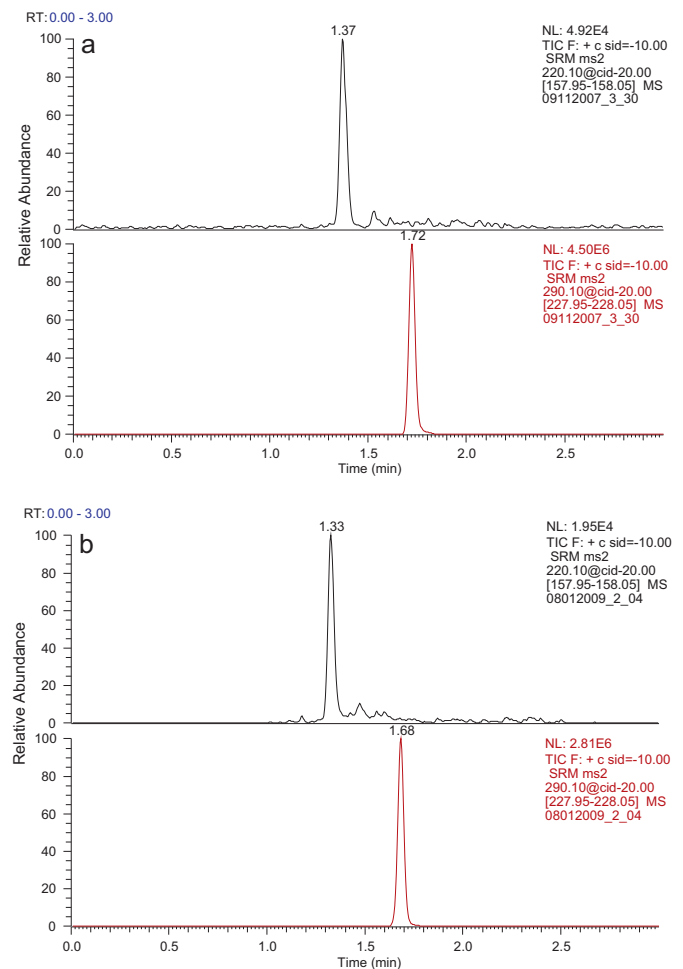
Fig. 3. SRM chromatograms of miglustat at QC1 concentration (mouse plasma, 3a) and at 20 ng/ml (human plasma, 3b) and the internal standard at a concentration of 500 ng/ml.

Fig. 2. Accurate mass MS/MS spectrum of miglustat.
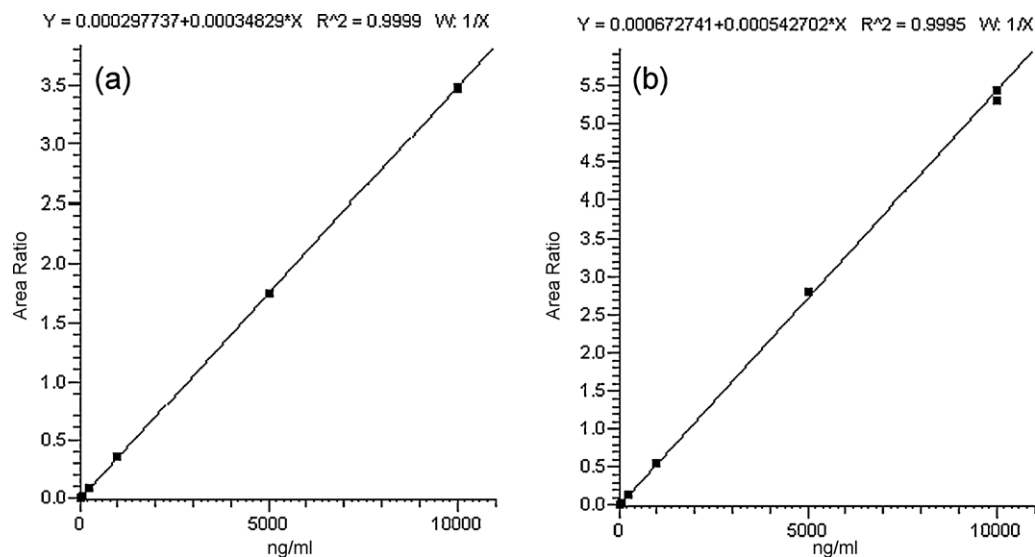
Fig. 4. Calibration curve of miglustat in mouse (a) and human (b) plasma.

3.3. Validation

3.3.1. Linearity

Three validation runs were performed for mouse plasma, each consisting of seven CAL levels and four QC concentrations in addition to a blank plasma sample and a QC0 (blank plasma with IS only).

Fig. 4 shows the calibration curves of miglustat, covering a range of 10.0–10,000 ng/ml for both mouse and human plasma. Considering the signal intensity at the lowest calibration point we estimate

Table 1
Intra-day and inter-day validation of miglustat in mouse plasma.

	QC_LLOQ 10.0 ng/ml		QC1 30.0 ng/ml		QC2 500 ng/ml		QC3 7500 ng/ml	
	Calc conc	%Diff	Calc conc	%Diff	Calc conc	%Diff	Calc conc	%Diff
Run 1	9.30	−7.0	32.5	8.3	572	14.4	8110	8.1
	9.60	−4.0	30.0	0.0	507	1.4	7900	5.3
	10.1	1.0	31.6	5.3	553	10.6	8130	8.4
	9.59	−4.1	34.0	13.3	506	1.2	8100	8.0
	9.01	−9.9	31.0	3.3	534	6.8	8080	7.7
	11.0	10.0	32.7	9.0	541	8.2	7890	5.2
Mean$_{intra}$ [ng/ml]	9.77		32.0		536		8040	
SD$_{intra}$ [ng/ml]	0.704		1.41		25.9		110	
CV$_{intra}$ [%]	7.2		4.4		4.8		1.4	
Accuracy$_{intra}$ [%]	97.7		106.7		107.2		107.2	
Run 2	8.92	−10.8	28.9	−3.7	488	−2.4	7710	2.8
	8.64	−13.6	28.4	−5.3	492	−1.6	7750	3.3
	8.05	−19.5	27.1	−9.7	486	−2.8	7920	5.6
	8.23	−17.7	26.3	−12.3	464	−7.2	7450	−0.7
	8.99	−10.1	30.0	0.0	487	−2.6	7580	1.1
	7.85	−21.5	26.8	−10.7	470	−6.0	7230	−3.6
Mean$_{intra}$ [ng/ml]	8.45		27.9		481		7610	
SD$_{intra}$ [ng/ml]	0.473		1.42		11.3		244	
CV$_{intra}$ [%]	5.6		5.1		2.3		3.2	
Accuracy$_{intra}$ [%]	84.5		93.0		96.2		101.5	
Run 3	7.36	−26.4	26.7	−11.0	473	−5.4	7650	2.0
	9.11	−8.9	27.0	−10.0	472	−5.6	7870	4.9
	9.32	−6.8	27.0	−10.0	479	−4.2	7900	5.3
	7.83	−21.7	27.9	−7.0	484	−3.2	7570	0.9
	10.2	2.0	27.4	−8.7	482	−3.6	7790	3.9
	10.6	6.0	27.6	−8.0	482	−3.6	7820	4.3
Mean$_{intra}$ [ng/ml]	9.07		27.3		479		7770	
SD$_{intra}$ [ng/ml]	1.28		0.446		5.05		130	
CV$_{intra}$ [%]	14.1		1.6		1.1		1.7	
Accuracy$_{intra}$ [%]	90.7		91.0		95.8		103.6	
Mean$_{inter}$ [ng/ml]	9.09		29.0		498		7800	
SD$_{inter}$ [ng/ml]	0.999		2.41		31.2		243	
N$_{inter}$	18		18		18		18	
CV$_{inter}$ [%]	11.0		8.3		6.3		3.1	
Accuracy$_{inter}$ [%]	90.9		96.8		99.7		104.0	

Table 2
Intra-day validation of miglustat in human plasma.

	QC_LLOQ 10.0 ng/ml		QC1 30.0 ng/ml		QC2 500 ng/ml		QC3 7500 ng/ml	
	Calc conc	%Diff	Calc conc	%Diff	Calc conc	%Diff	Calc conc	%Diff
Run1	8.12	−18.8	30.5	1.7	487	−2.6	7370	−1.7
	9.92	−0.8	32.1	7.0	452	−9.6	7460	−0.5
	10.8	8.0	28.8	−4.0	462	−7.6	7530	0.4
	10.2	2.0	31.1	3.7	473	−5.4	7660	2.1
	12.0	20.0	28.4	−5.3	473	−5.4	7170	−4.4
	9.05	−9.5	28.6	−4.7	463	−7.4	7090	−5.5
$Mean_{inter}$ [ng/ml]	10.0		29.9		468		7380	
SD_{inter} [ng/ml]	1.35		1.54		12.1		217	
CV_{inter} [%]	13.5		5.2		2.6		2.9	
$Accuracy_{inter}$ [%]	100.0		99.7		93.6		98.4	

that the limit of quantification could be further lowered by an order of magnitude, if required.

3.3.2. Intra- and inter-day precision and accuracy

The acceptance criteria were based on industry standards and accepted practices [8]. The coefficient of variation (CV), expressed as percentage, as well as the percentage difference between observed concentration and expected value (%Diff) are well within the acceptance criteria. For mouse plasma intra-day coefficients of variation were between 1.1% and 14.1%, intra-day accuracies

Table 3
Selectivity of analytical assay for miglustat and internal standard in mouse and human plasma.

Mouse	Area analyte QC_LLOQ, 10.0 ng/ml	Mean area analyte QC_LLOQ, 10.0 ng/ml	Blank area no analyte	Area ratio [%]
Blank A	37,584	38,177	1131	3.0
Blank B	37,476	38,177	423	1.1
Blank C	39,688	38,177	1225	3.2
Blank D	37,674	38,177	710	1.9
Blank E	35,188	38,177	1069	2.8
Blank F	41,453	38,177	1839	4.8
Mouse	Area IS 500 ng/ml	Mean area analyte 500 ng/ml	Blank area no IS	Area ratio [%]
Blank A	10,623,838	10,333,598	5814	0.1
Blank B	10,290,780	10,333,598	2198	<0.1
Blank C	10,438,243	10,333,598	764	<0.1
Blank D	10,360,790	10,333,598	5042	<0.1
Blank E	10,237,573	10,333,598	470	<0.1
Blank F	10,050,363	10,333,598	947	<0.1
Human	Area analyte QC_LLOQ, 10.0 ng/ml	Mean area analyte QC_LLOQ, 10.0 ng/ml	Blank area no analyte	Area ratio [%]
Blank A	17,554	11,925	794	6.7
Blank B	10,967	11,925	1141	9.6
Blank C	10,799	11,925	1146	9.6
Blank D	12,083	11,925	1264	10.6
Blank E	11,132	11,925	867	7.3
Blank F	9016	11,925	1950	16.4
Human	Area IS 500 ng/ml	Mean area analyte 500 ng/ml	Blank area no IS	Area ratio [%]
Blank A	3,258,295	3,315,046	1377	<0.1
Blank B	3,354,237	3,315,046	1667	0.1
Blank C	3,267,890	3,315,046	1324	<0.1
Blank D	3,243,547	3,315,046	1968	0.1
Blank E	3,423,636	3,315,046	1004	<0.1
Blank F	3,342,671	3,315,046	78,047	2.4

were between 84.5% and 107.2%. Inter-day coefficients of variation ranged from 6.3% to 11.0%, inter-day accuracies from 90.9% to 104.0% (Table 1). The intra-day coefficients of variation in human plasma were between 2.6% and 13.5% and intra-day accuracies were between 93.6% and 100.0% (Table 2).

3.3.3. Selectivity in mouse and human plasma

In order to verify the selectivity, blank plasma from six different subjects was analyzed and compared with plasma that was spiked with miglustat at LLOQ level. The peak area in none of the six samples at the retention time of the analyte exceeded 20% of the area of the analyte at the LLOQ. Selectivity was also shown for the signal of the IS. The results for mouse and human plasma are summarized in Table 3.

3.3.4. Matrix effects in human plasma

During method validation we tested plasma from six different subjects that were spiked with miglustat at the concentration of QC1 (30.0 ng/ml). Table 4 summarizes the ratio of $area_{miglustat}/area_{IS}$ as well as the deviation of each individual sample from the median value, showing the absence of matrix effects.

3.3.5. Recovery

Recovery from mouse and human plasma was determined by comparing the area of the miglustat peak of the low and high QC sample with the corresponding peak area of standard

Table 4
Matrix effects of miglustat in six individual human plasma samples.

Matrix	Area ratio	Area ratio mean
	Analyte/ISTD	Analyte/ISTD
Matrix A	0.00834	0.00818
	0.00801	
Matrix B	0.00793	0.00771
	0.00748	
Matrix C	0.00929	0.00917
	0.00904	
Matrix D	0.00761	0.0078
	0.00798	
Matrix E	0.0108	0.0101
	0.00937	
Matrix F	0.00958	0.00978
	0.00997	
Mean	0.00878	0.00879
SD	0.00105	0.00104
CV [%]	12	11.8

Table 5
Temperature stabilities of miglustat in mouse and human plasma.

Temperature stabilities	Mouse plasma	Human plasma
No. of freeze/thaw cycles	At least 3	At least 3
Short term stability	At least 27	At least 5
Post preparative stability	At least 22 at 8 °C	At least 18 at 8 °C
Reinjection stability	At least 14.5 at 8 °C	At least 18 at 8 °C
Long term stability	At least 13 month at −25 °C	At least 13 month at −25 °C

Table 6
Incurred Sample Reanalysis of miglustat from 11 patients.

Subject no.	Period	Study time point	Original value [ng/ml]	ISR value [ng/ml]	%Diff
101	1	D4-predose	1680	1460	−13.1
101	1	D8-8 h	1130	1040	−8.0
102	2	D8-1 h	3380	3140	−7.1
102	2	D8-6 h	1520	1440	−5.3
103	1	D8-2.5 h	3020	2300	−23.8
103	1	D8-8 h	1250	1220	−2.4
104	2	D8-2.5 h	2760	2460	−10.9
104	2	D8-6 h	1650	1780	7.9
105	1	D8-2.5 h	2290	2590	13.1
105	1	D8-8 h	1300	1310	0.8
106	2	D8-2.5 h	1730	1820	5.2
106	2	D8-8 h	716	656	−8.4
107	2	D8-2.5 h	2290	2320	1.3
107	2	D8-8 h	1110	1130	1.8
108	1	D8-2.5 h	2540	2440	−3.9
108	1	D8-8 h	1170	1110	−5.1
109	1	D8-2.5 h	1570	2520	60.5
109	1	D8-8 h	1370	1340	−2.2
110	2	D8-1 h	2230	2180	−2.2
110	2	D8-6 h	1190	1630	37.0
111	2	D8-2.5 h	1450	1840	26.9
111	2	D8-8 h	956	964	0.8
		ISR total		22	
		ISR failed		4	
		ISR passed [%]		81.8%	

solutions. Recovery from mouse plasma was between 91.4% and 98.0% for miglustat and the IS. Recovery from human plasma was between 97.7% and 114.2% for miglustat and 111.9% for N-(n-nonyl)deoxynojirimycin.

3.3.6. Stability

The results obtained for stability tests of miglustat in mouse and human plasma samples indicate that samples can be stored or processed over the given time intervals without degradation (Table 5).

3.3.7. Incurred Sample Reanalysis

The use of calibration standards and QC samples during validation may not mimic the samples of an actual study. Differences for instance in protein binding, back-conversion of known and unknown metabolites, sample inhomogeneity or concomitant
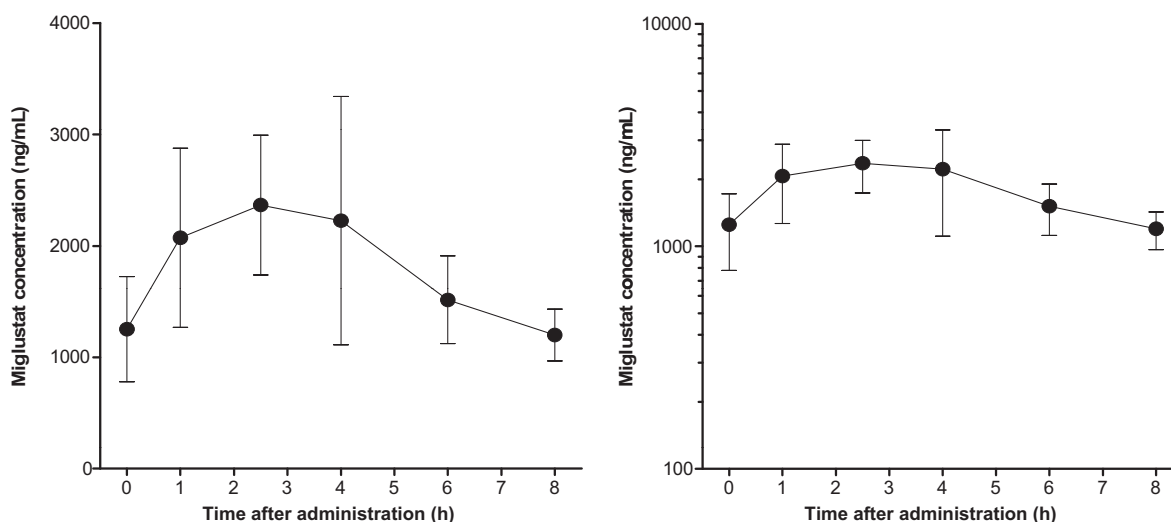
Fig. 5. Mean plasma concentration-time profile (Mean, SD, $n = 11$) of miglustat in cystic fibrosis patients treated with a dose regimen of 200 mg t.i.d. for 7 days. Left panel: linear scale, right panel: semi logarithmic scale.

medications, may affect the accuracy and precision of the analyte in study samples during processing and storage. It is, therefore, recommended to evaluate accuracy of incurred samples by reanalysis of study samples after a certain time. Incurred Sample Reanalysis (ISR) is done to provide sufficient confidence that the concentration being reported is accurate. In case ISR shows deviating results, this should be investigated, and adequate steps should be taken to minimize inaccuracy and imprecision. In addition ISR is an important part of the life cycle management of a method and it serves as a regular check of the laboratory processes.

Table 6 compares the original values and the respective ISR values of miglustat of randomly selected study samples. Approximately 10% (22 samples) of the total number of samples were chosen for ISR. Acceptance criteria were fulfilled, as 2/3 of all ISR results were within 20% of the original values.

4. Clinical study

The suitability of the method for use in clinical trials was demonstrated by the quantification of miglustat in plasma samples from 11 patients with cystic fibrosis who had been treated with miglustat 200 mg t.i.d. for 7 days in the context of a proof-of-concept study [9]. Plasma samples were collected after the last dose on study day 7. Fig. 5 presents the mean concentration–time curve of miglustat. The pharmacokinetics were characterized by a t_{max} of 2.5 h, a C_{max} of 2466 ng/ml, and an AUC_τ of 14,347 ng h/ml.

5. Conclusion

We described a new LC–MS/MS method for the analysis of miglustat in mouse and human plasma. The method is based on protein precipitation and analysis by APCI in SRM mode.

N-(n-nonyl)deoxynojirimycin was used as internal standard. The method is simple and robust and covers a range of 10.0–10,000 ng/ml; the cycle time of the method is only 3 min. It has been successfully applied in the assessment of pharmacokinetic parameters of miglustat in cystic fibrosis patients.

References

[1] G. Horne, F.X. Wilson, J. Tinsley, D.H. Williams, R. Storer, Iminosugars past, present and future: medicines for tomorrow, Drug Discov. Today 16 (2011) 107–118.

[2] http://www.ema.europa.eu/ema/index.jsp?curl=pages/medicines/human/medicines/000435/human_med_001171.jsp&murl=menus/medicines/medicines.jsp&mid=WC0b01ac058001d124&jsenabled=true (accessed 22.06.11).

[3] P.L.M. van Giersbergen, J. Dingemanse, Influence of food intake on the pharmacokinetics of miglustat, an inhibitor of glucosylceramide synthase, J. Clin. Pharmacol. 47 (2007) 1277–1282.

[4] A. Treiber, O. Morand, M. Clozel, The pharmacokinetics and tissue distribution of the glucosylceramide synthase inhibitor miglustat in rat, Xenobiotica 37 (2007) 298–314.

[5] G.H.B. Maegawa, P.L.M. van Giersbergen, S. Yang, B. Banwell, C.P. Morgan, J. Dingemanse, C.J. Tifft, J.T.R. Clarke, Pharmacokinetics, safety and tolerability of miglustat in the treatment of pediatric patients with GM2 gangliosidosis, Mol. Genet. Metab. 97 (2009) 284–291.

[6] J. Guitton, S. Coste, N. Guffon-Fouilhoux, S. Cohen, M. Manchon, M. Guillaumont, Rapid quantification of miglustat in human plasma and cerebrospinal fluid by liquid chromatography coupled with tandem mass spectrometry, J. Chromatogr. B 877 (2009) 149–154.

[7] R.F. Staak, G. Hopfgartner, New analytical strategies in studying drug metabolism, Anal. Bioanal. Chem. 22 (2007) 1365–1380.

[8] C.T. Viswanathan, S. Bansal, B. Booth, A.J. DeStefano, M.J. Rose, J. Sailstad, V.P. Shah, J.P. Skelly, P.G. Swann, R. Weiner, Workshop/conference report – quantitative bioanalytical methods validation and implementation: best practices for chromatographic and ligand binding assays, AAPS J. 9 (2007) E30–E42.

[9] A. Leonard, J. Dingemanse, P. Lebecque, T. Leal, Oral, miglustat in homozygous F508DEL CF patients, in: 33rd European Cystic Fibrosis Society Conference, Valencia, Spain, June 16–19, Poster 75, S20, 2010.

Therapeutic effect of Yunnan Baiyao on rheumatoid arthritis was partially due to regulating arachidonic acid metabolism in osteoblasts

Hongbing He [a,b], Xiaobin Ren [b], Xiyue Wang [a], Xianzhe Shi [a], Xiaolin Wang [a], Zhongjuan Ding [b], Peng Gao [a,*], Guowang Xu [a,*]

[a] CAS Key Laboratory of Separation Science for Analytical Chemistry, Dalian Institute of Chemical Physics, Chinese Academy of Sciences, 116023 Dalian, China
[b] The Affiliated Stomatology Hospital of Kunming Medical University, 650031 Kunming, China

ARTICLE INFO

ABSTRACT

In order to explore the potential therapeutic effect of Yunnan Baiyao (YNB) on rheumatoid arthritis (RA), rat models were constructed and orally administrated with YNB or methotrexate (MTX) in parallel. Clinical physical, histological and biochemical parameters showed trivial therapeutic difference between YNB and MTX applications. Urine and serum metabonomics results indicated that many endogenous metabolites differentially changed among the rats receiving diverse therapeutic interventions. Among them, the fluctuation of arachidonic acid (AA) was thought to make sense. Thus, its relevant metabolites were subjected to quantitation by using osteoblasts treated by YNB *in vitro*. It was found that YNB extract of 20 μg/mL could greatly activate the synthesis of intracellular prostaglandin E_2 and thromboxane B_2 in osteoblasts. Excretion of prostaglandin D_2 could be suppressed but not the thromboxane B_2. This study proved the efficacy of YNB on curing RA and its potential mechanism through modulating AA metabolism in osteoblasts to some extent.

© 2011 Elsevier B.V. All rights reserved.

1. Introduction

Rheumatoid arthritis (RA) is a systemic, chronic inflammatory autoimmune disease that primarily affects joints and leads to pain, deformity, joint destruction, and disability [1]. Similar to other autoimmune diseases, RA is a complex syndrome related to both genetic and environmental factors [2,3]. Currently, disease-modifying antirheumatic drugs, *e.g.* methotrexate (MTX), sulphasalazine and leflunomide, or a combined prescription of them, are the preferable solutions to the treatment of RA [4,5]. Traditional Chinese Medicine (TCM) has a very long history. Many ancient archives had detailed description on clinical prescriptions of TCM for curing RA [6]. Currently at least 6 herbal medicines have been reported to be effective in treating RA clinically [6]. Yunnan Baiyao (YNB), which was firstly introduced in 1914 commercially, is a well known patent medicine especially for its effect on different kinds of fracture and wounds. The reputation of YNB in the Chinese people is characterized with its potent activities of dephlogisticate, detumescence and regeneration of damaged bones (http://scholar.ilib.cn/A-QCode~szgygy200612131.html). The major components of YNB

are *Radix Notoginseng*, *Forest Musk*, *Borneolum Synthcticum*, *Rhizoma Paridis Chonglou*, *Radix Aconiti Kusnezoffii* and so on. In view of the modern Western Medicine, its main pharmaceutical effects include anti-inflammation, hemostasis, vasodilation especially for capillary, facilitating platelet agglutination, stimulating cortical hormone excretion, and activating macrophages. Although the exact composition of YNB is confidential, exploring its effective components and disclosing its new pharmaceutical merits have never ceased. Recently, experimental applications of YNB in curing gastrointestinal, respiratory, virus infection and pediatric diseases were reported and the results were exciting (http://scholar.ilib.cn/A-QCode~cfxyxb201005032.html). RA usually causes bone lesion and loss [7]. The fact that YNB shows perfect effects on the recovery of damaged bones prompts us to consider whether YNB might be effective in curing RA. To this end we constructed the RA rat models. The therapeutic effects of YNB on the model animals were compared with those of MTX by monitoring some well recognized physical, biochemical and pathological parameters. YNB is a compound recipe TCM and its influence on the metabolism is complex and multi-dimensional. In this light, systematic perturbation of YNB on organism metabolism was intended to be evaluated by a serum and urine metabonomics-based strategy. Although metabonomics is a new entry of systems biology toolbox, it can sensitively reflect perturbations of different origins on the metabolism by means of quantitating the metabolome in certain kinds of cells, organs or biofluid [8]. In the TCM research

* Corresponding authors. Tel.: +86 411 84379530; fax: +86 411 84379559.
E-mail addresses: xuhe@medmail.com.cn (P. Gao),
xugw@dicp.ac.cn, dicp402@mail.dlptt.ln.cn (G. Xu).

arena, this tactic has gained broad applications in many aspects, such as symptom subtyping [9], medicine quality control [10] and therapeutic effect evaluation [11]. In the current study, both the sera and urine samples were collected from the animals at a proper time point. The individual metabonome data were utilized to evaluate the influences of YNB and MTX on the metabolism of RA rat models. The most significantly changed metabolites found by metabonomic analysis were further evaluated. Biologically, the most valuable one was employed to assist the potential pharmaceutical mechanism exploration by using cultured cells.

2. Materials and methods

2.1. Reagents and chemicals

YNB was the product of Yunnan Baiyao Group Co., Ltd. (Kunming, China). MTX was purchased from SINE Pharmaceutical Co., Ltd., China. Arachidonic acid (AA), thromboxane B_2 (TXB$_2$), prostaglandin (PG) D_2, E_2, B_1 and J_2 were acquired from Cayman (Ann Arbor, MI, USA). 2,6-Di-tert-butyl-4-methylphenol (BHT), Freund's complete adjuvant (FCA) and bovine type II collagen (C-II) were all purchased from Sigma–Aldrich (St. Louis, MO, USA). 0.1 mol/L aseptic acetate solution containing 2 mg/mL C-II was settled at 4 °C overnight and then mixed with the same volume of FCA. The fresh mixture (containing C-II dissolved in acetate solution and FCA) was used as the model construction reagent (MCR). Interleukin-1β (IL-1β) and PGE$_2$ ELISA kits were all commercially acquired from Sigma–Aldrich and used to quantify serum IL-1β and PGE$_2$ according to the instructions provided by the manufacturer.

2.2. Model construction and treatment

Specific pathogen free male Sprague-Dawley (SD) rats were provided by the Experiment Animal Center of Kunming Medical University (KMU). Their average weights were about 220–250 g. Animal experiments were carried out under the survey of the Experiment Ethical Committee of KMU. In total 128 rats were enrolled in the study and randomly divided into 4 groups equally. Only 3 of them were subjected to model construction according to the procedures proposed by the literatures [12,13]. Briefly, each rat was treated with 0.2 mL MCR by the intracutaneous injection on multiple sites of the root of the tail on day 1. At the same time, injection of 0.1 mL MCR in left rear voix pedis was carried out for each rat. RA symptom appeared within 7 days. On days 7 and 21, only 0.2 mL MCR injection was repeated on the tail of each rat. RA model rats in group R received no treatment during the whole experiment period. From day 7 to day 35, the rats in the other three groups were treated differently. Every rat in group Y received intragastric administration of 1 mL YNB (50 mg/mL aseptic aqueous suspension) once every day. Group C consisted of 32 normal rats and they were treated as group Y did but the YNB was replaced with the same volume of physiological saline. Referred to clinical practice, the rats in group M received intragastric administration of 1 mL of 0.2 mg/mL MTX once every week [14]. For each group, every 8 rats were anaesthetized by ether on days 14, 21, 28 and 35. The relevant physical and pathological parameters were determined as necessary. On day 35, blood was sampled by cardiac puncture and the isolated sera were stored at −70 °C immediately for metabonomic analysis. The 24 h urine samples were also collected through automatic micturition on day 35. Some of the swelled limbs sampled on day 28 and day 35 were subjected to the histological check. During the experiment period, all the rats had free access to food and water. The lighting duration in every day was 12 h.

2.3. Observed physical parameters

Body weights and voix pedis thickness were determined every 4 days. Joint functionality scores of the limbs were evaluated by independent physicians according to the following criteria: 0, no appreciable symptom; 1, discernable red spot(s) or slight swell; 2, intermediate swell; 3, serious swell; 4, deformed joint(s) with stiffness. The highest score of total four limbs was 16 for each rat. Articulationes digitorum pedis of the affected limbs were subjected to pathological check after Hematoxylin–Eosin (HE) and tartrate-resistant acid phosphatase (TRAP) staining.

2.4. Cell experiments

Human origin osteoblastic sarcoma cell line MG-63 was commercially available and cultured in Hyclone MEM/EBSS medium (Logan, UT, USA) as recommended by the manufacturer with original inoculation density about 10^4 cell/mL. YNB powder was extracted by 75% alcohol with constant agitation for 48 h at room temperature. The supernatant was collected and condensed to 1 mg/mL as measured against the original powder weight using aseptic distilled water. The final application concentrations were 0, 5, 10 and 20 μg/mL in the media. Sampling time was after 9 days' culture and every sample was analyzed with five biological replicates.

2.5. Metabonomics analysis and AA metabolite analysis

Metabonomics analysis of the sera was performed according to our previous work with minor modification [15]. Basically, 400 μL acetonitrile was added to 100 μL serum. The mixture was shaken vigorously for 30 s and then centrifuged at 15,000 × g for 10 min at 4 °C. The supernatant was lyophilized and dissolved in 100 μL mixture of water and acetonitrile (v/v, 1:4). A quality control sample was prepared by mixing 10 μL of each sample and treated as the real samples. Serum separation was performed on a 2.1 mm × 100 mm (particle diameter of 1.7 μm) BEH C18 column (Waters, USA) using an ultra performance liquid chromatography system (Waters, USA) coupled to a Waters Q-TOF micro-MS system (Waters MS Technologies, Manchester, UK). A linear gradient elution was carried out at the flow rate of 0.35 mL/min. The mobile phase A was 0.1% formic acid in water and phase B was pure acetonitrile. The elution gradient of phase B was 12% (0–5 min), 12% up to 100% (5–25 min), kept 3 min. The sample injection volume was 5 μL for each run. The quality control sample was analyzed frequently at equal interval to monitor the stability of the analysis. MS scan was operated in either positive or negative ionization mode. The capillary voltage settings were 3100 V for the positive mode and −2400 V for the negative mode. The cone voltage was 35 V. Scan range was from (m/z) 100 to 1000. The leucine-enkephalin was used to calibrate the mass accuracy and reproducibility.

For urine metabonomics, 100 μL of urine sample was diluted with 300 μL of water, and centrifuged at 15,000 × g for 15 min at 4 °C. Every 4 μL of the diluted urine was injected and separated on an Agilent 1200 Rapid Resolution Liquid Chromatograph hyphenated to an Agilent 6510 Q-TOF mass spectrometer (Agilent, USA) using a Zorbax SB-AQ C18 column (1.8 μm, 2.1 mm × 100 mm, Agilent, USA) [16]. Gradient elution included 0.1% formic acid–water (phase A) and acetonitrile (phase B) at the flow rate of 0.3 mL/min. The elution gradient was 1% B (0–3 min), 30% B (3–10 min), and 100% B (10–20 min). MS scan was performed on a MassHunter workstation (Agilent, USA) with the following settings: scan mode, positive; gas temperature, 350 °C; drying gas flow rate, 11 L/min; capillary voltage, 4000 V; scan range, 80–950 m/z and scan rate, 2 spectra/s. The urine quality control sample was constructed by equally mixing each of the real samples. Metabolite identification
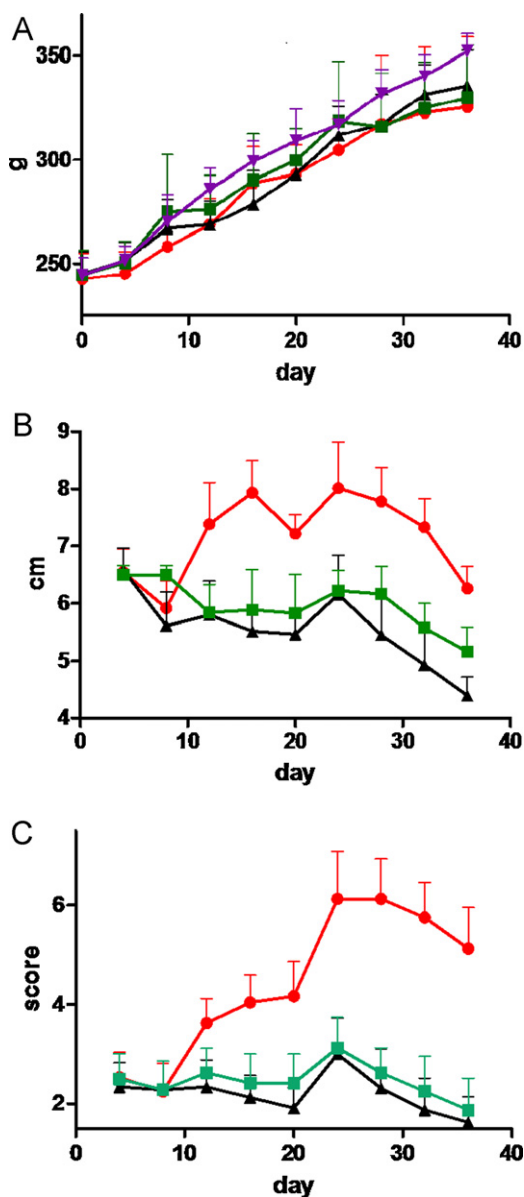
Fig. 1. Physical parameter comparisons among the studied groups. (A) Body weight gaining; (B) voix pedis thickness and (C) joint functionality scores. Data were presented as mean ± SEM. (▼) group C; (■) group M; (●) group R and (▲) group Y.
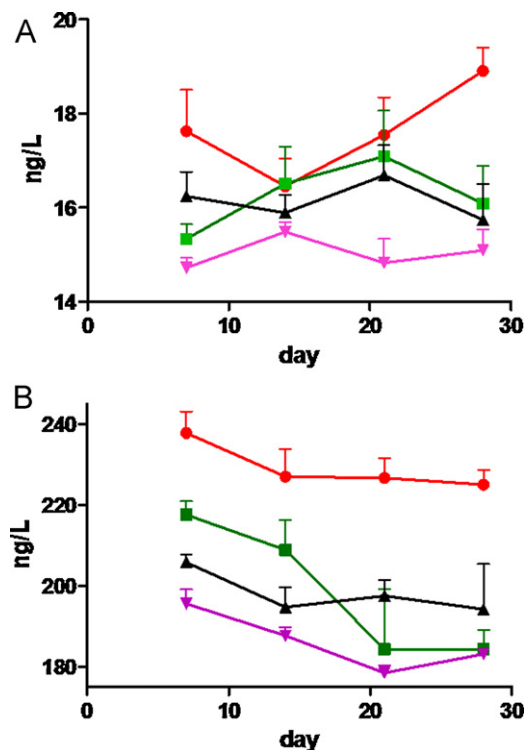

Fig. 2. Basic serum biochemical parameters of the studied groups. (A) Time-course changes of IL-1β and (B) PGE$_2$. Data were presented as mean ± SEM. (▼) group C; (■) group M; (●) group R and (▲) group Y.

was based on either comparing mass spectra with those of the commercial standards or the ion fragments of certain kinds of compounds.

For the measurement of extracellular AA metabolites every 2 mL supernatant was mixed with 1.4 mL methanol (containing 0.01 mol/L BHT), 30 μL formic acid and 20 μL of the internal standard PGB$_1$ (final concentration of 0.01 μg/mL). After centrifugation, the mixture was extracted by 2.8 mL ethyl acetate twice and lyophilized. The extract was redissolved in 40% methanol for analysis. For the quantitation of intercellular compounds the cells were firstly quenched by cold physiological saline [17] and then extracted as described above. The quantitation of downstream metabolites of AA was carried out on an Agilent 6460 Triple Quad LC/MS system scanned in the negative multiple reaction monitoring (MRM) mode. The liquid chromatography column was a BEH C18 column (100 mm × 2.1 mm, 1.7 μm particle size) from Waters MS Technologies (Manchester, UK). The mobile phase A was water with 0.05% formic acid and phase B was pure

acetonitrile. The elution gradient was 30–50% B (0–8 min), 50–90% B (8–9 min), 90% B (9–15 min), 90–30% B (15–15.1 min), and 30% B (15.1–18 min) at the flow rate of 0.2 mL/min at 35 °C. The fragmentor voltage, collision energy, retention time, m/z of the transmitted parent ion and the monitored product ion were as follows: TXB$_2$, 135 V, 10 V, 4.541 min, 369.3 → 169.1; PGE$_2$, 135 V, 10 V, 5.619 min, 351.2 → 271.3; PGD$_2$, 135 V, 10 V, 6.086 min, 351.2 → 189.1; PGB$_1$, 150 V, 20 V, 8.877 min, 335.2 → 113.1; PGJ$_2$, 100 V, 10 V, 8.397, 333.2 → 271.3. The Delta EMV(−) was 200 V. The mass spectrometer settings included: nitrogen gas temperature, 350 °C; gas flow, 8 L/min; nebulizer pressure, 40 psi and capillary voltage, 3500 V. The dwell time for each compound was 200 ms. Intercellular metabolite concentrations were normalized against cell dry weight and extracellular concentrations were normalized against cell wet weight. Under the above conditions, recovery of the interested compounds varied from 69.1% to 107.5%. The inter-day variance was from 3.0% to 16.9%.

2.6. Statistic analysis

Data processing for metabonomics was performed as described elsewhere [18]. In short, the raw serum metabonomics data were acquired by using the Micromass MarkerLynx Applications Manager version 4.0, allowing detection of the mass, retention time and intensity of each peak. After the peak alignment, the dataset was trimmed according to the 80% rule [19] and the ion intensities were normalized against the sum of the peak intensities in the corresponding samples.

The raw data of urine were analyzed using MassHunter molecular feature extraction algorithm (MFE). MFE deconvoluted the total ion chromatograms to generate retention time, exact mass and intensity information of each feature. After chromatogram matching by the GeneSpring MS 1.1 software (Agilent, USA), the resultant data were processed similarly as mentioned above.
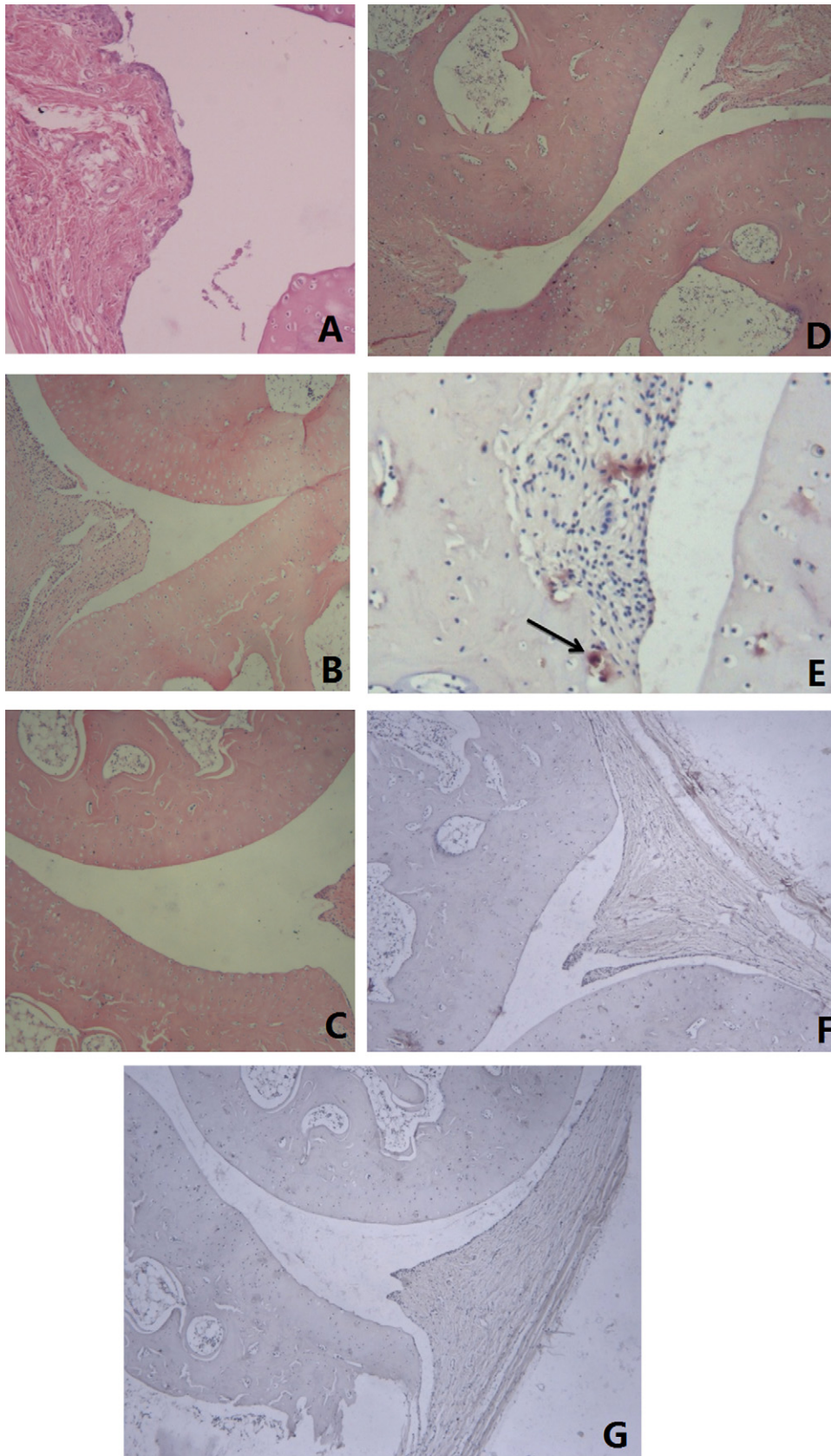
Fig. 3. Histopathological results of the normal and affected limbs (100×). HE stain of normal joint cavity (A) from group C and the affected joint cavity (B) from group R showed distinct appearance. Inflammation signs of YNB (C) and MTX (D) treated joint cavities from groups Y and M were all alleviated. Osteoclasts (TRAP positive ones, arrow indicated) could be found in samples from group R (E) but scarcely in samples from YNB (F) and MTX (G) treated groups.
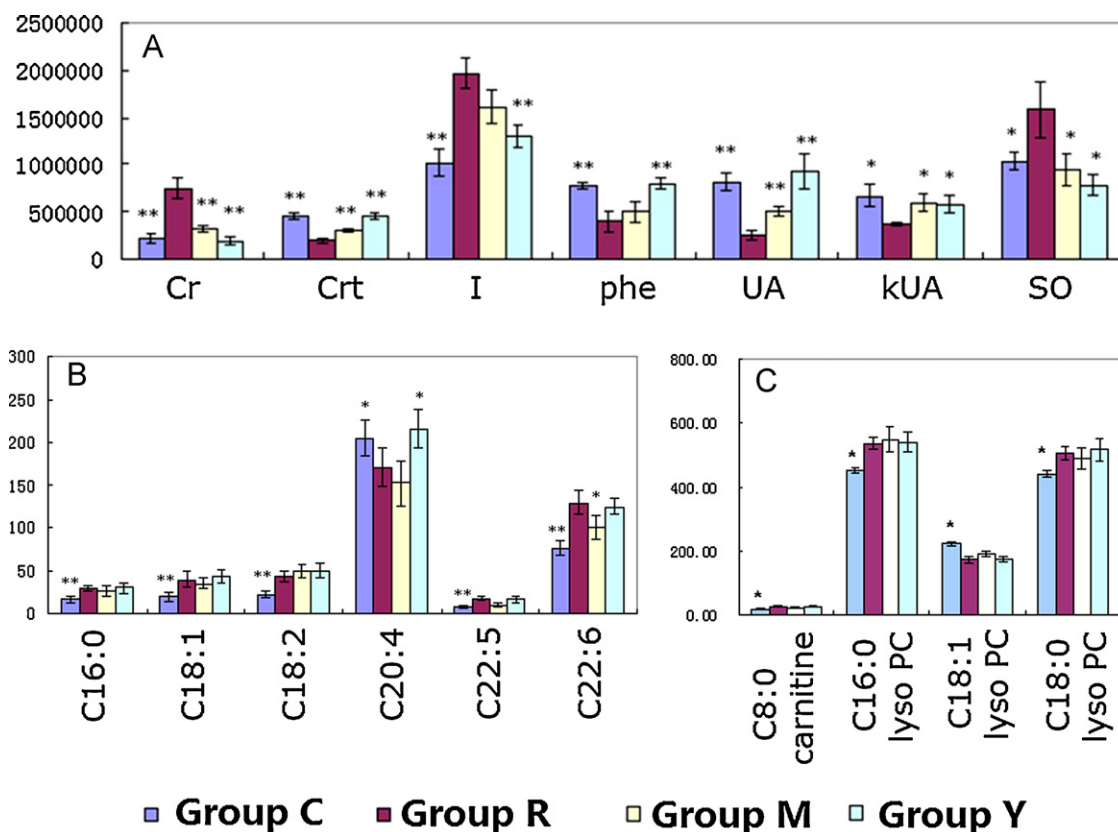
Fig. 4. Identified metabolites in the urine and sera that were statistically different among the 4 groups. (A) From the urine samples; (B) from the sera through the negative and (C) positive modes. Y axis: ion fragment intensity (compared to group R, $*p < 0.05$ and $**p < 0.01$). Cr, creatine; Crt, creatinine; I, hypoxanthine; phe, phenylalanine; UA, uric acid; kUA, kynurenic acid; SO, N_2-succinylornithine; lyso PC, lysophosphatidylcholine. Creatine, phenylalanine, uric acid, kynurenic acid, lyso PC of C16:0, lyso PC of C18:1, lyso PC of C18:0, C16:0, C20:4 and C22:6 were identified by commercial standards. The others were identified based on the ion fragments.

All the preprocessed data of sera and urine were fed to SIMCA-P (version 11.0; Umetrics, Umea, Sweden) for the analysis and visualization by multivariate statistical methods [18]. The interested metabolites were selected based on their fragment distribution in the loading plots [15]. Statistic analysis of ANOVA was performed using Minitab V15.0 (State College, PA, USA).

3. Results and discussion

3.1. Basic physical parameters

It was found that difference in the body weight gaining of the rats in the four groups was not evident ($p = 0.12$) with respect to the various treatments (Fig. 1A). The main factor affecting weight gaining was time ($p < 0.001$). The average voix pedis thickness of the affected limbs is depicted in Fig. 1B. The thickness was significantly different among the studied groups ($p < 0.001$). Both YNB and MTX could alleviate the symptom similarly ($p = 0.16$). Time effect was discernable on voix pedis thickness ($p = 0.002$). Joint functionality score evaluation indicated that therapeutic effect of YNB was superior to that of MTX ($p = 0.001$) and time effect was obvious ($p < 0.001$) among the groups (Fig. 1C).

3.2. Biochemical parameters

After day 7, blood samples were collected and serum IL-1β and PGE$_2$ were determined. The results are given in Fig. 2A and B. IL-1β and PGE$_2$ were all in higher concentrations in group R than in group C ($p < 0.001$). Both YNB and MTX could lower IL-1β ($p = 0.006$) and PGE$_2$ ($p < 0.001$) to the same extent ($p > 0.8$) although they could not

lower IL-1β and PGE$_2$ to the normal levels ($p < 0.02$). Time effect on IL-1β was not evident ($p > 0.3$) but PGE$_2$ tended to be affected by time factor during the experimental period ($p < 0.001$).

3.3. Histological results

In order to reflect the real disease state digiti pedis joint samples were collected on day 28 – one week after the second time MCR injection. The histological inspection results are shown in Fig. 3. Clearly, the structure of the normal joint was complete and no inflammation sign was found (Fig. 3A). Joints from group R were characterized with the inflammatory cell infiltration, distinct synovium hyperplasia and dirty narrowed joint space (Fig. 3B). The above mentioned pathological changes were alleviated by administrating both MTX (Fig. 3C) and YNB (Fig. 3D). TRAP stained positive osteoclasts could be found only in samples collected on day 35 from group R (Fig. 3E) but sporadically emerged in group Y (Fig. 3F) and group M (Fig. 3G).

3.4. Metabonomics results

To ensure the stability of the methods, the quality control samples were analyzed every six runs. The relative standard deviations (RSDs) of the retention times were less than 1%, and the RSDs of the peak areas were all less than 20%. These results indicated a satisfied quality of the adopted platform. For urine metabonomics, the average detectable fragments were 1532. In average, serum metabolic profiling generated 1550 fragments in the positive mode and 1452 in the negative mode. The typical urine total ion chromatograms (TICs) of the studied groups are shown in
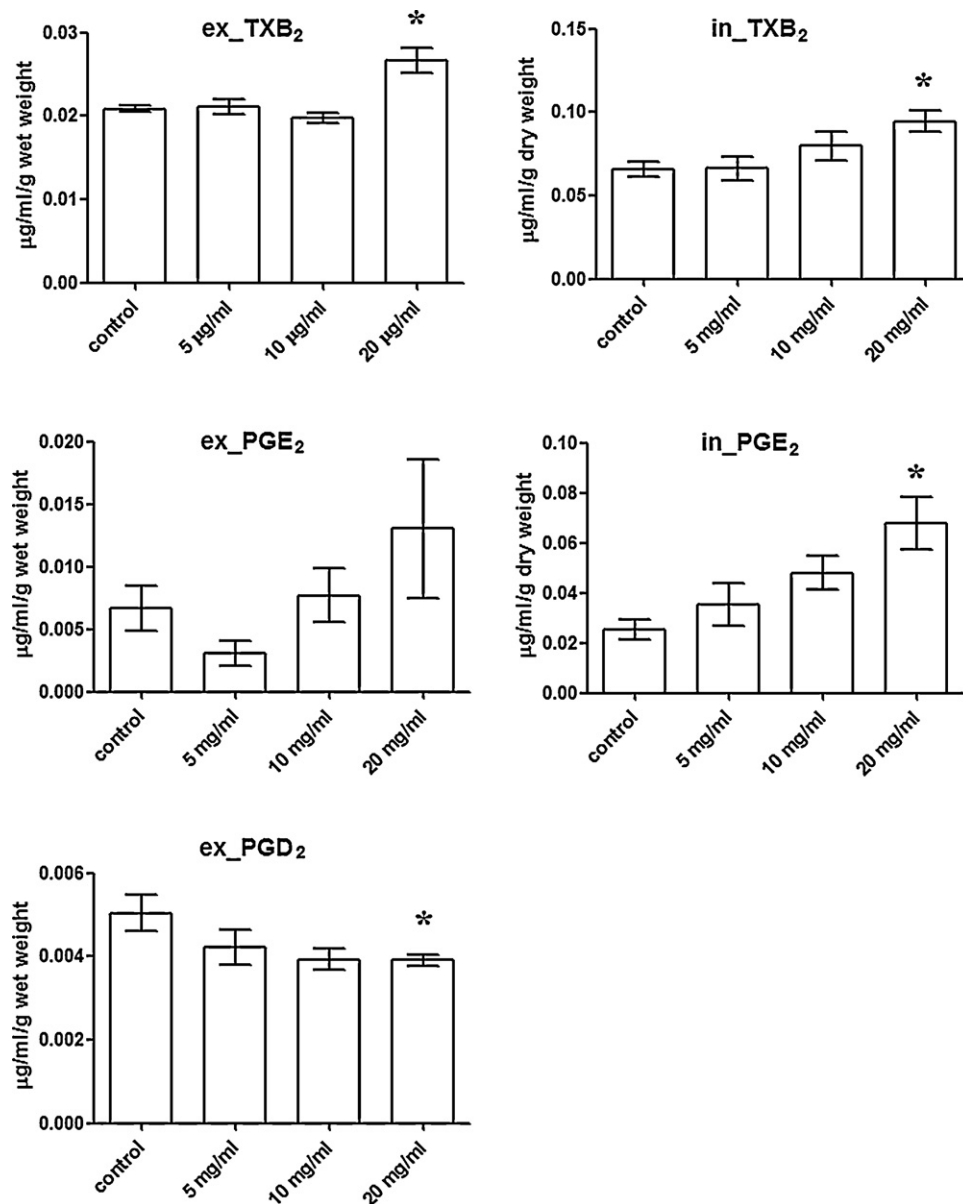
Fig. 5. Inter- (labeled with prefix of "in") and extra- (labeled with prefix of "ex") cellular contents of AA metabolites in MG-63 treated with varied concentrations of YNB extract. Data were presented as means ± SEM. *Statistically different to the control group.

Fig. S1 in Supplementary materials. The loading and score plots generated through partial least squares-discriminant analysis (PLS-DA) of these metabonomics data are given in Fig. S2. Meaningful metabolites were defined as corresponding fragments of variable importance for the projection larger than 1.0. These metabolites were then analyzed with ANOVA. Only those with $p < 0.05$ were kept and subjected to identification as possibly as we could. The representative TICs of sera are given in Figs. S3 and S4. The corresponding loading and score plots are shown in Fig. S5. Because of the overfitting's occurrence in processing the negative mode data, ANOVA was directly carried out to select the differential metabolites. Clearly, the score plot of urine metabonomics distinguished the four groups relatively unambiguously (Fig. S2). This meant that end products in the urine could be used to differentiate the groups and different interventions resulted in different urine metabolite profiles in the studied rats. For the serum metabonomics, separation of the studied groups by PLS-DA using the positive mode data was not good as using urine data (Fig. S5). The negative mode data nearly totally lost the differentiation ability (data not shown).

After sequential PLS-DA and ANOVA (Supplementary materials) were performed, the differentially changed metabolites in the urine and sera from different groups were identified. Most of the significantly changed metabolites in the urine were amino acids, nucleosides and their downstream metabolites (Fig. 4A). Most of them were not disease specific with respect to the current recognition of RA. In the negative scan mode, many serum-free fatty acids (FFAs) were found differently responsible to the interventions (Fig. 4B). Serum lysophosphatidylcholines were the most significantly changed metabolites in the positive scan mode (Fig. 4C). Of note, except AA (C20:4 in Fig. 4B), the other identified FFAs were in higher concentrations in group R.

3.5. Effect of YNB on the down-stream metabolism of AA in osteoblastic cell

The downstream metabolites of AA metabolism were profiled as possible in osteoblasts and totally three compounds could be quantified (Fig. 5). Both extra- and inter-cellular TXB$_2$ were increased

($p < 0.05$) when the cells were treated with 20 μg/mL YNB. Simultaneously, this concentration of YNB could lower the extracellular PGD_2 ($p < 0.05$). The intercellular PGD_2 could not be quantitated. Compared to group C, intercellular PGE_2 was elevated by 20 μg/mL YNB administration and was found to be positively correlated with the applied concentrations of YNB ($p < 0.05$). On the contrary, the extracellular PGE_2 was not affected.

TCMs are famous for their holistic, mild and multi-dimensional regulation on metabolism. Our results demonstrated that YNB exhibited the similar effects on curing RA compared with MTX. As a preferential cyclooxygenase-2 (COX-2) inhibitor, MTX gains wide applications in treating RA. Typical biochemical parameters used to evaluate therapeutic effects on RA showed trivial difference between YNB and MTX administration (Figs. 1–3). Disease specific metabolites could be hardly found through urine metabonomics (Fig. 4A). Findings from serum metabonomics partially ascertained the previous report that FFAs would increase in RA individuals [20,21]. A report indicated that fasting-associated increases in total plasma FFAs promoted lymphocyte proliferation *in vitro* and might not facilitate to alleviate inflammation [22]. Generally speaking, lysophosphatidylcholines involve in inflammation and inflammation is a key pathological event in RA. Thus, some species of them discovered through metabonomics analysis (Fig. 4C) was not unexpected.

The change of serum AA was deemed as most meaningful. First, AA is an important precursor of various bioactive molecules in regulating inflammation – the most dominant pathological event in RA. Secondly, among the identified FFAs, only AA decreased in the sera of untreated RA rats (Fig. 4B). Lastly, AA was the only altered FFA that could be recovered to the normal level after YNB administration (Fig. 4B). Because of the key roles in bone remodeling and repairing of osteoblasts, a MG-63 cell line was selected and treated with YNB *in vitro*. Its response to different concentrations of YNB was evaluated by quantitatively analyzing the down-stream metabolites of AA. In this study, only three AA metabolites were detectable (Fig. 5). The intercellular PGE_2 was substantially increased especially after treatment by 20 μg/mL YNB, but the extracellular PGE_2 content was not affected by any applied concentrations of YNB (Fig. 5). Seemingly, YNB could uncouple the osteoblasts' synthesis and excretion of PGE_2. It had been reported that PGE_2 could stimulate osteoclast-like cell formation in the presence of osteoblasts in mouse bone cell cultures [23]. This was thought to increase the bone-resorbing activity. In our study (Fig. 3E–G) osteoclasts could be scarcely found in the samples from YNB treated group. It might be partially ascribed to the fact that YNB could keep a constant extracellular PGE_2 content (Fig. 5). Additionally, PGE_2 could induce the IL-1β gene expression in osteoblasts and IL-1β closely associated with bone loss in RA status [24]. So the constant extracellular PGE_2 maintained by YNB should be in favor of bone recovery. This uncoupling effect was not evident in TXB_2. The inter- and extra-cellular TXB_2 were both increased. Although the exact pathological meanings of the elevated TXB_2 were not clear to date, this manifestation might indicate that, unlike MTX, COX-1 might also be a potential target of YNB [25]. Because the serum PGE_2 could be lowered by YNB (Fig. 2) and excretion of PGE_2 by osteoblasts was not severely suppressed (Fig. 5), other cell types involved in AA metabolism must be influenced by YNB. This deserved to be explored in the future. Serum IL-1β was also regulated by YNB (Fig. 2) and IL-1β positively affected the synthesis of PGE_2 [26]. This study also raised a new question that how YNB functionally coordinates the interactions between PGE_2 and IL-1β. Although the intercellular PGD_2 could not be quantitated, the 20 μg/mL YNB decreased the extracellular PGD_2 (Fig. 5). This was another evidence to prove YNB's therapeutic effects in that PGD_2 was thought to stimulate the synthesis of IL-6 in the immunocytes and higher PGD_2 caused excessive bone resorption [27,28].

Taken together, this study demonstrated the comparable pharmaceutical activities of YNB on curing RA. Its therapeutic effect on RA was partially due to suppression of some AA-derived proinflammatory mediators' excretion from osteoblasts. The diverse changes of PGs and TXB_2 implied that, at least in the osteoblasts, YNB's regulation of AA metabolism was not similar to that in MTX. Both COX-1 and COX-2 might be its targets. Definitely, new mechanisms of YNB's curing effects on RA deserved to be explored by systematic experiment design and further efforts.

Acknowledgements

Appendix A. Supplementary data

Supplementary data associated with this article can be found, in the online version, at doi:10.1016/j.jpba.2011.10.019.

References

[1] M.A. Mayoux-Benhamou, Fatigue and rheumatoid arthritis, Ann. Readapt. Med. Phys. 49 (2006) 301–308.
[2] L.A. Criswell, Gene discovery in rheumatoid arthritis highlights the CD40/NF-kappaB signaling pathway in disease pathogenesis, Immunol. Rev. 233 (2010) 55–61.
[3] G.J. Tobon, P. Youinou, A. Saraux, The environment, geo-epidemiology, and autoimmune disease: rheumatoid arthritis, J. Autoimmun. 35 (2010) 10–14.
[4] W.M. Kooloos, T.W. Huizinga, H.J. Guchelaar, J.A. Wessels, Pharmacogenetics in treatment of rheumatoid arthritis, Curr. Pharm. Des. 16 (2010) 164–175.
[5] J. Dale, N. Alcorn, H. Capell, R. Madhok, Combination therapy for rheumatoid arthritis: methotrexate and sulfasalazine together or with other DMARDs, Nat. Clin. Pract. Rheumatol. 3 (2007) 450–458.
[6] P. Zhang, J. Li, Y. Han, X.W. Yu, L. Qin, Traditional Chinese medicine in the treatment of rheumatoid arthritis: a general review, Rheumatol. Int. 30 (2010) 713–718.
[7] S.R. Goldring, E.M. Gravallese, Mechanisms of bone loss in inflammatory arthritis: diagnosis and therapeutic implications, Arthritis Res. 2 (2000) 33–37.
[8] J.K. Nicholson, I.D. Wilson, J.C. Lindon, Pharmacometabonomics as an effector for personalized medicine, Pharmacogenomics 12 (2011) 103–111.
[9] W.H. van, K. Yuan, C. Lu, P. Gao, J. Wang, C. Xiao, X. Yan, M. Wang, J. Schroen, A. Lu, G. Xu, J. van der Greef, Systems biology guided by Chinese medicine reveals new markers for sub-typing rheumatoid arthritis patients, J. Clin. Rheumatol. 15 (2009) 330–337.
[10] Z. Xiang, X.Q. Wang, X.J. Cai, S. Zeng, Metabolomics study on quality control and discrimination of three curcuma species based on gas chromatograph–mass spectrometry, Phytochem. Anal. (2011), doi:10.1002/pca.1296.
[11] Y. Qiu, M. Chen, M. Su, G. Xie, X. Li, M. Zhou, A. Zhao, J. Jiang, W. Jia, Metabolic profiling reveals therapeutic effects of Herba Cistanches in an animal model of hydrocortisone-induced 'kidney-deficiency syndrome', Chin. Med. 3 (2008) 3–10.
[12] M. Nishikawa, A. Myoui, T. Tomita, K. Takahi, A. Nampei, H. Yoshikawa, Prevention of the onset and progression of collagen-induced arthritis in rats by the potent p38 mitogen-activated protein kinase inhibitor FR167653, Arthritis Rheum. 48 (2003) 2670–2681.
[13] Q. Chen, W. Wei, Effects and mechanisms of glucosides of chaenomeles speciosa on collagen-induced arthritis in rats, Int. Immunopharmacol. 3 (2003) 593–608.
[14] V. Strand, D.L. Scott, P. Emery, J.R. Kalden, J.S. Smolen, G.W. Cannon, P. Tugwell, B. Crawford, Physical function and health related quality of life: analysis of 2-year data from randomized, controlled studies of leflunomide, sulfasalazine, or methotrexate in patients with active rheumatoid arthritis, J. Rheumatol. 32 (2005) 590–601.
[15] P. Yin, P. Mohemaiti, J. Chen, X. Zhao, X. Lu, A. Yimiti, H. Upur, G. Xu, Serum metabolic profiling of abnormal savda by liquid chromatography/mass spectrometry, J. Chromatogr. B: Anal. Technol. Biomed. Life Sci. 871 (2008) 322–327.
[16] Z. Wu, M. Li, C. Zhao, J. Zhou, Y. Chang, X. Li, P. Gao, X. Lu, Y. Li, G. Xu, Urinary metabonomics study in a rat model in response to protein-energy malnutrition by using gas chromatography–mass spectrometry and liquid chromatography–mass spectrometry, Mol. Biosyst. 6 (2010) 2157–2163.
[17] S. Dietmair, N.E. Timmins, P.P. Gray, L.K. Nielsen, J.O. Kromer, Towards quantitative metabolomics of mammalian cells: development of a metabolite extraction protocol, Anal. Biochem. 404 (2010) 155–164.

[18] P. Yin, X. Zhao, Q. Li, J. Wang, J. Li, G. Xu, Metabonomics study of intestinal fistulas based on ultraperformance liquid chromatography coupled with Q-TOF mass spectrometry (UPLC/Q-TOF MS), J. Proteome Res. 5 (2006) 2135–2143.

[19] S. Bijlsma, I. Bobeldijk, E.R. Verheij, R. Ramaker, S. Kochhar, I.A. Macdonald, B. van Ommen, A.K. Smilde, Large-scale human metabolomics studies: a strategy for data (pre-)processing and validation, Anal. Chem. 78 (2006) 567–574.

[20] P. Yin, D. Wan, C. Zhao, J. Chen, X. Zhao, W. Wang, X. Lu, S. Yang, J. Gu, G. Xu, A metabonomic study of hepatitis B-induced liver cirrhosis and hepatocellular carcinoma by using RP-LC and HILIC coupled with mass spectrometry, Mol. Biosyst. 5 (2009) 868–876.

[21] F. Zhang, Z. Jia, P. Gao, H. Kong, X. Li, J. Chen, Q. Yang, P. Yin, J. Wang, X. Lu, F. Li, Y. Wu, G. Xu, Metabonomics study of atherosclerosis rats by ultra fast liquid chromatography coupled with ion trap-time of flight mass spectrometry, Talanta 79 (2009) 836–844.

[22] D.A. Fraser, J. Thoen, A.C. Rustan, O. Forre, J. Kjeldsen-Kragh, Changes in plasma free fatty acid concentrations in rheumatoid arthritis patients during fasting and their effects upon T-lymphocyte proliferation, Rheumatology (Oxford) 38 (1999) 948–952.

[23] H. Kaji, T. Sugimoto, M. Kanatani, M. Fukase, M. Kumegawa, K. Chihara, Prostaglandin E2 stimulates osteoclast-like cell formation and bone-resorbing activity via osteoblasts: role of cAMP-dependent protein kinase, J. Bone Miner. Res. 11 (1996) 62–71.

[24] Y.G. Park, S.K. Kang, S.H. Noh, K.K. Park, Y.C. Chang, Y.C. Lee, C.H. Kim, PGE2 induces IL-1beta gene expression in mouse osteoblasts through a cAMP-PKA signaling pathway, Int. Immunopharmacol. 4 (2004) 779–789.

[25] S.B. Mello, D.M. Barros, A.S. Silva, I.M. Laurindo, G.S. Novaes, Methotrexate as a preferential cyclooxygenase 2 inhibitor in whole blood of patients with rheumatoid arthritis, Rheumatology (Oxford) 39 (2000) 533–536.

[26] C.A. Dinarello, J.G. Cannon, S.M. Wolff, H.A. Bernheim, B. Beutler, A. Cerami, I.S. Figari, M.A. Palladino Jr., J.V. O'Connor, Tumor necrosis factor (cachectin) is an endogenous pyrogen and induces production of interleukin 1, J. Exp. Med. 163 (1986) 1433–1450.

[27] M. Yoshida, Y. Kanno, A. Ishisaki, H. Tokuda, K. Hirade, K. Nakajima, Y. Katagiri, K. Shimizu, O. Kozawa, Methotrexate suppresses inflammatory agonist induced interleukin 6 synthesis in osteoblasts, J. Rheumatol. 32 (2005) 787–795.

[28] M. Yoshida, M. Niwa, A. Ishisaki, K. Hirade, H. Ito, K. Shimizu, K. Kato, O. Kozawa, Methotrexate enhances prostaglandin D2-stimulated heat shock protein 27 induction in osteoblasts, Prostaglandins Leukot. Essent. Fatty Acids 71 (2004) 351–362.

Comprehensive investigation of the influence of acidic, basic, and organic mobile phase compositions on bioanalytical assay sensitivity in positive ESI mode LC/MS/MS

Paul D. Rainville [a,b,∗], Norman W. Smith [a], David Cowan [a], Robert S. Plumb [a,b,c]

[a] King's College London, 150 Stamford Street, London SE1 9NH, United Kingdom
[b] Waters Corporation, 34 Maple Street, Milford, MA 01757, United States
[c] Imperial College, Division of Surgery and Cancer, South Kensington, London SA7 2AZ, United Kingdom

ARTICLE INFO

ABSTRACT

The sensitivity and accuracy of a bioanalytical method is critical in defining the pharmacokinetic (PK) parameters of a potential new chemical entity (NCE). Inhaled therapeutics and low dose NCEs present one of the most significant analytical challenges to the bioanalyst, due to their low systemic concentration. The sensitivity of a bioanalytical LC/MS/MS based assay can be influenced by multiple parameters, including: mobile phase composition, extraction efficiency and chromatographic performance. In this work, we discuss the influence of acidic (pH 3), and basic (pH 10) aqueous mobile phases in conjunction with the two most common organic modifiers used in HPLC, acetonitrile and methanol, on the assay sensitivity of twenty-four probe pharmaceuticals in solvent and biological fluid extract. The study showed that when the test probe pharmaceuticals were analyzed with basic aqueous mobile phases compared to standard acidic conditions the following results were observed: increases in chromatographic peak area ranging from 1.2 to 9.6 fold for twenty-one of the test compounds as well as increased signal-to-noise for greater than seventy percent of the compounds. This observed increase in the MS response was not necessarily related to the later elution of the analyte in a higher organic composition under basic conditions. This was demonstrated as seven out of the twenty-four (approximately thirty percent) of the probe pharmaceuticals tested, eluted earlier, or with the same retention time, under basic conditions, and still produced a greater signal-to-noise when analyzed under these basic conditions. Also observed were decreases in chromatographic peak width, and increases in the retention time of very hydrophilic pharmaceutical compounds. The effect of the mobile phase combinations on the retention and MS response of the choline-containing phospholipids present in precipitated plasma was also investigated, as these analytes are a major source of interference when developing a bioanalytical assay.

Published by Elsevier B.V.

1. Introduction

Recent regulatory guidelines and white papers have increased the scale and number of analytical challenges that the bioanalytical scientist is now facing. More stringent requirements around method development and validation, for example Incurred Sample Reanalysis (ISR) and Matrix Factor calculation has placed greater demands on the quality and robustness of the methodologies employed to support clinical and preclinical studies [1–3]. Since the introduction of the atmospheric pressure ionization source in the late 1980s, liquid chromatography coupled to mass spectrometry has, over the last 15–20 years, become the technology of choice for

quantification in bioanalysis [4–6]. The popularity of this approach for bioanalysis is due not only to the specificity and sensitivity of the technique but also ease of method development [7,8]. Such is the sensitivity of LC/MS/MS that assays with quantification limits of 10 pg/ml are routinely obtainable. However, despite this sensitivity, the analysis of circulating levels resulting from inhaled asthma medication as well as the low volume of sample available from micro-sampling and dried blood spot samples (DBS) provides new sensitivity challenges that must be addressed [9–11].

The sensitivity of bioanalytical assays can be increased by utilizing a variety of different techniques such as: first, sample pre-treatment, either by increasing the concentration of the sample often accomplished by drying down the sample and reconstituting in a lower volume, or by the implementation of sample clean-up protocols e.g. solid phase extraction; whereby samples are purified from endogenous matrix components that interfere with the ionization process in a mass spectrometer. Second,

∗ Corresponding author at: Waters Corporation, 34 Maple Street, Milford, MA 01757, United States. Tel.: +1 508 482 3539; fax: +1 508 482 3085.
E-mail address: paul_rainville@waters.com (P.D. Rainville).

Table 1
Probe pharmaceutical compounds utilized in study.
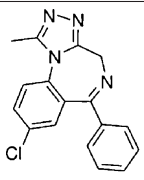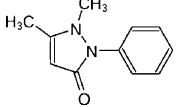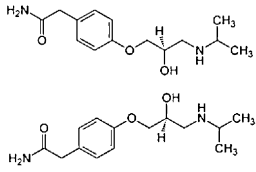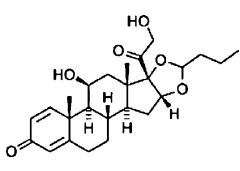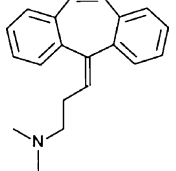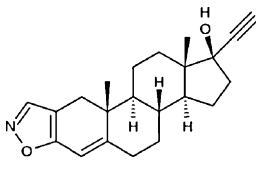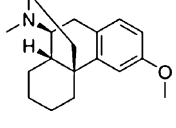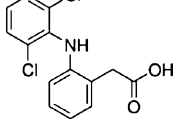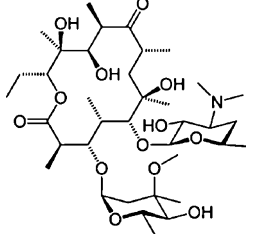
Number	Compound	Structure	Class	Indication
1	Alprazolam		• Benzodiazepines	Anti anxiety and sedative-hypnotic actions
2	Antipyrine		• Pyrazolones • Benzene and derivatives • Anilines	Analgesic
3	Atenolol		• Phenols and derivatives • Ethers • Phenethylamines • Anisoles	Cardioselective beta-adrenergic blocker
4	Budesonide		• Corticosteroids • Glucocorticoids	Management of asthma
5	Cyclobenzaprine		• Dibenzocycloheptenes	Skeletal muscle relaxant and a central nervous system (CNS) depressant
6	Danazol		• Steroids • Steroid derivatives	Treatment of endometriosis and some benign breast disorders
7	Dextromethorphan		• Morphinans • Benzylisoquinolines	Antitussives
8	Diclofenac		• Aminobenzoates • Phenylacetates	Antipyretic and analgesic
9	Erythromycin		• Macrolides	Macrolide antibiotic

Table 1 (*Continued*)
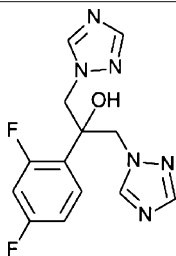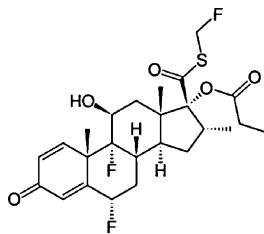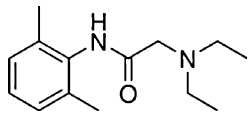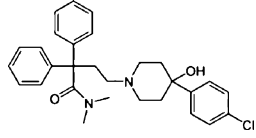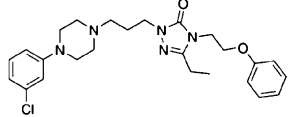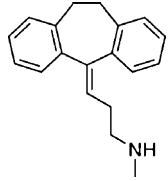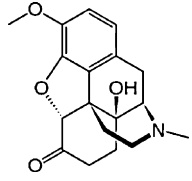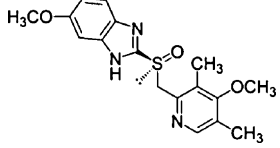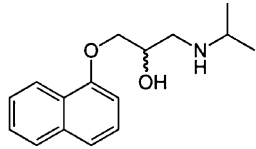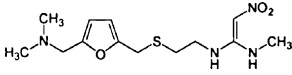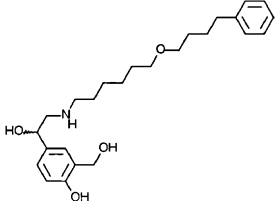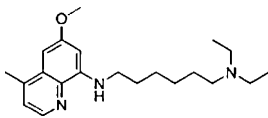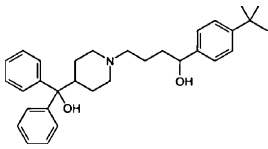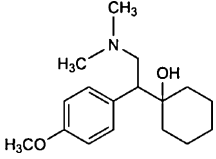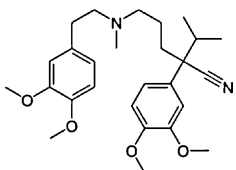
Number	Compound	Structure	Class	Indication
10	Fluconazole		• Benzyl alcohols and derivatives • Cumenes and derivatives • Phenethylamines	Antifungal
11	Fluticasone		• Steroids and steroid derivatives	Relieve inflammatory and pruritic symptoms of dermatoses and psoriasis, treatment of asthma.
12	Lidocaine		• Acetanilides	Local anesthetic and cardiac depressant
13	Loperamide		• Phenylpiperidines • Diphenylmethanes	Antidiarrheals
14	Nefazodone		• Phenols and derivatives • Ethers • Halobenzenes • Anisoles • Phenyl esters • Anilines	Antidepressant
15	Nortriptyline		• Dibenzocycloheptenes	Antidepressant
16	Oxycodone		• Morphinans • Benzylisoquinolines	Analgesic
17	Omeprazole		• Phenols and derivatives • Benzimidazoles • Ethers • Anisoles	Inhibitor of gastric acid secretion
18	Propanolol		• Naphthalenes	acute myocardial infarction, arrhythmias, angina pectoris, hypertension, hyperthyroidis, migraine, menopause, and anxiety.

Table 1 (*Continued*)

Number	Compound	Structure	Class	Indication
19	Ranitidine		• Furans	Mediate gastric secretion
20	Salmeterol		• Benzyl alcohols and derivatives • Phenols and derivatives • Phenethylamines	Treatment of asthma and chronic obstructive pulmonary disease
21	Sitamaquine		• Aminoquinolines	Potential treatment of visceral leishmaniasis
22	Terfenadine		• Diphenylmethanes	Antihistamine
23	Veneflaxine		• Phenols and derivatives • Ethers cumenes and derivatives • Phenethylamines anisoles	Antidepressant
24	Verapamil		• Catecholamines and derivatives	Anti-arrhythmia agent

high resolution chromatography, to provide sharper peaks and reduce co-elution [12–14]. Third, the utilization of a more sensitive detector, such as a high performance tandem quadrupole mass spectrometer.

Another approach for increasing LC/MS/MS sensitivity is improvement in the ionization efficiency of the analyte undergoing quantification. As previously mentioned, one way to increase the ionization of a target analyte is to remove or separate it from compounds that co-elute and interfere with the ionization process, a process known as ion suppression [7,15,16]. The importance of ion suppression in bioanalytical assays carried out by LC/MS/MS has been recognized by the FDA who has included requirements for the calculation of matrix-derived ion suppression in assay development and validation. Ionization efficiency can further be increased by promoting the ionization of analytes by proper desolvation temperature, gas flows and source settings. Mobile phase additives such as formic or acetic acid are often commonly utilized in bioanalysis to increase ionization with ESI positive MS as well [17–20].

Previous work has illustrated the benefit of using high pH mobile phases for LC/MS/MS analysis of basic compounds and peptides [21,22]. The use of high pH mobile phases was made possible by the development of new chromatographic stationary phases with the chemical stability in mobile phase above pH 8. The main advantage of using high pH mobile phases is the decrease in chromatographic peak tailing associated with basic compounds analyzed with acidic mobile phases. This produces sharp, symmetrical, chromatographic peak shapes which are important to increase assay sensitivity. There has also been evidence illustrating that the signal response of compounds analyzed increases when a basic mobile phase pH is employed, even with mass spectrometry operating in electrospray positive ionization mode [22–24].

In the work presented here, we compare the performance of pH 3 and pH 10 mobile phases on twenty-four probe pharmaceutical compounds spiked into protein precipitated plasma and into solvent. The probe pharmaceuticals chosen varied in pK_a, molecular weight, hydrophobicity, and functional groups (Table 1). The signal-to-noise, peak area, peak width, and retention time were calculated for each probe compound. The influence of the organic eluents: acetonitrile and methanol were also evaluated along with the acidic and basic aqueous mobile phase. Furthermore, the effect of the acidic and basic mobile phase on the choline-containing lipid fraction, a major matrix interference, present in the protein-precipitated rat plasma sample was evaluated.

2. Materials and methods

2.1. Chemicals and materials

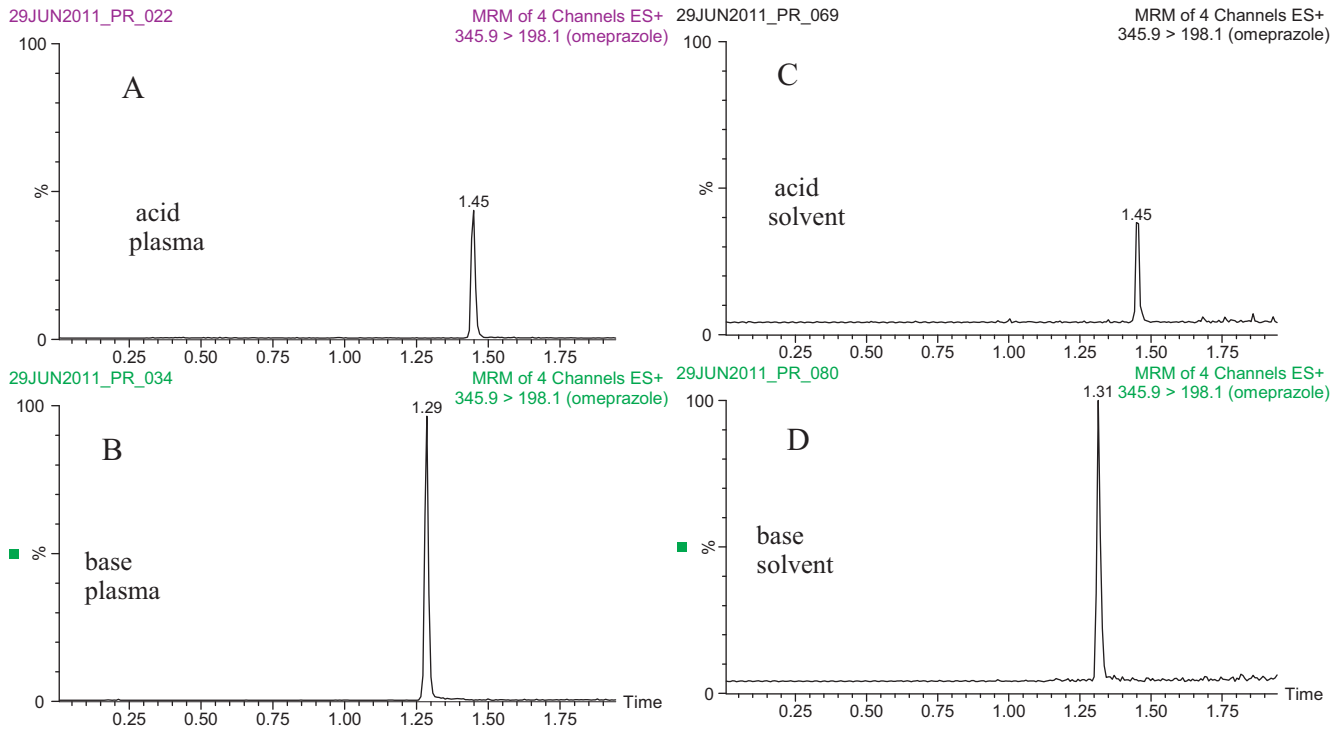Methanol and acetonitrile were obtained from Fisher Scientific (Waltham, MA, USA), Formic acid, dimethyl sulfoxide and

Fig. 1. Omeprazole spiked into precipitated rat plasma and analyzed with acidic (a) and basic mobile phase (b). Omeprazole spiked into solvent and analyzed with acidic (c) and basic mobile phase (d).

ammonium hydroxide were obtained from Sigma–Aldrich Chemicals (St. Louis, MO, USA). Rat plasma was purchased from Equitech-Bio (Kerrville, TX, USA) and stored frozen at 20 °C prior to use. Distilled water was generated in house using a Millipore water

system. Authentic standards for fluticasone and salmeterol was purchased from Toronto Research Chemicals (Toronto, Canada).

Authentic standards for acetaminophen, antipyrine, atenolol, budesonide, cyclobenzaprine, danazol, dextromethorphan, diclofenac, erythromycin, fluconazole, lidocaine, loperamide, nefazodone, nortriptyline, oxycodone, omeprazole, propranolol, ranitidine, sitamaquine terfenadine, veneflaxine, verapamil were
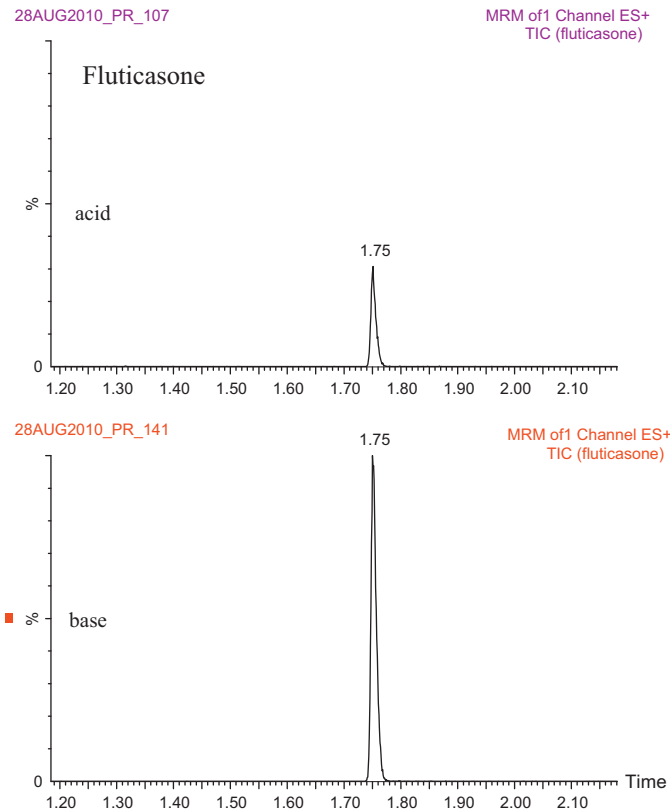
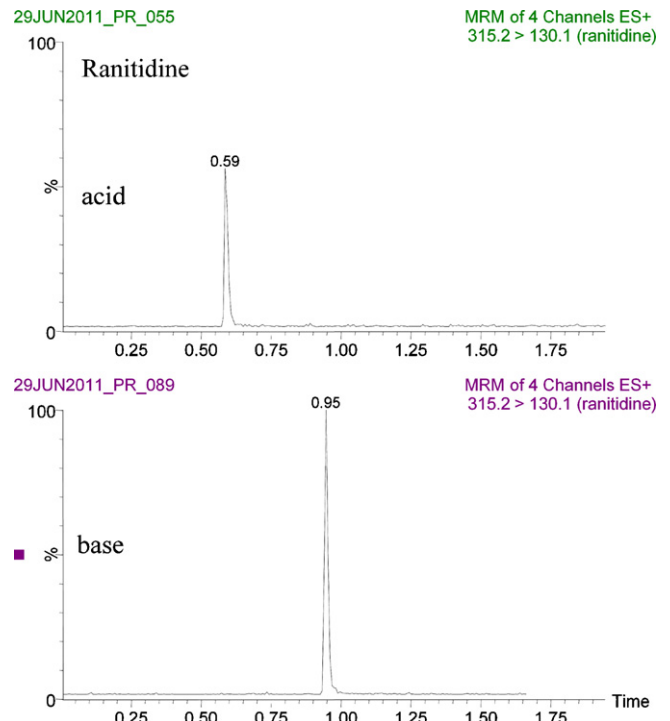**Fig. 2.** Effect of mobile phase pH on fluticasone spiked into solvent.

Fig. 3. Effect of mobile phase pH on ranitidine spiked into solvent.
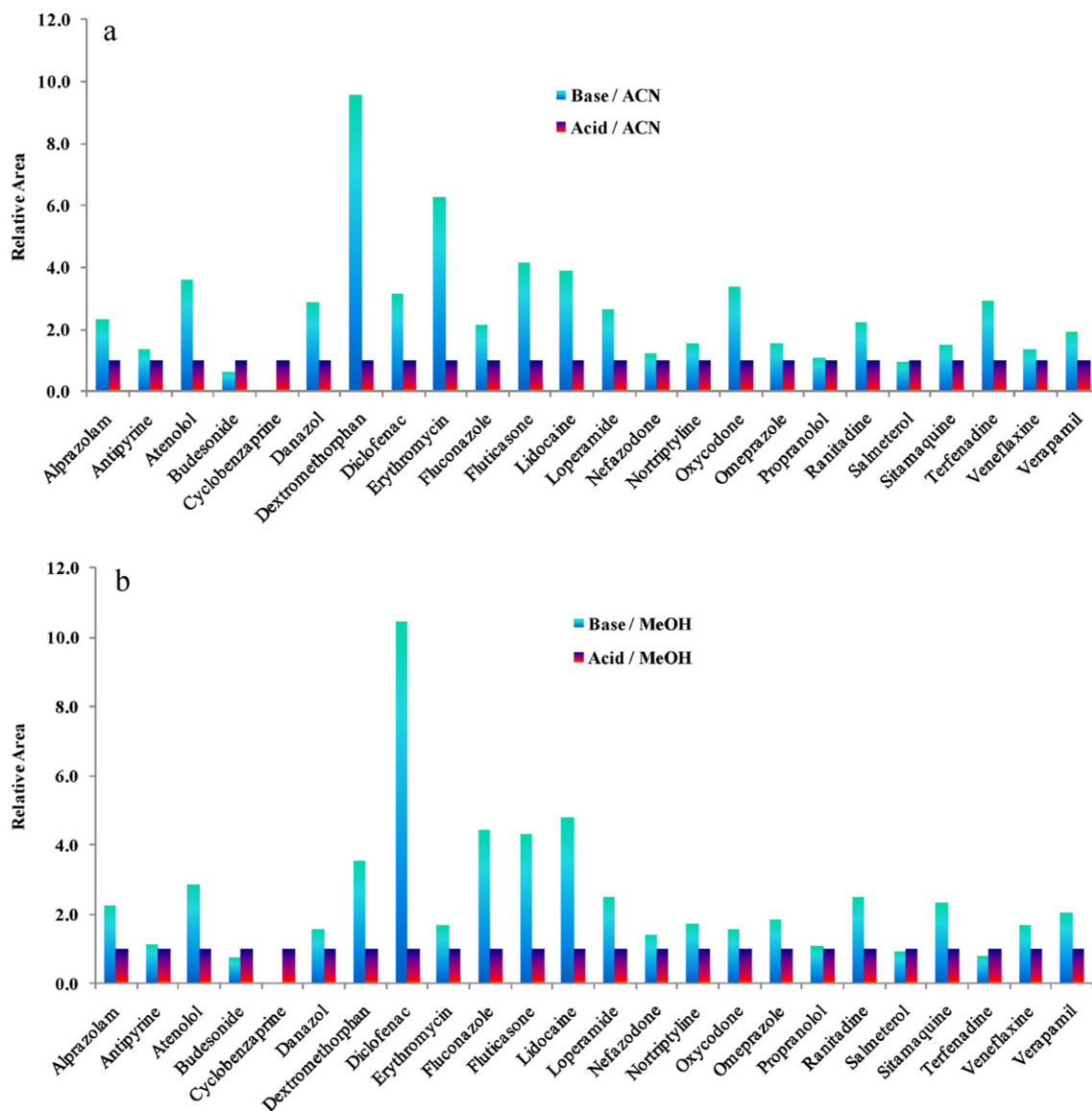
Fig. 4. (a and b) Relative MS response (peak area) for probe pharmaceuticals spiked into plasma, prepared by protein-precipitation, and analyzed with basic and acidic mobile phase pH combined with acetonitrile and methanol as the organic modifier.

purchased from (Sigma–Aldrich, St. Louis, MO, USA). Sample standard for alprazolam was purchased from Cerilliant (Round Rock, TX, USA).

2.2. Sample preparation

The standard compounds were dissolved in methanol, with the exception of fluticasone, which was dissolved in dimethyl sulfoxide, to produce a 1 mg/ml solution. The resulting solutions were then dissolved in aqueous methanol:water (5:95, v/v) to provide a series of spiking solutions. The standard solutions were then spiked into rat plasma or into aqueous methanol: water (5:95, v/v). The solvent composition was kept less than five percent in the plasma samples. Samples were then protein-precipitated by the addition of 100 μl of acetonitrile to 50 μl of sample in a 1.5 ml Eppendorf tube. Sample mixtures were then vortex mixed for 1 min and centrifuged at 15,000 rcf for 5 min. The supernatant was then removed and diluted with water using 1:5 protein-precipitated sample:water in order to match the initial generic gradient conditions utilized in

the study. Samples prepared to investigate the phospholipid component, present in the rat plasma, were prepared with the same previously described protein-precipitation method.

2.3. Liquid chromatography

A 5 μl injection of each sample was injected onto an ACQUITY® Ultra Performance LC® separations module (Waters Corporation, MA, USA). Chromatography was performed on a 2.1 mm × 50 mm 1.7 μm ACQUITY BEH C18. Mobile phase A consisted of water with formic acid (0.1%, v/v) or water with ammonium hydroxide (0.1%, v/v). Mobile phase B consisted of methanol or acetonitrile.

The column was maintained at 45 °C and eluted under linear gradient conditions from 5 to 95% B over 2.0 min at a flow rate of 0.6 ml/min.

2.4. Mass spectrometry

Mass spectrometry was performed on a Waters Xevo™ TQ mass spectrometer (Waters, Manchester, UK) equipped with an
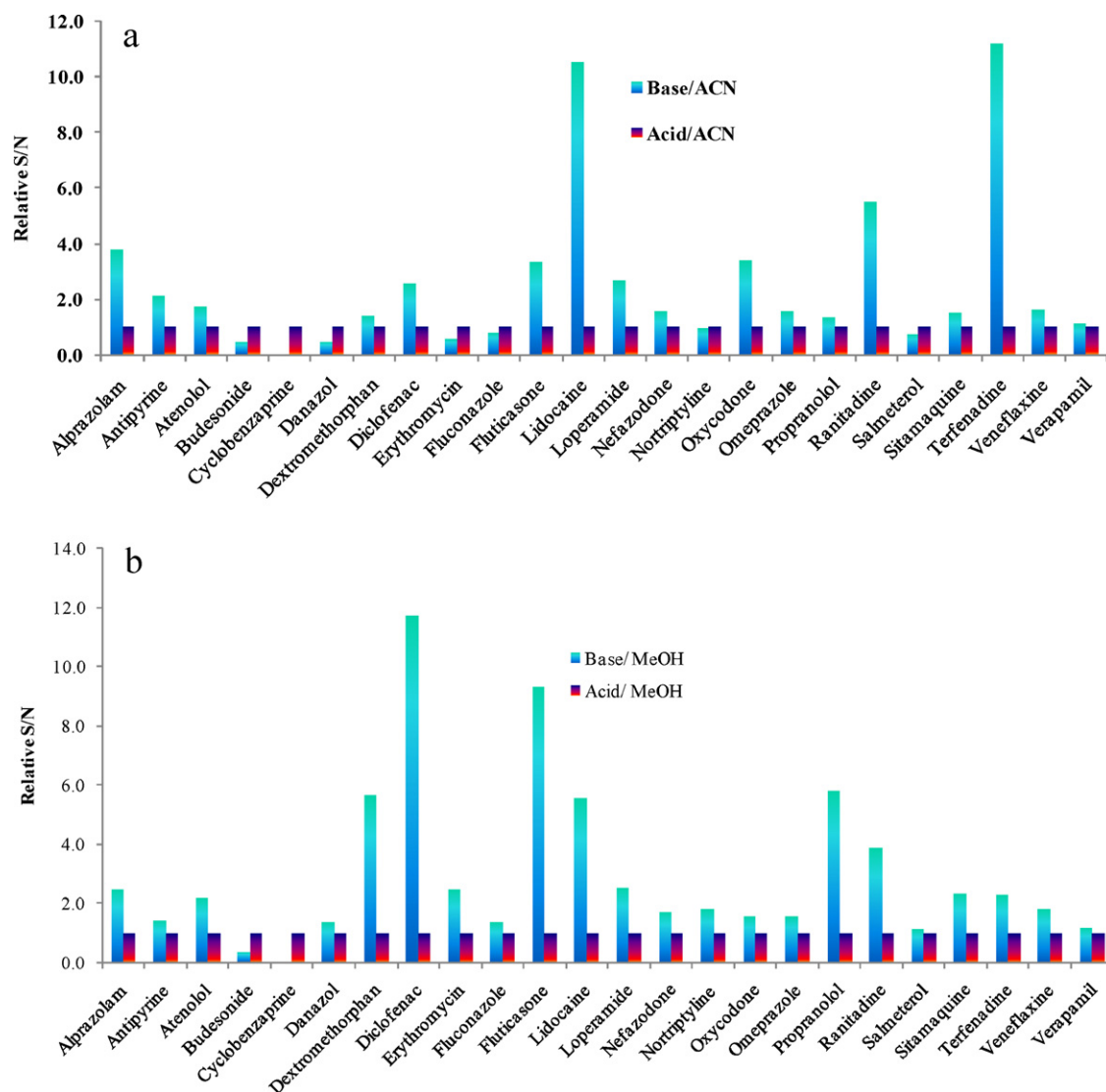
Fig. 5. (a and b) Relative MS response (signal-to-noise) for probe pharmaceuticals spiked into plasma, prepared by protein-precipitation, and analyzed with basic and acidic mobile phase pH combined with acetonitrile and methanol as the organic modifier.

electrospray interface. Settings were as follows: source temperature = 150 °C, desolvation temperature = 600 °C, desolvation gas flow rate = 1000 l/h, and cone gas flow = 40 l/h. Cone and collision energies were optimized for each compound. The mass spectrometer was operated in MRM, MRM with parent ion scan or MRM with full scan MS (RADAR^{TM} mode). Table 2 lists the transitions and conditions utilized for each of the compounds analyzed in this assay.

3. Results and discussion

The benefits of high pH mobile phases in reversed-phase chromatography are well known for compounds containing basic groups. Operation at a pH above the pK_a of these compounds allows them to be chromatographed as neutrals, resulting in greater, more reproducible retention as well as more symmetrical peak shapes. Peng and Farkas reported the use of high pH for the analysis of basic drug substances in 2008 [22]. As previously mentioned, the routine application of high pH mobile phases was made possible only by the development of organo-silica based stationary phases in the late 1990s [25]. These new phases employed the incorporation of a methyl group into the core silica structure, increasing

chemical stability and reducing phase dissolution. This allowed for operation with mobile phase in the range of 9–10 pH units. More recently, the development of a bridged-ethyl silica hybrid stationary phase has resulted in greater phase stability allowing continual operation at pH 10–11 [26]. The data presented here highlights the benefits and drawbacks of employing a high pH mobile phase for the LC/MS/MS analysis of a series of common pharmaceutical compounds that ionize under electrospray positive ionization mode. These compounds tested were selected due to their variation in chemical structure, polarity and lipophilicity. Each compound was individually spiked in solvent and protein-precipitated rat plasma. To compliment the evaluation of mobile phase pH, two common organic modifiers, acetonitrile and methanol, were also evaluated. Six consecutive, replicate injections were carried out for each compound under the acidic and basic mobile phase conditions. Further, the effect of the mobile phase pH in combination with organic modifier on endogenous molecules, such as phospholipids, present in biological matrix was also investigated.

A representative illustration of the effect of utilizing high pH mobile phase is shown in Fig. 1. The data displayed here shows the effect of mobile phase pH on the LC/MS/MS analysis of omeprazole, a protein pump inhibitor, spiked into solvent and into

Table 2
Optimized cone, collision energies and MRM transitions for probe test pharmaceutical compounds.

Compound name	Cone (V)	Collision energy (eV)	MRM
Alprazolam	40	25	309.2 > 281.0
Antipyrine	36	26	189.3 > 106.3
Atenolol	30	24	267.2 > 144.9
Budesonide	16	12	431.3 > 323.1
Cyclobenzaprine	28	38	276.2 > 215.2
Danazol	30	24	338.3 > 148.0
Dextromethorphan	40	38	272.3 > 171.0
Diclofenac	16	32	296.1 > 214.1
Erythromycin	28	32	716.8 > 158.1
Fluconazole	28	16	307.2 > 220.0
Fluticasone	18	20	501.2 > 293.3
Lidocaine	22	26	235.2 > 86.1
Loperamide	28	28	477.3 > 266.1
Nefazodone	48	34	470.3 > 246.1
Nortriptyline	24	14	262.2 > 233.0
Oxycodone	28	30	316.2 > 241.1
Omeprazole	16	10	345.9 > 198.1
Propranolol	25	20	260.1 > 183.1
Ranitadine	22	24	315.2 > 130.1
Salmeterol	28	24	416.5 > 232.2
Sitamaquine	30	21	344.3 > 271.2
Terfenadine	22	26	472.4 > 436.3
Veneflaxine	8	28	278.3 > 121.1
Verapamil	38	30	455.3 > 165.0

protein-precipitated rat plasma. As can be seen from the data, an approximate two-fold increase in response is realized when the compound was analyzed with the basic mobile phase compared to the acidic mobile phase, irrespective of the sample preparation. These results would indicate that the matrix components are not contributing to the increased response observed with the basic mobile phase analysis. Previous studies have contributed or suggested that the increase in response of compounds analyzed under basic mobile phase conditions, to increased retention time and therefore elution in a higher concentration of organic modifier [22]. However in this example, the retention time for omeprazole was actually decreased by 0.16 min when analyzed with the basic mobile phase and the response was greater than that when analyzed with traditional acidic conditions. This result suggests that the increase in analyte response may not due to a later elution time and higher organic solvent composition of the peak. A similar result was also observed for diclofenac analyzed under the acidic and basic conditions. An increase in MS response was also observed even when the retention time did not change with the change in mobile phase pH. This is illustrated in Fig. 2. Here the steroid, fluticasone propionate, was analyzed in the same manner as the previous omeprazole example. However, in this case, the retention time for fluticasone propionate was identical under both acidic and basic modified mobile phase conditions. Thus the organic solvent composition of the analyte peak entering the mass spectrometer is identical. This was the case for five of the twenty-four compounds (approximately twenty percent) tested during this study, these compounds were: alprazolam, antipyrine, danazol, fluconazole, and fluticasone. This data again leads us to conclude that the increase in MS response with the basic mobile phase may not be due to later chromatographic peak elution in a higher organic solvent composition. The data presented in Table 3 shows the retention times for the twenty-four compounds tested during the study. A significant increase in analyte retention times was observed for the more polar compounds. An example of this increase in retention time is illustrated with the analysis of the H2 receptor antagonist, ranitidine, as shown in Fig. 3. In this example, a retention time increase of 0.31 min was observed, equating to an increase in the gradient retention factor from 1.0 to 2.2. This observed increase in retention time under basic conditions for polar compounds has
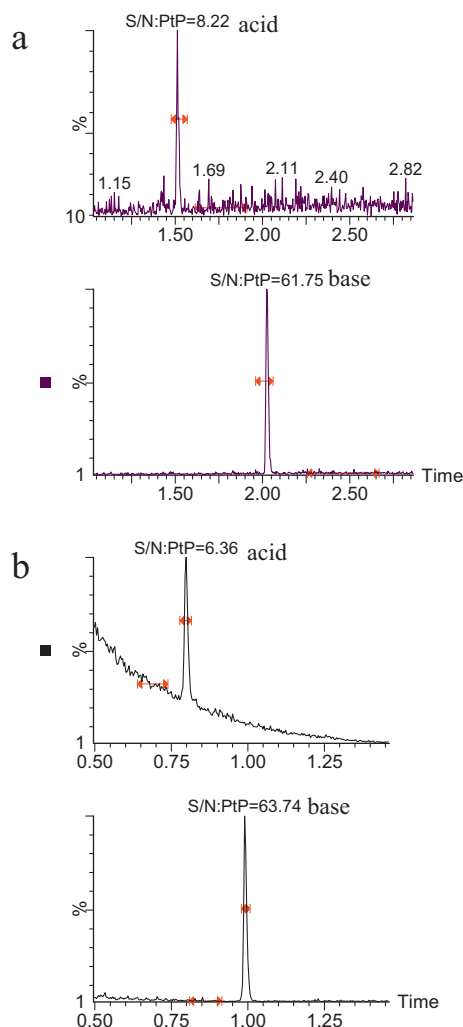

Fig. 6. (a and b) Signal-to-noise for propranolol (a) and lidocaine (b) spiked into plasma, prepared by protein-precipitation, near LLOQ analyzed with traditional acidic mobile phase compared to signal-to-noise obtained with basic mobile phase.

significant benefit in bioanalytical assays. By increasing analyte retention there is greater opportunity to separate the analyte from matrix interferences eluting near the void volume of the column. These matrix interferences could potentially lead to the incorrect measurement of the drug in a biofluid sample, leading to erroneous results due to ion suppression.

3.1. Effect on peak area

The chromatographic peak area is a measurement of the sensitivity or response of the system. The data displayed in Fig. 4a illustrates the average peak area values for each of the twenty-four probe pharmaceutical compounds, spiked into plasma prepared by protein-precipitation, and analyzed under basic and acidic conditions with acetonitrile as the strong eluent. The results obtained for the basic mobile phase analysis were normalized against the peak areas obtained with standard acidic conditions. One can see from Fig. 4a and b that of the twenty-four compounds tested under the previous stated conditions, twenty-one compounds had greater average peak area counts when run with the basic mobile phase; the exceptions being budesonide, cyclobenzaprine and salmeterol, which showed no increase in the average peak area counts under basic conditions over the standard acid conditions. The increases in peak area count ranged from 1.2 to 9.6 fold with propranolol

Table 3
Retention times for probe test pharmaceuticals under the four mobile phase compositions tested in the study.

| Compound	$n = 6$ (min)	ACID/MeCN	ACID/MeOH	BASE/MeCN	BASE/MeOH
Alprazolam	AVG	1.28	1.69	1.29	1.70
	ST DEV	0.00	0.00	0.00	0.00
	%RSD	0.00	0.00	0.00	0.00
Antipyrine	AVG	0.81	1.12	0.80	1.13
	ST DEV	0.01	0.00	0.01	0.01
	%RSD	0.63	0.36	1.05	0.97
Atenolol	AVG	0.54	0.71	0.82	1.30
	ST DEV	0.01	0.01	0.00	0.02
	%RSD	1.17	0.73	0.00	1.16
Budesonide	AVG	1.50	2.07	1.49	2.08
	ST DEV	0.01	0.01	0.01	0.01
	%RSD	0.35	0.25	0.35	0.25
Cyclobenzaprine	AVG	1.35	2.09		
	ST DEV	0.01	0.01		
	%RSD	0.73	0.58		
Danazol	AVG	1.76	2.09	1.76	2.09
	ST DEV	0.00	0.00	0.01	0.00
	%RSD	0.00	0.00	0.25	0.00
Dextromethorphan	AVG	1.32	1.70	1.92	2.21
	ST DEV	0.01	0.01	0.00	0.00
	%RSD	0.88	0.30	0.21	0.18
Diclofenac	AVG	1.62	2.59	1.01	1.86
	ST DEV	0.01	0.02	0.00	0.01
	%RSD	0.47	0.80	0.40	0.28
Erythromycin	AVG	1.53	1.96	1.74	2.10
	ST DEV	0.01	0.01	0.00	0.01
	%RSD	0.55	0.32	0.00	0.25
Fluconazole	AVG	0.83	1.16	0.83	1.16
	ST DEV	0.00	0.00	0.00	0.00
	%RSD	0.00	0.35	0.49	0.00
Fluticasone	AVG	1.75	1.98	1.75	1.98
	ST DEV	0.01	0.01	0.01	0.01
	%RSD	0.29	0.26	0.29	0.26
Lidocaine	AVG	0.91	1.13	1.60	1.90
	ST DEV	0.00	0.00	0.01	0.00
	%RSD	0.00	0.36	0.32	0.00
Loperamide	AVG	1.58	1.76	1.80	2.10
	ST DEV	0.01	0.00	0.01	0.01
	%RSD	0.33	0.00	0.29	0.29
Nefazodone	AVG	1.70	2.04	1.84	2.24
	ST DEV	0.01	0.00	0.00	0.00
	%RSD	0.44	0.20	0.00	0.00
Nortriptyline	AVG	1.32	1.73	1.97	2.16
	ST DEV	0.01	0.01	0.00	0.01
	%RSD	0.41	0.30	0.00	0.25
Oxycodone	AVG	0.79	0.88	1.37	1.65
	ST DEV	0.00	0.00	0.00	0.01
	%RSD	0.00	0.46	0.00	0.74
Omeprazole	AVG	1.02	1.46	0.82	1.31
	ST DEV	0.00	0.00	0.00	0.00
	%RSD	0.00	0.28	0.00	0.00
Propanolol	AVG	1.20	1.68	1.58	2.04
	ST DEV	0.01	0.01	0.00	0.01
	%RSD	0.43	0.33	0.00	0.25
Ranitadine	AVG	0.54	0.65	0.85	1.15
	ST DEV	0.01	0.00	0.00	0.00
	%RSD	0.95	0.00	0.48	0.00
Salmeterol	AVG	1.62	2.08	1.65	2.13
	ST DEV	0.01	0.01	0.00	0.00
	%RSD	0.55	0.36	0.00	0.00
Sitamaquine	AVG	1.62	1.93	1.83	2.43
	ST DEV	0.01	0.01	0.03	0.00
	%RSD	0.91	0.39	1.50	0.00
Terfenadine	AVG	1.70	2.44	2.27	2.37
	ST DEV	0.02	0.03	0.00	0.00
	%RSD	0.89	1.07	0.00	0.00
Veneflaxine	AVG	1.20	1.52	1.73	2.01
	ST DEV	0.01	0.00	0.00	0.00
	%RSD	0.43	0.27	0.00	0.00
Verapamil	AVG	1.27	1.53	1.83	2.03
	ST DEV	0.00	0.01	0.01	0.00
	%RSD	0.32	0.34	0.28	0.00
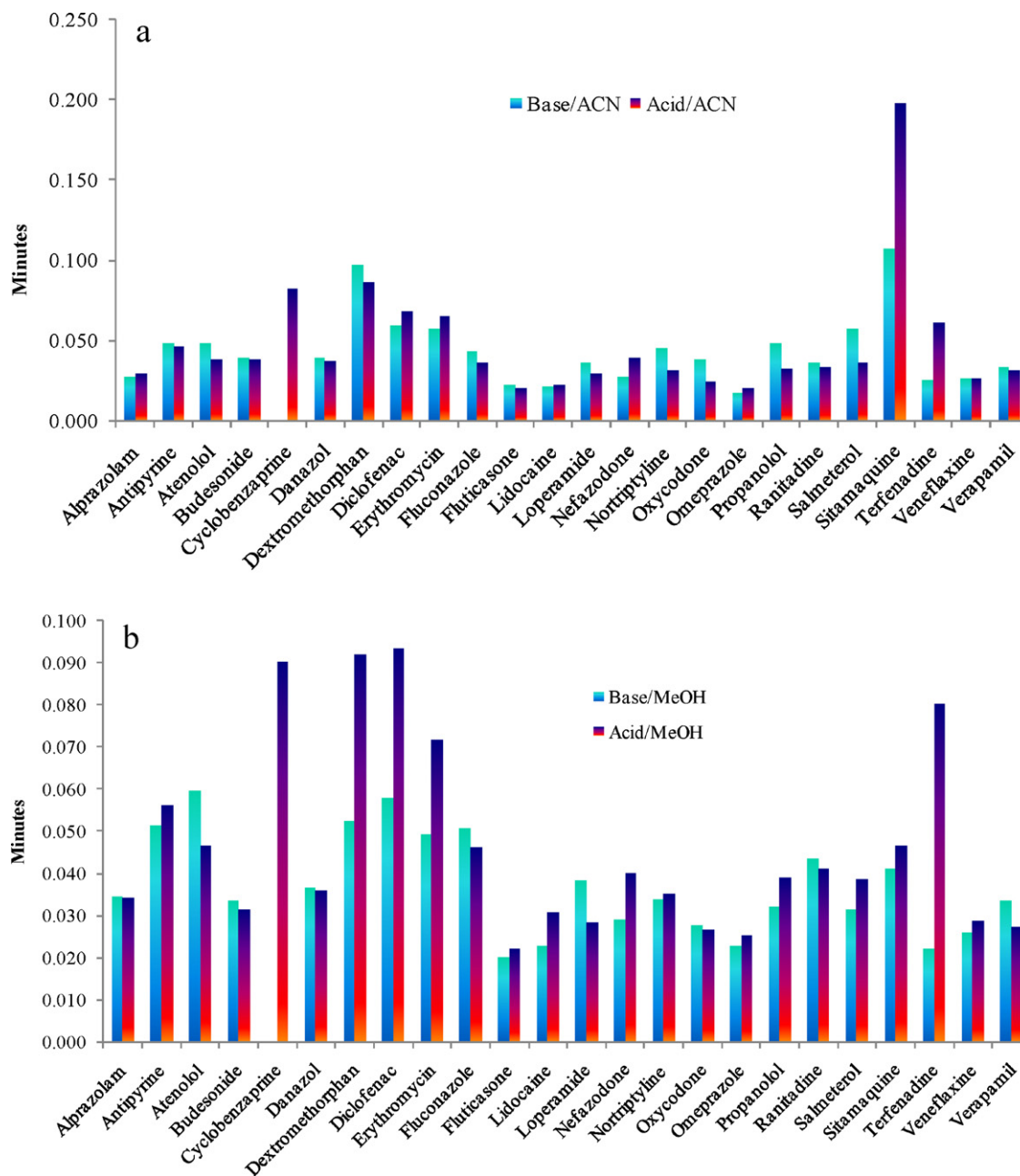
Fig. 7. (a and b) Effect of mobile phase pH on chromatographic peak width with acetonitrile and methanol as the organic modifier.

and dextromethorphan having respectfully the lowest and highest increases in peak area count. The experimental procedure was then repeated employing methanol in place of acetonitrile as the organic eluent. The data from this experiment is shown in Fig. 4b; here twenty out of twenty-four compounds showed an increase in average peak area count when analyzed with the basic mobile phase. Three of the compounds gave the same result as the previous experiment utilizing acetonitrile as the strong eluent: budesonide, cyclobenzaprine and salmeterol. Terfenadine, which exhibited a higher area count when analyzed with base and acetonitrile showed a decrease in area count when analyzed with base and methanol compared with the traditional acidic mobile phase.

3.2. Impact on signal-to-noise

Although an increase in area count may indicate an increase in the detection capability of the LC/MS system towards the probe

pharmaceuticals analyzed under the basic mobile phases; it is the signal-to-noise which is most important as this is the parameter which determines the lower limit of quantification of a bioanalytical assay [27]. Fig. 5a and b shows the average signal-to-noise values for the test compounds, spiked into plasma prepared by protein-precipitation, and run with either acetonitrile (Fig. 5a) or methanol (Fig. 5b) as the organic modifier under acidic and basic conditions. The signal-to-noise was calculated using the peak-to-peak algorithm within the MassLynx software version 4.1. Again, the data obtained under the basic mobile phase conditions is normalized against the signal-to-noise values for the acidic mobile phase analyses. The number of compounds showing an increase in the average signal-to-noise analyzed when using the basic/acetonitrile mobile phase was seventeen of the twenty-four compounds and twenty-two out of twenty-four when methanol was employed as the organic eluent. The calculated signal-to-noise value increases were more scattered when compared to the peak area data. The
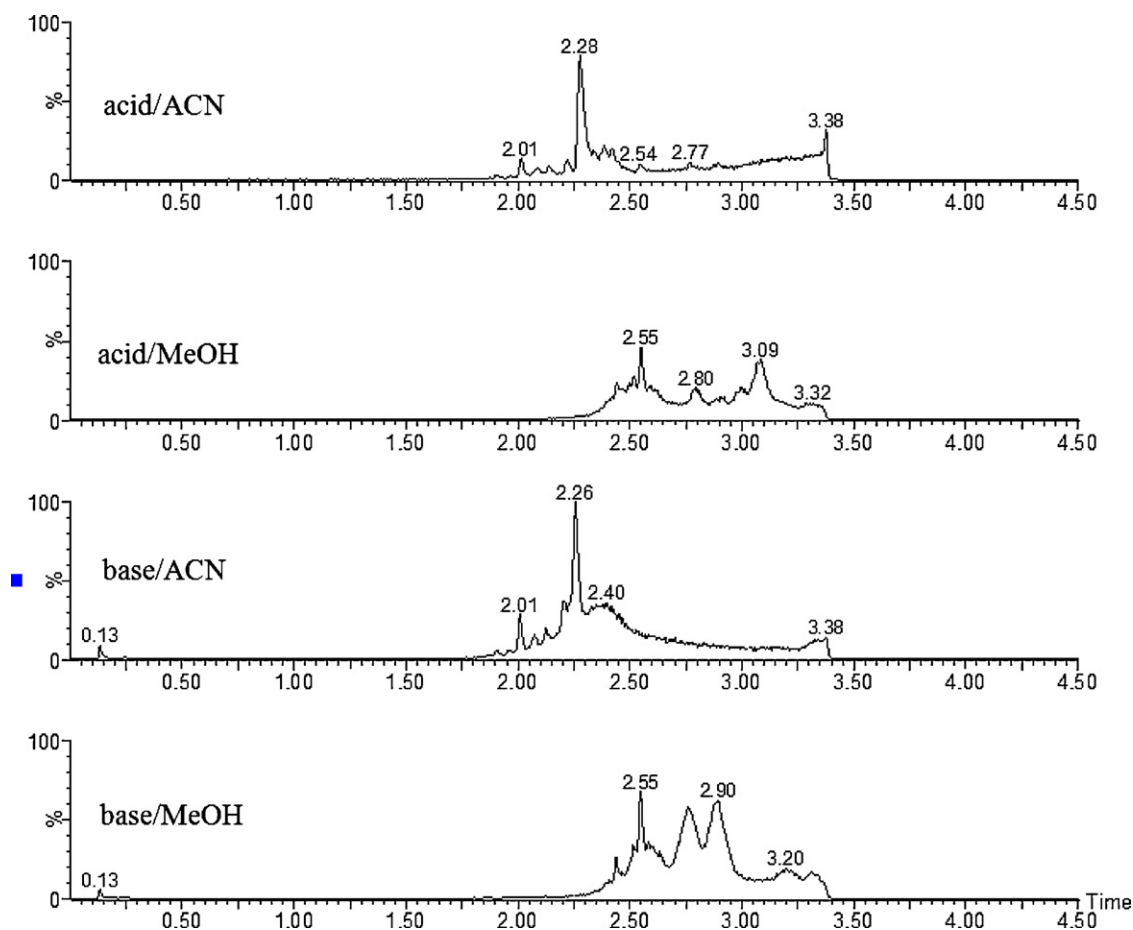
Fig. 8. Effect of mobile phase pH and organic modifier on elution profile of choline-containing phospholipids (axes linked).

chromatographic peak area data with both acetonitrile and methanol organic modifiers gave the same general trend for increases in area counts for the test compounds when the pH of the mobile phase was altered, with the exception of terfenadine. This can be contrasted with the signal-to-noise data where the trend is not as obvious. For example, the highest and lowest signal-to-noise responses with base and acetonitrile as the mobile phase were tefenadine and verapamil respectfully. Whereas with the basic methanol mobile phase combination the compounds that exhibited the highest and lowest signal-to-noise values were diclofenac and salmeterol. It was noted that the basic mobile phases produced greater signal-to-noise values for twenty-two out of twenty-four compounds tested when compared to traditional acidic mobile phases irrespective of the organic modifier. This result indicates that the organic modifier as well as the mobile phase pH needs to be considered when optimizing an assay. The effect of the basic mobile phase was then compared to acidic mobile phase near the LLOQ for propranolol (Fig. 6a) and lidocaine (Fig. 6b) analyzed with methanol as the organic eluent. The data in these figures show that an increase in the signal-to-noise of 7 and 10 fold for propanolol and lidocaine respectively. This result indicates that a lower LLOQ is obtainable with the basic mobile phase over the traditional acidic mobile phase.

3.3. Effect on peak width

Chromatographic peak widths have a direct effect on the signal-to-noise, as the narrower or sharper a chromatographic peak is, the greater the peak height resulting in improved signal-to-noise values. The chromatographic peak widths for the test compounds

were measured at ten percent peak height. Fig. 7a and b shows the resulting average peak width measurements using the four mobile phase combinations of the study. From the graph one can observe that eight of the twenty-four compounds tested had narrower peak widths with the basic/acetonitrile mobile phase combination. While fourteen of the twenty-four compounds tested had narrower peak widths with the basic/methanol mobile phase combination compared to the standard acidic conditions. All of the test compounds that had decreased peak width with the ammonium hydroxide modified mobile phase had a corresponding increase in signal-to-noise values. Therefore the narrower peak shape observed with the basic mobile phase did contribute to the improved signal-to-noise values obtained.

3.4. Effect on choline-containing lipids

While an increase in the signal-to-noise and therefore lower limit of quantification may be the main goal of a bioanalytical assay, careful consideration of matrix interferences is just as important if low levels of quantification are to be robustly achieved. Matrix interferences can arise from concomitant medications, metabolites, as well as endogenous compounds. These can inhibit or enhance MS response through a process referred to as ion suppression/ion enhancement [7,15,16]. One of the most common endogenous matrix components that can be the source of potential problems in blood derived matrices are the glycerphosphocholine-containing phospholipids (GPChos) [28–30]. Therefore, the effect of changing mobile phase pH on the retention time of GPChos was specifically identified as a point of investigation during this study. Fig. 8 illustrates the profile for the GPChos in protein-precipitated rat plasma

acquired by precursor ion scan of m/z 184, in positive ion electrospray with each of the four mobile phase conditions. Here we can observe that the retention time of the major choline-containing phospholipids present remained only slightly affected when the pH of the mobile phase was changed from an acidic to basic conditions. This is in contrast to the effect that the organic modifier had on these GPChos components. Changing the organic modifier from acetonitrile to methanol resulted in a significant increase in the retention time as well as the overall MS response for the GPChos. Therefore if one is to consider developing a bioanalytical assay using a basic mobile phase one must consider the effect of the mobile phase pH will have on the compound under analysis. If the retention time of the analyte under basic conditions is later than that with a standard acidic modified mobile phase, special consideration to matrix effects must be investigated as co-elution with the GPChos may occur. Also multiple lots of plasma must be evaluated as the GPCho profiles can differ between not only test subjects such as rat and humans but within the same species as well [31].

While it is not clear from these experiments as to why an increase in signal-to-noise is possible with the basic mobile phases, there is a definite increase in the MS response of the probe pharmaceuticals tested in this study. However, as stated earlier, the increase in MS response may not be due to increased retention time with the basic mobile phase. Also the contribution of narrower peaks and therefore increased peak height that was observed for some of the test compounds indicates that the use of a basic mobile phase in bioanalysis would be beneficial as compared to traditional acidic mobile phases. The results from this study are quite similar to results observed by Delatour and Leclercq, who showed the potential for incorporating high pH mobile phases for use in pharmaceutical analysis by LC/MS/MS [32]. They postulated different mechanisms to try to explain the observed MS response while using basic mobile phases. These mechanisms where based on the ionization process and included: gas-phase proton transfer from the ammonium ion to the compound undergoing analysis or collision-induced dissociation of the analyte-ammonium ion to the protonated analyte form and surface enrichment of protons in the surface layer of droplets from which ions are desorbed. An investigation across different MS instrument platforms may contribute information in order to evaluate whether the results shown here are also observed over a wide range of MS instruments that vary in source architecture. The observation that methanol gave an increase response for many of the compounds over that of acetonitrile may be explained by the fact that depending on the nature of the probe pharmaceutical under investigation, the organic modifier can enhance or suppress the signal observed by the MS [33]. The increase in GPCho response when methanol was utilized may be due to the increased solubility of these compounds in this particular organic modifier.

Future work will include an investigation with the same basic protocol to test the effect of basic mobile phases on common drug metabolites, such as glucuronides, to evaluate any conversion from the associated metabolite form to the parent drug form, either on column or in the MS source. This investigation is of rather importance as conversion of any drug associated metabolites to the parent drug during analysis could lead to erroneous results during a quantitative analysis due to the overestimation of the parent drug present in a sample [34].

4. Conclusion

The data presented here has indicated that the addition of a base, such as ammonium hydroxide, to modify the aqueous mobile phase, has significant benefits to LC/MS/MS based bioanalytical assays under electrospray positive ionization mode. An increase in the signal-to-noise was observed for twenty-two out of twenty-four of the probe pharmaceuticals tested indicating the importance of mobile phase pH optimization when developing an LC/MS/MS based assay. An increase in the chromatographic retention of poorly retained compounds was also observed. The increase in the MS response was not necessarily related to the later elution of the analyte in a higher organic composition under basic conditions. The results demonstrated that seven out of the twenty-four (approximately thirty percent) of the probe pharmaceuticals tested eluted earlier, or with the same retention time, compared to acidic mobile phase, produced a greater signal-to-noise when analyzed with the basic conditions. The effect of the pH of the mobile phase further showed that the phospholipid fraction present in protein precipitated rat plasma was slightly affected by the change in mobile phase pH. However, the basic modified aqueous mobile phase in combination with methanol yielded the highest response for the choline-containing lipid fraction of the prepared plasma sample. The results of these studies indicate that basic mobile phases may be an effective option in order to increase the signal-to-noise of LC/MS/MS bioanalytical assays run under ESI positive ionization mode.

References

[1] C.T. Viswanathan, Regulatory observances in bioanalytical determinations, Bioanalysis 2 (2010) 1325–1329.
[2] P. Timmerman, S. Luedtke, P. van Amsterdam, M. Brudny-Kloeppel, B. Lausecker, S. Fischmann, S. Globig, C. Sennbro, J.M. Jansat, H. Mulder, E. Thomas, M. Knutsson, D. Kasel, S.A. White, M.A. Kall, N. Mokrzycki-Issartel, A. Freisleben, F. Romero, M.P. Andersen, N. Knebel, M. de Zwart, S. Laakso, R.S. Hucker, D. Schmidt, B. Gordon, R. Abbott, P. Boulanger, Incurred sample reproducibility: views and recommendations by the European bioanalysis forum, Bioanalysis 1 (2009) 1049–1056.
[3] C.T. Viswanathan, S. Bansal, B. Booth, A. DeStefano, M.J. Rose, J. Sailstad, V.P. Shah, J.P. Skelly, P.G. Swann, R. Weiner, Quantitative bioanalytical methods validation and implementation: best practices for chromatographic and ligand binding assays, AAPS J. 9 (2007) E30–E42.
[4] P.D. Rainville, J.P. Wheaton, P.G. Alden, R.S. Plumb, Sub one minute inhibition assays for the major p450 enzymes utilizing ultra-performance liquid chromatography/tandem mass spectrometry, Rapid Commun. Mass Spectrom. 22 (2008) 1345–1350.
[5] M. Jemal, Y.Q. Xia, LC–MS development strategies for quantitative bioanalysis, Curr. Drug Metab. 7 (2006) 491–502.
[6] J. Bielawski, J.S. Pierce, J. Snider, B. Rembiesa, Z.M. Szulc, A. Bielawska, Comprehensive quantitative analysis of bioactive sphingolipids by high-performance liquid chromatography–tandem mass spectrometry, Methods Mol. Biol. 579 (2009) 443–467.
[7] Y.Q. Xia, M. Jemal, Phospholipids in liquid chromatography/mass spectrometry bioanalysis: comparison of three tandem mass spectrometric techniques for monitoring plasma phospholipids, the effect of mobile phase composition on phospholipids elution and the association of phospholipids with matrix effects, Rapid Commun. Mass Spectrom. 23 (2009) 2125–2138.
[8] W.A. Korfmacher, Principles and applications of LC–MS in new drug discovery, Drug Discov. Today 10 (2005) 1357–1367.
[9] F.M. Musteata, Pharmacokinetic applications of microdevices and microsampling techniques, Bioanalysis 1 (2009) 171–185.
[10] N. Spooner, R. Lad, M. Barfield, Dried blood spots as a sample collection technique for the determination of pharmacokinetics in clinical studies: considerations for the validation of a quantitative bioanalytical method, Anal. Chem. 81 (2009) 1557–1563.
[11] S. Aburuz, J. Millership, J. McElnay, Dried blood spot liquid chromatography assay for therapeutic drug monitoring of metformin, J. Chromatogr. B 832 (2006) 202–207.
[12] J.R. Mazzeo, U.D. Neue, M. Kele, R.S. Plumb, Advancing LC performance with smaller particles and higher pressure, Anal. Chem. 77 (2005) 460A–467A.
[13] S. Pedraglio, M. Rozio, P. Misiano, V. Reali, G. Dondio, C. Bigogno, New perspectives in bio-analytical techniques for preclinical characterization of a drug candidate: UPLC-MS/MS in in vitro metabolism and pharmacokinetic studies, J. Pharm. Biomed. Anal. 44 (2007) 665–673.
[14] J. Shen, H. Wang, S. Tadros, R. Hayes, Orthogonal extraction/chromatography and UPLC, two powerful new techniques for bioanalytical quantitation of desloratadine and 3-hydroxydesloratadine at 25 pg/mL, J. Pharm. Biomed. Anal. 40 (2006) 689–706.
[15] A. Van Eeckhaut, K. Lanckmans, S. Sarre, I. Smolders, Y. Michotte, Validation of bioanalytical LC-MS/MS assays: evaluation of matrix effects, J. Chromatogr. B 877 (2009) 2198–2207.
[16] B.K. Maturszowski, M.L. Conalanzer, C.M. Chaves-Eng, Strategies for the assessment of matrix effect in quantitative bioanalytical methods based on HPLC-MS/MS, Anal. Chem. 75 (2003) 3019–3030.

[17] V. Capka, S. Cater, Minimizing matrix effects in the development of a method for the determination of salmeterol in human plasma by LC/MS/MS at low pg/ml concentration levels, J. Chromatogr. B 856 (2007) 285–293.

[18] F. Bucelli, A. Fratini, P. Bavazzano, M. Comodo, Screening and quantitation of multiclass drugs of abuse and pharmaceuticals in hair by fast liquid chromatography electrospray time-of-flight mass spectrometry, J. Chromatogr. B 877 (2009) 3931–3936.

[19] T.M. Miller, M.K. Donnelly, E.A. Crago, D.M. Roman, P.R. Sherwood, M.B. Horowitz, S.M. Poloyac, Rapid, simultaneous quantitation of mono and dioxygenated metabolites of arachidonic acid in human CSF and rat brain, J. Chromatogr. B 877 (2009) 3991–4000.

[20] C. Ramirez-Moline, L. Burton, Screening strategy for the rapid detection of in vitro generated glutathione conjugates using high-performance liquid chromatography and low-resolution mass spectrometry in combination with LightSight software for data processing, Rapid Commun. Mass Spectrom. 23 (2009) 3501–3512.

[21] A.J. Tomlinson, R.M. Chicz, Microcapillary liquid chromatography/tandem mass spectrometry using alkaline pH mobile phases and positive ion detection, Rapid Commun. Mass Spectrom. 17 (2003) 909–916.

[22] L. Peng, T. Farkas, Analysis of basic compounds by reversed-phase liquid chromatography–electrospray mass spectrometry in high-pH mobile phases, J. Chromatogr. A 1179 (2008) 131–144.

[23] H. Sillen, N. Magnell, Screening ionisation and chromatography conditions for quantitative LC/MS methods, J. Chromatogr. B 877 (2009) 3581–3588.

[24] J. Mather, P.D. Rainville, W.B. Potts, N.W. Smith, R.S. Plumb, Development of a high sensitivity bioanalytical method for alprazolam using ultra-performance liquid chromatography/tandem mass spectrometry, Drug Test. Anal. 2 (2010) 11–18.

[25] Waters Corporation, Waters Technical Bulletin for XTerra Columns, 1999, WD164.

[26] Waters Corporation, Waters XBridge Columns Brochure, 2008. Available at http://www.waters.com/waters/library.htm?cid=511436&lid=10057202.

[27] FDA Guidance on Bioanalytical Method Validation, 2001. Available at http://www.fda.gov/downloads/Drugs/GuidanceComplianceRegulatoryInformation/Guidances/ucm070107.pdf.

[28] J.L. Little, M.F. Wempe, C.M. Buchanan, Liquid chromatography-mass spectrometry/mass spectrometry method development for drug metabolism studies: examining lipid matrix ionization effects in plasma, J. Chromatogr. B 833 (2006) 219–230.

[29] P. Bennett, H. Liang, Tandem Capabilities Publications. Available at http://www.tandemlabs.com/documents/PatrickASMSPaper.pdf.

[30] M. Meng, P. Bennett, Tandem Capabilities Publications. Available at http://www.tandemlabs.com/documents/MinASMSPaper.pdf.

[31] P.D. Rainville, C. Stumpf, J.P. Shockcor, R.S. Plumb, J.K. Nicholson, Novel application of reversed-phase UPLC-oaTOF-MS for lipid analysis in complex biological mixtures: a new tool for lipidomics, J. Proteome Res. 6 (2007) 552–558.

[32] C. Delatour, L. Leclercq, Positive electrospray liquid chromatography/mass spectrometry using high-pH gradients: a way to combine selectivity and sensitivity for a large variety of drugs, Rapid Commun. Mass Spectrom. 19 (2005) 1359–1362.

[33] S. Zhou, M. Hamburger, Effects of solvent composition on molecular ion response in electrospray mass spectrometry: investigation of the ionization process, Rapid Commun. Mass Spectrom. 9 (1995) 1516–1521.

[34] R. Plumb, G. Dear, D. Mallet, J. Ayrton, Direct analysis of pharmaceutical compounds in human plasma with chromatographic resolution using an alkyl-bonded silica rod column, Rapid Commun. Mass Spectrom. 15 (2001) 986–993.

Short communication

Development and validation of reversed phase high performance liquid chromatographic method for determination of moxonidine in the presence of its impurities

Svetlana Milovanović[a], Biljana Otašević[b], Mira Zečević[b,*], Ljiljana Živanović[b], Ana Protić[b]

[a] Medicines and Medical Devices Agency of Serbia, 458 Vojvode Stepe, 11152 Belgrade, Serbia
[b] Department of Drug Analysis, University of Belgrade, Faculty of Pharmacy, 450 Vojvode Stepe, 11221 Belgrade, Serbia

ARTICLE INFO

ABSTRACT

A simple, rapid, isocratic reversed-phase high-performance liquid chromatographic method was developed and validated for the analysis of moxonidine and its impurities in tablet formulations. The chromatographic separation was achieved on a Symmetry shield C18 column (250 mm × 4.6 mm, 5 μm) by employing a mobile phase consisting of methanol–potassium phosphate buffer (0.05 M) mixture (15:85, v/v) (pH 3.5) at a flow rate of 1 ml min^{-1}; detection at 255 nm. Central composite design technique and response surface method were used to evaluate the effects of variations of selected factors (buffer pH value, column temperature, methanol content) in order to achieve the best isocratic separation within short analysis time (less than 10 min), as well as for robustness test considerations. The method fulfilled the validation criteria: specificity, linearity, accuracy, precision, limit of detection and limit of quantitation. The method was successfully applied for the analysis of commercial moxonidine tablets.

1. Introduction

Moxonidine [4-chloro-N-(imidazolidin-2-ylidene)-6-methoxy-2-methylpyrimidin-5-amine (Fig. 1A)] is a second-generation centrally acting antihypertensive drug that activates I$_1$-imidazoline receptors in the rostroventrolateral medulla thereby reducing the activity of the sympathetic nervous system [1].

The official monographs in the European Pharmacopoeia [2] and in the British Pharmacopoeia [3] list four related substances of moxonidine: 4-chloro-moxonidine (Impurity A, Fig. 1B), 6-methoxy-moxonidine (Impurity B, Fig. 1C), 4-hydoxy-moxonidine (Impurity C, Fig. 1D), and 4-hydoxy-6-chloro-moxonidine (Impurity D, Fig. 1E), of which A and B are process related impurities while C and D are "others". There are a few weaknesses of the pharmacopoeial method such as the use of ion-pairing reagent as a mobile phase component, high column temperature and relatively long run time (about 23 min). No other HPLC method has been reported yet for the determination of moxonidine in the presence of related organic impurities in pharmaceutical dosage form. There are two recent reports describing LC–MS [4] and GC–MS methods for the determination of moxonidine in human plasma [5]. The main objective of the present study was to develop a simple, rapid

and sensitive HPLC method suitable for routine quality control analysis of moxonidine and related organic impurities in drug products (tablets).

2. Experimental

2.1. Drugs and reagents

The standard substances of moxonidine and its impurities were obtained from Chemagis Ltd. (Israel). Methanol gradient grade (Merck KGaA, Germany), potassium dihydrogen phosphate (JT Baker, Holland) and 85% orthophosphoric acid (Merck KGaA, Germany) were used for the mobile phase preparation. All reagents were of analytical grade. Water for chromatography was deionized using an Easy pure RF (USA) purification system. Ph. Eur. quality lactose monohydrate, povidone K-25, crospovidone and magnesium stearate were used as tablet excipients for placebo mixture preparation. The Moxogamma 0.4® tablets containing 0.4 mg of moxonidine (Artesan Pharma GmbH & Co. KG, Germany) were purchased from a local drugstore.

2.2. Equipment and experimental conditions

HPLC-UV analyses were done using Agilent 1100 series LC system (Agilent Technologies, Germany) consisting of binary pump, degasser, thermostated autosampler, thermostated column

* Corresponding author. Tel.: +381 11 3951 384; fax: +381 11 3972 840.
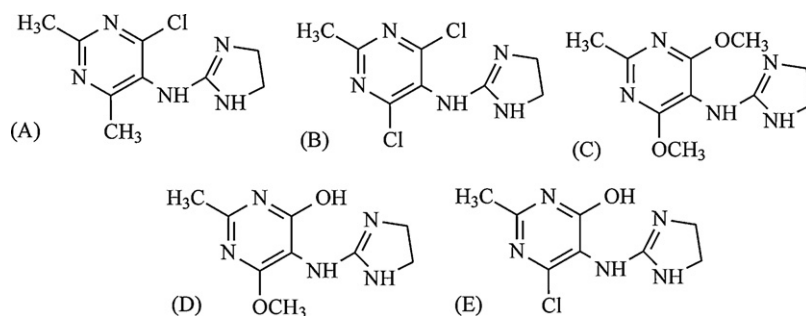E-mail address: mzecevic@pharmacy.bg.ac.rs (M. Zečević).

Fig. 1. Structures of moxonidine (A) and Impurities A (B), B (C), C (D) and D (E).

compartment and variable wavelength detector. For data collection and processing Chemstation software (Agilent Technologies, Germany) was used.

The separation was performed on a Symmetry shield C18 column (250 mm × 4.6 mm, 5 μm) (Waters, USA). The mobile phase consisting of methanol–potassium phosphate buffer (0.05 M, pH 3.5) mixture (15:85, v/v) was degassed and vacuum filtered prior to use through a 0.45 μm (47 mm diameter) nylon membrane filter (Millipore, USA), while Millex syringe driven filter units 0.45 μm (Millipore, USA) were used for filtration of the obtained supernatants. The column temperature was set at 25 °C. The flow rate was 1 ml min^{-1}, injection volume 20 μl and UV detection at 255 nm.

2.3. Solutions

Stock solution of moxonidine was prepared at a concentration of 1 mg ml^{-1} in a mixture of methanol–water (15:85, v/v). Further dilutions of stock solution were made with mobile phase in order to attain concentrations in the range of 0.05–0.15 mg ml^{-1} for a validation purposes. The concentrations of stock solutions of all impurities were 0.01 mg ml^{-1}. The same solvent was used as in case of moxonidine stock solution. Further dilutions of these stock solutions were made with mobile phase in order to obtain concentration ranges of 0.1–1.6 μg ml^{-1} and 0.05–0.80 μg ml^{-1} for Impurities C, D and A, B, respectively, also for a validation purposes. Preparation of stock solutions included ultrasonication for 10 min.

The standard mix solution was obtained by mixing the appropriate volumes of every stock solution and diluting the mixture with the mobile phase in order to obtain following target concentrations: 0.1 mg ml^{-1} for moxonidine, as well as 1.0 μg ml^{-1} and 0.5 μg ml^{-1} for Impurities C, D and A, B, respectively.

The sample solution was prepared from Moxogamma 0.4® tablets from which the film had previously been removed. A quantity of the pulverized tablet mass equivalent to 1 mg of moxonidine was transferred into 10 ml volumetric flask adding a part of mobile phase. After ultrasonication for 10 min, the mixture was made up to 10 ml with mobile phase, and then centrifuged at 4000 × g for 14 min. The supernatant was separated and filtered through Millex syringe driven filter units 0.45 μm prior to the injection. The concentration of moxonidine was 0.1 mg ml^{-1}.

2.4. Experimental design methodology

Application of experimental design enables examination of possible combination of several parameters that are changed at the same time and offers opportunity to perform faster and reliable analysis of results. The response surface design by means of central composite design (CCD) was therefore used to obtain a predictive model which describes the changes in the response within the experimental domain. The relationship between the inputs and the outputs in the CCD can be presented as a second order polynomial

with the form:

$$y = b_0 + b_1 x_1 + b_2 x_2 + b_3 x_3 + b_{12} x_1 x_2 + b_{13} x_1 x_3$$
$$+ b_{23} x_2 x_3 + b_{11} x_1^2 + b_{22} x_2^2 + b_{33} x_3^2$$

where x_1, x_2 and x_3 represent the coded levels of independent variables such as buffer pH value, column temperature and methanol content, respectively. The terms $x_1 x_2$ and x_i^2 ($i = 1$, 2 or 3) represent the interaction and quadratic terms, respectively. y represents observed system response associated with each factor level combination. b_0 represents polynomial equation intercept, while b_1–b_{33} are regression coefficients computed from observed experimental values of y. The experimental data are coded (the lower level is denoted as −1, central as 0 and the higher as +1) in order to have a better insight into the significance of the factors influences. In such a way, if the coefficient has larger value, this means that its significance is greater [6–8]. For all statistical analysis Microsoft Excel 2003 and StatSoft Statistica 5.0 software were used.

3. Results and discussion

3.1. Development of chromatographic method

Due to the similarity of the structures of moxonidine and its related substances (Fig. 1) their isocratic chromatographic separation is a difficult task. The main parts of each structure are pyrimidine and imidazolidine rings and they differ just in one substituent (C-4 or C-6 position of the pyrimidine ring). Due to its N–H group moxonidine is a weak acid (pK_b 5.48) but it contains a basic nitrogen center as well and thus may undergo protonation and/or deprotonation reactions. Based on these facts we tried to predict potential chromatographic conditions that enable efficient separation of the structurally similar components.

The official Ph. Eur. method uses RP8 stationary phase (250 mm × 4 mm, 5 μm chromatographic column) and mobile phase consisting of acetonitrile and ion-pair reagent (sodium pentansulphonate solution with pH adjusted to 3.5 with diluted sulphuric acid solution). The official method also implies heating of the column at 40 °C. In the initial experiments of the present study the same stationary phase was used while the main goals were to avoid ion-pair reagent in mobile phase as well as column heating. The well-known drawbacks of ion-pairing chromatography are long lasting equilibration time and, since the ion-pairing compounds interact strongly with the stationary phase, difficult elimination from the column and therefore poor retention time reproducibility. These facts and column heating lead to column deterioration, thus appeared inappropriate for routine analysis.

Preliminary experiments with different ratios of acetonitrile and water as the mobile phase without ion-pairing reagent as well as Zorbax SB C18 (4.6 mm × 250 mm, 5 μm) and XTerra C18 (4.6 mm × 250 mm, 5 μm) columns, resulted in inadequate chromatographic behavior of the analytes. Finally, the employment of
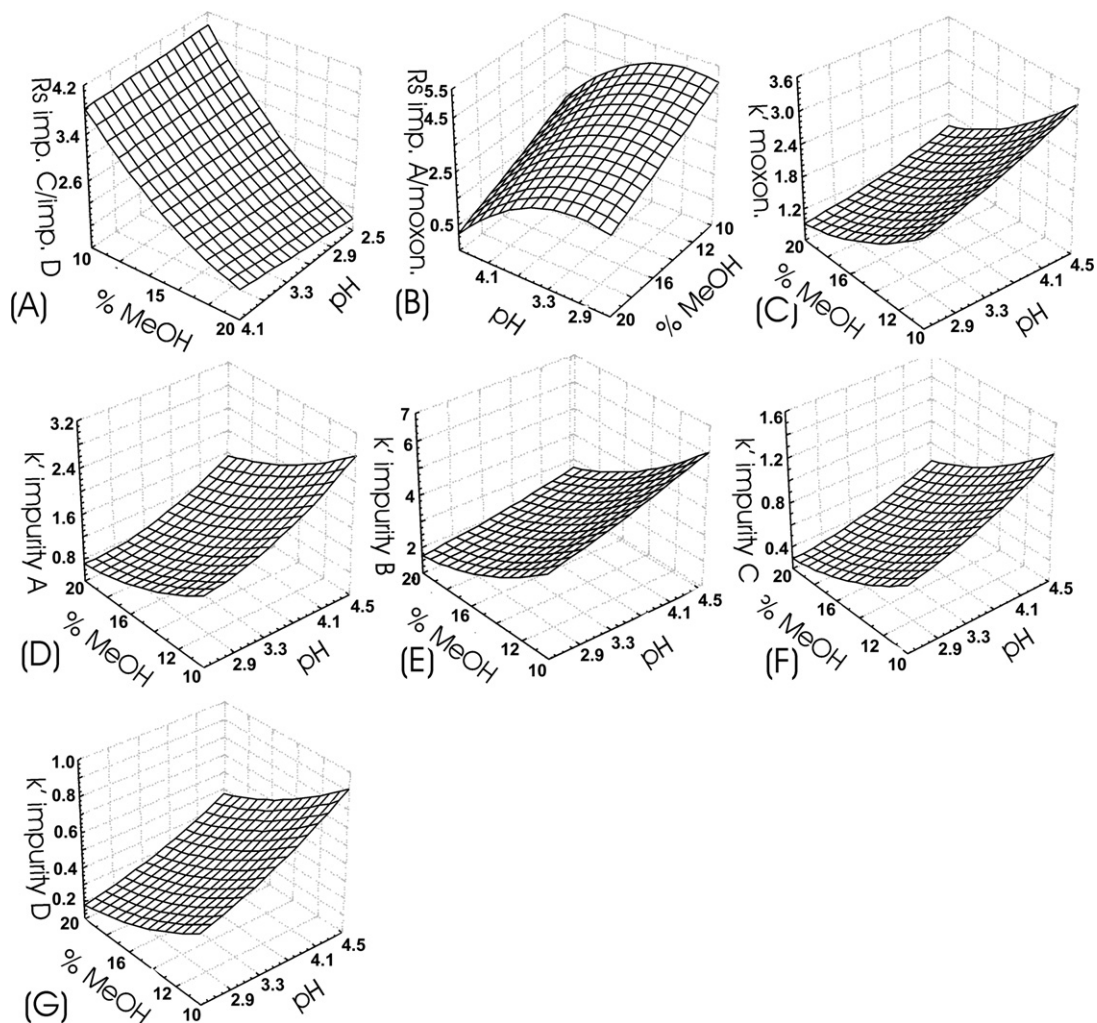
Fig. 2. 3D plots of the response surface for the resolution factors R for Impurity D/Impurity C (A) and Impurity A/moxonidine (B) and retention factors k' for moxonidine (C), Impurity A (D), Impurity B (E), Impurity C (F) and Impurity D (G): the variation of the response as a function of the content of methanol in the mobile phase and buffer pH value; fixed factor is column temperature $T = 25\,°C$.

Symmetry shield C18 (4.6 mm × 250 mm, 5 μm) column and appropriate adjustment of the pH and ratio of mobile phase components (methanol and aqueous buffer) resulted in satisfactory method selectivity and shortening of the runtime. These findings were strongly related to the chemical characteristics of the components. Considering moxonidine as weak acid, preparation of mobile phase with acidic buffer pH value suppressed the dissociation therefore providing longer retention on the RP stationary phase. On the other hand, the increase of methanol content speeded up elution of all components. During the method development, the critical separation pairs were identified and they were formed with Impurities C and D as well as with Impurity A and moxonidine. Polar hydroxyl groups on a C-4 position of pyrimidine rings in the structures of Impurities C and D provided earlier elution comparing with other components. At the same time, chlorine atom on a C-4 position of pyrimidine rings in the structures of moxonidine and Impurity A caused prolonged retention. Since moxonidine and Impurity C contain lipophilic methoxy groups at C-6 position in the pyrimidine ring, they remained slightly longer on stationary phase comparing to other component in the critical pair. Therefore, it was quite reasonable that Impurity B, having methoxy groups on both C-4 and C-6 positions of the pyrimidine ring, had been the last eluted component.

Moxonidine exhibits absorbance maxima at 230 nm and 255 nm with similar intensities [9]. 255 nm was selected as the wavelength of detection to increase the sensitivity for potentially present unknown degradation products.

Besides the influence of buffer:methanol ratio in mobile phase and buffer pH value, it is also well known that an increase in column temperature usually decreases retention and therefore it was expected that baseline separation of the components could be affected. Bearing all this in mind, it was decided to investigate more carefully the overall influence of methanol content, buffer pH value and column temperature. Central composite design (CCD) was used to study the effects of three finally selected factors and afterwards to define the optimal chromatographic conditions for the separation. Each factor was investigated in three levels. Buffer pH value was adjusted to 2.5, 3.5 and 4.5, column temperature was set at 20 °C, 25 °C and 30 °C and methanol content at 10%, 15% and 20%. The retention factor (k') and resolution (R) were chosen as responses. Moreover, the same information gathered from CCD experiments provided the method robustness evaluation as well.

The repetition of the center experimental point provided a precise estimate of the experimental error and a measure of the adequacy of the polynomial models (lack of fit). Regression lack of fit was determined with the assistance of the ANOVA method

Table 1
The estimates of the coefficients for CCD regression models and statistical parameters obtained from ANOVA.

	$R_{imp\ C/imp\ D}$	$R_{imp\ A/moxon.}$	$k'_{imp\ D}$	$k'_{imp\ C}$	$k'_{imp\ A}$	$k'_{moxon.}$	$k'_{imp\ B}$
Coefficients of the regression model							
b_0	2.5912	3.3257	0.4631	0.6595	1.3752	1.7702	3.183
b_1	0.1340	−1.1390	0.1800	0.2320	0.5140	0.4600	0.7510
b_2	0.0440	0.0120	−0.0060	−0.0110	−0.0190	−0.0400	−0.0930
b_3	−0.9970	−1.1550	−0.1980	−0.3140	−0.5490	−0.7850	−1.4760
b_{11}	−0.0274	−0.8564	−0.0012	0.0110	0.1295	0.0145	−0.0017
b_{22}	−0.0474	−0.1814	0.0388	0.0460	0.0545	0.0545	0.0683
b_{33}	0.2376	0.1636	0.0088	0.0310	0.0845	0.1395	0.3333
b_{12}	0.0163	−0.0500	−0.0087	−0.0100	0.0000	−0.0113	−0.0100
b_{13}	−0.0263	−0.1025	−0.0163	−0.0400	−0.0675	−0.1088	−0.2200
b_{23}	−0.0488	0.0125	0.0163	0.0175	0.0125	0.0387	0.0575
ANOVA							
SS_{pe}	11.0626	32.4027	0.7424	1.6173	6.2554	8.7634	29.5449
SS_{lof}	11.0118	32.2203	0.7338	1.6089	6.2199	8.7307	29.4913
F-ratio	0.9954	0.9944	0.9884	0.9948	0.9943	0.9963	0.9982
R^2	0.9879	0.9929	0.9893	0.9948	0.9946	0.9965	0.9981
R^2 adj.	0.9724	0.9839	0.9756	0.9880	0.9877	0.9921	0.9958

b_0, represents the mean value of the considered response; b_1, b_2 and b_3, the main effects of the factors; and b_{12}, b_{13} and b_{23}, the two-factor interactions.

by performing an F-test in order to compare the variance due to the lack of fit with the variance due to purely experimental uncertainty (Table 1). Since the calculated F-ratios were not greater than the tabled F-value for 5 and 2 degrees of freedom at 95% confidence level (19.30), there was no evidence of models lack of fit and the models provide an adequate representation of the data. The fraction of explained variation by means of coefficient of determination R^2 was also evaluated. The values of R^2 and R^2 adjusted taking into account the degrees of freedom indicated that the regression models fit the data very well [7].

According to the values of the coefficients from the polynomial models (Table 1), the column temperature had the least influence. Therefore, this factor was kept at a medium level while performing the new set of experiments in order to inspect and afterwards graphically visualize the dependence of retention factors and resolution factors from the other two variables (methanol content and buffer pH value). Therefore, three-dimensional response surfaces were plotted in order to easily and more precisely define the chromatographic behavior of the investigated substances (Fig. 2). In that way it was possible to predict the behavior of the analytes even slightly outside the selected experimental domain.

The values of the coefficients from the polynomial model of CCD and moreover the appearance of response surfaces revealed the significant influence of methanol content in the mobile phase. The increase of methanol content very evidently led to the decrease of resolution factors between both critical pairs. Due to the structural characteristics of substances, the presented data confirmed that the increase of the organic modifier content in the mobile phase shortens the retention. At the same time, the influence of buffer pH value was not the same on all observed responses. While the resolution between Impurities C and D slightly decreases with the decrease in pH, the resolution between Impurity A and moxonidine exerts more dramatic changes. At first, as the pH value of the buffer rises to 3.5, this response also increases, and afterwards it begins to decrease. At the same time, the increase of buffer pH value prolonged the retention of all investigated substances. The values of coefficients from the polynomial model of CCD as well as the steepness of the response surface plots demonstrate the great significance of this influence. In order to achieve the best separation performances and the reasonable retention of all substances in the isocratic system, the data analysis led to the conclusion that the final composition of the mobile phase should contain 15% of methanol and buffer pH value adjusted to 3.5. The temperature of the column should be maintained at 25 °C. Selected chromatographic conditions provided very attractive total run time (less than 10 min).

3.2. Validation of the method

The optimized method was validated by standard procedure to ensure adequate selectivity, sensitivity, linearity, precision, accuracy and robustness. The obtained data fully met the criteria of the ICH regulations for method validation [10]. The selectivity of the method was confirmed by observing potential interferences caused by tablet excipients: no interfering peaks were noticed in the chromatogram.

The linearity was evaluated by analyzing nine working solutions of moxonidine over the concentration range 0.05–0.15 mg ml^{-1} corresponding to 50–150% of intended test concentration (0.1 mg ml^{-1}) for quality control of moxonidine. In case of impurities, nine working solutions ranging 0.1–1.6 µg ml^{-1} for Impurities C, D and 0.05–0.8 µg ml^{-1} for Impurities A, B (corresponding to 10–160% from each target impurity concentration) were analyzed. All working solutions were prepared in mobile phase from appropriate stock solutions. The relationship between obtained peak areas and the concentrations was subjected to regression analysis. The calculated calibration equations were $y = 23970x − 12.482$, $y = 19.061x + 0.340$, $y = 20.408x + 0.579$, $y = 15.039x + 0.332$ and $y = 10.725x + 0.196$ for moxonidine and Impurities A, B, C and D, respectively. The obtained correlation coefficients (0.9986, 0.9988, 0.9973, 0.9996 and 0.9996, respectively) indicated high linearity over the entire concentration range. The statistical significance of the intercept was tested using the Student's t-test methodology. The calculated deviation values for the intercept (0.249, 2.165, 2.189, 2.214 and 1.958, respectively) were not greater than the tabular value ($t_{0.05} = 2.26$) which confirmed the absence of interferences. The method precision was perceived as inter-assay and intermediate precision including six repetitive measurements in target concentration level and the results were expressed as relative standard deviation values (Table 2). The accuracy of the method (Table 2) was evaluated at concentration levels of 80%, 100% and 120% of the target moxonidine concentration while impurities concentration ranges were spread and the selected points included 20%, 100% and 140% of each impurity target concentration. The solutions were made in triplicate.

According to the ICH regulation, the evaluation of robustness should be considered during the method development phase and it should reflect the reliability of an analytical procedure with respect to deliberate variations in method parameters [10]. The performed CCD experiments clearly marked factors which generally affected separation process and chromatographic

Table 2
Precision and accuracy of the proposed method and assay of commercial tablets.

Compound	Injected (μg ml^{-1})	Found (μg ml^{-1})	Recovery (%)	RSD (%)
Intra-assay precision				
Moxonidine	100	99.987 ± 0.143	99.99	0.14
Impurity A	0.5	0.508 ± 0.004	101.64	0.83
Impurity B	0.5	0.496 ± 0.004	99.26	0.78
Impurity C	1	0.998 ± 0.006	99.85	0.61
Impurity D	1	1.005 ± 0.006	100.48	0.57
Intermediate precision				
Moxonidine	100	100.041 ± 0.295	100.04	0.29
Impurity A	0.5	0.497 ± 0.006	99.42	1.23
Impurity B	0.5	0.503 ± 0.007	100.59	1.39
Impurity C	1	0.990 ± 0.011	99.04	1.07
Impurity D	1	0.997 ± 0.006	99.66	0.60
Accuracy				
Moxonidine	80.000	79.397 ± 0.008	99.25	0.01
	100.000	100.090 ± 0.056	100.09	0.06
	120.000	119.090 ± 0.037	99.24	0.03
Impurity A	0.100	0.102 ± 0.002	102.06	1.63
	0.500	0.496 ± 0.004	99.24	0.83
	0.700	0.711 ± 0.002	101.60	0.25
Impurity B	0.100	0.097 ± 0.003	97.46	3.22
	0.500	0.495 ± 0.008	99.09	1.62
	0.700	0.716 ± 0.011	102.25	1.51
Impurity C	0.200	0.183 ± 0.004	91.51	2.23
	1.000	0.980 ± 0.001	97.98	0.11
	1.400	1.436 ± 0.015	102.56	1.02
Impurity D	0.200	0.183 ± 0.010	91.52	5.42
	1.000	0.974 ± 0.005	97.35	0.55
	1.400	1.366 ± 0.014	97.59	1.05
Assay of commercial tablets				
Moxonidine	100	100.823 ± 0.244	100.84	0.24
Impurity A	0.500[a]	0.117 ± 0.002	0.12[b]	1.31
Impurity B	0.500[a]	0.079 ± 0.001	0.08[b]	1.46
Impurity C	1.000[a]	0.288 ± 0.005	0.29[b]	1.56
Impurity D	1.000[a]	0.270 ± 0.003	0.27[b]	1.28
Unknown impurity	0.500[a]	0.219 ± 0.003	0.22[b]	1.37

RSD, relative standard deviation.

[a] Max allowed content.

[b] Found (%).

behavior of the investigated substances. The column temperature demonstrated the least influence on every analyte while the other two factors, methanol content in the mobile phase and buffer pH value, demonstrated more significant influences on observed responses. Hence, it is necessary to suitably control the experimental parameter settings in order to maintain the reliability of the results. Experimentally determined values of limits of detection and quantification for moxonidine and Impurities A, B, C and D were 0.02 μg ml^{-1}, 0.03 μg ml^{-1}, 0.01 μg ml^{-1}, 0.03 μg ml^{-1} and 0.03 μg ml^{-1}, as well as 0.06 μg ml^{-1}, 0.05 μg ml^{-1}, 0.04 μg ml^{-1}, 0.07 μg ml^{-1}, and 0.07 μg ml^{-1}, respectively.

The proposed method was successfully applied for the analysis of investigated substances in the commercially available moxonidine tablets. The levels of moxonidine and Impurities A, B, C and D
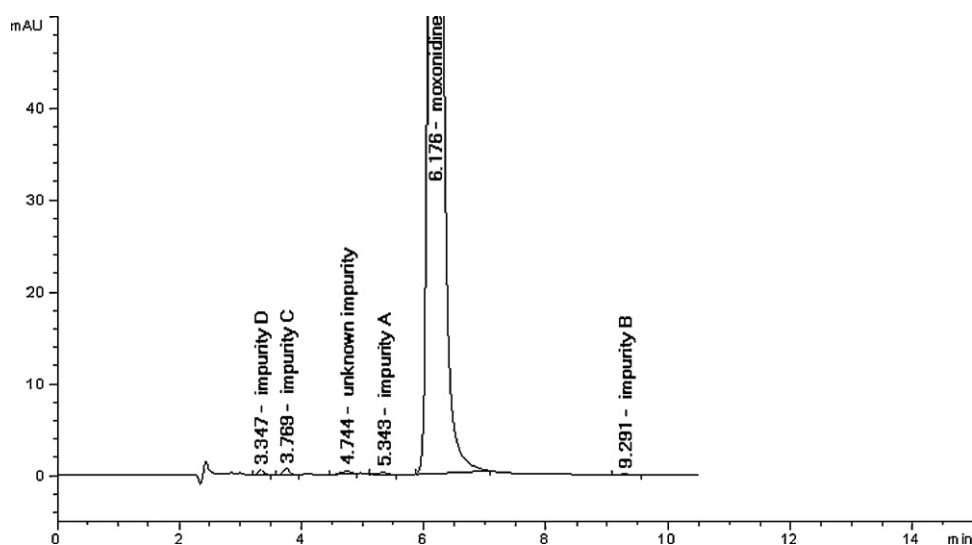
Fig. 3. The representative chromatogram of sample solution.

were in accordance with required criteria (Table 2, Fig. 3). Unknown impurity level of 0.22% was within requirement for single impurities (not more than 0.5%).

4. Conclusions

A simple and rapid isocratic RP-HPLC method was developed for the qualitative and quantitative determination of moxonidine in the presence of its impurities (including one unknown impurity) in tablet formulation. Once the optimized conditions were selected, the method was successfully validated showing good performances with respect to all investigated parameters. The main advantages of this method compared with the official Ph. Eur. method are avoiding ion-pair reagent and column heating, as well as significantly shortening of run time. This makes the proposed method suitable for routine quality control.

Acknowledgement

References

[1] D. Ziegler, M.A. Haxhiu, E.C. Kaan, J.G. Papp, P. Ernsberger, Pharmacology of moxonidine, an I_1-imidazoline receptor agonist, J. Cardiovasc. Pharm. 27 (1996) S26–S37.
[2] European Pharmacopoeia, 7th ed., Council of Europe, Strasbourg, France, 2011.
[3] British Pharmacopoeia, British Pharmacopoeia Commission, The Stationery Office (TSO), London, United Kingdom, 2011.
[4] L. Zhao, L. Ding, X. Wei, Determination of moxonidine in human plasma by liquid chromatography–electrospray ionisation-mass spectrometry, J. Pharm. Biomed. Anal. 40 (2006) 95–99.
[5] M. Rudolph, W. Janssen, M. Strassner, Determination of moxonidine (BDF 5895) in plasma by gas chromatography–negative ion chemical ionization mass spectrometry, J. Pharm. Biomed. Anal. 10 (1992) 323–328.
[6] B. Jocić, M. Zečević, Lj. Živanović, A. Protić, M. Jadranin, V. Vajs, Study of forced degradation behavior of Eletriptan hydrobromide by LC and LC–MS and development of stability-indicating method, J. Pharm. Biomed. Anal. 50 (2009) 622–629.
[7] S.L.C. Ferreira, R.E. Brun, E.G. Paranhos da Silva, W.N. Lopes dos Santos, C.M. Quintella, J.M. David, J. Bittencourt de Andrade, M.C. Breitkreitz, I.C.S.F. Jardim, B.B. Neto, Statistical designs and response surface techniques for the optimization of chromatographic systems, J. Chromatogr. A 1158 (2007) 2–14.
[8] B. Jocić, M. Zečević, Lj. Živanović, A. Ličanski, A chemometrical approach to optimization and validation of an HPLC assay for rizatriptan and its impurities in tablets, Anal. Lett. 40 (2007) 2301–2316.
[9] A.C. Moffat, D. Osselton, B. Widdop, Clarke's Analysis of Drugs and Poisons, third ed., Pharmaceutical Press, London, 2004.
[10] ICH topic Q2(R1), Validation of analytical procedures: text and methodology, Fed. Regist. 62 (1997) 27463–27467 (addendum incorporated 2005).

Short communication

Simultaneous determination of flucloxacillin and ampicillin in human plasma by ultra performance liquid chromatography–tandem mass spectrometry and subsequent application to a clinical study in healthy Chinese volunteers

Chenrong Huang, Jie Gao, Liyan Miao*

Clinical Pharmacology Research Laboratory, First Affiliated Hospital of Soochow University, Suzhou 215006, China

ARTICLE INFO

ABSTRACT

A novel method has been developed for the simultaneous determination of flucloxacillin and ampicillin in human plasma by ultra performance liquid chromatography combined with tandem mass spectrometry (UPLC–MS/MS).

The plasma was treated by single step of protein precipitation (PPT) with acetonitrile. The chromatographic separation was performed with a mobile phase consisting of 10 mM ammonium formate and acetonitrile (68:32, v/v). The analyses were carried out by multiple reaction monitoring (MRM) using the precursor-to-product combinations of m/z 454.1 → 160.3 (flucloxacillin), m/z 350.1 → 106.4 (ampicillin) and m/z 436.1 → 277.3 (IS).

Validation results indicated that the lower limit of quantification (LLOQ) were both 0.2 μg/mL and both assay exhibited a linear range of 0.2–500 μg/mL. The intra-batch precision (R.S.D.) was less than 10.6% and inter-batch R.S.D. was less than 11.2%, while accuracy was with ±8% and ±9.9%, determined from QC samples for flucloxacillin and ampicillin.

A rapid, sensitive and specific method for simultaneous quantifying flucloxacillin and ampicillin in human plasma have been devised and successfully applied to a clinic pharmacokinetic study.

© 2011 Elsevier B.V. All rights reserved.

1. Introduction

Compound preparation of flucloxacillin and ampicillin for injection, which kill bacteria by interfering with their ability to form cell walls, was used for kinds of infections. The inclusion of flucloxacillin which cannot be broken down by the penicillinase enzyme means that unlike other penicillins it can be used in infections caused by penicillin resistant bacteria called staphylococci. Therefore the combination of the two antibiotics allows a broader range of bacteria to be killed [1–3].

Several simultaneous analytical methods for flucloxacillin and ampicillin were reported, including spectrophotometer [4] and HPLC [5]. But the long analysis time (>15.3 min), low sensitivity (LLOQ of 5 μg/mL), 2 mobile phase and 2 detector monitored wavelengths may not meet the requirement of high throughput, rapid speed and sensitivity in biosample analysis. Some HPLC methods only for flucloxacillin [6–8] or for ampicillin [9,10] were reported, but cannot met the requirement for simultaneous determination.

Furthermore, no HPLC–MS/MS method for simultaneous determination of flucloxacillin and ampicillin was reported.

Therefore, in this paper, a simple, rapid and sensitive method by HPLC–MS/MS for simultaneous determination of flucloxacillin and ampicillin were developed and validated, and be successfully applied to clinical pharmacokinetic study in Chinese people.

2. Materials and methods

2.1. Chemical reagents

Ampicillin (purity = 86%), flucloxacillin (purity = 91.6%) and cloxacillin (purity = 96%) were purchased from the National Institute for Control of Pharmaceutical and Biological Products (PR China). HPLC grade acetonitrile and methanol were obtained from SK Chemicals (ROK). HPLC grade water was produced by a Milli-Q Reagent Water System (Millipore, MA, USA). Other chemicals and solvents used were analytical grade.

2.2. Instrumentation

The Ultra Performance™ liquid chromatography (UPLC) was equipped with a binary solvent delivery manager, and a sample

* Corresponding author. Tel.: +86 512 67780467; fax: +86 512 67780040.
  E-mail addresses: miaolysuzhou@163.com, sdfyy8467@126.com (L. Miao).

manager. Mass spectrometry (MS) was performed on a Waters Micromass® Quattro Premier™ tandem quadropole mass spectrometer. The LC–MS/MS system was controlled by a Masslynx™ 4.1 with QuanLynx™ Application Manager.

2.3. UPLC condition

The UPLC separation was performed on a Waters ACQUITY ethylene-bridged (BEH™) C_{18} column (50 mm × 2.1 mm, 1.7 μm) at 40 °C with a flow rate of 0.2 mL/min. The mobile phase was composed of 10 mM ammonium formate and acetonitrile (68:32, v/v). The auto-sampler was conditioned at 4 °C and the injection volume was 2.5 μL using partial loop mode for sample injection.

2.4. MS conditions

All quantifications were performed in MRM mode. The electrospray ionization (ESI) source was operated in positive ionization mode. Quantification was performed using MRM of the transitions of 454.1 → 160.3 (flucloxacillin), m/z 350.1 → 106.4 (ampicillin) and m/z 436.1 → 277.3 (IS), respectively (Fig. 1). The optimal MS parameters were as follows: capillary voltage 4 kV, the source temperature 120 °C, the desolvation gas flow 550 L/h, and cone gas flow 50 L/h.

2.5. Preparation of standards

A mixture stock solution of flucloxacillin and ampicillin was prepared by dissolving the accurately weighed references compound in 50% acetonitrile to give a final concentration of 1 mg/mL. The solution was then serially diluted with 50% acetonitrile to achieve standard working solutions for flucloxacillin and ampicillin.

2.6. Calibration curves and quality control samples

The resulting calibration curve consisted of eleven concentration levels (0.2, 0.5, 1, 2, 5, 10, 20, 50, 100, 200 and 500 μg/mL) for both flucloxacillin and ampicillin. The calibrators were extracted in the same manner as the unknown samples. Linear regression analysis was performed using QuanLynx 4.1.

For QC, samples were prepared by plasma at concentrations of 0.5 (low), 10 (medium) and 200 μg/mL (high) for both flucloxacillin and ampicillin.

2.7. Sample preparation

Aliquots (50 μL) of human plasma, spiked with internal standard working solution (6 μL), were vortex-mixed for 30 s and then precipitate with acetonitrile (0.5 mL) for 1 min using a vortex mixer, then add water 0.5 mL and vortex-mixed for 30 s. After centrifugation at 14,000 × g for 10 min at 4 °C, the supernatant was transferred and 2.5 μL was used for analysis.

2.8. Method validation

The method validation assays were performed according to the currently accepted US Food and Drug Administration (FDA) bioanalytical method validation guide.

2.8.1. Assay specificity

The specificity of the method was tested by screening six different batches of blank human plasma, comparing with those obtained for an aqueous solution of the analyte at a concentration near to the lower limit of quantification (LLOQ).

2.8.2. Linearity

The precision and accuracy of the assays were obtained by comparing the predicted concentration (obtained from the calibration curve) to the actual concentration of flucloxacillin and ampicillin spiked in plasma.

2.8.3. Precision and accuracy

The precision and accuracy were determined by back calculation of spiked plasma samples with respect to a calibration graph prepared each day. The precision was expressed as the inter-batch (LLOQ and QC samples) and intra-batch (QC samples) coefficient of variation (%). The accuracy was calculated as the mean deviation of each concentration from the theoretical value.

2.8.4. Extraction recovery and matrix effect

The extraction recoveries were calculated by comparing the peak areas of extracted standards to those prepared in mobile phase at corresponding concentrations. The matrix effect was evaluated by comparing the peak areas of post-extraction plasma spiked with analytes to those prepared in mobile phase.

2.8.5. Stability

The freeze and thaw stability study QC samples were frozen (−80 °C) and thawed (room temperature) three times before these samples were analyzed. The stability in a processed sample at 4 °C, during storage in the autosampler, was performed for a period of 24 h. The stability in plasma at an ambient temperature was assessed by processing and analysing plasma samples after storage for 3 h on the laboratory bench.

2.8.6. Dilution integrity

The dilution integrity was obtained by comparing the diluted samples (1000–200 μg/mL by blank plasma) to the actual concentration of flucloxacillin and ampicillin spiked in plasma.

2.9. Application of the method

The pharmacokinetic study was approved by the Health Authority Ethics Committee of the First Affiliated Hospital of Soochow University. All volunteers gave their signed informed consent prior to their participation in the study according to the principles of the Declaration of Helsinki. 24 adult volunteers were classified into 3 groups, aged between 20 and 30 years, weighing between 47 and 66, and height between 1.51 and 1.78 m. Three doses of injections (containing 1.5 g, 2.5 g and 5 g of flucloxacillin and ampicillin each) were intravenously guttae in 60 min. Approximately 2 mL blood samples were collected before and at 5 min, 15 min, 30 min, 1 h, 1.5 h, 2 h, 2.5 h, 3 h, 4 h, 5 h, 6 h, 7 h, 9 h, 11 h, 13 h post-dosing. The blood samples were centrifuged at 4000 rpm for 5 min and plasma was separated and stored immediately at −80 °C until analysis.

2.10. Statistical analysis of data

The PK parameters for flucloxacillin and ampicillin were evaluated by DAS 2.0. All analyses were performed with the Statistical Package for Social Science (SPSS 15.0, SPSS Science, IL, USA).

3. Results and discussion

3.1. LC–MS/MS method

Consideration about the long analysis time, two mobile phase and two detector monitored wave-lengths by HPLC method [5], we choose LC–MS/MS method.
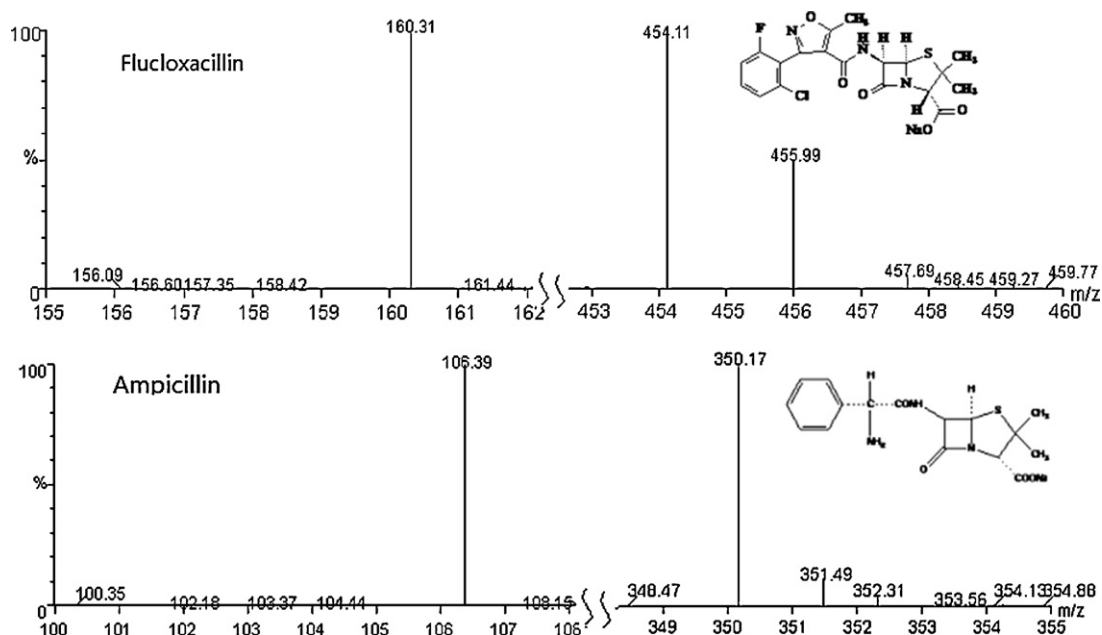
Fig. 1. The positive ion ESI-MS/MS spectrum of flucloxacillin and ampicillin and their chemical structures.

As shown in Fig. 2, flucloxacillin, ampicillin and cloxacillin (IS) were well separated with excellent peak shapes. The very narrow chromatographic peaks produced by UPLC^{TM} resulted in an increase in the chromatographic efficiency and sensitivity. Flucloxacillin, ampicillin and IS were rapidly eluted with retention times less than 3.5 min, which met the requirement for a high sample throughout.

3.2. Method validation

3.2.1. Specificity

Selectivity was assessed by comparing the chromatograms of six different batches of plasma samples with the corresponding spiked plasma. As shown in Fig. 2, there was no interference from endogenous substances observed at the retention time of the analytes.

3.2.2. Matrix effect

To evaluate the matrix effect, the peak areas of plasma extracts spiked with analyte (A) post-extraction were compared with those of the standard solutions dried directly and reconstituted with mobile phase (B). The ratios ($A/B \times 100$) % at concentration levels of 0.5, 10 and 200 µg/mL from plasma were $104.41 \pm 11.52\%$, $99.37 \pm 9.59\%$, $98.48 \pm 5.85\%$, respectively

for flucloxacillin, $93.32 \pm 16.22\%$, $86.70 \pm 9.46\%$, $91.04 \pm 5.37\%$, respectively for ampicillin, which meant no significant matrix effect in this method, indicating that no co-eluting substance could influence the ionization of the analytes.

3.2.3. Sensitivity and linearity

A typical equation for the calibration curve was (ampicillin) $y = 0.0213x + 0.0006$ ($r = 0.9983$) and (flucloxacillin) $y = 0.0229x + 0.0001$ ($r = 0.9984$). The LLOQ for both flucloxacillin and ampicillin were 0.2 µg/mL.

3.2.4. Accuracy and precision

The precision and accuracy data are presented in Table 1 . All these data indicated the adequate precision and accuracy of the present method for determination of flucloxacillin and ampicillin in human plasma.

3.2.5. Recovery and stability

The extraction recoveries of flucloxacillin and ampicillin at concentration levels of 0.5, 10 and 200 µg/mL from plasma were $115.07 \pm 9.61\%$, $135.55 \pm 18.15\%$, $134.59 \pm 21.59\%$, respectively for flucloxacillin, $112.62 \pm 17.22\%$, $118.66 \pm 13.22\%$, $117.31 \pm 14.87\%$, respectively for ampicillin.
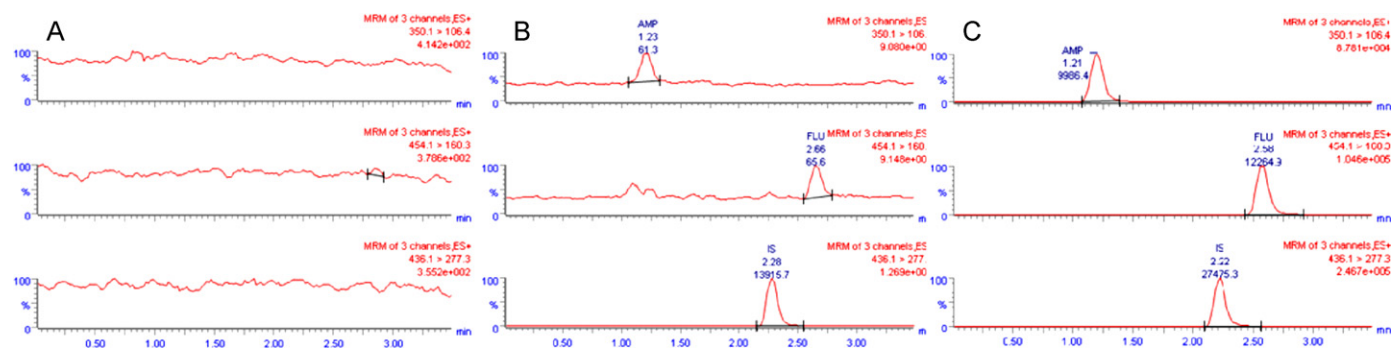
Fig. 2. Representative MRM chromatograms of ampicillin (peak 1, channel 1), flucloxacillin (peak 2, channel 2) and cloxacillin (peak 3, channel 3) in plasma. (A) A blank plasma sample; (B) a blank plasma spiked with warfarin at the LLOQ of 0.2 µg/mL and IS; (C) plasma sample from a volunteer after administration of flucloxacillin and ampicillin. The retention time for flucloxacillin, ampicillin and IS were 2.6, 1.2 and 2.2 min, respectively.

Table 1
The accuracy and precision assessment results for the established LC/MS/MS method of flucloxacillin and ampicillin in LLOQ and QC samples.

Concentration added (μg/mL)	Flucloxacillin						Ampicillin					
	Intra-batch ($n = 5$)			Inter-batch ($n = 15$)			Intra-batch ($n = 5$)			Inter-batch ($n = 15$)		
	Determined concentration (mean ± SD, μg/mL)	Accuracy (%)	Precision (%)	Determined concentration (mean ± SD, μg/mL)	Accuracy (%)	Precision (%)	Determined concentration (mean ± SD, μg/mL)	Accuracy (%)	Precision (RSD,%)	Determined concentration (mean ± SD, μg/mL)	Accuracy (%)	Precision (RSD,%)
0.2	0.20 ± 0.02	100.0	12.2	–	–	–	0.21 ± 0.02	105.0	10.1	–	–	–
0.5	0.47 ± 0.04	94.8	9.0	0.51 ± 0.06	102.0	11.2	0.47 ± 0.05	93.2	10.6	0.47 ± 0.04	94.7	8.2
10	9.95 ± 0.55	99.5	5.5	9.95 ± 0.39	99.5	3.9	9.30 ± 0.24	93.0	2.5	9.23 ± 0.36	92.3	3.9
200	187.66 ± 8.53	93.8	4.5	190.26 ± 7.10	95.1	3.7	183.95 ± 4.11	92.0	2.2	180.25 ± 6.43	90.1	3.6
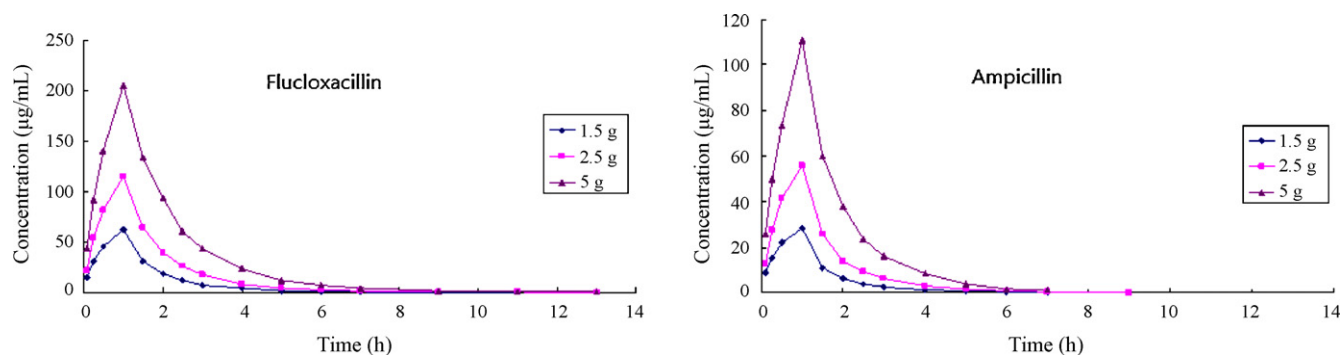
Fig. 3. Average concentration of flucloxacillin and ampicillin versus time in human plasma following 3 doses (1.5 g, 2.5 g and 5 g) of flucloxacillin and ampicillin.

Table 2
The pharmacokinetics (PK) parameters in human volunteers following administration of flucloxacillin and ampicillin at 3 different doses.

PK parameters	Flucloxacillin			Ampicillin		
	1.5 g Mean ± SD	2.5 g Mean ± SD	5 g Mean ± SD	1.5 g Mean ± SD	2.5 g Mean ± SD	5 g Mean ± SD
$AUC_{(0-t)}$ (mg/L h)	104.06 ± 13.32	202.77 ± 38.17	413.35 ± 126.70	41.22 ± 7.56	85.99 ± 13.38	185.44 ± 50.34
$AUC_{(0-\infty)}$ (mg/L h)	104.56 ± 13.30	203.55 ± 38.20	414.32 ± 126.80	41.65 ± 7.62	86.49 ± 13.32	185.90 ± 50.37
$t_{1/2}$ (h)	1.41 ± 0.25	1.69 ± 0.46	1.66 ± 0.23	1.02 ± 0.22	1.02 ± 0.19	1.24 ± 0.28
C_{max} (mg/L)	62.52 ± 10.33	114.92 ± 14.33	205.20 ± 55.38	28.16 ± 5.93	56.03 ± 6.17	110.62 ± 25.40

The results of stability experiments showed that no significant degradation occurred. QC samples obtained by extraction showed no significant degradation after at least 3 h at room temperature. The concentration variations found after three cycles of freezing and thawing were within ±15% of nominal concentrations, indicating no significant substance loss after three repeated freezings and thawings. When processed samples were stored at 4 °C in the autosampler, flucloxacillin and ampicillin showed a very good stability, and the responses varied no more than ±15.0% within 24 h of storage at the concentrations studied.

3.2.6. Dilution integrity

The results for dilution integrity were within ±15.0% of nominal concentrations, showing good dilution integrity.

3.3. Result of PK study

The mean plasma concentration–time profiles for both flucloxacillin and ampicillin was presented in Fig. 3.

As shown in Table 2, the $AUC_{(0-t)}$, $AUC_{(0-\infty)}$, C_{max} values of 3 different dosages increase linearly, and $t_{1/2}$ of 3 different dosages have no significant difference, which indicates the pharmacokinetic features of flucloxacillin and ampicillin among Chinese population.

4. Conclusions

A sensitive, simple and rapid UPLC–MS/MS method for simultaneous determination of flucloxacillin and ampicillin in human plasma are described. Compared with the published methods, the method has the superiority for high sensitivity, satisfactory selectivity and a short run time of 3.5 min. The method has been successfully applied to its pharmacokinetic study in Chinese healthy volunteers.

References

[1] S. Brooks, A.R. Dent, Comparison of bone levels after intramuscular administration of cephradine ('Velosef') or flucloxacillin/ampicillin in hip replacement, Pharmatherapeutica 3 (1984) 642–649.
[2] J. Lloyd-Williams, A.T. Robinson, The treatment of infections in general practice with magnapen: a multicentre trial, J. Int. Med. Res. 8 (1980) 417–423.
[3] R.E.S. Condon, D.H. Wittmann, The use of antibiotics in general surgery, Curr. Probl. Surg. 28 (1991) 801–949.
[4] B.C. McWhinney, S.C. Wallis, T. Hillister, J.A. Roberts, J. Lipman, J.P. Ungerer, Analysis of 12 beta-lactam antibiotics in human plasma by HPLC with ultraviolet detection, J. Chromatogr. B: Analyt. Technol. Biomed. Life Sci. 878 (2010) 2039–2043.
[5] G.G. Mohamed, Spectrophotometric determination of ampicillin, dicluxacillin, flucloxacillin and amoxicillin antibiotic drugs: ion-pair formation with molybdenum and thiocyanate, J. Pharm. Biomed. Anal. 24 (2001) 561–567.

[6] C.B. Landersdorfer, C.M. Kirkpatrick, M. Kinzig-Schippers, J.B. Bulitta, U. Holz-grabe, G.L. Drusano, F. Sörgel, Population pharmacokinetics at two dose levels and pharmacodynamic profiling of flucloxacillin, Antimicrob. Agents Chemother. 51 (2007) 3290–3297.

[7] Q. Zhou, Z. Ruan, H. Yuan, B. Jiang, D. Xu, RP-HPLC analysis of flucloxacillin in human plasma: validation and application to a bioequivalence study, Pharmazie 62 (2007) 101–104.

[8] B.G. Charles, C.C. Foo, J. Gath, Rapid column liquid chromatographic analysis of flucloxacillin in plasma on a microparticulate pre-column, J. Chromatogr. B: Biomed. Sci. Appl. 660 (1994) 186–190.

[9] H.Z. Wu, M.Y. Liu, S. Wang, W.Y. Feng, W.F. Yao, H.S. Zhao, M.J. Wei, Pharmacokinetic properties and bioequivalence of two compound formulations of 1500 mg ampicillin (1167 mg)/probenecid (333 mg): a randomized-sequence single-dose, open-label, two-period crossover study in healthy Chinese male volunteers, Clin. Ther. 32 (2010) 597–606.

[10] M. Ishida, K. Kobayashi, N. Awata, F. Sakamoto, Simple high-performance liquid chromatography determination of ampicillin in human serum using solid-phase extraction disk cartridges, J. Chromatogr. B: Biomed. Sci. Appl. 727 (1999) 245–248.

Short communication

Development and validation of a stability indicating HPLC method for simultaneous determination of four novel fluoroquinolone dimers as potential antibacterial agents

Muzaffar Khan [a,*], C. Naveen Kumar Reddy [b], G. Ravindra [a], K.V.S.R. Krishna Reddy [a], P.K. Dubey [c]

[a] *Analytical Development, Aptuit Laurus Private Limited, ICICI Knowledge Park, Turkapally, Shameerpet, Hyderabad, Andhra Pradesh 500078, India*
[b] *Process Development, Aptuit Laurus Private Limited, ICICI Knowledge Park, Turkapally, Shameerpet, Hyderabad 500078, India*
[c] *Department of Chemistry, Jawaharlal Nehru Technological University, Kukatpally, Hyderabad 500072, India*

A R T I C L E   I N F O

A B S T R A C T

A series of novel 6-fluoro1,4-dihydro-4-oxo-3-quinoline carboxylic acid dimers were synthesized as potential antibacterial agents from commercially available substituted fluorobenzoic acids. A stability indicating HPLC method was developed to determine these novel fluoroquinolone dimers using a systematic method development approach. Samples were subjected to stress conditions of hydrolysis, oxidation, photolysis and thermal degradation; and analyzed to demonstrate the specificity and stability indicating ability of the developed method. The precision for all four fluoroquinolone dimers was within 2.0% RSD. Calibration curves were linear (LOQ, 150%), with regression coefficients >0.99 for all dimers. The method was conveniently applied for determining purity and assay of these four novel fluoroquinolone dimers.

© 2011 Elsevier B.V. All rights reserved.

1. Introduction

1,4-Dihydro-4-oxo-6-fluoroquinoline-3-carboxylic acids and their ester derivatives are quinolone class of anti-bacterial agents [1,2] which are effective against a variety of gram-negative microorganisms. A number of fluoroquinolone antibacterial agents such as aspefloxacin, norfloxacin, ofloxacin, ciprofloxacin, levofloxacin, lomefloxacin and sparfloxacin are in clinical use. Since there is a continuous demand for new antibacterials and fluoroquinolones, many researchers have been working on modified quinolones to potentiate them further [3–5]. The antibacterial activity of ciprofloxacin modified dimers [6,7] against drug resistant strains of bacteria has been evaluated.

A series of novel N1-quinolone dimers (Fig. 1) were synthesized as potential antibacterial agents which have demonstrated promising antibacterial activities [8]. The separation of quinolone drugs by HPLC coupled with UV detection [9], fluorescence detection [10], MS detection [11] and by capillary electrophoresis-fluorescence detection [12] is reported in literature. The purpose of this research was to develop a stability indicating HPLC method for simultaneous determination of the four novel fluoroquinolone dimers, before

they could be evaluated for their antibacterial activities. In this paper the development and validation of a simple HPLC method for determining a series of novel fluoroquinolone dimers is presented.

2. Materials and methods

2.1. Chemicals and materials

The fluoroquinolone dimers were synthesized at Research and Development Centre, Aptuit Laurus Pvt. Ltd. (Hyderabad, India). Reference standards of the dimers were prepared in-house by semi-preparative LC purification. Inertsil ODS analytical and preparative columns were purchased from GL Sciences (Tokyo, Japan). X-Terra RP 18 and Acquity UPLC® BEH C8 columns were procured from Waters Corporation Ltd. (Milford, MA, USA). Zorbax Eclipse XDB-C18 column was procured from Agilent Technologies (Waldbronn, Germany). Trifluoro acetic acid (TFA, HPLC grade), hydrochloric acid (HPLC grade) and maleic acid (Analytical grade) were procured from Fluka (Steinheim, Germany). Hydrogen peroxide (30% solution, AR grade), sodium hydroxide (AR grade), methanol (MeOH, HPLC grade) and acetonitrile (MeCN, HPLC grade) were procured from Rankem Fine Chemicals Ltd. (New Delhi, India). Water was filtered and deionized with a Milli-Q, Millipore system (Milford, MA, USA).

* Corresponding author. Tel.: +91 40 230413531; fax: +91 40 23045438.
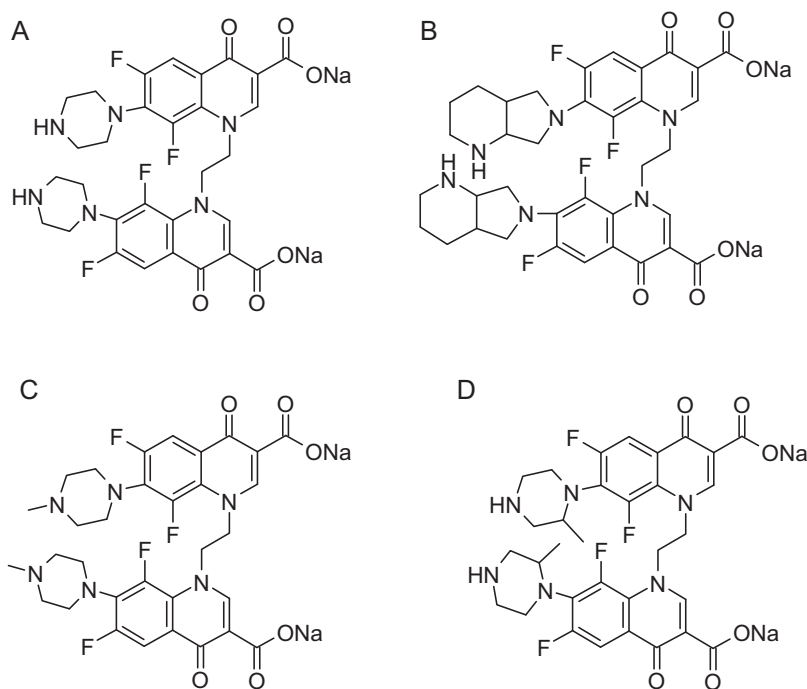*E-mail address:* muzaffarkhan76@rediffmail.com (M. Khan).

Fig. 1. Structures and chemical names of novel fluoroquinolone dimers. (A) 1-[2-(3-carboxy-6,8-difluoro-4-oxo-7-piperazino-1,4-dihydro-1-quinolinyl)ethyl]-6,8-difluoro-4-oxo-7-piperazino-1,4-dihydro-3-quinolinecarboxylic acid disodium salt. (B) 1-{2-[3-carboxy-6,8-difluoro-7-(4-methylpiperazino)-4-oxo-1,4-dihydro-1-quinolinyl]ethyl}-6,8-difluoro-7-(4-methylpiperazino)-4-oxo-1,4-dihydro-3-quinoline carboxylic acid disodium salt. (C) 1-{2-[3-carboxy-6,8-difluoro-7-(3-methylpiperazino)-4-oxo-1,4-dihydro-1-quinolinyl]ethyl}-6,8-difluoro-7-(3-methylpiperazino)-4-oxo-1,4-dihydro-3-quinoline carboxylic acid disodium salt. (D) 1-{2-(3-carboxy-6,8-difluoro-4-oxo-7-perhydropyrrolo[3,4-b]pyridin-6-yl-1,4-dihydro-1quinolinyl)ethyl}-6,8-difluoro-4-oxo-7-perhydropyrrolo[3,4-b]pyridin-6-yl-1,4-dihydro-3-quinolinecarboxylic acid disodium salt.

2.2. Instrumentation

A Waters Alliance 2695 separations module appended with a 2996 PDA detector and Empower software (Version 5.0) were used throughout the studies. Purification was performed on Agilent Technologies 1200 series Preparative LC system equipped with Chemstation software. A Buchi Rotavapor R-215 was used for solvent distillation. An XP205 Mettler Toledo balance (Greifensee, Switzerland), Bruker AVANCE II 300 MHz NMR Spectrometer (Fällanden, Switzerland) Newtronic NW-CON-51 Oven (Mumbai, India), Newtronic NEC 108RSPI photostability chamber (Mumbai, India) and Bandelin RK 510 Sonicator (Berlin, Germany) were used during the studies.

2.3. Chromatographic conditions

The separation was performed on a Zorbax Eclipse XDB-C18 (150 mm × 4.6 mm), 5 μm column maintained at 45 °C. The mobile phase A [0.1%, v/v, aqueous TFA] and mobile phase B [MeOH:MeCN:TFA (85:15:0.1, v/v/v)] were pumped in a gradient mode [(time in min vs. % mobile phase B) = 0:20, 10:30, 15:50, 20:80 and 20.1:20]. The flow rate was 1.0 mL/min and the injection volume was set to 5 μL. Data was acquired on a PDA detector and chromatograms were extracted at 285 nm. All the four compounds and their related impurities were well separated within 15 min. and the total run time was 20.1 min.

2.4. Preparation of standard and sample solutions

Stock solutions of the standard compounds were prepared (0.5 mg/mL) in diluent (Water:MeOH:TFA 80:20:0.1, v/v/v) by ultra sonication for 10 min. A standard mixture of the four compounds was prepared by diluting 5 mL of each stock solution to 100 mL in a single volumetric flask, obtaining a final concentration of about 0.025 mg/mL of each compound.

About 12.5 mg of each sample was dissolved in 25 mL diluent by ultra sonication for 10 min. These stock solutions were diluted 20 folds (5–100 mL) and 5 folds (5–25 mL) with diluent to obtain the sample solutions for assay and purity analysis respectively.

2.5. Method validation

2.5.1. Specificity, sensitivity and linearity

Forced degradation studies were performed on the four compounds under stress conditions of acid hydrolysis (1 N HCl for 48 h), base hydrolysis (1 N NaOH for 48 h), oxidative degradation (3% H_2O_2 for 6 h), heat (60 °C for 7 days) and photo-degradation (as per ICH Q1B) [13]. The stressed samples were analyzed; and peak purities of the dimers were assessed from the spectral signals obtained by a photo diode array detector.

The detector response was obtained for a series of dilute solutions with known concentrations of the dimers considering signal-to-noise ratios of 3:1 and 10:1 for LOD and LOQ, respectively. The linearity solutions were prepared at seven concentration levels—LOQ, 5, 50, 75, 100, 125 and 150% of nominal analyte concentration and analyzed.

2.5.2. Precision and accuracy

Repeatability was assessed as %RSD by analyzing as per method, six sample solutions containing each dimer spiked at LOQ and analyte concentrations. The inter-day precision was evaluated by repeating the procedures on three consecutive days. The intermediate precision (ruggedness) was evaluated by a different analyst, using a different column on a different instrument in the same laboratory. For determining accuracy of the method, triplicate sample solutions at LOQ level, 80, 100, 120 and 150% of the nominal analyte concentration were prepared and analyzed. The mean

Table 1
System suitability results for optimization trials.

Chromatographic conditions	Parameter	Comp-A	Comp-B	Comp-C	Comp-D
Inertsil ODS 3 V (150 mm × 4.6 mm), 5 μm	N	834	13,980	3394	1.61
MP: 0.025 M Phosphoric acid and MeCN + TEA	T_f	–	1.83	–	1.32
	α	1.24	5.01	–	2.35
	R_s	1.08	7.09	–	2.05
X-Terra RP18 (150 mm × 4.6 mm), 3.5 μm	N	24,787	70,291	–	39,111
MP: 0.025 M Phosphoric acid and MeCN + TEA	T_f	1.04	1.10	–	1.04
	α	–	1.23	–	1.23
	R_s	–	14.78	–	8.16
X-Terra RP18 (150 mm × 4.6 mm), 3.5 μm	N	56,245	106,419	34,649	75,805
MP A: 0.1% TFA in water	T_f	–	1.13	–	1.18
MP B: 0.1% TFA in MeCN	α	1.01	1.15	–	1.10
	R_s	0.71	10.43	–	6.10
X-Terra RP18 (150 mm × 4.6 mm), 3.5 μm	N	24,599	158,416	21,508	32,683
MP A: 0.1% TFA in water	T_f	1.00	1.12	–	0.95
MP B: 0.1% TFA in MeOH:MeCN (85:15, v/v)	α	1.05	1.14	–	1.26
	R_s	1.59	7.60	–	8.81
Zorbax XDB C18 (150 mm × 4.6 mm), 5 μm	N	14,409	98,265	12,077	17,565
MP A: 0.1% TFA in water	T_f	1.01	1.02	1.01	1.02
MP B: 0.1% TFA in MeOH:MeCN (85:15, v/v)	α	1.14	1.37	–	1.46
	R_s	3.30	14.20	–	10.63

MP, mobile phase; MeCN, acetonitrile; MeOH, methanol; TEA, triethylamine.

%recoveries calculated against the standards at each level were used as a measure of accuracy.

2.5.3. Robustness and stability of analytical solutions

Deliberate changes to the standard experimental conditions were made and the resolution (R_s) between the fluoroquinolone dimers was evaluated. The impact of flow rate (0.9, 1.0 and 1.1 mL/min) and the column temperature (40, 45 and 50 °C) on resolution was studied. The %TFA in mobile phase was varied between 0.05 and 0.15% (v/v). Gradient runs were performed by varying the absolute % of mobile phase B within ±2% of the set composition. The ratio of MeCN in mobile phase B was varied between ±5% (v/v).

Standard solutions were analyzed immediately after preparation and divided into two parts. One part was stored at 2–8 °C in a refrigerator and the other at bench top in tightly capped volumetric flasks. The stored solutions were reanalyzed after 6, 12, 24 36 and 48 h.

3. Results and discussion

3.1. Method development

Initial separation trials were made in accordance with Ph.Eur. monograph of Ciprofloxacin hydrochloride monohydrate on an Inertsil ODS (150 mm × 4.6 mm), 5 μm column using a mobile phase that consisted of aqueous phosphoric acid (0.025 M, adjusted to pH 3.0 with TEA) and MeCN in a gradient mode. Under these chromatographic conditions, all the four dimers exhibited poor peak efficiencies (N) and peak symmetries (T_f); and a partial resolution (R_s) between Comp-A and Comp-C was achieved (Table 1). With the same mobile phase, peak symmetries and peak efficiencies improved on an X-Terra RP18 (150 mm × 4.6 mm), 3.5 μm column but selectivity for Comp-A and Comp-C was lost.

While Comp-A and Comp-C could not be resolved on an Inertsil ODS column, a low resolution between the two was obtained on an X-Terra RP 18 column with a mobile phase that consisted of 0.1% aqueous TFA and 0.1% TFA in MeOH. The use of MeOH provided an alternate selectivity which could not be obtained with MeCN. A baseline separation between these critical pair components (Comp-A and Comp-C) could be achieved with the same mobile phase on a Zorbax Eclipse XDB-C18 column. To increase the efficiency while retaining selectivity, mixtures of MeOH and MeCN in different proportions were evaluated and the organic phase containing MeOH:MeCN:TFA (85:15:0.1, v/v/v) was found to be the most optimum, providing satisfactory separation, symmetric peaks and high efficiencies for all the four compounds.

In order to increase the throughput time, the separation was attempted on an Acquity UPLC® BEH C8 (100 mm × 2.1 mm) 1.7 μm column on a UPLC system using 0.1% aqueous TFA and 0.1% TFA in MeOH:MeCN (85:15, v/v) as mobile phase in a gradient mode. No separation could be achieved between Comp-A and Comp-C, therefore no further trials were made on the UPLC system.

A shallow gradient facilitated improved resolution between Comp-A and Comp-C. The resolution increased at elevated temperatures therefore the column temperature was optimized to 45 °C. Representative chromatograms of the four fluoroquinolone dimers, spiked standard and stressed samples in the optimized method are shown in Fig. 2.

3.2. Purification of crude fluoroquinolone dimers

The crude fluoroquinolone dimers (purity 72–94% area/area) were purified by preparative LC for evaluating their biological activities and preparing reference standards. On an Inertsil ODS 3 V (250 mm × 50 mm, 7 μm) preparative column, a mobile phase comprising of water and MeOH in gradient proportions [(time in min – % MeOH) of 0:10, 10:45, 13.50:45, 14:100, 17:100, 17.10:10 and 20:10] was pumped at a flow rate of 80 mL/min. A 1.5 mL aliquot of the crude sample solutions (20 mg/mL) was injected and the eluent was monitored at 285 nm. The desired fractions were collected from several injections and evaporated to obtain the standard compounds. After purification, the purities of the dimers were improved in the range of 97–98% area/area. The potencies (%w/w) of purified dimers were determined by quantitative ^{1}H NMR spectroscopy using maleic acid as an internal standard.

3.3. Method validation

3.3.1. Specificity, sensitivity and linearity

No degradation of the dimers was observed under stress conditions of acid hydrolysis, base hydrolysis, thermal stress and
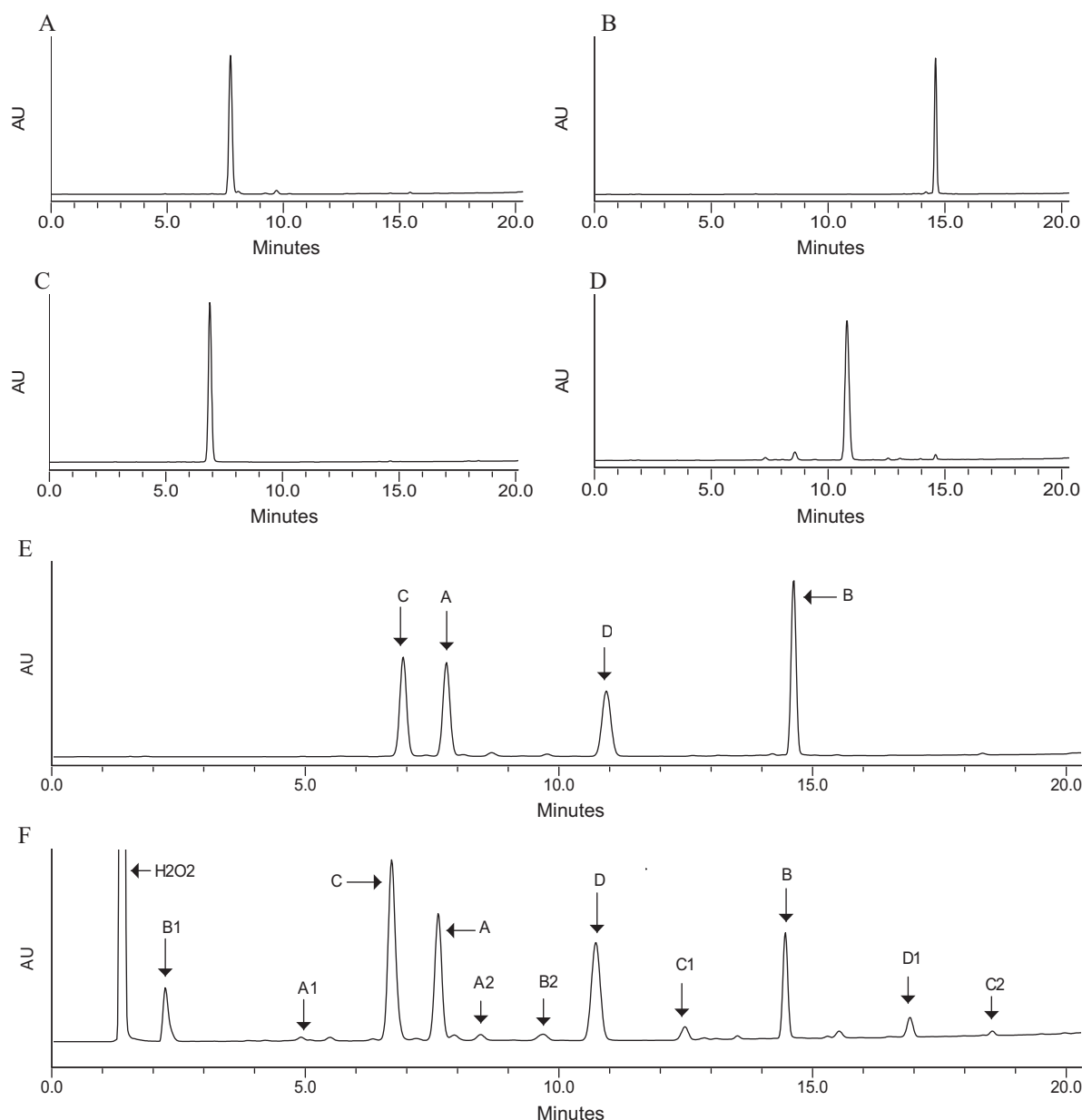
Fig. 2. Representative chromatograms of (A) compound-A; (B) compound-B; (C) compound-C; (D) compound-D; (E) spike of four fluoroquinolone dimer standards and (F) spike of stressed samples (A1 and A2 = degradants of compound-A; B1 and B2 = degradants of compound-B; C1 and C2 = degradants of compound-C; D1 = degradant of compound-D).

photo-degradation. However the dimers showed considerable degradation (10–15%) when oxidized in 3% H_2O_2. The degradants were well separated from the fluoroquinolone dimers (Fig. 2F) and the spectral peak purity tests confirmed the homogeneity of dimer peaks in the stressed samples.

The limits of detection of the four compounds were in the range 0.04–0.1 μg/mL and limits of quantification were in the range 0.1–0.3 μg/mL. The detector response linearity to varying analyte concentrations was established by analyzing standard solutions at seven different concentrations ranging from LOQ to 150% of nominal analyte concentration. Linearity curves (area vs. conc.) were plotted for each compound and the data was subjected to regression analysis. The test results confirm linear relationships between detector response and concentrations (Table 2). From the results of validation tests that were performed, the range for this method is LOQ to 150% of the nominal analyte concentration.

Table 2
Linearity results.

Fluoroquinolone dimer	Range	Equation	R^2	LOQ (μg/mL)
Comp-A	LOQ–150%	$y = 21057x + 1253$	0.9991	0.3
Comp-B	LOQ–150%	$y = 21921x + 952$	0.9997	0.1
Comp-C	LOQ–150%	$y = 18043x + 4843$	0.9910	0.3
Comp-D	LOQ–150%	$y = 13175x + 1630$	0.9995	0.3

3.3.2. Precision and accuracy

The %RSD in area at LOQ levels for all four compounds was not more than 10.0% during the repeatability, inter-day and intermediate precision experiments. At the nominal analyte concentration, the %RSD for the four compounds was better than 2.0% for all precision experiments which assert the suitability of the developed method.

Table 3
Accuracy results.

Fluoroquinolone dimer	Accuracy level				
	LOQ	80%	100%	120%	150%
% Mean recovery[a] ± std. dev.					
Comp-A	96.15 ± 0.81	101.09 ± 0.26	98.82 ± 0.63	99.83 ± 0.28	98.27 ± 0.55
Comp-B	98.84 ± 0.32	99.32 ± 0.61	100.82 ± 1.38	99.96 ± 0.15	99.51 ± 0.17
Comp-C	96.54 ± 0.27	98.13 ± 0.35	99.83 ± 0.49	101.64 ± 0.24	101.04 ± 0.28
Comp-D	97.25 ± 0.18	100.11 ± 0.18	100.84 ± 0.44	99.65 ± 0.26	100.45 ± 0.03

[a] $n = 3$ determinations.

For all compounds, the recoveries at LOQ ranged from 96.2 to 98.8%, and the recoveries at other concentrations ranged from 98.1 to 101.6% (Table 3). It is noteworthy that these recoveries attest the suitability and performance of the developed method.

3.3.3. Robustness and stability of analytical solutions

A robustness test is expected to confirm the reliability of an analysis to deliberately made alterations to the method parameters. Analyses results obtained in robustness studies under varied chromatographic conditions (flow rate, %TFA, %organic phase and column temperature) illustrate that the resolution between the dimers and in particular the most critical pair (Comp-A and Comp-C) was always greater than 1.5 vindicating robustness of the method.

The %RSD for the four dimers reanalyzed after 6, 12, 24, 36 and 48 h of storage was not more than 2.0%, indicating that the sample solutions were stable for at least 48 h when stored at 2–8 °C or room temperature.

4. Conclusion

A simple and effective stability indicating HPLC method was developed and validated for simultaneous quantitative determination of four novel fluoroquinolone dimers. The method was found to be suitable for determining the dimers within the range LOQ–150% of nominal analyte concentration and was conveniently applied to determine the real samples before evaluating their biological activities.

References

[1] H. Koga, A. Itoh, T. Murayama, S. Suzue, T. Irikura, Structure-activity relationships of antibacterial 6,7- and 7,8-disubstituted 1-alkyl-1,4-dihydro-4-oxoquinoline-3-carboxylic acids, J. Med. Chem. 23 (1980) 1358–1363.

[2] R. Wise, J. Andrews, L. Edward, In vitro activity of Bay 09867, a new quinolone derivative, compared with those of other antimicrobial agents, Antimicrob. Agents Chemother. 23 (1983) 559–564.

[3] D.T.W. Chu, P.B. Fernandes, A.K. Claiborne, E. Pihuleac, C.W. Nordeen, R.E. Maleczka, A. Pernet, Synthesis and structure–activity relationship of 1-aryl-6,8-difluoroquinolone antibacterial agents, J. Med. Chem. 30 (1987) 504–509.

[4] D.T.W. Chu, R.E. Maleczka, Synthesis of 4-oxo-4H-quino[2, 3,4-i,j][1,4]-benoxazine-5-carboxylic acid derivatives, J. Hetrocycl. Chem. 24 (1987) 453–456.

[5] J.A. David, H.F. Andrew, F.K. Edward, Synthesis and antibacterial activity of 2, 3-dehydroofloxacin, J. Hetrocycl. Chem. 27 (1990) 509–1511.

[6] X. Zhao, B. Quinn, R.J. Kerns, K. Drlica, Bactericidal activity and target preference of a piperazinyl-cross-linked ciprofloxacin dimer with *Staphylococcus aureus* and *Escherichia coli*, J. Antimicrob. Chemother. 58 (2006) 1283–1286.

[7] K.A. Gould, X. Pan, R.J. Kerns, L.M. Fisher, Ciprofloxacin dimers target gyrase in *Streptococcus pneumonia*, Antimicrob. Agents Chemother. 48 (2004) 2108–2115.

[8] N.R. Chepyala, R.R. Durgi, L.K. Tatini, G.V. Subbaraju, R.M. Hindupur, M.R. Dhanvada, Quinolone dimers as potential antibacterial agents, Lett. Org. Chem. 8 (2010), in press.

[9] E. Nemutlu, S. Kır, ö. özyüncü, M.S. Beksaç, Simultaneous Separation and determination of seven quinolones using HPLC: analysis of levofloxacin and moxifloxacin in plasma and amniotic fluid, Chromatographia 66 (2007) S15–S24.

[10] S. Schulte, T. Ackermann, N. Bertram, T. Sauerbruch, W.D. Paar, Determination of the newer quinolones levofloxacin and moxifloxacin in plasma by high-performance liquid chromatography with fluorescence detection, J. Chromatogr. Sci. 44 (2006) 205–208.

[11] D.A. Volmer, B. Mansoori, S.J. Locke, Study of 4-quinolone antibiotics in biological samples by short-column liquid chromatography coupled with electrospray ionization tandem mass spectrometry, Anal. Chem. 69 (1997) 4143–4155.

[12] M. Ferdig, A. Kaleta, T.D. Thanh, W. Buchberger, Improved capillary electrophoretic separation of nine (fluoro)quinolones with fluorescence detection for biological and environmental samples, J. Chromatogr. A 1047 (2004) 305–311.

[13] Stability testing of new drug substances and products Q1A (R2), in: International Conference on Harmonization, IFPMA, Geneva, 2003.

Short communication

Quantitative analysis of tris(2-carboxyethyl)phosphine by anion-exchange chromatography and evaporative light-scattering detection

Zhijun Tan[a], Peter M. Ihnat[b,*], Vikram S. Nayak[a], Reb J. Russell[b]

[a] Biological Process and Product Development, Bristol-Myers Squibb Company, 6000 Thompson Road, East Syracuse, NY 13057, USA
[b] Biological Process and Product Development, Bristol-Myers Squibb Company, 311 Pennington-Rocky Hill Road, Pennington, NJ 08534, USA

ARTICLE INFO

ABSTRACT

Tris(2-carboxyethyl)phosphine (TCEP) belongs to the trialkylphosphine class of reducing agents that are widely used in research and industry. In this paper, we discuss a sensitive high-performance liquid chromatography (HPLC) method equipped with an evaporative light scattering detector (ELSD) for the determination of TCEP in pharmaceutical samples containing therapeutic protein and stabilizing additives. TCEP was first completely oxidized with hydrogen peroxide to form TCEP oxide (TCEPO). Proteins and salts were removed from the sample by solid phase extraction. TCEPO concentrations were determined by anion exchange chromatography coupled with ELSD. Because of the 1:1 oxidation stoichiometry for the reaction, the concentration of TCEP in the sample is directly proportional to the measured concentration of TCEPO. A good linearity fit of ELSD response versus TCEPO concentration was observed over the range of 20–2000 μM. The specificity, precision, accuracy, and robustness of the method were evaluated and suitable for the quantitation of TCEP in biological samples. Moreover, selective treatment with peroxide prior to solid-phase extraction may be used to determine the mass balance of TCEP species or track the oxidation rate in pharmaceutical samples.

1. Introduction

Tris (2-carboxyethyl) phosphine (TCEP) is extensively used in a wide range of applications to reduce disulfide bonds, to maintain free sulphydryl groups and for subsequent structural analysis in proteins (TCEP structure Fig. 1). Generally, one equivalent of TCEP and water irreversibly reduces one disulphide bond to form one equivalent of P-oxide TCEP (TCEPO) and two free sulphydryl groups. Once oxidized, TCEPO does not participate in additional thio-disulphide reactions. TCEP accomplishes reduction of disulphide bonds over a much wider pH range than thiol reductants such as dithiothreitol (DTT). Additionally, TCEP is often preferred to thiol reductants due to its higher solution stability, irreversibility and odorless nature [1–5].

TCEP is often used to reduce cysteine disulphides prior to site-directed conjugation of therapeutic proteins with chemically modified polymers [6]. Following reduction, the TCEP may be removed to improve efficiency of the conjugation reaction. When used as a reducing agent during preparative purification processes, TCEP and TCEPO are often removed from the reaction by hydrophobic inter-action chromatography [4]. However, confirmation of the TCEP concentration following specific process steps is essential to ascertain the efficiency of reactions and quality of the final product. An accurate assessment of purity is also important when planning processes or when designing reactions to achieve complete reduction of disulphide bonds. In addition to protein, the TCEP in these samples is likely combined with buffer species, reactants and excipients [6]. Therefore, an accurate, high throughput and robust method for quantitative analysis of TCEP, in complex pharmaceutical samples, would be a useful tool in the standard bioanalytical laboratory.

Currently, the most widely used method for quantitative analysis of TCEP is indirect UV spectrophotometry. The sample containing TCEP is combined with a known molar excess of 5,5′-dithiobis(2-nitrobenzoic acid) (DTNB or Ellman's reagent). The spectrophotometric assay measures the concentration of 2-nitro-5-thiobenzoate (NTB) at 412 nm (molar extinction coefficient of $14,150 \, M^{-1} \, cm^{-1}$). One equivalent of TCEP reduces one equivalent of DTNB to one equivalent of TCEPO and two equivalents of NTB [7]. However, DTNB was found to react with thiolate anions in a thiol–disulfide exchange reaction in proteins and other biological systems to form NTB. Therefore, measured NTB concentrations may overestimate TCEP in the presence of free thiols [2,8].

To date, a direct measurement of TCEP has not been reported in the literature. Direct measurement of structurally similar, hydrophobic organophosphate triesters following extraction from environmental sediments has been reported. The sample

* Corresponding author at: Biological Process and Product Development, Bristol-Myers Squibb Company MS3-1.05, 311 Pennington-Rocky Hill Road, Pennington, NJ 08534, United States. Tel.: +1 609 818 5401; fax: +1 609 818 6935.
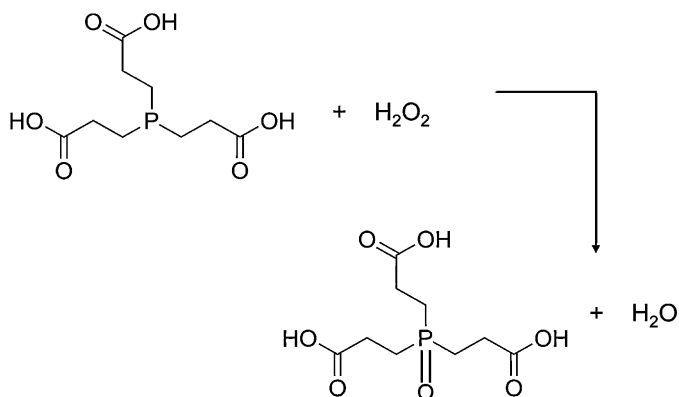 E-mail address: peter.ihnat@bms.com (P.M. Ihnat).

Fig. 1. Conversion of TCEP to P-oxide TCEP (TCEPO) by hydrogen peroxide.

preparation consists of several extraction steps that involve mixing with organic solvents under high pressure and temperature and complex SPE. Analysis was performed by gas chromatography coupled with an ion trap mass spectrometer [9,10]. Because of the hydrophilic properties of TCEP and TCEPO and the composition of the samples, such extensive preparation is not necessary or appropriate. Nevertheless, the lack of a distinct chromophore as well as the amphipilic nature of TCEP provides challenges for separation and direct detection [2,5,11].

The properties of TCEPO appear to be more amenable to separation by ion exchange than TCEP. TCEPO has three acidic pK_a values (pK_1 3.55, pK_2 4.22, pK_3 4.86) that confer strong anionic character at pH > 7 [5]. The conversion of TCEP to TCEPO is rapid and complete by reaction with hydrogen peroxide (Fig. 1). The total concentration of TCEP in the sample is directly proportional to the measured TCEPO concentration [8].

The problem of detection may be overcome by evaporative light scattering (ELSD). Evaporative light scattering detection, often referred as a sensitive universal detector, has been widely used for the determination of organic cations and anions by using volatile mobile phases during chromatography [12–16]. This method is based on TCEP oxidation to TCEPO with H_2O_2 adjusting pH to fully deprotonate TCEPO, separation of TCEPO from protein and salts in the sample by anionic solid phase extraction (SPE) and analytical anion exchange chromatography (AEX-HPLC) with ELSD detection (Figs. 1 and 2).
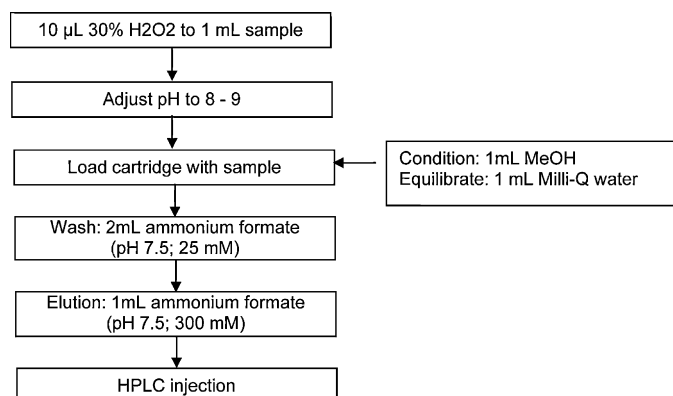
Fig. 2. Scheme of TCEP sample preparation and extraction.

2. Materials and methods

2.1. Reagents and supplies

Buffered 0.5 M TCEP solution and ammonium formate were purchased from Sigma–Aldrich. Nebulizer gas nitrogen for the ELSD detector (≥99.99%, UHP) was purchased from Airgas. HPLC grade methanol was purchased from EM Science. Phenomenex Strata-X-A cartridges (33 μm, polymeric SAX, Cat #8B-S123-UBJ, Phenomenex, Torrance, CA) were used for solid phase extraction. High purity water purified by a Milli-Q Ultrapure Water System (Millipore, USA) was used for mobile phase and sample preparation. Hydrogen peroxide 30% solution and buffer salts (sodium chloride, sodium acetate, sodium phosphate, tromethamine) were all purchased from EMD (Darmstadt, Germany). A 92 kD Fc fusion protein that contains nine disulphide bonds (eight intramolecular and one intermolecular) (50 mg/mL in 10 mM phosphate, 25 mM sodium chloride pH 7.5) used in method validation was produced by Bristol-Myers Squibb (BMS, East Syracuse, NY) [17]. Also, a PEGylated protein (2.5 mg/mL in 50 mM sodium acetate buffer pH 5.5), used in confirming selectivity, was produced by Bristol-Myers Squibb (BMS, East Syracuse, NY).

2.2. Sample preparation

Samples containing TCEP were oxidized by spiking 10 μL of 30% H_2O_2 into 1 mL of samples for 10 min at room temperature. After oxidation, the sample pH was adjusted to 8–9 by adding acetic acid or ammonium hydroxide based on the original sample pH value. Afterwards, the pH adjusted samples were subjected to solid-phase extraction clean-up using conditioned cartridges, to trap the TCEPO onto the resin. Impurities were eluted with 2 mL 25 mM ammonium formate pH 7.5. The TCEPO sample was eluted with 1 mL, 300 mM ammonium formate pH 7.5 and injected onto the HPLC (Fig. 2).

2.3. Instrumentation and HPLC analysis

Chromatographic separations were accomplished using a Waters 2695 module and a Sedex 75 ELSD system was used for detection. The TCEPO was separated on a Hamilton anion exchange column (PXP-X100 4.1 × 250 mm, 10 μm, product no.: 79433, Hamilton, Reno, NV) with a mobile phase consisting of 250 mM ammonium formate and 5% methanol (adjusted to a pH of 7.5 with ammonium hydroxide). The separation was performed under an isocratic condition for 20 min at a flow rate of 1 mL/min. The mobile phase was filtered by 0.22 μm filters and degassed prior to use. The ELSD settings were temperature 50 °C, nebulizer (nitrogen) gas pressure 3.0 bar, and detector gain 9. Data were collected with Empower software from Waters.

2.4. Method development

2.4.1. Selectivity

Selectivity was established by spiking TCEP into commonly used buffer matrices at low concentrations. For this purpose, five buffer matrices (H_2O as control, 1 mM sodium chloride, 1 mM sodium acetate, 1 mM sodium phosphate, and 1 mM Tris) were used with TCEP spiking level of 1 mM. The spiked samples were directly injected onto the HPLC system after H_2O_2 oxidation. The selectivity was challenged by preparing a lower level of TCEP sample (~0.1 mM TCEP) in a complex sample matrix containing 50 mg/mL Fc fusion protein, 10 mM sodium phosphate, and 25 mM sodium chloride. After H_2O_2 oxidation, the sample with and without SPE preparations was injected on the HPLC system for comparison. The selectivity was further evaluated by other sample matrices respectively: 50 mM of sodium acetate, 50 mM sodium phosphate, 50 mM

Table 1
Precision, linearity, accuracy and robustness for determination of TCEP.[a]

	Mean r^2	Mean value (μM TCEP)	Accuracy (%)	RSD[b] (%)
Precision				
Instrumental ($n = 6$)				1.8
Repeatability ($n = 6$)				4.2
Linearity ($n = 3$)	0.9997			0.02
Accuracy ($n = 3$)				
20 μM		20.7	103.5	3.8
50 μM		48.9	97.7	1.4
100 μM		102.1	102.1	2.7
500 μM		516.3	103.3	3.0
2000 μM		1993.5	99.7	7.0
Sensitivity				
LOD ($n = 3$)		7.7	–	1.2
LOQ ($n = 3$)		16.3	93.6	1.2
Robustness (0.1 mM TCEP with Fc fusion protein, $n = 3$)				
0 mg/mL protein			94.2	0.1
1 mg/mL protein			100.9	1.6
5 mg/mL protein			96.1	1.1
10 mg/mL protein			98.9	1.3
50 mg/mL protein			99.3	1.4

[a] 50 mg/mL Fc fusion protein in 10 mM phosphate/25 mM sodium chloride pH 7.5 prior to SPE.
[b] Relative standard deviation: RSD = (sd/mean) × 100.

Tris, and a PEGylated protein. The samples were oxidized with H_2O_2 prior to SPE clean-ups followed by HPLC analysis (Fig. 2).

2.4.2. Precision

The repeatability of injection, separation and detector response was evaluated by replicate injections ($n = 6$) of 0.1 mM TCEP in 50 mg/mL Fc fusion protein buffered solution after SPE clean-up. Using the ELSD detector response for the individual injections, average response, standard deviation and relative standard deviation were calculated. In order to evaluate the repeatability of the overall method, 0.1 mM TCEP in 50 mg/mL Fc fusion protein buffered solution were prepared separately ($n = 6$) and following peroxidation and SPE (Section 2.2, Fig. 2), were sequentially injected into the system. Using the ELSD detector responses for all the TCEP standards, mean response, standard deviation and relative standard deviation were calculated (Table 1).

2.4.3. Linearity and accuracy

The range of the calibration curve was from 0.02 mM to 2 mM and consisted of five TCEP concentrations (0.02, 0.05, 0.10, 0.50 and 2.00 mM) in the Fc fusion protein sample matrix (50 mg/mL protein, 10 mM phosphate, 25 mM sodium chloride pH 7.5). Calibration curves were replicated in triplicate. All TCEP solutions were oxidized with H_2O_2 and passed through SPE prior to the HPLC injections. For each calibration curve the TCEPO peak area was plotted against the TCEP concentration by a log–log linear relationship. The coefficient of determination (r^2) of each curve was determined by linear regression.

Accuracy was determined across the linear range from 0.02 mM to 2 mM with triplicate sample preparations in the protein sample. Accuracy was calculated using the equation:

$$\text{Accuracy} = \left(\frac{\text{calculated concentration}}{\text{spiked concentration}} \right) \times 100 \qquad (1)$$

The mean, standard deviation and relative standard deviation (RSD) of triplicate determinations was calculated for each concentration.

2.4.4. Limits of quantitation and detection

The limits of quantitation (LOQ) and detection (LOD) were calculated based on signal-to-noise ratios of 3 and 10, respectively [15]. The lowest concentration (0.02 mM) of TCEP on the calibration curves, which were prepared in the Fc fusion protein matrix, was used for the signal determination and the noise was from the sample blank. The mean values and the relative standard deviations of LOQ and LOD of the three preparations were calculated and reaffirmed by injection onto the HPLC system.

2.4.5. Robustness

Robustness was demonstrated by obtaining acceptable method results when deliberate variations were made. The SPE clean-up is a critical step in sample purification by removing protein and high concentration of salts. The method recovery of TCEP was evaluated by varying protein concentrations in the sample matrix. For this purpose, triplicate preparations of 0.1 mM of TCEP in five protein concentrations in the range of 0 to 50 mg/mL were performed. The mean recovery at each protein concentration and the overall recovery of all protein concentrations were determined.

3. Results and discussion

The direct analysis of TCEP using AEX-HPLC and ELSD shows poor recovery and a broad, poorly symmetrical peak. Because the phosphonium center $pK_a \approx 7.7$, TCEP does not bind efficiently to the anion exchange column [5]. Oxidation of TCEP to TCEPO removes the charge from the phosphonium center and confers anionic character to the molecule. At pH > 7, TCEPO is completely deprotonated and suitable for binding to anion exchange resins. Because of the charged state of TCEPO, options based on anionic solid-phase extraction for sample clean-up and anionic chromatography for separation became appropriate for development.

The SPE cartridge type was selected using the same principle as anion exchange chromatography. After evaluating several sample-clean up approaches, solid-phase extraction using the Strata-X-A Cartridge, provided the best recovery of TCEPO. The Strata-X-A is a polymeric strong anion exchange sorbent that combines a hydrophobic backbone with dimethyl butyl quaternary amines. By manipulating the ionic strengths of the buffers, the TCEPO in the sample was efficiently loaded, washed and eluted while removing protein and the weakly bound salts. Furthermore, the method sensitivity can be increased by changing the sample loading and eluting volumes. For example, by loading 1 mL of sample and introducing 0.5 mL of eluent, the sample will be 2-fold concentrated. As long as total sample load is not beyond the maximum capacity of the cartridge and enough eluent is used to remove all bound TCEPO in
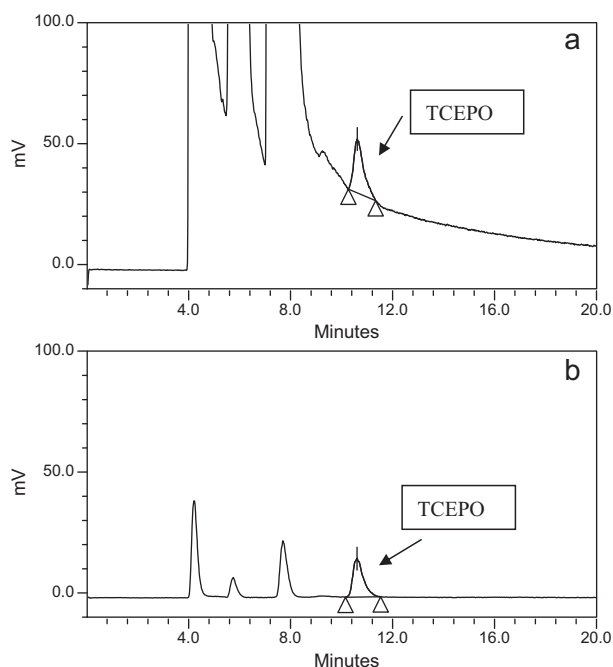
Fig. 3. HPLC chromatograms of 0.1 mM TCEP in the Fc fusion protein sample matrix without SPE clean-up (a) and with SPE clean-up (b).

the cartridge, the ratio of sample load and eluent volume can be optimized.

After applying the sample preparation method and assay conditions described in this study, the retention time for TCEPO was approximately 11.4 min. By implementing the SPE clean-up step, it is apparent that the resolution and smoothness of the baseline has been significantly improved by removing protein and high concentration of salts in the sample matrix (USP tailing = 1.3, theoretical plate count >3500) (Figs. 3 and 5). Volatile pure water gives a peak at 8 min. In matrices of various buffers, interfering peaks were still detected between 4 and 8 min following SPE but to a much lesser extent. Nevertheless, at 1 mM buffer concentrations, these peaks did not interfere with the detection of TCEPO (Fig. 4). At lower concentrations of TCEPO, higher concentrations of cosolutes interfere in detection without prior SPE (data not shown). Even though buffer and protein may be detected following SPE, there is baseline resolution between the peaks and TCEPO (Fig. 5). Phosphate buffer (50 mM pH 7.5) showed a large peak at approximately 5.5 min possibly as a result of the diversity of ionized species (pK_a values 2, 6.8 and 12.5) (Fig. 5d) [19]. Trace Fc fusion protein appeared to coelute with the 8 min peak (Fig. 5f). The lower concentration of the PEGylated protein likely facilitated more efficient removal by SPE compared with the Fc fusion protein (Fig. 5g).

Following preparation and SPE of the Fc fusion protein samples (50 mg/mL protein in 10 mM phosphate, 25 mM sodium chloride, pH 7.5), the calibration curve for TCEP was linear over the range of 0.02–2.00 mM with regression coefficient, $r^2 = 0.9997$ ($n = 3$, Eq. (2)).

$$\log(\text{peak area TCEPO}) = 1.4019 \log(\mu M TCEP) + 2.8374 \qquad (2)$$

The average LOD and LOQ were determined to be 7.7 μM and 16.3 μM with signal to noise ratios of 3 and 10, respectively (Table 1). The method demonstrated good precision and accuracy over the linearity range. The 1.8% RSD of the ELSD responses obtained from the six injections is an indication that the HPLC injection is reproducible. The 4.2% RSD of the ELSD responses obtained from the six SPE preparations is an indication that the overall method repeatability is good. Over the linearity range of
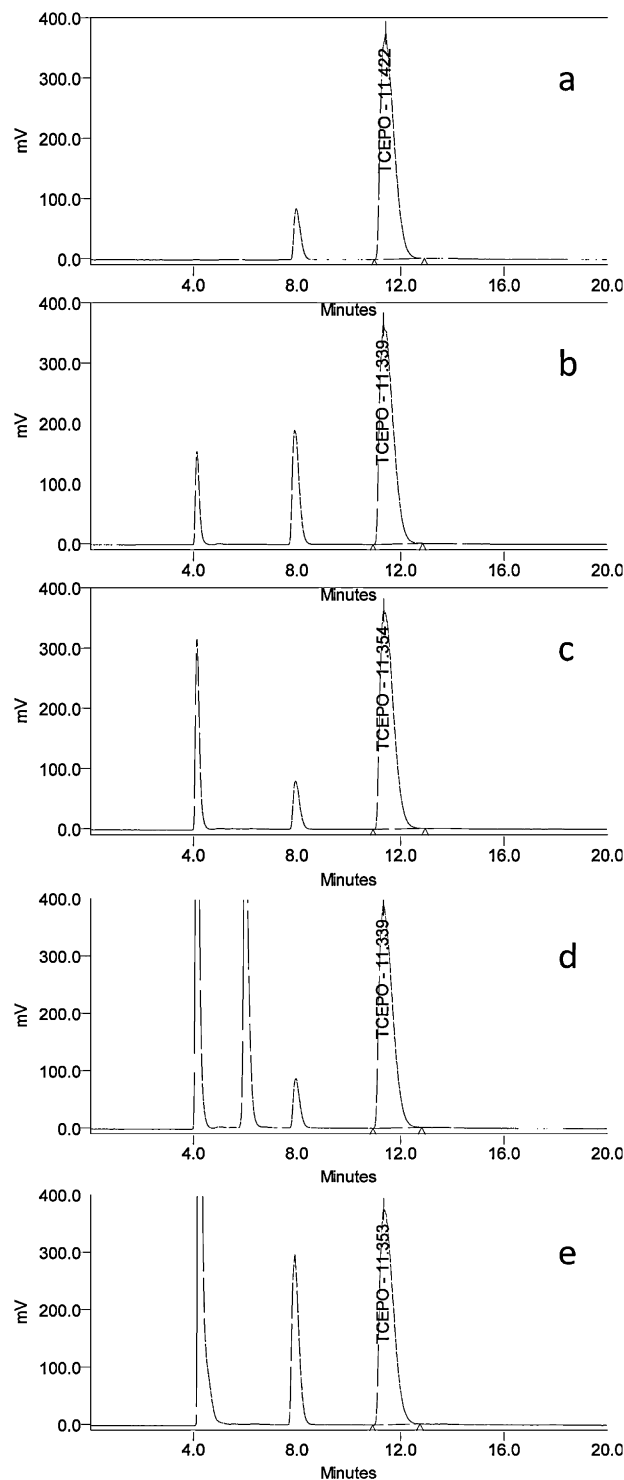
Fig. 4. Representative HPLC chromatograms of TCEPO: 1 mM TCEP in water (a); 1 mM TCEP in 1 mM NaCl (b); 1 mM TCEP in 1 mM sodium acetate (c); 1 mM TCEP in 1 mM sodium phosphate (d); 1 mM TCEP in 1 mM Tris (e).

0.02–2.00 mM, the mean accuracy was 97.7–103.5% and the RSD was 1.4–7.0% for the triplicate preparations at each concentration. The accuracy was 94.2–100.9% with TCEP level of 0.1 mM at the Fc fusion protein sample matrix at various protein concentrations. The RSD was 0.1–1.6% for the triplicate preparations at each protein concentration (Table 1). The results of spiking TCEP into various matrices showed that good resolution and selectivity of the method were achieved (Figs. 4 and 5). SPE clean-up step was able to remove
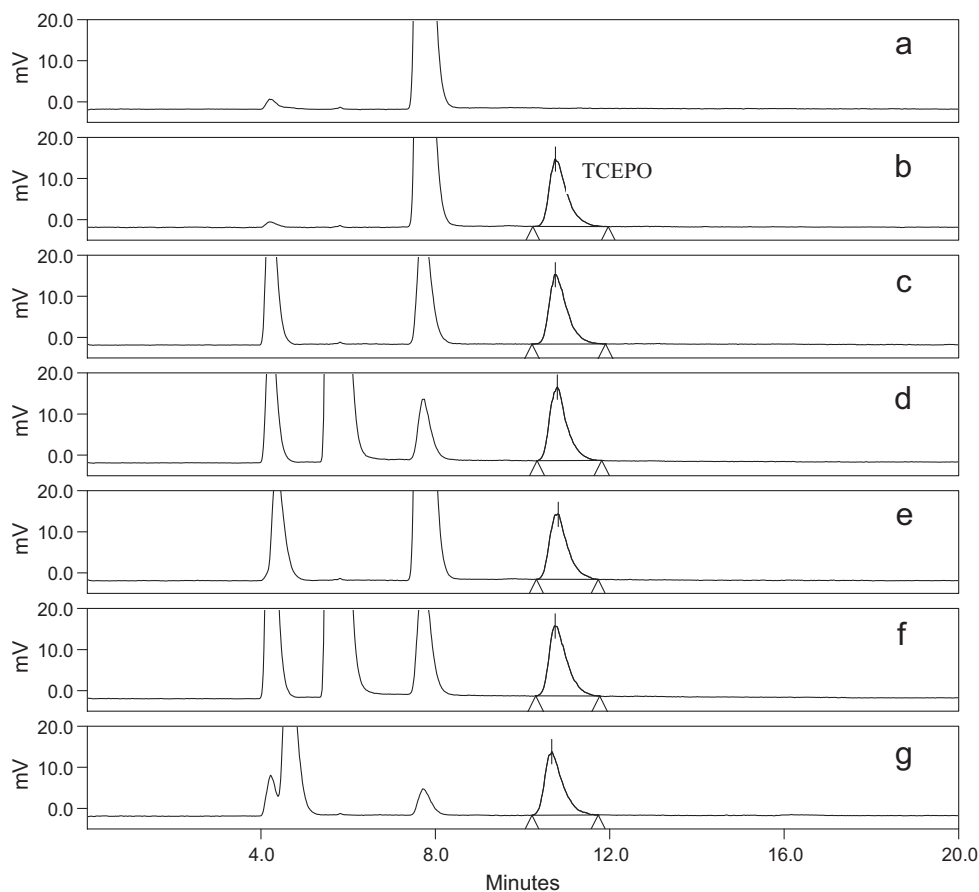
Fig. 5. HPLC chromatograms of 0.1 mM TCEP spiked samples, treated with H_2O_2, followed by SPE clean-up: water blank (a); TCEP in water (b); TCEP in 50 mM sodium acetate pH7.5 (c); TCEP in 50 mM sodium phosphate pH 7.5 (d); TCEP in 50 mM Tris pH7.5 (e); TCEP in 50 mg/mL Fc fusion protein, 10 mM phosphate, 25 mM sodium chloride (f); TCEP in 2.5 mg/mL PEGylated protein, 50 mM sodium acetate, pH5.5 (g).

or reduce the high concentration of salts and proteins, improved method selectivity, extended column lifetime, and enhanced detector performance.

The AEX-HPLC/ELSD method for TCEP detection is at least as comparable in sensitivity to reduction of DTNB to NTB. Although an LOQ was not determined, 10 μM (±3%) NTB was detected at 412 nm after reaction with 5 μM TCEP in Tris–HCl pH 7.5 solution rather than a more complex matrix [7]. By comparison, the LOQ for chromatographic analysis and ELSD detection of TCEP (converted to TCEPO) was determine to be 16.3 μM following SPE from a buffered Fc protein solution (Table 1). Previously, the performance of TCEP and DTT as reducing agents in biological matrices was evaluated with NTB detection at 0.1–10 mM compared with the present assay that is shown to be approximately 5 times more sensitive [3].

Another advantage of this method is the ability to determine consumed TCEP as well as total TCEP in the sample. As illustrated in this report, the entire sample is oxidized with H_2O_2 prior to SPE clean-up and HPLC analysis to determine the total amount of TCEP. However, a sample without H_2O_2 pretreatment followed by SPE clean-up would only yield the portion of consumed TCEP. Therefore, the rate of disulphide reduction may be followed by splitting a sample into two portions and pretreating only one aliquot with peroxide prior to SPE and AEX-HPLC of both. The disulphide reduction rate would be proportional to the difference between oxidized and total TCEP in the sample at any given time. NTB detection would only provide the concentration of the consumed TCEP in a sample [18].

4. Conclusion

An uncomplicated HPLC method using evaporative light scattering detection for quantitative determination of TCEP has been developed. In this method, the sample containing TCEP is first incubated with an excess amount of H_2O_2 to completely convert TCEP to p-oxide TCEP (TCEPO) (Fig. 1). Solid phase extraction (SPE, Strata-X-A cartridges) was used to remove protein and buffer species prior to AEX-HPLC/ELSD detection of oxidized TCEP. The protein and salts were removed or reduced by SPE and high resolution of the TCEPO peak was achieved (Figs. 4 and 5).

This method is sensitive enough to measure micro molar concentrations of TCEP in complex pharmaceutical sample matrices that contain proteins and salts. The Fc fusion protein at 50 mg/mL in phosphate buffer, used in development, represented an appropriate and typical complex pharmaceutical matrix to challenge the method. The protein concentration was relatively high and provided an opportunity to interact with TCEP (through multiple disulphide bonds) or interfere with the SPE method by competing for binding sites on the resin. In general, the buffer species that were evaluated are commonly used in pharmaceutical process and formulation development (Figs. 4 and 5). Because buffered solutions containing TCEP would likely contain protein as well as reacting additives, this method could be used to confirm TCEP removal following purification steps or the degree of TCEP consumption when developing a cysteine-specific protein conjugation reaction [6]. Therefore, the method presented in this report is suitable for measuring total as well as consumed TCEP in practical samples of

protein therapeutics. While the detection of NTB remains useful for measuring TCEP concentrations, the direct AEX-HPLC/ELSD method provides an additional robust and sensitive option.

References

[1] J.A. Burns, J. Butler, J. Moran, G. Whitesides, Selective reduction of disulfides by tris(2-carboxyethyl)phosphine, J. Org. Chem. 56 (1991) 2648–2650.

[2] R. Hansen, J. Winther, An introduction to methods for analyzing thiols and disulfides: reactions, reagents, and practical considerations, Anal. Biochem. 394 (2009) 147–158.

[3] E. Burmeister Getz, M. Xiao, T. Chakrabarty, R. Cooke, P.R. Selvin, A comparison between the sulfhydryl reductants tris(2-carboxyethyl)phosphine and dithiothreitol for use in protein biochemistry, Anal. Biochem. 273 (1999) 73–80.

[4] D.E. Shafer, J.K. Inman, A. Lees, Reaction of tris(2-carboxyethyl)phosphine (TCEP) with maleimide and α-haloacyl groups: anomalous elution of TCEP by gel filtration, Anal. Biochem. 282 (2000) 161–164.

[5] A. Krezel, R. Latajka, G.D. Bujacz, W. Bal, Coordination properties of tris(2-carboxyethyl)phosphine, a newly introduced thiol reductant, and its oxide, Inorg. Chem. 42 (2003) 1994–2003.

[6] D.H. Doherty, M.S. Rosendahl, D.J. Smith, J.M. Hughes, E.A. Chlipala, G.N. Cox, Site-specific PEGylation of engineered cysteine analogues of recombinant human granulocyte-macropage colony stimulating factor, Bioconjug. Chem. 16 (2005) 1291–1298.

[7] J.C. Han, G.Y. Han, A procedure for quantitative determination of tris(2-carboxyethyl)phosphine, an odorless reducing agent more stable and effective than dithiothreitol, Anal. Biochem. 220 (1994) 5–10.

[8] J. Han, S. Yen, G. Han, P. Han, Quantitation of hydrogen peroxide using tris(2-carboxyethyl)phosphine, Anal. Biochem. 234 (1996) 107–109.

[9] M. Garcia-Lopez, I. Rodriguez, R. Cela, K.K. Kroening, J.A. Caruso, Determination of organophosphate flame retardants and plasticizers in sediment samples using microwave-assisted extraction and gas chromatography with inductively couples plasma mass spectrometry, Talanta 79 (2009) 824–829.

[10] M. Garcia-Lopez, I. Rodriguez, R. Cela, Pressurized liquid extraction of organophosphate triesters from sediment samples using aqueous solutions, J. Chromatogr. A 1216 (2009) 6986–6993.

[11] P. Liu, B.W. O'Mara, B.M. Warrack, W. Wu, Y. Huang, Y. Zhang, R. Zhao, et al., A tris (2-Carboxyethyl) phosphine (TCEP) related cleavage on cysteine-containing proteins, J. Am. Soc. Mass Spectrom. 21 (2010) 837–844.

[12] M.D. Lantz, D.S. Risley, J.A. Peterson, Simultaneous resolution and detection of a drug substance, impurity, and couter ion using a mixed-mode HPLC column with evaporative light scattering detection, J. Liq. Chromatogr. Relat. Technol. 20 (1997) 1409–1422.

[13] C. Elfakir, P. Chaimbault, M. Dreux, Determination of inorganic anions on porous graphitic carbon using evaporative light scatterring detection using of carboxylic acids as electronic competitors, J. Chromatogr. A 829 (1998) 193–199.

[14] F. Mouchere, M. El Haddad, C. Elfakir, M. Dreux, Determination of inorganic cations and anions by ion-exchange chromatography with evaporative light-scattering detection, J. Chromatogr. A 914 (2001) 167–173.

[15] N. Megoulas, M. Koupparis, Development and validation of a novel LC/ELSD method for the quantitation of gentamicin sulfate components in pharmaceuticals, J. Pharm. Biomed. Anal. 36 (2004) 73–79.

[16] H.S. Park, C.K. Rhee, Simultaneous determination of nonionic and anionic industrial surfactants by liquid chromatography combined with evaporative light-scattering detection, J. Chromatogr. A 1046 (2004) 289–291.

[17] J.L. Fast, A.A. Cordes, J.F. Carpenter, T.W. Randolph, Physical instability of a therapeutic Fc fusion protein: domain contributions to conformation and colloidal stability, Biochemistry 48 (2009) 11724–11736.

[18] P.W. Riddles, R. Blakeley, B. Zerner, Reassessment of Ellman's reagent, Methods Enzymol. 91 (1983) 49–60.

[19] W.D. Kumler, J.J. Eiler, The acid strength of mono and diesters of phosphoric acid. The n-alkyl esters from methyl to butyl, the esters of biological importance, and the natural guanidine phosphoric acids, J. Am. Chem. Soc. 65 (1943) 2355–2361.

Short communication

Development and application of a validated gradient elution HPLC method for simultaneous determination of 5-fluorouracil and paclitaxel in dissolution samples of 5-fluorouracil/paclitaxel-co-eluting stents

Weiluan Chen, Yuanyuan Shen*, Haojun Rong, Lei Lei, Shengrong Guo

School of Pharmacy, Shanghai Jiao Tong University, Shanghai 200240, China

ABSTRACT

The combined use of 5-fluorouracil and paclitaxel is common in clinical trials. However, there are few methods for simultaneous determination of 5-fluorouracil and paclitaxel; most reported approaches can only quantitate either 5-fluorouracil or paclitaxel. This paper proposes a new gradient elution HPLC method for simultaneous determination of 5-fluorouracil and paclitaxel using a photodiode array detector, C_{18} column (250 mm × 4.6 mm, 5 μm) with methanol and 0.5% H_3PO_4 aqueous solution as the mobile phase components. The injection volume was 50 μl and the column temperature was maintained at 30 °C. The method was validated according to USP Category I requirements. The validation characteristics included system suitability, linearity, analytical range, LOD, LOQ, accuracy, precision, specificity, stability, ruggedness and robustness. The calibration curves exhibited linear concentration ranges of 0.2–40 μg/ml for 5-fluorouracil and 1.5–150 μg/ml for paclitaxel with correlation coefficients larger than 0.99990. The lower limits of quantitation were 2 ng/ml for 5-fluorouracil and 0.75 μg/ml for paclitaxel, respectively. The intra and inter-day precision and accuracy were found to be well within acceptable limits (i.e., 5%). The results demonstrate that this method is reliable, reproducible and suitable for simultaneous quantitation of the two drugs in the release media of 5-fluorouracil/paclitaxel-co-eluting stents.

1. Introduction

Paclitaxel (PTX), a plant product isolated from the bark of the Pacific yew tree, *Taxus brevifolia*, is an antimicrotubular agent which binds to the microtubules, promotes microtubule assembly and stabilizes tubulin polymer formation [1]. 5-Fluorouracil (5-FU) has been one of the mainstays of drugs for patients with solid tumors. As PTX exerts its cytotoxic effects through a mechanism different from that of 5-FU, and it has no cross-resistance with 5-FU [2], clinical combinational use of PTX and 5-FU have been widely reported [3,4]. However, long-term systemic use of 5-FU and PTX are associated with unwanted side effects [5,6]. Localized drug delivery has been proved to be a favorable option for those two drugs, and delivery of paclitaxel or 5-fluorouracil through localized implantable devices (such as drug-eluting stents) have been reported [7,8].

As combined use of 5-FU and PTX is very common in clinical trials, more and more anti-tumor pharmaceutical preparations are co-loaded with both of them [1,9,10]. Hereby, a reliable, accurate and sensitive method which can simultaneously quantify 5-FU and PTX is in great demand. Though there is no shortage of methods for determination of 5-FU and PTX individually [11–14], only a few methods for simultaneous determination of them are reported [15–17]. 5-FU and PTX were not very well separated by using isocratic elution [15]. The run time was as long as 60 min [16,17]. The aim of this study was to develop and validate a simple, rapid gradient elution HPLC method for simultaneous determination of 5-FU and PTX and quantitatively analyze the stent containing the two drugs.

2. Experimental

2.1. Reagents and solvents

HPLC grade methanol was purchased from Shanghai Xingke Biochemistry Co., Ltd (China). Water was purified by a Milli-Q water purifier system from Millipore (Bedford, MA, USA). 5-FU was purchased from Nantong Jinghua Pharmaceutical Co., Ltd (Nantong City, China) and PTX was from Xi'an Haoxuan Biological Technology Co., Ltd (Xi'an, China). Ethylene vinyl acetate (EVA) copolymer (with VAc of 42% and melt index of 60 g/min) was purchased from Shanghai Research Institute of Chemical Industry (Shanghai, China).

* Corresponding author. Tel.: +86 21 34204793; fax: +86 21 34204793.
E-mail address: shenyuanyuan@sjtu.edu.cn (Y. Shen).

2.2. Preparation of drug-eluting stents

Drug-eluting stents were prepared by two steps: (1) the bare nitinol stent (diameter 1 cm, length 2 cm, supplied by Micro-Tech Co., Ltd, Nanjing, China) was first dip-coated to obtain a thin EVA protective layer (about 100 μm) by immersion into a viscous methylene chloride solution containing 20% (w/v) of EVA for 10 min and subsequent evaporation of the solvent; and then (2) a drug-loaded film was wrapped around the outside surface of the protective layer-coated nitinol stent.

The drug-loaded film was prepared by hot-compressing the fully blended mixture of 5-FU and PTX particles with molten EVA at various ratios with a heat source. In brief, 3.5 g EVA and the micronized 5-FU and PTX particles were added slowly into the chamber of a Haake Mini-Lab twin screw extruder (Thermo Fischer Scientific, Waltham, Mass) at weight ratios of 30/20/50 or 20/30/50 (5-FU/PTX/EVA) and then blended at 90 °C for 30 min. The concentrations were chosen according to the dosage of 5-FU and PTX in the clinical applications. The resulting EVA-5-FU-PTX blends were further compressed into films on a Compression Molding Machine (XLB-D, Shanghai No. 1 Rubber Machine Factory) at 100 °C and 5 MPa. The obtained drug-loaded films had a thickness of 200 μm. The drug content was defined as the weight percentage of the drug in the film.

2.3. Dissolution analysis of drug-eluting stents

Each drug-eluting stent was placed in a polyethylene tube containing 15 ml of phosphate-buffered saline (PBS) (pH 7.4; 0.05 M, 1% sodium dodecyl sulfate). The tubes were placed in a shaking water bath at 37 °C with a shaking speed of 110 rpm. At predetermined time points, the release medium was completely withdrawn and replaced with 15 ml of fresh PBS to maintain sink conditions. 5-FU and PTX concentrations in the retrieved release media were assessed by HPLC.

2.4. Preparation of 5-FU and PTX stock solutions

5-FU and PTX stock solutions (200 and 300 μg/ml, respectively) were prepared in 75% ethanol aqueous solution, they were stored at 4 °C and were used within one month.

2.5. Instrumentation and chromatography conditions

The analyses of the samples were performed by HPLC using a Waters system consisting of an autosampler (2707), a binary HPLC pump (1525) and a photodiode array detector (2998). The analytical signal was monitored and integrated using Empower^{TM} 2 chromatography software. A Venusil RP-C$_{18}$ column (250 mm × 4.6 mm, particle size 5 μm, Agelatina Technologies, Tianjin, China), which has a wide pH range of applicability (1–10) was used. The mobile phase was composed of solvent A (methanol) and solvent B (0.5% H$_3$PO$_4$ aqueous solution). The flow rate was 1.0 ml/min. The gradient elution conditions are described in Supplementary Table S1. The photodiode-array UV absorbance at 266 nm (for 5-FU) and 227 nm (for PTX) were monitored. The column temperature was controlled at 30 °C and the injection volume was 50 μl.

2.6. Method validation procedure

2.6.1. System suitability

System suitability standard solution (at concentrations of 10 μg/ml for 5-FU and 15 μg/ml for PTX) was prepared daily using the stock solutions. System suitability was determined from six replicate injections of the system suitability standard solution before sample analysis. The acceptance criteria were less than 2% relative standard deviation (RSD) for the peak area and retention time, greater than 3000 column plates, USP tailing factor less than 1.5, and capacity factor (k') greater than 3.0.

2.6.2. Linearity and range

The calibration standard solutions (containing 5-FU and PTX) were prepared by mixing the 5-FU and PTX stock solutions and then serially diluting the mixture. The concentrations of 5-FU and PTX in the 6 calibration standard solutions were 0.2 and 1.5, 1 and 7.5, 5 and 15, 10 and 30, 20 and 60, 40 and 150 μg/ml, respectively. The data of peak area versus drug concentration were treated by linear least square regression analysis. The analytical ranges were established by the highest and lowest concentrations of analytes where acceptable linearity, accuracy and precision were obtained.

2.6.3. LOD and LOQ

Limits of detection (LOD) and quantitation (LOQ) were estimated from the signal-to-noise ratio. The detection limit was determined as the lowest concentration level resulting in a peak area of three times the baseline noise. The quantitation limit was determined as the lowest concentration level that provided a peak area with signal-to-noise ratio of 10.

2.6.4. Precision and accuracy

PTX and 5-Fu stock solutions and 75% ethanol aqueous solution were used to prepare a working standard containing 60 μg/ml PTX and 40 μg/ml 5-FU. Quality control (QC) standard solutions were prepared by diluting the working standard to final QC standard solutions with PTX and 5-FU concentrations of 60 and 40 (high), 15 and 10 (intermediate), and 1.5 and 1 (low) μg/ml. QC solutions were then transferred to an autosampler for HPLC analysis. Each QC solution was analyzed six times.

Precision and accuracy of the method were determined for PTX and 5-FU by analyzing the above QC standard samples. The precision was established by six injections of each QC sample within one day for the intra-day precision and 6 days for intermediate precision. Precision was expressed as the RSD of the analyte peaks. Accuracy was determined by the QC samples and evaluated as an average drug content percentage.

2.6.5. Specificity

Specificity of the method was determined by analyzing the system suitability standard, drug-free release media and drug dissolution samples. All chromatograms were examined to determine if the active compound had any co-elution with the surfactant peak from the dissolution medium.

2.6.6. Stability

Short-term stability was evaluated by using the QC standard solutions stored at room temperature for 24 h. The long-term stability test was performed by using the QC standard solutions stored at 4 °C for 1 month. Autosampler stability was also tested with the QC standard samples for 24 h.

2.6.7. Ruggedness and robustness of the method

To evaluate the intermediate precision (also known as ruggedness) of the method, precision was performed on different days by using columns from different manufacturers of the same dimensions. Method robustness was carried by changing the flow rate and mobile phase composition to evaluate the impact on the performance of the method.
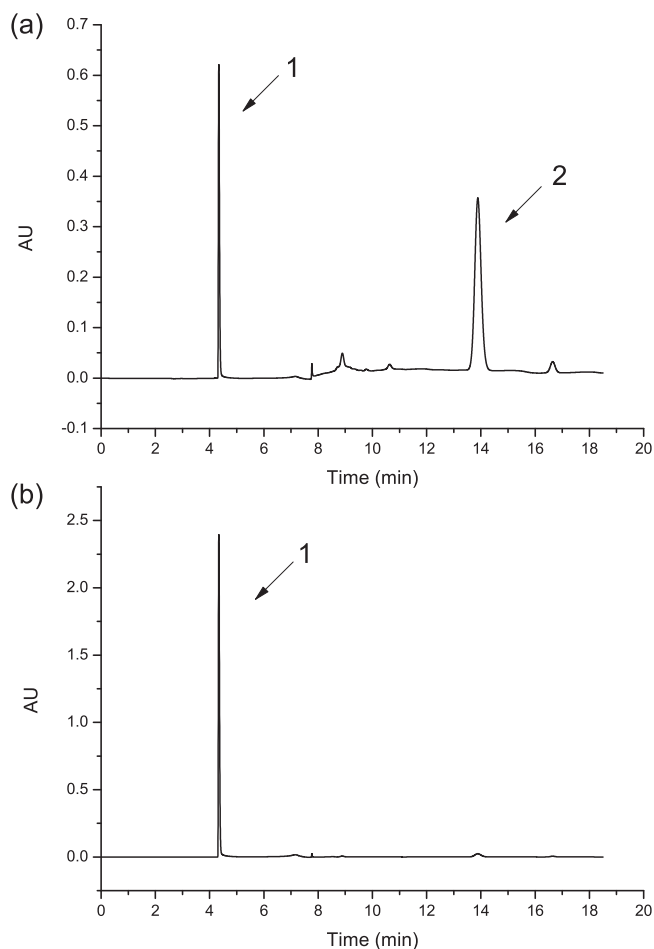
Fig. 1. Representative chromatograms of the system suitability standard solution containing 5-FU and PTX. UV detection was set at 227 (a) and 266 (b) nm. 1, 5-FU; 2, PTX.
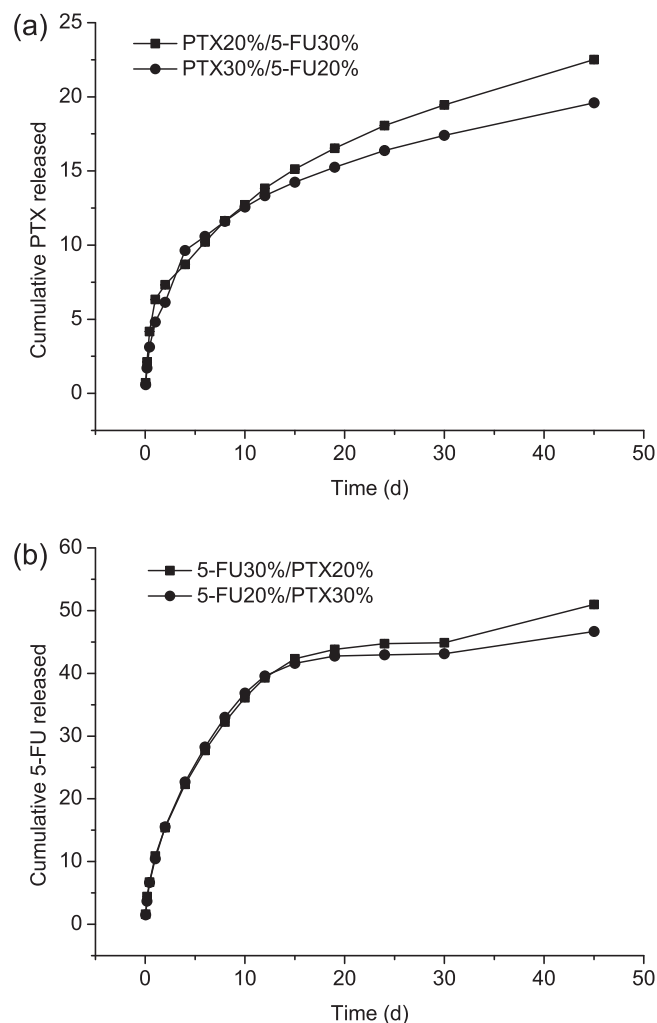

Fig. 2. Drug release curves of the 5-FU/PTX-co-eluting stents. The release curve of PTX from the 5-FU/PTX-co-eluting stents (a), and the release curve of 5-FU from the 5-FU/PTX-co-eluting stents (b).

3. Results and discussion

3.1. Preparation of drug-eluting stents

The drug-eluting stents consisted of a bare nitinol stent and a bilayered coating composed of one 5-FU/PTX loaded EVA layer and one protective EVA layer. The thickness of the protective EVA layer could be adjusted by altering the solution viscosity (concentration of the EVA) or the time of dipping.

3.2. Method development

In order to optimise the chromatographic parameters, the effect of mobile phase composition on the tailing factor (T_f) was investigated. The results showed that the T_f of 5-FU was decreased below 0.95 with decreasing percentage of H_3PO_4 in aqueous solution (data not shown), however, the increase of H_3PO_4 percentage in aqueous solution led to a poorly shaped peak of PTX. The H_3PO_4 aqueous solution (0.1–1%) were tested and with a H_3PO_4 percentage of 0.5 in the aqueous solution (pH 1.75), good baseline, adequate separation and well-shaped peaks within an acceptable elution time could be achieved. Under these chromatographic conditions, 5-FU and PTX were well separated (with retention times of 4.3 and 13.8 min, respectively).

3.3. Method validation

The method was validated according to the United States Pharmacopeia (USP 30) Category I requirements. The following

validation characteristics were addressed: system suitability, linearity, range, LOD, LOQ, precision, accuracy, specificity, stability, ruggedness and robustness.

3.3.1. System suitability

The system suitability test, which ensures the validity of the analytical procedure as well as confirms the resolution between different peaks of interest, was performed according to USP 30 prescriptions [18]. All the obtained critical parameters met the acceptance criteria (Supplementary Table S2). The system suitability test established instrument performance parameters such as retention time, peak area, capacity factor and USP tailing factor for 5-FU and PTX peaks. All the parameters maintained a %RSD of <1. All critical parameters tested met the acceptance criteria on all days. A typical chromatogram of the system suitability standard solution containing both 5-FU and PTX is shown in Fig. 1.

3.3.2. Linearity and range

The linearity of the calibration curves for PTX and 5-FU was calculated and constructed by least square regression method. The peak area ratios of the 5-FU and PTX were linear in the ranges of 0.2–40 μg/ml and 1.5–150 μg/ml, respectively. The correlation coefficients (R^2) of both 5-FU and PTX calibration curves for the first day were all greater than 0.99990 and the correlation
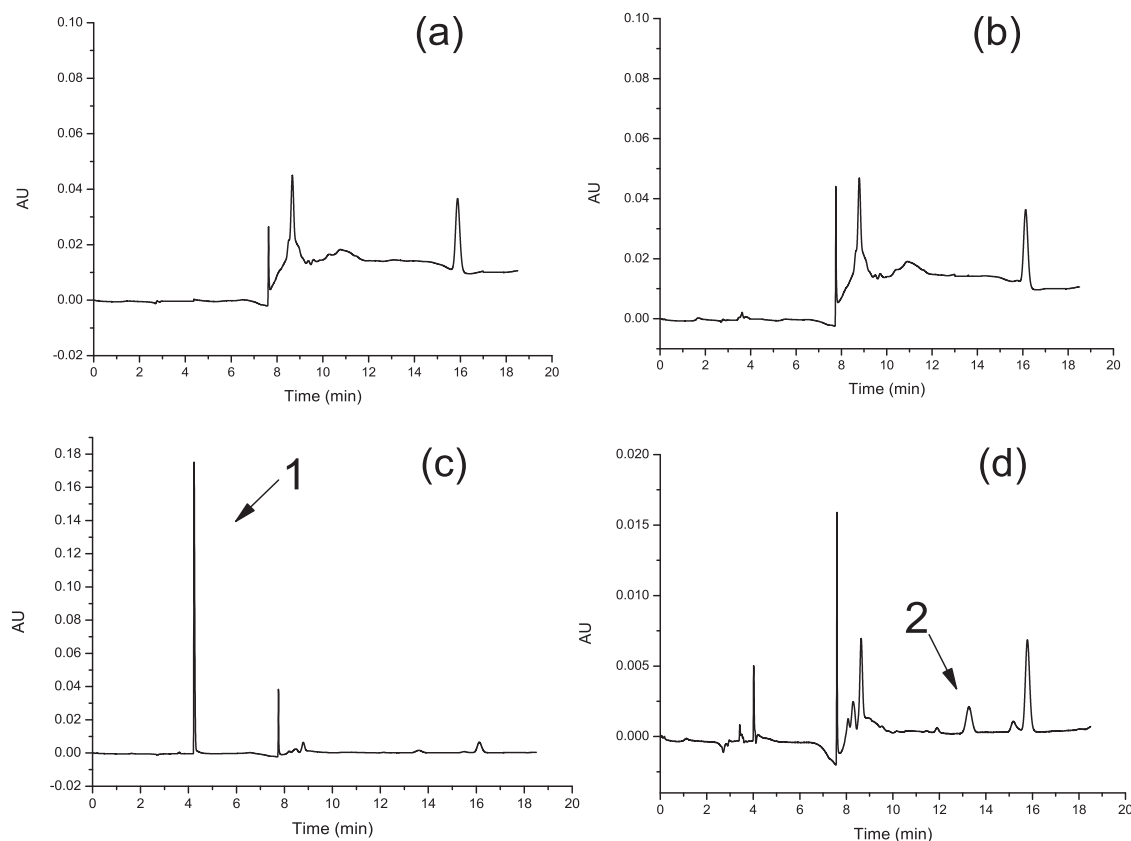
Fig. 3. Representative chromatogram of 0.05 M phosphate buffer: 75% ethanol aqueous solution (a) and (b); and dissolution media of the 5-FU/PTX-co-eluting stents (c) and (d). UV detection was set at 266 (a) and (c) nm; and 227 (b) and (d) nm. 1, 5-FU; 2, PTX.

coefficients (R^2) of all the calibration curves were greater than 0.999 (Supplementary Table S3).

3.3.3. LOD and LOQ

The LOD were 0.6 ng/ml for 5-FU and 0.3 μg/ml for PTX at a signal-to-noise ratio of 3:1. The limits of quantitation were determined as 2 ng/ml for 5-FU and 0.75 μg/ml for PTX at a signal-to-noise ratio of 10:1. The LOD and LOQ of 5-FU and PTX were lower than those reported [17], thus, our method can simultaneously determine relatively low concentrations of 5-FU and PTX, which has advantages for the quantitatively analysis of some sustained release preparations, such as implants or drug-eluting stents.

3.3.4. Accuracy and precision

Accuracy and precision were established within the analytical ranges for 5-FU and PTX. The intra- and inter-day precision and accuracy were calculated from the QC standard samples. Results for the intra- and inter-day precision of 5-FU and PTX are summarized in Supplementary Table S4. Results for the intra- and inter-day accuracy of 5-FU and PTX are summarized in Supplementary Table S5. All the data were within the accepted criteria of 5%.

3.3.5. Specificity

Specificity of the method was demonstrated by good separation of the two drugs (5-FU and PTX) and no additional peaks were co-eluted with the analytes, evidencing the good specificity of this method.

3.3.6. Stability

Stability results indicated that the samples were stable for 24 h at ambient temperature at bench top or in the autosampler

chamber, and for 1 month at 4 °C, respectively. The detailed results are given in Supplementary Table S6.

3.3.7. Ruggedness and robustness of the method

Method robustness and ruggedness was determined by analyzing the same sample at normal operating conditions and also by changing some operating analytical conditions, such as column manufacturers, mobile phase composition, flow rate, and analysts. Supplementary Table S7 represents the ruggedness and robustness of the method. The robustness and ruggedness of the method shows that the assay value of 5-FU and PTX were both less than 2.0%.

3.4. Application of the method to drug-loaded stents

The method was successfully applied to simultaneously determine the 5-FU and PTX concentrations in the release media of the 5-FU/PTX-co-eluting stents. At predetermined time points, the retrieved release media were collected and diluted four times with 75% ethanol aqueous solution. 5-FU and PTX concentrations in the dilutions were determined using the above HPLC method, and the cumulative amount of drug released was plotted versus the release time. The drug release curves for the stents are shown in Fig. 2. The release curves of 5-FU and PTX showed differences: 5-FU was released faster than PTX in the 5-FU/PTX-co-eluting stents. After 45 days, about 51% of the incorporated 5-FU was released, whilst about 23% of the PTX was released from the drug-eluting stent with 5-FU content of 30% and PTX content of 20%. For another stent with different drug loadings (with 5-FU content of 20% and PTX content of 30%), less drugs were released. About 47% and 20% of the 5-FU and PTX were released, respectively. As shown in Fig. 3, there were no interfering peaks at the retention times of 5-FU and PTX in the retrieved release media.

4. Conclusion

A simple, efficient and rapid gradient elution HPLC analytical method was developed and validated for simultaneous quantitation of 5-FU and PTX. The system suitability, linearity and range, LOD, LOQ, precision, accuracy, specificity, stability, ruggedness and robustness met the USP acceptance criteria. The method can be used for quantitative analysis of the *in vitro* drug dissolution samples for the drug-eluting stents. Because of its lower LOD and LOQ, compared with the published methods, our method can be used to measure samples containing relatively low amounts of 5-FU and PTX, suitable for quantitative analysis of drug sustained release preparations, such as drug-eluting stents or implants.

Acknowledgements

Appendix A. Supplementary data

Supplementary data associated with this article can be found, in the online version, at doi:10.1016/j.jpba.2011.10.005.

References

[1] D.H. Ilson, J. Ajani, K. Bhalla, A. Forastiere, Y. Huang, P. Patel, L. Martin, J. Donegan, R. Pazdur, C. Reed, D.P. Kelsen, Phase II trial of paclitaxel, fluorouracil, and cisplatin in patients with advanced carcinoma of the esophagus, J. Clin. Oncol. 16 (1998) 1826–1834.

[2] R.S. Gupta, Cross-resistance of Vinblastine- and Taxol-resistant Mutants of Chinese Hamster Ovary Cells to Other Anticancer Drugs, US Department of Health, Education and Welfare, Silver Spring, MD, ETATS-UNIS, 1985.

[3] Y.H. Kim, S.W. Shin, B.S. Kim, J.H. Kim, J.G. Kim, Y.J. Mok, C.S. Kim, H.S. Rhyu, J.H. Hyun, J.S. Kim, Paclitaxel, 5-fluorouracil, and cisplatin combination chemotherapy for the treatment of advanced gastric carcinoma, Cancer 85 (1999) 295–301.

[4] A.A. Meluch, J.D. Hainsworth, J.R. Gray, M. Thomas, P.L. Whitworth, J.L. Davis, F.A. Greco, Preoperative combined modality therapy with paclitaxel, carboplatin, prolonged infusion 5-fluorouracil, and radiation therapy in localized esophageal cancer: preliminary results of a Minnie Pearl Cancer Research Network Phase II Trial, Cancer J. 5 (1999) 84–91.

[5] N. Goyal, A. El Achchabi, E. Goldberg, G. Hochhaus, Simultaneous determination of dexamethasone, dexamethasone 21-acetate, and paclitaxel in a simulated biological matrix by RP-HPLC: assay development and validation, J. Liq. Chromatogr. Relat. Technol. 31 (2008) 1478–1491.

[6] J.J. Monsuez, J.C. Charniot, N. Vignat, J.Y. Artigou, Cardiac side-effects of cancer chemotherapy, Int. J. Cardiol. 144 (2010) 3–15.

[7] L. Lei, X. Liu, S. Guo, M. Tang, L. Cheng, L. Tian, 5-Fluorouracil-loaded multilayered films for drug controlled releasing stent application: drug release, microstructure, and ex vivo permeation behaviors, J. Control. Release 146 (2010) 45–53.

[8] X. Liu, L. Lei, J.W. Hou, M.F. Tang, S.R. Guo, Z.M. Wang, K.M. Chen, Evaluation of two polymeric blends (EVA/PLA and EVA/PEG) as coating film materials for paclitaxel-eluting stent application, J. Mater. Sci.-Mater. M. 22 (2011) 327–337.

[9] A. Gupte, K. Ciftci, Formulation and characterization of paclitaxel, 5-FU and paclitaxel + 5-FU microspheres, Int. J. Pharm. 276 (2004) 93–106.

[10] K. Liu, D. Zhong, H. Zou, X. Chen, Determination of tegafur, 5-fluorouracil, gimeracil and oxonic acid in human plasma using liquid chromatography–tandem mass spectrometry, J. Pharm. Biomed. Anal. 52 (2010) 550–556.

[11] R. Pisano, M. Breda, S. Grassi, C.A. James, Hydrophilic interaction liquid chromatography–APCI-mass spectrometry determination of 5-fluorouracil in plasma and tissues, J. Pharm. Biomed. Anal. 38 (2005) 738–745.

[12] O.T. Fahmy, M.A. Korany, H.M. Maher, High performance liquid chromatographic determination of some co-administered anticancer drugs in pharmaceutical preparations and in spiked human plasma, J. Pharm. Biomed. Anal. 34 (2004) 1099–1107.

[13] G. Basileo, M. Breda, G. Fonte, R. Pisano, C.A. James, Quantitative determination of paclitaxel in human plasma using semi-automated liquid–liquid extraction in conjunction with liquid chromatography/tandem mass spectrometry, J. Pharm. Biomed. Anal. 32 (2003) 591–600.

[14] S.C. Kim, J. Yu, J.W. Lee, E.-S. Park, S.-C. Chi, Sensitive HPLC method for quantitation of paclitaxel (Genexol®) in biological samples with application to preclinical pharmacokinetics and biodistribution, J. Pharm. Biomed. Anal. 39 (2005) 170–176.

[15] A.M.P.d.P. Alcântara, R.V. Vitor, E.P. Vieira, I. Martins, Simultaneous detection of three antineoplastic drugs on gloves by liquid chromatography with diode array detector, Braz. J. Pharm. Sci. 46 (2010) 731–740.

[16] R.R. Larson, M.B. Khazaeli, H.K. Dillon, A new monitoring method using solid sorbent media for evaluation of airborne cyclophosphamide and other antineoplastic agents, Appl. Occup. Environ. Hyg. 18 (2003) 120–131.

[17] R.R. Larson, M.B. Khazaeli, H.K. Dillon, Development of an HPLC method for simultaneous analysis of five antineoplastic agents, Appl. Occup. Environ. Hyg. 18 (2003) 109–119.

[18] T.U.S., Pharmacopeia, The United State Pharmacopeia (2007).

Short communication

Thermal stability of vitamin C: Thermogravimetric analysis and use of total ion monitoring chromatograms

Márta Juhász, Yuki Kitahara, Seiji Takahashi, Toshihiro Fujii *

Department of Chemistry, Faculty of Sciences and Engineering, Meisei University, Hodokubo 2-1-1, Hino, Tokyo 191-8506, Japan

ARTICLE INFO

ABSTRACT

The thermal decomposition kinetics and shelf life of vitamin C in nitrogen or air were studied by using thermogravimetric analysis (TGA) and evolved-gas analysis–lithium-ion attachment mass spectrometry (EGA–Li$^+$IAMS). Arrhenius parameters obtained via TGA were reported for thermal decomposition. For vitamin C in a nitrogen atmosphere, the activation energy (E_a) was 25.1 kcal/mol and the pre-exponential factor (A) was 2.5×10^{11} min^{-1}. The kinetic parameters estimated via TGA agreed with values estimated from a pyrogram when the weight loss observed by TGA was shown to be due to gas evolution as a result of decomposition of the compound. Thermal stability was expressed by calculating the time for 10% of the vitamin C to decompose at 25 °C ($t_{90\%,25\,°C}$). The $t_{90\%,25\,°C}$ for vitamin C obtained via TGA or EGA–Li$^+$IAMS was higher in nitrogen (2.0 and 2.0 years, respectively) than in air (1.3 and 1.6 years, respectively). This indicates that the type of atmosphere influences vitamin C stability.

© 2011 Elsevier B.V. All rights reserved.

1. Introduction

Vitamin C is important as a pharmaceutical agent, cosmetic ingredient, and dietary supplement. Products containing vitamin C are often subjected to thermal treatment during preparation, processing, and storage [1–5], so it is important to ascertain vitamin C's thermal decomposition kinetics and shelf life. Thermal stability is of particular interest because the results of thermal decomposition kinetic studies may lead to improvements in the stability of the formulations of many pharmaceutical and food products.

Studies on decomposition kinetics of vitamin C in various food products under different storage and processing conditions revealed that decomposition of vitamin C follows first order kinetics and the temperature dependence of the rate of reaction is described by the Arrhenius equation [1–5].

A number of instrumental methods, such as differential scanning calorimetry, differential thermal analysis, and thermogravimetric analysis (TGA), are available for the study of decomposition kinetics. Recently, evolved-gas analysis–mass spectrometry, which is considered to be the second generation of pyrolysis mass spectrometry, has been successfully applied to characterization of the thermal decomposition process [6–9]. In addition, total ion monitoring (TIM) or selected ion monitoring (SIM) chromatograms against temperature can be used as

alternatives to pyrograms to provide information for thermal decomposition kinetic studies.

This paper presents the thermal decomposition kinetics (E_a, A) and shelf life ($t_{90\%,25\,°C}$) predictions for vitamin C in nitrogen or air, as obtained via TGA or EGA–Li$^+$IAMS. This paper also compares the TGA method with the EGA–Li$^+$IAMS method with regards to the determination of thermal stability.

2. Methods

2.1. Thermogravimetric analysis and evolved-gas analysis–lithium-ion attachment mass spectrometry (EGA–Li$^+$IAMS)

TGA was conducted with a Shimadzu DT-40 Thermal Analyzer (Shimadzu, Kyoto, Japan) under a nitrogen or air atmosphere at a flow rate of 80 mL/min. Vitamin C samples of 3 mg were heated from 50 °C to 500 °C at a rate of 4 °C/min. EGA–Li$^+$IAMS experiments were conducted with a Li Ion Attachment Mass Spectrometer (Canon ANELVA Corporation, Kanagawa, Japan) and samples of 0.1 mg were heated from 50 °C to 500 °C at a rate of 4 °C/min under a nitrogen or air atmosphere.

3. Results and discussion

3.1. Thermogravimetric analysis

In a nitrogen atmosphere (Fig. 1(a) solid line), vitamin C started to decompose at approximately 191 °C, with the maximum rate

---

* Corresponding author. Tel.: +81 42 591 5595; fax: +81 42 591 5595.
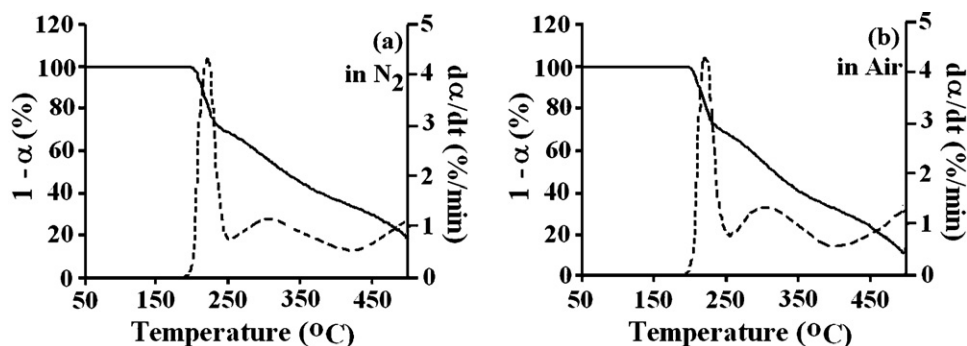*E-mail address:* fujii@chem.meisei-u.ac.jp (T. Fujii).

Fig. 1. TG and DTG curves for vitamin C heated in nitrogen (a) and air (b) from 50 °C to 500 °C at a rate of 4 °C/min at atmospheric pressure. DTG curves are represented by a dotted line.

of decomposition occurring at approximately 221 °C. This maximum was followed by two additional decomposition steps in the 251–500 °C temperature range. At 500 °C approximately 11% of the initial sample remained as charred residue.

In an air atmosphere (Fig. 1(b) solid line) degradation also took place in three stages. The decomposition profile was similar to that observed in nitrogen, although the temperature of the initial weight loss (188 °C) was lower than that recorded in nitrogen (191 °C) and at 500 °C approximately 4% of the initial sample remained as charred residue. Since vitamin C is sensitive to the presence of oxygen [10], it is reasonable to expect that, in air, vitamin C starts to decompose at lower temperatures and at a higher rate than in nitrogen.

3.2. Evolved-gas analysis–lithium-ion attachment mass spectrometry

The TIM curves (Fig. 2) closely reproduced the three maxima appearing in the DTG curves (Fig. 1(a and b) dotted line) owing to the evolution of thermal decomposition products. Under EGA–Li$^+$IAMS conditions, vitamin C starts decomposing at lower temperatures than under TG conditions.

In a nitrogen atmosphere (Fig. 2(a)), the initial weight loss started at 182 °C and at 500 °C approximately 5% of the initial sample remained as charred residue while in air (Fig. 2(b)), the first decomposition step of the vitamin C thermal decomposition process started at approximately 180 °C and at 500 °C approximately 2% of the initial sample remained as charred residue.

3.3. Decomposition kinetics analysis

TIM chromatograms obtained from the EGA–Li$^+$IAMS give the relative number of decomposition product molecules, thereby

indicating the production rate. The degree of conversion (α) at any temperature (T) is equal to the integrated area under the TIM curve between the temperature at the signal start (T_0) and T. Assuming a first-order reaction [11,12], the ionic signal acquired from real-time total-ion monitoring of chemicals released from a thermally decomposing specimen was used to obtain the functional forms of the following kinetic rate equation:

$$\ln\left[\frac{(d\alpha/dT)\beta}{(1-\alpha)}\right] = \ln A - \frac{E_a}{RT} \tag{1}$$

where α is the degree of yield of the decomposed specimen, T is the temperature, β is the heating rate, A is the pre-exponential factor, E_a is the activation energy, and R is the universal gas constant. Activation energy and pre-exponential factor were determined from plots of $\ln[(d\alpha/dT)\beta/(1-\alpha)]$ versus $1/T$.

In TGA, the DTG plot acquired from real-time weight loss due to the release of chemicals from the thermally decomposing sample was used to obtain the functional forms of the kinetic rate expression.

We evaluated the kinetic data from both the DTG and the TIM curves of the first decomposition step, since these curves represented the most substantial rate of decomposition. We investigated the decomposition kinetics over the 181–231 °C temperature range in nitrogen or in air to obtain rate expressions for vitamin C degradation. The slopes of the plots of temperature versus signal intensity were constant (Fig. 3(a–d)). Activation energies and pre-exponential factors were calculated from the plots (Table 1).

The activation energies for the thermal decomposition of vitamin C obtained from both the TGA and EGA–Li$^+$IAMS experiments were lower in air than in nitrogen. These results were expected, since the initial temperatures for vitamin C decomposition were
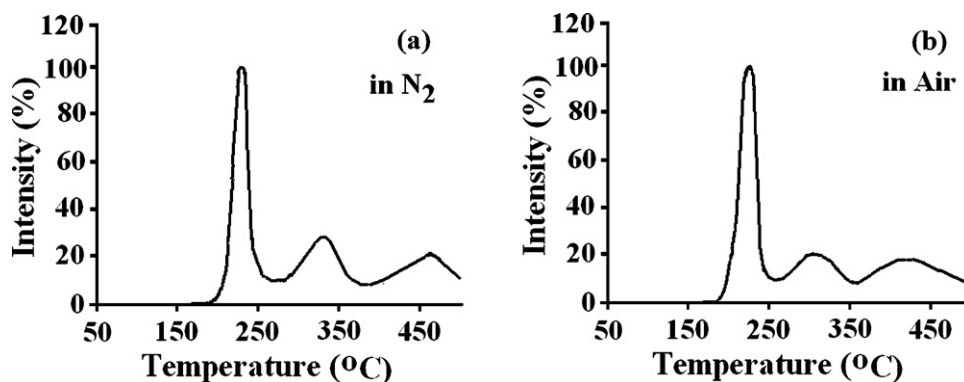

Fig. 2. TIM curves for vitamin C heated in nitrogen (a) and air (b) from 50 °C to 500 °C at a rate of 4 °C/min at *ca.* 40 Pa.
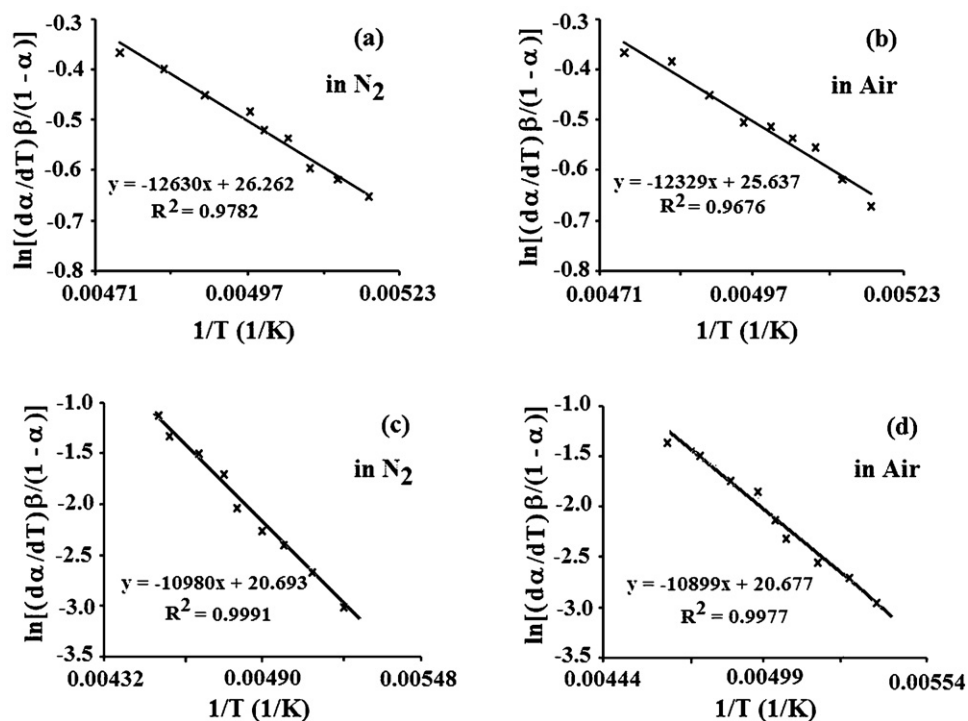
Fig. 3. Arrhenius plots for data calculated from the DTG curves of vitamin C decomposition in nitrogen (a) and in air (b), and Arrhenius plots for data calculated from the TIM curves of vitamin C decomposition in nitrogen (c) and in air (d).

also lower in air than in nitrogen. The same pattern was observed in the calculated pre-exponential factors.

3.4. Prediction of shelf life ($t_{90\%,25°C}$)

The time for 10% of a target molecule to decompose ($t_{90\%}$) is generally used as the estimation of shelf life. In a nitrogen or air atmosphere, the $t_{90\%,25°C}$ of vitamin C determined by using TGA or EGA–Li$^+$IAMS are given in Table 1. The values of $t_{90\%,25°C}$ for vitamin C decomposition were lower in air than in nitrogen, indicating that vitamin C was more stable in nitrogen than in air and that the type of atmosphere (nitrogen versus air) influenced the thermal stability of vitamin C.

We compared our calculated $t_{90\%,25°C}$ values with the $t_{70\%,25°C}$ values obtained by Zhan et al. [13–15]. They investigated the shelf life of solid vitamin C tablets under different programmed-heating conditions and reported a $t_{70\%,25°C}$ value of approximately 7.0 years. This corresponds to 2.3 years when defined as $t_{90\%,25°C}$. The difference between our results and the results of Zhan et al. may be due to the difference in the form of the sample used: our sample was powdered, whereas their sample was a tablet.

4. Conclusions

We used TGA and EGA–Li$^+$IAMS with non-isothermal heating to study the thermal decomposition kinetics and predict the lifetime of vitamin C. The results for the thermal decomposition of vitamin C showed that the thermal stability of vitamin C was greater in nitrogen than in air. Estimated shelf lives ($t_{90\%,25°C}$) in nitrogen of 2.0 years were obtained from both the TGA and EGA–Li$^+$IAMS experiments. The identical predictions of shelf life indicate that the results obtained from TGA can be reproduced by using EGA–Li$^+$IAMS.

Table 1
Thermal decomposition kinetic parameters for vitamin C decomposition determined by TGA or EGA–Li$^+$IAMS in nitrogen or air, and the associated predicted values of shelf life.

Method	Atmosphere	E_a (kcal/mol)	A (min^{-1})	$t_{90\%,25°C}$ (years)
TGA	Nitrogen	25.1	2.5×10^{11}	2.0
	Air	24.5	1.4×10^{11}	1.3
EGA–Li$^+$IAMS	Nitrogen	21.8	9.7×10^{8}	2.0
	Air	21.7	9.5×10^{8}	1.6

A = pre-exponential factor, E_a = activation energy, $t_{90\%,25°C}$ = shelf life (time for 10% of the target molecule to decompose at 25°C), EGA–Li$^+$IAMS = evolved-gas analysis–lithium-ion attachment mass spectrometry, TGA = thermogravimetric analysis.

References

[1] P.S. Taoukis, P. Panagiotidis, N.G. Stoforos, P. Butz, H. Fister, B. Tauscher, Kinetics of vitamin C degradation under high pressure-moderate temperature processing in model systems and fruit juices, in: N.S. Isaacs (Ed.), High Pressure Food Science, Bioscience and Chemistry, The Royal Society of Chemistry, Cambridge, 1998, pp. 310–316.
[2] P. Nisha, R.S. Singhal, A.B. Pandit, A study on degradation kinetics of ascorbic acid in amla (*Phyllanthus emblica* L.) during cooking, Int. J. Food Sci. Nutr. 55 (2004) 415–422.
[3] M. Karhan, M. Aksu, N. Tetik, I. Turhan, Kinetic modeling of anaerobic thermal degradation of ascorbic acid in rose hip (*Rosa canina* L) pulp, J. Food Qual. 27 (2004) 311–319.
[4] R.M.S. Cruz, M.C. Vieira, C.L.M. Silva, Effect of heat and thermosonication treatments on watercress (*Nasturtium officinale*) vitamin C degradation kinetics, Innovat. Food Sci. Emerg. Technol. 9 (2008) 483–488.
[5] C. Dhuique-Mayer, M. Tbatou, M. Carail, C. Caris-Veyrat, M. Dornier, M.J. Amiot, Thermal degradation of antioxidant micronutrients in citrus juices: kinetics and newly formed compounds, J. Agric. Food Chem. 55 (2007) 4209–4216.
[6] M. Kamruddin, P.K. Ajikumar, S. Dash, A.K. Tyagi, B. Raj, Thermogravimetry-evolved gas analysis–mass spectrometry system for materials research, Bull. Mater. Sci. 26 (2003) 449–460.
[7] T. Tsugoshi, T. Nagaoka, M. Nakamura, Y. Shiokawa, K. Watari, Application of ion attachment mass spectrometry to evolved gas analysis for in situ monitoring of porous ceramic processing, Anal. Chem. 78 (2006) 2366–2369.

[8] J.A. Jansen, in: V.B.F. Mathot (Ed.), Calorimetry and Thermal Analysis of Polymers, Hanser, Munich, 1994, pp. 335–352.

[9] M. Juhász, Y. Kitahara, T. Fujii, Thermal decomposition of vitamin C: an evolved gas analysis–ion attachment mass spectrometry study, Food Chem. 129 (2011) 546–550.

[10] S.P. Gladkikh, Ascorbic acid and methods of increasing its stability in drugs, Technology (1971) 699–705.

[11] J. Kirk, D. Dennison, P. Kokoczka, D. Heldman, Degradation of ascorbic-acid in a dehydrated food system, J. Food Sci. 42 (1977) 1274–1279.

[12] A.N. Hiatt, L.S. Taylor, L.J. Mauer, Influence of simultaneous variations in temperature and relative humidity on chemical stability of two vitamin C forms and implications for shelf life models, J. Agric. Food Chem. 58 (2010) 3532–3540.

[13] X. Zhan, G. Yin, B. Ma, New heating controller and computation for linear heating stability experiment, Int. J. Pharm. 115 (1995) 161–166.

[14] X. Zhan, J. Jiang, S. Liu, G. Yin, Computer-controlled heating system and new computation for reciprocal heating stability experiment, Int. J. Pharm. 115 (1995) 167–173.

[15] X. Zhan, G. Yin, L. Wang, B. Ma, Exponential heating in drug stability experiment and statistical evaluation of nonisothermal and isothermal prediction, J. Pharm. Sci. 86 (1997) 709–715.

Short communication

Determination of resveratrol and its sulfate and glucuronide metabolites in plasma by LC–MS/MS and their pharmacokinetics in dogs

Miguel Muzzio [a,*], Zhihua Huang [a], Shu-Chieh Hu [a], William D. Johnson [a], David L. McCormick [a], Izet M. Kapetanovic [b]

[a] *Life Sciences Group, IIT Research Institute, Chicago, IL 60616, USA*
[b] *Division of Cancer Prevention, National Cancer Institute, Bethesda, MD 20892, USA*

ARTICLE INFO

ABSTRACT

An analytical approach for the determination of *trans*-resveratrol (3,5,4′-trihydroxy-*trans*-stilbene) and its glucuronide and sulfate conjugates in dog plasma by LC–MS/MS (without enzymatic hydrolysis of the conjugates) was validated to support pre-clinical toxicological and pharmacological studies. The approach required two independent sample extractions and consequent instrument runs. Samples for resveratrol determination were prepared by protein precipitation with acetonitrile; acetonitrile–methanol was used instead for resveratrol metabolites. Chromatographic separation was performed using a C18 column (30 mm × 2.0 mm) at a flow rate of 0.25 mL/min. For resveratrol the mobile phase consisted of A: 5 mM ammonium acetate in water–isopropanol (98:2, v/v) and B: methanol–isopropanol (98:2, v/v) and for metabolites the mobile phase was modified as follows: A: 0.1% (v/v) formic acid in water and B: 0.1% (v/v) formic acid in acetonitrile. Total run time was 12 min for each run with retention times of about 4–5 min for all analytes. A turbo ion spray source was used operating in negative mode for resveratrol and resveratrol sulfate and in positive mode for resveratrol glucuronide. Calibration curves were linear from 5 to 1000 ng/mL for resveratrol and its glucuronide, and 10–2000 ng/mL for resveratrol sulfate. Linearity was assessed using the internal standard method for resveratrol and the external standard method for the metabolites. Method accuracy was 90–112% of the true value for all analytes with precision of 9% RSD or less for all validation experiments. The validated method was applied to a preclinical toxicology study in dogs after oral administration (200–1200 mg/kg) of the agent. Peak plasma resveratrol concentration (C_{max}) for most animals was observed within 1–5 h of dosing, with group mean values in the 1.7–9.9 μg/mL (7.5–43 μM) range. Area under the plasma concentration–time curve (AUC) mean values for resveratrol ranged from 3.6 to 44 h μg/mL for all study groups and were generally proportional to the dose, with no consistent statistically significant changes observed for gender or number of doses. Mean molecular-weight adjusted ratios of resveratrol metabolites to resveratrol for AUC ranged from 1 to 9 for resveratrol glucuronide and from 2 to 11 for resveratrol sulfate.

1. Introduction

The polyphenolic natural product *trans*-resveratrol (5-[(*E*)-2-(4-hydroxyphenyl)ethenyl]benzene-1,3-diol; Fig. 1; referred to hereafter as resveratrol), found in grapes, berries, peanuts and other foodstuffs, continues to be the subject of numerous studies probing into its diverse properties and potential health benefits. Literature about its varied biological activity derived from in vivo and in vitro studies and about its potential as a disease-preventing agent is extensive and includes cancer prevention, cardioprotection and life span prolongation [1–7]. However, in spite of the large volume of published research, complete understanding of resveratrol's fundamental properties as a therapeutic remains elusive [8–10]. For example, resveratrol's health benefits when ingested in the diet, the efficacy of supplementation for disease prevention, and its therapeutic window and toxicity at the high doses proposed as necessary for beneficial effects have yet to be fully researched.

Resveratrol's low oral bioavailability and fast first-pass metabolism have been reported in species including human, mouse, rat, rabbit and pig [11–16]. Specifically, oral bioavailability was reported as 1.5% in rabbit [15] and up to 30% in rat [13]. In human studies, resveratrol plasma levels have been reported at below the limit of quantitation or low levels after oral administration of the agent [17]. Although metabolic profiles may differ, all species have in common an acceptable absorption after oral administration followed by fast conversion of the agent to glucuronide and sulfate metabolites, with plasma levels of the metabolites
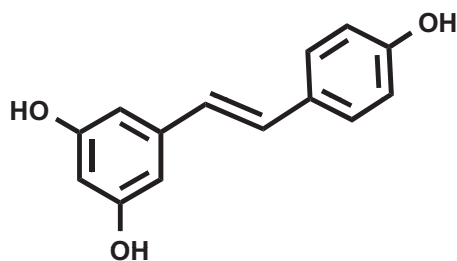
Fig. 1. Chemical structure of resveratrol.

larger than those of the parent compound. Whether the prevalent metabolites are biologically active [8,18,19] or serve as a systemic repository of the agent through, for example, enterohepatic recirculation [14] is not completely understood. It is therefore apparent that the complete assessment of resveratrol's potential as a therapeutic should include not only the agent's pharmacokinetics but that of its prevalent conjugate metabolites as well.

A number of references are available with validated methods for the determination of resveratrol in plasma from multiple species [14,20–25]. Additionally, resveratrol metabolite identification following oral administration of the agent has been performed for multiple species, with results consistently identifying mono-glucuronides and mono-sulfates as two of the prevalent metabolites [13,14,20,26,27]. Published methodologies for the determination of resveratrol metabolites in plasma and tissues include HPLC with UV detection [11,20,21,28,29] and tandem mass spectrometry [14,30]. With few exceptions [28,29], in these earlier methods enzymatic hydrolysis of the conjugates and indirect determination from the increases observed in the concentration of resveratrol were necessary to estimate the degree of Phase II metabolism. HPLC methods are long, approximately 25 min per run, and sample preparation is demanding, often requiring solid phase extraction (SPE) to purify the extracts and remove interferences. The indirect approach using LC–MS/MS with selective hydrolysis requires three separate extractions and its accuracy depends heavily on the selectivity of the enzymatic hydrolysis and the extent to which the reaction is carried out. A direct determination approach for resveratrol mono-sulfate by LC–MS/MS was published earlier; however, resveratrol mono-glucuronide concentrations were estimated using the parent compound calibration curve and method validation results were not provided [26].

In this work, we present a fully validated LC–MS/MS analytical approach for the determination of resveratrol and of resveratrol glucuronide and resveratrol sulfate without previous enzymatic hydrolysis to free resveratrol. The chromatographic separation of resveratrol is based on an HPLC method published earlier [20] and optimized here for throughput and performance using tandem mass spectrometry detection. This modified approach was first validated for resveratrol and later validated for the direct determination of resveratrol mono-glucuronide and mono-sulfate metabolites after additional modifications using a separate protein precipitation sample preparation and instrumental analysis. The approach was applied to examine the pharmacokinetics of resveratrol, resveratrol glucuronide and resveratrol sulfate in dogs after a 13 week oral administration of resveratrol, a study that was performed as part of the preclinical investigation of resveratrol as a candidate chemopreventive agent by the US National Cancer Institute.

2. Experimental

2.1. Chemicals and reagents

Resveratrol (Sochinaz SA, Vionnaz, Switzerland) was provided by the Division of Cancer Prevention, National Cancer

Institute (Bethesda, MD, USA). *trans*-Resveratrol-3-O-β-D-glucuronide (Toronto Research Chemicals, Inc., North York, Ontario, Canada) and *trans*-resveratrol-3-O-sulfate (SynFine Research, Inc., Richmond Hill, Ontario, Canada) were used as reference standards for the determination of conjugated resveratrol. *trans*-Resveratrol-$^{13}C_6$ (Toronto Research Chemicals, Inc.) was used as the internal standard for the determination of resveratrol. Acetonitrile, methanol, isopropanol, ammonium acetate and formic acid (all HPLC grade) were purchased from Fisher Scientific (Pittsburgh, PA, USA). HPLC-grade water was generated using a PURELAB Ultra system from ELGA (Lowell, MA, USA) followed by filtration with a Millipore (Billerica, MA, USA) 0.25 μm filter. Blank dog plasma was obtained from Bioreclamation Inc. (Westbury, NY, USA).

2.2. Animals

Twenty male and twenty female healthy naive beagle dogs (approximately five months old; Ridglan Farms, Inc., Mount Horeb, WI, USA) were held in quarantine for approximately 4 weeks and observed daily for survival and general health status. Prior to randomization into experimental groups, each animal underwent a detailed physical examination to ensure suitability as a test animal. Dogs were housed individually in pens in accordance with standard protocols [31]. Animal rooms were held within a temperature range of approximately 20–25 °C and a humidity range of approximately 30–70%. Fluorescent lighting in the animal rooms was provided on a cycle of 12 h of light followed by 12 h of darkness. Each dog was provided with 400 g of commercial chow (Certified Canine Diet 2021C, Harlan Teklad, Madison, WI, USA) daily for a minimum of 2 h during the treatment period. Drinking water was available *ad libitum* by automatic watering systems.

2.3. Preparation of analytical stock and standards solutions

Stock solutions of resveratrol, *trans*-resveratrol-$^{13}C_6$, resveratrol-3-O-β-D-glucuronide and resveratrol-3-O-sulfate were prepared in methanol at 1, 0.1, 0.2 and 0.4 mg/mL concentrations, respectively, and stored at −20 °C when not in use. Stock standards were prepared by further diluting the stock solutions in methanol–water (50:50, v/v) to 50, 100, 200, 500, 2000, 5000 and 10,000 ng/mL for resveratrol and its glucuronide, and to 100, 200, 400, 1000, 2000, 4000, 10,000 and 20,000 ng/mL for resveratrol sulfate. The internal standard working solution was prepared by diluting the stock solution with acetonitrile to a concentration of 25 ng/mL.

2.4. Extractions

Plasma samples (100 μL) were transferred to 2-mL microcentrifuge plastic vials (placed in ice and protected from light) and mixed with 10 μL of stock standards (for plasma calibrators and QC samples) and 1 mL of internal standard solution in acetonitrile. The samples were vortex-mixed for 1 min, centrifuged at 4 °C in a Sorvall RC 5C Super Speed centrifuge (Thermo Fisher Scientific, Waltham, MA, USA) at 8000 × g for 10 min to remove precipitated proteins, and the supernatant was transferred to a clean tube and dried under nitrogen flow at room temperature (about 25 °C). After evaporation was complete, the residue was reconstituted in 100 μL of methanol with five min of sonication, added to 400 μL of water, vortex-mixed and centrifuged again. The resulting supernatant was transferred to a sample vial for instrumental analysis. For the determination of conjugated resveratrol metabolites, the protein precipitation procedure was performed instead with 1 mL of acetonitrile–methanol (1:1, v/v) solution. All other steps were the same.

2.5. Instrumentation

Samples were analyzed on an API 3000 MS/MS system (Applied Biosystems/MDS Sciex, Foster City, CA, USA) equipped with an Agilent 1100 HPLC (Agilent Technologies, Wilmington, DE, USA) and run by Analyst^{TM} 1.4.2 software.

Separation of resveratrol from plasma components was achieved using a Luna 3 μm C18(2) 100 Å 30 mm × 2.0 mm column (Phenomenex, Torrance, CA, USA). The column was maintained at room temperature, the flow rate was 0.25 mL/min, and the injection volume was 25 μL. For the resveratrol determination method, the mobile phase consisted of A: 5 mM ammonium acetate in water–isopropanol (98:2, v/v) and B: methanol–isopropanol (98:2, v/v). The mobile phase gradient was as follows: after injection, initial conditions with Solvent A at 90% were held for 0.5 min, decreased to 5% in 3.5 min and held constant for 5 min, returning to initial conditions for another 3 min of reequilibration time. The mobile phase was changed for the analysis of resveratrol metabolites as follows: A: 0.1% (v/v) formic acid in water and B: 0.1% (v/v) formic acid in acetonitrile. All other chromatographic conditions were the same.

Retention times of resveratrol, resveratrol glucuronide and resveratrol sulfate were approximately 5.2, 4.0 and 4.9 min, respectively. Total run time was 12 min for each analytical run.

A turbo ion spray interface was used as the ion source, operating in negative ion mode for the resveratrol determination and with polarity switch for the metabolites determination (negative ion mode for resveratrol sulfate and positive mode for resveratrol glucuronide). Acquisition was performed in multiple reaction monitoring (MRM) mode using m/z 227 ($[M-H]^-$) → 185 (loss of 42 (C_2H_2O)) [32]; 233 ($[M-H]^-$) → 191 (loss of 42 (C_2H_2O)); 405 ($[M+H]^+$) → 229 (resveratrol, $[M+H]^+$); and 307 ($[M-H]^-$) → 227 (resveratrol, $[M-H]^-$) at unit resolution for resveratrol, resveratrol-$^{13}C_6$, resveratrol glucuronide and resveratrol sulfate, respectively. Ion spray voltage and collision energy were −3000 and −30 V, 4500 and 24 V, and −4500 and −24 V for resveratrol, resveratrol glucuronide and resveratrol sulfate, respectively. The collision gas was nitrogen; the ion spray temperature was 450 °C; and dwell time was 200 ms.

2.6. Method validation

Method validation was performed following the FDA's *Guidance for Industry: Bioanalytical Method Validation* [33]. Selectivity, linearity, precision, accuracy, recovery and stability were used to assess assay performance.

Selectivity was assessed by analyzing extract from six individual animals for the presence of analytical interferences and comparing the results to those obtained from spiking blank plasma sources with the analytes at the lowest limit of quantitation (LLOQ; 5 ng/mL for resveratrol and resveratrol glucuronide, 10 ng/mL for resveratrol sulfate).

Linearity was assessed using the internal standard method for resveratrol and the external standard method for its conjugated metabolites and up to eight calibrators prepared with blank dog plasma and analyte concentrations in the 5–1000 ng/mL (resveratrol and its glucuronide) and 10–2000 ng/mL (resveratrol sulfate) ranges. Curves were built from peak area ratios to the internal standard (resveratrol) or peak areas (resveratrol metabolites) using least-squares linear regression with a ($1/x^2$) weighting factor that was chosen based on goodness-of-fit criteria, including coefficient of determination (r^2), the back-calculated concentration of individual calibrators, and minimization of the intercept value.

Precision and accuracy were determined from three validation runs with dog plasma quality control (QC) samples ($n = 6$) spiked at the LLOQ (5 ng/mL) and at low (12 ng/mL), mid (400 ng/mL)

and high (800 ng/mL) concentrations for resveratrol and its glucuronide and corresponding concentrations of 10, 24, 800 and 1600 ng/mL, respectively, for resveratrol sulfate. Within-run precision and accuracy were assessed from the results from a single day, while between-run precision and accuracy were determined from the results from the three validation runs on different days.

Dog plasma extraction recovery of resveratrol and metabolites was determined by comparison of peak area results of dog plasma QC samples ($n = 6$) to peak area results of extracted blank dog plasma samples spiked post extraction with analyte concentrations at the same levels. For matrix effect evaluation, the peak areas were also compared to those from the corresponding standards prepared in the reconstitution solvent.

Bench-top stability was determined by analyzing low and high level QC samples for the analyte concentrations after 4 and 24 h of storage at ambient temperature and comparing the results to those obtained from freshly prepared samples. The 24 h stability experiment was repeated for resveratrol under refrigerated conditions (approximately 4 °C). Similar experiments were performed for the long-term stability evaluation of the analytes in dog plasma after 50 days storage at −70 °C. Freeze–thaw stability of the low and high level QC samples was determined at −70 °C and over three cycles. Stability was also determined for low and high level QC samples that were extracted and stored in the instrument autosampler under refrigerated conditions (approximately 4 °C); sample extracts were injected on the LC–MS/MS instrument and the concentrations determined after approximately 6 days of storage using freshly prepared calibrators.

To evaluate the impact of sample dilution on the method's accuracy and precision, six replicate QC samples were prepared in blank dog plasma at 4000 ng/mL (resveratrol and its glucuronide) and 8000 ng/mL (resveratrol sulfate) and diluted 5-fold with additional blank plasma prior to analysis.

2.7. Application to a pre-clinical toxicological study

Resveratrol was administered to beagle dogs to evaluate the toxicity and pharmacokinetics of the agent following daily oral administration for 91 consecutive days. Animals were randomly assigned to a control or one of three treatment groups at the end of the quarantine period using a computerized body weight stratification procedure that produced similar group mean body weight values. Body weights for the animals assigned to the study ranged from 5 to 10 kg. The study groups, each consisting of four male and four female dogs, received capsules with neat doses of resveratrol at 0, 200, 600 and 1200 mg/kg (control, low, mid and high groups, respectively).

Blood samples for determination of plasma levels of resveratrol, resveratrol glucuronide and resveratrol sulfate were collected from all treated animals after the first dose and during the last week (week 13) of the study. Blood samples (approximately 3 mL) were collected from the jugular or cephalic vein into Vacutainer tubes (Fisher Scientific, Pittsburgh, PA, USA) containing EDTA at 9 time points (0, 0.25, 0.5, 1, 2, 4, 8, 12 and 24 h post-dose). Tubes were inverted several times to mix; placed on ice until centrifuged to separate plasma (within 1 h); transferred into storage tubes (0.5 mL); and stored frozen (approximately −70 °C) until analyzed.

2.8. Pharmacokinetics analysis

Plasma concentration–time profiles of resveratrol, resveratrol glucuronide and resveratrol sulfate for individual animals were analyzed using a noncompartmental model for extravascular administration with WinNonlin® Professional Edition software, Version 5.0.1 (Pharsight Corporation, Mountain View, CA, USA). Pharmacokinetic parameters reported for all target
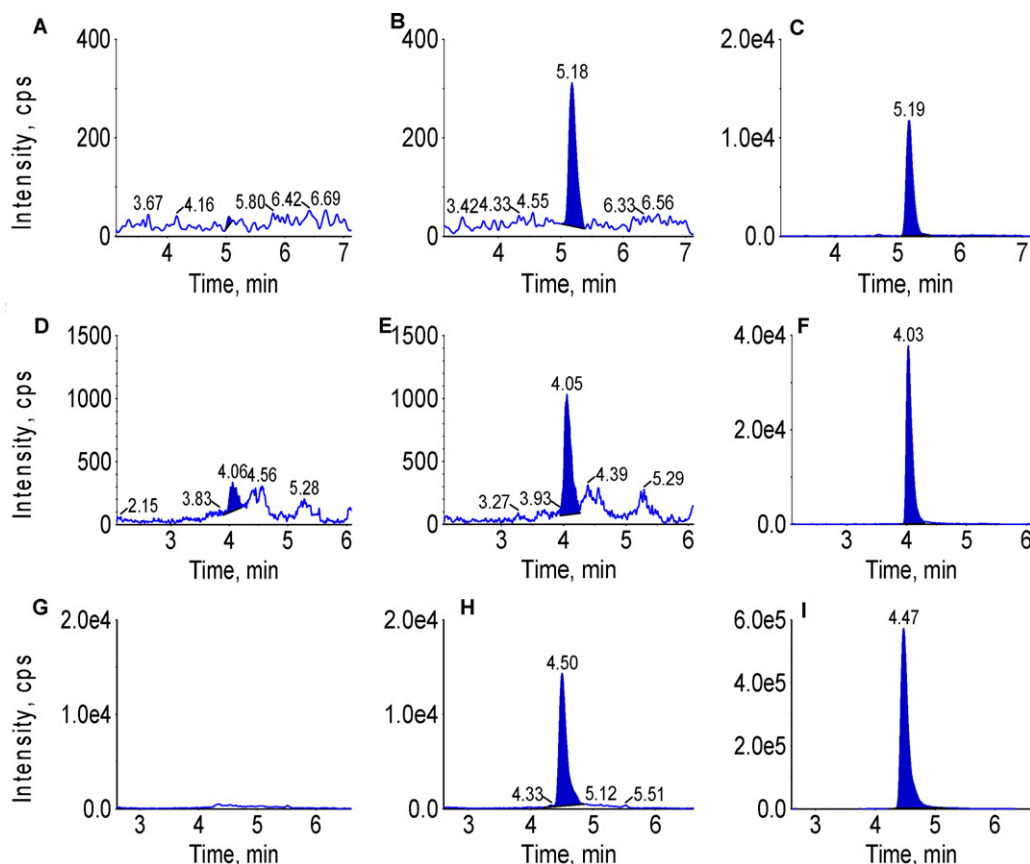
Fig. 2. (A) Resveratrol – blank dog plasma; (B) resveratrol – calibrator at the LLOQ (5 ng/mL) in dog plasma; (C) resveratrol – calibrator at 200 ng/mL in dog plasma; (D) resveratrol glucuronide – blank dog plasma; (E) resveratrol glucuronide – calibrator at the LLOQ (5 ng/mL) in dog plasma; (F) resveratrol glucuronide – calibrator at 200 ng/mL in dog plasma; (G) resveratrol sulfate – blank dog plasma; (H) resveratrol sulfate – calibrator at the LLOQ (10 ng/mL) in dog plasma; (I) resveratrol sulfate – calibrator at 400 ng/mL in dog plasma.

analytes included: time to maximum plasma concentration (T_{max}), peak plasma concentration (C_{max}), area under the plasma concentration–time curve (AUC), and elimination half-life ($t_{1/2}$). Clearance (CL/F) and apparent volume of distribution (V_z/F) were calculated only for resveratrol. AUC from time zero to the last measured concentration (AUC_{0-t}) was estimated by the linear trapezoidal rule up to C_{max}, followed by the log trapezoidal rule for the remainder of the curve. AUC extrapolated to infinity ($AUC_{0-\infty}$) is defined as $AUC_{0-t} + C_t/\lambda_z$, where λ_z is the disposition rate constant estimated using log-linear regression during the terminal elimination phase and C_t is the last measureable plasma concentration.

Statistical comparisons of the data to assess changes due to dose level, gender, or study day were performed using Systat software (Version 10.2). Data was analyzed via analysis of variance (ANOVA) followed, as necessary, by the *post hoc* Tukey's test (inter-group comparison) or via *t*-test (Day 1 vs. Week 13 and male vs. female); $p \leq 0.05$ (all comparisons); data was log-transformed (with the exception of $t_{1/2}$ and T_{max}); C_{max} and AUC parameters were normalized to the body surface area dose (i.e., mg resveratrol/m^2) prior to log-transformation [34].

3. Method validation results

3.1. Specificity

No significant peaks interfering with the quantitation of resveratrol and metabolites were detected in the chromatograms of blank dog plasma at the method's LLOQ for the three analytes. Fig. 2 shows representative chromatograms of blank dog plasma extract, LLOQ

(5 ng/mL or 10 ng/mL for resveratrol sulfate), and a 200 ng/mL calibrator (400 ng/mL for resveratrol sulfate) in dog plasma for each of the analytes.

3.2. Calibration curves

Calibration curves were linear from 5 to 1000 ng/mL (resveratrol and glucuronide) and 10 to 2000 ng/mL (resveratrol sulfate). Calibrators that fell outside the range of 85–115% were not used to calculate the standard curve (two instances for the 200 ng/mL calibrator for resveratrol glucuronide). Mean r^2 values were 0.995 or greater for all analytes. Representative regression equations for the calibration curves were $y = 0.0365x + 0.0031$, $y = 1780x + 876$ and $y = 6340x + 1380$ for resveratrol, resveratrol glucuronide and resveratrol sulfate, respectively. The mean accuracy (% of true value) of individual calibrators used to determine the calibration curves ranged from 97 to 103%, 93 to 112% (106% without the 200 ng/mL calibrator), and 97 to 108% of the true value for resveratrol, resveratrol glucuronide and resveratrol sulfate, respectively. Between-run precision [% relative standard deviation (RSD)] for the back-calculated calibrator concentrations ranged from 1 to 8% for the three analytes.

3.3. Precision and accuracy

Precision and accuracy experiment results are presented in Table 1. For all QC samples and analytes the method precision was 9% RSD or less. Accuracy was within 15% of the true value for all determinations.

Table 1
Within-run and between-run precision and accuracy for QC dog plasma samples.

Nominal concentration[a] (ng/mL)	Method precision and accuracy (%)[b,c]		
	Resveratrol	Resveratrol glucuronide	Resveratrol sulfate
5 or 10 (LLOQ)			
Within-run	98.2, 101, 105	103, 98.2, 109	100, 115, 109
% RSD	4.8, 6.2, 6.2	3.0, 5.8, 4.3	3.8, 3.5, 3.3
Between-run	101	103	108
% RSD	6.1	6.0	6.8
12 or 24 (low QC)			
Within-run	91.9, 93.2, 98.5	97.4, 89.7, 96.5	92.9, 97.6, 95.5
% RSD	6.5, 2.7, 9.1	1.0, 1.9, 3.2	1.7, 3.1, 4.7
Between-run	94.3	94.5	95.1
% RSD	7.2	4.4	3.7
400 or 800 (mid QC)			
Within-run	101, 102, 105	112, 107, 111	108, 104, 105
% RSD	2.5, 1.7, 5.8	1.8, 1.7, 4.1	2.4, 5.4, 1.4
Between-run	102	110	106
%RSD	4.0	3.3	3.6
800 or 1600 (high QC)			
Within-run	104, 103, 106	109, 105, 112	110, 106, 102
% RSD	4.3, 2.3, 6.9	1.3, 3.6, 5.2	1.7, 5.0, 4.5
Between-run	104	109	106
% RSD	4.8	4.3	4.7

[a] QC dog plasma samples were prepared at 5, 12, 400 and 800 ng/mL for resveratrol and its glucuronide and 10, 24, 800 and 1600 ng/mL for resveratrol sulfate.
[b] For all experiments, the number of QC samples (*n*) was 6 and 18 for individual validation runs (within-run) and between-run, respectively.
[c] Accuracy expressed as % of true value, precision as % relative standard deviation (RSD).

3.4. Recovery

Average recovery for the low, mid and high QC replicate samples was 95%, 98% and 90%; 74%, 77% and 73%; and 83%, 81% and 78% for resveratrol, resveratrol glucuronide, and resveratrol sulfate, respectively. Precision ranged from 4% to 7%, 2% to 9% and 3% to 9% RSD for resveratrol, resveratrol glucuronide, and resveratrol sulfate, respectively. Comparison of the peak areas of the above experiments to those from the analytes in the reconstitution solvent did not show any significant matrix ion suppression.

3.5. Lower limit of quantitation

Results for the LLOQ determination experiments are included in Table 1. For samples prepared at the LLOQ, method precision was 7% RSD or less for all analytes. Accuracy was within 15% of the true value for all determinations.

3.6. Stability studies

The experiments designed to evaluate the bench-top stability of the target analytes in dog plasma after 4 or 24 h at room temperature had recoveries within ±10% of their nominal concentration for all analytes and concentrations, with the exception of resveratrol after 24 h (the low and high QC samples degraded to 65 and 49%, respectively, of their initial concentrations) and resveratrol glucuronide (high QC, 4 h time period, 113% recovery). Recovery of resveratrol in dog plasma improved under refrigerated conditions, at 96 and 95%, respectively, of the initial concentrations for the low and high QC samples after 24 h. The changes after three freeze–thaw cycles for the low and high QC samples were within ±10% of their nominal concentrations. The changes after six days of storage of the QC sample extracts in the instrument refrigerated autosampler were within ±10% of their nominal concentrations. No degradation was observed for resveratrol or metabolites in dog plasma after 50 days storage at −70 °C.

Table 2
Stability assessment in dog plasma and dog plasma extracts.

Nominal concentration[a] (ng/mL) – time	Mean measured (SD) recovery (% of true value)		
	Resveratrol	Resveratrol glucuronide	Resveratrol sulfate
Plasma bench-top stability (room temperature)			
12 or 24 – 4 h	92.4 (2.6)	98.5 (1.8)	96.3 (6.6)
12 or 24 – 24 h	65.1 (4.4)	94.1 (1.6)	102 (5.6)
800 or 1600 – 4 h	93.9 (3.3)	113 (2.2)	92.3 (3.4)
800 or 1600 – 24 h	49.0 (2.9)	106 (1.7)	95.2 (2.8)
Plasma refrigerated stability (4 °C)			
12 or 24 – 24 h	95.5 (1.0)	–[b]	–[b]
800 or 1600 – 24 h	95.2 (2.2)	–[b]	–[b]
Plasma freeze–thaw stability (3 cycles)[c]			
12 or 24	97.6 (10)	109 (1.5)	99.9 (6.0)
800 or 1600	102 (3.4)	105 (2.7)	90.7 (8.0)
Plasma extract autosampler stability (4 °C)			
12 or 24 – 6 days	103 (9.3)	99.4 (5.8)	102 (12)
800 or 1600 – 6 days	106 (4.4)	95.4 (4.6)	97.9 (1.8)
Plasma long term stability (−70 °C)			
12 or 24 – 50 days	101 (17)	100 (2.0)	105 (15)
800 or 1600 – 50 days	100 (2.9)	105 (16)	107 (2.7)

[a] QC dog plasma samples (*n* = 6) prepared at 12 and 800 ng/mL for resveratrol and its glucuronide and 24 and 1600 ng/mL for resveratrol sulfate.
[b] Experiment not performed for the indicated target analyte.
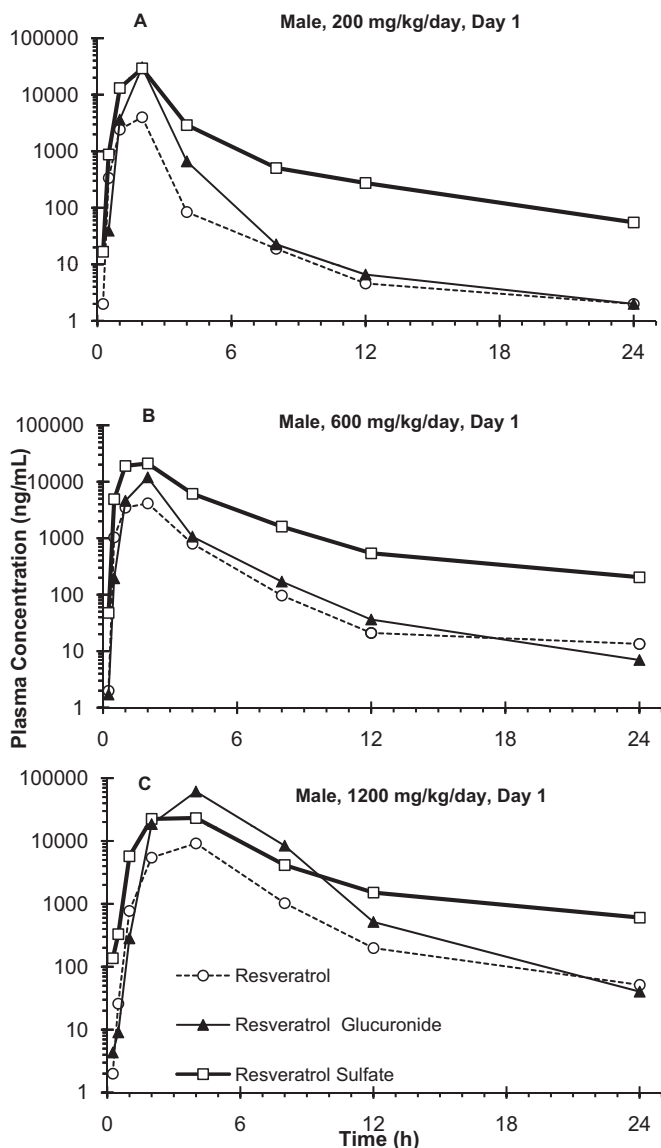[c] Plasma samples were kept frozen at −70 °C.

Fig. 3. Representative plasma concentration–time curve for resveratrol, resveratrol glucuronide and resveratrol sulfate: (A) male dog, 200 mg/kg/day group, Day 1; (B) male dog, 600 mg/kg/day group, Day 1; (C) male dog; 1200 mg/kg/day group, Day 1.

Results for all stability experiments performed are presented in Table 2.

3.7. Sample dilution

For the 6-replicate set of QC dog plasma samples prepared at 4000 or 8000 ng/mL and diluted 5-fold before analysis, accuracy was 98.3, 101 and 106% of the target value, with a precision of 2, 3 and 1% RSD for resveratrol, resveratrol glucuronide and resveratrol sulfate, respectively.

4. Pharmacokinetics results

Representative individual animal plasma concentrations (ng/mL) of resveratrol and its metabolites are presented graphically for males and females from the low, mid and high dosing groups in Fig. 3A–C, respectively. Group mean value ranges for resveratrol, resveratrol glucuronide and resveratrol sulfate are summarized in Table 3.

4.1. Resveratrol results

Following oral administration, C_{max} for most animals was observed within 1–5 h of dosing; with group mean values in the 1.7–9.9 µg/mL (7.5–43 µM) range. Statistical comparisons indicated proportional increases with the dose; however, no other consistent statistically significant changes were observed. Although T_{max} appeared to shift to larger values with the dose, no consistent statistically significant changes were observed related to dose, gender, or study day. Mean $t_{1/2}$ values for the different study groups were similar (ranging from 2 to 4 h). No statistically significant changes were observed for $t_{1/2}$ related to dose level, gender, or study day. AUC mean values ranged from 3.6 to 44 h µg/mL for all study groups and were proportional to the dose. V_z/F mean values ranged from 120 to 440 L/kg; CL/F mean values ranged from 22 to 110 L/h/kg. No consistent statistically significant changes were observed for V_z/F or CL/F.

4.2. Metabolites results

Resveratrol metabolized rapidly to resveratrol glucuronide and resveratrol sulfate, producing similar plasma concentration time profiles; no significant changes were apparent for T_{max} between resveratrol and its metabolites.

Resveratrol glucuronide: T_{max} mean values (2–7 h) were similar to those observed for resveratrol and also appeared to increase with the dose. Mean C_{max} values were in the 3.8–210 µg/mL range and statistical comparisons indicated proportional increases with the dose. Mean $t_{1/2}$ values were comparable to those for resveratrol and did not change significantly among the study groups. AUC mean values ranged from 7.2 to 560 h µg/mL for all study groups and were mostly proportional to the dose.

Resveratrol sulfate: T_{max} mean values for resveratrol sulfate were similar to those observed for resveratrol. Mean C_{max} values were in the 17–30 µg/mL range and did not change significantly among the study groups. Mean $t_{1/2}$ values ranged from 4 to 9 h and were, in general, larger than those for resveratrol. AUC mean values ranged from 40 to 170 h µg/mL for all study groups and although in general they increased with the dose, the changes were not proportional for Day 1 and less apparent for Week 13.

Mean molecular-weight adjusted ratios of resveratrol metabolites to resveratrol for AUC ranged from 1 to 9 for resveratrol glucuronide and from 2 to 11 for resveratrol sulfate. Although the AUC ratio for resveratrol glucuronide appeared to increase with the dose, the changes were not statistically significant. The statistical comparisons for resveratrol sulfate AUC ratios indicated a general decrease with the dose.

5. Discussion and conclusions

5.1. Method development

Initial attempts in our laboratory to use the resveratrol plasma extraction and chromatographic conditions for the conjugated metabolites analysis were unsuccessful due to poor reproducibility. Recovery for resveratrol sulfate improved from about 45% to approximately 75% with the use of acetonitrile–methanol for the extractions; although still not optimal, this proved consistent and reproducible. In addition, we found better method performance for resveratrol glucuronide with the mass spectrometer operating in positive mode and with the addition of formic acid in the mobile phase. A reference standard for resveratrol di-sulfate, another conjugated metabolite found in multiple species, was not commercially available at the time of the study, thus the method could not be validated for this metabolite.

Table 3
Summary of pharmacokinetic results – group mean value ranges.

Resveratrol dose (mg/kg/day)	$t_{1/2}$ (h)	T_{max} (h)	C_{max} (µg/mL)	AUC[a] (h µg/mL)	AUC ratio[b]	V_z/F[c] (L/kg)	CL/F[c] (L/h/kg)
Resveratrol							
200	2–4	1–2	1.7–2.6	3.6–5.0	1	120–280	41–58
600	3–4	3–4	3.7–9.0	13–30	1	120–300	22–51
1200	3–4	3–5	5.1–9.9	21–44	1	130–440	28–110
Resveratrol glucuronide							
200	1–5	2–3	3.8–12	7.2–17	1–2	–	–
600	2–3	2–5	19–110	48–260	2–5	–	–
1200	2–3	4–7	40–210	160–560	3–9	–	–
Resveratrol sulfate							
200	4–8	2–3	17–23	40–58	8–11	–	–
600	4–7	2–3	20–28	83–120	2–7	–	–
1200	4–9	2–5	18–30	76–170	2–4	–	–

[a] AUC, $AUC_{0-\infty}$ for Day 1 and AUC_{0-24h} for Week 13.
[b] AUC ratio was calculated as $(AUC/MW)_{metabolite}/(AUC/MW)_{resveratrol}$, where MW = molecular weight: 228, 404 and 308 for resveratrol, resveratrol glucuronide and resveratrol sulfate, respectively.
[c] V_z/F and CL/F were not determined for resveratrol metabolites.

5.2. Assay performance

As presented, the determination of resveratrol and target metabolites required two independent sample extractions and consequent instrument runs. Although the approach worked acceptably, the assay throughput could be substantially improved by combining the sample preparation and instrumental analysis into a single method for all analytes; in our work we could not find the right analysis conditions to achieve this. The utilization of deuterated analogs of the Phase II metabolites as internal standards, not commercially available at the time of the study, could further improve the method's performance. Additionally, if resveratrol di-sulfate reference material were to become available, the method could also be validated for its determination.

5.3. Pharmacokinetics of resveratrol in dogs

The plasma concentration individual results and concomitant concentration–time profiles for this study contained several irregularities based on expected pharmacokinetics. Some animals showed occasional delayed absorption, while others presented sudden increases in plasma concentrations approximately 8 h after oral administration, with significant prolongation of the terminal elimination half-life. This last observation is consistent with results from similar studies with resveratrol in other species and is attributed to enterohepatic recirculation [13,14]. The limited number of blood collection time points in the 8–24 h post-dose period for this study did not allow the modeling and estimation of the two apparent elimination phase rate constants believed to exist in the pharmacokinetic profile of resveratrol. Therefore, the pharmacokinetic parameters presented correspond to the estimation of the average elimination rate constant as permitted by the experimental data.

There were no consistent statistically significant changes in the C_{max} or AUC group mean values between Day 1 and Week 13 that would indicate evidence of induction or accumulation for either resveratrol or its metabolites. Similarly, statistical comparisons of C_{max} or AUC group mean values did not provide consistent evidence of differences among experimental groups due to gender.

For resveratrol and resveratrol glucuronide, statistical comparison of AUC data indicated proportional increases with the dose for Day 1; however, for Week 13 AUC increases lacked proportionality to the dose. For resveratrol sulfate, changes for AUC on Day 1 were not proportional to the dose increases, while at Week 13, AUC changes were proportional to the dose changes, with one exception [low vs. high (females)].

Statistical comparison of mean AUC resveratrol glucuronide values normalized to resveratrol AUC values did not provide evidence of differences for the study groups. However, similar statistical comparisons performed for resveratrol sulfate indicated significant decreases relative to resveratrol AUC values with the dose for both Day 1 and Week 13.

Details of the toxicological observations for this dog study are presented elsewhere [35].

5.4. Comparison of resveratrol pharmacokinetics in dog, human and rat studies

Resveratrol pharmacokinetic results from experiments with a single oral dose in humans at 42 and 83 mg/kg (1500 and 3100 mg/m^2; assuming 60 kg subjects) [36] and rats at 50 and 150 mg/kg (300 and 900 mg/m^2) [13] as compared to our dog study at 200–1200 mg/kg (4000–24,000 mg/m^2) are as follows:

Mean T_{max} values in human and rat groups were 1.5 and 1.0 h, respectively, which compares well with 1.8 and 1.1 h (male and female, respectively) for our 200 mg/kg dog dose group, although increased to 3–5 h for the higher dose groups. Dose-normalized C_{max} mean values were 6.4 and 6.5, 1.5 and 5.6, and 4.3–13 ng/mL kg/mg for human, rat and dog, respectively.
Mean $t_{1/2}$ values were 4.2 and 8.5 h for human, 12 and 3.6 h for rat and 1.9 and 3.8 h for dog.
Dose-normalized AUC mean values were 19 and 16, 27 and 17, and 20–37 h ng/mL kg/mg for human, rat and dog, respectively.
Mean AUC ratios of resveratrol glucuronide to resveratrol were 13 and 14 (sum of glucuronide isomers), 8.6 and 8.8, and 1.8 to 3.4 for human, rat and dog, respectively. Similarly, the AUC ratios for resveratrol sulfate were 22 and 23, 9.3 and 18, and 2.9 to 11 for human, rat and dog, respectively. Although comparable, these results seem to indicate more extensive conjugation of the agent in humans.

Acknowledgements

References

[1] J.A. Baur, D.A. Sinclair, Therapeutic potential of resveratrol: the in vivo evidence, Nat. Rev. Drug Discov. 5 (2006) 493–506.

[2] F. Brisdelli, G. D'Andrea, A. Bozzi, Resveratrol: a natural polyphenol with multiple chemopreventive properties, Curr. Drug Metab. 10 (2009) 530–546.

[3] D.K. Das, Resveratrol in cardioprotection: a therapeutic promise of alternative medicine, Mol. Interv. 6 (2006) 36–47.

[4] F.Z. Marques, M.A. Markus, B.J. Morris, Resveratrol: cellular actions of a potent natural chemical that confers a diversity of health benefits, Int. J. Biochem. Cell Biol. 41 (2009) 2125–2128.

[5] S. Pervaiz, A.L. Holme, Resveratrol: its biologic targets and functional activity, Antioxid. Redox Signal. 11 (2009) 2851–2897.

[6] J.M. Pezzuto, Resveratrol as an inhibitor of carcinogenesis, Pharm. Biol. 46 (2008) 443–573.

[7] L. Pirola, S. Frojdo, Resveratrol: one molecule, many targets, IUBMB Life 60 (2008) 323–332.

[8] L. Subramanian, S. Youssef, S. Bhattacharya, J. Kenealey, A.S. Polans, P.R. van Ginkel, Resveratrol: challenges in translation to the clinic—a critical discussion, Clin. Cancer Res. 16 (2010) 5942–5948.

[9] A.J. Gescher, W.P. Steward, Relationship between mechanisms, bioavailability, and preclinical chemopreventive efficacy of resveratrol: a conundrum, Cancer Epidemiol. Biomarkers Prev. 12 (2003) 953–957.

[10] E. Wenzel, V. Somoza, Metabolism and bioavailability of trans-resveratrol, Mol. Nutr. Food Res. 49 (2005) 472–481.

[11] T. Walle, F. Hsieh, M.H. DeLegge, J.E. Oatis Jr., U.K. Walle, High absorption but very low bioavailability of oral resveratrol in humans, Drug Metab. Dispos. 32 (2004) 1377–1382.

[12] S. Sale, R.D. Verschoyle, D. Boocock, D.J.L. Jones, N. Wisher, K.C. Ruparelia, G.A. Potter, P.B. Farmer, W.P. Steward, A.J. Gescher, Pharmacokinetics in mice and growth-inhibitory properties of the putative cancer chemopreventive agent resveratrol and the synthetic analogue trans-3,4,5,4′-tetramethoxystilbene, Br. J. Cancer 90 (2004) 736–744.

[13] I.M. Kapetanovic, M. Muzzio, Z. Huang, T.N. Thompson, D.L. McCormick, Pharmacokinetics, oral bioavailability, and metabolic profile of resveratrol and its dimethylether analog, pterostilbene, in rats, Cancer Chemother. Pharmacol. 68 (2011) 593–601.

[14] J.-F. Marier, P. Vachon, A. Gritsas, J. Zhang, J.-P. Moreau, M.P. Ducharme, Metabolism and disposition of resveratrol in rats: extent of absorption, glucuronidation, and enterohepatic recirculation evidenced by a linked-rat model, J. Pharmacol. Exp. Ther. 302 (2002) 369–373.

[15] M. Asensi, I. Medina, A. Ortega, J. Carretero, M.C. Baño, E. Obrador, J.M. Estrela, Inhibition of cancer growth by resveratrol is related to its low bioavailability, Free Radic. Biol. Med. 33 (2002) 387–398.

[16] M. Azorín-Ortuño, M.J. Yañes-Gascón, F.J. Pallarés, F. Vallejo, M. Larrosa, M.T. García-Conesa, F. Tomás-Barberán, J.C. Espín, Pharmacokinetic study of trans-resveratrol in adult pigs, J. Agric. Food Chem. 58 (2010) 11165–11171.

[17] C.-H. Cottart, V. Nivet-Antoine, C. Laguillier-Morizot, J.-L. Beaudeux, Resveratrol bioavailability and toxicity in humans, Mol. Nutr. Food Res. 54 (2010) 7–16.

[18] J. Hoshino, E.J. Park, T.P. Kondratyuk, L. Marler, J.M. Pezzuto, R.B. van Breemen, S. Mo, Y. Li, M. Cushman, Selective synthesis and biological evaluation of sulfate-conjugated resveratrol metabolites, J. Med. Chem. 53 (2010) 5033–5043.

[19] B. Calamini, K. Ratia, M.G. Malkowski, M. Cuendet, J.M. Pezzuto, B.D. Santarsiero, A.D. Mesecar, Pleiotropic mechanisms facilitated by resveratrol and its metabolites, Biochem. J. 429 (2010) 273–282.

[20] D.J. Boocock, K.R. Patel, G.E.S. Faust, D.P. Normolle, T.H. Marczylo, J.A. Crowell, D.E. Brenner, T.D. Booth, A. Gescher, W.P. Steward, Quantitation of trans-resveratrol and detection of its metabolites in human plasma and urine by high performance liquid chromatography, J. Chromatogr. B 848 (2007) 182–187.

[21] M.E. Juan, M. Maijó, J.M. Planas, Quantification of trans-resveratrol and its metabolites in rat plasma and tissues by HPLC, J. Pharm. Biomed. Anal. 51 (2010) 391–398.

[22] L. Almeida, M. Vaz-da-Silva, A. Falcão, E. Soares, R. Costa, A.I. Loureiro, C. Fernandes-Lopes, J.-F. Rocha, T. Nunes, L. Wright, P. Soares-da-Silva, Pharmacokinetic and safety profile of trans-resveratrol in a rising multiple-dose study in healthy volunteers, Mol. Nutr. Food Res. 53 (2009) S7–S15.

[23] M.E. Juan, R.M. Lamuela-Raventós, M.C. de la Torre-Boronat, J.M. Planas, Determination of trans-resveratrol in plasma by HPLC, Anal. Chem. 71 (1999) 747–750.

[24] X. Chen, H. He, G. Wang, B. Yang, W. Ren, L. Ma, Q. Yu, Stereospecific determination of cis- and trans-resveratrol in rat plasma by HPLC: application to pharmacokinetic studies, Biomed. Chromatogr. 21 (2007) 257–265.

[25] M. Urpí-Sardà, O. Jáuregui, R.M. Lamuela-Raventós, W. Jaeger, M. Miksits, M.I. Covas, C. Andres-Lacueva, Uptake of diet resveratrol into the human low-density lipoprotein. Identification and quantification of resveratrol metabolites by liquid chromatography coupled with tandem mass spectrometry, Anal. Chem. 77 (2005) 3144–3149.

[26] C. Yu, Y.G. Shin, A. Chow, Y. Li, J.W. Kosmeder, Y.S. Lee, W.H. Hirschelman, J.M. Pezzuto, R.G. Mehta, R.B. van Breemen, Human, rat, and mouse metabolism of resveratrol, Pharm. Res. 19 (2002) 1907–1914.

[27] A. Burkon, V. Somoza, Quantification of free and protein-bound trans-resveratrol metabolites and identification of trans-resveratrol-C/O-conjugated diglucuronides—two novel resveratrol metabolites in human plasma, Mol. Nutr. Food Res. 52 (2008) 549–557.

[28] E. Wenzel, T. Soldo, H. Erbersdobler, V. Somoza, Bioactivity and metabolism of trans-resveratrol orally administered to Wistar rats, Mol. Nutr. Food Res. 49 (2005) 482–494.

[29] K.R. Patel, V.A. Brown, D.J.L. Jones, R.G. Britton, D. Hemingway, A.S. Miller, K.P. West, T.D. Booth, M. Perloff, J.A. Crowell, D.E. Brenner, W.P. Steward, A.J. Gescher, K. Brown, Clinical pharmacology of resveratrol and its metabolites in colorectal cancer patients, Cancer Res. 70 (2010) 7392–7399.

[30] X. Liu, Z. Teng, Y. Zhang, M. Huan, S. Zhou, High performance liquid chromatography–tandem mass spectrometric determination of resveratrol and its metabolites in rat tissues, Anal. Lett. 43 (2010) 557–569.

[31] Guide for the Care and Use of Laboratory Animals (National Research Council, 1996) and U.S. Department of Agriculture Animal Welfare Standards (Title 9, Code of Federal Regulations, Part 3, 1991 Revision).

[32] D. Wang, T. Hang, C. Wu, W. Liu, Identification of the major metabolites of resveratrol in rat urine by HPLC–MS/MS, J. Chromatogr. B 829 (2005) 97–106.

[33] U.S. Department of Health and Human Services, Food and Drug Administration, Center for Drug Evaluation and Research (CDER), Center for Veterinary Medicine (CVM), May 2001.

[34] E.J. Freireich, E.A. Gehan, D.P. Rall, L.H. Schmidt, H.E. Skipper, Quantitative comparison to toxicity of anticancer agents in mouse, rat, hamster, dog, monkey and man, Cancer Chemother. Rep. 50 (1966) 219–244.

[35] W.D. Johnson, R.L. Morrissey, A.L. Usborne, I. Kapetanovic, J.A. Crowell, M. Muzzio, D.L. McCormick, Subchronic oral toxicity and cardiovascular safety pharmacology studies of resveratrol, a naturally occurring polyphenol with cancer preventive activity, Food Chem. Toxicol. (2011), doi:10.1016/j.fct.2011.08.023.

[36] D.J. Boocock, G.E.S. Faust, K.R. Patel, A.M. Schinas, V.A. Brown, M.P. Ducharme, T.D. Booth, J.A. Crowell, M. Perloff, A.J. Gescher, W.P. Steward, D.E. Brenner, Phase I dose escalation pharmacokinetic study in healthy volunteers of resveratrol, a potential cancer chemopreventive agent, Cancer Epidemiol. Biomarkers Prev. 16 (2007) 1246–1252.

QSRR models for potential local anaesthetic drugs using high performance liquid chromatography

Tatiana Durcekova[a], Katarina Boronova[a], Jan Mocak[a,*], Jozef Lehotay[a,b], Jozef Cizmarik[c]

[a] *Department of Chemistry, University of SS. Cyril and Methodius, J. Herdu 2, Trnava SK-91701, Slovak Republic*
[b] *Institute of Analytical Chemistry, Slovak University of Technology, Radlinskeho 9, Bratislava SK-81237, Slovak Republic*
[c] *Department of Pharmaceutical Chemistry, Comenius University, Odbojarov 10, Bratislava SK-83232, Slovak Republic*

ARTICLE INFO

ABSTRACT

Quantitative structure–retention relationships (QSRR) were proposed for Separon SGX C18 and Separon SGX Phenyl columns using physico-chemical molecular descriptors for the compounds, which are potential local anaesthetic drugs. Chemometrical methods were used for the QSRR studies of the HPLC retention factor k of 59 esters of alkoxyphenylcarbamic acid, which exhibit surface and/or infiltration anaesthetic activity. Four separation systems were used: phenyl column and acetonitrile/water mobile phase, phenyl column and methanol/water mobile phase, C18 column and acetonitrile/water mobile phase, and C18 column and methanol/water mobile phase. The values of $\log P$ and $\log S$ and ^{13}C and ^{1}H NMR chemical shifts were simulated and utilized in calculating the corresponding QSRR models and predicting the retention factors by artificial neural networks (ANN). In addition, principal component analysis and cluster analysis were used for a closer characterization of alkoxyphenylcarbamic acid esters. The proposed ANN models, based on optimally selected species descriptors, showed a high degree of correlation between k predicted and k measured. The intercepts and the slopes of the obtained dependences were close to the theoretically expected values of 0 and 1, respectively.

© 2011 Elsevier B.V. All rights reserved.

1. Introduction

Like quantitative structure–activity relationships (QSAR), the main advantage of quantitative structure–property relationships (QSPR) lies in the fact that once such a relationship is ascertained (with an adequate statistical degree of confidence) it can be of valuable assistance in the prognosis of the behaviour of new molecules, even before they are actually synthesized. Taking this advantage into account, pharmaceutical scientists have extended the QSPR concept to develop correlations with physico-chemical, pharmaceutical and organoleptic properties, such as solubility, stability, reactivity, drug release, retention (partition), permeability, transportability, pharmacokinetics, toxicity and mutagenicity [1].

The quantitative structure–retention relationships (QSRR) are relationships between chromatographic properties and the descriptors characterizing molecular structure of the investigated analytes. The retention is here modelled as a function of structural or molecular descriptors. Since the structural datasets can be very large, the selection of most informative variables is often required [2]. A very advantageous feature of QSRR is that it allows the prediction of retention data of novel, not yet synthesized compounds, solely from their structural descriptors [3,4].

The QSRR approach has been spread out and applied in many studies. Let us introduce some interesting recent articles. Quantitative relationships between the retention data describing biopartitioning and the selected pharmacodynamic parameters of local anaesthetics were obtained by micellar chromatography and micellar electrokinetic chromatography in [5]. The use of the experimental molecular descriptors and some possible alternatives were evaluated in the QSRR study of the peptides [6]. A similar study was performed in QSRR modelling of the peptides behaviour in reversed phase liquid chromatography and shown in [2]. The QSRR were also employed in the study of the retention behaviour of non-steroidal anti-inflammatory drugs in high-performance liquid chromatography [7]. QSRR study of β-blocking agents by micellar liquid chromatography revealed good correlations between $\log P$ and *in vitro* biological variables [8]. Despite the ever increasing usage of HPLC for the separation and analysis of various compounds, drugs, metabolites, etc., the selection of appropriate chromatographic conditions is still a tedious, time-consuming procedure, often performed by the trial and error approach. *A priori* knowledge of the retention time of a given solute simplifies the selection of working conditions. No wonder that the generally accepted task is to rationalize and predict retention data using available and interpretable descriptors [3]. The HPLC retention factor k is

---

usually well correlated with the lipophilicity parameter $\log P$ (for 1-octanol/water) and can be used as an alternative measure of lipophilicity [3].

In addition, the application of chromatographic parameters in structure–activity relationships gives rise to a new field, the quantitative retention–activity relationships (QRAR) [3,5].

Several chemometrical techniques have been frequently used in the QSAR or QSRR studies [9], mainly multiple linear regression [10], partial least-square (PLS) regression [2,11–13], artificial neural networks [14–17], principal component analysis [18–20] and cluster analysis [18,21,22]. The latter three techniques are complementarily used also in this work. QSRR studies are here applied to the derivatives of alkoxyphenylcarbamic acid esters, which have been hitherto proved as efficient potential local anaesthetics [23,24].

2. Materials and methods

2.1. HPLC retention data of drugs

A Hewlett–Packard HPLC system consisting of a pump with a degasser, a diode-array detector (DAD), a 20 µl injector and AGILENT Chem A1002 software was employed for chromatographic measurements of alkoxyphenylcarbamic acid esters. The retention factors of the studied compounds were determined isocratically on Separon SGX C18 and Separon SGX Phenyl columns 15 cm × 0.32 cm and particle size 5 µm. Two mobile phases were used: (1) acetonitrile (Merck, Germany)–water (80/20), (2) methanol (Merck, Germany)–water (80/20). The mobile phase flow-rate was 1.0 ml/min. The wavelengths in the range 210–290 nm were used. The compound sample weight 50 µg was dissolved in 1 cm³ of methanol, then a 20 µl of the final solution was injected onto the column. The observed retention factors were obtained from the retention time (t_r) and the dead-time (t_0) according to the usual relationship $k = (t_r - t_0)/t_0$. Four chromatographic systems were investigated: (a) phenyl stationary phase, mobile phase acetonitrile–water, (b) phenyl stationary phase, mobile phase methanol–water, (c) C18 stationary phase, mobile phase acetonitrile–water and (d) C18 stationary phase, mobile phase methanol–water; the corresponding designation of the retention factors is *kPhAcN*, *kPhMeOH*, *kC18AcN* and *kC18MeOH*, respectively.

2.2. Structural descriptors and target variables

The molecular structure of the compounds investigated in this paper and the corresponding retention factors are shown in Table 1.

The esters of alkoxyphenylcarbamic acid (EAPCA) were prepared in the way described by [23] and [24]. Four HPLC retention factors *kPhAcN*, *kPhMeOH*, *kC18AcN*, *kC18MeOH*, explained in Section 2.1, were used as the target variables. The following descriptors were employed as independent variables: (a) Nine 1-octanol/water partition coefficients $\log P$, calculated in various ways by ALOGPS 2.1 software – *ALOGPs*, *ACLogP*, *miLogP*, *ALOGP*, *MLOGP*, *KOWWIN*, *XLOGP2*, *XLOGP3*, *AvlogP* [25–27]. (b) Four physico-chemical properties – molar mass M and three differently calculated compound solubilities $\log S$ in water – *ALOGpS*, *ACLogS*, *AvlogS* [25–27]. (c) Eleven selected ¹³C NMR chemical shifts designed by the variable names according to the carbon numbers: *C1*, *C2*, *C3*, *C4*, *C5*, *C6*, *C8*, *C10*, *C11*, *C12*, and their mean *Call*, together with ten selected ¹H NMR chemical shifts designed as *H4*, *H5*, *H6*, *H7*, *H10*, *H11a*, *H11b*, *H12a*, *H12b*, and their mean *Hall*. Software package ACD Labs [28] was used for the NMR simulation; a good reliability of the obtained chemical shifts was confirmed by comparison to available experimentally measured values. (d) The length of the side alkoxy chain

represented by the corresponding number of carbon atoms n. (e) In addition, two independent categorical variables were used: the ester type *RType* and the position of the side alkoxy chain *Pno* (two possibilities – ortho and meta), as shown in Table 1.

3. Results and discussion

3.1. Correlation analysis

The performed correlation analysis shows the measure of all possible pair correlations of the studied variables expressed by the Spearman correlation coefficient, R, which is a robust substitute of more common Pearson correlation coefficient [29] and is advantageous due to its independence of the assumption on the error distribution. In this study, 35 continual variables (descriptors) were correlated mutually, but mainly to four target variables – the retention factors *kPhAcN*, *kPhMeOH*, *kC18AcN* and *kC18MeOH*. Due to a large number of originally exploited variables the correlation analysis was utilized for their reduction so that only the best of them were used in further studies. Therefore the reduced lists of variables were prepared from four calculated correlation tables, achieved under different separation conditions, which contains only the variables most correlated to the given retention factor k (Table 2). Since $\log P$ and $\log S$ were calculated in several ways, only the best correlated descriptors of these two quantities are present in the reduced lists.

The correlations are considered significant at two different two-tailed p-value levels: at $p < 0.05$ for the correlations with respect to *kC18AcN* and *kC18MeOH*, and at $p < 0.01$ regarding *kPhAcN* and *kPhMeOH* since in this case the correlations are weaker. It is evident from the reduced correlation tables in Table 2 that the list of most significant variables and their number are moderately different for any of four investigated chromatographic systems. Ten variables were found significantly correlated to *kPhAcN*, 13 variables were significantly correlated to *kPhMeOH*, 16 variables to *kC18AcN* and 14 variables to *kC18MeOH*. It is also evident that similar descriptors are detected among the lists of most correlated variables even though their exact order by the R-value is different – especially in case of the NMR chemical shifts.

3.2. Principal component analysis

Principal component analysis, PCA, is a linear multidimensional data analysis technique that finds the most efficient representation of the data variability [30–32]. PCA is usually employed as a tool to reduce the dimensionality of the investigated set of data, which may allow one to visualize a multivariable data more easily. PCA calculates the linear combinations of the original variables in the form of principal components PC1, PC2, etc., whose importance corresponds to the eigenvectors of the corresponding correlation matrix. In the PCA, the original data set is decomposed into the PC scores and loadings, which can be displayed together in a biplot. The PCs are constructed in such a way as to maximize the data variance. They are mutually orthogonal [33], i.e. mutually independent. In this work, the PCA was used to find the descriptors significantly related to the retention factors of four chromatographic systems. It was found by inspecting the positions of the variable rays in the PCA biplot (Fig. 1) that the variables mostly related to four retention factors are *ALOGPs* and *XLOGP2*, *M*, and NMR chemical shifts *C12* and *C10*. Due to their close position to the retention factors in the biplot, these relations are positive. A strong negative relation to the retention factor (and the opposite biplot position) exhibit NMR chemical shifts *H10*, *H11a*, *H11b*, *C11* and, partly, the solubility descriptors *ACLogS* and *ALOGpS*. Two groups of objects are observed in the biplot graph representing the meta- (at high PC2 values) and

Table 1
Chemical structure of investigated derivatives of alkoxyphenylcarbamic acid esters and their retention factors.
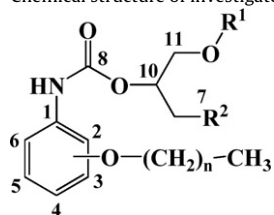
No.	R^1	R^2	P	n	kPhAcN	kPhMeOH	kC18AcN	kC18MeOH	No	R^1	R^2	P	n	kPhAcN	kPhMeOH	kC18AcN	kC18MeOH
1	CH_3	PP	o	2	0.833	1.492	1.188	1.470	31	CH_3	PP	m	2	0.800	1.367	0.933	1.201
2	CH_3	P	o	2	1.277	1.756	1.309	1.250	32	CH_3	PP	m	3	0.867	1.544	1.148	1.622
3	CH_3	PP	o	3	0.907	1.690	1.499	1.957	33	C_2H_5	P	m	3	1.316	1.992	1.258	1.957
4	CH_3	P	o	3	1.356	1.932	1.634	1.665	34	C_2H_5	PP	m	3	0.875	1.673	1.343	2.247
5	C_2H_5	PP	o	3	0.996	1.878	1.904	3.037	35	C_3H_7	P	m	3	1.154	2.015	1.705	2.226
6	C_3H_7	P	o	3	1.277	2.191	2.280	2.797	36	C_3H_7	PP	m	3	0.815	1.752	1.566	0.508
7	C_3H_7	PP	o	3	1.008	2.138	2.379	3.594	37	C_3H_7	A	m	3	1.074	2.370	2.326	4.288
8	C_3H_7	A	o	3	1.327	2.919	3.589	6.434	38	C_4H_9O	PP	m	3	0.837	1.812	1.295	2.126
9	C_4H_9O	PP	o	3	0.950	1.970	1.693	2.687	39	CH_3	PP	m	4	1.007	1.941	1.537	2.348
10	CH_3	PP	o	4	1.068	2.133	2.099	2.970	40	CH_3	P	m	4	1.530	2.424	1.692	1.976
11	CH_3	P	o	4	1.481	2.267	2.076	2.305	41	C_2H_5	P	m	4	1.449	2.284	1.800	2.616
12	C_2H_5	P	o	4	1.511	2.318	2.384	3.683	42	C_2H_5	PP	m	4	0.999	2.021	1.753	3.243
13	C_2H_5	PP	o	4	1.126	2.222	2.494	4.401	43	C_3H_7	P	m	4	1.300	2.423	2.236	3.116
14	C_2H_5	A	o	4	1.483	3.125	3.873	6.598	44	C_3H_7	PP	m	4	0.953	2.158	2.073	0.586
15	C_3H_7	P	o	4	1.449	2.589	2.921	3.942	45	C_3H_7	A	m	4	1.270	2.962	3.090	6.239
16	C_3H_7	PP	o	4	1.182	2.607	3.194	5.287	46	CH_3	P	m	5	1.714	2.895	2.215	2.768
17	CH_3	PP	o	5	1.225	2.546	2.769	4.250	47	CH_3	PP	m	5	1.149	2.322	2.073	3.445
18	C_2H_5	P	o	5	1.639	2.626	2.964	5.189	48	C_2H_5	P	m	5	1.659	2.754	2.382	3.982
19	C_2H_5	PP	o	5	1.298	2.746	3.271	6.345	49	C_2H_5	PP	m	5	1.125	2.381	2.248	4.673
20	C_2H_5	A	o	5	1.755	3.819	5.235	9.658	50	C_3H_7	P	m	5	1.520	2.984	2.831	4.507
21	C_3H_7	P	o	5	1.680	3.123	3.950	5.500	51	C_3H_7	PP	m	5	1.105	2.629	2.780	0.679
22	C_3H_7	PP	o	5	1.400	3.203	4.280	7.483	52	C_3H_7	A	m	5	1.562	3.622	4.127	9.192
23	C_3H_7	A	o	5	1.930	4.522	6.610	13.95	53	CH_3	PP	m	6	1.302	2.724	2.676	4.817
24	C_4H_9O	PP	o	5	1.228	2.870	3.003	5.651	54	CH_3	A	m	6	1.697	3.731	3.847	6.573
25	CH_3	P	o	6	1.904	3.271	3.810	4.543	55	C_2H_5	P	m	6	1.851	3.386	3.091	5.848
26	C_2H_5	P	o	6	1.982	3.274	4.263	8.000	56	C_2H_5	PP	m	6	1.351	3.016	1.951	6.966
27	C_2H_5	PP	o	6	1.573	3.422	4.524	9.465	57	C_3H_7	P	m	6	1.755	3.632	3.817	6.195
28	C_2H_5	A	o	6	2.136	4.790	7.066	14.20	58	C_3H_7	PP	m	6	1.341	3.310	3.682	0.794
29	C_3H_7	PP	o	6	1.709	4.061	5.973	1.029	59	C_3H_7	A	m	6	1.803	4.752	5.831	13.89
30	C_4H_9O	PP	o	6	1.445	3.352	3.993	8.191									

Notes: No., the compound number; C_4H_9O in R^1 column denotes $(CH_2)_2OC_2H_5$; R^2: P, pyrrolidine (NC_4H_8), PP, piperidine (NC_5H_{10}), A, azepane (NC_6H_{12}); P: position of the side alkoxy chain; o, ortho, m, meta; n, number of carbons in the side alkoxy chain; *kPhAcN, kPhMeOH, kC18AcN, kC18MeOH*: the HPLC retention factors.

Table 2
Four reduced correlation tables of the variables best correlated with individual retention factors characterized by Spearman correlation coefficients R and the corresponding two-tailed p-values.

kPhAcN

Variable (order)	XLOGP2 (1)	AClogS (10)	C6 (12)	C3 (13)	H5 (17)	H11b (18)	C10 (19)	C4 (20)	Call (21)
R	0.606	-0.504	0.433	-0.402	-0.289	-0.284	0.263	0.248	-0.248
p	1.0E−6	4.8E−5	6.1E−4	0.002	0.026	0.030	0.045	0.058	0.058

kPhMeOH

Variable (order)	ALOGPs (1)	ALOGpS (3)	M (11)	H12b (14)	C6 (15)	C5 (19)	H5 (20)	C10 (22)	C11 (23)	C4 (24)
R	0.886	-0.874	0.754	-0.370	0.429	0.264	0.245	0.234	-0.223	0.221
p	1.0E−6	1.0E−6	1.0E−6	0.004	0.001	0.043	0.062	0.075	0.090	0.092

kC18AcN

Variable (order)	ALOGPs (1)	ALOGpS (2)	M (3)	C6 (12)	C3 (15)	H12b (16)	H12a (17)	C4 (18)	H5 (19)	H7 (20)	Call (21)	C8 (22)	C12 (23)	C10 (24)	C2 (25)	C11 (26)
R	0.859	-0.824	0.740	0.610	-0.555	-0.442	-0.441	0.432	-0.430	0.410	-0.382	-0.331	0.326	0.273	0.263	-0.257
p	1.0E−6	1.0E−6	1.0E−6	1.0E−6	5.2E−6	4.6E−4	4.7E−4	6.4E−4	6.8E−4	0.001	0.003	0.011	0.012	0.036	0.044	0.050

kC18MeOH

Variable (order)	ALOGPs (1)	ALOGpS (2)	M (11)	C6 (14)	C3 (15)	C11 (16)	H7 (17)	C4 (18)	H5 (19)	C10 (20)	H11b (21)	Call (22)	H11a (23)	H10 (24)
R	0.663	-0.638	0.621	0.474	-0.404	-0.380	0.365	0.335	-0.325	0.316	-0.312	-0.29	-0.288	-0.271
p	1.0E−6	1.0E−6	1.0E−6	1.5E−4	0.002	0.003	0.005	0.010	0.012	0.015	0.016	0.026	0.027	0.038

Note: 59 EAPCA derivatives were studied. The variables significantly correlated to $kPhMeOH$ and $kPhAcN$ are those where $p < 0.10$ and the variables significantly correlated to $kC18AcN$ and $kC18MeOH$ are with $p < 0.05$. Software SPSS 15.0.
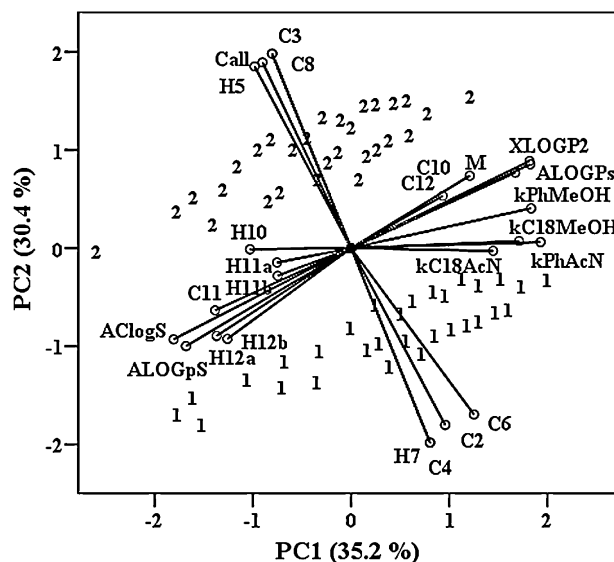
Fig. 1. Biplot of principal component analysis for 59 objects (EAPCA compounds), four studied retention factors and further 21 significant variables. 1: ortho derivatives, 2: meta derivatives. Software SPSS 15.0.

ortho-EAPCA derivatives (low PC2). The main, first principal component is mostly influenced by the retention factors. The position of the solubility descriptors at the negative PC1 values is understandable – the retention factor is large when the solubility is low and *vice versa*.

When assessing the general credit of the PCA results it is important to note that the first principal component (PC1) accounts for 35.2% and the second one (PC2) for about 30.4% of the explained total variance in the original data set (65.6% for PC1 + PC2 altogether). The eigenvalues of the first five principal components are larger than 1 and account for 90.3% of the total variance.

25 descriptors, found as optimal by correlation analysis, was investigated with regard to their impact on the first principal component, PC1. Their importance is given by the calculated component weights – the coefficients of the following linear equation, where the order of the descriptor terms is arranged by the absolute values of the weights:

$$
\begin{aligned}
\text{PC1} ={}& 0.931kC18AcN + 0.900ALOGPs - 0.896AClogS + 0.890kPhMeOH \\
& + 0.885XLOGP2 - 0.841ALOGpS + 0.807kC18MeOH + 0.802M + 0.670kPhAcN \\
& - 0.587C11 - 0.518H12a - 0.506H12b + 0.437C10 + 0.426C12 + 0.397Call \\
& + 0.345C6 - 0.335C3 - 0.332H5 + 0.328C4 - 0.327C8 + 0.323C2 + 0.285H7 \\
& - 0.265H10 - 0.191H11a - 0.138H11b
\end{aligned}
$$

It is evident that the largest terms correspond to the retention factors, lipophilicity (the log P descriptors), solubility (log S), and molar mass M (related both to lipophilicity and solubility). Most important among ^{13}C NMR shifts are C11, C10 and C12, and H11a and H11b among ^{1}H NMR shifts. In general, the PC1 expresses the main effect investigated in the given problem, however, sometimes its assignment is difficult. Taking into consideration the most influencing descriptors, the PC1 in this work may be articulated as the composed anaesthetical activity variable.

With regard to the position of the ortho- and meta-derivatives (number 1 and 2 in Fig. 1), forming distinct clusters in the biplot, it is evident that they have different PC2 values and differ mainly in some NMR shifts (H5, Call, C3, C8 and H7, C4, C2, C6) corresponding to C and H atoms of the aromatic ring or close to it, which is understandable due to a dual position of the substituents of the aromatic ring. On the other hand, when accepting the PC1 as the axis of anaesthetical activity, the ortho- or meta-derivatives do not exhibit basically different activity since both clusters of compounds are widespread along the PC1 axis and in both groups very active
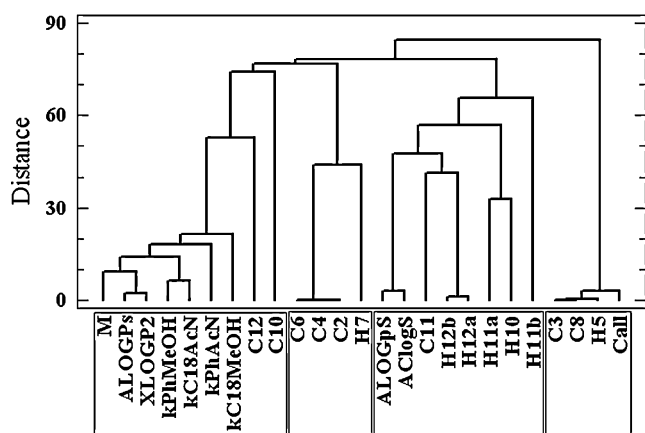
Fig. 2. Dendrogram of cluster analysis for four retention factors and further 21 significant variables. Ward's clustering method, squared Euclidean distance. Software Statgraphics Centurion 16.0.09. Autoscaled data of 59 EAPCA derivatives.
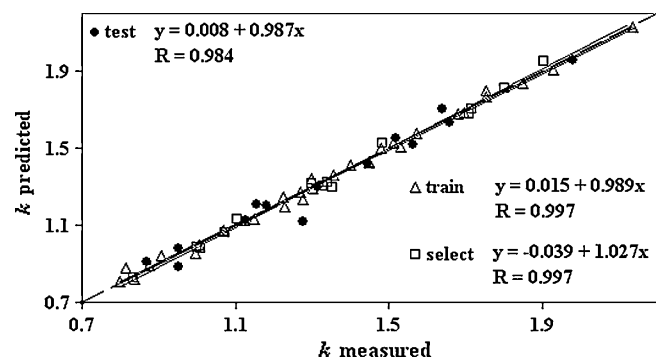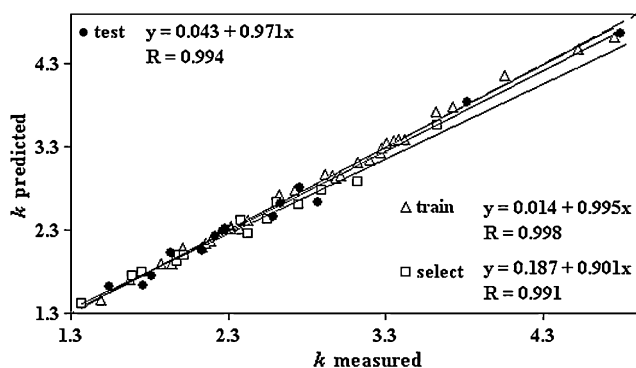

Fig. 3. Plot of the fitted linear model kPhAcN predicted vs. kPhAcN measured for three data subsets of 59 studied EAPCA compounds. Prediction was performed by MLP ANN for phenyl stationary phase and acetonitrile–water mobile phase (80/20). The number of input–hidden–output neurons is 13–2–1. Statistica Neural Networks 8.0.

as well as low active compounds can be found. Similarly, the ortho- and meta-derivatives cannot be distinguished by the lipophilicities, solubilities as well as by retention factors.

3.3. Cluster analysis

Cluster analysis, CA, is designed to detect hidden groups or clusters in (1) a set of objects described by their variables (descriptors) or (2) a set of variables such that the members of each cluster behave similarly to each other. Clustering techniques are the basic chemometric tools used for data exploration [34,35]. In this case, CA was performed using Ward method of *variable clustering* and squared Euclidean distances [29]. Cluster analysis was made extra for each chromatographic system and also for all four systems jointly (Fig. 2), in which four retention factors and the variables selected as significant by correlation analysis were used (the same as in PCA). The most important cluster in Fig. 2 is created by all four retention factors and the variables most similar to them – *ALOGPs* and *XLOGP2*, the two best calculated forms of log *P*, molar mass *M*, as well as ^{13}C NMR chemical shifts *C12* and *C10*. It is rather interesting that among retention factors mutually closest and therefore most similar are *kPhMeOH* and *kC18AcN*. The second cluster, closest to the retention factor cluster, comprises four further relative NMR variables *C6*, *C4*, *C2* and *H7*. The third cluster contains those NMR variables which are most influencing the solubility of the investigated compounds. The least important variables inhere in the fourth cluster. The found results of CA are in a very good agreement with the results of principal component analysis. In general, the combined use of statistical tools may provide more objective view on the investigated problem and the credibility of achieved results is higher if they are confirmed by two or more methods.

When individual chromatographic systems are considered, the retention factor *kPhAcN* creates a mildly different main cluster compared to remaining three systems since the variables *XLOGP2*, *M* and *C10* are here grouped without *C12*; in the remaining three systems *ALOGPs* was selected instead of *XLOGP2* according to the correlation analysis results.

3.4. Artificial neural networks

Artificial neural networks (ANN) [36,37], are more robust (in terms of sensitivity to noise) and more versatile than linear techniques. If a continual output is chosen, ANN can be considered as the nonlinear regression analysis tool.

In this work, multilayer perceptron (MLP) neural networks were fitted to the studied data of 59 EAPCA derivatives. MLP is a common type of artificial neural networks, which is widely used in computer science and engineering for object recognition, discrimination and classification, and have more recently found use also in process monitoring and control [38]. The ANN calculations were performed with STATISTICA Neural Networks [39]. The complete original data set was divided into the training subset of 31 compounds, the selection subset of 14 compounds and the test subset of 14 compounds by random selection automatically made by software, independently of the user. For determination of the final predictive ability of neural network the test subset results are decisive. It is worth mentioning that the term selection subset is often denominated as the validation set or subset. It contains the data which are not included into the training and the test data sets and are used for the selection of the best neural network.

Continual variables selected by the best correlation to the retention factor (Table 2) and two categorical variables (*RType* and *Pno*) were used at the ANN input for each chromatographic system. Variable reduction made by correlation analysis is fundamental since their large number adversely influence the ANN performance, especially the prediction ability. At the output the corresponding retention factor *k* was used; separate ANN models were generated for each retention factor using a separate training data set.

The selection data set was used for optimisation of the ANN architecture. The following optimal three-layer perceptron neural networks were used (composed of the input–hidden–output neurons): (a) 13–2–1 for the prediction of *kPhAcN*; (b) 16–3–1 for the prediction of *kPhMeOH*; (c) 19–2–1 for the prediction of *kC18AcN*. The selection of the best type of the ANN for each separation system was made by the minimum mean squared error, MSE, calculated for the selection subset (evaluated as the sum of squares between the calculated and the known retention factor values). In general, the same way of the error evaluation was performed for the training and test subsets; the results are summarized in Table 3. For *kC18MeOH* prediction significantly worse results were obtained and will not be further commented.

The final ANN results are visualized by the linear regression graphs of the predicted *k* values vs. the measured *k* values (Figs. 3–5). The intercepts and the slopes of the obtained linear dependences were close to the theoretically expected values of 0 and 1, respectively (represented by the diagonal in all three figures). The statistical significance of the slope was confirmed by *t*-test at the significance level 0.05, in the same way the insignificance of the intercept was approved in all cases.

The most important regression results are those for the test subset. The comparison of the measured and predicted *k* values of the test subset compounds is summarized in Table 4. The analysis of relative error shows that (a) for the *kPhAcN* prediction the median

Table 3
Mean squared errors (MSE) of retention factors as the ANN outputs for three separation systems and three data subsets.

Phenyl column and acetonitrile–water mobile phase, retention factor *kPhAcN*			
ANN model MLP 13-2-1	Training set ($n = 31$)	Selection set ($n = 14$)	Test set ($n = 14$)
MSE	5.8E−04	7.8E−04	0.0033

Phenyl column and methanol–water mobile phase, retention factor *kPhMeOH*			
ANN model MLP 16-3-1	Training set ($n = 31$)	Selection set ($n = 14$)	Test set ($n = 14$)
MSE	0.0024	0.0071	0.0092

C18 column and acetonitrile–water mobile phase, retention factor *kC18AcN*			
ANN model MLP 19-2-1	Training set ($n = 31$)	Selection set ($n = 14$)	Test set ($n = 14$)
MSE	0.0332	0.0349	0.0359

Fig. 4. Plot of the fitted linear model kPhMeOH predicted vs. kPhMeOH measured for three data subsets of 59 studied EAPCA compounds. Prediction was performed by MLP ANN for phenyl stationary phase and methanol–water mobile phase (80/20). The number of input–hidden–output neurons is 16–3–1. Statistica Neural Networks 8.0.
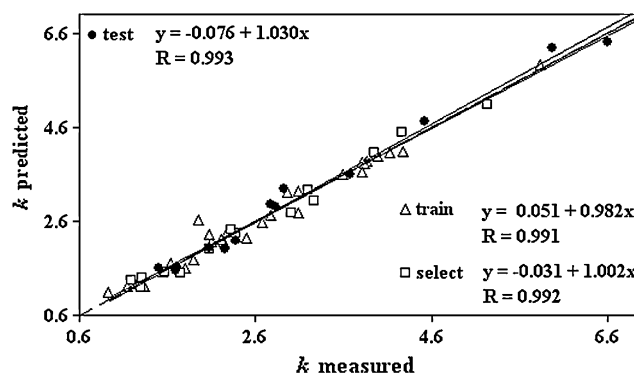
Fig. 5. Plot of the fitted model kC18AcN predicted vs. kC18AcN measured for three subsets of 59 studied EAPCA compounds. Prediction was performed by MLP ANN for C18 stationary phase and acetonitrile–water mobile phase (80/20). The number of input–hidden–output neurons is 19–2–1. Statistica Neural Networks 8.0.

relative error is −0.68%, the maximum relative error is +5.18% and the minimum relative errors is −12.31%, (b) for the *kPhMeOH* prediction the median relative error is +0.01%, the maximum relative error is +5.04% and the minimum relative error is −7.98%, (c) for the *kC18AcN* prediction the median relative error is −2.09%, the maximum relative error is +12.58% and the minimum relative error is −10.72%. Thus, the best prediction result provides the Phenyl column and 80% methanol–water mobile phase.

The sensitivity analysis, SA [40], gives some information about the relative importance of the input variables used in ANN. SA tests the performance of neural network if one of the input variables is unavailable – each variable is in turn treated as missing and the resulting network error is computed. If an important variable is removed then the error increase is extensive; if unimportant one is missing, the error does not increase considerably. In this work, SA was enabled by the applied Statistica package as a special

Table 4
Measured and predicted values of the retention factors *kPhAcN*, *kPhMeOH* and *kC18AcN* for 14 EAPCA compounds in three test data subsets.

kPhAcN				kPhMeOH				kC18AcN			
Predicted	Measured	ε_{rel}, %	No	Predicted	Measured	ε_{rel}, %	No	Predicted	Measured	ε_{rel}, %	No
1.12	1.13	−0.24	13	2.63	2.63	−0.09	51	2.04	2.07	−1.77	47
1.96	1.98	−1.12	26	2.22	2.22	0.11	13	3.59	3.68	−2.42	58
1.64	1.66	−1.38	48	3.84	3.82	0.66	20	2.91	2.83	2.80	50
1.29	1.32	−1.63	33	2.29	2.27	1.10	11	6.42	6.61	−2.87	23
1.42	1.45	−1.71	30	2.32	2.28	1.46	41	4.72	4.52	4.40	27
1.20	1.18	1.73	16	2.81	2.75	2.07	48	1.63	1.70	−4.54	35
1.55	1.52	2.04	50	4.67	4.79	−2.53	28	1.60	1.69	−5.25	40
1.52	1.56	−2.60	52	1.75	1.81	−3.53	38	6.30	5.97	5.40	29
0.98	0.95	2.93	44	2.05	2.13	−3.67	10	1.60	1.50	6.67	3
1.70	1.64	3.84	18	2.02	1.93	4.65	4	2.95	2.77	6.72	17
1.21	1.15	4.48	35	2.47	2.59	−4.77	15	2.20	2.38	−7.79	48
0.91	0.87	5.18	32	1.62	1.54	5.04	32	1.55	1.69	−8.43	9
0.88	0.95	−7.21	9	1.63	1.76	−7.30	2	2.01	2.25	−10.72	49
1.12	1.28	−12.31	2	2.64	2.87	−7.98	24	3.29	2.92	12.58	15
	Median (ε_{rel})	−0.68%			Median (ε_{rel})	0.01%			Median (ε_{rel})	−2.09%	
	Max (ε_{rel})	5.18%			Max (ε_{rel})	5.04%			Max (ε_{rel})	12.58%	
	Min (ε_{rel})	−12.31%			Min (ε_{rel})	−7.98%			Min (ε_{rel})	−10.72%	

Note: The retention factors *kPhAcN*, *kPhMeOH* and *kC18AcN* express given chromatographic separation conditions: *kPhAcN* – phenyl column, mobile phase acetonitrile–water, *kPhMeOH* – phenyl column, mobile phase methanol–water, *kC18AcN* – C18 column, mobile phase acetonitrile–water. The compound number (No.) corresponds to the data in Table 1.

evaluation tool. The order of significance among the exploited variables found by SA in k prediction is as follows (a) for *kPhAcN*: *n*, *Rtype*, *AClogS*, *M*, *Pno*, *C4*, *H5*, *XLOGP2*, *C3*, *Call*, *H11b*, *C6* and *C10*; (b) for *kPhMeOH*: *n*, *Rtype*, *ALOGPs*, *ALOGpS*, *C12*, *H12a*, *Pno*, *H5*, *C4*, *C6*, *M*, *C3*, *C5*, *C11*, *H12b* and *C10*; (c) for *kC18AcN*: *n*, *Rtype*, *H12a*, *C12*, *C8*, *ALOGpS*, *C11*, *M*, *C3*, *C10*, *ALOGPs*, *C2*, *C6*, *H5*, *Call*, *Pno*, *H12b*, *H7* and *C4*. In addition to the variables used in correlation analysis three categorical variables were used here – *n* and *Rtype* were found very important and *Pno* less important. To sum up the significance of further factors, log *S* and log *P* were found important under all examined chromatographic conditions. Molar mass was found also important, mainly for *kPhAcN* and *kC18AcN* prediction. All three mentioned continuous variables were also found highly correlated to the retention factors in correlation analysis. According to the rank, the importance of the NMR descriptors in correlation analysis and sensitivity analysis is different but the same rank cannot be expected due to different principles of these two approaches. Nevertheless, in general, *H5* and *C4* are more important when phenyl column is used, *C3* is important for all three retention factors, several other NMR descriptors are important for a particular combination of the column and mobile phase, e.g. *C12* for *kPhMeOH* and *kC18AcN*.

3.5. Determination and interpretation of the most significant descriptors

A very difficult problem is determination of the most significant descriptors. First of all – this task depends upon the bunch of originally chosen descriptors. Contemporary QSAR literature [41] describes about 3000 molecular descriptors calculable e.g. by Dragon software and several hundreds of them are now and then used in a single scientific paper. Nevertheless, the number of descriptors selected in this work is relatively small and all of them are experimentally accessible; even though they were calculated from various databases, which originated from experimental values.

Another problem in explicating the best descriptors is connected to the applied method. Correlation analysis in part 3.1 revealed that all retention factors are significantly correlated to lipophilicity (to log *P*) and solubility (to −log *S*, a negative correlation). Unambiguously significant is also their correlation to molar mass *M* and several NMR descriptors, as it will be mentioned later on. The most important principal component PC1 is linearly combined from all chosen descriptors with the weighting coefficients proportional to their influence upon PC1. However, the PC1 expresses mainly the anaesthetic activity, which is secondarily strongly dependent on all four retention factors as well as log *P*, log *S* and *M*. The third way of indicating the influential descriptors is selectivity analysis, which allows also the use of categorical variables – in contrast to previous two methods. The found most important variables *n* and *Rtype* relate to the length of the side alkoxy chain and R^2 substituent in the ester part, respectively. In all cases a larger *n* corresponds to larger retention factor. A more close inspection of the effect of pyrrolidine (P), piperidine (PP) and azepane (A) R^2 substituents upon retention factors in correlation analysis revealed that, assuming equal R^1 and *n*, the azepane derivatives exhibit the largest retention factors *k* (except *kPhAcN* which are slightly larger for pyrrolidine derivatives). Piperidine derivatives exhibit larger *k* values than pyrrolidine ones for all investigated separation systems in case of ortho position of alkoxy chain, the opposite is valid for the compounds with meta position of alkoxy chain. In contrast to the discussed variables the categorical variable *Pno*, indicating the position of the alkoxy substituents, is much less influential upon the retention factors.

When considering the used NMR descriptors, all three applied methods indicated that the most significant are chemical shifts of aromatic carbons *C6* and *C3* and hydrogen atom *H5*; very important is also *C4* but mainly for the systems with Phenyl column. Chemical shifts are closely related to the shift of electron density throughout the molecule, which depends on the quality and position of the substituents in the molecule skelet. A deeper elucidation of such effects may contribute to understanding of the interaction of the potential drug molecule with the receptor.

4. Conclusions

Computer calculation of molecular descriptors, simulation of NMR chemical shifts and the application of chemometrical techniques are likely to become an important part of future research and development in pharmaceutical chemistry. Theoretical calculations and predictions can be successfully compared to the experimental results. The principal aim of QSRR is to predict retention data from the molecular structure reflected in the selected properties/descriptors. The multivariate approach, combining in this study principal components, correlation and cluster analysis and artificial neural networks, allows revealing relations between the target property and the selected structural descriptors and determining those of them, which are most important. The ANN implementation, due to its speed and better prediction ability compared to conventional calculation methods, exhibits a strong potential for use in pharmaceutical product development.

The retention factors of the EAPCA derivatives, the potential local anaesthetic drugs, were experimentally determined under various HPLC conditions and also predicted by QSRR. Correlation analysis was used as a suitable tool for elimination of those EAPCA properties that are weakly correlated to retention factors. Three of four examined final models, differing by the applied chromatographic conditions, provided very successful ANN predictions of the retention factors. The regression dependences of the predicted vs. the measured retention factor exhibit the best results for Phenyl column and acetonitrile/water mobile phase, but also the slopes and intercepts in other two cases are close to the theoretical values. The correlation coefficients for the training, selection and test data subsets are high and confirm reliable predictions.

The demonstrated results prove that the ANN is an adequate tool for prediction of the retention factor values if the optimal descriptors of the investigated compounds are selected. A joined assessment of descriptors by sensitivity analysis, correlation analysis and principal component analysis facilitates identification of the descriptors most influencing the predicted retention factors.

References

[1] M. Grover, B. Singh, M. Bakshi, S. Singh, Quantitative structure–property relationships in pharmaceutical research – part 2, Pharm. Sci. Technol. Today 3 (2000) 50–57.
[2] K. Bodzioch, A. Durand, R. Kaliszan, T. Baczek, Y. Vander Heyden, Advanced QSRR modelling of peptides behaviour in RPLC, Talanta 81 (2010) 1711–1718.
[3] K. Héberger, Quantitative structure–(chromatographic) retention relationships, J. Chromatogr. A 1158 (2007) 273–305.
[4] P. Nemeček, J. Mocak, J. Lehotay, K. Waisser, Prediction of HPLC retention factor of potential antituberculotics by QSRR, J. Liq. Chromatogr. 36 (2011) 168–181.
[5] N. Canós-Rius, Y. Martín-Biosca, S. Sagrado, R.M. Villanueva-Camañas, M.J. Medina-Hernández, Estimation of the effect of the acidosis and alkalosis on the anesthetic potency of local anesthetics by biopartitioning micellar chromatography and micellar electrokinetic chromatography, Eur. J. Med. Chem. 40 (2005) 215–223.

[6] K. Bodzioch, T. Baczek, R. Kaliszan, Y. Vander Heyden, The molecular descriptor logSumAA and its alternatives in QSRR models to predict the retention of peptides, J. Pharm. Biomed. Anal. 50 (2009) 563–569.

[7] G. Carlucci, A.A. D'Archivio, M.A. Maggi, P. Mazzeo, F. Ruggieri, Investigation of retention behaviour of non-steroidal anti-inflammatory drugs in high-performance liquid chromatography by using quantitative structure–retention relationships, Anal. Chim. Acta 601 (2007) 68–76.

[8] A. Detroyer, Y. Vander Heyden, S. Carda-Broch, M.C. Garcia-Alvarez-Coque, D.L. Massart, Quantitative structure–retention and retention–activity relationships of β-blocking agents by micellar liquid chromatography, J. Chromatogr. A 912 (2001) 211–221.

[9] R. Kaliszan, Retention data from affinity high-performance liquid chromatography in view of chemometrics, J. Chromatogr. B 715 (1998) 229–244.

[10] R. Put, Y. Vander Heyden, Review on modelling aspects in reversed-phase liquid chromatographic quantitative structure–retention relationships, Anal. Chim. Acta 602 (2007) 164–172.

[11] E. Borges de Melo, J.P.A. Martins, T.C.M. Jorge, M.C. Friozi, M.M.C. Ferreira, Multivariate QSAR study on the antimutagenic activity of flavonoids against 3-NFA on Salmonella typhimurium TA98, Eur. J. Med. Chem. 45 (2010) 4562–4569.

[12] L.-T. Qin, S.-S. Liu, H.-L. Liu, J. Tong, Comparative multiple quantitative structure-retention relationships modelling of gas chromatographic retention time of essential oils using multiple linear regression, principal component regression, and partial least squares techniques, J. Chromatogr. A 1216 (2009) 5302–5312.

[13] T. Hancock, R. Put, D. Coomans, Y. Vander Heyden, Y. Everingham, A performance comparison of modern statistical techniques for molecular descriptor selection and retention prediction in chromatographic QSRR studies, Chemometr. Intell. Lab. Syst. 76 (2005) 185–196.

[14] A. Mendyk, P. Kleinebudde, M. Thommes, A. Yoo, J. Szlek, R. Jachowicz, Analysis of pellet properties with use of artificial neural networks, Eur. J. Pharm. Sci. 41 (2010) 421–429.

[15] M. Fernández, J. Caballero, A. Tundidor-Camba, Linear and nonlinear QSAR study of N-hydroxy-2-[(phenylsulfonyl)amino]acetamide derivatives as matrix metalloproteinase inhibitors, Bioorg. Med. Chem. 14 (2006) 4137–4150.

[16] V. Tantishaiyakul, Prediction of the aqueous solubility of benzylamine salts using QSPR model, J. Pharm. Biomed. Anal. 37 (2005) 411–415.

[17] D. Weekes, G.B. Fogel, Evolutionary optimization, backpropagation and data preparation issues in QSAR modeling of HIV inhibition by HEPT derivatives, BioSystems 72 (2003) 149–158.

[18] A. Dallos, H.S. Ngo, R. Kresz, K. Héberger, Cluster and principal component analysis for Kováts' retention indices on apolar and polar stationary phases in gas chromatography, J. Chromatogr. A 1177 (2008) 175–182.

[19] Z. Kánya, E. Forgács, T. Cserháti, Z. Illé, Reducing dimensionality in principal component analysis – a method comparison, Chromatographia 63 (2006) 129–134.

[20] Y. Chen, D. Chen, C. He, S. Hu, Quantitative structure–activity relationships study of herbicides using neural networks and different statistical methods, Chemom. Intell. Lab. Syst. 45 (1999) 267–276.

[21] T. Körtvélyesi, M. Görgényi, K. Héberger, Correlation between retention indices and quantum-chemical descriptors of ketones and aldehydes on stationary phases of different polarity, Anal. Chim. Acta 428 (2001) 73–82.

[22] J. Olivero, K. Kannan, Quantitative structure–retention relationships of poly-chlorinated naphthalenes in gas chromatography, J. Chromatogr. A 849 (1999) 621–627.

[23] Ľ. Búčiová, A. Borovanský, J. Čižmárik, J. Csöllei, P. Švec, J. Kozlovský, E. Račanská, L. Beneš, Study of the effect of modification in the connective chain on the biological activity in a group of basic phenylcarbamates (in Slovak), Ceska Slov. Farm. 36 (1987) 339–344.

[24] Ľ. Búčiová, J. Csöllei, A. Borovanský, J. Čižmárik, E. Račanská, Preparation and effectiveness of 1-etoxymetyl-2-(1-pyrolidinyl), 2-piperidino- and 2-(1-perhydroazepinyl)-etylesters of o- and m-alkoxyphenylcarbamic acid (in Slovak), Ceska Slov. Farm. 40 (1991) 102–105.

[25] VCCLAB, Virtual Computational Chemistry Laboratory, 2005, http://www.vcclab.org.

[26] R. Mannhold, G.I. Poda, C. Ostermann, I.V. Tetko, Calculation of molecular lipophilicity: state-of-the-art and comparison of log P methods on more than 96,000 compounds, J. Pharm. Sci. 98 (2009) 861–893.

[27] I.V. Tetko, J. Gasteiger, R. Todeschini, A. Mauri, D. Livingstone, P. Ertl, V.A. Palyulin, E.V. Radchenko, N.S. Zefirov, A.S. Makarenko, V.Y. Tanchuk, V.V. Prokopenko, Virtual computational chemistry laboratory – design and description, J. Comput. Aid. Mol. Des. 19 (2005) 453–463.

[28] ACDLabs, Advanced Chemistry Development, Inc., 2010, http://www.acdlabs.com/products/adh/.

[29] B. Vandeginste, D.L. Massart, L. Buydens, S. De Jong, P. Lewi, J. Smeyers-Verbeke, Handbook of Chemometrics and Qualimetrics, Part B, Elsevier, Amsterdam, 1998.

[30] I.T. Jolliffe, Principal Component Analysis, Springer-Verlag, New York, 2002.

[31] M. Otto, Chemometrics: Statistics and Computer Application in Analytical Chemistry, Wiley, Weinheim, 1999.

[32] D.L. Massart, B.G.M. Vandeginste, L.M.C. Buydens, S. De Jong, P.J. Lewi, J. Smeyers-Verbeke, Handbook of Chemometrics and Qualimetrics, Part A, Elsevier, Amsterdam, 1997.

[33] M. Daszykowski, From projection pursuit to other unsupervised chemometric techniques, J. Chemom. 21 (2007) 270–294.

[34] M. Daszykowski, B. Walczak, D.L. Massart, Density-based clustering for exploration of analytical data, Anal. Bioanal. Chem. 380 (2004) 370–372.

[35] H.H. Bock, Probabilistic models in cluster analysis, Comput. Stat. Data Anal. 23 (1996) 5–28.

[36] J. Zupan, J. Gasteiger, Neural Networks for Chemists, Wiley, Weinheim, 1993.

[37] J. Zupan, J. Gasteiger, Neural Networks in Chemistry and Drug Design, Wiley, Weinheim, 1999.

[38] M. Aitkin, R. Foxall, Statistical modelling of artificial neural networks using the multi-layer perceptron, Stat. Comput. 13 (2003) 227–239.

[39] StatSoft Inc., Statistica Neural Networks v.8.0 (software), Tulsa, USA, 2009.

[40] D. Patterson, Artificial Neural Networks, Prentice Hall, Singapore, 1996.

[41] R. Todeschini, V. Consonni, Molecular Descriptors for Chemoinformatics, vols. 1–2, Wiley-VCH, 2009.

Corrigendum

Corrigendum to "Paclitaxel/sirolimus combination coated drug-eluting stent: In vitro and in vivo drug release studies" [J. Pharm. Biomed. Anal. 54 (2011) 807–811]

Xiaodong Ma [a,b], Shizu Oyamada [c], Fan Gao [d], Tim Wu [a,b,*], Michael P. Robich [c], Hao Wu [b], Xingwei Wang [a], Bryan Buchholz [a], Stephen McCarthy [a], Zhiyong Gu [d], Cesario F. Bianchi [c], Frank W. Sellke [c], Roger Laham [e,**]

[a] Biomedical Engineering and Biotechnology Doctoral Program, University of Massachusetts, Lowell, MA 01854, USA
[b] VasoTech, Inc., Lowell, MA 01854, USA
[c] Division of Cardiothoracic Surgery, Brown Medical School, Providence, RI 02903, USA
[d] Department of Chemical Engineering, University of Massachusetts, Lowell, MA 01854, USA
[e] Department of Cardiology, Beth Israel Deaconess Medical Center, Harvard Medical School, Boston, MA 02215, USA

DOI of original article: 10.1016/j.jpba.2010.10.027.
* Corresponding author at: VasoTech, Inc., Lowell, MA 01854, USA. Tel.: +1 617 686 2770; fax: +1 617 446 1518.
** Corresponding author. Tel.: +1 617 632 9204; fax: +1 617 975 5201.
E-mail addresses: tiangenwu@yahoo.com (T. Wu), laham@caregroup.harvard.edu (R. Laham).